Search for Planetary Transits and Stellar Variability with BEST II and ASTEP

vorgelegt von
Dipl.-Phys. Thomas Fruth
Marburg

Von der Fakultät II – Mathematik und Naturwissenschaften
der Technischen Universität Berlin
zur Erlangung des akademischen Grades

Doktor der Naturwissenschaften
– Dr. rer. nat. –

genehmigte Dissertation

Promotionsausschuss:

Vorsitzender:	Prof. Dr. Mario Dähne
Berichter:	Prof. Dr. Heike Rauer
	Prof. Dr. Rolf Chini

Tag der wissenschaftlichen Aussprache: 1. Februar 2013

Berlin 2013
D 83

Abstract

Two decades ago, the first evidence of planets orbiting stars other than our Sun opened a new field of astronomy and astrophysics. Today, more than 850 such extrasolar planets are known, and their detections have revealed a wide diversity regarding, e.g., the planetary size, mass, density, or orbital distance. As a result, more and more intriguing scientific questions can now be investigated quantitatively, while all previous knowledge was solely based upon our Solar System.

The space mission CoRoT successfully applies the transit method to find new planets; it is supported, e.g., by the two Berlin Exoplanet Search Telescopes (BEST and BEST II) with ground-based photometric observations.

The main aim of this thesis is to search for new exoplanets. Within this work, the first BEST II transit survey was planned, realized, and analyzed scientifically: During 138 nights in 2009/2010, three target fields were monitored. Optimizations of their selection, observations, the data pipeline, and transit search improved the expected detection yield significantly compared to previous BEST II surveys, and simulations suggest a reasonable chance for a detection. The sensitivity of the optimized BEST II system is competitive with leading ground-based surveys such as SuperWASP.

Furthermore, this work aims to probe the potential for transit search from Antarctica. While previous studies indicate excellent conditions, it was yet to be shown whether a real transit survey can benefit from these in practice. In this work, first data from the ASTEP 400 telescope (Dome C) were analyzed, and parallel observations were obtained with BEST II (Chile) for a direct comparison. These show that ASTEP 400 achieves sub-mmag precision on favorable nights, but systematic effects still limit the overall photometric quality. However, within two weeks, ASTEP yields an observational coverage of planetary transits that is comparable to a whole season in Chile. An optimal performance is achieved when data from both sites are combined, which increases the detection yield by up to $\sim 30\%$.

Overall, 256,026 low-noise light curves have been analyzed for transiting planets. Using state-of-the-art procedures for detection and false alarm exclusion, 20 high-quality "hot Jupiter" candidates were identified (14 in BEST II, four in ASTEP, and two in combined time series). Eleven host stars were characterized spectroscopically, and radial velocity analyses were proposed to eventually confirm the planetary nature and derive masses of the two best candidates. These are important findings since they orbit early F-type dwarf stars, which are expected to host giant exoplanets more frequently than later types, but very few such systems are currently known.

In addition, photometric data allow the study of stellar variability. New detections enable new and/or more detailed astrophysical studies (e.g., stellar interior models). This thesis presents a new method to decrease the false alarm rate in variable star searches significantly. It was recently published (Fruth et al. 2012) and applied successfully to five BEST II data sets: Out of 329,660 light curves analyzed here, 2,791 new and 806 suspected variable stars were found and classified, thus increasing the yield of BEST/BEST II by 258%. Where possible, the results were compared with other surveys such as CoRoT, and were found to be in excellent overall agreement.

Zusammenfassung

Während vor etwa zwanzig Jahren der erste Planet außerhalb des Sonnensystems nachgewiesen wurde, so sind mittlerweile mehr als 850 solcher extrasolaren Planeten bekannt. Sie unterscheiden sich z.B. hinsichtlich ihrer Radien, Massen, Dichten und Bahneigenschaften sowohl untereinander als auch von den bisher bekannten Begleitern unserer Sonne und ermöglichen nun die quantitative Untersuchung einer Vielzahl alter und neuer wissenschaftlicher Fragestellungen.

Die Weltraummission CoRoT sucht mithilfe der Transitmethode nach extrasolaren Planeten. Sie wird u.a. von den beiden "Berlin Exoplanet Search Telescopes" (BEST und BEST II) mit bodengebundenen photometrischen Beobachtungen unterstützt.

Die Suche nach Exoplaneten stellt auch das primäre Ziel dieser Dissertation dar. In einer eigens geplanten BEST II Transitsuchkampagne wurden drei Sternfelder 2009/2010 insgesamt 138 Nächte lang beobachtet. Im Vergleich zu vorangegangenen BEST II Studien steigerten Verbesserungen in der Feldauswahl, der Datenauswertung, sowie des Beobachtungsumfangs die Leistungsfähigkeit des Systems erheblich. Simulationen zeigen, dass die Empfindlichkeit von BEST II vergleichbar mit führenden Projekten wie SuperWASP und eine erste Planetenentdeckung realistisch ist.

Einen weiteren Schwerpunkt bildet eine Studie zu den Bedingungen der Transitsuche in der Antarktis. In dieser Arbeit wurden erste Daten des ASTEP 400 Teleskops (Dome C) analysiert und mit BEST II (Chile) verglichen. Die Analyse zeigt, dass ASTEP in einzelnen Nächten sub-mmag Präzision erzielt, aber systematische Effekte die photometrische Genauigkeit über die gesamte Kampagne limitieren. Die Polarnacht bewirkt während eines zweiwöchigen Beobachtungszeitraums eine gute Abdeckung kurzperiodischer Planeten, die in Chile nur während einer kompletten Saison erzielt wird. Optimal ist eine Kombination beider Standorte, wodurch bis zu $\sim 30\%$ mehr Entdeckungen erzielt werden können.

Insgesamt wurden 256.026 hochpräzise Lichtkurven auf extrasolare Transitplaneten untersucht. Mithilfe aktueller Techniken zur Detektion konnten 20 sehr gute "heiße Jupiter" Kandidaten (14 in BEST II, vier in ASTEP und zwei in kombinierten Daten) identifiziert und von falsch-positiven Signalen abgegrenzt werden. Elf Sterne wurden bereits spektroskopisch klassifiziert, und die besten zwei Kandidaten wurden für Nachfolgebeobachtungen vorgeschlagen, um ihre Masse zu bestimmen und den Planetenstatus zu bestätigen bzw. zu widerlegen. Dies sind wichtige Entdeckungen, da die Sterne frühe F-Zwerge sind: Bei diesen erwartet man häufiger Riesenplaneten als bei sonnenähnlichen Sternen, kennt aber bisher nur sehr wenige solcher Systeme.

Photometrische Zeitreihen werden zudem auf Variabilität untersucht, da die Entdeckung variabler Sterne neue bzw. genauere astrophysikalische Studien ermöglicht. Diese Arbeit präsentiert eine Methode, die die Suche nach variablen Sternen in photometrischen Daten signifikant verbessert. Sie wurde bereits veröffentlicht (Fruth et al. 2012) und erfolgreich auf fünf BEST II Datensätze angewandt: In 329.660 Lichtkurven wurden 2.791 variable und 806 mutmaßlich variable Sterne entdeckt und klassifiziert, wodurch die Anzahl der mit BEST/BEST II identifizierten Variablen um 258% ansteigt. Die Ergebnisse stimmen sehr gut mit vergleichbaren Studien überein.

Contents

Part I

Introduction

1 Background and Purpose

Nicolaus Copernicus dramatically changed our world view through the publication of his book *"De Revolutionibus Orbium Coelestium"* in 1543. Locating the Earth in an orbit around our Sun instead of being the center of the Universe not only laid the foundation for modern astronomy, but also triggered a rethinking of age-old philosophical and religious dogmas. For example, the Italian philosopher Giordano Bruno was inspired by the new Copernican system and extrapolated it: He claimed that our Sun was only another star and that the Universe consisted of an infinite number of solar systems.

The existence of such distant worlds, *extrasolar planets*, has been long debated since. However, immense technical difficulties hinder their discovery, and although important detection methods were first envisioned by Struve (1952), they could only recently be applied successfully. In 1992, Wolszczan and Frail found two extrasolar planets around the neutron star PSR1257+12 in a rather peculiar environment, being bathed in high-energy pulsar radiation. Shortly after, the uniqueness of our own Solar System was finally disproven through the detection of a planet orbiting another Sun-like star, 51 Peg (Mayor and Queloz 1995).

These first detections initiated an enormous research effort from various disciplines. Meanwhile, more than 850 confirmed extrasolar planets[1] continuously improve our knowledge in this young field, e.g., to learn about their composition, formation, and evolution. Since, however, the diversity of the planets found is huge, their classification into categories – e.g., analogous to the pioneering work of Hertzsprung and Russell for stars – is only about to start. Moreover, first planetary abundance estimations strongly imply that our present detections only mark the very tip of the iceberg. If at least 5–10% of all solar-type stars harbour massive planets (Perryman 2011), and 1–3% have Earth analog planets (Catanzarite and Shao 2011), we can expect billions of planetary systems just in our own Galaxy, the Milky Way.

Could *life* have evolved on one of these systems? A common conclusion drawn from the astronomical count estimations is that extraterrestrial life is likely to exist, but the final proof is still beyond reach for present-day instrumentations. However, the question as to whether our world is unique remains today as intriguing as it was in the 16th century.

This chapter gives a brief overview about the scientific topics covered in the following thesis. Section 1.1 introduces the research field of extrasolar planets and highlights some of the most important discoveries. It is followed by a short introduction to stellar variability in Section 1.2 and a brief motivation for astronomical research from Antarctica in Section 1.3. Finally, Section 1.4 outlines the purpose and structure of this work.

[1] See, e.g., *www.exoplanet.eu* (described by Schneider et al. 2011)

1.1 Extrasolar Planets

Diversity

The detections of extrasolar planets have revealed a wide diversity of systems. For example, both their orbital distances and planetary masses vary over several orders of magnitude (Figure 1.1). Confirmed planets range in size from Earth up to giants that are much larger than Jupiter. Some have orbital periods of a few hours, i.e., they are located very close to their star in an extremely hot environment, while the most distant receive only little starlight and require up to a thousand years for one revolution. A detailed description how exoplanets are being detected will be given in Chapter 2.

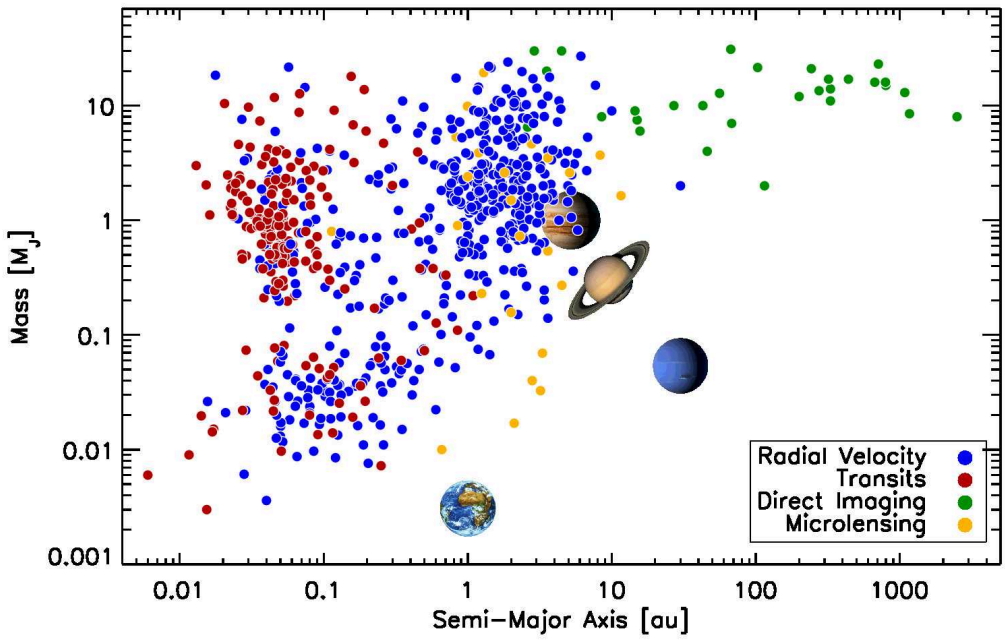

Figure 1.1: Detection ranges of different methods to find extrasolar planets. The masses and semi-major axes are shown for planets found by the radial velocity method (*blue*, $M \sin i$), microlensing *(orange)* and direct imaging *(green)*. Transiting planets are marked *red*, regardless if they were initially found using the transit method. The positions of the Solar System bodies Earth, Neptune, Saturn and Jupiter are shown for comparison (with sizes not to scale). Exoplanet data are from *www.exoplanet.eu* (Schneider et al. 2011), as of 19th November 2012. For a description of detection methods, see Chapter 2.

Most intriguingly, many of the planets found so far are not at all similar to those in our Solar System (for a recent overview, see, e.g., Perryman 2011): Large numbers of exoplanets have rather elliptical orbits, high masses, and/or they are found in very close orbits, i.e., closer than Mercury to the Sun. Furthermore, the orbital plane is often highly inclined towards the equatorial plane of the star, and some exoplanets even orbit in the opposite direction compared to the stellar spin. A large variety is also found regarding the host stars, which include main sequence stars, giants, stars of low and high metallicity, pulsars, white dwarfs and multiple stars.

While single planets have been detected in most cases, systems with up to seven bodies have been reported (HD 10180; Lovis et al. 2011). In fact, multiple systems

with small planets are expected to be very common: In a sample of 170 candidate systems with no planet larger than Neptune, Latham et al. (2011) recently found 78% to be composed of more than one planet.

Definition

As the number of high-mass planets and low-mass stars grows, the distinction between both populations requires a definition of what should be considered a planet. The IAU Working Group on Extrasolar Planets gives the following recommendation (IAU 2003):

> *Objects with true masses below the limiting mass for thermonuclear fusion of deuterium (currently calculated to be 13 Jupiter masses for objects of solar metallicity) that orbit stars or stellar remnants are "planets" (no matter how they formed). The minimum mass/size required for an extrasolar object to be considered a planet should be the same as that used in our Solar System.*

Towards the lower boundary, a planet is thus required to (a) have sufficient mass for its self-gravity to overcome rigid body forces so that it assumes a hydrostatic equilibrium (nearly round) shape, and (b) have cleared the neighborhood around its orbit (analogous to Solar System planets, IAU 2006).

Bodies above 13 Jupiter masses (M_J) are considered stars or sub-stellar objects, depending on their mass: *Stars* must be able to sustain a stable hydrogen fusion, which is generally the case for masses above ~ 75–$90\,M_J$, depending on the metallicity (Burrows et al. 2001). Objects in the intermediate mass range, i.e., within $13\,M_J \lesssim M \lesssim 75\,M_J$, are typically denoted as *brown dwarfs*. Their mass is insufficient to raise the core density high enough to initiate hydrogen burning, but still allows for some nuclear reactions with lower threshold temperatures, e.g., the fusion of lithium or deuterium. However, the distinction between planets and brown dwarfs is still ambiguous, because both mass distributions overlap (see, e.g., Baraffe et al. 2010; Spiegel et al. 2011). Schneider et al. (2011) therefore concluded that the mass alone is likely not sufficient to decide about the nature of an object in this regime. Finally, more detections of intermediate bodies like CoRoT-3b ($22\,M_J$, Deleuil et al. 2008) are needed for a better understanding of this boundary.

Formation and Evolution

When stars are born through the collapse of a molecular cloud, remaining dust and gas forms an accretion disk. The most widely accepted model for the formation of terrestrial planets assumes that a gradual agglomeration of small grains to rocks, planetesimals and protoplanets can finally build up large planetary bodies. Even though this *solar nebula theory* was first suggested some centuries ago, the detection of extrasolar planets enables today's models to be constrained statistically by comparing theoretical predictions with observational data (e.g., Mordasini et al. 2009a, b, 2012; Alibert et al. 2011). Though many details of the formation and evolution of planetary systems are now known, some processes are not well understood. For example, the mechanisms that are responsible for the growth of cm-sized particles to planetesimals of ca. 1 km diameter are rather unclear (e.g., Papaloizou and Terquem 2006).

The formation and evolution of giant planets like Jupiter or Saturn is also subject to ongoing research. Two scenarios are mainly being considered: The *core accretion model* assumes that these first grow in the same way as terrestrial planets to sizes of 5–10 $M_\oplus$ (Kennedy and Kenyon 2008) and then gravitationally bind large gas envelopes, whereas the *disk instability model* assumes that giant planets form directly via gravitational instabilities in the protoplanetary disk (for a recent overview, see, e.g., D'Angelo et al. 2010).

In both scenarios, giant planets are expected to form at rather large orbital distances. For example, the favored core accretion model constrains the range of giant planet formation to beyond the *snow line* at about 6 au (Kennedy and Kenyon 2008), where ice allows to build large cores, but to within $\sim$50 au (Rafikov 2011), as core formation is considered too slow at larger orbital distances for binding large gas envelopes before the protoplanetary disk dissipates.

As many giant exoplanets have been detected well below and above this range (cf. Figure 1.1), they are considered to have *migrated* from their initial orbit in- or outward. Proposed causes for migration include tidal interactions with gas in the protoplanetary disk (type I–III migration; see, e.g., Papaloizou and Terquem 2006), scattering with other planets or planetesimals (Nagasawa et al. 2008; Raymond et al. 2010), and perturbations by a distant companion star together with tidal friction (Fabrycky and Tremaine 2007). The same processes are invoked to explain the large frequency of planets with high eccentricities and inclinations (e.g., Morton and Johnson 2011), but more detections are required to identify the dominant mechanism.

Internal Composition

Planets in our Solar System can be probed *in situ* to learn about their internal composition, which is not possible for extrasolar planets. However, the knowledge of some basic planetary parameters usually suffices for a first assessment of their main constituents. Important in this respect are *transiting* exoplanets, for which both the radius and the mass, and, thus, the mean density can be determined (see Section 2.2). These measurements can be compared with the mass-radius relationship of theoretical predictions, and hence distinguish between different possible compositions (Figure 1.2a).

Four basic planetary types are known in the Solar System, namely: (a) terrestrial planets with a dense iron core and a rocky mantle (Mercury, Venus, Earth, and Mars), (b) dwarf planets made of rock and ice (e.g., Pluto and Eris), (c) gas giants with huge envelopes of hydrogen and helium (Jupiter and Saturn), and (d) giants largely made of ice (Uranus and Neptune). Planets of these types are probably very common in extrasolar systems, assuming their accretion disks show similar elemental abundances (Lodders 2010). However, discoveries are also revealing exotic planets unlike any Solar System body, e.g., the *"super-Earth"* exoplanet GJ 1214b (e.g., Charbonneau et al. 2009; Rogers and Seager 2010; de Mooij et al. 2012).

So far, most planets found are of Jupiter-type, which is largely due to detection biases (see Chapter 2). However, these planets exhibit a large diversity, and most detections have actually raised more questions than they have answered. In particular, *hot Jupiters*, i.e., giant planets in very close orbits (with periods $p \lesssim 5$ days), are encountered with densities ranging from $\rho = 0.16$ to 26 g/cm^3 (Ketchum et al. 2011). This large range cannot be fully explained by standard planetary models:

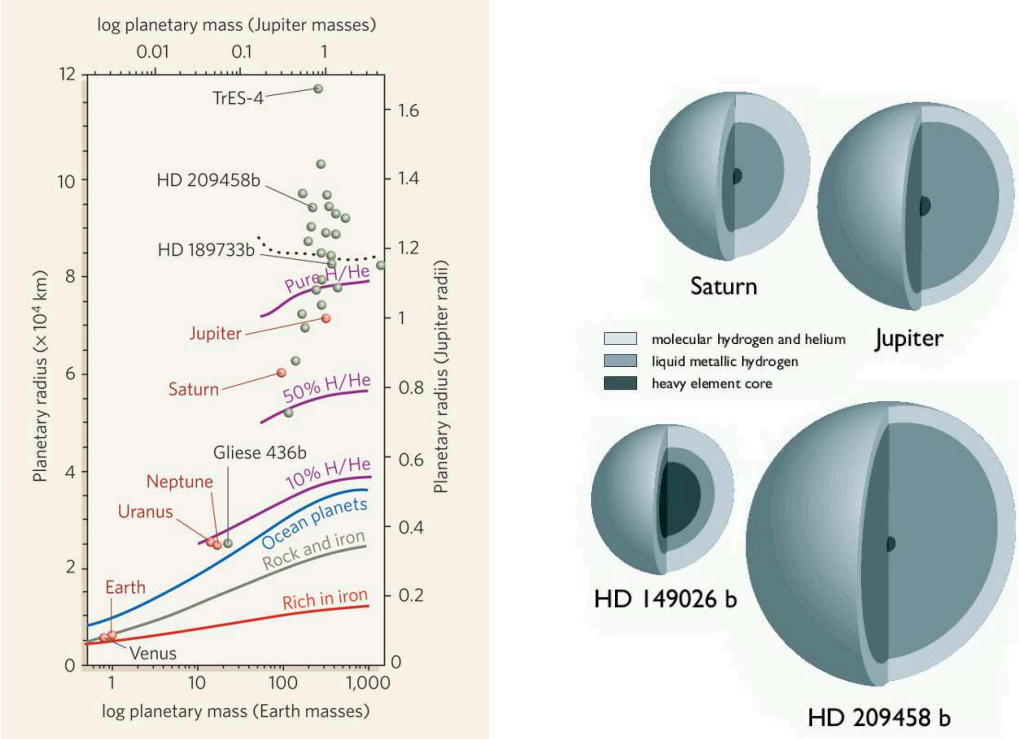

(a) (b)

Figure 1.2: (a) Mass and radius of an exoplanet are used to constrain its interior composition by comparing the measurements with models for different bulk constituents. *(Adapted by permission from Macmillan Publishers Ltd: Nature (Sasselov 2008), copyright 2008.)* (b) Observations have revealed a particularly large variety of giant planets. *(Figure from Protostars and Planets V edited by Bo Reipurth, David Jewitt, and Klaus Keil (Charbonneau et al. 2007). © 2007 The Arizona Board of Regents. Reprinted by permission of the University of Arizona Press.)*

While dense objects such as HD 149026 b (Figure 1.2b, Sato et al. 2005) are considered small due to an enrichment of heavy elements in the core (Burrows et al. 2007), an explanation of the anomalous inflation of planets like HD 209458 b (Figure 1.2b, Charbonneau et al. 2000) remains an open scientific question (e.g., Bodenheimer et al. 2001; Guillot 2005; Winn and Holman 2005; Burrows et al. 2007; Baraffe et al. 2010; Batygin and Stevenson 2010; Fortney and Nettelmann 2010; Laughlin et al. 2011). A statistically significant sample of well-characterized hot Jupiters with low densities is thus required in order to better understand these objects.

Astrobiology, Habitability, and the Search for Life

Astrobiology encompasses the study of the origin, evolution, distribution, and future of life in the Universe. In addition to the practical search for life within the Solar System and beyond, this interdisciplinary field also addresses fundamental topics such as the definition of life (e.g., Benner 2010; Tirard et al. 2010).

Although the fact that life formed early on Earth suggests that abiogenesis is an effective process, further evidence for life is finally required to rule out that our world is a rare exception (Spiegel and Turner 2011). For carbon-based life as we know it, biologists consider the presence of water a prime necessity (e.g., Owen 1980; Brack 1993). The concept of *habitability* follows this assumption by investigating

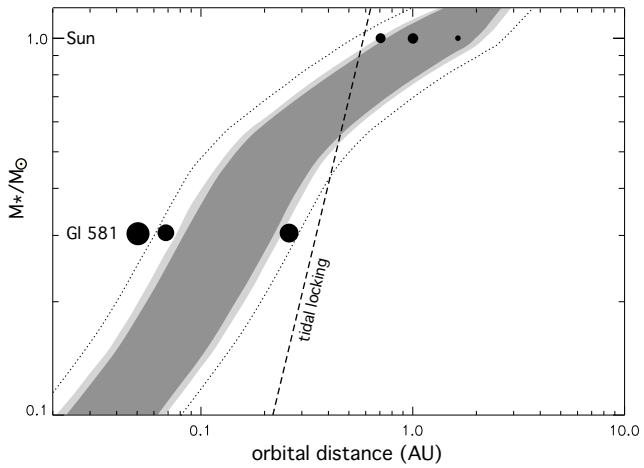

Figure 1.3: Habitable zone as a function of orbital distance and stellar mass – some planets of Gliese 581 and the Solar System are shown as an example. *(Figure 3 from Selsis et al. (2007), reproduced with permission, copyright ESO.)*

environments that can sustain liquid water for a long time; a circumstellar region that meets this requirement is accordingly termed the *habitable zone*. Whether a given planet is considered habitable or not is largely determined by the stellar flux it receives, i.e., the stellar type and its semi-major axis (Figure 1.3), but also depends on its eccentricity, rotation, other heat sources, and atmospheric properties.

Thus, the search for life motivates large efforts that are currently being undertaken in order to detect terrestrial planets in the habitable zone of a distant star. Once such worlds are known, a central goal is to analyze their atmospheres spectroscopically and to search for *biomarkers*, i.e., molecules that are considered to arise from biological activity. Important examples are O_2, O_3, and N_2O (e.g., Kaltenegger and Traub 2009; Pallé et al. 2009; Rauer et al. 2011).

Although some *super-Earths*, i.e., planets with masses up to $\sim 10\,M_\oplus$, have been found in or very close to the habitable zone (e.g., GJ 667C c with $4.5\,M_\oplus$, Anglada-Escudé et al. 2012), a thorough characterization of such small planets will only be in reach of future space instrumentation such as the JWST (Gardner et al. 2006) or EChO (Tinetti et al. 2012).

1.2 Variable Stars

The luminosity of all stars varies throughout their lifetime. While the change is typically slow for main sequence stars, evolved stars can undergo unstable phases with rapid and large brightness variations, e.g., due to expansion and contraction of their outer layers. Therefore, a commonly adopted definition suggests that *"a star is called variable when its brightness or colour variations are detectible on time scales of the order of the mean life time of man"* (Sterken and Jaschek 1996). Such variations may be periodic, semi-periodic, irregular, or chaotic, and the timescales can range from seconds up to more than a century.

Figure 1.4 shows some types of variability that are regularly encountered at different evolutionary stages in the Hertzsprung-Russell diagram. These are typically *intrinsic*, i.e., due to physical processes in the stellar atmosphere, eruptions, or gen-

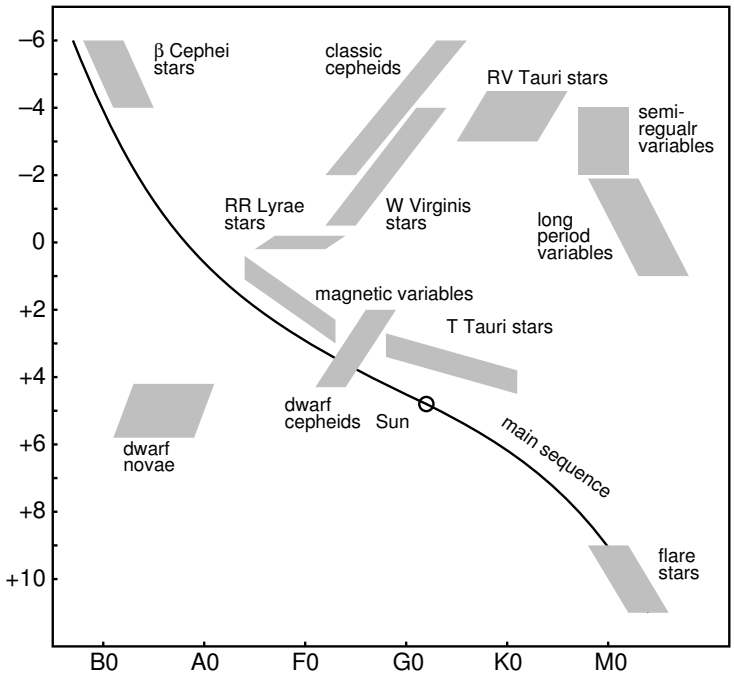

Figure 1.4: Schematical Hertzsprung-Russell diagram with locations of some typical variable stars (Karttunen et al. 2007, Figure 13.2). Shown are absolute magnitudes vs. spectral classes. Most stars – including the Sun – are found on the main sequence, where they spend most of their lifetime. *(Reproduced with permission of Ursa Astronomical Association.)*

eral stellar activity. In contrast to that, *extrinsic* variability can either be caused by rotation (e.g., spots) or by two or more stars orbiting each other. In the latter case, variability is encountered because the objects obscure each other in *eclipses* and/or have tidally distorted surfaces.

Variability can be detected by monitoring the stellar brightness over time. The resulting *light curves* reveal characteristic shapes, amplitudes and periodicity for different types of variable stars and thus allow a first classification. To gain a better understanding of the origin of variability, the photometric data are often complemented with spectroscopic measurements which yield spectral types, luminosity classes, and chemical compositions of the targeted objects.

Variable stars are crucial for addressing fundamental astrophysical questions (for a recent overview, see, e.g., Eyer and Mowlavi 2008; Walkowicz et al. 2009). In particular, the period-luminosity relation of *Cepheids* makes them to important *"standard candles"* for determining Galactic and extragalactic distances (e.g., Majaess et al. 2009). Furthermore, *eclipsing binaries* are essential to astronomy, because they allow an accurate determination of stellar parameters such as mass, radius, luminosity, or temperature, as well as to study internal and external processes of stars, their composition, internal structure, and evolution (e.g., Ribas 2006).

A dramatic increase in the detection rate of variable stars has been achieved through the advent of charge-coupled devices (CCDs) and the capability for automated data processing with modern computers. Large ground-based photometric surveys like MACHO (Alcock et al. 2000), EROS (Derue et al. 2002), ASAS (Pojmanski 2002), OGLE (Soszyński et al. 2008), and the space missions CoRoT (Section 3.1)

and Kepler (Borucki et al. 2010) together monitor millions of stars. Even though many of these projects have a different scientific focus, their light curves are commonly searched for variable stars which are collected in large catalogs such as the General Catalogue of Variable Stars (GCVS; Samus et al. 2009) or the Variable Star Index (VSX; Watson et al. 2006).

1.3 Antarctica – the Best Place for Astronomy?

To obtain a better understanding of our Universe, astronomers have constantly sought to improve their observing conditions. While the limiting factors can be many and diverse, the selection of an observing site particularly impacts the quality of the astronomical data recorded. Among the most important constraints are the fraction of clear skies, the level of astronomical seeing and scintillation, the accessibility of a large spectral range, and a low sky brightness due to emission, scattered light, and light pollution. In particular, an excellent observing site is of key importance for detecting and characterizing extrasolar planets.

Best conditions are generally achieved high above the atmosphere, i.e., using airborne or space observatories. However, such projects are limited by extensive costs, and technical considerations impose further constraints. For instance, very large telescope apertures ($d > 10\,\mathrm{m}$) can today only be realized on ground, and the possibilities for instrument maintenance and upgrades are very limited in space. Therefore, the search for excellent observational sites on ground is being pursued with unwaned interest. Over the last few decades, high-altitude sites such as in the Chilean Atacama desert or the mountain tops of Hawaii have generally been recognized to provide the best observing conditions for large ground-based observatories.

Antarctica is the highest, driest and coldest continent on Earth. Figure 1.5 shows a topographic map of the continent with some locations of current and planned astronomical instrumentation. The extreme Antarctic environment yields a number of very favorable conditions for astronomy:

- The polar night allows for observations with a very **high duty cycle**. This is particularly beneficial for observations that rely on continuous time series, e.g., transit search (Caldwell et al. 2004; Pont and Bouchy 2005; Fruth 2008; Rauer et al. 2008a, b; Crouzet et al. 2010; Rauer and Deeg 2010) or asteroseismology (Grec et al. 1980; Mosser and Aristidi 2007; Mosser et al. 2009; Damé et al. 2010).

- The **clear sky fraction** in Antarctica is comparable to excellent temperate sites or better. While the South Pole is covered by clouds about half of the time (Town et al. 2007), sites on the Antarctic plateau experience a significantly larger number of good nights (e.g., Saunders et al. 2009). For Dome C, different projects have measured a very good fraction of ca. 75–90% photometric nights during winter (Ashley et al. 2004, 2005; Mosser and Aristidi 2007; Moore et al. 2008; Crouzet et al. 2010), while Wang et al. (2011) reported for Dome A remarkable conditions of 96% clear skies during winter 2008.

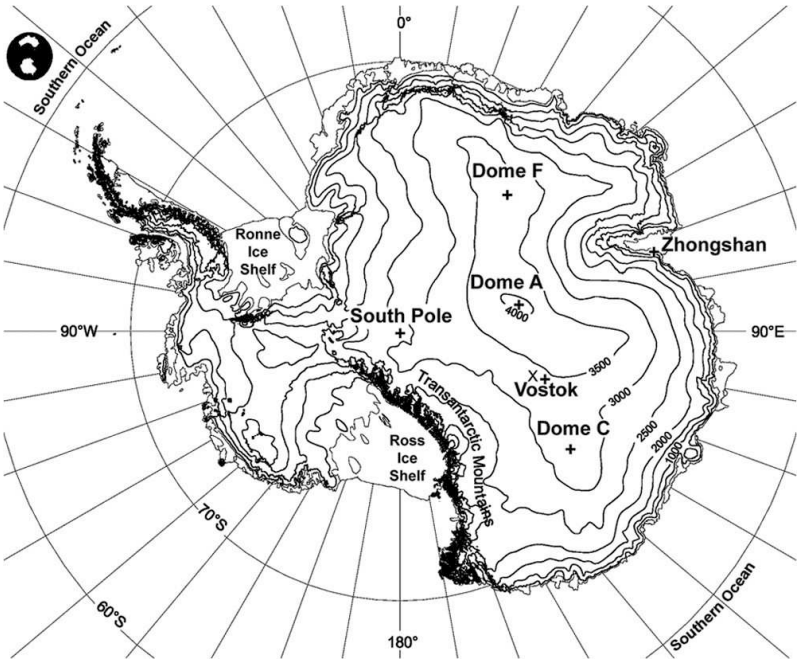

Figure 1.5: Map of Antarctica (Yang et al. 2009, Figure 1). *(Reproduced with permission of the University of Chicago Press; copyright Australian Antarctic Data Center.)*

- Average winter temperatures of around −60° and a largely reduced aerosol content account for a **low sky background**, especially in the mid and far infrared. For wavelengths $\lambda \approx 2$–$30\,\mu\text{m}$, the Antarctic sky is found to be about 10–50 times darker compared to the best temperate sites (Ashley et al. 1996; Nguyen et al. 1996; Smith and Harper 1998; Phillips et al. 1999; Lawrence 2004), thus yielding a significant increase in sensitivity for background-limited infrared observations.

- An extreme dryness leads to a significantly **increased transmittivity** of the Antarctic atmosphere. While the atmosphere above normal observing sites such as Siding Springs (Australia) or Kitt Peak (USA) typically contains about 1 cm of precipitable water vapor, the most arid temperate places like the Chajnantor plateau (Chile) can occasionally experience levels as low as 300 µm (Burton 2010). In Antarctica, however, such small amounts of water vapor are regularly encountered: For example, Dome A shows values below 100 µm during 25% of the winter (Yang et al. 2010). Because the absorption of water is strongly reduced, the Antarctic atmosphere becomes transparent for a number of important infrared and sub-mm wavelength ranges that are inaccessible from any other site on Earth (Lawrence 2004; Yang et al. 2010).

- Light from distant sources is refracted when it passes through the Earth's atmosphere. Turbulences in the air cause temporal variations in the refractive index, which yield an angular widening of the incident light (seeing) and intensity variations (scintillation). In most of Antarctica, the **atmospheric turbulence** is confined to a thin boundary layer (Swain and Gallée 2006). It extends on average 200–300 m above the South Pole (Marks et al. 1999; Travouillon et al. 2003), about 25 m at Dome C (Aristidi et al. 2009), and only 14 m at

Dome A (Bonner et al. 2010). Above this layer, the average seeing is with $\sim 0.3''$ about 2–3 times smaller than at the best temperate sites (Lawrence et al. 2004; Aristidi et al. 2009; Giordano et al. 2012). Because the path between turbulent cells and the telescope is short, scintillation noise is also – even for observations from the ground – significantly reduced: Kenyon et al. (2006) measured a gain of factor 2–4 compared to Chilean sites for Dome C. Furthermore, both adaptive optics and interferometry benefit from a large isoplanatic angle and a long coherence time above the thin ground layer (Lawrence et al. 2004, 2008; Storey 2004).

While a number of projects have initially favored the South Pole largely due to the available infrastructure, a more recent development focuses on sites at the East Antarctic plateau (Gillingham 1991; for a review on astronomy from Antarctica, see Indermuehle et al. 2005; Burton 2010). All summits of the Antarctic plateau, i.e., Dome A, Dome C, and Dome F (Figure 1.5) are considered to provide an outstanding environment for astronomy (for a comparison, see Saunders et al. 2009). They are particularly interesting for astronomical research at high angular resolution in the near infrared and sub-mm, which could largely benefit both from the unequaled atmospheric transmission in this spectral range and the exceptional seeing.

However, the infrastructural development and knowledge about site conditions differs largely. Dome C is best characterized through site testing, and the French-Italian Concordia station (Candidi and Lori 2003) allows for year-round attendance of scientists since 2005. Dome A is less accessible, and was only first visited in 2004. Meanwhile, however, a number of measurements have been performed (Yang et al. 2009, 2010; Bonner et al. 2010; Zhou et al. 2010; Wang et al. 2011; Sims et al. 2012a, b), a station has been erected, and the Chinese Center for Antarctic Astronomy has ambitious plans for large-scale telescopes (Cui 2010). Dome F is currently least studied among these summits, but is also being considered for future astronomical facilities (Ichikawa 2010).

1.4 About this Study

This thesis has been prepared at the Institute of Planetary Research, which is part of the German Aerospace Center (DLR), Berlin. Its department *Extrasolar Planets and Atmospheres*[2] focuses on the search and characterization of extrasolar planetary systems and atmosphere modeling of planets in and out of the Solar System.

The department's participation in the CoRoT space mission (Section 3.1) forms an integral part for its work on extrasolar planets. Through careful analysis of the satellite data, new planets are found using the transit method (Section 2.2) and characterized. CoRoT has made invaluable contributions to the field of extrasolar planets, i.e., by finding small objects such as the first detected terrestrial exoplanet CoRoT-7b.

In addition, the department operates two ground-based telescopes that support the follow-up process of the CoRoT mission: The *Berlin Exoplanet Search Telescopes* BEST and BEST II (Section 3.2); they are used to confirm or reject planetary candidates from the satellite (Deeg et al. 2009). BEST is located in France, while BEST II resides in the Chilean Atacama. Both are operated remotely.

[2] http://www.dlr.de/caesp

1.4.1 Purpose

This thesis addresses the following scientific questions:

- **Transit Search with BEST II**
  Small telescopes such as BEST II can also be used to search for extrasolar planets. During long-term monitoring of CoRoT target fields, BEST II has already shown its potential to obtain a photometric precision better than 1% together with a long duty cycle (Kabath 2009). It should thus be capable of detecting planets of Jupiter size, which can help to understand some important questions in exoplanet research. For example, different migration theories have been put forward to explain the large population of systems in orbits that are eccentric and/or highly inclined towards the stellar equatorial plane (see also Section 1.1), but more planets are required to finally identify the dominant mechanism (Morton and Johnson 2011). In a similar way, more inflated hot Jupiters are required to decide statistically between theories that are considered to explain their low densities (Laughlin et al. 2011).

  The detection of more such planets using a dedicated transit search program with BEST II is the main focus of this thesis.

- **Transit Search from Antarctica**
  The East Antarctic Plateau is considered a prime site for transit search and has been investigated through site testing and theoretical comparisons (Section 1.3). In particular, joint observations of Dome C together with a mid-latitude site such as in Chile imply a theoretical advantage for transit searches (Fruth 2008; Rauer et al. 2008b). Since 2010, the ASTEP 400 telescope (Section 3.3) operates as the first full exoplanet survey from Antarctica at Dome C.

  The thesis aims to probe the potential for transit search under real conditions through an analysis of first ASTEP 400 data, to compare the results with Chile, and to investigate the feasibility of detecting extrasolar planets using a network of telescopes.

- **Variable Star Detections**
  The analysis of stellar variability complements photometric surveys such as BEST, CoRoT, or ASTEP. Detections are generally announced in large catalogs so that they can be investigated further by an interested scientific community. With BEST and BEST II, previously unknown variability has been reported for almost one thousand cases (Karoff et al. 2007; Kabath et al. 2007, 2008, 2009a, b; Pasternacki et al. 2011). However, the methods used to analyze photometric data sets are known to be strongly affected by systematic trends that are present in ground-based observations (see, e.g., Pepper and Burke 2006; Karoff et al. 2007; Kabath et al. 2009a; Hartman et al. 2011a). Such effects generally lead to a higher ranking of non-variable stars, which in turn increases both the number of false alarms and the number of missed detections.

  The thesis aims to increase the yield of variable star searches through a better treatment of systematic variability.

1.4.2 Structure

The thesis is structured into three main parts, which are outlined briefly in the following text.

I. Introduction

The first part gives an introduction to the topics covered. It includes this chapter, which states the scientific background and the motivation for the presented work. The following Chapter 2 explains important methods of detecting extrasolar planets, including the transit method. The latter is used by all projects that are relevant for this thesis, namely CoRoT, BEST/BEST II and ASTEP. These projects are described in Chapter 3, which concludes the introduction.

II. Observations and Methods

The second part focuses on the observations and methods that are used to obtain scientific results, and improvements that were achieved in the framework of this thesis. Topics covered include the whole process of data acquisition, i.e., from target field selection through telescope operations and observations to photometric data reduction, and the methods for scientific analysis of the light curves obtained.

Chapter 4 first gives an updated summary of the BEST II observing strategy, including the first dedicated transit search that was performed with the instrument on three target fields (F17–F19) during 2009/2010, an evaluation of the photometric quality of BEST II, and the expected number of planet detections. Chapter 5 then gives a description of the photometric pipeline, i.e., the set of routines that are used to construct light curves from raw observational data.

The last two chapters of this part deal with the scientific data analysis of light curves. Chapter 6 describes the adaptation and validation of a transit search procedure for BEST II. Chapter 7 presents the method to search for variable stars in photometric data sets, including an improved procedure to account for systematic variability.

III. Scientific Results

The last part presents the scientific results. Chapter 8 presents a large number of planetary candidates that were found in the analyzed target fields F17–F19, including a thorough description of the tests and follow-up observations that have been performed to exclude false positive signals. Chapter 9 summarizes the corresponding results of a search for stellar variability in these fields, and additional BEST II findings that were obtained via a reanalysis of the CoRoT target field LRa02; these are presented together in a large variable star catalog in Appendix E.

The analysis of the first photometric time series obtained with the ASTEP 400 telescope is the subject of Chapter 10. It contains an outline of observations and transit search performed on two target fields together with BEST II, compares the photometric quality and detection yield, and discusses the advantages and difficulties of such a joint campaign.

Finally, Chapter 11 summarizes the thesis, discusses its results and gives an outlook to future work.

2 Detection Methods

Direct vs. Indirect Methods

In our Solar System, all planets can be observed *directly*, and their reflected and emitted light contains a plethora of information. For example, a view of the surface of Mars gives hints on its composition, and Venus' atmosphere can be deciphered through spectroscopy. Unfortunately, it is substantially more difficult to obtain direct measurements for extrasolar planets mainly because:

- The orbital separation between a star and its planet is vanishingly small compared to their mutual distance to us. Thus, their apparent angular separation on the sky is usually well below the resolving power of any present-day observatory. For example, a planet in an Earth-like orbit around our closest neighbor, the star $\alpha\,\mathrm{Cen\,C}$ (4.22 light years away), would be placed at a small angular distance of $0.8''$ from its host star and could thus only be resolved by a few of the largest facilities on Earth or from space.

- The contrast ratio between stars and planets is immense. In the optical, stars typically outshine their planetary companions by a factor of $\sim 10^8$–10^{10} (for orbital distances of 0.2–15 au and masses from 0.5–8 M_J, Burrows et al. 2004).

Together, these boundary conditions place considerable limitations on the direct detection and characterization of exoplanets. Only a few observationally favorable massive planets in large orbital distances have been observed directly (for a recent review, see Kalas 2011), and the direct measurement of Earth-like planets will not be possible using any currently available or planned facility (Angel 2003).

The majority of extrasolar planets known today has thus been detected using *indirect* methods. Several techniques have been developed to infer the existence of a planetary companion through observations of its host star. Figure 1.1 gives an overview of exoplanetary masses and orbital distances – they range from Earth-sized bodies up to the lower boundary of stars, and from orbits lasting only a few hours up to a thousand years. Depending on the underlying physical principles and technical limitations, each method is targeting a slightly different type of planetary systems and thus likewise important towards an overall picture of exoplanets.

Since this work focuses on the transit method, this technique will be described in more detail in Section 2.2. It is preceded by an introduction to the radial velocity method in Section 2.1, which is complementary to the transit method and thus of likewise importance for this thesis. Other indirect methods will be mentioned briefly at the end of this chapter in Section 2.3. For a recent in-depth overview of all methods and their findings, see, e.g., Perryman (2011).

2.1 Radial Velocity Method

Any two gravitationally bound bodies revolve in elliptical orbits (Figure 2.1a). The center of mass coincides with the focus of each ellipse, and the relative dimension of

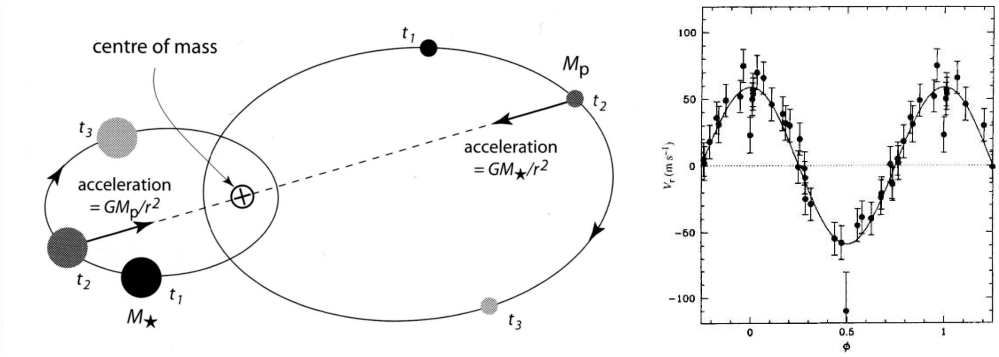

(a) (b)

Figure 2.1: (a) Motion of two bodies orbiting each other due to their mutual gravitational attraction (Perryman 2011, Figure 2.3). *(Reproduced with permission of Cambridge University Press.)* (b) First RV measurement of an exoplanet (51 Peg b; Mayor and Queloz 1995). *(Adapted by permission from Macmillan Publishers Ltd: Nature (Mayor and Queloz 1995), copyright 1995.)*

both orbits is determined by the inverse mass ratio, i.e., $a_\star/a_p = M_p/M_\star$. In planetary systems, the mass of the star ($M_\star$) is much larger than that of the planet (M_p), which is why the stellar orbit $a_\star \ll a_p$ can often be neglected.

However, the small stellar movement around the barycenter can be used to indirectly infer the existence of a planet. The radial velocity (RV) method uses the Doppler effect to detect tiny motions of a star in the direction towards or away from the observer. By comparing the distortion $\Delta\lambda$ of absorption lines in the stellar spectrum compared to their reference wavelength λ_0, it is possible to measure the radial velocity v_r of the star through

$$\frac{v_r}{c} = \frac{\Delta\lambda}{\lambda_0} \quad . \tag{2.1}$$

The presence of a secondary object can then be deduced from a periodic variation of v_r in time. Furthermore, the amplitude of $v_r(t)$ yields information about its mass, whereas orbital parameters such as the eccentricity can be derived from the shape. The variation is largest if the orbital plane is parallel to the line of sight (inclination $i = 90°$), and zero if it is perpendicular to it ($i = 0$). More precisely, the radial velocity can theoretically be described through

$$v_r(t) = K\left[\cos(\omega + \nu(t)) + e\cos\omega\right] \ , \tag{2.2}$$

whereby K is the semi-amplitude of variation, e the eccentricity, and ω the argument of periastron. The true anomaly $\nu(t)$ specifies the angle between barycenter, periastron and the current orbital position of the star at time t and can be calculated if the orbital period p, eccentricity e, and the time of periastron passage t_p are known. Fitting Equation (2.2) to the measurement data $v_r(t)$ thus yields the five parameters p, e, t_p, ω, and K.

Using Kepler's third law, it is possible to derive further physical parameters from K. First, the planetary mass M_p can be accessed by (Cumming et al. 1999)

$$K = \left(\frac{2\pi G}{p}\right)^{1/3} \frac{M_p \sin i}{(M_p + M_\star)^{2/3}} \cdot \frac{1}{\sqrt{1-e^2}} \ , \tag{2.3}$$

if the stellar mass $M_\star$ can be approximated appropriately, e.g., through spectroscopic characterization or asteroseismology. Note that because the inclination i cannot be

Table 2.1: Planetary parameters (semi-major axis a_p, orbital period p, mass M_p) and resulting stellar movement (semi-major axis $a_\star$, RV semi-amplitude K) for some Solar System bodies and the first RV exoplanet 51 Peg b.

Planet	a_p [au]	p [yr]	M_p [$M_\star$]	$a_\star$ [$r_\star$]	K [m/s]
Mercury	0.387	0.241	$1.7 \cdot 10^{-7}$	$1.38 \cdot 10^{-5}$	0.00812
Earth	1	1	$3.0 \cdot 10^{-6}$	$6.45 \cdot 10^{-4}$	0.0894
Jupiter	5.2	11.9	$9.6 \cdot 10^{-4}$	1.07	12.5
Neptune	30.1	164	$5.2 \cdot 10^{-5}$	0.335	0.284
51 Peg b	0.0567	0.0116	$4.0 \cdot 10^{-4}$	$3.79 \cdot 10^{-3}$	59

Notes. The semi-amplitude K of the RV curve $v_r(t)$ was calculated using Equation (2.4) and assuming an edge-on observer, i.e., $i = 90°$, for the Solar System planets. Parameters are taken from Karttunen et al. (2007) for the Solar System, and from Mayor and Queloz (1995) and Poppenhäger et al. (2009) for 51 Peg b. For the latter, values correspond to $\{a_p, M_p, a_\star\} \cdot \sin i$.

determined with the RV method, M_p cannot be calculated directly; instead, $M_p \sin i$ only yields a lower limit for the mass of a planet. Second, the semi-major axis $a_\star$ can be obtained from the semi-amplitude K using (e.g., Perryman 2011)

$$K = \frac{2\pi}{p} \cdot \frac{a_\star \sin i}{\sqrt{1-e^2}} \ . \tag{2.4}$$

Figure 2.1b shows the RV curve of 51 Peg that lead to the first detection of an exoplanet around a Sun-like star (Mayor and Queloz 1995). Although the method had already been applied successfully to binary stars, an improved experimental precision then allowed for the first time to measure the much smaller signal of a planetary companion. While stars are typically orbiting each other at a few km/s, 51 Peg – with a minimum mass of $M_p \sin i = 0.47\, M_J$ – showed an RV semi-amplitude K of only 59 m/s. For comparison, Table 2.1 shows how much the Sun moves due to planetary orbits. Jupiter, the largest planet in the Solar System, shifts the Sun-Jupiter barycenter to slightly above the Solar surface and causes a maximum RV amplitude of 12.5 m/s.

As follows immediately from Equation (2.3), the RV method is most sensitive to large bodies in tight orbits. Therefore, the first detected exoplanets belong to the class of so-called *hot Jupiters*.

Instrumental Precision

State-of-the-art RV spectrographs such as HARPS (Mayor et al. 2003) today achieve precisions slightly below 1 m/s (Lovis et al. 2008), which is sufficient to detect Earth-sized planets at very short orbital distances, or slightly larger bodies – so-called *Super-Earths* ($M_p \approx 1$–$10\, M_\oplus$) – with orbital periods of up to about 100 days (e.g., the planetary system HD 20794, Pepe et al. 2011; see also Figure 1.1). With a signal of 51 cm/s, the most recent detection of an Earth-sized planet around the nearby star α Cen B ($p = 3.236$ days, $M_p \sin i = 1.13\, M_\oplus$, Dumusque et al. 2012) sets the current benchmark for RV detections.

Earth itself would cause an RV signal of 9 cm/s and is therefore still below the detection threshold of present instruments. However, Pepe and Lovis (2008) expect an improvement to 20–30 cm/s in the near future, and claim that Earth-like planets will be in reach by next-generation facilities such as the E-ELT with an aimed-for precision of 5–10 cm/s.

Constraints of the Method

With 497 detected exoplanets (Schneider et al. 2011, as of 21th November 2012), the RV technique is the most successful detection method to date. However, it involves some important observational constraints: First, the achievable precision strongly depends on the luminosity of the target star (e.g., Bouchy et al. 2001), making it particularly difficult to detect or confirm exoplanets around stars fainter than $V \approx 15\,\mathrm{mag}$. Second, RV measurements are affected by various types of additional noise: The star itself can generate a jitter through magnetic activity, rotation, or pulsation that might well exceed the signal imposed by a planetary companion. On the one hand, this leads to a sample of RV planets that is biased against very young and active stars. On the other hand, the smaller a planet, the more difficult it gets to disentangle its signal from the stellar jitter (e.g., requiring intensive activity monitoring, Boisse et al. 2011).

2.2 Transit Method

Transiting extrasolar planets periodically eclipse their host stars as seen from Earth (Figure 2.2). While passing the stellar disk, they cause a temporary decrease of the stellar flux that can be measured. The transit method uses long-term photometric observations to detect this characteristic signal and infer the existence of a planetary companion.

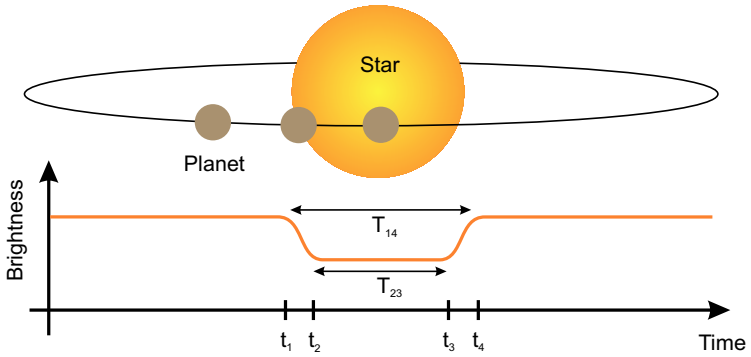

Figure 2.2: The transit method. When a distant planet is crossing the line-of-sight towards us, four important events can be observed during the primary eclipse: The beginning of the transit (t_1), the moment at which the planet is first (t_2) and last (t_3) completely in front of the star, and when it finally uncovers the stellar disk (t_4). The time ranges $[t_1, t_2]$ and $[t_3, t_4]$ are called *ingress* and *egress* phases, respectively. The complete time in transit is denoted by $T_{14} = t_4 - t_1$, while $T_{23} = t_3 - t_2$ denotes the duration of the lower part of the transit.

Observables

An analysis of the *light curve*, i.e., the stellar flux $f(t)$ as a function of time, allows the direct measurement of the orbital period p. It is determined by the time between adjacent transits and thus requires the observation of at least two such events. More recorded transits help to improve the measurement error of p (see also Section 8.2) or can be used to detect a third body in the system (see later in this section).

Further observables can be deduced from the shape of the light curve during eclipse. Under the simplifying assumption that the stellar luminosity is uniformly distributed

over its disk (i.e., neglecting limb darkening), transits have a trapezoidal profile, which can thus be described using the depth δF, the total duration T_{14}, and the duration of the flat part T_{23} (see Figure 2.2). Thereby, the depth is simply defined as the relative difference between the stellar flux before/after ($f_{\rm out}$) and during transit ($f_{\rm in}$), i.e.,

$$\delta F = \frac{f_{\rm out} - f_{\rm in}}{f_{\rm out}} \ . \tag{2.5}$$

Physical Parameters

The four observables p, δF, T_{14}, and T_{23} can be used to derive physical quantities. Seager and Mallén-Ornelas (2003) showed that a unique solution can be obtained for transiting planets in circular orbits under the assumptions that the light curve is not contaminated by light from a third object, limb darkening is negligible, and that $M_p \ll M_\star$. First, the flux decrease during transit is determined by the ratio of planetary to stellar disk, and the radius ratio can be approximated through

$$\frac{r_p}{r_\star} \approx \sqrt{\delta F} \ . \tag{2.6}$$

Second, the impact parameter b, i.e., the projected distance between planet and stellar center during mid-transit, is given by

$$b \equiv \frac{a}{r_\star} \cos i = \left\{ \frac{(1-\sqrt{\delta F})^2 - \left[\sin^2(\pi T_{23}/p)/\sin^2(\pi T_{14}/p)\right](1+\sqrt{\delta F})^2}{1 - \left[\sin^2(\pi T_{23}/p)/\sin^2(\pi T_{14}/p)\right]} \right\}^{1/2} . \tag{2.7}$$

Third, the semi-major axis a can be calculated in units of stellar radii $r_\star$,

$$\frac{a}{r_\star} = \left\{ \frac{(1+\sqrt{\delta F})^2 - b^2\left[1-\sin^2(\pi T_{14}/p)\right]}{\sin^2(\pi T_{14}/p)} \right\}^{1/2} , \tag{2.8}$$

which in turn yields the fourth quantity, the stellar density

$$\frac{\rho_\star}{\rho_\odot} \equiv \frac{M_\star/M_\odot}{(r_\star/r_\odot)^3} = \frac{4\pi^2}{G\,p^2}\left(\frac{a}{r_\star}\right)^3 . \tag{2.9}$$

The approximation $r_\star \ll a$ can be used to further simplify Equations (2.7)–(2.9), for example

$$\frac{\rho_\star}{\rho_\odot} = \frac{32}{G\pi}\,p \cdot \frac{\delta F^{3/4}}{\left(T_{14}^2 - T_{23}^2\right)^{3/2}} \ . \tag{2.10}$$

With an additional stellar mass-radius relation $r_\star = k M_\star^x$, the physical quantities a, r_p, $r_\star$, and i can be disentangled (Seager and Mallén-Ornelas 2003, Equations (10)–(14)).

The parameters from Equations (2.6)–(2.10) represent to a good first-order approximation the real physical parameters. These can be used, for example, to identify massive companions which might be less interesting to follow up. However, the assumptions made are often over-simplifications, and a more precise light curve fitting is obtained by including the effects of limb darkening and eccentric orbits. This first requires a model to describe the light curve theoretically as a function of the physical parameters, e.g., using the formulation of Mandel and Agol (2002). In a second step, all parameters are varied numerically within physically meaningful ranges in order to obtain the best agreement between modeled and measured stellar flux.

Complementarity to the Radial Velocity Method

Since transiting exoplanets are orbiting in a plane that is almost parallel to the line of sight ($i \approx 90°$), both the stellar reflex motion and the RV amplitude are close to maximal (Equation (2.3)). Provided it can be measured with sufficient precision, additional RV data bring two important advantages. First, the planet is then confirmed with an independent method. Second, the planetary mass M_p can be determined exactly by combining the inclination i from the transit light curve with the mass estimation $M_p \sin i$ from the RV method. Thus, together with the radius r_p, the combination of both methods yields the *density* of extrasolar planets. This enables an initial characterization, e.g., to distinguish between gas and rocky planets. Such information is only available for transiting planets to date.

Discoveries

The first extrasolar transits were observed independently by Henry et al. (2000) and Charbonneau et al. (2000) for the planet HD 209458 b that was previously known from RV measurements. Two years later, Udalski et al. (2002b) reported the first planet discovered by the transit method. Today, we know 234 transiting extrasolar systems with a total of 289 planets[1], having orbital periods as short as 11 hours (Kepler-42c; Muirhead et al. 2012) up to 303 days (Kepler-47c; Orosz et al. 2012) and radii between $0.57\,r_\oplus$ (Kepler-42d; Muirhead et al. 2012) and $2.0\,r_J$ (HAT-P-32b; Hartman et al. 2011b).

Detection Probability

The probability to detect a transiting exoplanet is constrained by a number of factors, including the number of stars surveyed, the achievable photometric precision, the geometric probability for a favorable orbital alignment, and the observational time series. Beatty and Gaudi (2008) derived a general formalism to predict the detection yield N_{det} based on the parameters of a given survey. They define (Equation (1))

$$\frac{d^6 N_{\mathrm{det}}}{dr_p\; dp\; dM_\star\; dr\; dl\; db} = \rho_\star(r,l,b)\; r^2 \cos b\; \frac{dn}{dM_\star}\; \frac{df(r_p,p)}{dr_p\; dp} \cdot\; p_{\mathrm{det}}(M_\star, r, r_p, p), \quad (2.11)$$

whereby r, l, and b specify galactic coordinates, $\frac{dn}{dM_\star}$ the present day mass function, and $\frac{df(r_p,p)}{dr_p\; dp}$ the probability that a star will possess a planet of radius r_p and orbital period p. The function p_{det} describes the probability that a planetary system around a star of mass $M_\star$ at distance r presents a *detectable* transit. It comprises the probability p_g for a transit geometry, observational coverage p_{win} of the transit, and the probability $p_{\mathrm{S/N}}$ of a sufficient signal-to-noise ratio (SNR), i.e.,

$$p_{\mathrm{det}}(M_\star, r, r_p, p) = p_{\mathrm{S/N}}(M_\star, r, r_p, p) \cdot p_g(p) \cdot p_{\mathrm{win}}(p)\;. \quad (2.12)$$

The geometric probability for observing a transit is given by (e.g., Barnes 2007, Equation (8))

$$p_g(a(p)) = \frac{r_\star + r_p}{a \cdot (1 - e^2)}, \quad (2.13)$$

[1] *www.exoplanet.eu* (Schneider et al. 2011), as of 21th November 2012

Table 2.2: Transit method characteristics – the Solar System as a showcase (after Titz-Weider 2006).

Planet	a [au]	p [yr]	r_p [$r_\oplus$]	δF [%]	T_{14} [h]	p_g [%]
Mercury	0.39	0.24	0.38	0.0012	8.1	1.2
Venus	0.72	0.62	0.95	0.0075	11	0.64
Earth	1.0	1.0	1.0	0.0084	13	0.47
Mars	1.5	1.9	0.53	0.0024	16	0.31
Jupiter	5.2	12	11	1.0	30	0.089
Saturn	9.6	30	9.4	0.75	40	0.048
Uranus	19	85	4.0	0.14	57	0.024
Neptune	30	165	3.9	0.12	71	0.015

Notes. In addition to the orbital period p, the semi-major axis a, and the planetary radius r_p, the relative decrease in solar flux δF, the total transit duration T_{14}, and the geometric probability p_g (Equation (2.13)) are given for each planet.

whereby a indicates the planet's semi-major axis, e its eccentricity, and $r_\star$ and r_p the stellar and planetary radius, respectively. The proportionality to $1/a$ causes the transit method to be most sensitive to close-in planets, for which p_g can reach values larger than 10% (see, e.g., Kane and von Braun 2009, Table 1). For comparison, Table 2.2 lists the geometric probability to see a Solar System planet transiting if observed from a random direction. While Mercury has a probability of 1.2%, Earth could only be seen in transit from 0.47% of all possible viewing angles. In order to counter such relatively small chances, transit searches commonly target very large ($N_\star \gg 10^4$) stellar samples.

Typically, a transit detection requires the observation of at least three transit events (Rauer and Erikson 2007). From ground, the diurnal cycle limits the orbital coverage p_{win} to periods of up to a few weeks; however, it can be increased significantly through observations with networks, or from space (see, e.g., Rauer et al. 2008a; von Braun et al. 2009).

Photometric Precision and Current Detection Limits

The decrease in flux that is to be measured by the transit method is typically in the range $\delta F \lesssim 1\%$. Table 2.2 gives δF in the Solar System: Jupiter, the largest planet, would occult about 1% of the solar disk if transiting – a signal that is well detectable with current technology. The signals of Neptune and Uranus ($\delta F \approx 0.1\%$) are at the limit of present ground-based instrumentation (e.g., the 60 cm TRAPPIST telescope with a photometric error of $\sim$0.1%, Gillon et al. 2012), but can be quite easily detected from space. Transits of Earth-sized planets cause only a tiny decrease of about 0.01% in the stellar flux and are thus the exclusive domain of space-based observatories such as CoRoT and Kepler. Their precision enabled the first detection of a terrestrial planet (Corot-7b; Léger et al. 2009; Queloz et al. 2009; Hatzes et al. 2011) and has today reached a level that is sufficient to measure transit signals of Earth-sized extrasolar planets around Sun-like stars (Kepler-20e with $0.868\,r_\oplus$ and Kepler-20f with $1.03\,r_\oplus$; Fressin et al. 2012).

Since the transit signal is determined by the radius ratio of planet to star (Equation (2.6)), the *stellar size* also constrains the detectability of a transit. On the one hand, large early-type stars significantly complicate the transit detection, and the vast size of giants makes it – at least for now – impossible to measure planetary transits for such stars. On the other hand, the smaller size of late-type stars facil-

itates the detection of transit signals. Thus, the detection limit is shifted towards smaller planets for M-type stars (e.g., GJ 1214b, a $2.68\,r_\oplus$ small planet detected from ground; Charbonneau et al. 2009), which are expected to show transit depths of up to 7% (Haghighipour et al. 2010).

Another complication arises from intrinsic stellar variability, e.g., due to the rotation of spots. At least for small planets, the corresponding variation is typically larger than the transit signal itself (Alapini and Aigrain 2009). Especially for the detection of Earth-sized planets with space-based surveys, several techniques have thus been set up to filter stellar variation (e.g., Aigrain et al. 2004; Bonomo and Lanza 2008; Bonomo et al. 2009).

False Alarms

A small periodic decrease in the stellar flux can have various causes other than a planetary transit. First, instrumental effects can induce systematic trends into the light curve that can be mistaken as a transit. However, such false alarms can usually be identified relatively easily by careful analysis of the photometric time series alone. Second, certain stellar configurations can also mimic a planetary transit – Figure 2.3 shows some prevalent cases. Most commonly, binary stars are mistaken for planetary transits because the eclipse can be grazing (a), a large primary (e.g., a giant star) can yield a small radius ratio (b), or the target PSF can be diluted with third light from an unresolved background binary (d). Less frequently, spots can mimic a transit-like signal (c).

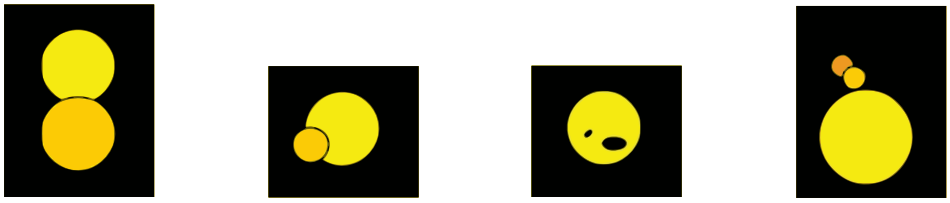

(a) (b) (c) (d)

Figure 2.3: Common causes for false alarms in transit searches: (a) Grazing eclipses, (b) small stellar companions, (c) star spots and (d) background eclipsing binaries. (*Copyright R. Titz-Weider, reprinted with permission (see also Titz-Weider 2006).)*

Unfortunately, the number of astrophysical false positives is generally much higher than the final number of detections. Recent studies have shown that one confirmed planet is only contained in a sample of approximately 10–20 candidates that require follow-up observations (e.g., Brown 2003; Pont et al. 2005; Alonso et al. 2007; Almenara et al. 2009; Evans and Sackett 2010; Carone et al. 2012).

Astrophysical false positives often pose a significant challenge to the transit method and frequently require additional observations to be solved without ambiguity. However, the capacity of suitable facilities to perform such observations is regularly outnumbered by the number of candidates. Therefore, all successful transit surveys have developed extensive strategies to exclude false positives (see, e.g., SuperWASP – Collier Cameron et al. 2007; Kane et al. 2008; OGLE – Pont et al. 2005; CoRoT – Cabrera et al. 2009; Deeg et al. 2009; Moutou et al. 2009). After careful light curve analysis, these generally aim for a candidate prioritization, which is used to schedule further observations with increasing order of complexity. The follow-up process

includes photometry at higher angular resolution to exclude background eclipsing binaries with a higher confidence and an initial spectral classification which allows rejection of large host stars. For the candidates presented in this work, these procedures are described in detail in Chapter 8. If all tests are passed successfully, then RV measurements are obtained for the best and most interesting candidates in order to finally confirm the planetary nature and to determine the planetary mass.

Additional Characterization for Transiting Exoplanets

In addition to the important density estimation, transiting planets uniquely provide a multitude of additional characterization possibilities which are not available for other planets. Most importantly, the occultations allow the disentanglement of the planetary signal from the starlight and, thus, a spectrum of the planet can be obtained (e.g., Burrows et al. 2008). Its analysis can yield important information about the planet, such as its atmospheric temperature or composition.

Further examples include the measurement of the angle between the stellar rotation axis and the orbit using the Rossiter-McLaughlin effect (e.g., Triaud et al. 2010), or the possibility to detect additional bodies in the system through Transit Timing Variations (TTV; see, e.g., Heyl and Gladman 2007).

Therefore, despite the challenges of the method such as its need for a rare geometric alignment, the search for transiting systems is continuing with unwaning interest.

2.3 Other Indirect Methods

Astrometry

The measurement of celestial positions is termed *astrometry*. If a star has a planet, it revolves periodically around the common barycenter (Figure 2.1). Astrometry aims to detect this movement by obtaining precise positions during different phases of the orbit. In comparison to the RV method (Section 2.1), astrometry also probes the stellar reflex motion, but perpendicular to the line of sight. With measurements in the two angular dimensions, it is – in contrast to the RV method – in principle able to determine the orbital inclination and planetary mass.

The astrometric signature is given by Perryman (2011) as

$$\alpha \cong \left(\frac{M_p}{M_\star}\right)\left(\frac{a}{1\,\mathrm{au}}\right)\left(\frac{d}{1\,\mathrm{pc}}\right)^{-1}\mathrm{arcsec}, \tag{2.14}$$

whereby a is the planetary semi-major axis, and d denotes the distance to the star in parsec. The value α is the stellar semi-major axis projected onto the celestial sphere, i.e., it determines the maximum signal (for inclination $i = 0$) that can be expected in astrometric measurements for a given star-planet configuration.

As Equation (2.14) shows, the astrometric method is most sensitive to heavy planets in large orbits around nearby stars. However, the amplitude is typically very low ($\alpha \ll 1''/1000 \equiv 1\,\mathrm{mas}$) for currently known exoplanets. As an example, the Sun shows an apparent angular orbit of $\alpha = 0.5\,\mathrm{mas}$ when seen from 10 pc distance.

Since the achievable precision is only starting to enter this range, no confident extrasolar planet detection has been announced via astrometry up to now. With a precision of $\sim 1\,\mathrm{mas}$, the Hipparcos mission (ESA 1997) and the Fine Guidance

Sensor on the Hubble Space Telescope (HST; Bradley et al. 1991; Benedict et al. 1994) provide the most accurate astrometry available to date. The latter has been used successfully for dedicated observations of exoplanets, yielding either a confirmation of the planetary nature (e.g., GJ 876b, a $1.89\,M_J$ planet with a signal of $\alpha = (0.25 \pm 0.06)$ mas; Benedict et al. 2002), or a rejection because the secondary object is too heavy to be a planet (e.g., the brown dwarf companion to HD 136118; Martioli et al. 2010). A breakthrough could come with the next-generation space mission Gaia (Perryman et al. 2001; Lindegren 2010): With an astrometric precision of 8 µas, it is expected to find several thousands of giant planets with orbital separations up to 3–4 au within 200 pc distance (Casertano et al. 2008).

Microlensing

The microlensing method uses an effect of general relativity to detect extrasolar planets. Since matter changes the geometry of spacetime, light passing a massive body is deflected. In astronomy, this phenomenon can be observed if two objects are aligned almost perfectly along the line of sight. The light of the background object (source) can then be amplified through the gravitational perturbation of the foreground object (lens). The effect is called microlensing if both objects cannot be spatially resolved, but only be detected indirectly through the magnification.

Since the configuration of source, lens, and observer changes due to their relative motion, the magnification event can be sampled with photometric time series. The careful analysis of the light curve thereby forms the basic principle for detecting extrasolar planets: If a planet is accompanying the foreground star, it can cause additional lensing events (see, e.g., Wambsganss 2011).

Search projects monitor a very large number of stars and focus on dense regions in the sky, e.g., the galactic bulge, because the probability for observing a single microlensing event is in the order of 10^{-8} (Perryman 2011). The necessity to cover a lensing event as continuously as possible by photometric measurements sets further observational constraints. However, the two large microlensing surveys MOA (Abe et al. 1997) and OGLE (Udalski 2003) have meanwhile detected a total of 16 extrasolar planets.[2]

Main limitations of the method are that the observed systems are typically rather distant (few kpc), and the uniqueness of the geometry does not allow for any additional measurements. In spite of that, microlensing surveys exhibit several advantages over other methods: Microlensing can more easily detect small planets (Earth mass and below), or so-called "floating planets" which are not bound to any star (Sumi et al. 2011). Furthermore, the method is most sensitive to orbital distances of 0.6–1.6 au, i.e., including the interesting habitable zone of main sequence stars. It is also not biased towards a particular type of host star, so that the surveyed stellar sample can usually be considered more representative compared to other methods (e.g., Gould et al. 2010). However, the statistics drawn from microlensing surveys – such as the recent analysis of planetary abundance by Cassan et al. (2012) – still involve rather large uncertainties due to the small number of detected planets.

[2] *www.exoplanet.eu* (Schneider et al. 2011), state of 21th November 2012

3 Transit Search Projects

Since the first discovery of an extrasolar planet, numerous projects have been set up for detecting transiting planetary systems using large photometric surveys.

Ground-based projects have mainly developed two different strategies to meet the requirements of monitoring as many stars as possible with a high photometric precision. One is to survey bright stars in relatively large fields of $\sim 50\,\mathrm{deg}^2$ (e.g., SuperWASP, Pollacco et al. 2006; HAT, Bakos et al. 2002, 2004; XO, McCullough et al. 2005), while the other aims to monitor fainter stars in small fields of $\sim 1\,\mathrm{deg}^2$ (e.g., OGLE, Udalski et al. 2002a; Lupus, Bayliss et al. 2009). Projects targeting large fields have been more successful in planet detections. In particular, they survey brighter host stars which enable better follow-up confirmation and planetary characterization.

Figure 3.1: Transit search with BEST II in the southern sky.

Transit searches from space generally yield superior results to ground-based projects for two main reasons. First, the absence of atmospheric disturbances increases the achievable photometric precision and thus allows the detection of significantly smaller planets. Second, observations from space can yield largely uninterrupted time series, so that the range of detected planets is extended towards larger orbits.

A first transit search from space was performed using the HST for seven days in 2004 (Sahu et al. 2006). Two years later, CoRoT was launched as the first space mission with transit search as one of its prime scientific objectives. In 2009, CoRoT was followed by a second-generation transit search mission, the Kepler space-

craft (Borucki et al. 2010). Several additional space missions are currently being planned and proposed. They focus in particular on the detection and characterization of small planets around bright targets (e.g., PLATO, Catala 2009; TESS, Deming et al. 2009; THESIS, Swain et al. 2010; EChO, Tinetti et al. 2012).

This chapter introduces three transit search projects that are covered in this thesis, namely CoRoT (Section 3.1), BEST/BEST II (Section 3.2), and ASTEP (Section 3.3). For a comprehensive overview of past, present, and future transit search projects, see, e.g., Perryman (2011).

3.1 CoRoT

The CoRoT space mission (Baglin et al. 2006) has two main scientific objectives: To measure the oscillations of stars (termed *asteroseismology*), and to search for transiting extrasolar planets. It is led by the French Space Agency (CNES) in collaboration with several international partners, including DLR.

CoRoT was launched on 27th December 2006 into a polar orbit, which constrains the observations to two large *"eyes"* in the sky. Fields are either monitored in *Long Runs* (LR, 60–150 days) or *Short Runs* (SR, 20–60 days). The nominal duration of CoRoT was 2.5 years, but the mission has already been extended twice; it is now foreseen to operate until 2015. By 30th April 2012, 155,303 stars have been observed in 23 fields.

The telescope has an aperture of 27 cm, covers a FOV of $2\overset{\circ}{.}70 \times 3\overset{\circ}{.}05$, and is equipped with four 2k × 2k Pixel CCDs (two for asteroseismology and two for transit search) to perform high-precision photometric measurements at optical wavelengths (Bodin 2006). Since March 2009, only one CCD is operational in each science topic. In the exoplanet channel, starlight passes a bi-prism so that light curves are obtained in three different spectral bands. This additional color information can be used to distinguish the nearly achromatic transit signal from color-dependent stellar fluctuations (Barge et al. 2006).

So far, the scientific results of the CoRoT mission have already made an invaluable contribution to both of its main fields of research:

In **asteroseismology**, CoRoT can measure stellar oscillations on the ppm level. For the first time, this allowed the precise characterization of solar-type oscillations on stars other than the Sun (e.g., Appourchaux et al. 2008; Michel et al. 2008). It also initiated extensive research through its capability to study different types of stars, e.g., red giants (e.g., De Ridder et al. 2009; Baudin et al. 2011), massive stars (e.g., Belkacem et al. 2009; Degroote et al. 2010a, b), or δ Scuti pulsators (e.g., Poretti et al. 2009, 2010). Furthermore, an asteroseismic analysis of stars accompanied by a planet yielded improved parameters for both the host star and its companion in two cases (HD 46375, Gaulme et al. 2010; HD 52265, Ballot et al. 2011).

In the **exoplanet field**, CoRoT has discovered 26 confirmed transiting planets to date (two of them detected by RV follow-up) and one brown dwarf. These include some very interesting objects which have been subject to extensive further characterization and theoretical studies. For example, the ultradense planet CoRoT-20b ($r_p = 0.84\,r_J$, $M_p = 4.24\,M_J$, Deleuil et al. 2012) is currently challenging planetary

formation models. With a small radius of $r_p = (1.68 \pm 0.09)\, r_\oplus$, CoRoT-7b was the first transiting Super-Earth and set a new benchmark for photometric detections (Léger et al. 2009; Queloz et al. 2009; Hatzes et al. 2011).
Furthermore, CoRoT's precision proved to be sufficient to measure secondary eclipses and phase variations in the optical (Alonso et al. 2009; Snellen et al. 2009), which can be used to constrain the planetary albedo and heat distribution. The long duty cycle and photometric precision achievable from space also allowed the detection of transiting planets with very long orbital periods (CoRoT-9b with 95 days, Deeg et al. 2010), and planets around very active stars like CoRoT-2 (Alonso et al. 2008). The careful analysis of such light curves cannot only yield valuable information about the planet itself, but also about its interaction with the star (for a recent review, see Lanza 2011) and the stellar surface (e.g., Fröhlich et al. 2009; Wolter et al. 2009; Huber et al. 2010; Silva-Valio et al. 2010).

3.2 Berlin Exoplanet Search Telescopes (BEST/BEST II)

The *Berlin Exoplanet Search Telescopes* BEST (Rauer et al. 2004) and BEST II are two small aperture telescopes that are operated by the Institute of Planetary Research at DLR Berlin. The specifications of both are summarized in Table 3.1.

Their primary science objective is to support CoRoT (Section 3.1) by characterizing the stellar variability in its target fields. Although the space mission provides a much better photometric precision, the confirmation of planetary candidates generally requires additional measurements from ground. In particular, the relatively large CoRoT PSF of $35'' \times 23''$ (Deeg et al. 2009) can include unresolved background stars that are the most common source for false positive detections (see also Section 2.2). BEST II can solve some of these cases through separating the light of individual objects. Both BEST telescopes are part of a broad effort of photometric follow-up for CoRoT planetary candidates as described by Deeg et al. (2009).

Until August 2011, BEST and BEST II light curves have been analyzed as part of the follow-up process of 253 CoRoT planetary candidates (109 with BEST and 144 with BEST II; Titz-Weider, DLR internal report 2011). Out of these, eight could

Table 3.1: Technical specifications of BEST and BEST II.

	BEST		BEST II	
	Main Telescope	Guider	Main Telescope	Guider
Telescope	Schmidt-Cassegrain	Lichtenknecker	Takahashi BRC-250	TEC APO 140 ED
— Aperture	195 mm	90 mm	250 mm	140 mm
— Focal Ratio	$f/2.7$	$f/10$	$f/5$	$f/7$
Instrument	Apogee AP 10	SBIG ST-4	[1] FLI IMG-16801E2 [2] FLI PL16801-1	SBIG ST-1603 ME
— CCD Size	2048×2048	192×164	4096×4096	1530×1020
— Pixel Size	$14\,\mu m \times 14\,\mu m$	$14\,\mu m \times 16\,\mu m$	$9\,\mu m \times 9\,\mu m$	$9\,\mu m \times 9\,\mu m$
— Pixel Scale	$5\farcs5$/Px	$1\farcs4$–$1\farcs6$/Px	$1\farcs5$/Px	$1\farcs9$/Px
— Field of View	$3\fdg1 \times 3\fdg1$	$4\farcm5 \times 4\farcm5$	$1\fdg7 \times 1\fdg7$	$0\fdg8 \times 0\fdg5$
Mount	M100B German equatorial		GM4000 German equatorial (10micron)	
Location	Observatoire de Haute-Provence E05°42′44″ N43°55′54″ (650 m)		Observatorio Cerro Armazones W70°11′35″ S24°35′24″ (2840 m)	

[1] until 07/2011
[2] from 08/2011 – For details on the main BEST II instrument, see also Appendix A.1.

be rejected because they were found to be contaminated by a close eclipsing binary or variable star. For two candidates, the small signal was confirmed on target. The rest either showed no contamination within the angular and photometric resolution of BEST/BEST II or were not observed during expected transit times (in particular when measurements had been obtained prior to the satellite). Furthermore, transits of the two planets CoRoT-1b and CoRoT-2b were observed by BEST before CoRoT detected them (Rauer et al. 2010). Although the limited duty cycle of BEST was not sufficient to directly detect them in the data, the light curves were readily available to confirm the detection.

In addition, each BEST/BEST II data set is analyzed for stellar variability. In total, more than 300,000 light curves have already been investigated (not including this work; see Chapter 9 and Table 9.5 for a comparison). The results are regularly announced to the scientific community and have led to the detection of several hundred variable stars (Karoff et al. 2007; Kabath et al. 2007, 2008, 2009a, b; Pasternacki et al. 2011).

BEST

The first BEST system was installed at the Thüringer Landessternwarte Tautenburg (TLS), Germany, in 2002. In 2004, it was moved to the Observatoire de Haute-Provence (OHP) in France with improved weather conditions in order to increase the observational duty cycle. While the commissioning phase in Tautenburg focused on transit search (Rauer et al. 2004; Voss 2006), the observation of CoRoT fields was started at OHP (Kabath 2009).

BEST is described in detail by Rauer et al. (2004) and Voss (2006). It consists of a 19.5 cm aperture Schmidt telescope and a small refractor for guiding. The main instrument comprises a CCD with 2k×2k Pixel that covers a FOV of $3.^{\circ}1 \times 3.^{\circ}1$, resulting in a scale of $5.''5$/Px. An observer can operate the system from Berlin.

BEST II

A second telescope, BEST II (Figure 3.1), was installed in the Chilean Atacama desert in 2007. It is located at the Observatorio Cerro Armazones (OCA, Figure 3.2), which is operated by the Astronomical Institute of the Ruhr-Universität Bochum. The OCA is located 22 km away from the large ESO (European Southern Observatory) facilities at Cerro Paranal, and in the immediate vicinity to Cerro Armazones. The latter has recently been selected in an extensive site testing campaign for the future 40 m-class European Extremely Large Telescope (E-ELT, ESO 2010).

The Chilean location has much more favorable conditions for finding extrasolar planets compared to BEST. First, the duty cycle is significantly increased and thus allows for a better time coverage: Disregarding technical or planned downtime, observations with BEST II yielded a duty cycle of 66% in the period from 2009–2012 (see Section 4.1), while BEST typically reached a value of 40% (Kabath 2009). Second, the photometric conditions in the Chilean desert are excellent, allowing mmag-precision over a whole observing season (see Section 4.3).

Figure 3.2: BEST II in the Chilean Atacama. The Observatorio Cerro Armazones sits on the smaller mountain on the left (Cerro Murphy, 2840 m), while Cerro Armazones rises 3060 m high in the background. The basecamp facilities can be seen at the lower right corner of the picture.

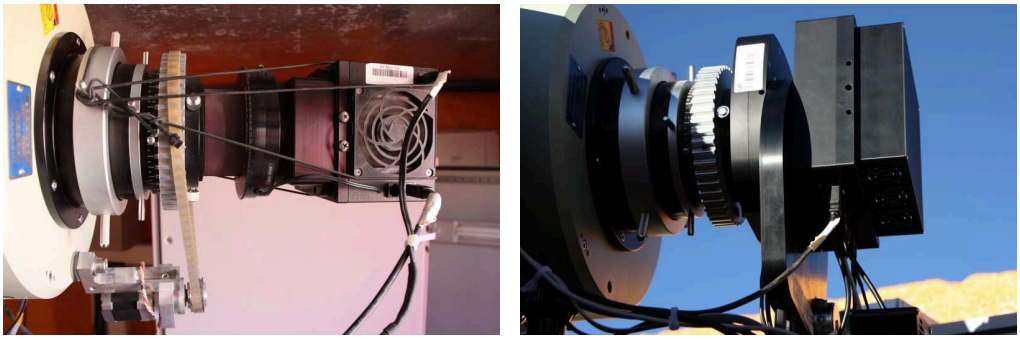

(a) First generation (until July 2011) (b) Second generation (since August 2011)

Figure 3.3: Main BEST II instrumentation.

BEST II consists of a 25 cm-aperture Baker-Ritchey-Chrétien reflector and a 14 cm-aperture guiding refractor. The main instrument is a 4k×4k CCD by Finger Lakes Instrumentation with a pixel scale of $1\farcs5$/Px and a FOV of $1\fdg7 \times 1\fdg7$ (Table 3.1). The system and its implementation phase are described in detail by Kabath (2009).

The instrumentation was changed by myself during a maintenance visit from 19th July to 4th August 2011 (Figure 3.3): While BEST II observed without filter and a fixed focal length in its initial setup, the new instrument contains a CCD with a shorter readout time, a five-position filter wheel (FLI CFW-4-5) and a focus unit (FLI ATLAS). The technical performance of the new instrument and the advantages for scientific observations are described in Appendix A.1; however, all data and results presented in this thesis have been obtained with the original camera.

The pointing stability of the telescope is very good, i.e., stars close to the edge of the FOV are also covered well over a whole observing season. Within this work, it was be optimized from an initial variation of several arc minutes ($286\,\mathrm{Px} \equiv 7\farcm15$) down to ~ 10–$15''$. The pointing improvement is described in Appendix A.2.

Observations are performed in a robotic mode and require a minimum of user interaction. It is limited to the preparation of an observing script, the assessment of the local weather situation using forecasts from Paranal and life data from an on-site weather station, and a remotely controlled opening and closing of the roof. The system is very stable and usually requires only one or two maintenance visits per year. Due to a small communication bandwidth, such visits were also necessary to transport the observational data on hard disks to Europe. This situation changed with the establishing of a fiber link connection in October 2010, after which all data can be transfered through the network. An overview of the observations obtained with BEST II will be presented in Chapter 4.

3.3 ASTEP

The *Antarctic Search for Transiting ExoPlanets (ASTEP)* project comprises two small telescopes at Dome C, Antarctica. Its main scientific objectives are first, to assess the photometric quality of Dome C and second, to search for transiting planets (Fressin et al. 2006; for the motivation to perform astronomy from Antarctica, see also Section 1.3). It is operated by an international consortium under the responsibility of the Observatoire de la Côte d'Azur and the Laboratoire Universitaire d'Astrophysique de Nice. Figure 3.4 shows the two ASTEP telescopes in Antarctica.

Figure 3.4: ASTEP at Dome C, Antarctica. The dome in the foreground houses ASTEP 400, while the small box to its left contains its smaller predecessor ASTEP South. Further AstroConcordia instruments are operated from the two wooden mounts on the left, while the Concordia station itself can be seen in the background on the right. (*Copyright E. Aristidi (winterover 2011); reprinted with permission.)*

ASTEP South

ASTEP South (Crouzet et al. 2010) is a small telescope with an aperture of 10 cm that has been operating at Dome C since 2008. Its design is as simple as possible without moving parts. It is maintained in a thermalized enclosure on a fixed mount and constantly points at the South Pole. The instrument is a 4k × 4k Pixel CCD (FLI ProLine 16801, i.e., the same as the new camera for BEST II) that covers a FOV

of $3\overset{\circ}{.}88 \times 3\overset{\circ}{.}88$ with an angular resolution of $3\overset{''}{.}41$/Px. A long pass filter is used to exclude wavelengths $\lambda \lesssim 600\,\mathrm{nm}$.

A preliminary analysis of the data set from winter 2008 yielded initial insights into the photometric quality of Dome C. Crouzet et al. (2010) showed that the Sun affects the photometric measurements if it rises higher than $-13°$ above the horizon, and that influences due to the Moon or aurorae are negligible. Excellent weather conditions were reported for 56–68% of the winter time, which yields a significantly increased detection efficiency estimate compared to temperate sites such as La Silla. The detailed analysis of the ASTEP South observations including the search for transiting planets is ongoing (Crouzet et al. 2012).

Figure 3.5: The ASTEP 400 telescope covered with ice after a period of high humidity. *(Copyright D. Mekarnia (winterover 2011); reprinted with permission.)*

ASTEP 400

ASTEP 400 (Fressin et al. 2006; Daban et al. 2010; Crouzet et al. 2011) is at the heart of the project. It has an aperture of 40 cm and is being operated on an Astrophysics AP3600 mount that was modified to operate down to $-80°$C (Figure 3.5). In order to stabilize the optical path and to allow for all electronic devices to operate properly, all focal instrumentation is kept in a thermalized enclosure (Figure 3.6). It contains two CCDs, correction lenses, and a dichroic mirror. The latter is used to forward the blue part ($\lambda \lesssim 550\,\mathrm{nm}$) of the light beam to the guiding camera (SBIG ST402M), while the red part ($\lambda \gtrsim 550\,\mathrm{nm}$) is reflected to the main focus with the science camera. It is the same instrument as used for ASTEP South and BEST II (FLI ProLine 16801). The 4k × 4k Pixel CCD covers a FOV of $1\overset{\circ}{.}0 \times 1\overset{\circ}{.}0$, thus providing an angular resolution of $0\overset{''}{.}9$/Px.

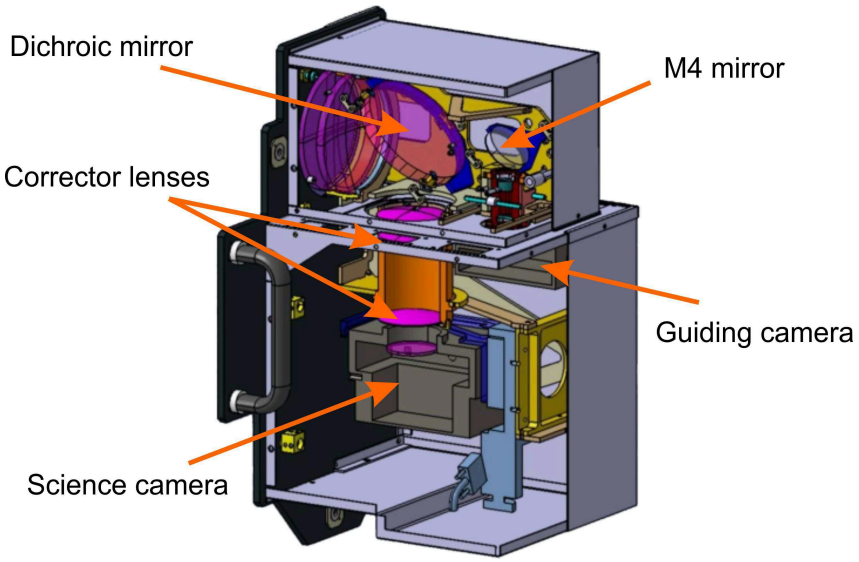

Figure 3.6: Focal box of ASTEP 400, containing the two CCDs. *(Copyright Daban et al. (2010); reprinted with permission of the authors.)*

The ASTEP 400 telescope was installed at Dome C during the summer campaign 2009/2010 and achieved first astronomical light on 25th March 2010. While the first half of the winter 2010 was interrupted by some technical problems with the mount/guiding and icing on the main mirror, observations ran rather smoothly during the second half (June to September). The scientific program of the first season consisted mainly of

- continuous monitoring of five subsequent target fields (ASTEP-Exo1–Exo5) which had been selected for transit search and
- long time series observations of the two transiting planets WASP-18b and WASP-19b.

The above was complemented by shorter observations of four M dwarfs for transit search and the follow-up of a few microlensing alerts. The second season in 2011 focused on ten target fields for transit search (including the ASTEP-Exo5 field already observed in 2010), which were monitored for periods between 3 and 15 days (Aristidi and Mekarnia 2011).

Since the amount of data acquired exceeds the communication bandwidth of the Concordia base (e.g., 7.5 TB of ASTEP 400 data in 2011 compared to a bandwidth of 1 MB per day and scientist), the bulk of data must be transported to Europe on hard disk. Thus, the full data analysis typically starts at least half a year after the observations.

In 2010, two of the ASTEP target fields and the planet WASP-18b were observed with ASTEP 400 and BEST II together. These data were analyzed within this work in order to compare the two sites regarding the potential for transit search and to assess the feasibility of such joint observations. The data reduction and scientific analysis will be presented in Chapter 10.

Part II

Observations and Methods

4 BEST II Observations

This chapter describes the current observing strategy of BEST II and characterizes new target fields that were selected and monitored for transit search.

The first Section 4.1 gives an overview of the data obtained with BEST II from 2007–2011. This includes observations that were taken explicitly for the purposes of this work (such as transit search or joint observations with ASTEP), as well as measurements obtained in other contexts (such as observations of known planets). While the telescope maintenance and planning of observations formed an integral part of this work, observations themselves have been distributed equally amongst a team of observers[1].

Figure 4.1: First light of the new BEST II camera with filters (see technical description in Section 3.2 and Appendix A.1). The image shows a color-composite of the Lagoon nebula (M8), a giant interstellar cloud in Sagittarius. It is stacked from 44 individual frames taken in B, V and R filters during the nights of 25th and 29th July 2011. The total exposure time is 382 s.

Section 4.2 introduces the BEST II target fields F17–F19 that have been selected and observed for the purpose of transit search. These are characterized further concerning their photometric quality (Section 4.3) and the expected detection yield of transiting planets (Section 4.4). Finally, Section 4.5 summarizes this chapter.

[1] J. Cabrera, Sz. Csizmadia, P. Eigmüller (since August 2011), T. Fruth, P. Kabath (until June 2009), and T. Pasternacki

4.1 Overview

BEST II was built to support the CoRoT mission with ground-based observations (see Section 3.2), which is why the observing strategy is strongly focused on CoRoT target fields. However, since there exists a reasonable amount of time between CoRoT observations, the BEST II schedule can be assigned additional scientific targets.

The BEST II project obtained scientific data during more than 500 nights within its first five years of operation, i.e., from 2007 to 2011. Observations have been performed about every second night when the system is fully operational (Figure 4.2). However, larger technical problems such as the breakdown of the main PC in summer 2008 or of the uninterruptible power supply in winter 2010/11 required maintenance visits and therefore caused longer observing breaks.

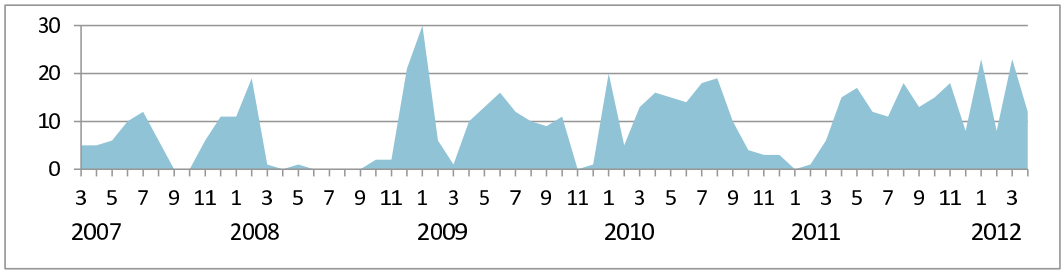

Figure 4.2: Number of nights observed with BEST II (per month).

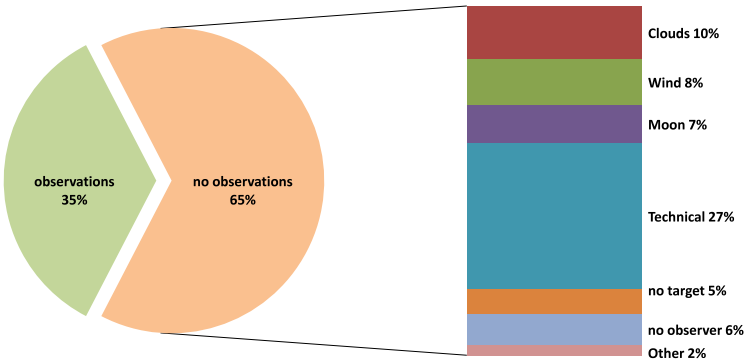

Figure 4.3: Usage of BEST II, compiled from manual entries in the observer's log for 1,051 consecutive nights (21/04/2009 to 30/04/2012). The conditions are assessed on a nightly basis by the observer; normally excluded are three nights around full Moon, nights with clouds visible at the local sky at dusk, or with wind speeds larger than 15 m/s.

Since early 2009, an improved nightly log is kept that includes both the observed target fields as well as information about nights in which no observations could be obtained. In average, BEST II acquired data in about every third night within this period. As can be seen in Figure 4.3, technical problems are the dominant reason for not observing. Thereafter, the main environmental limitations are given by strong winds and clouds, together preventing observations for about two months per year in total.

Table 4.1: Field observations obtained with BEST II during the years 2007–2011

Field	Coordinates (J2000.0) α	δ	Season	#Nights obs./phot.	ΔT	#Frames	#Stars Total	$\sigma \leq 0.01$
LRc02ax†	$18^h41^m02^s$	$+07°12'54''$	16/07/07–21/08/07	20 / 20	240 s	373	43,616	660
LRc02by†	$18^h43^m33^s$	$+05°59'53''$	16/07/07–21/08/07	17 / 17	240 s	232	54,603	2,130
LRa02a *(v5)*	$06^h50^m46^s$	$+03°59'31''$	29/11/07–28/02/08	41 / 41	240 s	765	44,124	2,512
LRa02b *(v4)*	$06^h51^m14^s$	$+05°26'16''$	29/11/07–28/02/08	40 / 40	240 s	759	76,466	3,004
SRa01a	$06^h40^m27^s$	$+09°40'00''$	06/12/08–10/02/09	50 / 48	120 s	1,384	41,119	628
SRa01b	$06^h40^m38^s$	$+08°21'00''$	06/12/08–10/02/09	47 / 45	120 s	1,183	54,522	668
SRc02	$18^h59^m47^s$	$-03°08'12''$	04/05/09–27/07/09	32 / 32	120 s	1,288	86,944	3,751
F17	$14^h24^m29^s$	$-54°07'20''$	20/04/09–22/07/09	40 / 39	120 s	2,259	68,317	3,700
F18	$22^h52^m00^s$	$-44°12'00''$	19/08/09–27/10/09	28 / 27	120 s	2,266	13,551	448
F19 *(v2)*	$16^h26^m00^s$	$-56°12'00''$	24/03/10–21/09/10	70 / 62	300 s	2,855	127,202	11,681
ASTEP-Exo2	$16^h04^m32^s$	$-65°50'35''$	29/07/10–04/08/10	6 / 6	120 s	391	90,330	8,229
ASTEP-Exo3	$15^h46^m11^s$	$-64°53'33''$	05/08/10–21/08/10	11 / 11	10 s	360	29,225	206
				12 / 12	90 s	437	134,222	6,436

† Due to pointing problems, field LRc02 was split into several subfields. LRc02ax and LRc02by refer to the largest overlap area of individual frames for each of the two directions (see Fruth (2008) for details).

Notes. Shown are the center coordinates, the time range between the first and last observing night, the number of observed/photometric nights within this range, the exposure time ΔT, the number of acquired frames, and the number of total/low-noise light curves for each target field.

Field observations obtained with BEST II since its commissioning in 2007 until the end of 2011 are shown in Table 4.1. The four most important scientific projects are the follow-up observations of CoRoT, the planet surveys on BEST II target fields, joint observations with the ASTEP project, and the observations of known transiting planets, which are all briefly described in the following text.

- **CoRoT**

  The mode of ground-based support changed for BEST/BEST II as the CoRoT mission evolved. During the initial phase of the project, most target fields were selected well in advance of the CoRoT observations. Hence, the strategy of BEST and BEST II was to observe the CoRoT fields at least one year before the satellite's pointings. The data were analyzed and could immediately be checked for candidates once the first satellite observations became available. Furthermore, catalogs of stellar variability were published for several CoRoT fields based upon BEST/BEST II observations (Karoff et al. 2007; Kabath et al. 2007, 2008, 2009a, b).

  Since 2009/2010, the coordinates of target fields are selected on a shorter notice, so that they could not be observed with BEST II prior to the satellite. Photometric measurements are thus scheduled immediately after CoRoT raises an alarm on an individual target. Such observations usually cover the full eclipse event as indicated by CoRoT, plus a reasonable period of time before and after.

  Altogether, BEST II forms a valuable part of the CoRoT follow-up process (Deeg et al. 2009). In addition to the rejection of several transit candidates before they would have been observed spectroscopically (see summary in Section 3.2), BEST II data helped in the confirmation process of the planets CoRoT-17b (Csizmadia et al. 2011) and CoRoT-24b (Alonso et al. 2012).

- **BEST II Field Survey**

  Since, by 2009 the changed BEST II observing strategy of CoRoT targets increased the number of otherwise allocatable nights significantly, it was decided

to perform an additional transit survey. The three fields F17–F19 selected within this work have been observed for a total of 138 nights in 2009/2010.

- **ASTEP**

  The purpose of joint BEST II observations with the ASTEP project is to compare the photometric quality of these two excellent sites and to extend the phase coverage of transit searches. The planet WASP-18b and two fields selected by the ASTEP team for transit search have been observed by BEST II for a total of 37 nights in 2010.

- **Known Transits**

  Known transiting exoplanets are observed with BEST II for the following reasons: First, the performance of the whole system can be judged by evaluating the quality of a real transit light curve, and its limitations – e.g., the observable magnitude range – can be assessed. Second, deviations from the predicted transit timings could be measured and then be used to draw conclusions about a possible third companion in the system (e.g., Agol et al. 2005; Holman and Murray 2005). Third, from observations in different filters, the planetary parameters can be improved (e.g., Knutson et al. 2007), and conclusions can be drawn about the host star's atmosphere from the shape of the transit in different colors (e.g., Howarth 2011).

  Similar to the CoRoT on/off observations, a full transit is usually observed together with a few hours spend on the target before and after the predicted event. Meanwhile, BEST II has acquired a large photometric data set on such planets; a first analysis regarding their transit timing variations has recently been presented by Stilz (2012).

This thesis focuses on the BEST II transit survey and joint observations with ASTEP. The selection of BEST II target fields was solely obtained in the framework of this thesis and is described together with the observations and their photometric quality in Sections 4.2 and 4.3. A comparison of BEST II observations with ASTEP data is presented in Chapter 10.

4.2 BEST II Target Fields F17–F19

4.2.1 Selection

The process of target field selection evolved during the lifetime of the BEST/BEST II project. For BEST, 16 target fields, F1–F16, were proposed by Voss (2006), from which F2, F8, and F15 were observed extensively from both the TLS and OHP. The fields are separated in right ascension such that at least one is well observable during each season. They have been selected manually with the aid of star counts from the SIMBAD database and checked not to contain a large number of galaxies. Since they were also required to culminate close to zenith, the resulting declinations of $\delta = 50° \pm 2°$ make them unsuitable for observations from Chile.

In this work, a quantitative field selection was implemented to provide targets for the new transit survey with BEST II. Albeit devised for BEST II, the observing site and instrumental configuration enter the simulation only as parameters, so that it could easily be adapted to other projects.

For ground-based surveys, the detection efficiency of transit searches is especially sensitive to the following three criteria:

- **Duty Cycle.** The amount of time that a target field is visible on the night sky sets the astronomical limit on the duty cycle. Together with target-independent issues such as bad weather or technical problems, it defines the window function of any observational campaign.
- **Photometric Quality.** Transits can only be detected in high-precision photometric time series. For bright stars, one of the main error sources is atmospheric extinction. As the sky position of a target determines its time-varying airmass X, different fields show different photometric quality.
- **Number of dwarf stars.** The number of observed stars should be maximized in order to yield a high detection probability (cf. Equation (2.11)). However, more overlapping PSFs increase the number of false positive transit signals in very dense target fields (depending on the spatial resolution), which must be balanced against the need for quantity. Furthermore, planets transiting large stars – such as giants and early-type dwarfs – produce a very small signal that is not detectable by ground-based surveys, so that these are usually not considered suitable targets.

The simulation used in the following aims at a quantitative assessment of these three parameters: After the observing time T_1, photometric quality (through mean airmass $\overline{X}$) and number N_{st} of suitable dwarf stars are estimated, they are weighted against each other in order to compare a single quantity $\Theta\left(T_1, \overline{X}, N_{\mathrm{st}}\right)$ for different pointings. The procedure is described in detail in Appendix B.

The selection itself is subject to some input parameters; most important are the observing site and the time range for which observations should be obtained. A common example would be to find the optimal target field for an upcoming observing season at a given site. This then translates into the task of finding the field *longest* observable but with the *smallest airmass* within the given period of time and with a *maximum number* of suitable target stars.

F17 and F18

A first transit survey was planned for BEST II in 2009. Since unallocated time was available at rather short notice, the first two target fields had to be selected using already available procedures. For that, the times of planned observations (April/May for F17 and August/September for F18) were used to calculate possible observing times and mean airmasses for fields throughout the sky. The resulting map of weighted observing times $\Theta\left(T_1, \overline{X}, 1\right)$ (see Figure 4.4) was then used to constrain the coordinate ranges to fields visible longest during these periods with a minimum average airmass. F17 and F18 were then selected in a similar way as in Voss (2006): A star catalog was reviewed around the maxima of Figure 4.4 in order to exclude

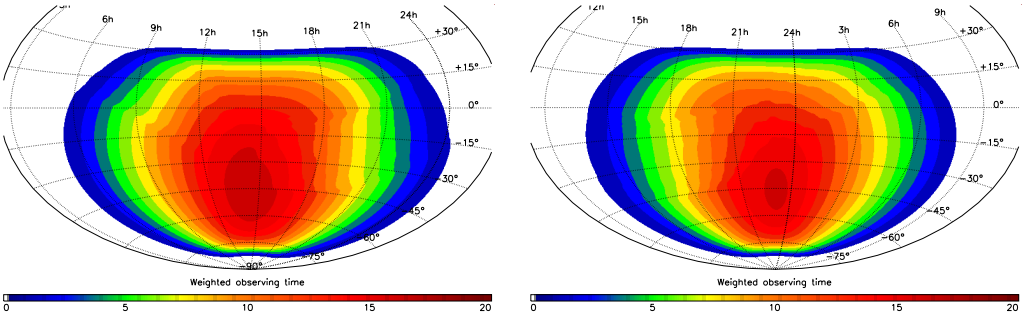

(a) F17 (01/04–31/05/2009) (b) F18 (05/08–04/10/2009)

Figure 4.4: Weighted observing time $\Theta\left(T_1, \overline{X}, 1\right)$ for two planned seasons of field observations in 2009 (Equation (B.7) without the dependence on stellar density, i.e., with $N_{\mathrm{st}} = 1$).

pointings with very bright stars ($V < 6\,\mathrm{mag}$) or a large number of contaminating objects such as nebulae or galaxies. After a night of test observations, the field coordinates were then fixed (Table 4.1).

F19

After the first observations of F17 and F18 had been reduced, it was recognized that both fields differed significantly in the numbers of stars suitable for transit search. Although the photometric quality is well comparable, only 448 stars were recorded in F18 with a precision better than 1%, compared to 3,700 in F17 (Table 4.1). This difference of almost one order of magnitude raised the need for a more quantitative consideration of stellar densities for the BEST II field selection.

Thus, the simulation of duty cycle and airmasses was complemented by including an approximation of the number of suitable target stars for the BEST II transit search (Appendix B.2). This simulation was first used to select a new field for an observing season lasting from March to August 2010. Figure 4.5 illustrates the selection process: First, the number of *suitable* target stars (Figure 4.5a) was estimated for each direction in the sky from the target count in the Besançon input catalog by subtracting contaminated stars (Figure 4.5b). Second, observing times were weighted against the mean airmass of possible fields (Figure 4.5c) and combined with the suitable target count (Figure 4.5a) to the weighting function $\Theta\left(T_1, \overline{X}, N_{\mathrm{st}}\right)$ (Equation (B.7), Figure 4.6d). Third, this map was searched for maxima indicating well observable fields with a large number of target stars. Since significant observing time was available for the beginning of the planned season, the expanded area shown in Figure 4.5e was favored over regions with similar values of Θ but with higher right ascension. Fourth, all local maxima in Figure 4.5e were reviewed using a real star catalog. The same rejection criteria as already applied for fields F1–F18 (i.e., no bright stars, few nebulae or galaxies) left two promising pointings (white squares in Figure 4.5e) which were subject to test observations with BEST II. Finally, F19 was selected because a first count yielded about 10% more stars than in the second test field.

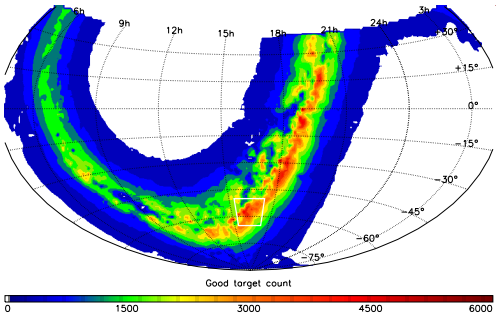

(a) Suitable targets $N_{\mathrm{st}}(\alpha, \delta)$

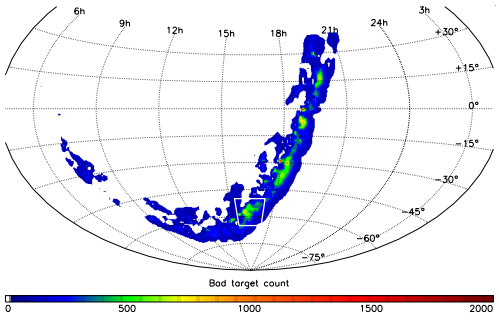

(b) Contaminated targets $N_{\mathrm{ct}}(\alpha, \delta)$

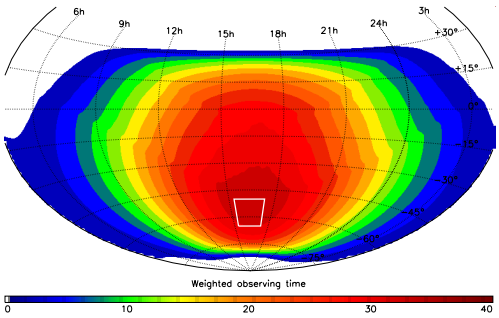

(c) Weighted observing time $\Theta\left(T_1, \overline{X}, 1\right)$

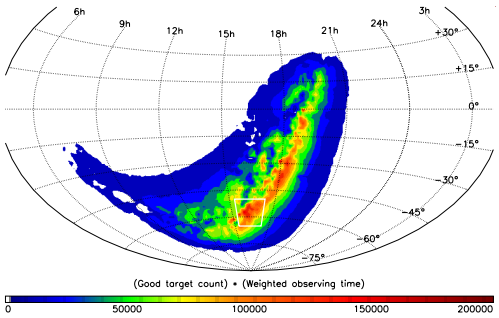

(d) Weighting function $\Theta\left(T_1, \overline{X}, N_{\mathrm{st}}\right)$

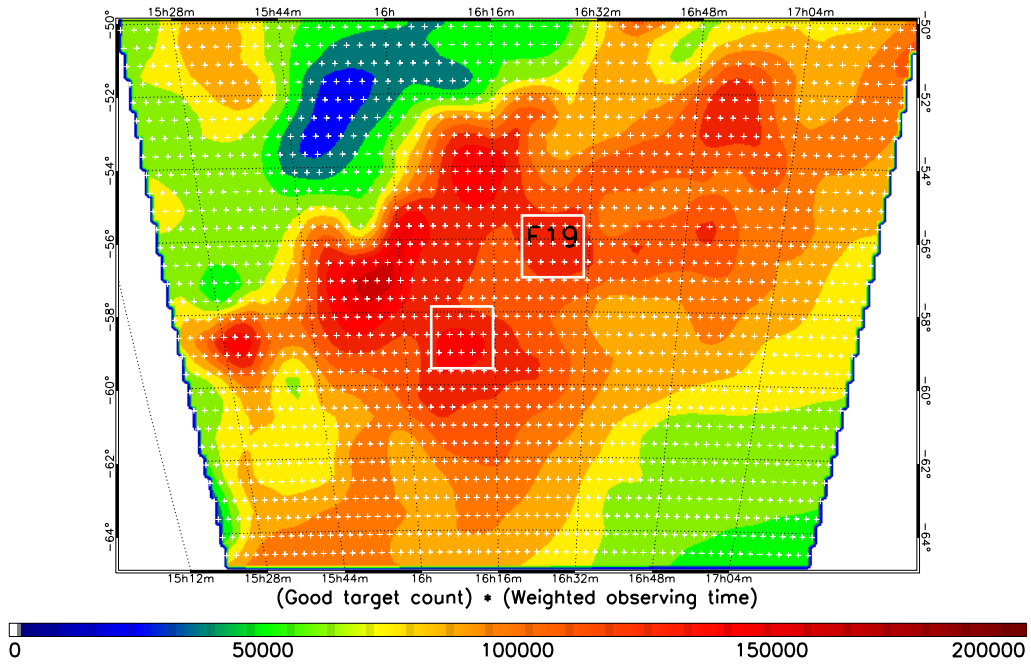

(e) Weighting function $\Theta\left(T_1, \overline{X}, N_{\mathrm{st}}\right)$ (Equation (B.7)), region of interest

Figure 4.5: Results of BEST II target field simulations (see Appendix B) for selection of F19. The small upper plots (a–d) show the numbers of suitable and contaminated stars, as well as the weighted observing time and the final weighting function Θ for the whole sky in the period 24/03–10/08/2010. The surrounding of F19 is marked with a *white polygon* in Figures (a–d); the same area is shown expanded in (e) for the main result Θ. The two *white boxes* in (e) refer to two selected target field pointings; one of them was finally observed as F19.

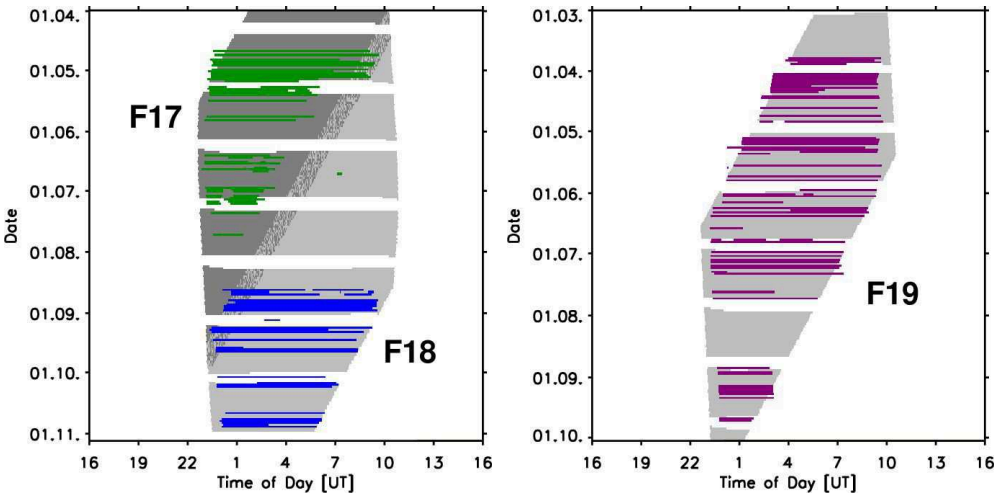

(a) 2009 (b) 2010

Figure 4.6: BEST II field observations during Chilean winters 2009 and 2010. Times of observations are shown for the fields F17 *(green)*, F18 *(blue)*, and F19 *(violet)*. For comparison, *gray* areas indicate the maximum astronomical visibility b (Equation (B.3), i.e., target field 30° above the horizon, Sun below −8°, etc.) of each respective field.

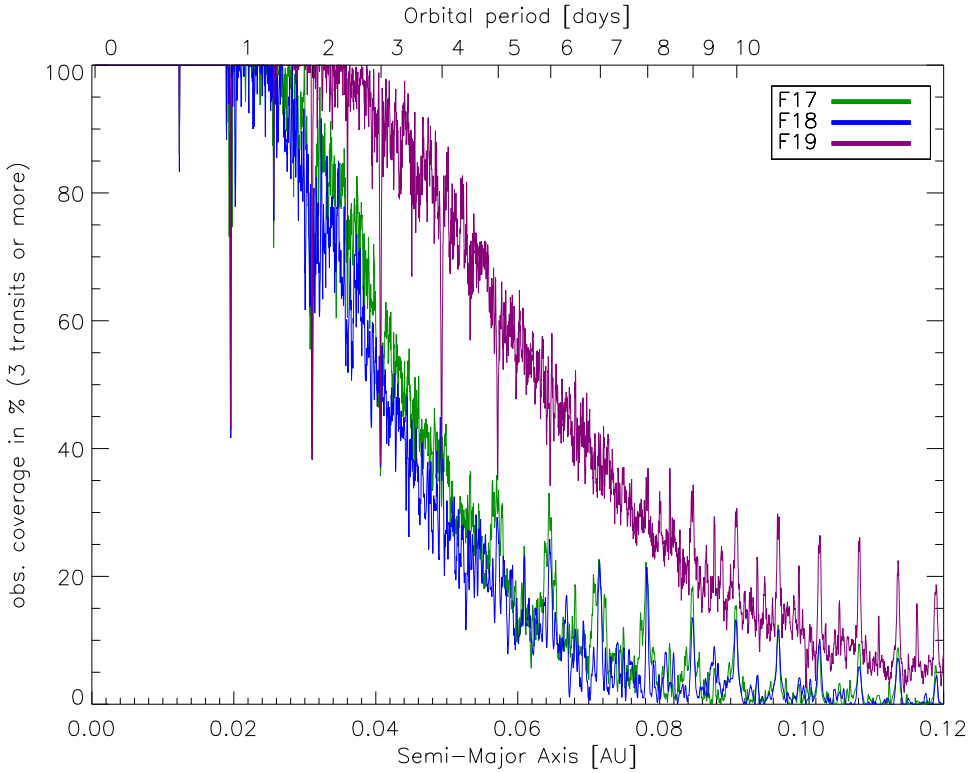

Figure 4.7: Orbital phase coverage of three or more transits for the window functions of F17, F18, and F19 (from real observations in 2009 and 2010, see Figure 4.6).

4.2.2 Observations

All three selected fields were observed with BEST II (Table 4.1): F17 from April to July 2009 for 40 nights, F18 from August to October 2009 for 28 nights, and F19 from March to September 2010 for 70 nights.

Periods of observations are shown and compared with the theoretical observability in Figure 4.6. During phases of a few weeks, each of the fields was observed almost continuously when visible in the night sky. However, interruptions due to bad weather, full Moon and higher priority targets are also clearly visible during large parts of each observing run.

The real observing times can be used to estimate the orbital phase coverage of transit events. Figure 4.7 shows the probability $p_{c3}(p)$ to cover at least three transits as a function of the assumed orbital period p for each of the three data sets. As expected for ground-based surveys, a reasonable chance to cover three or more events is only achieved for close-in planets, i.e., for periods of less than about 10 days. The two fields F17 and F18 show a similar probability, covering orbits up to 1–2 days completely. However, the coverage is significantly improved for F19: Due to its significantly larger window function, periods up to about 3–4 days are covered well.

4.2.3 Number of Stars

An important difference between the three fields is encountered in the number of observed stars (Table 4.1): The F18 data set contains only about 13,500 light curves, whereas F17 has ca. 68,000, and measurements have been obtained for more than 127,000 stars in F19 (for the latter, the flux threshold $f_{\min}$ (Section 5.2.1) was raised in order to focus the reduction on bright targets in this crowded field). Most important is the number of high-precision light curves: The number of stars having standard deviations $\sigma \leq 0.01\,\mathrm{mag}$ is for F19 with 11,681 stars 3.2 times higher than for F17, and strongly increased by a factor 26 compared to F18.

4.3 Photometric Quality

The procedures of photometric data reduction will be the subject of Chapter 5, and the reduction of fields F17–F19 will be described together with the search for transiting planets in Chapter 8. In this Section 4.3 and the next Section 4.4, the photometric quality of BEST II is discussed in a more general context.

The photometric variation of a single light curve i can be described with its standard deviation σ_i. Stellar variability adds to σ_i, so the value only yields a lower boundary for the photometric noise, but the whole set $\{\sigma_i\}$ can provide an estimate of the overall noise level. Furthermore, the photometric quality of light curves largely depends on the stellar flux f, which is why it is often investigated in a brightness-σ diagram. Figure 4.8 shows such an *rms plot* for the largest data set of this work.

The noise level is governed by three factors. First, errors due to systematic effects or atmospheric scintillation are proportional to f and yield a constant relative noise level σ_r. Second, the signal itself is produced by photons arriving at random and

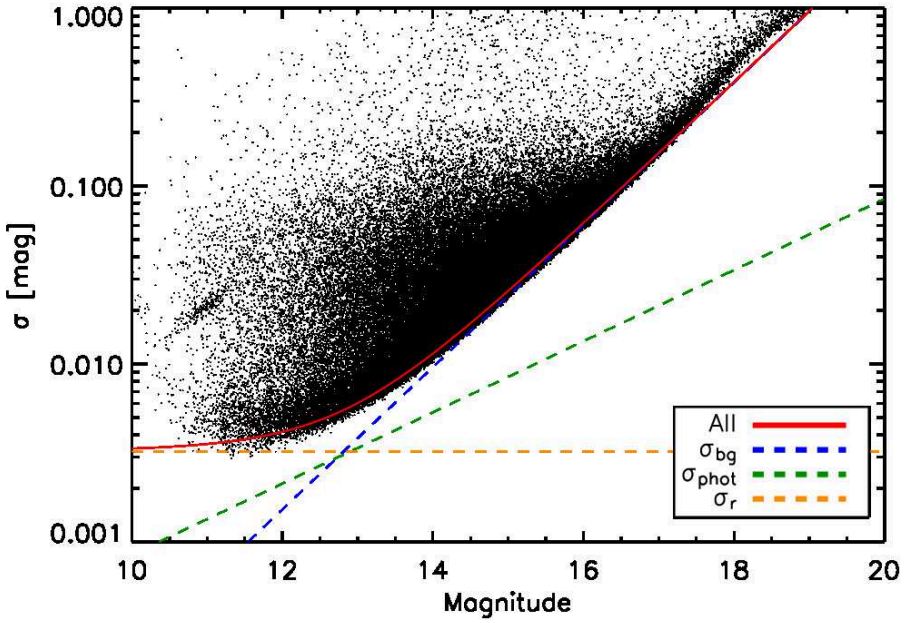

Figure 4.8: Light curve standard deviation σ_i vs. median stellar magnitudes $\widetilde{m}_i$ for all stars i in the BEST II data set F19. The *solid red* line shows the fit obtained with Equation (4.1), while the *dashed* lines show the individual noise factors $\sigma_r = \text{const}$ *(orange)*, $\sigma_{\text{phot}} \propto 1/\sqrt{f}$ *(green)*, and $\sigma_{\text{bg}} \propto 1/f$ *(blue)*. The fit yields $\sigma_r = 3.23\,\text{mmag}$ and $\Delta f_{\text{bg}} = 26.5\,\text{ADU}$.

thus follows a Poisson distribution, i.e., the corresponding photon noise σ_{phot} is proportional to $1/\sqrt{f}$. Third, uncertainties in the background flux level estimation and noise from the calibration process (Equation (5.2)) add up to a constant absolute error Δf_{bg} in each pixel, thus yielding a relative noise component $\sigma_{\text{bg}} \propto 1/f$. The combined relative photometric error σ can be described analytically (after Newberry 1991, Equation (12)):

$$\sigma \approx \sqrt{\sigma_r^2 + \frac{1}{g \cdot f} + n_\star^{\text{ap}} \left(1 + \frac{1}{n_{\text{sky}}^{\text{ap}}}\right) \cdot \left(\frac{\Delta f_{\text{bg}}}{f}\right)^2}, \tag{4.1}$$

whereby Δf_{bg} and the stellar flux f are given in ADU, g denotes the CCD gain factor, and $n_\star^{\text{ap}}$ and $n_{\text{sky}}^{\text{ap}}$ specify the number of pixels in the stellar aperture and the background annulus (Section 5.2), respectively. (The conversion of σ and σ_r to the magnitude scale can be obtained via $\sigma[\text{mag}] = 1.0857 \cdot \sigma$.)

Equation (4.1) was used to fit the lower boundary of the rms plots for all data sets reduced in this work (see example in Figure 4.8). The fit yields an estimate for the systematic noise σ_r and the constant term Δf_{bg} – these results are summarized in Table 4.2 (cf. Table 10.3 for ASTEP data).

The noise component σ_r readily yields a first characterization of the photometric quality of a given data set. For the fields F17–F19 which have been observed and reduced in the framework of this thesis, BEST II reaches a minimum overall noise level of $\sigma_r \approx 3\,\text{mmag}$ (Table 4.2), which underlines the quality of the Chilean site to enable a very high photometric stability over a whole observing season.

However, of similar importance for the detection efficiency of photometric surveys

Table 4.2: Photometric noise levels determined by fitting Equation (4.1) to rms plots $(\sigma, \widetilde{m})$ of BEST II analyzed in this work.

Field	σ_r	Δf_{bg}
LRa02a	5.08 mmag	21.9 ADU
LRa02b	6.99 mmag	22.5 ADU
F17	2.77 mmag	15.7 ADU
F18	3.14 mmag	14.2 ADU
F19	3.23 mmag	26.5 ADU

are the *time scales* at which this systematic noise is encountered. For example, the value σ_r will be assessed on a *nightly* basis in Chapter 10 for a site comparison between Dome C and Chile. For detecting extrasolar planets, however, the amount of systematic noise within the duration of a transit (i.e., a few hours for hot Jupiters) is critical. Kabath (2009) applied the method of Pont et al. (2006) to BEST II observations and found that about half the overall systematic noise σ_r was also present at a typical transit time scale (2–4 mmag at 2.5 hours compared to $\sigma_r = 6$–9 mmag in the first reduction of the LRa02 field). Within this work, the transit detection yield is estimated directly from the photometric noise budget of each analyzed data set.

4.4 Expected Detection Yield of BEST II

Given its high photometric quality, BEST II should be able to find transits of Jupiter-sized planets (having signals of $\delta F \approx 1\%$) with a sufficient signal-to-noise ratio. In addition, the success of transit search is constrained by the stellar and planetary population in a given field, the geometric transit probability, and the observational duty cycle (see Section 2.2).

This section presents all relevant characteristics for the fields investigated in this work, aiming at an estimation of the detection yield of BEST II. The idea is to identify factors that are important for its efficiency through the comparison of different fields, so that the observing strategy can possibly be optimized. Finally, the estimates of this section will be compared with actual findings in Section 8.4.

Model and Assumptions

The following model for estimating the detection yield builds on the theoretical framework of Beatty and Gaudi (2008), but uses some simplifying assumptions.

First, the calculation of N_{det} (using Equation (2.11)) can be simplified by assuming a single planetary radius of interest ($r_p \equiv r_{p0}$), and by neglecting the period dependency of the probability $p_{\mathrm{S/N}}$ for a system to show a detectable transit, i.e.,

$$p_{\mathrm{S/N}}(M_\star, r, r_p, p) \approx p_{\mathrm{S/N}}(M_\star, r) \cdot \delta(r_{p0}). \tag{4.2}$$

The latter assumption can be made since the number of transits covered with BEST II observations is typically constrained to a small range of $\sim$2–4 events, so that averaging individual transits does not yield a significant difference in the detection sensitivity within the relevant period range (in contrast to space missions; cf. the detection of CoRoT-7b based on 153 individual transits, Léger et al. 2009).

Second, the probability $df(p)/dp$ that a star possesses a planet of radius r_{p0} is approximately constant if the period range $[p_0, p_1]$ is small (e.g., for hot Jupiters). Thus, it can be estimated with a mean value f_{p0}, i.e.,

$$f_{p0} = \int_{p_0}^{p_1} \frac{df(p)}{dp}\, dp \approx (p_1 - p_0) \cdot \frac{df(p)}{dp}\ . \tag{4.3}$$

Finally, integration of Equation (2.11) yields

$$N_{\mathrm{det}} = N_{\mathrm{S/N}} \cdot f_{p0} \cdot f_t, \tag{4.4}$$

whereby

$$N_{\mathrm{S/N}} = \iiiint \rho_\star(r, l, b)\ r^2 \cos b\ \frac{dn}{dM_\star} \cdot p_{\mathrm{S/N}}(M_\star, r)\ dr\ dl\ db\ dM_\star \tag{4.5}$$

describes the number of stars in the field with a sufficient SNR to detect a transit, and the timing factor

$$f_t = \frac{1}{p_1 - p_0} \int_{p_0}^{p_1} p_g(p) \cdot p_{\mathrm{win}}(p)\ dp \tag{4.6}$$

encompasses the observational coverage $p_{\mathrm{win}}(p)$ folded with the geometric probability $p_g(p)$. The latter is calculated using Equation (2.13), Kepler's third law, and the approximations $e = 0$, $r_\star = r_\odot$, $M_\star \gg M_p$, and $r_\star \gg r_p$, thus yielding

$$p_g(p) \approx \frac{r_\odot + r_{p0}}{p^{2/3}} \tag{4.7}$$

(with p in years, $r_\odot$ and r_{p0} in astronomical units).

Simulations and Parameters

The calculation of $N_{\mathrm{S/N}}$ (Equation (4.5)) requires more knowledge than is usually available a priori: Since the stellar radii determine the transit depth (Equation (2.6)), any comparison between the *achieved* precision and the precision that is actually *necessary* for transit detection requires information about the stellar population in a given field. The modeling of stellar fields and its link to observational data now presented follows the approach of Bayliss and Sackett (2011).

First, the Besançon model of the Galaxy (Robin et al. 2003) is used to assess the stellar content of target fields. For each pointing, stars are simulated within the magnitude range $R \in [10, 17]$, and the results are compared and adjusted to catalog data: Stars are assigned to bins of 0.1 mag within $10 \leq R \leq 14.5$, and the total number difference between model and star catalog is minimized by varying the Besançon input parameter a_v for interstellar extinction in steps of 0.1 mag/kpc (Figure 4.9a). For all fields investigated in this work, the R band of the GSC2.2 catalog (Lasker et al. 2008) showed the best agreement with the Besançon results from a group of several catalogs tested (e.g., UCAC3, USNO-A2, NOMAD; for a direct comparison with GSC2.2, see also Reylé et al. (2010); Crouzet et al. (2010) use the same combination in a very similar context).

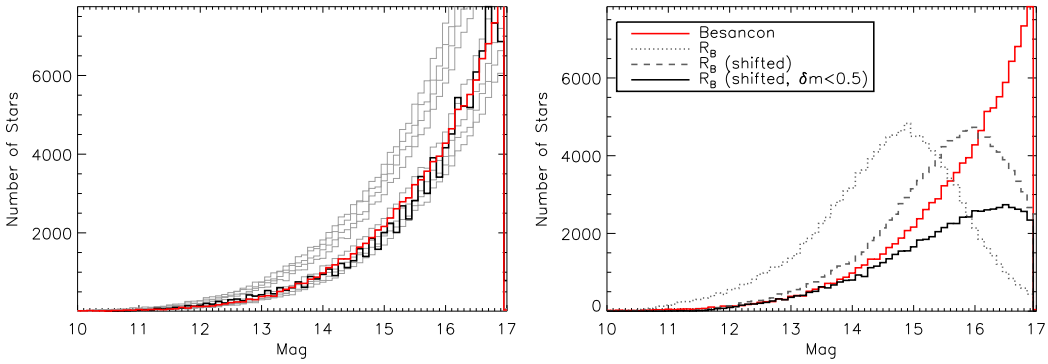

(a) Besançon and GSC2.2 (b) Besançon and BEST II

Figure 4.9: Comparison between stellar magnitudes of BEST II, GSC2.2, and the Besançon model of the Galaxy; example for field F19. Both graphs show star counts within bins of 0.1 mag. (a) Besançon (*gray* and *red*, m_i^{sim}) and GSC2.2 magnitudes (*black*, m_i^{cat}). The total difference within $10 \leq R \leq 14.5$ is calculated for varying interstellar extinctions a_v (different *gray* lines), and the Besançon catalog with the minimum value is finally selected *(red)*. (b) Besançon (*red*; as in (a)) and BEST II magnitudes. For BEST II, the plot shows $\widetilde{m}_i$ *(dotted)* and shifted magnitudes $\widetilde{m}_i + \delta m$, the latter both for all stars *(dashed)* and a subset that is used to model the rms distribution *(solid)*.

Second, each BEST II star is matched with the GSC2.2 catalog (within $2''$ radius), and the median difference δm between BEST II magnitudes and the GSC2.2 R band is calculated (cf. Equation (5.20)). Since the same catalog as in the first step is used, *shifted* BEST II magnitudes $\widetilde{m}_i + \delta m$ match the Besançon catalog reasonably well (see example in Figure 4.9b), and the stellar content can be compared homogeneously.

Third, each simulated star i is assigned a photometric noise level σ_i^{sim} that is typical for its magnitude m_i^{sim} in the given data set. For that, each light curve is binned to a typical transit time scale of 30 minutes, and the corresponding standard deviation σ^{bin} is calculated. The noise σ_i^{sim} is then determined as a random value following the σ^{bin}-distribution of all BEST II stars with *similar brightness*, i.e., having $\left|\widetilde{m}_i + \delta m - m_i^{\mathrm{sim}}\right| \leq 0.04\,\mathrm{mag}$. In order to limit the effect of crowding and other systematic factors, only stars which differ by less than 0.5 mag from their corresponding catalog magnitude (i.e., with $\left|\widetilde{m}_i + \delta m - m_i^{\mathrm{cat}}\right| < 0.5\,\mathrm{mag}$) are included in the determination of σ_i^{sim}.

With σ_i^{sim} at hand, it is possible to estimate if the photometric precision of star i allows the detection of the transit of a Jupiter-sized planet. In the following,

$$\sigma_i^{\mathrm{sim}} \leq c \cdot \delta F \quad \text{with} \quad \delta F \equiv \left(\frac{r_J}{r_\star}\right)^2 \tag{4.8}$$

is used as a simple criterion for sufficient SNR. As in Equation (4.2), the period dependency on the detection threshold is considered small. In Section 6.2.3, the validity of Equation (4.8) will be discussed using a test with artificial transit signals in BEST II data, and the constant c will be approximated (Equation (6.10)). Note that since both σ_i^{sim} and c refer to photometric data binned to 30 minutes, the simulation also enables comparing the detection yield between data sets that are obtained with a different time sampling.

The stellar radii $r_\star$ for δF in Equation (4.8) are derived from the masses $M_\star$ (Besançon output) using the power law (Cox 2000)

$$\log_{10}(r_\star/r_\odot) = 0.917 \log_{10}(M_\star/M_\odot) - 0.020 \tag{4.9}$$

for the main sequence. Other luminosity classes are disregarded for possible detections, as planetary transits for these are generally well below the threshold of the surveys investigated in this work. The simulation is repeated five times for each star and yields $N_{\mathrm{S/N}} = f_{\mathrm{S/N}} \cdot N_\star$, i.e., the number of dwarf stars for which Equation (4.8) holds, whereby $N_\star$ denotes the total count of simulated Besançon stars.

Fourth, f_t is calculated using Equations (4.6) and (4.7) within the period range of $p \in [1, 10]$ days that is relevant for BEST II. The observational coverage is calculated for three or more transits, i.e., $p_{\mathrm{win}} \equiv p_{\mathrm{c3}}$ as described in Section 4.2.2. The validity of this assumption will be addressed in Section 6.3 using artificial transit signals.

Finally, the probability f_{p0} for stars to host a planet is taken from the literature for hot Jupiters, i.e., for the same period range and planetary radius as before. Depending on the probed stellar populations and detection limits, values vary for different surveys (see Table 6 by Bayliss and Sackett (2011) for a recent overview). For comparison, two values are used for the calculation of N_{det}: Bayliss and Sackett (2011) find the rather low value of $f_{p0}^{(1)} = 0.10\%$ ($r_{p0} = 1.1\,r_J$, $p \in [1, 10]$ days) from the SuperLupus survey, a transit search similar to BEST II. Larger values are found in RV surveys, of which $f_{p0}^{(2)} = 0.43\%$ ($M_\star = M_J$, $p < 11.5$ days; Cumming et al. 2008) from the Keck Planet Search is used as a second reference value for comparison. Note that the latter value agrees with the occurance rate as determined by the two transit surveys from space, which both found 0.4% for hot Jupiters with periods of $p < 10$ days (CoRoT with $M_p = 0.45$–$2.5\,M_J$, Guenther et al. 2012; Kepler with $r_p = 8$–$32\,r_\oplus$, Howard et al. 2012).

Results

The results of the BEST II detection yield simulations are summarized in Table 4.3. In addition to the expected number of detections for each target field investigated in this work, it shows the number of simulated stars, the number of stars with a sufficient SNR to find transits, and the time coverage combined with the geometric probability (f_t; Equation (4.6)).

The quantitative estimation of N_{det} now allows to address the question *how many* planets are expected to be found, and which parameters place the most important constraints upon the detection efficiency:

Target field F19 shows a reasonable chance to find a transiting planet. Having by far the highest number of light curves with sufficient SNR ($N_{\mathrm{S/N}} = 2{,}058$, i.e., more than F17 and F18 together), 0.14–0.62 planets are expected to be found in this

Table 4.3: Expected number of hot Jupiter detections in BEST II target fields.

Field	a_v [mag/kpc]	$N_\star$	$N_{\mathrm{S/N}}$	$f_{\mathrm{S/N}}$	f_t	$N_{\mathrm{det}}^{(1)}$	$N_{\mathrm{det}}^{(2)}$
F17	2.7	39,514	1,103	2.79%	4.65%	0.05	0.22
F18	0.8	2,508	886	35.32%	4.19%	0.04	0.16
F19	1.1	113,635	2,058	1.81%	7.02%	0.14	0.62
LRa02*a (v1)*	1.4	24,530	161	0.66%	4.74%	0.01	0.03
LRa02*a (v5)*	1.4	24,530	657	2.68%	4.74%	0.03	0.13
LRa02*b (v1)*	1.0	24,606	278	1.13%	4.74%	0.01	0.06
LRa02*b (v4)*	1.0	24,606	516	2.10%	4.74%	0.02	0.11

Notes. Stellar populations have been simulated using the Besançon model of the Galaxy. The interstellar extinction a_v has been adjusted for each field such that the star counts resample the BEST II observations (see example in Figure 4.9a). $N_\star$ gives the total count of modeled stars ($R \in [10, 17]$) within the FOV, whereas $N_{\mathrm{S/N}}$ gives the number of stars that show transit depths $\delta F \geq \sigma_i^{\mathrm{bin}}/0.64$ (cf. Equations (6.10) and (4.8) with $r_p \equiv r_J$), and $f_{\mathrm{S/N}}$ gives the ratio $N_{\mathrm{S/N}}/N_\star$. The geometric probability is combined with the orbital coverage to the parameter f_t (Equation (4.6)). The expected detection yield N_{det} is given for $f_{p0}^{(1)} = 0.10\%$ (Bayliss and Sackett 2011) and $f_{p0}^{(2)} = 0.43\%$ (Cumming et al. 2008), respectively.

field. In addition, the high duty cycle of F19 yields a factor of $f_t = 7\%$ for short-period planets, while the same value only reaches 4.2–4.7% for all other investigated fields. A transit detection in the other two fields seems rather unlikely, showing a detection yield of 0.05–0.22 planets in F17, and 0.04–0.16 in F18, respectively. Thus, the differences in the estimated detection yield between fields F17–F19 are in good agreement with the qualitative differences already identified in Section 4.2.2 regarding the time coverage and number of high-precision light curves.

The two BEST II target fields within the CoRoT pointing LRa02, which have been reanalyzed for variable star search in the framework of this thesis (Chapter 7), show with $N_{\mathrm{det}} = 0.05$–0.24 a combined yield that is comparable to the F17 field. For comparison, the detection yield has also been calculated for the initial version of these data sets (v1), for which N_{det} is 2–4 times smaller than with the latest reductions. The differences are largely due to pipeline improvements, which will be described in the next chapter (e.g., the new frame quality criterion, see Section 5.2.2 and Figure 5.7). The improved quality could motivate a second transit search in this field, which has not been performed in this work.

Overall, 0.28–1.14 detectable transiting planets are expected in 329,660 light curves within five BEST II target fields (F17–F19 and LRa02a/b, see Tables 4.1 and 4.3), thus corresponding to one detection in 290,000–1,200,000 stars surveyed. For comparison, the most successful transit survey from ground, SuperWASP, reported 70 planets from an analysis of 30 million light curves (Norton et al. 2011), corresponding to one detection per 430,000 stars. Thus, the *relative* detection yield is well comparable, which indicates that both the photometric quality as well as the observational coverage of BEST II are highly competitive. In contrast to that, the *overall* number of stars surveyed clearly causes a significant difference in the detection yield, since SuperWASP acquired 91 times more light curves than BEST II. Together with the actual findings of this work, Chapter 11 discusses this issue in the perspective of future transit surveys with BEST II .

4.5 Summary

Since its commissioning in 2007, BEST II observed approximately every third night. The observations focused on the follow-up of CoRoT planetary candidates, and were complemented since 2009 with a transit survey on three fields, joint observations with the ASTEP project, and monitoring of known transiting planets. This work focuses on the planning, conducting, reduction, and analysis of observations for *transit search* and for *comparison with ASTEP*. The latter are covered together with observations from Antarctica in Chapter 10.

To perform a dedicated transit search with BEST II, a new observing strategy was implemented. Most importantly, this included the selection of suitable target fields. The first two fields, F17 and F18, were selected to be observable longest at low airmasses within a given period of time using procedures of Rauer et al. (2008a, b) and Fruth (2008). For the selection of the third field, F19, the method was complemented by a simulation of the expected number of suitable target stars.

F17 was observed for 40 nights between 20th April and 22nd July 2009, F18 for 28 nights between 19th August and 27th October 2009, and F19 for 70 nights from 24th March to 21st September 2010. The time series of the first two fields provide a full phase coverage for three transit events up to orbital periods of 1–2 days, while F19 covers up to 3–4 days well. The photometric quality of all three data sets is excellent, showing a low systematic error of $\sigma_r \approx 3\,\mathrm{mmag}$ over the whole observing campaign. However, there are large differences regarding the number of stars and low-noise light curves: F19 contains 127,202 light curves (11,681 with $\sigma \leq 0.01\,\mathrm{mag}$), F17 68,317 (3,700), and F18 only 13,551 (448).

Both the better orbital phase coverage as well as the large number of high-precision light curves imply a clearly improved probability to find transits in field F19 compared to F17 and F18. A simulation of the stellar population was used, together with literature values for the fraction of stars hosting a planet, to estimate how many hot Jupiters could be detected within each of these three data sets. The estimate yields 0.05–0.22 planets in F17, 0.04–0.16 in F18, and 0.14–0.62 in F19 (i.e., 0.23–1.00 planets in total). The differences are dominated by the unequal stellar densities in each pointing; however, the better duty cycle for F19 also increases the expected detection yield by about a factor 1.6 compared to F17 and F18. While the phase coverage of F17 and F18 was limited by observational constraints, the significant difference in the number of low-noise light curves was achieved by switching to a quantitative field selection including the simulation of suitable target stars. The latter is thus considered a mandatory criterion to reach the aims of this thesis.

The results of transit search in fields F17–F19 will be described in Chapter 8; an analysis of stellar variability in BEST II fields is covered in Chapter 9.

5 Data Reduction

Photometric data obtained with a telescope require a number of operations before the measurements can be interpreted scientifically. The data sets usually comprise a number of raw scientific images taken with a digital camera. In a first step, the *calibration*, instrumental effects are removed with the aid of calibration images that have to be recorded together with the observations. The second step, the *photometry*, comprises the identification of stars in the field and the calculation of their flux as a function of time, i.e., it yields a *light curve* for each star. Finally, the last step, the scientific *analysis*, invokes the investigation of the light curves obtained. A schematic overview is shown in Figure 5.1.

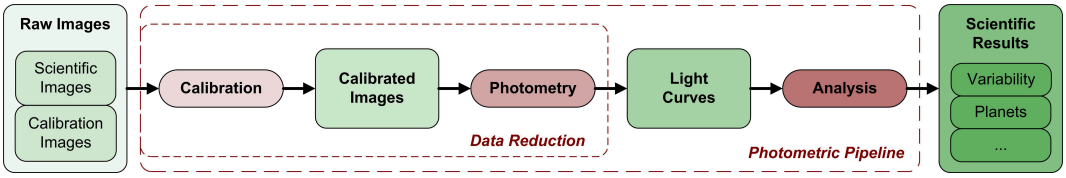

Figure 5.1: Schematic overview of the data flow from observations to scientific results. Calibration and photometry are summarized under the term *data reduction*, while the whole chain is called the *photometric pipeline*. Details on the data reduction can be found in Figure 5.2 (calibration) and Figure 5.4 (photometry). An overview on the analysis of transit planets is given in Figure 8.1.

Since the two processes of calibration and photometry together yield the processed light curves, they are often summarized under the term *data reduction*. The whole set of programs for photometric data analysis, i.e., from raw images to scientific results, is called the *pipeline*. The term is based on the fact that huge astronomical data sets require a well automated approach to mass data processing.

This chapter describes the data reduction procedures which were used to obtain the results in this work. They are part of the DLR photometric pipeline, which has already been used to analyze various BEST/BEST II data sets (Rauer et al. 2004, 2010; Voss 2006; Kabath et al. 2007, 2008, 2009a, b; Karoff et al. 2007; Wiese 2007; Fruth 2008; Kabath 2009; Pasternacki 2009; Pilello 2010; Schulze 2010; Pasternacki et al. 2011). It is largely written in IDL (Interactive Data Language) and described in detail by Fruth et al. (2011).

The pipeline has constantly been improved concerning both the quality of the reduction and the level of automation. Likewise, some major parts had to be adapted in order to reach the scientific objectives of this work. For example, the pipeline was modified to be independent of projects or platforms, which was particularly necessary to reduce ASTEP data.

In the following, the procedures for calibration (Section 5.1) and photometric reduction (Section 5.2) are outlined briefly. Section 5.3 summarizes this chapter with a focus on the pipeline improvements that were implemented in the framework of this thesis. The scientific analysis part is then covered in Chapters 6 and 7.

5.1 Calibration

In astronomy, predominantly CCDs are used for observations. Incident photons produce charges on a two-dimensional array of small semi-conductor capacitors (pixels) which are transported, electronically read out and converted into Analog-to-Digital Units (ADU). However, the final reading of an individual pixel consists not only of a value proportional to the incident flux, but also includes components which are caused by the acquisition process. In order to retrieve the photometric signal itself, these instrumental effects are removed during the calibration phase.

Bias

For readout, each CCD pixel is offset by a constant voltage in order to avoid negative digital values. Therefore, all measurements contain a *bias level* N_B that must be subtracted, and an associated readout noise σ_B. The bias level may vary with time and/or during the readout process (the latter resulting in small structures across the frame). It can be determined by obtaining frames with integration time $\Delta T = 0$.

Dark

Electronic charges in the CCD are not only generated by photons, but also by thermal agitation. The additional dark current N_D is read out together with the signal and becomes part of the measurement. It can be accessed by subtracting the bias level N_B from *dark frames*. These are taken with the same integration time and temperature as scientific frames, but without light falling on the CCD.

Flat

If the same star is observed at different positions on the CCD, it can appear to have a different brightness. Instrumental causes for this include optical effects and different pixel sensitivities. They can be determined by observing a uniformly illuminated area in a sequence of *flat fields* and be reduced via dividing each pixel by the normalized flat field count η_{flat}.

Procedure

The raw measurement

$$N_{\mathrm{raw}} = \eta_{\mathrm{flat}} \cdot N_{\mathrm{phot}} + N_B + N_D \tag{5.1}$$

comprises the photometric signal N_{phot}, the bias level N_B, the dark current N_D and the sensitivity variations η_{flat}. In order to retrieve N_{phot}, bias and dark frames are collected to determine and subtract N_B and N_D from N_{raw}, and flat fields are obtained to divide the dark- and bias-subtracted frames by η_{flat}. For the present pipeline setup, the error of the reduced signal is given by

$$\begin{aligned}\sigma_{\mathrm{cal}}^2 = \sigma_{\mathrm{phot}}^2 &+ \sigma_{\mathrm{flat}}^2 \cdot \frac{N_{\mathrm{phot}}^2}{\eta_{\mathrm{flat}}^2}\left(1 + \frac{1}{n_{\mathrm{flat}}}\right) + \sigma_{\mathrm{D}}^2 \cdot \left(1 + \frac{1}{n_{\mathrm{D}}}\right) \\ &+ \sigma_{\mathrm{B}}^2 \cdot \left(1 + \frac{1}{n_{\mathrm{B}}}\right)\left(2 + \frac{1}{n_{\mathrm{D}}} + \frac{N_{\mathrm{phot}}^2}{\eta_{\mathrm{flat}}^2}\left(1 + \frac{1}{n_{\mathrm{flat}}}\right)\right).\end{aligned} \tag{5.2}$$

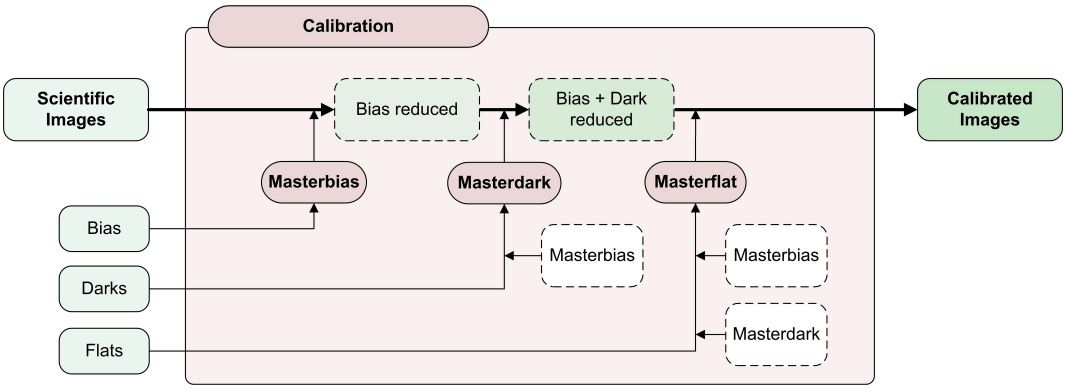

Figure 5.2: Schematic overview of the data calibration. Calibration images are combined into master frames, which are used to remove instrumental effects from each scientific image. Temporary frames are indicated with dashed boxes.

Thereby, σ_{phot} denotes the noise component of the signal N_{phot} itself, and σ_B, σ_D, and σ_{flat} give the corresponding uncertainties in a *single* calibration frame. A number of n_B, n_D, and n_{flat} calibration images are averaged to *master* frames in order to decrease the errors that are introduced by these operations. Samples are typically chosen in the range of $n \approx 10$–20 as a compromise between noise improvement and loss of observing time. Figure 5.2 summarizes the procedure schematically.

Implementation

The building of master frames and the implementation of Equation (5.1) are straightforward. However, the calibration does face some challenges, such as the treatment of outlier frames and an effective processing of a large amount of data.

Note that before this work, each BEST II night typically covered a single target field, and the calibration started once all observations concluded. However, a changed observing strategy (see Section 4.1) caused several fields to be observed within one night, in which some had to be reduced immediately. As part of this thesis, the calibration part of the pipeline was recreated in order to adapt to the new mode of observations. The aim was to enforce a standard calibration scheme that could be executed on-site directly after the observations, and which is independent of the target fields observed.

The new implementation follows a semi-automatic approach. Its idea is that all relevant information on the quality of individual images is collected and presented in a condensed form to the observer, reviewing the observations on a nightly basis. It includes an automatic preselection of suitable frames that can quickly be confirmed or adjusted before the calibration is started.

The new program `CAL_WIZARD` provides the framework to operate the calibration and to track its progress on individual nights through status flags. It starts with raw instrumental data (c0 status) which are first duplicated (c1), and continues through the collection of additional information on individual frames (c2), the manual review (c3) and the automatic calibration itself (c4) down to completion by deleting all temporary data (c5).

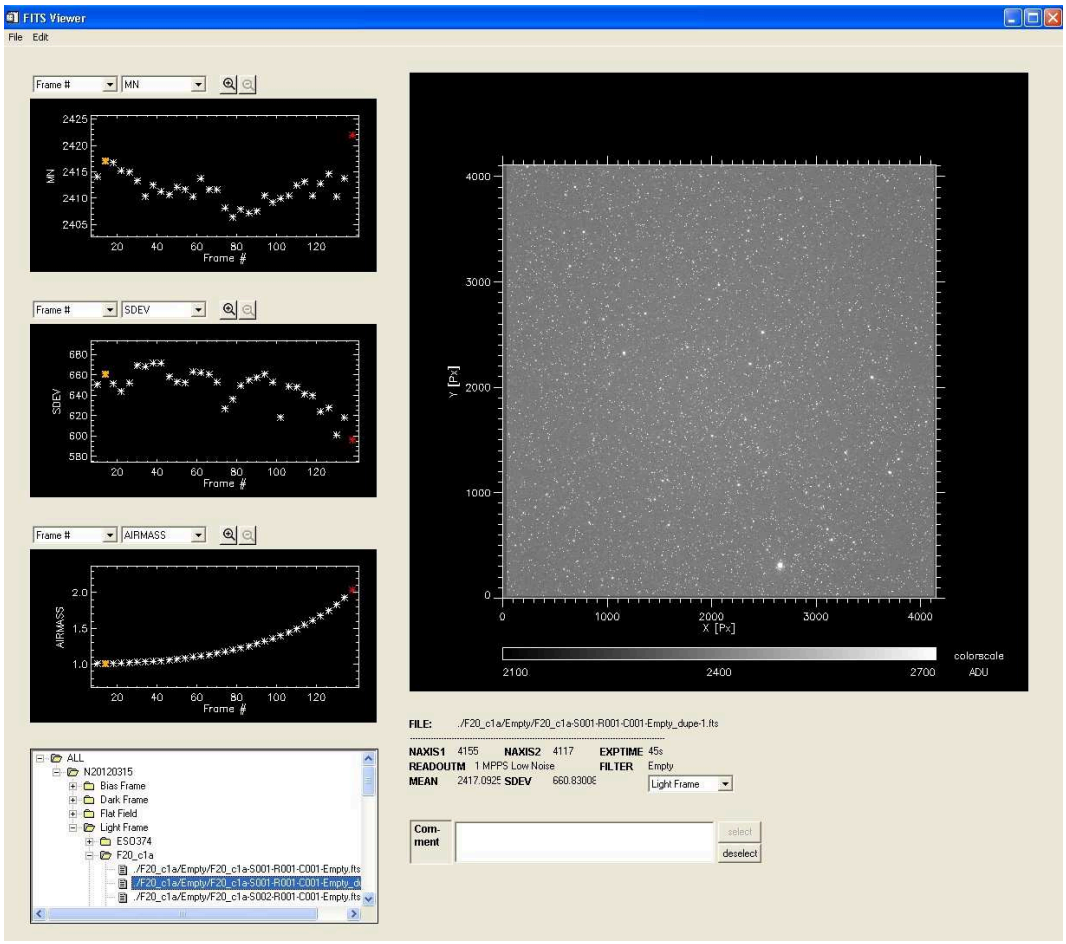

Figure 5.3: The program `FITS_VIEWER` – an interface to quickly assess the image quality during calibration. The small three panels on the *upper left* can be adjusted to show any image parameter; in this example, the mean, standard deviation and the airmass are each plotted vs. the frame index. Outliers are marked in *red* and can be quickly (de)selected in any plot. The tree on the *lower left* shows all frames sorted by category and target; it can be used to browse through the night's data. The panel on the *right* summarizes information about a selected frame, including its exposure time, filter, readout mode, and a thumbnail image.

For the third step (c3), the program `FITS_VIEWER` provides a user-friendly interface to review the quality of individual frames (Figure 5.3). It works on a small meta file that is produced by reading all images in a given night automatically. Standard parameters include the mean, standard deviation, type, filter, exposure time and readout mode of each frame. By setting configuration parameters, they can easily be complemented with project-specific data from the image headers, e.g., the airmass, CCD temperature, or focus position. In addition, a small thumbnail image is stored.

`FITS_VIEWER` groups all frames into meaningful categories (i.e., same image type, readout mode, etc.). For each group, all available parameters can be reviewed as a function of frame index or time in order to identify outliers. Thereby, the frame mean and standard deviation are used for an automatic preselection (using 3σ-clipping). Outliers marked by these criteria are deselected, but the observer makes the final decision, i.e., as to which calibration frames are used to build the master frames. A first assessment of scientific images is also possible: Already at this stage, some

problems such as clouds or bad guiding can easily be identified to exclude bad frames.

Improvements

The most important improvements of the new calibration method, as implemented by this thesis, are:

- **Project-independent calibration.** The calibration works with standard parameters from the image header. Project-dependent parameters are stored in a separate configuration file and can be quickly adjusted.
- **Possibility for on-site calibration.** The meta file containing information on all frames is small and can be transfered with small bandwidths. The procedure was implemented and used successfully in 2010/2011 for the on-site calibration of BEST II images; it helped particularly to decrease the response time for CoRoT follow-up observations (since 2012, all raw data is transfered through the new fiber link and the calibration is performed in Berlin).
- **Improved quality control.** A better quality assessment is achieved due to the condensed presentation of many available parameters. Therefore, problems with the observations are encountered more easily and can be accounted for immediately.
- **Switch from target to nightly calibration.** Earlier versions of the pipeline needed all nights of an observing run for calibration. With a changed observing strategy of BEST II, different observing runs often overlap, and several targets are observed within the same night. Therefore, the calibration procedures were adjusted to work on a nightly basis, i.e., independent of the observed target fields.

5.2 Photometry

The photometric part of the pipeline extracts the flux of all stars in a target field from individual images, combines the measurements into light curves and cleans them from systematic effects. An overview of the most important procedures and temporary data products is shown in Figure 5.4.

5.2.1 From Calibrated Images to Raw Light Curves

Image Alignment

A prerequisite for the following procedures is that all scientific images are aligned to a common coordinate system. Since the telescope pointing is usually not stable enough to keep stars on the same pixel (for BEST II pointing accuracy, see Section A.2), an automatic procedure is required for adjustment.

The image alignment for the DLR pipeline has been implemented and described by Pasternacki (2009). First, it obtains the positions of all stars in each calibrated science frame using the *Source-Extractor* program (Bertin and Arnouts 1996). In a

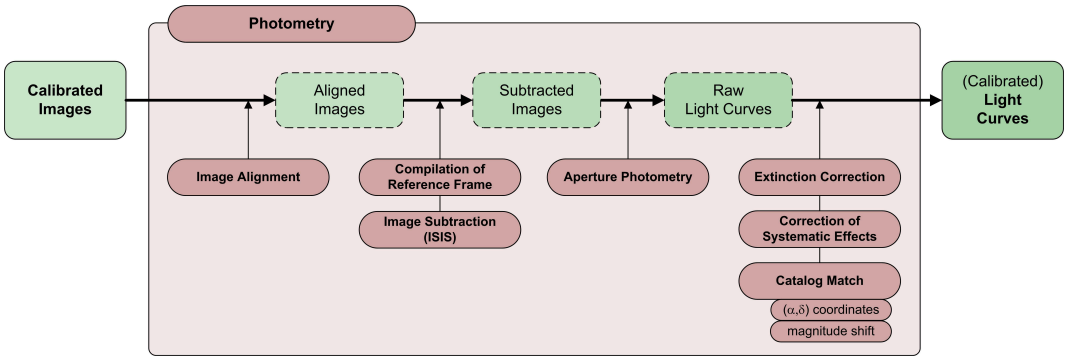

Figure 5.4: Schematic overview of the photometric part of the pipeline. It starts with calibrated frames (see Section 5.1 and Figure 5.2) and yields a light curve for each star in the field. In a first step, all images are aligned to a common coordinate system. Second, a reference frame is stacked from the images with the best seeing and subtracted from each image. Third, stars are located on the reference image and their flux is integrated for both the reference and each subtracted image. Finally, the initial light curves are corrected for extinction and systematic effects, and CCD positions are matched with a catalog for astrometric coordinates and to transfer instrumental magnitudes into a standard photometric system.

second step, these positions are used to find a transformation to a reference coordinate system with the routine `grmatch` (Pál and Bakos 2006). Third, all frames are interpolated to this reference grid.

Image Subtraction

The DLR pipeline uses image subtraction and is thus optimized for crowded field photometry (Karoff et al. 2007). By subtracting the aligned frames from a reference image, *constant* field stars vanish and brightness *variations* can be measured with higher precision (Figure 5.5).

To obtain subtracted images, the ISIS package is used (Alard and Lupton 1998; Alard 2000). It involves three steps: First, a reference image $\mathrm{Ref}(x, y)$ is created by averaging some 10–20 images with the best seeing in a data set. Second, the reference frame is fitted to each image $\mathrm{I}_j(x, y)$ by determining the optimum Kernel that minimizes the expression

$$\sum_{x,y} \left[\mathrm{Ref}(x, y) \otimes \mathrm{Kernel} - \mathrm{I}_j(x, y)\right]^2 . \tag{5.3}$$

Third, each subtracted frame $\mathrm{S}_j(x, y)$ is calculated as

$$\mathrm{S}_j(x, y) = \mathrm{Ref}(x, y) \otimes \mathrm{Kernel} - \mathrm{I}_j(x, y). \tag{5.4}$$

The selection of images that are stacked to the ISIS reference frame was done manually in previous versions of the pipeline. In the framework of this thesis, an automatic criterion was introduced to make the selection faster and more reliable, which operates as follows: In order to maximize the overlap area, the program `BESTREF` first excludes frames that were shifted by more than $N_{\mathrm{shift}}^{\mathrm{max}}$ pixels to the common coordinate system (default $N_{\mathrm{shift}}^{\mathrm{max}} = 5\,\mathrm{Px}$). It then uses the mean PSF width σ_j^{fwhm} and

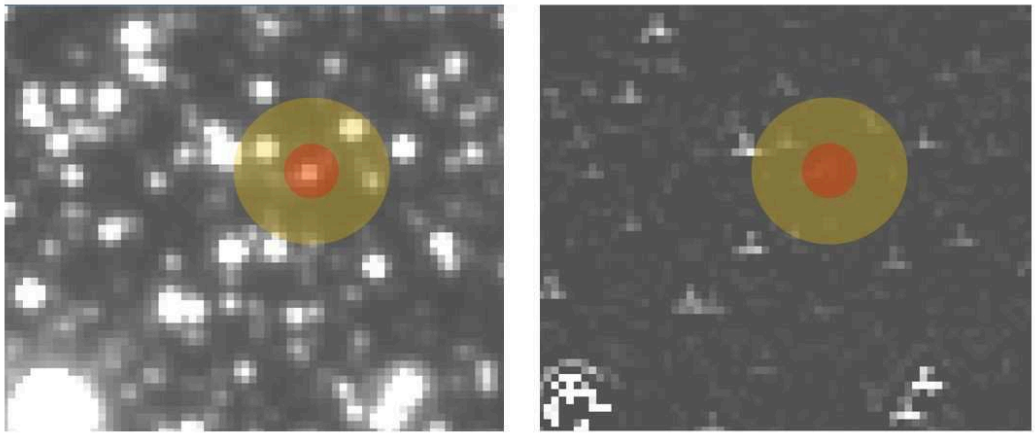

Figure 5.5: Principle of image subtraction. The *left image* shows a small area of a BEST II reference frame $\mathrm{Ref}(x, y)$, the *right image* the same area but for a subtracted frame $S_j(x, y)$. Measurements are obtained for each star as the sum of all pixels in a fixed radius aperture (indicated in *red* and *orange*, the latter for the background flux). Because the flux of most stars remains largely constant (i.e., they vanish in the subtracted images), relative changes can be measured more accurately using this method, especially on crowded fields.

the number of bright stars N_j^{bs} in each frame j to assess its seeing, i.e., all frames are sorted by the quantity

$$q_j^{\mathrm{ref}} = N_j^{\mathrm{bs}} / \sigma_j^{\mathrm{fwhm}} \ , \tag{5.5}$$

and frames with the largest value of q_j^{ref} are preselected for the reference frame. Considering the combination of both parameters turned out to be more robust than one of them alone. This procedure was successfully applied to many data sets.

Aperture Photometry

Simple unit-weight aperture photometry is used to obtain stellar fluxes in the reference frame and all subtracted images (for a discussion of PSF-weighted vs. unit-weighted aperture photometry for BEST, see Karoff et al. 2007).

To measure integrated fluxes, stars must first be identified in the reference image; the IDL routine `FIND` (Landsman 1993) is used to identify the (x, y) positions of all stars. It excludes stars whose PSF strongly deviates from a Gaussian shape and that have fluxes f_i below a threshold parameter f_{min}. The latter is usually chosen close to the photometric noise limit with the help of the `PRE_PHOT` program (Fruth 2008).

In a second step, a circular aperture A_i with radius r_{ap} is placed around the CCD center coordinates $(x, y)_i$ of each star i in the reference frame. The flux of all pixels contained within is added to

$$f_{i,\mathrm{ref}} = \sum_{(x,y)\in A_i} \left(\mathrm{Ref}(x, y) - N_i^{\mathrm{bg}} \right), \tag{5.6}$$

whereby N_i^{bg} denotes the background flux per pixel. The latter is determined through an iteration in the annulus $r_{\mathrm{ap}} < r \leq r_{\mathrm{sky}}$ around the stellar aperture (Karoff 2008). The radii r_{ap} and r_{sky} must be chosen such that the PSFs are fully covered by the

aperture, yet keeping the overlap with neighboring stars small. For BEST II, the default values are $r_{\mathrm{ap}} = 5\,\mathrm{Px}$ and $r_{\mathrm{sky}} = 20\,\mathrm{Px}$.

The same process is repeated on all subtracted images to obtain measurements for all times t_j and stars i, i.e.,

$$f_{ij} = f_{i,\mathrm{ref}} - \sum_{(x,y)\in A_i} \left(\mathrm{S}_j(x,y) - N_{ij}^{\mathrm{bg}} \right), \tag{5.7}$$

with N_{ij}^{bg} denoting the corresponding background estimation for the aperture in the subtracted frame S_j. Finally, fluxes are converted into magnitudes by

$$m_{ij} = 25 - 2.5 \cdot \log_{10}\left(f_{ij}\right). \tag{5.8}$$

Note that the choice of the zero-point $m = 25$ is arbitrary because the magnitude scale is adjusted later via cross-correlation with a catalog (Section 5.2.3, Equation (5.21)).

5.2.2 Light Curve Cleaning

The raw light curves that are obtained by image subtraction and aperture photometry can still contain outliers and systematic effects. Thus, a number of additional procedures are included in the pipeline to remove them as well as possible.

Extinction Correction

Stars appear fainter when observed from the ground due to scattering and absorption of light in the atmosphere. The apparent magnitude m depends on the airmass X at which a star is observed and its color index C as follows (Hardie 1962)

$$m = m_0 + k'X + k''CX, \tag{5.9}$$

where m_0 denotes the magnitude outside the atmosphere and k' and k'' are first and second order extinction coefficients ($k' \gg k''$).

In the DLR pipeline, a first extinction correction is implicitly obtained through the subtraction of the differential background flux N_{ij}^{bg} in Equation (5.7). A second correction is applied by the program `ZEROOFFSET`. It calculates for each frame j and a subset of stars i the median deviation

$$\delta m_j = \underset{i}{\mathrm{median}}\left(m_{ij} - \widetilde{m}_i\right) \tag{5.10}$$

from the median magnitude $\widetilde{m}_i$ and subtracts it from all measurements, i.e.,

$$m'_{ij} = m_{ij} - \delta m_j. \tag{5.11}$$

The calculation of δm_j in Equation (5.10) is typically obtained using several thousand stars which have the lowest standard deviation in a data set. As such, it is equivalent to the calculation of a comparison star. The corrections δm_j are typically in the order of a few mmag for BEST II, but can increase the photometric precision in particular for bright stars significantly.

SysRem

The corrections discussed so far successfully resolve average trends and are sensitive to globally affected scientific images. However, systematics can remain in subsets of light curves. Such effects may be associated with, e.g., color-dependent extinction (Equation (5.9)), PSF changes due to a variation of temperature and/or seeing, or other instrumental effects.

Detrending algorithms aim at the detection and removal of such residual systematic effects. The most important in the context of photometric measurements are the *Trend Filtering Algorithm* (TFA; Kovács et al. 2005) and *SysRem* (Tamuz et al. 2005). These do not require any prior knowledge regarding the origin of systematics; instead, they simply identify trends which are commonly encountered in a set of light curves.

The SysRem algorithm is used for detrending in the DLR pipeline. Its basic idea is to find coefficients c_i for each star i and a_j for each frame j that minimize the expression

$$\sum_{ij} \frac{(r_{ij} - c_i a_j)^2}{\Delta m_{ij}^2} \ , \tag{5.12}$$

whereby $r_{ij} = m'_{ij} - \overline{m}_i$ are the mean-subtracted stellar magnitudes and Δm_{ij} the corresponding uncertainties. The coefficients are used to subtract systematic trends, i.e., the correction

$$r_{ij}^{(1)} = r_{ij} - c_i a_j \tag{5.13}$$

is applied to the data. The whole procedure can be repeated with the corrected data set to find higher order effects, i.e., new vectors $(c_i^{(2,3,\ldots)})$ and $(a_j^{(2,3,\ldots)})$. Finally, cleaned light curves are obtained by

$$m''_{ij} = \overline{m}_i + r_{ij}^{(n\mathrm{sys})} \ , \tag{5.14}$$

whereby n_{sys} denotes the number of SysRem iterations. It must be chosen carefully so that physical variability is not removed; most important criteria in this respect are the fraction of light curves which have been improved by the k-th iteration, and a visual inspection of the corresponding frame vector $(a_j^{(k)})$.

The pipeline implementation of the SysRem algorithm was initially adapted and applied successfully to BEST data (Wiese 2007; Pasternacki 2009). It was tested as well on the first BEST II data sets, but showed only minimal improvements (Kabath 2009). The main problem was that the algorithm often removed real variability instead of systematics already during the first few iterations. While this effect was also encountered with BEST, it only occurred at later iteration steps due to generally larger systematic trends in the data. A second, more technical challenge was experienced with the most recent BEST II and ASTEP data sets. Since these include both a large number of frames and stars, the matrices (r_{ij}) exceeded the memory capacity of IDL.

A solution to both problems was found in the framework of this thesis by applying two limits. First, faint stars with $\overline{m}_i > m_{\mathrm{sys}}^{\mathrm{max}}$ are completely excluded from detrending, because their intrinsic photon noise is typically much larger than any

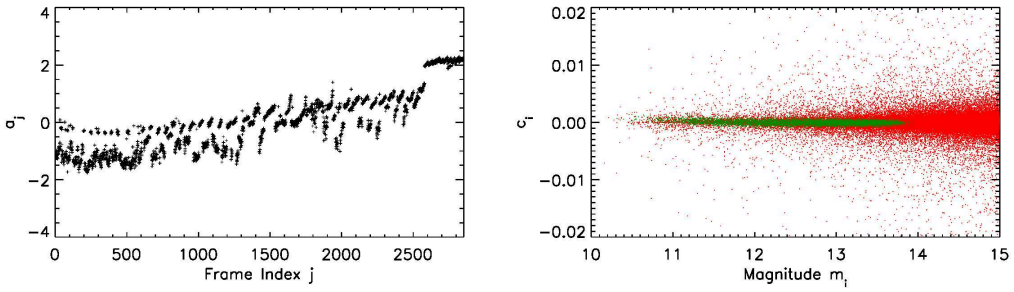

(a) First set of SysRem coefficients – left plot $(j, a_j^{(1)})$, right plot $(\overline{m}_i, c_i^{(1)})$

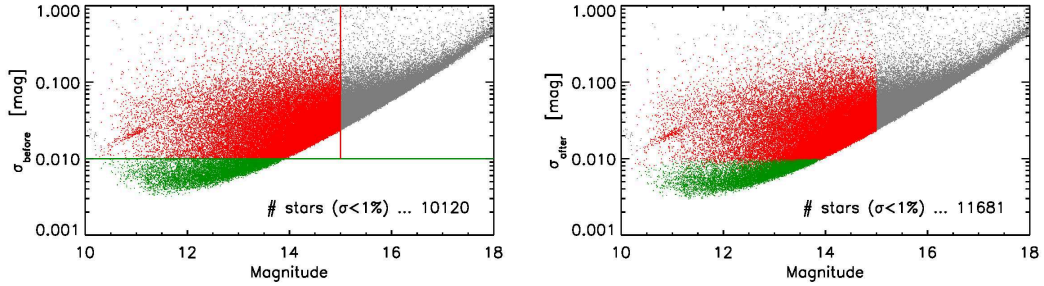

(b) RMS plots *before* (left) and *after* SysRem (right)

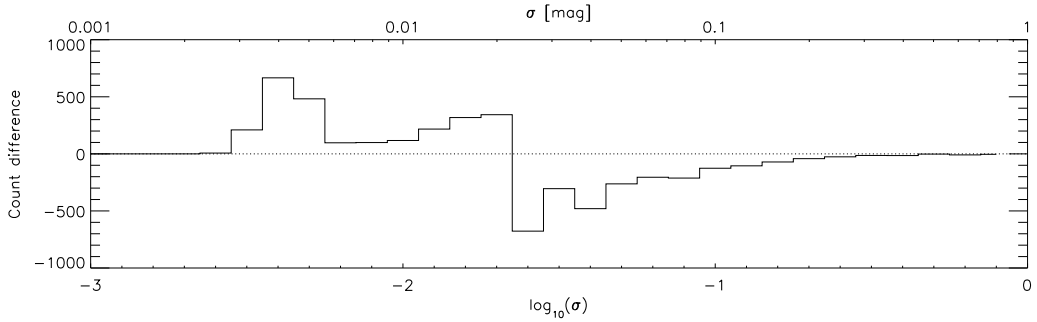

(c) Differences in the number of light curves (*after* minus *before* SysRem), in bins of $0.1 \log_{10}(\sigma)$

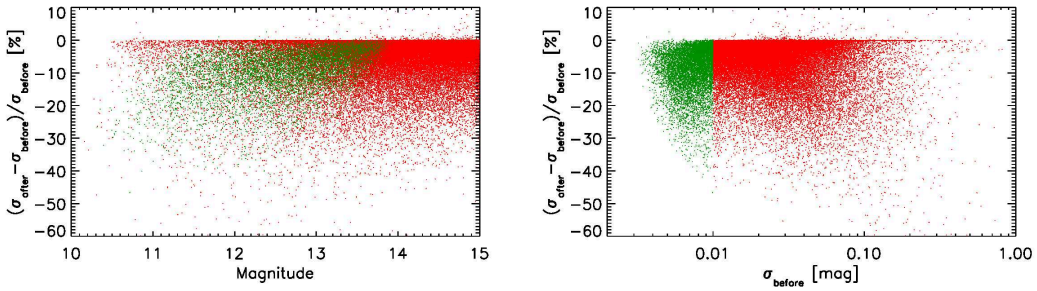

(d) Relative RMS change through SysRem, shown as a function of magnitude (left) and σ (right)

Figure 5.6: Photometric improvement through the SysRem algorithm – example of the BEST II data set F19. Five SysRem runs have been applied to detrend the light curves ($n_{\mathrm{sys}} = 5$, cf. Section 6.2). Stars that were used for the calculation of the SysRem coefficients (c_i) and (a_j) (Equation (5.12)) are marked *green* ($\sigma_{\mathrm{sys}}^{\mathrm{max}} = 1\%$), while *red* data points correspond to stars that were only corrected by the algorithm (Equation (5.13)). Completely excluded stars are shaded *gray* ($m_{\mathrm{sys}}^{\mathrm{max}} = 15$).

systematic trend. Through this limit, the size of all investigated data sets could be sufficiently decreased in order to apply the algorithm. Second, systematic effects are only determined on a subset

$$S_\star^{\mathrm{sys}} = \{i \mid \sigma_i \leq \sigma_{\mathrm{sys}}^{\mathrm{max}}\} \tag{5.15}$$

of low-noise light curves. These are then used to detrend bright stars, i.e., all light curves with $\overline{m}_i \leq m_{\mathrm{sys}}^{\mathrm{max}}$. With the assumption that residual systematic effects are much smaller than stellar variability, a limit in the order of $\sigma_{\mathrm{sys}}^{\mathrm{max}} = 1\%$ can be used to exclude most variable stars from the calculation of (c_i) and (a_j).

Figure 5.6 shows an example for the application of SysRem. The large BEST II data set F19 was detrended by five iterations (see Section 6.2 for a discussion on n_{sys} in this field). The coefficients $(c_i^{(1)})$ and $(a_j^{(1)})$ of the first effect are displayed in Figure 5.6a and show how SysRem can remove residual trends that are not identified through frame averaging; depending on the stellar coefficient c_i, the vector (a_j) is either subtracted or added to light curve i. The left panel of Figure 5.6b shows the new limits for the SysRem implementation in a $(\overline{m}_i, \sigma_i)$ plot: Green stars are used for the calculation, green and red stars are detrended, and gray stars are not included at all. The improvement of photometric precision is significant – Figure 5.6c gives the relative change of star counts in bins for different noise levels. In particular, it shows a large increase of light curves with mmag precision, which is especially important for the search of transit signals with amplitudes of $\delta F \approx 1\%$. Finally, a comparison of the noise levels σ_{before} and σ_{after} is given in Figure 5.6d as a function of the magnitude $\overline{m}_i$ and the initial standard deviation σ_{before}. In addition to the clear overall increase of photometric quality, it shows that the new distinction into two groups of stars works very well: Although the SysRem coefficients have only been determined on the (green) subset $S_\star^{\mathrm{sys}}$ of low-noise stars, they can be applied successfully to remove systematic effects from the (red) remainder of stars with $\sigma_i > \sigma_{\mathrm{sys}}^{\mathrm{max}}$ but $\overline{m}_i \leq m_{\mathrm{sys}}^{\mathrm{max}}$.

The influence of the adapted SysRem algorithm on the BEST II transit search performance will be studied in Section 6.2.

Frame Quality

Poor scientific images can be encountered for various reasons, e.g., bad guiding, or thin cirrus clouds. If they have not been sorted in previous steps of the pipeline, they can yield outliers in the light curves of many stars. As such, even a few bad frames can significantly affect a scientific analysis such as the search for transit signals. To reject them automatically, a criterion for the frame quality has been implemented in the framework of this thesis.

A frame j is considered "bad" if many data points m''_{ij} deviate from their respective stellar mean magnitude $\overline{m}_i$. In order to be more sensitive to low-noise light curves, these deviations are weighted with the stellar standard deviation σ_i. Quantitatively, this corresponds to defining a frame quality parameter

$$\gamma_j = \frac{1}{N_\star^{\mathrm{fq}}} \sum_{i \in S_\star^{\mathrm{fq}}} \frac{\left(m''_{ij} - \overline{m}_i\right)^2}{\sigma_i^2}, \tag{5.16}$$

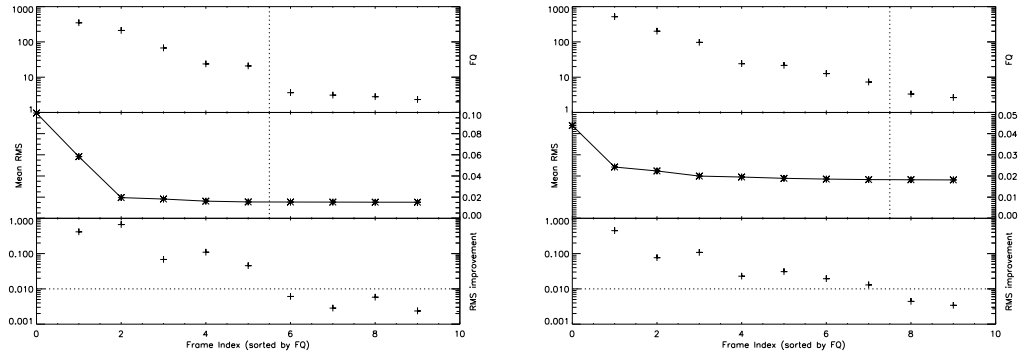

(a) Cutoff criteria for bad frames: Frame quality γ_j, mean $\overline{\sigma}_k^{\mathrm{fq}}$ and improvement $\delta\sigma_k$

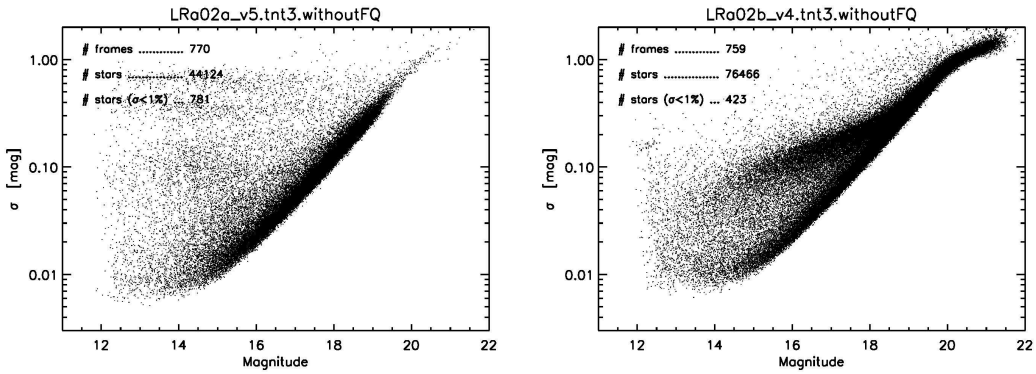

(b) RMS plots *before* removing frames with high γ_j values

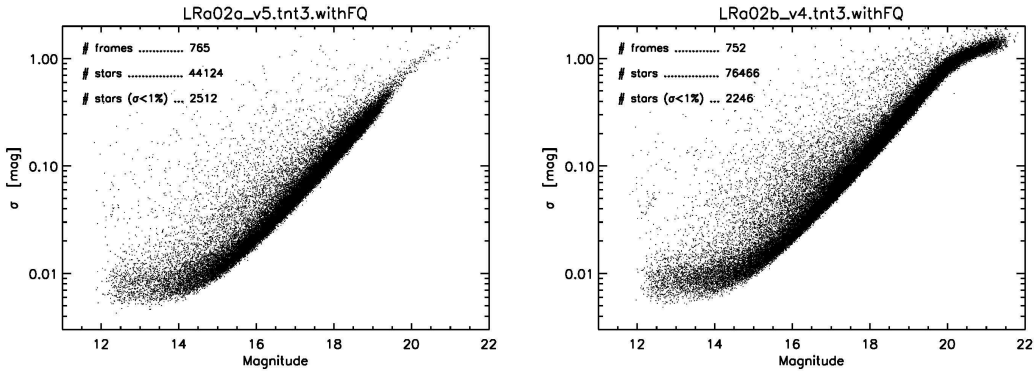

(c) RMS plots *after* removing frames with high γ_j values

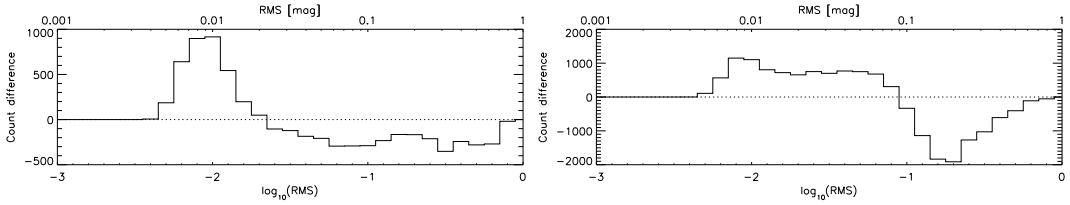

(d) Differences in the number of light curves (*after* minus *before* removing bad frames)

Figure 5.7: Exclusion of bad frames using the frame quality parameter γ_j (Equation (5.16)) for the data sets LRa02*a (left panels)* and LRa02*b (right)*. (a) shows the quality parameter γ_j, the mean standard deviation $\overline{\sigma}_k^{\mathrm{fq}}$ and its relative improvement $\delta\sigma_k$, starting with the worst frame (i.e, sorted in descending order of γ_j). (b/c) plots the light curve's standard deviation σ vs. stellar magnitudes before/after removal of bad frames. (d) shows the distribution of star count difference after minus before in bins of photometric noise (bins are $0.1\log_{10}(\sigma)$ wide).

whereby $S_\star^{\mathrm{fq}}$ denotes a subset of $N_\star^{\mathrm{fq}}$ stars that are taken into account for the calculation of γ_j. Typically, these are the brightest stars which show small photometric noise (the brightest 10% are used by default). Independently from this work, Bayliss and Sackett (2011) recently presented an almost identical parameter that is used to exclude bad frames from SuperLupus (Bayliss et al. 2009) data.

Ideally, outliers are identified by rejecting the null hypothesis of pure noise with high statistical confidence, i.e., by comparing the real distribution of γ_j with a theoretical expectation. Unfortunately, extensive tests to model the distribution of γ_j failed because the required assumption of Gaussian noise was not valid for the tested BEST II data.

Therefore, manual cuts are applied to distinguish between good and bad frames. The pipeline includes two options: The first is to set a limit $\gamma_{\max}$ which excludes all frames with $\gamma_j > \gamma_{\max}$. The second uses a relative improvement of the photometric precision as a criterion. For that, the mean standard deviation $\overline{\sigma}_k^{\mathrm{fq}}$

$$\overline{\sigma}_k^{\mathrm{fq}} = \frac{1}{N_\star^{\mathrm{fq}}} \sum_{i \in S_\star^{\mathrm{fq}}} \sigma_{ik} \tag{5.17}$$

is calculated for the brightest $N_\star^{\mathrm{fq}}$ stars as a function of k. The parameter k denotes the number of bad frames sorted in descending order of γ_j. Likewise, σ_{ik} gives the standard deviation of light curve i *without* the k worst frames. The quantity

$$\delta\sigma_k = \frac{\overline{\sigma}_{k-1}^{\mathrm{fq}} - \overline{\sigma}_k^{\mathrm{fq}}}{\overline{\sigma}_{k-1}^{\mathrm{fq}}} \tag{5.18}$$

is finally used to evaluate the improvement of the photometric quality. It gives the relative photometric noise improvement by removal of the k-th frame. Low values of $\delta\sigma_k$ and/or a sharp drop in the $(k, \delta\sigma_k)$ diagram can be used to distinguish outliers from normal images. In this second option, the number of removed frames k_{fq} is then defined through a limit $\delta\sigma_{\mathrm{limit}}$ such that

$$\delta\sigma_{k_{\mathrm{fq}}} > \delta\sigma_{\mathrm{limit}} > \delta\sigma_{k_{\mathrm{fq}}+1} \ . \tag{5.19}$$

As an example, Figure 5.7 shows the frame quality procedure at work on the BEST II data set LRa02. The uppermost panel, Figure 5.7a, shows the quality parameter γ_j, followed by the mean standard deviation $\overline{\sigma}_k^{\mathrm{fq}}$, and finally its relative improvement $\delta\sigma_k$ as a function of the parameter k (i.e., starting with the worst frame). In this example, a limit of $\delta\sigma_{\mathrm{limit}} = 0.01$ works well to separate outliers. It excludes five frames in LRa02a and seven in LRa02b. Although the number of outliers is relatively small, the improvement of the photometric quality is remarkable: Figures 5.7b and 5.7c show the standard deviations and magnitudes of all stars, before and after the removal, respectively. While many light curves showed large noise levels of $\sigma \gg 10\%$ even for bright stars before, the procedure yields a significant decrease. In particular, the number of stars with $\sigma < 1\%$ increases by a factor of four (from 1,204 to 4,758, both data sets). Figure 5.7d shows the relative change before/after as a function of the initial photometric noise.

5.2.3 Catalog Match

In a last step, all stars are matched with an astrometric catalog. This procedure has two aims: To assign equatorial coordinates (α, δ) to each star and to adjust the instrumental magnitudes to a standard magnitude system. The latter yields best results if the catalog system matches the photometric response of the instrument well.

Astrometry

The pipeline program `HATASTROMETRY` first retrieves the astrometric positions (α, δ) for all catalog stars around a given pointing coordinate. Therefore, the catalog is chosen to closely match both the instrumental resolution and magnitude range; for BEST II, optimal results are obtained with USNO-A2.0 (Monet 1998) and UCAC3 (Zacharias et al. 2010). The subroutine `grmatch` is then used to find the transformation between CCD (x, y) and equatorial (α, δ) coordinates, while `grtrans` finally applies it to all stars in the data set (both by Pál and Bakos 2006).

Magnitude Adjustment

Typically more than 90% of all light curves can be matched with a catalog star. For this subset $S_\star^{\mathrm{cat}}$ it is possible to compare the median instrumental magnitude $\widetilde{m}_i$ with a corresponding catalog value m_i^{cat}. In order to obtain a brightness calibration, the median difference

$$\delta m = \underset{i \in S_\star^{\mathrm{cat}}}{\mathrm{median}}(m_i^{\mathrm{cat}} - \widetilde{m}_i) \tag{5.20}$$

is used to shift the whole magnitude range, i.e.,

$$m_{ij}''' = m_{ij}'' + \delta m. \tag{5.21}$$

The goodness of this calibration largely depends on how well the spectral range of the observation matches the catalog. For BEST II, a good agreement is reached with the R band of USNO-A2.0 or UCAC3 (cf. Figure A.2). However, in this approach the different photometric systems usually yield an average calibration accuracy of only about 0.5 mag. Therefore, *absolute* photometric magnitudes obtained in this way are only used as an estimation. In contrast, only *relative* brightness variations are important for detecting transiting extrasolar planets and stellar variability, which is the scientific focus of photometric surveys like BEST II. In fact, these can be measured to a much higher precision: For example, BEST II reaches a noise level of 2–3 mmag for the brightest stars in a field over a whole observing season (see Section 4.3).

5.3 Summary

The DLR photometric pipeline is used to reduce the data sets presented in this work: Calibration procedures remove instrumental effects from raw images, the processed frames are aligned and subtracted, and unit-weight aperture photometry is applied to extract light curves for stars within the FOV. The photometric noise level is improved further through corrections of atmospheric extinction and systematic effects, as well as the removal of outliers. Finally, a catalog match yields equatorial coordinates for each star and an adjustment of instrumental magnitudes.

The described pipeline has been used within the BEST/BEST II project before (Rauer et al. 2004, 2010; Voss 2006; Kabath et al. 2007, 2008, 2009a, b; Karoff et al. 2007; Wiese 2007; Fruth 2008; Kabath 2009; Pasternacki 2009; Pilello 2010; Schulze 2010; Pasternacki et al. 2011) and is constantly being improved. In order to achieve the aims of this thesis, various changes have been applied to the pipeline. While being too numerous to be listed individually, they can broadly be assigned to the following improvements:

Platform- and project-independent. The pipeline has been developed further to reduce data of projects other than BEST/BEST II and to run flexibly on different systems. All project- or system-dependent parameters are stored in configuration files which can easily be adjusted. For this work, these changes were particularly necessary to reduce ASTEP data (Chapter 10). However, the improved pipeline has also been applied successfully by other projects, e.g., to reduce data from the *Tautenburg Exoplanet Search Telescope* (TEST, Eigmüller and Eislöffel 2009), the *Variable Young Stellar Object Survey* (VYSOS 6, Buda 2011), or a prototype of the *Next Generation Transit Survey* (NGTS, Chazelas et al. 2012).

Photometric quality. The photometric quality could be improved through an automatic identification of bad frames and the adaptation of the SysRem detrending algorithm to BEST II and ASTEP. SysRem is especially important to reveal the small signals of transiting planets (see Chapter 6).

CoRoT follow-up. Delays in the analysis of BEST II follow-up observations could significantly be reduced. A new and clear procedure is used for calibration on a nightly basis, i.e., immediately after observing, and if necessary on-site.

Semi-automatic approach. Where possible, repetitive manual interaction is avoided. The pipeline is designed to instead use valuable manpower for a quality assessment of automatically generated results, thus yielding a more consistent and/or better photometric quality. Examples include the new calibration procedures, the automatic selection of reference frames, and the rejection of bad images.

Within this work, the improved pipeline has been used to reduce eight BEST II and three ASTEP 400 data sets (see Appendix D for details). The scientific results are presented in Part III: BEST II light curves are analyzed in Chapter 8 for transiting planets, and for stellar variability in Chapter 9. Joint observations of ASTEP and BEST II are presented in Chapter 10.

6 Transit Search – Description and Validation

Many algorithms that are used for periodicity search in photometric time series try to fit the light curve with a set of orthogonal functions. For example, the Analysis of Variance algorithm (Schwarzenberg-Czerny 1996), used to characterize stellar variability in BEST II data sets (see Chapter 7), is based upon Fourier series. However, such algorithms are generally not well adapted to the special shape of a transit light curve: A star with a transiting planet shows very few variation throughout the largest part of its light curve, but for a very short fraction of the orbital period, the transit causes a small but steep intensity drop.

An algorithm by Kovács et al. (2002) uses the *Box-Fitting Least Squares* (BLS) method to account for this special shape. It is the most commonly used tool to search for transit-like signals in photometric time series, being applied by leading ground-based projects such as SuperWASP (Collier Cameron et al. 2006), HAT (e.g., Johnson et al. 2011), and OGLE (Udalski et al. 2004), as well as partly by the space missions CoRoT (Surace et al. 2008) and Kepler (Latham et al. 2011). Tingley (2003a, b) has tested several algorithms and shown that BLS yields the best detection performance; the same conclusion was drawn from a competitive approach to find artificial transits in simulated CoRoT data (CoRoT *blind tests*; Moutou et al. 2005, 2007).

Transit Search with BEST/BEST II

The first transit search within the DLR pipeline was implemented by Voss (2006) to analyze BEST data. It used a box fitting algorithm similar to BLS, but the detection efficiency of BEST was strongly affected by its low duty cycle. For example, several candidates were found with single transit-like events (Wiese 2007), and the transits of CoRoT-1b and CoRoT-2b were only found after being detected by the CoRoT team, despite being observed prior to CoRoT (Rauer et al. 2010).

For BEST II, BLS was used to search for transits in the first observed CoRoT fields. However, the first version was not optimized for BEST II and was particularly time-consuming, thus limiting the analysis to a small subset of light curves. Due to these issues, the first four planetary candidates of BEST II could only be identified using stellar variability algorithms (Kabath 2009).

A large improvement for the BEST II transit search was achieved in the framework of the master thesis by Schulze (2010). By using a BLS implementation of Juan Cabrera (DLR), it was possible to reduce the computation time by several orders of magnitude, thus enabling the analysis of more stars with a better numerical precision. Furthermore, the signal-to-noise ratio of detections could be improved significantly through tests with artificial transit light curves and an optimization of parameters such as the binning size or the usage of error weighting.

This chapter describes the BEST II transit search method and evaluates its performance. Section 6.1 gives a brief overview of the BLS algorithm used and its current implementation. In Section 6.2, the detection efficiency is tested and evaluated with light curves from the largest BEST II data set at hand, F19, into which artificial transits were inserted. Finally, Section 6.3 summarizes this chapter and discusses the performance with regard to the system specifications.

6.1 BLS Algorithm

Theoretical Description

The BLS algorithm anticipates the shape of a transit signal to build a mathematically very simple model. First, the light curve $\{(t_j, f_j, \Delta f_j)\}$ is folded with a given test period p to $\{(t'_j, f'_j, \Delta f'_j)\}$. The model assumes only two discrete values:

- L for $j \in [j_1, j_2]$ (in transit)
- H otherwise

The indices j_1 and j_2 thereby denote the the first and last measurement in transit, respectively.

Kovács et al. (2002) showed that the best box fit to the light curve is obtained by maximizing the signal residue

$$SR = \sqrt{\frac{s^2}{r(1-r)}} \tag{6.1}$$

using the definitions

$$s = \sum_{j \in [j_1, j_2]} w'_j f'_j \quad \text{and} \quad r = \sum_{j \in [j_1, j_2]} w'_j \tag{6.2}$$

with weights w'_j corresponding to each flux value f'_j. For any given period p, the BLS algorithm probes the parameters L, H, j_1, and j_2 within physically reasonable ranges (e.g., with an upper limit on the transit depth $H - L$) for a maximum of SR. Subtracting the average flux from all measurements yields an additional relation between H and L that can be used to decrease the number of free parameters by one. Furthermore, the performance of BLS is improved by rejecting unphysical "inverse" transits (i.e., with $H < L$; Tingley 2003b).

Period Determination

The parameter

$$\Theta_{\mathrm{bls}}(p) = \max(SR) \tag{6.3}$$

is calculated for each test period p to form the BLS *power spectrum* $p \to \Theta_{\mathrm{bls}}(p)$. Its maximum $\Theta_{\mathrm{bls}}(p_{\mathrm{bls}}) = \max(\Theta_{\mathrm{bls}}(p))$ is used to determine p_{bls}, i.e., the period with the most evident transit-like signal (see Figure 6.1).

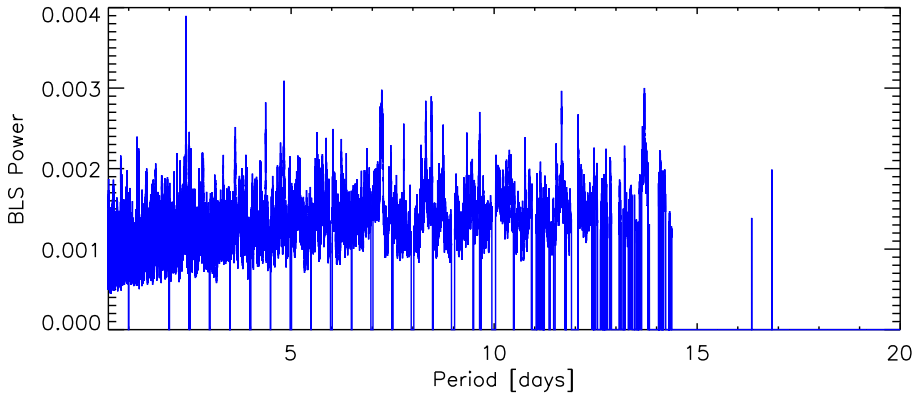

Figure 6.1: Example BLS power spectrum $\{p_m, \Theta_{\mathrm{bls}}(p_m)\}$ for a BEST II planetary candidate (F19_068690; see Chapter 8). The maximum value of Θ_{bls} is encountered at $p_{\mathrm{bls}} = 2.41246^d$. (Note that periods with a phase coverage of less than $n_{\mathrm{box}}^{\mathrm{min}} = 80\%$ have been excluded from the analysis.)

The significance of the fit is quantified by comparing the peak power to the overall noise level, i.e., the signal-to-noise ratio

$$S_{\mathrm{bls}} = \frac{\Theta_{\mathrm{bls}}(p_{\mathrm{bls}})}{\sigma(\Theta_{\mathrm{bls}})} \tag{6.4}$$

is obtained through division of $\Theta_{\mathrm{bls}}(p_{\mathrm{bls}})$ by the power spectrum's standard deviation $\sigma(\Theta_{\mathrm{bls}})$.

Binning

In order to increase the detection efficiency, adjacent measurements are binned. The folded light curve is divided into equidistant "boxes" B_k that are each assigned a number of N_k measurements via

$$B_k = \{j \mid \lfloor N_{\mathrm{box}} \cdot t_j/p \rfloor \bmod N_{\mathrm{box}} = k-1\} \text{ with } k = 1, 2, \ldots, N_{\mathrm{box}}. \tag{6.5}$$

Thereby, the box count N_{box} is calculated from the number N_t of measurements through $N_{\mathrm{box}} = N_t/\widetilde{N}_K$, with the parameter $\widetilde{N}_K$ specifying a targeted mean box occupancy. Individual measurements f'_j and weights w'_j are replaced by box-averaged values f_k^{box} and w_k^{box} in Equation (6.2). The fluxes are calculated via

$$f_k^{\mathrm{box}} = \frac{\sum_{j\in B_k} w_j\, f_j}{\sum_{j\in B_k} w_j} \quad \text{with} \quad w_j = 1/\Delta f_j^2 \ , \tag{6.6}$$

and weighted standard deviations

$$\Delta f_k^{\mathrm{box}} = \left(\frac{N_k}{N_k - 1} \cdot \frac{\sum_{j\in B_k} w_j \left(f_j - f_k^{\mathrm{box}}\right)^2}{\sum_{j\in B_k} w_j} \right)^{1/2} \tag{6.7}$$

are used to obtain box weights $w_k^{\mathrm{box}} = 1/(\Delta f_k^{\mathrm{box}})^2$.

Implementation

The current implementation of the algorithm is described in detail by Fruth et al. (2011). First, a BLS spectrum is obtained on a grid of discrete periods

$$p_m = \left(1 + \frac{\Delta E_{\mathrm{lim}}}{t_N - t_1}\right)^m \cdot p_{\mathrm{bls}}^{\mathrm{min}} \tag{6.8}$$

within a defined range of $\left[p_{\mathrm{bls}}^{\mathrm{min}}, p_{\mathrm{bls}}^{\mathrm{max}}\right]$. Thereby, the parameter ΔE_{lim} defines the maximum error in the ephemeris, and t_1 and t_N denote the first and last observing date, respectively. For each period p_m, the light curve is folded and binned into N_{box} boxes (Equations (6.5)–(6.7)), and the BLS power Θ_{bls} is calculated (Equation (6.3)). Periods having less than $N_{\mathrm{box}} \cdot n_{\mathrm{box}}^{\mathrm{min}}$ boxes with at least one measurement are excluded from the analysis. Finally, the spectrum $\{p_m, \Theta_{\mathrm{bls}}(p_m)\}$ is used to determine the final period p_{bls} and its significance S_{bls} (Equation (6.4)). Figure 6.1 shows an example.

Default parameters for the usage of BLS with BEST II data were obtained and described by Schulze (2010); they are used in this work and listed in Appendix D.

6.2 Validation of BLS for BEST II

Simulated transits can be used to characterize the transit search performance of both BEST II and its detection pipeline. Are transits found successfully in the expected range of photometric precision and orbital periods? First tests with real BEST II light curves by Schulze (2010) showed that the BLS algorithm can successfully identify the majority of simulated transits with large depths ($\delta F \geq 3\%$) for the brightest stars in a data set ($m \lesssim 15\,\mathrm{mag}$). The detection efficiency decreased rapidly with increasing orbital periods and reached vanishingly small values for $p \gtrsim 3$ days. However, this first study used the same orbital phase for all artificially inserted transits. Since the number of observed transits is strongly correlated to the selected phase, the results were highly affected by the observational window function. In order to assess the detection efficiency of BEST II quantitatively, it was thus necessary to set up a second test run with random orbital phases and periods; the procedures are first described in the following Sections 6.2.1 and 6.2.2 and then applied to BEST II data in Section 6.2.3.

6.2.1 UTM

The *Universal Transit Modeller (UTM)* is a program to simulate light curves of various configurations of eclipsing and transiting objects (Deeg 2009). It can be used to either generate whole light curves and/or to add a certain transit signal to real photometric time series. Modeled systems can include an arbitrary number of stars, planets, moons, and rings.

Due to its flexibility for a large variety of modeled star-planet configurations, it is widely used within the transit search community. Its main two applications are the fitting of model light curves to observations and the evaluation of detection algorithm performances. In the CoRoT team, it was for instance used successfully as part of a study to compare different transit search algorithms (Moutou et al. 2005).

The UTM package was included into the DLR pipeline as a standard tool to insert planetary transits into BEST/BEST II light curves. The new routine `APPLY_UTM` can be used to insert artificial transits with a fixed depth, but having random phases and orbital periods (within a given range) into any given data set. Transits can either be applied to every light curve or to only a fraction of stars.

6.2.2 Test Setup

In order to validate the DLR transit search, artificial transits were inserted into BEST II data with the aim to recover them using BLS. Real light curves of target field F19 were selected for this purpose, being the largest data set recorded by BEST II so far. From all 127,202 stars in F19, only those with a low photometric noise provide a realistic chance of finding small transit-like signals. Therefore, a sub-sample of 10,120 light curves with standard deviations $\sigma_i \leq 0.01\,\mathrm{mag}$ was selected for the exercise.

The performance of search algorithms not only depends on the number of transits identified correctly, but also on those falsely identified. Stars that have been identified as candidates although there is no real signal present are called *false positives*. In order to study this effect, artificial transits were only inserted into every 10th star.

The validation was set up as follows. First, 1,012 light curves (10%) were randomly selected from the 10,120 low-noise stars of data set F19. Second, transit signals of equal depth were included into these light curves using UTM. Thereby, all orbits are circular and have central transits ($i = 90°$), and limb-darkening is neglected. The periods follow a uniform random distribution between 0.5 and 10 days[1], and orbital phases are randomly distributed between 0 and 1. Third, the data set was analyzed using the DLR implementation of BLS (parameters as in Table D.1 for F19). The range of test periods was set to $p_{\mathrm{bls}} = \left[0.5^d, 20^d\right]$; its upper limit was purposely extended further than the maximal artificial period to allow for false alarms.

Finally, the whole procedure was carried out with three different transit depths of $\delta F = 0.5\%, 1\%$, and 2% in order to assess the influence of the signal-to-noise ratio on the transit detection efficiency.

Performance Evaluation

In order to evaluate the success of the transit search quantitatively, BLS results are compared with the artificially introduced UTM signals. Thereby, a correctly identified period is considered the prime and mandatory condition for detection.

For every artificial planet, the orbital period p_{utm} is compared with p_{bls} from BLS, yielding three main quantities/categories:

[1] Shorter periods are not expected around solar-like stars (Cabrera et al. 2012) and longer orbits yield a vanishingly small phase coverage for the given data set (cf. Figure 4.7)

1. $N_{\rm bls}^{\rm correct}$ – the number of "planets" with a *correctly* identified period. To account for numerical errors, periods $p_{\rm bls}$ within a 1% tolerance range of $p_{\rm utm}$ are considered as correct.
2. $N_{\rm bls}^{\rm multi}$ – the number of "planets" with *multiples* of the correct period. Values of $p_{\rm bls}$ within 1% of $\frac{m}{n} \cdot p_{\rm utm}$ (with $m, n \in \{1, 2, 3, 4, 5\}$ and $m \neq n$) are accepted as almost correct detections, because such small integral multiples of the correct period can often easily be identified by additional light curve analysis.
3. $N_{\rm bls}^{\rm miss}$ – the number of "planets" that are *missed*, i.e., not contained in 1 or 2.

Depending on the focus, the three quantities are either evaluated in respect to the whole set of 1,012 artificial planets, or as a function of an additional interesting parameter, such as the orbital period or the significance of the BLS result. Furthermore, the first two categories are usually combined to a total number of *detections* $N_{\rm bls}^{\rm det} = N_{\rm bls}^{\rm correct} + N_{\rm bls}^{\rm multi}$.

For the performance of a transit search, it is also important to investigate the number of false alarms. Therefore, a fourth quantity is calculated:

4. $N_{\rm bls}^{\rm false}$ – the number light curves that are *falsely* identified as candidates.

It requires a criterion to distinguish planetary candidates from non-significant box-like signals. In the following, a light curve is considered to contain a significant transit-like signal, if its highest BLS peak is found at least $S_{\rm bls}^{\rm min}$ times above the noise level, i.e.,

$$S_{\rm bls} \geq S_{\rm bls}^{\rm min} \ . \tag{6.9}$$

6.2.3 Results

An initial BLS test was applied to search in unfiltered F19 light curves, i.e., after artificial transits had been inserted to the data set including all calibration steps except the removal of systematics (SysRem; see Section 5.2.2). Table 6.1 shows the numbers of correct and missed detections, as well as the false alarm count for an SNR limit of $S_{\rm bls}^{\rm min} = 6.12$ (the determination of this limit will be discussed later in this section). Due to bad phase coverage, BLS automatically skipped the range of long periods $14.5^d \lesssim p_{\rm bls} \leq 20^d$ almost entirely (see also Figure 6.1).

Table 6.1: Results from the BLS tests in the F19 data set.

	Without SysRem				After SysRem			
δF	$N_{\rm bls}^{\rm det}$	$N_{\rm bls}^{\rm miss}$	$N_{\rm bls}^{\rm false}$	$S_{\rm bls}^{\rm eq}$	$N_{\rm bls}^{\rm det}$	$N_{\rm bls}^{\rm miss}$	$N_{\rm bls}^{\rm false}$	$S_{\rm bls}^{\rm eq}$
0.5%	(2.6%) 33	(6.4%) 81	(91.0%) 1146	–	(11.5%) 84	(7.1%) 52	(81.3%) 592	8.61
1%	(9.2%) 120	(5.0%) 65	(85.8%) 1121	9.13	(27.2%) 232	(4.2%) 36	(68.5%) 584	7.22
2%	(24.6%) 384	(3.3%) 52	(72.1%) 1126	7.59	(42.0%) 456	(3.4%) 37	(54.6%) 592	6.35

Notes. The number of stars identified with a BLS significance of $S_{\rm bls} \geq 6.12$ (Equation (6.4)) is given for each of the tested transit depths before and after application of SysRem ($n_{\rm sys} = 5$). For light curves with artificial transits, the number of candidates identified with the correct or a multiple period ($N_{\rm bls}^{\rm det} = N_{\rm bls}^{\rm correct} + N_{\rm bls}^{\rm multi}$) is compared to those with a wrong period ($N_{\rm bls}^{\rm miss}$). The number of light curves with $S_{\rm bls} \geq 6.12$ which contained no artificial signal is denoted by $N_{\rm bls}^{\rm false}$. The quantity $S_{\rm bls}^{\rm eq}$ gives the largest value of $S_{\rm bls}^{\rm min}$ at which $N_{\rm bls}^{\rm false} \geq N_{\rm bls}^{\rm det}$ (cf. Figure 6.9).

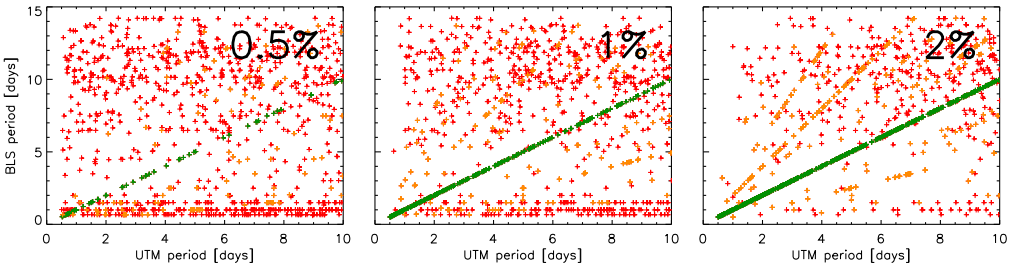

(a) Without SysRem

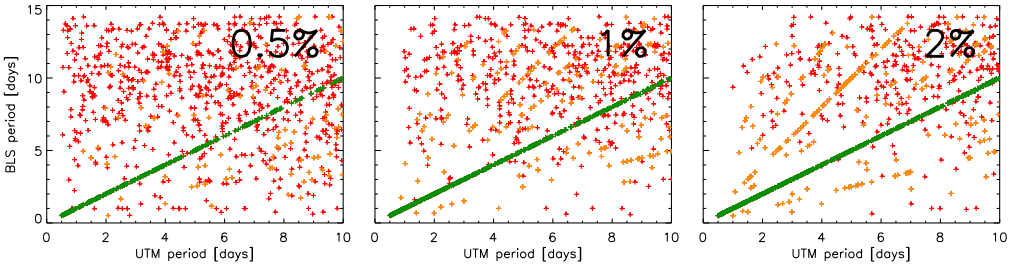

(b) After SysRem

Figure 6.2: Periods p_{bls} determined by BLS vs. orbital periods p_{utm} for light curves with artificially inserted UTM signals. Results are shown for all three tested transit depths, as well as before (a) and after application of SysRem (b, with $n_{\mathrm{sys}} = 5$). Correctly identified periods are shown in *green*, multiples in *orange*, and wrong periods in *red* color.

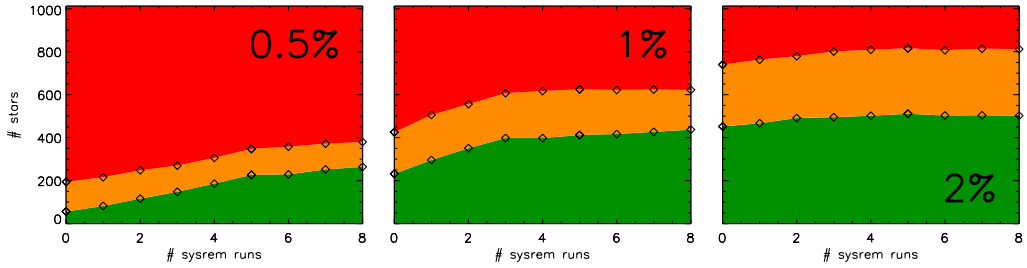

Figure 6.3: Detected test planets as a function of the number of SysRem runs, n_{sys}, and transit depth δF. The cumulative counts of transits identified with the correct period ($N_{\mathrm{bls}}^{\mathrm{correct}}$, *green*), multiples thereof ($N_{\mathrm{bls}}^{\mathrm{multi}}$, *yellow*), and wrong periods ($N_{\mathrm{bls}}^{\mathrm{miss}}$, *red*) are determined for *all* light curves with artificially introduced planets, i.e., independent of the BLS significance S_{bls} of individual results.

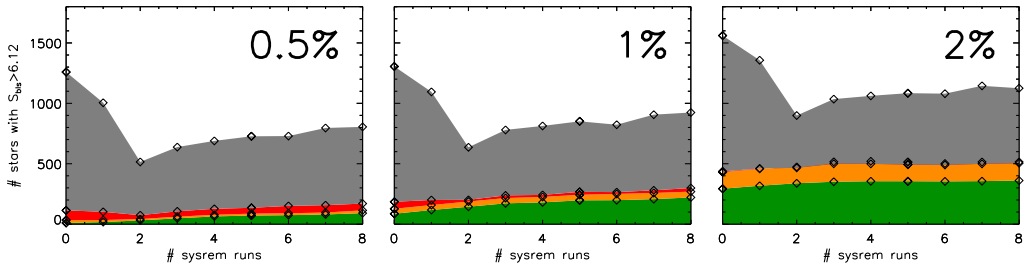

Figure 6.4: Test planets detected with a significance of $S_{\mathrm{bls}} \geq 6.12$ as a function of the number of SysRem runs, n_{sys}, and transit depth δF. On top of the cumulative counts $N_{\mathrm{bls}}^{\mathrm{correct}}$ *(green)*, $N_{\mathrm{bls}}^{\mathrm{multi}}$ *(yellow)*, and $N_{\mathrm{bls}}^{\mathrm{miss}}$ *(red)*, the number $N_{\mathrm{bls}}^{\mathrm{false}}$ of light curves without artificial transit but with $S_{\mathrm{bls}} \geq 6.12$ is shown in *gray*.

From the 1,012 light curves with artificial transits of $\delta F = \{0.5\%, 1\%, 2\%\}$ depth, only $N_{\rm bls}^{\rm det} = \{194, 425, 740\}$ were found by BLS in the first test with the correct or multiple period (disregarding their significance $S_{\rm bls}$). With a reasonable SNR limit of $S_{\rm bls}^{\rm min} = 6.12$, the detection counts decrease significantly (see Table 6.1), in particular for the small signals of 0.5% and 1%. Furthermore, the number of false alarms was found to be very high. From all light curves with significant transit-like signals of $S_{\rm bls} \geq 6.12$, only 9–28% contain a simulated transit signal (Table 6.1).

A visual inspection of unfiltered F19 light curves, folded with the periods found by BLS, revealed most signals to be caused by systematic effects. The most prevalent features fitted by BLS were flux changes after the nightly meridian flip of the German mount of BEST II, and other systematic trends that are most likely due to uncorrected higher order extinction effects. Due to the diurnal periodicity of these effects, most missed detections are – especially for the small transit depths of 0.5% and 1% – falsely identified with $p_{\rm bls} = 1^d$ or multiples thereof. Figure 6.2a shows how the corresponding false detections build up in lines of constant $p_{\rm bls}$. This clear influence on the transit search performance underlines the need for an automatic treatment of systematics. It motivated an adaptation and application of the SysRem algorithm (Tamuz et al. 2005) to BEST II data as described in Section 5.2.2.

Performance Improvements using SysRem

In order to study the influence of detrending on the transit search performance, the tests were repeated using a varying number of $n_{\rm sys} = 0, \ldots, 8$ SysRem runs applied to the data: Figure 6.3 shows how many artificial planets are detected or missed as a function of $n_{\rm sys}$. In addition to the results for unfiltered data, Table 6.1 shows the corresponding counts after five SysRem runs. Figure 6.4 shows the same quantities, but with the additional requirement of a significant SNR ($S_{\rm bls} \geq 6.12$).

The application of SysRem to the test data set F19 has two important effects on the transit search performance:

1. The number $N_{\rm bls}^{\rm det}$ of detected artificial transits increases significantly. An application of five SysRem runs doubles the count of correct or multiple periods for the two smallest tested signals (see Table 6.1; $N_{\rm bls}^{\rm det}$ increases from 33 to 84 for $\delta F = 0.5\%$, and from 120 to 232 for $\delta F = 1\%$). However, the performance increase is less distinct for the 2% signal ($N_{\rm bls}^{\rm det} = 384$ to 456), indicating that the removed systematic signals are predominantly in the order of $\delta F \lesssim 1\%$. For $n_{\rm sys} > 5$, the performance in Figure 6.3 does not show significant improvement.
2. The false alarm rate is reduced significantly. $N_{\rm bls}^{\rm false}$ decreases from ~ 1130 to ~ 590 after SysRem was used to remove systematic trends (for all tested depths, see Table 6.1). The first two SysRem runs result in the largest false alarm reduction, whereas $N_{\rm bls}^{\rm false}$ is slightly increasing with more iterations (Figure 6.4).

Based on these test results, a number of five SysRem runs ($n_{\rm sys} = 5$) has been selected and applied for transit search in the F19 data set.

Dependence on Orbital Period, Phase, and Light Curve Noise

The yield of BLS depends on the number of data points *in transit* and the signal-to-noise ratio. Both factors are determined by the simulated orbital period, phase, and transit depth, as well as the observational duty cycle and the photometric precision. Correlations between these parameters are now described.

Figure 6.5 shows the relative number of detections as a function of the photometric noise σ_i^{bin} (binned to a transit timescale of 30 minutes) and of the number of points in transit for each star i with an artificial signal. It shows that the detection yield is largely independent of the noise for signals of $\delta F \geq 1\%$, while detections of the smallest transit with $\delta F = 0.5\%$ are rather noise-limited. The latter case can thus be used to approximate a detection criterion of the evaluated search method: For

$$\sigma_i^{\mathrm{bin}} \leq 3.2\,\mathrm{mmag} \equiv 0.64 \cdot \delta F \ , \tag{6.10}$$

the detection efficiency (i.e., the fraction of detected to all transits) steeply rises

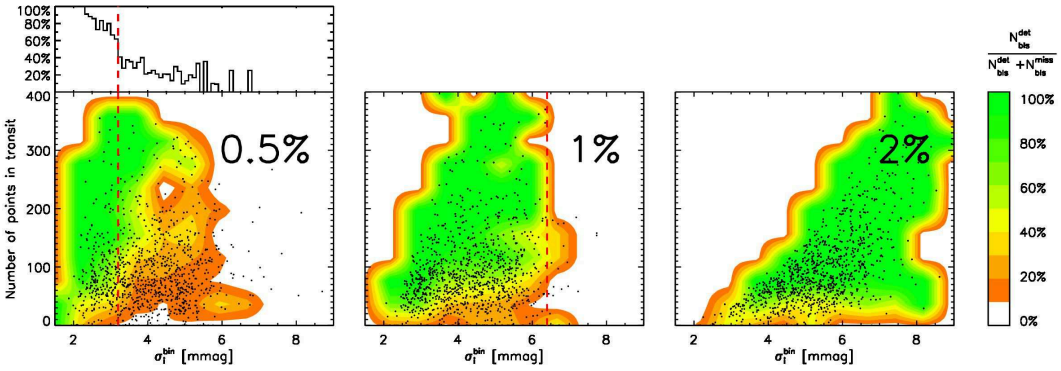

Figure 6.5: Dependency of transit search performance on the photometric noise level σ_i^{bin} (binned to 30 min) and the number of data points in transit (for transit depths $\delta F = 0.5\%$, 1%, and 2%). Individual stars i with a transit are shown as circles. In addition, the fraction $N_{\mathrm{bls}}^{\mathrm{det}} / \left(N_{\mathrm{bls}}^{\mathrm{det}} + N_{\mathrm{bls}}^{\mathrm{miss}}\right)$ of successful detections is color-coded as indicated on the right. For $\delta F = 0.5\%$, the same fraction is shown in a histogram of σ_i^{bin}, but for all light curves that contain at least 50 data points in transit. The *red dashed* line at $0.64 \cdot \delta F$ indicates the approximated detection limit (Equation (6.10)).

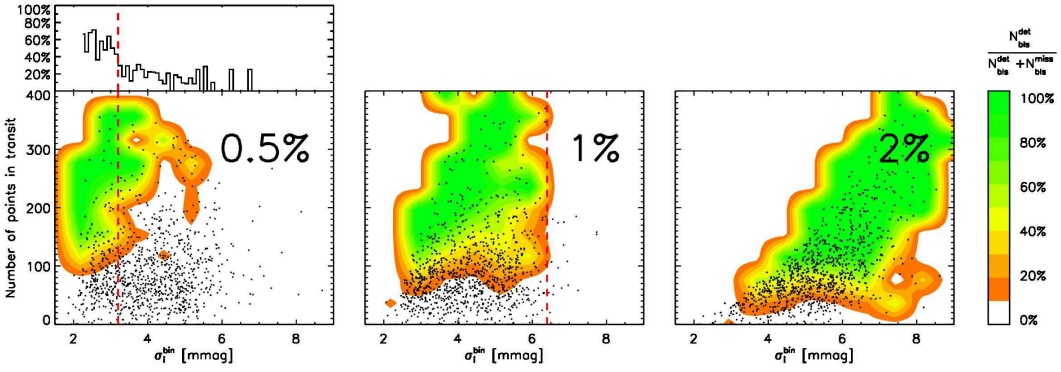

Figure 6.6: As Figure 6.5, but with the requirement of a significant detection ($S_{\mathrm{bls}} \geq 6.12$).

above 50%. Equation (6.10) remains valid if only detections with $S_{\rm bls} \geq S_{\rm bls}^{\rm min}$ are being considered, because transits with $\sigma_i^{\rm bin} \leq 0.64 \cdot \delta F$ remain significant as long as the observations cover enough ($\gtrsim$ 50–100) data points in transit (Figure 6.6). Furthermore, Equation (6.10) is consistent with the results for the larger transit depths of 1% and 2% (Figures 6.5 and 6.6), and independent of the actual observational time sampling (since the considered noise level $\sigma_i^{\rm bin}$ is determined on binned data). The criterion is used to estimate the detection yield of transit searches in several data sets in Chapters 4 and 10.

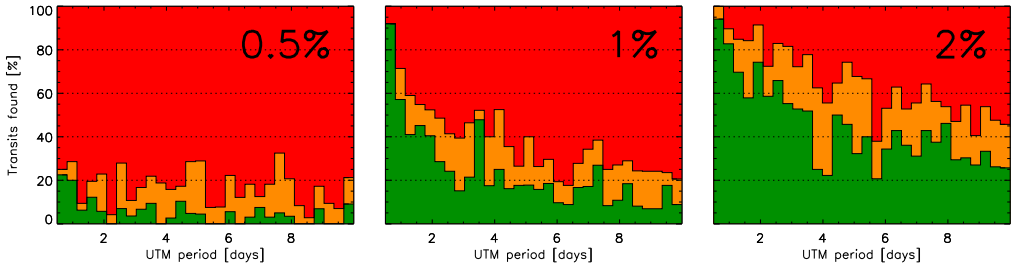

(a) Without SysRem

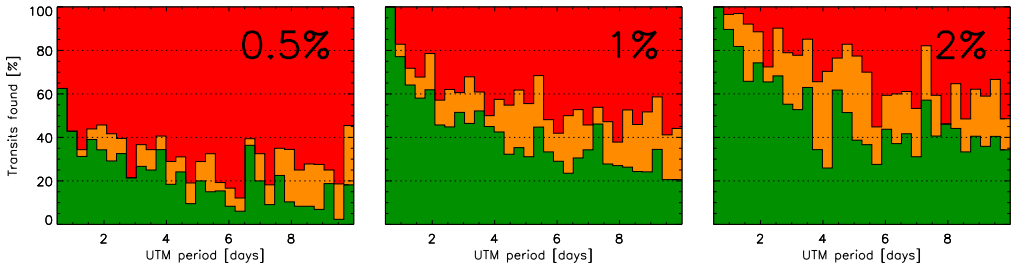

(b) After SysRem

Figure 6.7: Fraction of detected test planets as a function of their orbital period $p_{\rm utm}$ and transit depth δF. The numbers of transits identified with the correct period ($N_{\rm bls}^{\rm correct}$, *green*), multiples thereof ($N_{\rm bls}^{\rm multi}$, *yellow*), and wrong periods ($N_{\rm bls}^{\rm miss}$, *red*) are calculated and normalized separately within each period bin. Results are shown for all three tested transit depths, as well as before (a) and after application of SysRem (b, with $n_{\rm sys} = 5$). They are determined for *all* light curves with artificially introduced planets, i.e., independent of the BLS significance $S_{\rm bls}$.

Figure 6.7 shows the statistics of detected and missed artificial transits as a function of the orbital period: While ca. 60–100% of the short orbits ($p \lesssim 4^d$) are recovered in the high SNR cases of $\delta F = 1\%$ and 2% (after SysRem), the performance drops to about 50% for long periods $p \gtrsim 6^d$. The low SNR case $\delta F = 0.5\%$ is dominated by noise and shows a significantly lower fraction of detected planets for all periods.

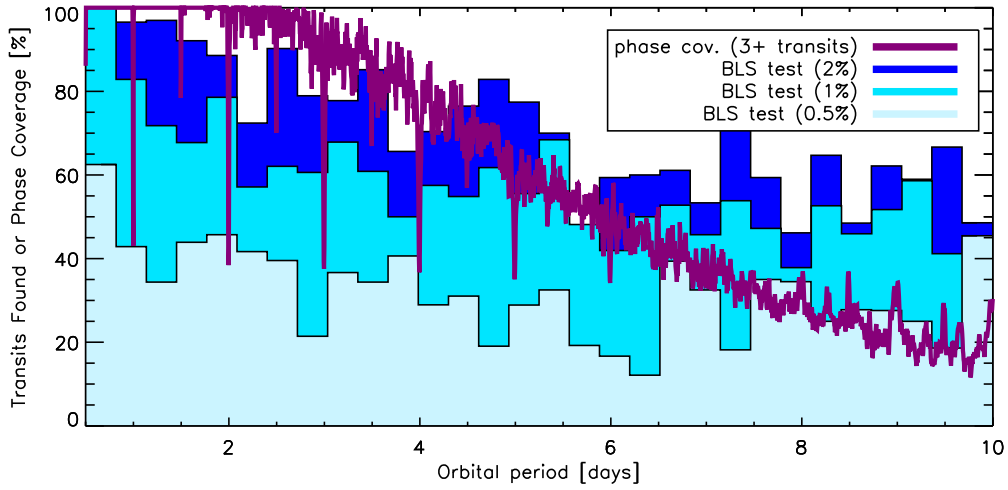

Figure 6.8: Comparison of BEST II transit search performance with orbital phase coverage for F19. For each period bin, the number of *detected* test planets $N_{\mathrm{bls}}^{\mathrm{det}}$ is divided by the total count of signals that have been introduced to F19 within this range. Blue histogram bars show the results for the tested transit depths of 0.5%, 1%, and 2%. They were obtained on the filtered data set F19, i.e., after five SysRem runs (see Figure 6.7b). The orbital coverage for three or more transits is derived from the real observational window function of F19 (see Chapter 4, in particular Figures 4.6 and 4.7).

Figure 6.8 compares the results of the BLS test with the observational coverage $p_{\mathrm{c3}}(p)$ of F19 as presented in Section 4.2.2; the latter was calculated from the times of observation by requiring that they cover at least three transit events. While the line corresponding to $\delta F = 0.5\%$ does not reach this benchmark in Figure 6.8 due to an insufficient SNR, the larger depths of 1% and in particular 2% largely follow the observational coverage. A slight lack of detections with $p \lesssim 5^d$ can be explained with the assumption of vanishing transit duration in the calculation of $p_{\mathrm{c3}}(p)$, while a surplus for $p \gtrsim 5^d$ indicates that the correct period could also be recovered if less than three events are covered.

BLS detection limit

The signal to noise ratio S_{bls} (Equation (6.4)) was introduced to quantify the significance of a BLS fit. Its performance in distinguishing between noise and real signals is now evaluated using the F19 data set with artificial transits.

Figure 6.9 displays the number of detected and missed planets, and the number of false alarms as a function of the BLS SNR limit $S_{\mathrm{bls}}^{\mathrm{min}}$. It shows that for larger tested transit depths δF, higher values of S_{bls} are obtained for correct detections, which can in turn be distinguished better from false alarms. Therefore, this parameter can be considered a good criterion for candidate prioritization.

In order to determine a reasonable limit $S_{\mathrm{bls}}^{\mathrm{min}}$ for real transit searches, a quantity $S_{\mathrm{bls}}^{\mathrm{eq}}$ has been determined for each tested transit depth (Table 6.1). It gives the largest value of $S_{\mathrm{bls}}^{\mathrm{min}}$ at which the number of false alarms exceeds the number of detections, i.e., $N_{\mathrm{bls}}^{\mathrm{false}} \geq N_{\mathrm{bls}}^{\mathrm{det}}$ (in Figure 6.9, $S_{\mathrm{bls}}^{\mathrm{eq}}$ can be seen as the interception of

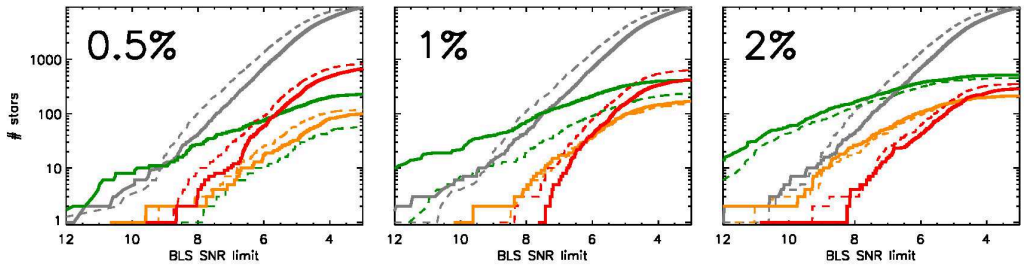

Figure 6.9: Number of detections above a given BLS SNR limit $S_{\rm bls}^{\rm min}$. The counts of artificial transits identified with the correct period ($N_{\rm bls}^{\rm correct}$, *green*), multiples thereof ($N_{\rm bls}^{\rm multi}$, *yellow*), and wrong period ($N_{\rm bls}^{\rm miss}$, *red*), as well as the false alarm count ($N_{\rm bls}^{\rm false}$, *gray*) are shown as a function of $S_{\rm bls}^{\rm min}$. Solid thick lines correspond to filtered data ($n_{\rm sys} = 5$), whereas thin dashed lines give the respective counts for the original data set F19 (without SysRem).

the gray and the green line). For the small depth of $\delta F = 0.5\%$, the number of false alarms exceeds the number of detections at $S_{\rm bls}^{\rm min} = 8.61$. In the case of larger transits, the false alarm rate only reaches a significant number at values of $S_{\rm bls}^{\rm min} = 7.22$ (1%) and 6.35 (2%). For all three cases, small SNR limits $S_{\rm bls}^{\rm min} \ll S_{\rm bls}^{\rm eq}$ lead to very high false alarms rates and should be avoided, i.e., a limit in the order of $S_{\rm bls}^{\rm min} \approx 6$ is considered appropriate for field F19.

Unfortunately, the BLS statistic used here is *not* comparable between different data sets, i.e., the actual distribution of $S_{\rm bls}$ depends on the time/frequency sampling, and the duration of the observations (Kovács et al. 2002). In order to obtain consistent results for transit search in different fields, a fixed fraction of low-noise light curves is chosen instead, i.e., the limit $S_{\rm bls}^{\rm min}$ is determined by the actual distribution of $S_{\rm bls}$. For F19, $S_{\rm bls}^{\rm min} = 6.12$ corresponds to 5% of all light curves in the field with $\sigma \leq 0.05\,$mag. Under the reasonable assumption that significant transit signals are always found within the 5% largest values of $S_{\rm bls}$ (for similiar approaches, see, e.g., Moutou et al. 2005; Mochejska et al. 2006; Bayliss and Sackett 2011; Nascimbeni et al. 2012), this criterion is used as the default for the inspection of potential transit signals within this work.

6.3 Summary and Discussion

The transit search procedure of BEST II was tested on its largest data set F19. Using an adaptation of the UTM program (Deeg 2009), artificial transit signals of depths $\delta F = 0.5\%$, 1%, and 2% were inserted into every 10th light curve of all 10,120 stars with $\sigma_i < 0.01\,$mag with the aim of recovering them using BLS.

The validation yields two main conclusions: First, a removal of systematic trends with SysRem significantly improves the detection performance. Second, the detection performs satisfactorily and within expectations.

SysRem

The transit search was investigated with no removal of systematic effects, and with up to eight runs of the SysRem algorithm. It was found that the number of detections

significantly increases after the first runs, especially for artificial signals with $\delta F \lesssim \sigma$, for which it virtually doubles. Moreover, the number of false alarms (i.e., light curves without transit but with a significant BLS peak of $S_{\rm bls} \geq 6.12$) decreases by a factor of two through the application of SysRem.

A number of five SysRem runs was found to be optimal for F19 using a deep analysis of the transit detection efficiency; therefore, $n_{\rm sys} = 5$ is used as the default value for transit search with BEST II. However, the actual number might vary from field to field depending on the systematic effects present in the data. It should be used as a guideline, but be adapted if necessary using the quality assessment of the SysRem results as discussed in Section 5.2.2.

Detection Performance

As discussed in Section 2.2, the probability of transit detection depends on various factors such as the number of surveyed stars, the photometric precision, or the observational duty cycle (Equation (2.11)). The corresponding yield was estimated for several BEST II target fields in Section 4.4. That simulation comprised two basic criteria to decide if a transit could be detected at star i: First, that the transit depth δF is larger than its photometric noise σ by a factor c (Equation (4.8)), and second, that at least three transit events are covered by observations.

The validation presented in this chapter neglects the stellar population within the field by inserting transits of fixed depth into a number of light curves that is much larger than expected in reality, e.g., concerning the number of stars actually hosting a planet. Thus, a comprehensive simulation is required to estimate the detection yield (cf. Section 4.4). However, the tests presented in this chapter probe crucial parts in the chain of transit detection; as such, the results allow to rate the performance of the given search procedure in general, and to verify the assumptions of Section 4.4 in particular.

First, for cases with a sufficient observational coverage of the transit phase, it has been shown that the detection limit can be approximated with $\sigma_i^{\rm bin} \leq 0.64 \cdot \delta F$, whereas $\sigma_i^{\rm bin}$ refers to the standard deviation in data binned to a typical transit time scale of 30 minutes. At the noise limit, e.g., if only three two-hour transits[2] are observed with $\sigma_i^{\rm bin} = 0.64 \cdot \delta F$, this corresponds to an overall SNR of 5.4. The criterion is used within this work to estimate and compare the detection yield for different data sets and projects (i.e., with $c = 0.64$ in Equation (4.8); cf. Sections 4.4 and 10.3).

Second, the rate of detections decreases with the simulated orbital period as expected from the observational duty cycle. If the transit signal is larger than the photometric noise, about 60–100% of all artificial planets are found up to periods $p \lesssim 4^d$. The performance can be approximated with the theoretical observational coverage $p_{\rm c3}(p)$ of three or more transit events (Section 4.2.2). The latter can thus be used to estimate the detection yield.

[2] together covering 44 individual data points with the average F19 time sampling

7 Improved Variable Star Search

During the last decade, ground- and space-based surveys have been very successful in detecting transiting exoplanets. In addition to their primary science goal, the large photometric data sets acquired by them allow studying millions of stars for variability. Numerous projects thus provide an exceedingly increasing number of detections that are collected by variable star catalogs such as the General Catalogue of Variable Stars (GCVS; Samus et al. 2009) or the Variable Star Index (VSX; Watson et al. 2006). Such catalogs not only broaden the statistical sample of variable stars, but are also important to gain further knowledge about the different processes that cause stellar variability.

Several methods have been proposed to search for periodic signals in astronomical time series (for a good overview, see, e.g., Schwarzenberg-Czerny 1999). One of the most widely applied algorithms is the analysis of variance (AoV) statistic (Schwarzenberg-Czerny 1996), which provides an optimal period search in uneven sampled observations. It has been used very successfully by projects like HAT (Bakos et al. 2004), SuperWASP (e.g., Maciejewski et al. 2011), or OGLE (e.g., Soszyński et al. 2008). In addition, the J index (Stetson 1996) is frequently used to quantify variability in general and/or for selecting candidate stars prior to a period search in order to minimize computation time (e.g., Zhang et al. 2003; Pepper and Burke 2006; Pasternacki et al. 2011).

However, both methods, the AoV period search and Stetson's variability index, are strongly affected by systematic trends present in ground-based data sets (see, e.g., Pepper and Burke 2006; Karoff et al. 2007; Kabath et al. 2009a; Hartman et al. 2011a). Most dominant are diurnal systematics, introducing artificial variability with periods of one day or multiples thereof. Such trends generally yield a higher ranking of non-variable stars, thus increasing the false alarm rate. A common approach to account for candidates with systematic variability is to set limits, e.g., to exclude detections within certain period ranges. However, any such manual mechanism is usually not well applicable to other data sets or projects, and the number of missed detections (false negatives) is often unknown. Therefore, a more sophisticated treatment of systematic variability in combination with period search and ranking is needed.

A first characterization of periodic stellar variability in the CoRoT field LRa02 with BEST II has been published by Kabath et al. (2009a). Following the detections from this first publication (denoted as Paper I hereafter), it was possible to optimize the DLR photometric pipeline. The large, well-characterized data set LRa02 was used as a proxy to analyze and automatically exclude systematic biases from the variable star candidate selection and period search, yielding a significantly reduced false alarm rate.

Outline

This chapter describes an optimized procedure to rank periodic variable stars. The results form an integral part of this thesis and have been published recently (Fruth et al. 2012). In addition, the publication includes a large catalog extension to the variable star classification in LRa02 that was obtained through the reanalysis. Together with variable stars from the BEST II fields F17–F19, these new detections are presented in Chapter 9.

While the following Section 7.1 recaps the observations and results from Paper I, Section 7.2 outlines the reanalysis that was performed in the framework of this thesis. Section 7.3 describes the limitations of the old method, and introduces the new method together with a quantitative framework to test and optimize its performance. Finally, Section 7.4 shows the results of the new procedure on the LRa02 data set, and Section 7.5 summarizes this chapter.

7.1 First Variability Study in Field LRa02

The CoRoT long-run field LRa02 was observed by BEST II for 41 nights from November 2007 to February 2008 prior to the satellite observations (see Table 4.1). As the FOV of CoRoT is slightly larger than BEST II, we split the field into two subfields (called LRa02*a* and LRa02*b*, respectively) and pointed at them alternating. Paper I indicates their corresponding center coordinates, and Figure 7.1 shows the orientation with respect to the CoRoT FOV.

The acquired data set was calibrated and reduced using the DLR automated photometric data pipeline as outlined in Chapter 5 (see Appendix D for parameters).

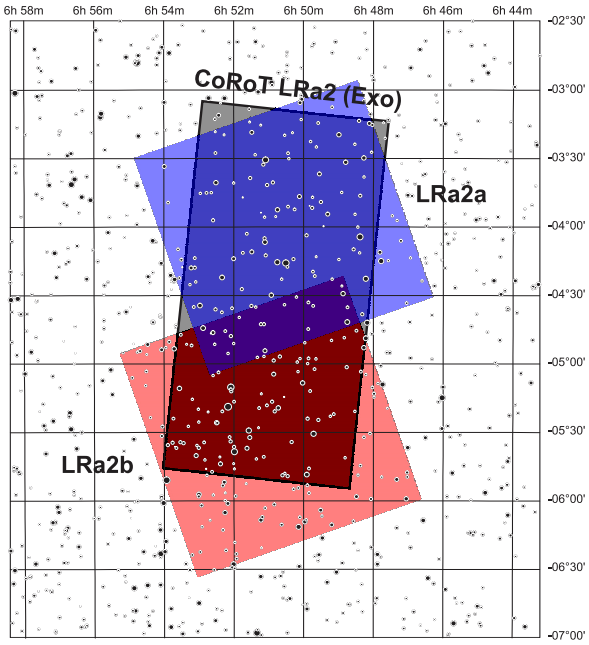

Figure 7.1: Relative position of CoRoT field LRa02 *(gray)* and the BEST II pointings LRa02*a* *(blue)* and LRa02*b* *(red)* (cf. Kabath et al. 2007, Figure 1).

Variability Criteria

In Paper I, Kabath et al. reported the detection of 350 periodic variable stars (of which five were previously known). Their selection was based upon the variability index J (Stetson 1996), calculated for each star by

$$J = \frac{\sum_{k=1}^{n-1} w_k \operatorname{sgn}(P_k)\sqrt{|P_k|}}{\sum_{k=1}^{n-1} w_k}, \tag{7.1}$$

where k is indexing individual data points. P_k is calculated from each pair of subsequent magnitudes m_k and m_{k+1} using the corresponding normalized residuals δ_k and δ_{k+1}:

$$P_k = \delta_k \delta_{k+1} \quad \text{with} \quad \delta_k = \sqrt{\frac{n}{n-1}} \left(\frac{m_k - \overline{m}}{\Delta m_k} \right), \tag{7.2}$$

where Δm_k denotes the uncertainty of measurement k, $\overline{m}$ the mean magnitude, and n the number of measurements for the selected star. The weights w_k in Equation (7.1) were calculated following the approach of Zhang et al. (2003) as

$$w_k = \exp\left(-\frac{t_{k+1} - t_k}{\Delta t} \right), \tag{7.3}$$

where t_k denotes the time of observation k and Δt is the median of all pair time spans $(t_{k+1} - t_k)$.

In Paper I, the limit of $J \geq 0.5$ was applied in order to distinguish variable from constant field stars. This preselection yielded 1,858 stars in LRa02*a* and 1,868 stars in LRa02*b*, respectively. For each star, the AoV statistic Θ (Schwarzenberg-Czerny 1996) was calculated for a period range of 0.1–35 days. The light curves were folded with the frequency $\omega_{\max}$ corresponding to the maximum AoV value,

$$\Theta(\omega_{\max}) = \max\left(\Theta(\omega)\right), \tag{7.4}$$

and then inspected visually. Most folded light curves showed no clear periodic variability or an artificial period of one day or multiples thereof, which can be caused by systematic effects due to the observational cycle. Kabath et al. (2009a) finally identified 173 periodic variables in LRa02*a* and 177 in LRa02*b*.

7.2 Reanalysis

In the BEST archive, some stars are marked as clear variables with large J indices (up to 10 and higher). Figure 7.2 shows the count of all stars in subfield LRa02*b* and the corresponding number of variable star detections in Paper I as a function of the J index. Altogether, the large number of false positives shows that the J index alone is not an effective criterion for selecting variable stars. Furthermore, a number of clear detections with low J values indicates that several variables must have been missed in Paper I due to the cutoff.

In order to improve the quality of our preselection process and to maximize the detection yield, we performed a deeper analysis of our data set LRa02. Field LRa02

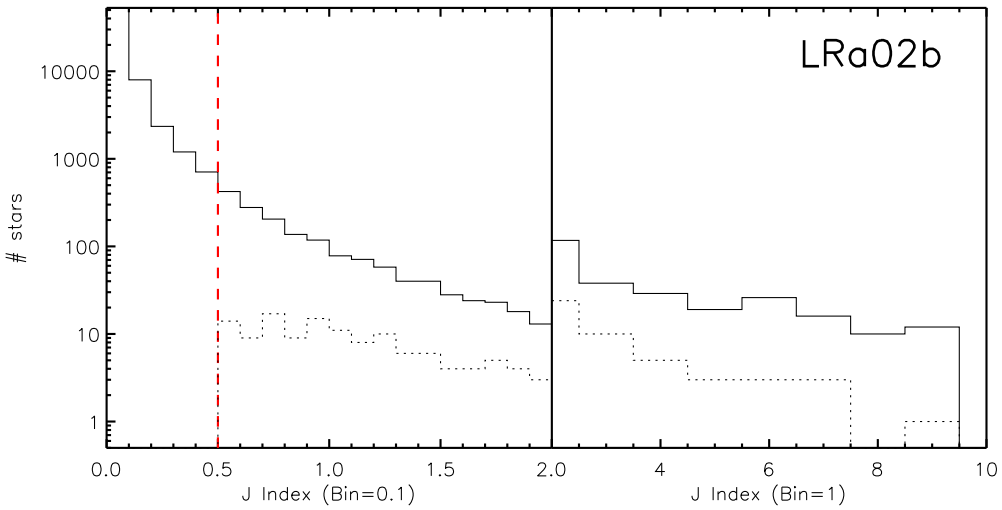

Figure 7.2: J index histogram for subfield LRa02*b* (qualitatively equal to LRa02*a*). The *solid* line shows the total star count in bins of 0.1 ($J < 2$) and 1 ($J \geq 2$), whereas the *dotted* line shows the number of variable star detections from Paper I. The *red dashed* line denotes the cutoff limit of $J = 0.5$ as applied in Paper I. *(Published as Figure 1 by Fruth et al. 2012.)*

was chosen for this purpose because it provided the longest time series within the BEST project at the time of the reanalysis.

The performed reanalysis consisted of three main steps.

First, the best period was searched in all light curves from the initial data set without any preselection criterion, i.e., directly using the AoV multiharmonic algorithm for *all* stars in both subsets. Each of the resulting 37,361 folded light curves in LRa02*a* and 66,974 in LRa02*b* was then examined visually for periodic stellar variability. In addition to the variable stars from Paper I, this first step already revealed 189 *additional* variable stars that were not detected in the first publication. During this step, we also discovered a bug in our implementation of the J index that yielded systematically lower values especially for short periods, which is why many of these detections show periods of less than a day.

Second, the combined data set of variable stars from Paper I and the additional manual detections were used to optimize the BEST II selection process (see next Section 7.3). With a very good knowledge of this data set, it was possible to compare different selection methods and to adjust their corresponding parameters.

Third, the new search algorithm was applied to the data set with optimized parameters. The improvements to the pipeline finally lead to an increase of detections by another 135 variable stars that were not found during all previous steps (see Section 7.4).

7.3 Improvements on Variability Search

The deep analysis of the BEST II data set LRa02 gives the opportunity to study the performance of variability search algorithms in detail. The aim is to recover

all variable stars in the data set automatically and to minimize the number of false alarms (and manpower) at the same time.

This section introduces the limitations of the J index with regard to systematic trends (Section 7.3.1), describes how to quantify the performance of a variability search (Section 7.3.2), presents the algorithms tested (Sections 7.3.3 and 7.3.4), and finally shows the performance of different approaches and parameters in comparison (Section 7.3.5).

7.3.1 Limitations of the Variability Index J

After the first step of the reanalysis, the visual inspection, the majority of new detections showed J indices below the limit of 0.5 applied before, which is why they were not detected in Paper I. The relation between periods and variability is shown

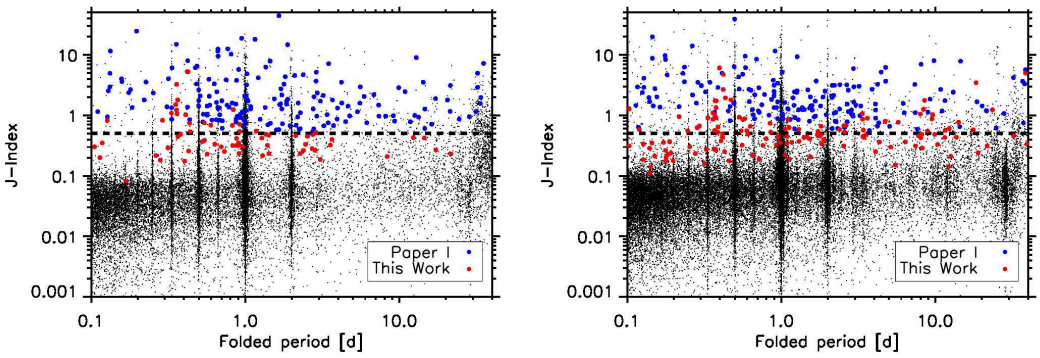

Figure 7.3: Variability J index plotted vs. determined period without treatment of systematic effects for all stars in the BEST II field LRa02*a* *(left)* and LRa02*b* *(right)*. Variable stars identified in Paper I are marked with *blue* dots, whereas variable stars from the manual reanalysis appear *red*. The dashed line shows the selection limit of $J = 0.5$ as applied in Paper I. *(Published as Figure 2 by Fruth et al. 2012.)*

in Figure 7.3. A clear bulk of stars can be found at about $0.01 \leq J \leq 0.1$, with the limits being widely period independent and populated by stars showing noise only. Most new variable star detections are found in the region between $J = 0.1$ and the cutoff limit of $J = 0.5$ from Paper I. A small number of new variables with $J > 0.5$ were not detected in Paper I because their J indices have been initially underestimated (see Section 7.2).

The dominant variation in many light curves is due to diurnal systematics, aliasing, or a combination of both. Figure 7.3 shows a large accumulation of stars having periods of one day or integral fractions/multiples thereof, often in combination with large J indices. Consequently, this leads to a very high number of false alarms when using the Stetson index as the only criterion for variability selection. In the example of the data set LRa02, a cutoff limit of $J = 0.1$ would be sufficient to include all variable stars in the selection sample, but only 74% of all light curves would be sorted out. The remaining large sample of 31,000 stars is mainly affected by systematic effects and contains only 681 stars with real physical variability (see Section 7.4). The corresponding false alarm rate of about 98% shows the need for an automated treatment of systematic variability, which is not part of the J index.

7.3.2 Quantitative Assessment of Period Search Algorithms

Two fundamental criteria are used to assess the quality of period search algorithms: the significance of the detection itself and the correct determination of the frequency of variability.

First, a quantity ξ is introduced to evaluate the detection efficiency of any given search algorithm. Detection methods are usually based upon a single numerical value q (e.g., the Stetson index, $q \equiv J$) that can be used to prioritize a candidate list. The success of ranking variable stars high in the list is measured with ξ for each tested search algorithm. It ranges from 0 for the perfect algorithm (all previously identified variable stars listed first) to 1 (listed last). For details on the calculation of ξ, see Appendix C.2.

The second criterion is tested by comparing the frequency $\omega_{\mathrm{correct}}$ that was verified manually with the frequency of a tested algorithm. A tolerance range of 2% around $\omega_{\mathrm{correct}}$ is considered here for a correct determination. Also included are 2% deviation around half or twice that value, because the distinction between these is often ambiguous from the light curve itself. The fraction n_ω of correctly identified frequencies can then be used for a quantitative comparison between tested algorithms.

7.3.3 Frequency Determination and Exclusion of Systematics

Because systematics and their aliases are usually limited to a set of few well-defined frequencies $\{\omega_{\mathrm{sys}}\}$, they can be excluded by searching the best frequency ω_{max} only on a subset $\Omega^\star = \{\omega^\star\} = \{\omega\}\backslash\{\omega_{\mathrm{sys}}\}$ (Figure 7.4). Three different methods to account for systematic frequencies were tested, both independent of each other as well as in combination.

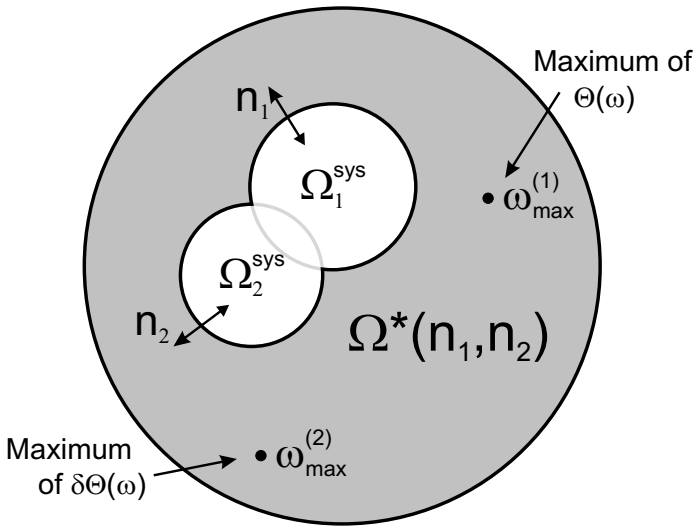

Figure 7.4: Schematic view on the rejection of systematic frequencies. The set $\Omega^\star(n_1, n_2)$ of non-systematic frequencies is obtained by excluding the subsets Ω_1^{sys} (master power spectrum cut) and Ω_2^{sys} (empty phases). The size of both can be adjusted with the parameters n_1 and n_2. Maxima of $\Theta(\omega)$ and $\delta\Theta(\omega)$ are searched within $\Omega^\star(n_1, n_2)$ to obtain the frequencies $\omega_{\mathrm{max}}^{(1)}$ and $\omega_{\mathrm{max}}^{(2)}$, respectively. *(Published as Figure 3 by Fruth et al. 2012.)*

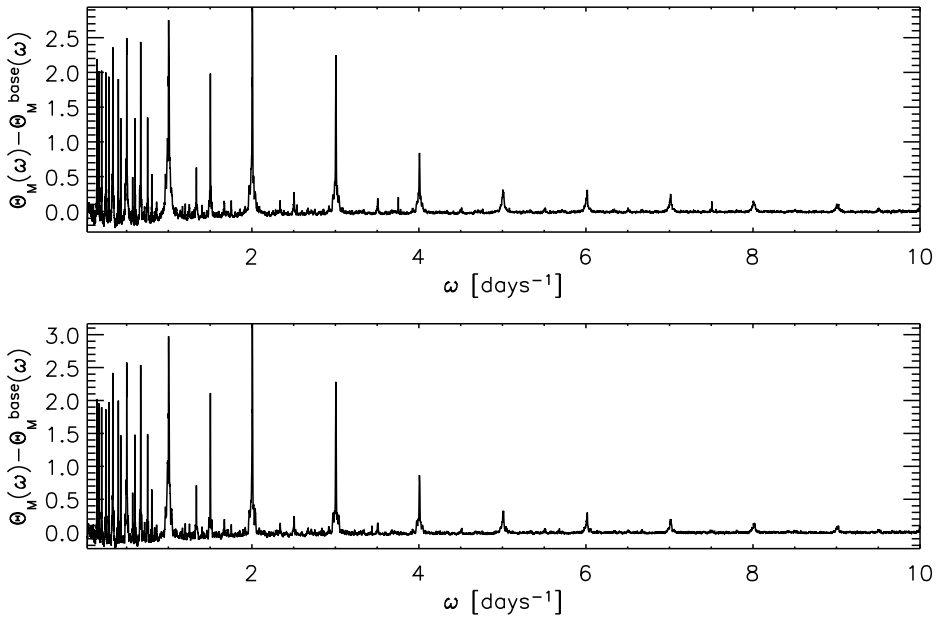

Figure 7.5: Master power spectrum for data sets LRa02*a* *(top)* and LRa02*b* *(bottom)*. *(Published as Figure 4 by Fruth et al. 2012.)*

1. *Master power spectrum.* Systematic periodic signals affect many light curves in a data set and can thus be distinguished from real stellar variability by analyzing many power spectra $\Theta_i(\omega)$ of individual stars i statistically. The mean of all $N_\star$ spectra is used to build a *master* spectrum

$$\Theta_M(\omega) = \frac{1}{N_\star} \sum_{i=1...N_\star} \Theta_i(\omega). \tag{7.5}$$

In order to identify significant peaks in the master spectrum, a baseline fit is determined. Among several investigated functions, a polynomial log-log fit,

$$\ln(\Theta_M^{\rm base}(\omega)) = \sum_{i=0}^{N_\Theta^{\rm c}} c_i \cdot (\ln \omega)^i, \tag{7.6}$$

with coefficients c_i maps the baseline best and most reliable for various tested data sets. The baseline-subtracted spectrum can then be searched for systematics. Figure 7.5 shows how $\Theta_M - \Theta_M^{\rm base}$ peaks clearly at the diurnal frequencies that we aim to identify.

Finally, a simple cutoff using the standard deviation $\sigma_M^{\rm base}$ of the subtracted spectrum $\Theta_M - \Theta_M^{\rm base}$ is applied to filter systematics automatically. The corresponding set of frequencies having peaks at least $n_1 \cdot \sigma_M^{\rm base}$ above the average power spectrum is defined by

$$\Omega_1^{\rm sys}(n_1) = \{\omega \mid \Theta_M(\omega) > \Theta_M^{\rm base}(\omega) + n_1 \cdot \sigma_M^{\rm base}\}, \tag{7.7}$$

where the parameter n_1 can be adjusted to quantify the degree of exclusion.

2. *Frequencies with empty phases.* Ground-based observations are strongly affected by periodic gaps in the data, most commonly due to the diurnal cycle. The

incomplete phase coverage leads to aliasing and can often cause false positive detections. We use a simple model to exclude frequencies with poor phase coverage: First, the folded light curve is split into $N_{\mathrm{boxes}} = 100$ intervals of the same length. The number of empty intervals $N^{\mathrm{empty}}_{\mathrm{boxes}}(\omega)$ is then counted for each sampled frequency. A frequency is considered systematic by this criterion if the fraction of empty intervals is larger than a relative threshold parameter n_2, i.e.,

$$\Omega^{\mathrm{sys}}_2(n_2) = \{\omega \mid N^{\mathrm{empty}}_{\mathrm{boxes}}(\omega) > n_2 \cdot N_{\mathrm{boxes}}\}. \tag{7.8}$$

Both criteria (7.7) and (7.8) are merged to exclude systematic frequencies determined in either way, i.e., the overall set of non-systematic frequencies (Figure 7.4) is defined by

$$\Omega^{\star}(n_1, n_2) = \{\omega\} \setminus [\Omega^{\mathrm{sys}}_1(n_1) \cup \Omega^{\mathrm{sys}}_2(n_2)] \tag{7.9}$$

and the search for ω_{max} is restricted from the whole frequency range (Equation (7.4)) to the subset $\Omega^{\star}(n_1, n_2)$:

$$\forall \omega \in \Omega^{\star}(n_1, n_2) : \Theta(\omega) \leq \Theta(\omega^{(1)}_{\mathrm{max}}). \tag{7.10}$$

Note that the function $N^{\mathrm{empty}}_{\mathrm{boxes}}(\omega)$ is similar but not equivalent to the window function $\gamma_N(\omega)$ (Deeming 1975). Limiting the latter was tested as an alternative criterion; it shows a very similar ranking performance, but slightly less correctly determined frequencies. Being more simple, the empty phase criterion was chosen for the final test setup.

3. *Power spectrum scaling.* In addition to the exclusion of systematic frequencies, we also investigated a method to include the information about systematics into the AoV results directly. Instead of searching for the maximum of $\Theta(\omega)$, an artificial spectrum

$$\delta\Theta(\omega) = \Theta(\omega)/\Theta_M(\omega) \tag{7.11}$$

is created by dividing the AoV spectrum Θ of every star by the master power spectrum Θ_M. Its maximum is found at the frequency $\omega^{(2)}_{\mathrm{max}}$ in analogy to Equation (7.10):

$$\forall \omega \in \Omega^{\star}(n_1, n_2) : \delta\Theta(\omega) \leq \delta\Theta(\omega^{(2)}_{\mathrm{max}}) \ . \tag{7.12}$$

7.3.4 Variable Star Ranking

In addition to the J index, two methods to prioritize variable star candidates were tested.

The first method takes the AoV result directly, i.e.,

$$q^{(1)}_1 = \Theta(\omega^{(1)}_{\mathrm{max}}). \tag{7.13}$$

In its special case of no excluded systematic frequencies ($n_1 \to \infty$, $n_2 = 1$), this is a widespread method for prioritizing variable star candidates. Likewise, the maximum of the divided power spectrum $\delta\Theta$ could serve as a variability indicator:

$$q^{(2)}_1 = \delta\Theta(\omega^{(2)}_{\mathrm{max}}). \tag{7.14}$$

The AoV statistic $\Theta \equiv \frac{(n-n_\parallel)\|x_\parallel\|^2}{n_\parallel\|x-x_\parallel\|^2}$ compares the quadratic norm of a model $x_\parallel$ (with $n_\parallel$ free parameters) with the residuals that remain after subtraction of the model from n observations x (Schwarzenberg-Czerny 1999). Because it has optimum period detection properties (Schwarzenberg-Czerny 1996), q_1 is expected to yield the best ranking. However, the light curve's standard deviation with and without the periodic signal obtained by the AoV multiharmonic fit was also tested as an empirical alternative:

$$q_2^{(1)} = \frac{\sigma}{\sigma'(\omega_{\max}^{(1)})} \quad \text{and} \quad q_2^{(2)} = \frac{\sigma}{\sigma'(\omega_{\max}^{(2)})} \tag{7.15}$$

It is dependent upon the frequency $\omega_{\max}$ determined in the previous section, which is why different choices of $\omega_{\max}$ lead to different rankings. The quoted σ' refers to the standard variation *after* subtraction of the corresponding fit (for calculation of coefficients, see Schwarzenberg-Czerny and Kaluzny 1998).

7.3.5 Comparison of Variability Search Performance

The quantities ξ and n_ω have been calculated for both frequencies $\omega_{\max}^{(1)}$ and $\omega_{\max}^{(2)}$ and both tested ranking methods $q_{1,2}^{(k)}$. For each run, the parameters n_1 and n_2 were varied independently on the following values:

$$\begin{aligned} n_1 &= \{0, 0.01, 0.05, 0.1, 0.2, 0.5, 1, 2, 5, 10, 1000\} \\ n_2 &= \{0\%, 10\%, 20\%, 30\%, 40\%, 50\%, 60\%, 70\%, 80\%, 90\%, 100\%\} \end{aligned}$$

The results of the comparison are summarized in Table 7.1, which shows the best value for ξ and n_ω achievable with each tested method.

Number of Harmonics

Paper I and the first step of the reanalysis (Section 7.2) determined the stellar variability using AoV periodograms with two harmonics, which was also used for this comparison. Furthermore, the number of harmonics was set to $N = 7$ in a second test in order to increase the sensitivity on sharp signals that are, e.g., caused by eclipsing binaries (for the sensitivity dependence on the number of harmonics, see, e.g., Schwarzenberg-Czerny 1999). Both results show very similar ranking performances (for the best ranking method q_1, we find $\xi_7 \approx \xi_2 \pm 0.001$ in both data sets), but the $N = 2$ test naturally yields a slightly better (12%–15%) frequency match with the initial run that was obtained using the same number of harmonics. However, the test with seven harmonics revealed a number of additional interesting eclipsing binaries that could not be detected using the smaller number of model parameters (see Sections 7.4 and 9.1). Therefore, we prefer the latter for our improved variability search (Section 7.3.6) and focus in the following on the details of the search performance with $N = 7$ harmonics.

Table 7.1: Results of the tested variable star ranking methods and parameters.

		$\omega_{\max}^{(1)}$		$\omega_{\max}^{(2)}$		J
		$q_1^{(1)}$	$q_2^{(1)}$	$q_1^{(2)}$	$q_2^{(2)}$	Index
ξ (n_1,n_2)	LRa02a	$(0,0)$ 0.0051	$(0,0)$ 0.010	$(0.2,10\%)$ 0.0035	$(0.2,\geq 70\%)$ 0.010	0.032
	LRa02b	$(0,0)$ 0.0035	$(0,0)$ 0.0056	$(0,0)$ 0.0027	$(0,0)$ 0.0062	0.034
n_ω (n_1,n_2)	LRa02a	$(5-10,10\%)$ 65%		$(\geq 5,10\%)$ 84%		
	LRa02b	$(\geq 10,0)$ 63%		$(\geq 5,10\%)$ 81%		

Notes. The quantities ξ and n_ω are shown for each tested ranking parameter q, both methods of determining the best frequency $\omega_{\max}^{(k)}$ and both analyzed data sets. For clarity, only the best value achievable by variation of the parameters n_1 (master power spectrum cut) and n_2 (empty phases) is shown for each method. The corresponding values/ranges of n_1 and n_2 are shown in small brackets above each value.

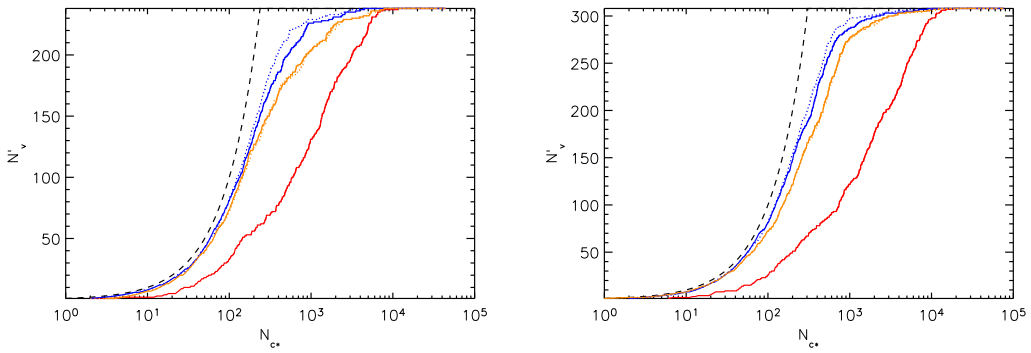

Figure 7.6: Number of variable stars N_v' as a function of the number of inspected stars $N_{c\star}$ for LRa02a *(left)* and LRa02b *(right)*. The different lines represent tested ranking methods: $q_1^{(k)}$, $q_2^{(k)}$, and the Stetson J index (left to right). *Solid* lines represent the unweighted case ($k = 1$), whereas *dotted* lines include the effect of master power spectrum division ($k = 2$). Only the parameters n_1 and n_2 of the most successful sorting are used for each method (compare Table 7.1). The *black dashed* line shows the optimal ranking for comparison. *(Published as Figure 5 by Fruth et al. 2012.)*

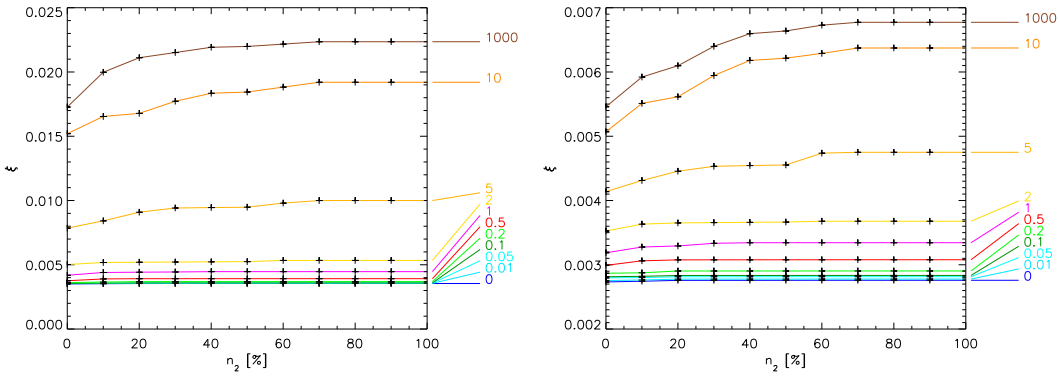

Figure 7.7: Influence of systematic frequency exclusion method on variable star ranking efficiency for the data set LRa02b. The quantity ξ is shown on the y-axis as a function of the model parameters n_1 (lines) and n_2 (x-axis) for the best tested ranking method using q_1. The *left* plot shows the results with $\omega_{\max}^{(1)}$ as the maximum frequency, whereas the effect of division by the master power spectrum ($\omega_{\max}^{(2)}$) can be seen on the *right*. *(Published as Figure 6 by Fruth et al. 2012.)*

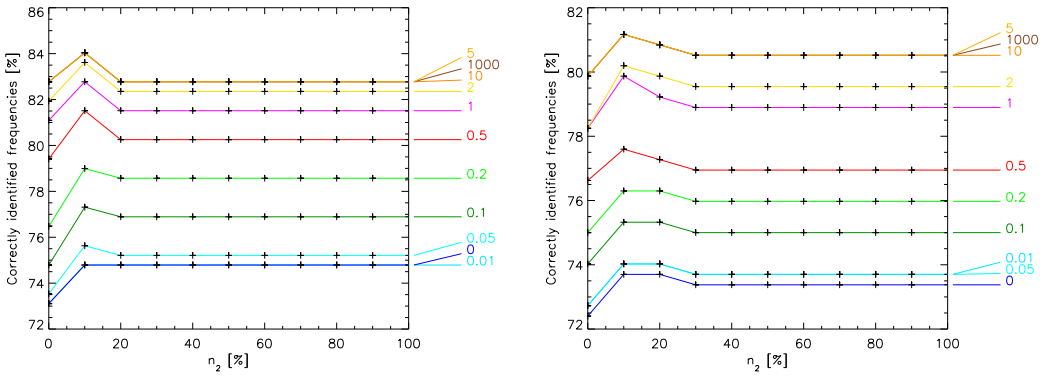

Figure 7.8: Fraction n_ω of correctly identified frequencies $\omega^{(2)}_{\max}$ as a function of model parameters n_1 (lines) and n_2 (x-axis) for variable stars in data set LRa02*a* *(left)* and LRa02*b* *(right)*, respectively. *(Published as Figure 7 by Fruth et al. 2012.)*

Ranking

The performance of the ranking differs only slightly between the tested methods. Figure 7.6 shows how the quantities q_1 (AoV) and q_2 (σ-ratio) both provide a sorting that lists stars with real variability first. The numerical quantity ξ yields with ~ 0.003 for $q_1^{(2)}$ a minimum close to the optimal ranking ($\xi = 0$). It is an order of magnitude lower than the previously used J index ($\xi \approx 0.03$) and significantly lower than ranking the AoV power without exclusion of systematics ($\xi \approx 0.022$ for $q_1^{(1)}$ with $n_1 = 1000$ and $n_2 = 100\%$). In particular, this corresponds to a drastically decreased false alarm rate: For example, using $q_1^{(2)}$ for ranking, only 1,125 LRa02 light curves have to be inspected in order to detect 491 variable stars (i.e., 90% of all in this test). In contrast to that, if only the J index was used for ranking, the *same* detection yield could only be obtained after an analysis of 11,689 light curves.

Figure 7.7 shows the dependence of the ranking performance on the parameters n_1 and n_2 for the two best methods $q_1^{(1)}$ and $q_1^{(2)}$. In both cases, the most restrictive exclusion of systematic frequencies yields the best sorting. Thereby, the cut in the master power spectrum (Equation (7.7)) has a slightly larger impact than the exclusion of empty phases (Equation (7.8)). The minimum of ξ is reached for $n_1 = n_2 = 0$, but is almost independent of n_2, because the first criterion is more restrictive.

Frequency Determination

The frequencies found in Paper I and by manual reanalysis of the data set are in good agreement with the values of $\omega^{(k)}_{\max}$ (see Table 7.1 and Figure 7.8). Without master spectrum division ($k = 1$), about two-thirds of the frequencies are recovered. However, the yield increases to about 80% if the procedure is applied ($k = 2$).

Interestingly, the frequency exclusion from the first criterion (Equation (7.7)) now has the reverse effect – the maximal agreement is reached if it is almost switched

off by setting $n_1 \geq 5$. Smaller values of n_1 are too restrictive and can increase the number of wrong periods by up to about 10%. On the other hand, the exclusion of empty phases has again a small influence, although a value of $n_2 = 10\%$ yields a slight improvement for the majority of tested scenarios (Figure 7.8).

The remaining small group of variable stars detected with a different period has been analyzed carefully. The majority of them shows multi-period variation and was identified with a rational multiple (e.g., 1/7, 2/5) of the original frequency. For some stars, the original period had to be revised during the reanalysis (see also Section 7.4). A small rest shows amplitudes close to the noise level, such that the period could not be determined unambiguously.

7.3.6 New Selection Method

Based upon the results from the comparison, a new procedure was set up to search for variable stars within the BEST project.

1. The J index is used to exclude non-variable stars in order to save computation time. High values of J can originate from either real variability or systematic trends, leading to a very high false alarm rate when being used as the only ranking criterion. However, low J indices give a reliable criterion for non-variability, i.e., neither physical nor systematic variations. In the studied data set LRa02, *no* star shows clear variability below $J = 0.1$. This limit is therefore used for analyses of BEST II data sets, for which it typically excludes 50%–75% of all stars.
2. The AoV algorithm is applied with $N = 7$ harmonics to the selected subset ($J \geq 0.1$) in order to obtain power spectra.
3. The improved selection method is applied to rank all investigated stars. Following the results from Section 7.3.5, a master power spectrum is calculated, the number of empty boxes is counted for each test period, and each individual power spectrum is divided by the master power spectrum (Equation (7.11)). For the ranking, the frequency $\omega^{(2)}_{\max}$ is determined from the subset of non-systematic frequencies in the divided spectrum $\delta\Theta(\omega)$ by following Equations (7.7)–(7.9) and (7.12) with the parameters $n_1 = 0$ and $n_2 = 10\%$. The corresponding maximum $\delta\Theta(\omega^{(2)}_{\max})$ (Equation (7.14)) serves as the quantity q for priorization (see example in Figure 7.9). However, in order to improve the final period ω_f, $\omega^{(2)}_{\max}$ is recalculated without exclusion of systematic frequencies from the master power spectrum, i.e., by setting $n_1 \to \infty$, $n_2 = 10\%$ and applying Equations (7.7)–(7.9) and (7.12) again.
4. All light curves are folded with their respective final periods ω_f and analyzed visually in descending order of $q = \delta\Theta(\omega^{(2)}_{\max})$.

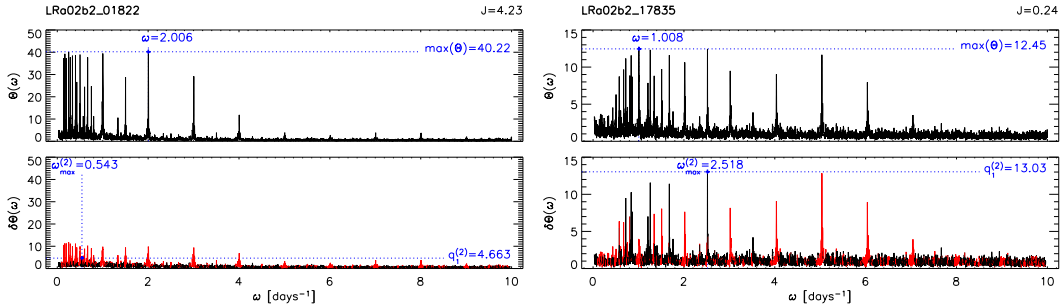

Figure 7.9: Example for power spectra $\Theta(\omega)$ (*upper* plots) and $\delta\Theta(\omega)$ (*lower* plots, see Equation (7.11)) – the star LRa02b2_01822 (*left* plots) is strongly affected by systematic noise, while LRa02b2_17835 (*right* plots) shows both physical and systematic variability. In each plain AoV spectrum $\Theta(\omega)$ (*upper* plots), the position of the overall maximum is marked – it is found at systematic frequencies for both cases. Furthermore, the maximum of $\Theta(\omega)$ and the J index are both much larger for the first star, leading to a false alarm when using these quantities to rank the variability. The functionality of the new variable star search algorithm is shown in the *lower* plots. In addition to the division by the master power spectrum, systematic frequencies are filtered out (Equations (7.7)–(7.9) with parameters $n_1 = 0$ and $n_2 = 10\%$, marked *red* in the spectrum), and the maximum $\omega^{(2)}_{\max}$ is determined on the non-systematic subset of frequencies (Equation (7.12)). To use the corresponding maximum $q_1^{(2)} = \delta\Theta(\omega^{(2)}_{\max})$ for ranking is much more sensitive to real variability. The second star LRa02b2_17835 is a new detection of this work (Table E.1 and Figure 9.1). *(Published as Figure 8 by Fruth et al. 2012.)*

7.4 Application of the New Method to LRa02

A large number of 189 new variable stars was already identified in the BEST II data set LRa02 by the first step of the reanalysis, the manual screening (see Section 7.2). After the search procedure was tested and optimized using the results from Paper I and this additional sample of detections, the most successful sorting method (see description in Section 7.3) was finally applied to search the data set LRa02 once more.

In addition to the 350 variable stars published in Paper I and the 189 found by the manual reanalysis, this improved search yielded another 135 previously unknown variable stars. Reasons why these went undetected by previous searches are as follows.

- Systematic trends or aliases were found instead of the real periodicity.
- The AoV algorithm was run with $N = 2$ harmonics for Paper I and the manual reanalysis, but with $N = 7$ for the latest search. This leads to a higher sensitivity for non-sinusoidal variations, which is particularly important for the detection of Algol type eclipsing binaries (at least 27 additional EA variables with long periods ($P > 2$ days) can be attributed to the increase of N, some of them being very eccentric).
- A total of 21 variable stars on the edge of the BEST II FOV with few data points were excluded by earlier reductions of the data set.

Due to an improved data quality (see Figure 5.7, Section 5.2.2) and increased sensitivity for non-sinusoidal events, we could also refine the periods for 17 of the variable stars published in Paper I (see Table E.2).

7.5 Summary

The CoRoT target field LRa02 was observed with BEST II during 41 nights from November 2007 to February 2008 (see Section 4.1 and Paper I). In the framework of this thesis, the data set was reanalyzed in order to improve the detection method and to maximize the number of detections.

From a manual inspection of all light curves without any preselection criterion, it turned out that many periodic variable stars went undetected in Paper I because the applied variability criterion using the Stetson J index was too restrictive. But because the J index is heavily biased by systematic effects, a smaller cutoff limit leads to very high false alarm rates ($\sim 98\%$) and is therefore not a practical alternative. However, although the J index is not capable to distinguish between systematic and stellar variability, it can still be used to exclude non-variable stars from the analysis: no variable star is falsely rejected if light curves with low variability indices $J < 0.1$ are sorted out in both LRa02 data sets. This separation can be particularly useful if the full AoV process is too time consuming for a whole data set.

The deep characterization of the data set enabled comparing and training of different automatic methods for an improved variability ranking. In particular, a master power spectrum was calculated as the mean of all individual AoV spectra. This method proved a valuable tool for exclusion of systematic frequencies and hence the ranking of real variability. The best algorithm found separates variable stars very effectively from the non-variable background population and in parallel recovers their frequencies well. The new ranking method is particularly superior to the J index in regimes where the amplitude of variation becomes comparable to the noise level, i.e., close to the detection limit of the photometric system. It shows an almost equal performance for both independent subsets LRa02a and LRa02b, and is easily applicable to other data sets (cf. the search for stellar variability in the three BEST II target fields F17–F19 in Section 9.2).

Part III

Scientific Results

8 BEST II Transit Candidates

Three target fields, F17–F19, have been observed in 2009/2010 for 138 nights in total to search for exoplanets (Chapter 4). The data have been reduced and analyzed for transiting planets using the procedures described in Chapters 5 and 6.

This chapter describes the data analysis, the different stages of candidate selection, and the scientific outcome of the transit search. Figure 8.1 illustrates schematically the processes involved in obtaining a candidate list from an initial set of light curves.

In addition, joint observations with ASTEP on the two fields ASTEP-Exo2 and ASTEP-Exo3 have been searched for transits using the same procedures; the results will be presented in Chapter 10. An analysis of stellar variability in the BEST II target fields F17–F19 is the subject of Chapter 9.

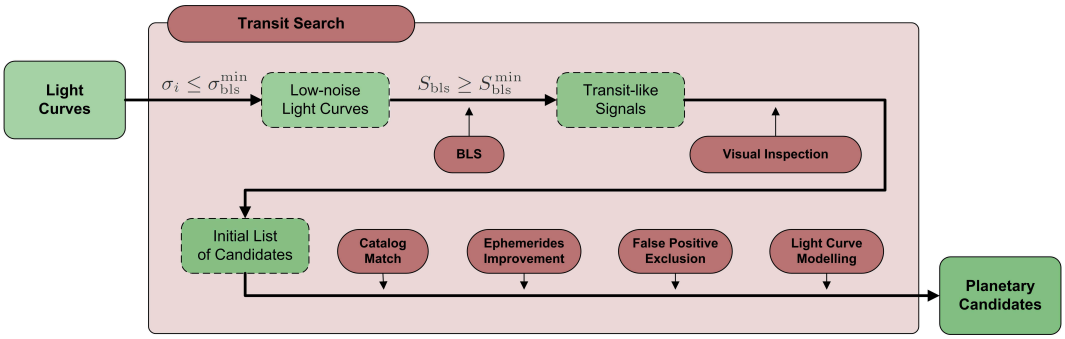

Figure 8.1: Schematic overview on the transit search as part of the photometric data analysis (see overview in Figure 5.1). Shown are the steps from fully processed light curves to planetary candidates, which are then subject to additional follow-up measurements.

Transit-like signals that are detected by algorithms like BLS can have multiple causes other than an exoplanet (see Section 2.2). It is therefore essential to exclude all other scenarios in order to eventually confirm the planetary nature. For the candidates presented in this work, this follow-up process is still ongoing. Using BEST II photometry, information from star catalogs and spectroscopic measurements, a large number of false positive candidates has already been excluded.

The first Section 8.1 of this chapter covers the transit search in the BEST II fields F17–F19. A procedure to improve the orbital ephemerides of each candidate identified therein is outlined in Section 8.2, and the measures to exclude false positives from light curve analysis are detailed in Section 8.3. The BEST II candidates themselves are presented in Section 8.4, including a description of their light curve modeling and a first spectroscopic characterization. Finally, Section 8.5 summarizes this chapter and outlines the current status of the follow-up process.

8.1 Transit Search in Fields F17–F19

Data Reduction

The three BEST II target fields F17–F19 have been reduced using the DLR photometric pipeline as described in Chapter 5; the most important parameters of the data processing are listed in Appendix D. Scientific images were recorded together with standard calibration frames (bias, dark, and flats) and calibrated on a nightly basis. As soon as an entire data set had arrived from Chile, the reduction continued with image alignment and subtraction, aperture photometry, extinction correction, and a match with the UCAC3 catalog (Zacharias et al. 2010). In preparation of transit search in these fields, SysRem was applied for detrending (see Chapter 6 for a discussion). However, SysRem has not been used for the analysis of stellar variability in Chapter 9, as will be discussed there.

Catalog Match

White light observations from BEST II or ASTEP provide neither a precise absolute photometry nor color information. As a first step in the follow-up analysis, catalogs are therefore searched for additional data. To obtain this information, the NOMAD (Zacharias et al. 2004) and 2MASS (Skrutskie et al. 2006) catalogs are cross-matched by equatorial coordinates with each data set. The closest catalog star is determined for each BEST II star and considered to match it, if the two coordinates, i.e., from the catalog and from the data reduction (Section 5.2.3), differ by less than $2''$.

Transit Search

Finally, the data sets F17–F19 have been searched for transit-like signals using the BLS algorithm (Chapter 6). Figure 8.2 illustrates this process, while Table 8.1 summarizes the selection criteria and lists the results for each field individually.

At first, the criterion $\sigma_i \leq \sigma_{\mathrm{bls}}^{\mathrm{min}} = 0.05\,\mathrm{mag}$ was applied to select low-noise light curves; in total, 115,740 (55%) of all 209,070 stars in F17–F19 have been analyzed with BLS. Out of these, the 5% most significant signals were inspected visually, i.e.,

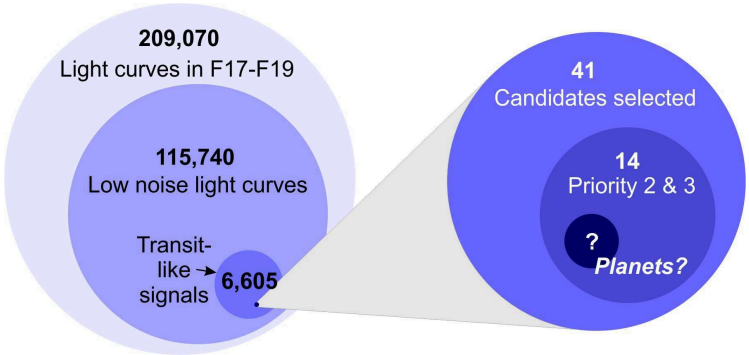

Figure 8.2: Planetary candidate selection process in BEST II fields F17–F19 (schematically). Circle areas are proportional to the respective counts.

Table 8.1: Star and candidate counts in BEST II fields F17–F19.

Field	Star Count			Limits		Candidate Count.	
	Total	$\sigma_i \leq \sigma_{\rm bls}^{\rm min}$	$S_{\rm bls} \geq S_{\rm bls}^{\rm min}$	$\sigma_{\rm bls}^{\rm min}$ [mag]	$S_{\rm bls}^{\rm min}$	initial	after all tests
F17	68,317	26,383	1,337 (5%)	0.05	5.84	3	2
F18	13,551	1,534	769 (50%)	0.05	4.12	0	0
F19	127,202	87,823	4,500 (5%)	0.05	6.12	38	12
Total	209,070	115,740	6,605			41	14

Notes. Shown are the total number of stars in each data set, the number of low-noise ($\sigma_i \leq \sigma_{\rm bls}^{\rm min}$) light curves analyzed with BLS, and the number of light curves with $S_{\rm bls} \geq S_{\rm bls}^{\rm min}$ that were inspected visually for transit signals. The latter is chosen such that a fixed fraction of low-noise light curves is inspected.

with the largest values of $S_{\rm bls}$ (Equation (6.4); see Section 6.2.3 for the motivation of the limit). For the less dense field F18, half of the low-noise light curves were inspected visually.

In an initial screening, 6,605 light curves with a significant transit-like signal have been analyzed visually. Most of them could already be rejected as clear eclipsing binaries at this stage, e.g., due to secondary eclipses, strongly $\bigvee$-shaped transits, or obvious out-of-transit variations. With decreasing SNR of the BLS result, most light curves either showed no significant signal or the signal was clearly of a systematic origin. In total, 6,564 candidates were rejected at this stage. This large number is consistent with the findings of other ground-based surveys (e.g., over 95% with SuperWASP; Kane et al. 2008).

A total number of 41 stars made up the initial candidate list. Their light curves show transit-like signals which could have arisen from a planetary cause (i.e., periods $p \gtrsim 0.5^d$ and depths $\delta F \lesssim 5\%$), no immediate false alarm indicator, and the observations cover a minimum of three events, including at least one full transit. The selection was made rather conservative in order to minimize the number of false rejections, i.e., ambiguous cases were all included into the initial candidate set for solving them through further tests. These are first described in the following two Sections 8.2 and 8.3, while the candidates themselves are presented in Section 8.4.

8.2 Ephemerides Improvement

The orbital period of a transiting exoplanet (candidate) needs to be measured as accurately as possible, because, from this one calculates the semi-major axis, a key property. Furthermore, small deviations in the period can alter the transit shape significantly when the data are phase-folded. First, this can affect the determination of additional stellar and planetary parameters through light curve modeling. Second, the shape of the transit itself is used as a criterion for rejecting eclipsing binaries (Section 8.3.1).

A first approximation of the orbital period is obtained from the transit search algorithm. However, the BLS routine is optimized for *detection*: It searches for strictly box-like signals on a grid of discrete frequencies. After detection, a three-step procedure is applied in order to improve the orbital ephemerides for each candidate.

First, the light curve is folded with the initial period as determined by the BLS

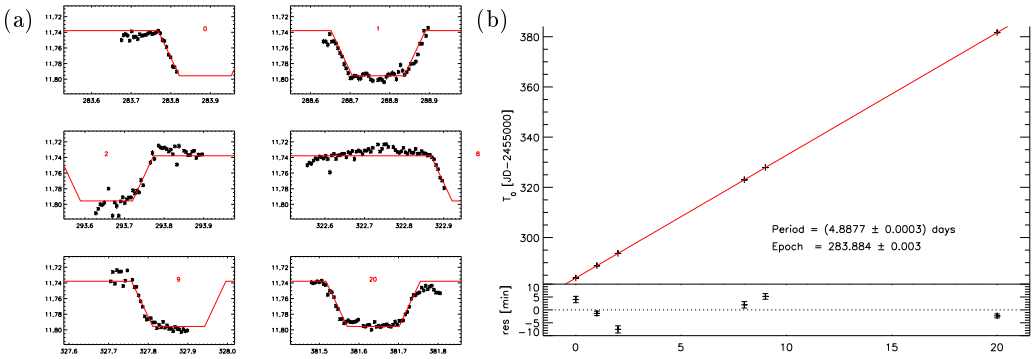

Figure 8.3: Example for period improvement of planetary candidate F19_043426. (a) The trapezoid from the fit to the folded light curve is fitted to each recorded event with the mid-point $T_0^{(i)}$ as the only free parameter. (b) All mid-points $T_0^{(i)}$ are then plotted vs. the orbital index i of the event. Improved ephemerides are finally obtained from a linear fit to these results; residuals of the fit are shown in the lower part of the plot.

algorithm. Instead of the step function from BLS, a trapezoid is fitted to the data. Thereby, the free parameters are the depth, the full duration T_{14}, and the duration T_{23} of the bottom part of the transit (cf. Figure 2.2). The magnitude out of transit and the zero point T_0 stay fixed.

Second, the shape determined on the folded light curve is fitted to each individual transit-like event (Figure 8.3a). In this step, the shape remains fixed and is only allowed to be shifted along the time axis, i.e., the mid-point $T_0^{(i)}$ is the only free parameter of each fit. The index i denotes the i-th orbital period after the first observed transit at date $T_0 \equiv T_0^{(0)}$.

Third, a line $y = T_0 + p \cdot i$ is fitted to the paired data $(i, T_0^{(i)})$ of all indices and mid-points (Figure 8.3b). It directly yields revised values for T_0 and the orbital period p as well as an estimation of the corresponding errors. Since the uncertainties of $T_0^{(i)}$ tend to be over- or underestimated for some cases, an unweighted linear fit proved to show more robust results.

The improved value of p might still point to an alias/multiple of the true orbital period. Therefore, the unfolded light curve, the BLS spectrum, and the index set $\{i\}$ are inspected carefully for different period solutions. For example, if *all* individual transit events were recorded with even indices i, the light curve would be folded with half the initial period and inspected visually. If a solution is found to match the observed sequence of transit-like events better, the period p is updated and the procedure of ephemerides improvement is repeated.

8.3 False Positives Exclusion from Light Curve Analysis and Catalog Information

8.3.1 Transit Shape

The shape and depth of a suspected transit signal are the prime rejection criteria available from photometry.

First, deep transits indicate a stellar secondary object rather than a planetary companion. The most inflated transiting hot Jupiters found so far show transit depths of $\delta F \lesssim 2\%$ (e.g., HAT-P-32 b; Hartman et al. 2011b). Large transit depths $\delta F \geq 3\%$ correspond to radius ratios of $r_p/r_\star \geq 0.17$ (Equation (2.6)), which can only be observed for Jupiter-sized planets around small M-type stars (see also Figure 8.12). It is therefore most likely – especially in the magnitude range of ground-based surveys – for such a scenario to be caused by an ordinary eclipsing binary.

Second, transiting planets are expected to cause a $\bigcup$-shaped signal in the majority of cases. Long ingress and egress phases otherwise indicate two more equally sized bodies that are eclipsing each other. Seager and Mallén-Ornelas (2003) showed that the probability of observing *planetary* transits decreases strongly with an increasing duration of ingress and egress phase. In particular, less than 20% of all transits with depths $\delta F \leq 5\%$ yield configurations with $T_{23} \leq 0.4\,T_{14}$ (see their Figure 10), i.e., significant $\bigvee$-shapes.

If found in conjunction with a large transit depth ($\delta F \gtrsim 5\%$), clear $\bigvee$-shaped transits are already rejected during the first visual inspection of the BLS results (see Section 8.1). However, all unclear cases enter the initial candidate list and are subject to additional quantitative tests.

8.3.2 Check for Transit Depth Variations

When an extrasolar planet is transiting a distant star, two events can be observed: The transit itself, when the planet is in front of the star, and the secondary eclipse, when the star is occulting the planet (Figure 2.2). Although secondary eclipses of planets can in principle be detected, the contrast ratio is very small at optical wavelengths (see, e.g., Burrows et al. 2006). Therefore, ground-based telescopes like BEST II are not able to measure them even for the most luminous planets (e.g., CoRoT-1b with $\delta F = 1.26 \cdot 10^{-4}$; Snellen et al. 2009). The measurement of a secondary eclipse with such instruments can thus only be explained with the presence of a stellar companion, leading to the rejection of the object as a planetary candidate.

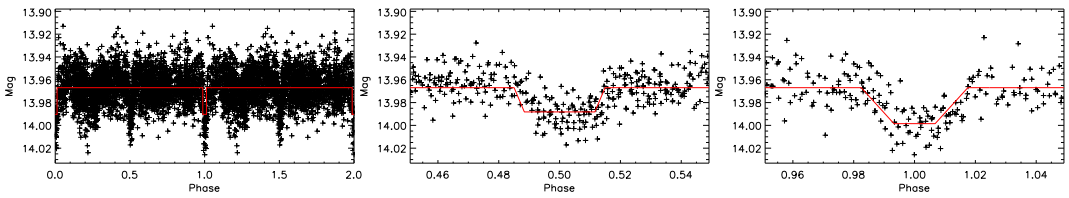

(a) Full phase-folded light curve (b) secondary: (21 ± 2) mmag (c) primary: (32 ± 3) mmag

Figure 8.4: Example of a transit depth variation test: BEST II planetary candidate F19_111745. (a) The light curve is phase-folded with twice the BLS period ($p = 2 \times 1.34445^d$). The primary (c) is significantly deeper than the secondary eclipse (b), and the candidate was rejected.

For the candidates presented in this work, the check for secondary eclipses proceeds in two steps. First, the folded light curve is inspected visually at phase $\varphi \approx \frac{1}{2}$. If the depth of the secondary eclipse is larger than the noise, it should be visible in this time range. However, if primary and secondary eclipses are of similar depths, the transit search will usually not be able to distinguish between both events and

therefore obtain the best fit with half of the orbital period (Collier Cameron et al. 2007). To test this, in a further check the period is then doubled, and trapezoids are fitted independently to the folded light curve around $\varphi = \frac{1}{2}$ and $\varphi = 1$, respectively. If both signals differ significantly in shape and/or depth, the candidate is rejected as an eclipsing binary (see example in Figure 8.4).

8.3.3 Out-Of-Transit Variation

Binary stars and planetary systems can show brightness variations that are correlated with the orbital phase of the secondary object due to ellipsoidal and/or reflection effects, or relativistic beaming (e.g., Snellen et al. 2009; Mazeh and Faigler 2010; Welsh et al. 2010). However, the amplitude for planetary systems is typically well below 0.1 mmag (for a theoretical approximation, see Mazeh and Faigler 2010) and can therefore not be detected by small ground-based telescopes like BEST II. A significant out-of-transit variation is therefore used here as a clear criterion for candidate rejection.

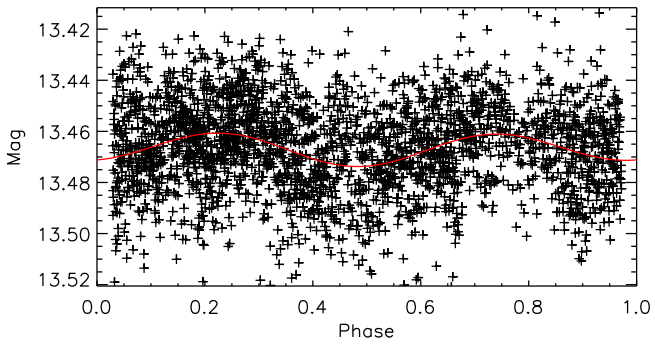

Figure 8.5: Example of an out-of-transit variation check: BEST II planetary candidate F19_097429. The folded light curve is shown without transits. A second-order sinusoidal fit to the remaining data points is shown in *red*; its amplitude is 13 mmag $= 0.74\,\sigma_{\rm oot}$, and the minimum is reached at phase $\varphi_{\rm oot} = 0.48$.

For estimating the variation quantitatively, a second-order sinusoidal is fitted to the folded light curve of each candidate. Data in transit are excluded before fitting. In order to assess the significance of the variation, the out-of-transit (oot) amplitude $A_{\rm oot}$ of the fit is divided by the standard deviation $\sigma_{\rm oot}$ of the out-of-transit, fit-subtracted light curve; values of $(A_{\rm oot}/\sigma_{\rm oot}) \gtrsim 1$ can be considered significant. Furthermore, the phase $\varphi_{\rm oot}$ of the fit minimum is determined. Eclipsing binaries can show ellipsoidal variation or a reflection effect which both are – in contrast to stellar activity – in a fixed phase relation with the eclipses. For instance, if $\varphi_{\rm oot}$ is close to $\frac{1}{2}$ or 1, this is another indicator for binary variation. Both parameters $A_{\rm oot}$ and $\varphi_{\rm oot}$ together can therefore lead to the rejection of a candidate, that might otherwise not be considered significant from the amplitude criterion alone (see example in Figure 8.5).

8.3.4 Contamination from Stellar Neighbors

Two false alarm scenarios are commonly encountered due to stellar crowding: First, light of a nearby binary leaks into the target aperture. Second, the target is itself a binary, but a significant amount of third light is recorded together with the target flux. In both cases, the depths of eclipses appear smaller and can thus mimic a transit-like signal (see also Section 2.2 and Appendix C.3).

For the candidates presented in this work, the first check for stellar contamination consists of the visual light curve inspection of all stars within 20 Px of the candidate's host star. Each light curve is then folded with the suspected orbital period of the candidate. If one of the neighboring stars shows variability with the same period but a larger amplitude, the candidate is rejected (see example in Figure 8.6).

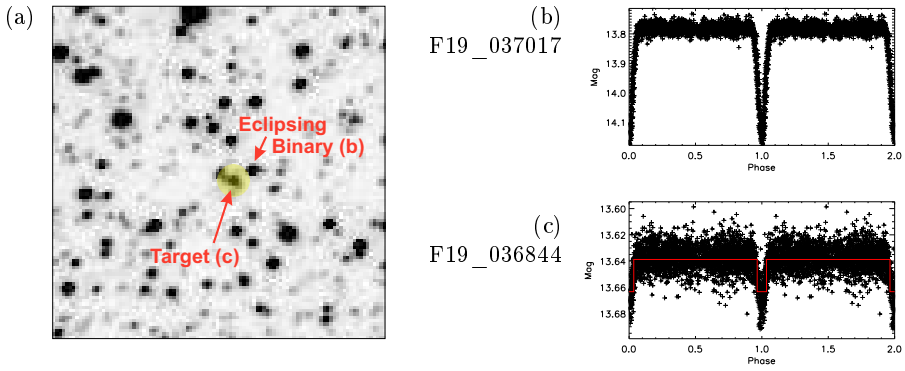

Figure 8.6: Example of a contamination test. (a) The left plot shows a cutout of the BEST II reference frame Ref(x, y) (cf. Section 5.2.1) centered on the transit candidate F19_036844. (c) Its light curve has a transit-like signal of 3%. However, the neighboring star F19_037017 (b) is a binary with eclipses that are about one order of magnitude deeper. Its light leaks into the aperture of the target (marked *yellow* in (a)) and mimics a transit.

In a second step, catalog information is used to estimate stellar contamination quantitatively. The stellar neighborhood of a candidate is assessed searching the NOMAD catalog for the closest objects within 20 Px radius. Their PSFs are then simulated assuming Gaussian shapes with $\sigma_{\mathrm{fwhm}} = 3\,\mathrm{Px}$ width. Thereby, the cataloged R magnitudes are used to estimate the flux leaking into the candidate's host star aperture (for details on the calculation, see Appendix C.1). If the fraction of third light is large enough to increase the transit depth above the range expected for planetary objects ($\delta F \gg 1\%$), a candidate is given lower priority or rejected.

8.3.5 Spectral Class and Stellar Radius

The transit signal δF is determined by the radius ratio $r_p/r_\star$ of the companion and its host star (Equation (2.6)). Therefore, the size of the secondary object can only be assessed if the stellar radius $r_\star$ is known. The latter can be estimated from the host star's spectral class, which hence forms the key to the physical nature of a candidate: It allows to distinguish between stellar and planetary objects, and to obtain a first size estimation.

Unfortunately, the color information available from catalogs (Section 8.1) usually enables only a very broad first estimation of the spectral class. In the following

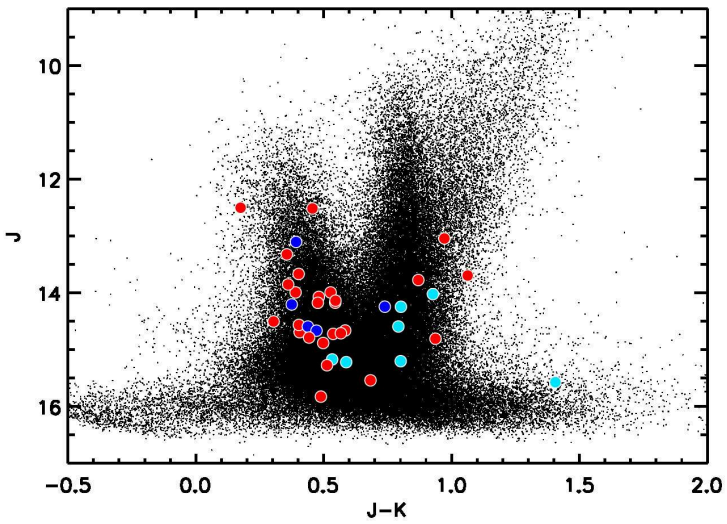

Figure 8.7: Color-magnitude diagram for target field F19. 2MASS J magnitudes are plotted vs. $(J-K)$ colors for every star that was matched with the catalog. Transit candidates are marked by circles; they appear *red* if they were excluded by the light curve analysis, and *blue* if they survived all tests (*dark blue* for $p_{\mathrm{cand}} = 2$, *light blue* for $p_{\mathrm{cand}} = 3$; for the priority definition, see page 99).

analysis, it is used for two purposes: To distinguish between giant and dwarf host stars, and to estimate the spectral class and stellar radius. This information is then used to limit the observational effort for precise class determinations to candidates for which either criterion does not indicate a stellar companion.

Dwarf or Giant?

In order to distinguish between dwarf and giant host stars, a color-magnitude diagram is created for all stars in each field. Although *absolute* magnitudes would be needed for a proper mapping of the main sequence and the giant branch, a $(J, J-K)$ plot with 2MASS *apparent* magnitudes can be used for a first approximation. Figure 8.7 shows an example, namely field F19. For stars brighter than $J \approx 14$, the distinction between dwarfs and giants is becoming visible. Unfortunately, the $(J-K)$ colors become highly unreliable for fainter stars ($J \gtrsim 15$), so that the method is not applicable to most of the candidates presented in this work, and further observations are needed to obtain a proper separation.

Class and Radius

In the literature, intrinsic colors are given for average main sequence and giant stars as a function of spectral classes. For this work, 2MASS colors are used to estimate the corresponding spectral class from tabulated values. Thereby, it is assumed that all stars are located on the main sequence, intermediate stellar classes are interpolated linearly, and interstellar reddening is neglected.

Figure 8.8a displays how stellar classes are assigned to candidate stars. For each of the three 2MASS colors $(J-H)$, $(H-K)$, and $(J-K)$, spectral classes are de-

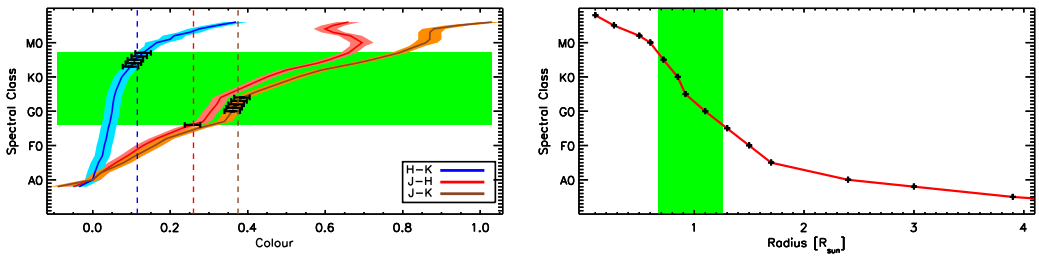

(a) Spectral class from colors

(b) Stellar radius from spectral class

Figure 8.8: Spectral class estimation – example of BEST II candidate F19_067715. (a) The correlation between spectral classes and colors is shown for main sequence stars. Values are from Bessell and Brett (1988), uncertainties from Cox (2000). Missing sub-classes are interpolated linearly. For each candidate and color, the spectral range is estimated from sub-classes having the same tabulated color (within uncertainties). The maximal spectral range supported by all colors *(green)* is used as a first estimate. (b) The maximal spectral class range from (a) is translated to a corresponding stellar radius range using a linear interpolation of Table 15.8 by Cox (2000).

termined that are compatible with tabulated values (Bessell and Brett 1988) within the uncertainties as given by Cox (2000, Table 7.6). The corresponding class ranges are given in the following Section 8.4 for each planetary candidate (cf. Table 8.2). Depending on unquantified effects on the 2MASS color measurements such as reddening or crowding, the ranges derived from the three different colors either overlap well or can be in mismatch. In addition, an inconclusive result can point to a giant star (for which the used relations are not valid), or a binary.

The class ranges are used to estimate the stellar radius $r_\star$ and therefore yield, together with the transit depth δF (Equation (2.6)), a first hint for the planetary radius r_p. Given the spectral class estimations, stellar radii are assigned to each star using the relation in Table 15.8 by Cox (2000). In order to account for uncertainties in the stellar class determination, maximum ranges, i.e., comprising all possible spectral types of the three colors, are formed and translated into radius ranges. Figure 8.8 shows an example of the radius estimation from 2MASS colors.

8.3.6 Estimation of Stellar Density $\rho_\star$

The stellar density $\rho_\star$ can be used for a quantitative identification of giants, which show very low densities compared to main sequence stars. Similar to the approximation of spectral classes from tabulated values, catalog colors are used to estimate the density $\rho_\star$ for each candidate's host star. However, $\rho_\star$ can also be calculated from the light curve itself, and the comparison of both approaches forms an important analysis technique: If both densities differ significantly, this can indicate a blend scenario. The procedure used for BEST II is described in the following text; it is based upon Tingley et al. (2011).

First, the color information from 2MASS is used to estimate the stellar density $\rho_\star$ (denoted as ρ_{JK} in the following). For each candidate, the $(J-K)$ color is used to look up the corresponding stellar densities from tabulated values in *Allen's Astrophysical Quantities* (Cox 2000); in analogy to Tingley et al. (2011), a fourth-order polynomial interpolates intermediate colors (Figure 8.9). The stellar density can be estimated

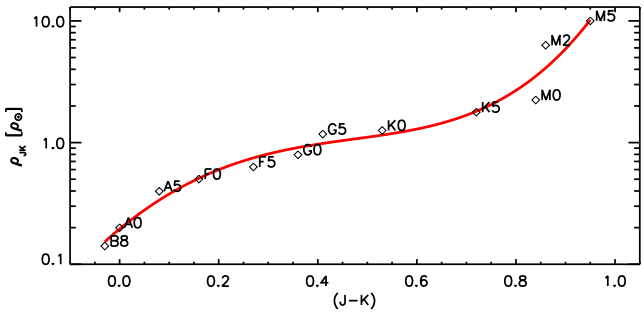

Figure 8.9: Stellar density estimations from 2MASS $(J-K)$ color, following Tingley et al. (2011). Diamonds show values for main sequence stars as listed in Cox (2000). A fourth-order polynomial fit *(red)* is used to interpolate for intermediate colors.

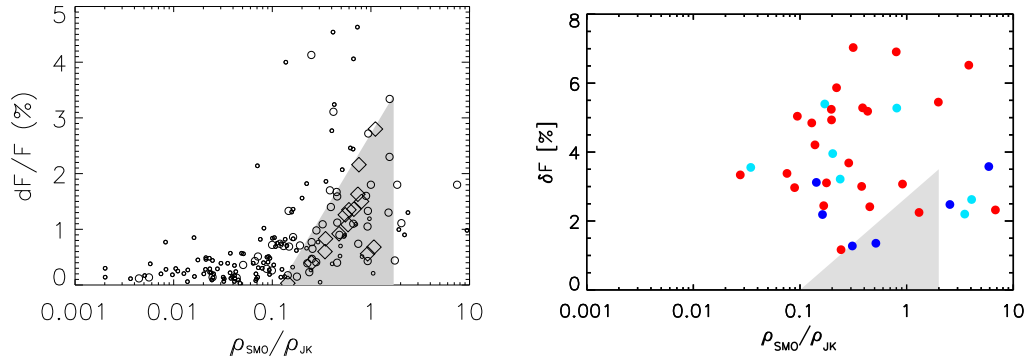

(a) (b)

Figure 8.10: Transit depths δF vs. density ratios $\rho_{\mathrm{SMO}}/\rho_{\mathrm{JK}}$. (a) Figure 4 from Tingley et al. (2011) for CoRoT candidates (circles) and confirmed planets (diamonds). (b) BEST II candidates in F17–F19 with parameters from Table 8.2. Colors as in Figure 8.7, i.e., *red* for rejected, *dark blue* for $p_{\mathrm{cand}} = 2$, and *light blue* for $p_{\mathrm{cand}} = 3$ (for the priority definition, see page 99).

very easily this way, but the method involves some systematic uncertainties. In particular, the fit in Figure 8.9 is only valid for the main sequence, so the derived densities ρ_{JK} are not correct for evolved stars.

Second, the stellar density is estimated from the light curves themselves. Seager and Mallén-Ornelas (2003) have shown that it is possible to obtain $\rho_\star$ from a simple trapezoid fit to the transit measurements (see Section 2.2; $\rho_\star$ denoted as ρ_{SMO} in the following). For the BEST II candidates, the full transit length T_{14}, the duration of the bottom part T_{23}, and the transit depth δF are determined by fitting a trapezoid to the folded light curve around the transit (i.e., $T_0 \pm 2\,T_{14}$). Together with the orbital period p, these parameters are used to calculate ρ_{SMO} with Equation (2.10).

Finally, both densities are compared by calculating the ratio $\delta\rho = \rho_{\mathrm{SMO}}/\rho_{\mathrm{JK}}$. Cases with $\delta\rho \ll 1$ either point to blend scenarios or giant stars (for which Figure 8.9 yields incorrect values of ρ_{JK}) that can both be rejected. Furthermore, Tingley et al. (2011) found that CoRoT confirmed planets are located in a triangular region in a diagram of transit depth vs. density ratio (Figure 8.10a). For each candidate in this work, $\delta\rho$ is calculated and reviewed in a similar way (Figure 8.10b), i.e., candidates that appear far off the shaded region are assigned a low priority.

8.4 Candidates in Fields F17–F19

As described in Section 8.1, a visual screening of BEST II light curves in the target fields F17–F19 yielded an initial list of 41 extrasolar planet candidates. For each candidate in the list, information from star catalogs was obtained, the ephemerides were improved through light curve fitting (Section 8.2), and false alarm indicators were evaluated (Section 8.3). Reports summarizing all available information were created for each candidate and reviewed carefully. Table 8.2 gives the most important properties for each candidate, e.g., the ephemerides, transit depth, or host star brightness.

According to the scheme applied within the CoRoT team (Cabrera et al. 2009; Erikson et al. 2012), priorities were assigned to each candidate:

- $p_{\mathrm{cand}} = 1$ for candidates that passed all false alarm tests without problems,
- $p_{\mathrm{cand}} = 2$–3 for candidates that show some inconclusive results, i.e., where the available information was neither sufficient to disregard a false alarm scenario nor to reject the candidate. The decision between priority 2 and 3 is made depending on the number of uncertain indicators and the photometric quality.

Candidates that clearly failed one or more of the tests were rejected. From the initial list of 41 candidates in F17–F19, six were given $p_{\mathrm{cand}} = 2$, eight were ranked with $p_{\mathrm{cand}} = 3$, and 27 were rejected as false alarms. Due to the relatively low SNR of all transit signals, no candidate was given the highest priority.

Comparison with Estimations

The number of detected candidates is in good agreement with the theoretical estimates of Section 4.4. If one assumes a planet-to-candidate ratio of $\sim$1:10–1:20 as obtained in other studies (e.g., Brown 2003; Pont et al. 2005; Alonso et al. 2007; Almenara et al. 2009; Evans and Sackett 2010; Carone et al. 2012), the overall expected yield in F17–F19 of 0.23–1.00 planets translates into 2–20 candidates.

In accordance with the expectations, the majority of initial candidates is found in F19, and none is found in the most sparsely populated field F18 (see Table 8.1). However, the number of candidates in F19 compared to F17 and F18 is higher than the ratio of the corresponding detection yields N_{det} that were estimated in Section 4.4. Most probably, this indicates a larger false alarm rate in F19 due to crowding. This issue could be addressed in the selection of future target fields by applying an additional limit to the fraction of contaminating stars in the simulation (see Appendix B; for F19, the *absolute* number of suitable target stars was maximized).

The fraction of candidates found is also in reasonable agreement with other ground-based surveys, albeit the selection criteria and observing strategies vary between different projects. For example, Kane et al. (2008) describes a data set of 130,566 low-noise SuperWASP light curves, from which 5,445 (4.2%; for comparison, BEST II: 5.7%) were raised by their detection algorithm for visual inspection, 36 (0.028%; BEST II: 0.035%) formed the initial candidate list, six (0.0046%; BEST II: 0.012%) remained after applying a full set of test procedures to the photometric data similar to those presented here, and one was finally confirmed as a planet through follow-up

Table 8.2: Transit candidates in BEST II fields F17–F19 (sorted by priorities) — results from photometry.

	Magnitude					Color	Stellar Type		St. Density [$\rho_\odot$]		BLS	Ephemerides		Trapezoid Fit		
ID	R_B	V	R	J	K	J-K	H-K;J-H;J-K	$r_\star$ [$r_\odot$]	$\rho_{\rm SMO}$	$\rho_{\rm JK}$	$S_{\rm bls}$	T_0 [rHJD†]	p [d]	δF	T_{14} [h]	T_{23} [h]
PRIORITY 2																
F17_064507	15.7	15.2	15.5	13.8	13.2	0.60	M4-M5;F8-G2;K2	0.7 ± 0.5	7.59	1.29	8.3	-57.406 ± 0.002	1.5220 ± 0.0002	3.6%	2.12	1.91
F19_057757 ⋆	14.7	15.9	15.9	14.6	14.2	0.44	K0-K5;G2-G5;G6-G7	0.9 ± 0.2	2.60	1.02	6.9	282.526 ± 0.002	2.10781 ± 0.00005	2.5%	2.84	2.50
F19_067715 ⋆	14.3	15.3	15.3	14.2	13.8	0.38	K3-K7;F6;G0-G4	1.0 ± 0.3	0.29	0.93	12.0	280.851 ± 0.005	0.93670 ± 0.00005	1.3%	2.14	1.15
F19_068690 ⋆	13.8	15.7	14.3	14.7	14.2	0.47	K8-M0;F9-G4;G7-G8	0.9 ± 0.3	0.55	1.07	6.9	281.523 ± 0.006	2.4123 ± 0.0002	1.4%	3.39	2.72
F19_083743 ⋆	13.1	14.2	14.2	13.1	12.7	0.39	A7-G7;G4-G5;G2-G5	1.3 ± 0.4	0.16	0.96	6.2	299.790 ± 0.004	2.4576 ± 0.0002	2.2%	3.52	0.31
F19_106774 ⋆	14.6	16.3	16.3	14.2	13.5	0.74	K9-M0;K4-M4;K5-K6	0.5 ± 0.2	0.28	1.96	11.1	282.033 ± 0.006	1.7248 ± 0.0002	3.1%	3.52	2.13
PRIORITY 3																
F17_006239	15.6	15.6	15.0	13.8	13.2	0.67	K9-M0;K2;K4	0.7 ± 0.1	6.15	1.51	6.4	-55.2039 ± 0.0006	5.13317 ± 0.00009	2.6%	2.39	1.95
F19_010403 ⋆	15.1	15.9	16.0	15.2	14.6	0.53	M0-M2;G5-G6;K0	0.7 ± 0.3	0.93	1.16	10.0	282.357 ± 0.008	4.7317 ± 0.0004	5.3%	3.00	···
F19_013266 ⋆	14.3	···	14.8	15.6	14.2	1.41	–;K4;–	0.746 ± 0.001	1.12	···	6.9	281.915 ± 0.003	1.76879 ± 0.00005	2.7%	1.72	···
F19_041059 ⋆	14.7	15.8	15.3	14.6	13.8	0.79	K7-M0;K6-M6;K7	0.5 ± 0.3	0.44	2.56	9.7	280.73 ± 0.01	3.2617 ± 0.0005	5.4%	3.50	0.76
F19_047826	14.8	16.3	15.8	15.2	14.6	0.59	M1-M2;G6-G7;K2	0.7 ± 0.3	0.26	1.26	9.9	281.745 ± 0.003	1.63226 ± 0.00006	4.0%	3.42	1.64
F19_064524 ⋆	14.9	16.4	15.0	14.2	13.4	0.80	K4-K8;K7-M6;K7-K8	0.5 ± 0.3	0.09	2.71	8.4	281.154 ± 0.006	1.1915 ± 0.0001	3.6%	3.73	0.63
F19_103706 ⋆	14.8	15.9	15.4	14.0	13.1	0.93	M4-M5;K5-M5;M5	0.5 ± 0.3	1.86	7.80	7.8	281.214 ± 0.003	1.13080 ± 0.00004	3.2%	2.07	1.61
F19_108764 ⋆	14.3	14.8	14.9	15.2	14.4	0.80	M3-M4;K3;K7-K8	0.6 ± 0.3	9.45	2.70	10.9	280.772 ± 0.003	1.91355 ± 0.00008	2.2%	1.80	1.61
REJECTED																
F17_061245	16.4	15.4	16.1	14.5	14.0	0.51	G4-K2;G9-K0;G9-K0	0.88 ± 0.08	0.35	1.13	6.6	-55.556 ± 0.005	2.2519 ± 0.0004	7.0%	3.85	1.68
F19_000014 ⋆	15.3	···	···	15.8	15.3	0.49	–;K4-M4;G8-G9	0.6 ± 0.3	2.16	1.09	11.2	280.674 ± 0.004	1.88445 ± 0.00008	5.4%	1.98	1.05
F19_021095 ⋆	13.9	16.1	15.5	15.3	14.8	0.51	A6-G5;K1;G9-K0	1.2 ± 0.5	0.16	1.13	12.9	284.303 ± 0.008	6.2320 ± 0.0008	4.2%	5.83	1.52
F19_021164	13.8	15.3	14.2	14.0	13.5	0.53	K8-M0;G5-G6;K0	0.8 ± 0.2	0.19	1.15	8.2	284.30 ± 0.02	6.234 ± 0.002	2.4%	5.27	2.61
F19_030342	14.8	···	16.0	14.8	13.9	0.94	K8-M0;–;M5	0.5 ± 0.2	0.24	8.73	9.3	280.92 ± 0.02	2.9765 ± 0.0004	3.3%	3.79	1.22
F19_030727‡⋆	13.9	15.3	14.6	14.0	13.6	0.39	F1-G9;G2-G5;G2-G5	1.2 ± 0.3	···	0.96	7.7	280.914‡	2.97633‡	1.1%	1.09	1.30
F19_035193 ⋆	14.1	15.2	15.0	14.5	14.2	0.30	A6-G4;F6-F7;F6	1.3 ± 0.4	0.74	0.81	6.9	281.380 ± 0.004	1.58329 ± 0.00007	3.1%	2.05	0.63
F19_036844	13.6	15.0	···	14.7	14.3	0.41	G8-K4;G0-G4;G5	0.9 ± 0.2	0.09	0.98	11.0	280.849 ± 0.004	1.67727 ± 0.00008	3.0%	4.12	0.80
F19_036930 ⋆	14.5	···	15.2	14.7	14.1	0.58	M3-M4;G0-G4;K2	0.7 ± 0.4	0.22	1.25	9.9	281.289 ± 0.006	0.72450 ± 0.00005	3.1%	2.42	0.87
F19_043426 ⋆	11.7	13.1	13.0	12.5	12.3	0.18	K1-K5;A5-A7;F0-F2	1.2 ± 0.5	0.23	0.54	7.5	283.884 ± 0.003	4.8877 ± 0.0003	5.2%	5.72	3.15
F19_044625	14.0	···	16.3	15.5	14.9	0.68	M6;G0-G4;K4	0.7 ± 0.5	6.07	1.59	14.6	281.381 ± 0.004	2.23018 ± 0.00008	6.5%	2.19	1.75
F19_044803	14.6	16.0	16.1	14.6	14.2	0.40	G6-K3;G0-G4;G4-G5	0.9 ± 0.2	1.27	0.97	9.2	281.250 ± 0.008	2.6440 ± 0.0003	2.2%	2.96	2.36
F19_046366 ⋆	13.0	14.0	13.5	13.3	13.0	0.36	K2-K6;F6;F7-G2	1.0 ± 0.3	0.22	0.90	6.1	281.702 ± 0.004	1.45427 ± 0.00005	1.2%	2.67	1.45
F19_047833 ⋆	13.9	15.6	15.2	13.0	12.1	0.97	M1-M2;–;–	0.52 ± 0.03	0.11	···	10.7	281.782 ± 0.003	1.28750 ± 0.00004	2.4%	3.49	1.17
F19_048335 ⋆	14.5	···	14.4	14.9	14.4	0.50	G5-K2;G8-G9;G8-G9	0.86 ± 0.07	0.24	1.10	10.9	288.242 ± 0.005	11.5640 ± 0.0007	5.9%	6.58	1.19
F19_063165 ⋆	13.6	14.5	13.0	13.9	13.5	0.36	A5-G2;G1-G4;F8-G2	1.3 ± 0.4	0.73	0.91	15.7	280.902 ± 0.002	2.53011 ± 0.00006	6.9%	2.86	0.47
F19_079670 ⋆	13.9	···	···	13.8	12.9	0.87	M1-M2;K7-M6;M0-M4	0.4 ± 0.3	0.58	4.46	7.8	283.88 ± 0.02	6.5763 ± 0.0007	4.8%	3.89	0.63
F19_081853 ⋆	14.1	15.2	15.8	14.1	13.6	0.48	K3-K7;G5-G6;G8	0.8 ± 0.2	0.10	1.08	10.3	283.282 ± 0.003	2.7516 ± 0.0001	5.0%	5.34	1.37
F19_097429 ⋆	13.5	15.4	14.7	14.2	13.7	0.48	K1-K6;G6-G7;G8	0.8 ± 0.2	0.41	1.07	6.4	281.624 ± 0.008	2.2157 ± 0.0003	3.0%	3.52	2.31
F19_097625 ⋆	13.7	14.4	···	14.2	13.6	0.55	F1-G8;K1-K2;K0-K1	1.1 ± 0.4	0.23	1.18	17.5	281.879 ± 0.003	1.55162 ± 0.00005	5.2%	3.35	0.72
F19_101062 ⋆	14.5	15.5	14.8	14.7	14.2	0.54	K9-M1;G5-G6;K0	0.7 ± 0.2	0.23	1.16	6.3	284.466 ± 0.009	5.1582 ± 0.0008	4.9%	4.83	···
F19_104521 ⋆	14.2	15.2	14.9	14.1	13.6	0.55	A0-F0;K3;K0-K1	1.6 ± 0.9	0.34	1.18	12.6	284.701 ± 0.005	8.3322 ± 0.0005	3.7%	4.73	0.95
F19_108882	14.3	16.2	···	13.7	12.6	1.06	M0-M2;–;–	0.55 ± 0.05	2.78	···	6.7	280.772 ± 0.007	1.9133 ± 0.0002	1.8%	1.60	1.08
F19_111745 ⋆	14.0	15.5	15.4	14.8	14.3	0.44	–;K4-M5;G6-G7	0.6 ± 0.4	0.46	1.03	7.0	281.860 ± 0.002	1.34450 ± 0.00004	2.4%	2.25	0.95
F19_114106 ⋆	12.5	13.6	13.4	12.5	12.1	0.46	F7-K1;G7-G8;G7	1.0 ± 0.2	0.08	1.05	6.2	280.748 ± 0.007	4.4595 ± 0.0004	3.4%	6.47	2.48
F19_115366 ⋆	13.5	15.1	14.7	13.7	13.3	0.40	A3-F8;G6-G7;G4-G5	1.4 ± 0.6	0.38	0.97	6.3	283.116 ± 0.009	6.4637 ± 0.0007	5.3%	4.68	1.30
F19_115603 ⋆	14.4	16.1	15.9	14.7	14.1	0.57	K3-K7;K0-K1;K1	0.76 ± 0.09	8.28	1.22	8.0	281.770 ± 0.002	1.62565 ± 0.00005	2.3%	2.35	2.20

† rHJD = HJD − 2,455,000

‡ Ephemerides fit (see Section 8.2) failed because individual events are not precise enough. BLS results are shown instead.

⋆ Stellar spectrum obtained with AAOmega.

Notes. Magnitudes are obtained by BEST II and coordinate matches to the NOMAD (V,R) and 2MASS (J,K) catalogs. Spectral type ranges and stellar radii $r_\star$ are estimated from 2MASS colors (Section 8.3.5). The stellar densities $\rho_{\rm SMO}$ and $\rho_{\rm JK}$ are derived independently using the transit shape and the 2MASS ($J-K$) color, respectively (Section 8.3.6). Ephemerides T_0 and p are the result of the mid-point fit to individual events (Section 8.2). The transit depth δF, the duration of the full transit T_{14}, and the main eclipse duration T_{23} are all determined from a trapezoid fit to the folded light curve (Section 8.2).

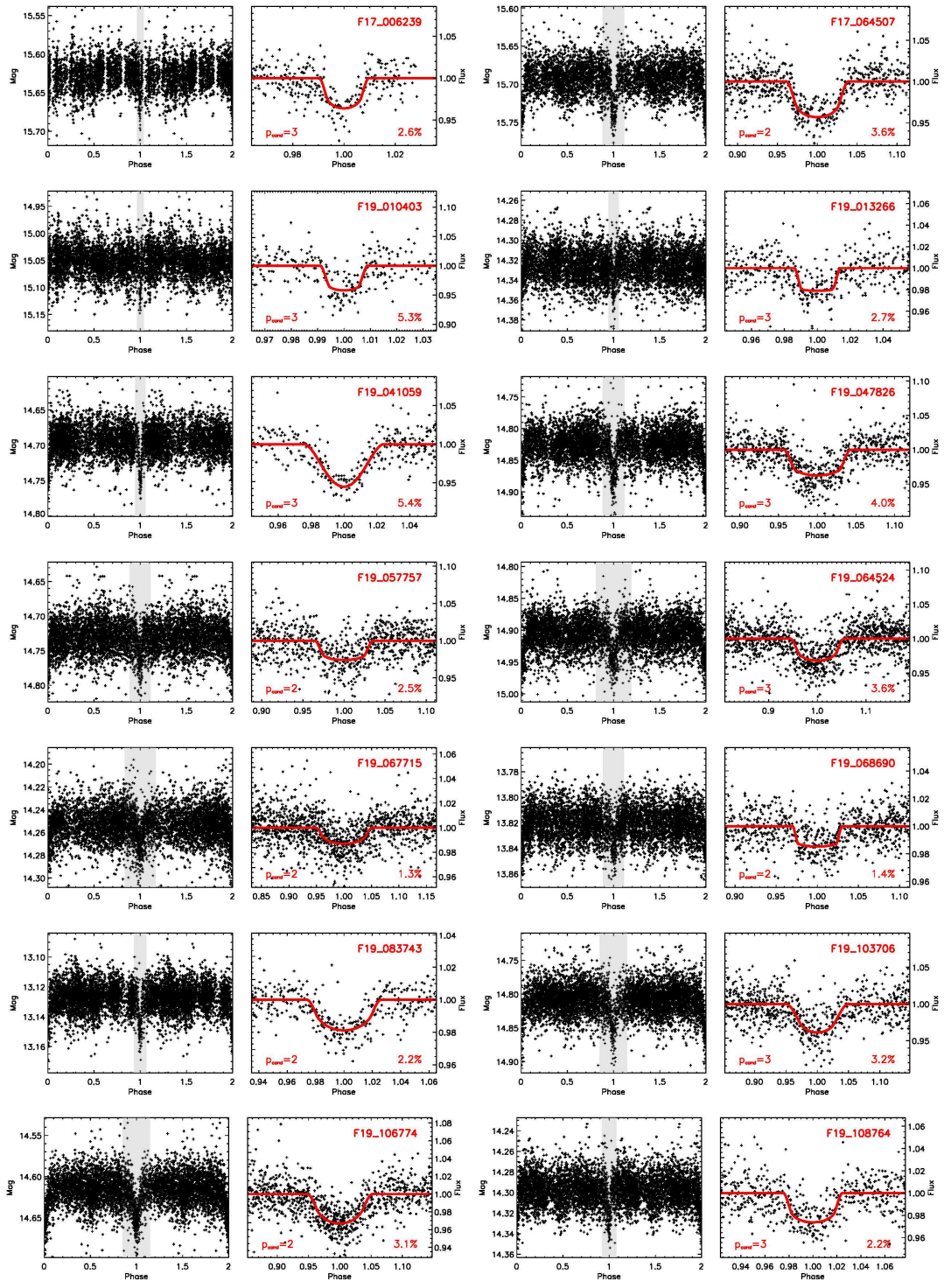

Figure 8.11: Folded light curves of transit candidates in fields F17–F19. The left side of each panel shows the folded light curve in BEST II magnitudes. A phase range around the transit-like signal is marked *gray* and shown enlarged on the right plot of each panel, which displays measured fluxes together with the modeled fit *(red line)*. In addition, priorities p_{cand} and transit depths δF are given for information (see also Table 8.2).

Table 8.3: Light curve modeling results for BEST II planetary candidates in F17–F19.

ID	R_B	J-K	Modeling Results				r_p/r_J
			$a/r_\star$	$r_p/r_\star$	b	χ^2	
PRIORITY 2							
F17_064507	15.7	0.60	4.81 ± 0.35	0.1855 ± 0.0094	0.25 ± 0.22	0.594	1.31 ± 0.83
F19_057757	14.7	0.44	5.00 ± 0.54	0.1503 ± 0.0070	0.36 ± 0.27	0.259	1.25 ± 0.21
F19_067715	14.3	0.38	3.14 ± 0.15	0.1028 ± 0.0038	0.499 ± 0.090	0.445	0.97 ± 0.30
F19_068690	13.8	0.47	5.88 ± 0.29	0.1149 ± 0.0032	0.20 ± 0.22	0.728	0.97 ± 0.31
F19_083743	13.1	0.39	6.22 ± 0.30	0.1211 ± 0.0037	0.481 ± 0.076	0.803	1.48 ± 0.44
F19_106774	14.6	0.74	3.34 ± 0.15	0.1602 ± 0.0043	0.450 ± 0.068	0.569	0.85 ± 0.32
PRIORITY 3							
F17_006239	15.6	0.67	18.4 ± 3.5	0.169 ± 0.025	0.36 ± 0.38	0.595	1.15 ± 0.24
F19_010403	15.1	0.53	20.1 ± 2.9	0.1952 ± 0.0078	0.41 ± 0.23	0.433	1.35 ± 0.41
F19_013266	14.3	1.41	12.2 ± 1.5	0.1425 ± 0.0062	0.46 ± 0.31	0.813	1.03 ± 0.05
F19_041059	14.7	0.79	6.44 ± 0.35	0.258 ± 0.038	0.806 ± 0.072	0.487	1.14 ± 0.63
F19_047826	14.8	0.59	4.43 ± 0.16	0.1770 ± 0.0062	0.12 ± 0.15	0.436	1.21 ± 0.36
F19_064524	14.9	0.80	3.33 ± 0.19	0.1578 ± 0.0061	0.27 ± 0.23	0.370	0.74 ± 0.42
F19_103706	14.8	0.93	3.298 ± 0.099	0.1877 ± 0.0044	0.656 ± 0.025	0.527	0.90 ± 0.42
F19_108764	14.3	0.80	7.23 ± 0.61	0.1461 ± 0.0058	0.29 ± 0.24	0.344	0.80 ± 0.31

Notes. The semi-major axis a and the planet radius r_p are given in units of stellar radii $r_\star$. In addition, the impact parameter b and the goodness-of-fit value χ^2 (Equation (8.1)) are shown, and the instrumental magnitude R_B and the $(J-K)$ color are repeated from Table 8.2 for information. Planetary radii r_p are given in units of Jupiter radii and are derived by combining the modeling result $r_p/r_\star$ with the estimate of $r_\star$ from Table 8.2. Note that several candidates have been observed spectroscopically, in which case much more accurate estimates on $r_\star$ and r_p are available (see Table 8.4).

observations. In contrast to that, the photometric precision and extended duty cycle of space-based surveys yield a significantly higher fraction of candidates. For example, CoRoT identified a total of 195 (0.49%) planetary candidates in the 39,662 light curves of its first four target fields (Carpano et al. 2009; Cabrera et al. 2009; Carone et al. 2012; Erikson et al. 2012).

8.4.1 Light Curve Modeling

The light curves of transit candidates ranked with $p_{\text{cand}} \leq 3$ have been modeled by Szilárd Csizmadia (DLR) using the *Transit Light Curve Modeling (TLCM)* package (e.g., used for the modeling of CoRoT-17b; Csizmadia et al. 2011). It it based on an analytic light curve description given by Mandel and Agol (2002) with quadratic limb-darkening, and uses a genetic algorithm to fit the following free parameters to the observations: The radius ratio $r_p/r_\star$, the impact parameter b, the transit mid-point T_0, the transit duration T_{14} (in phase units), and the two limb-darkening coefficients u_1 and u_2. From T_{14}, the semi-major axis a can be approximated in units of the stellar radius $r_\star$. The goodness of the fitted function g_{fit} to the data $\{(t_j, f_j)\}$ is evaluated through χ^2 statistics, i.e.,

$$\chi^2 = \frac{1}{N_t - N_p - 1} \cdot \sum_{j=1}^{N_t} \left(\frac{f_j - g_{\text{fit}}(t_j)}{\Delta f_j} \right)^2 , \tag{8.1}$$

where N_t defines the number of data points and N_p denotes the number of free parameters.

Figure 8.11 shows the phase-folded light curves together with the best model fit, and Table 8.3 lists the fitting results $a/r_\star$, $r_p/r_\star$, b, and χ^2. In addition, $r_p/r_\star$ is combined with $r_\star$ of Table 8.2 (see Section 8.3.5) to estimate the planetary radius r_p.

8.4.2 Spectroscopic Characterization

Photometry from BEST II or catalogs such as 2MASS cannot provide reliable spectral types, luminosity classes, or radii of the candidate's host stars: Figure 8.12 compares the radius ratios $r_p/r_\star$ of BEST II candidates with planets of Neptune- and Jupiter-size around different stellar types; it shows that a more accurate spectral characterization is essential to determine the physical nature of each candidate. Therefore, the next step is to obtain these parameters through spectral classification.

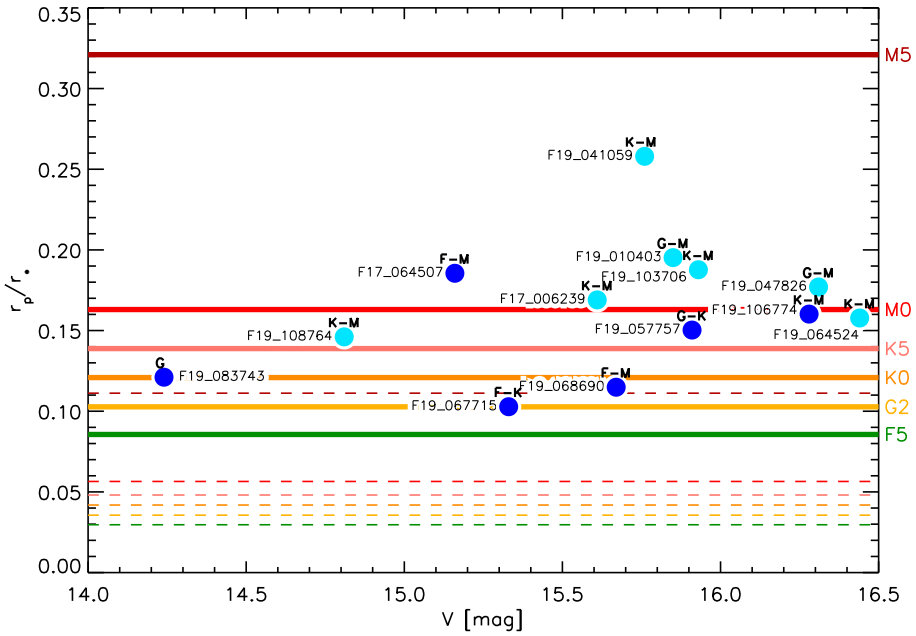

Figure 8.12: Radius ratio $r_p/r_\star$ of BEST II planetary candidates plotted vs. their corresponding V magnitude from the NOMAD catalog. Priority 2 candidates are shown in *dark blue*, priority 3 candidates in *light blue*. Thick solid lines indicate the radius ratio of Jupiter ($r_p = 0.10\,r_\odot$) for selected stellar types, whereas thin dashed lines show the ratios of Neptune ($r_p = 0.036\,r_\odot$). Also given are first rough spectral type estimations for each host star based on catalog colors (see Section 8.3.5).

Most importantly, this allows to exclude two types of stars from the further follow-up process:

- Evolved stars, for which the transit depth corresponds to an eclipsing low-mass star rather than a planetary companion.
- Early-type stars and rapidly rotating objects, for which high-precision RV measurements are not feasible.

The best results are obtained via low-resolution spectroscopy covering a wide spectral range *(reconnaissance spectroscopy)*. The relative faintness of the presented candidates requires observations with a medium sized telescope (2–4 m class) to obtain spectra with a reasonable SNR. Altogether, the AAOmega spectrograph (Smith et al. 2004) at the 3.9 m *Anglo-Australian Telescope (AAT)* in Australia has been identified as the most suitable instrument for initial spectral characterization of BEST II candidates. It is able to obtain spectra for up to 392 objects in a single pointing,

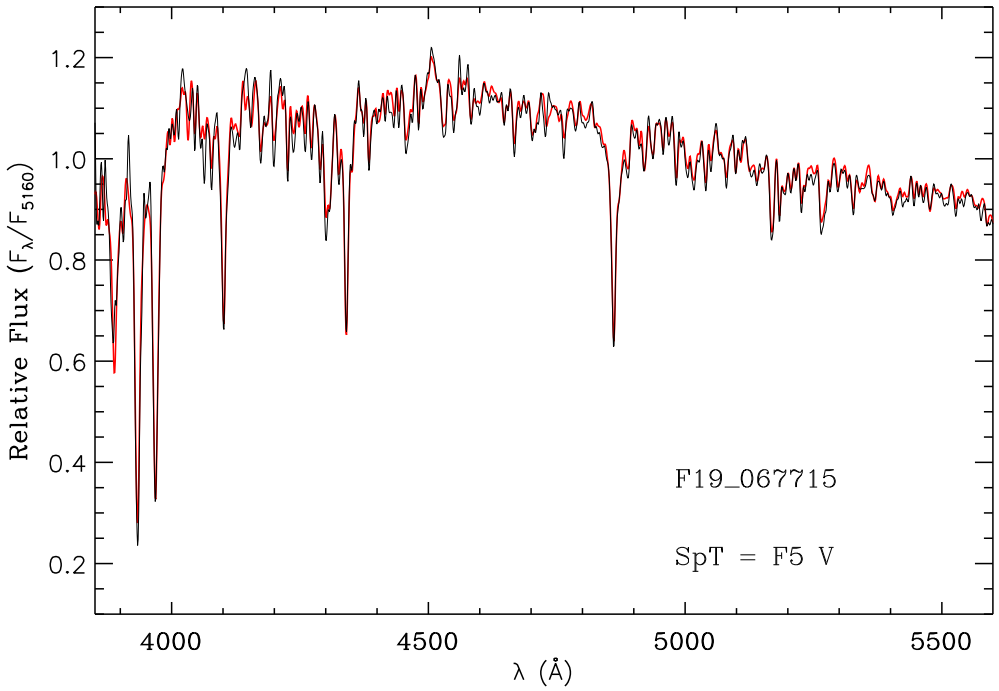

Figure 8.13: AAOmega spectrum of BEST II planetary candidate F19_067715 (*black* line). Overplotted with a *red* line is the best-fitting F5V template as derived using the spectrum fitting procedure described by Gandolfi et al. (2008). The spectra are normalized to the flux at 5,160 Å.

Table 8.4: Results from the spectroscopic characterization of planetary candidates in field F19.

ID	$p_{\rm cand}$	.. Photometry .. R_B	p [d]	δF	..... Spectroscopy ..... Type	$T_{\rm eff}$ [K]	$\log g$	$r_\star$ [$r_\odot$]	r_p [r_J]
Luminosity Class V (main sequence stars)									
F19_010403	3	15.1	4.73	4.0%	G0 V	5,900	4.4	1.10	2.09 ± 0.23
F19_013266	3	14.3	1.77	1.7%	G5 V	5,550	4.3	0.92	1.28 ± 0.14
F19_067715	2	14.3	0.94	1.5%	F5 V	6,450	4.3	1.30	1.30 ± 0.14
F19_083743	2	13.1	2.46	2.0%	F1 V	6,900	4.2	1.46	1.72 ± 0.18
F19_108764	3	14.3	1.91	2.3%	G6 V	5,450	4.3	0.91	1.29 ± 0.14
F19_041059	3	14.7	3.26	5.4%	K0 IV/V	5,200	4.0–4.4	0.85	2.13 ± 0.39
Luminosity Class IV (subgiants)									
F19_057757*	2	14.7	2.11	2.5%	F6 IV	6,400	4	(1.3)*	(1.8 ± 0.3)*
F19_068690*	2	13.8	2.41	1.3%	F6 IV	6,420	4	(1.3)*	(1.4 ± 0.2)*
Luminosity Class III (giants)									
F19_064524	3	14.9	1.19	2.9%	G8 III	4,900	2.5	13	20 ± 3
F19_103706	3	14.8	1.13	3.6%	K2 III	4,400	2.3	19	35 ± 4
F19_106774	2	14.6	1.72	3.1%	G8 III	4,900	2.8	13	17 ± 2

* Due a lack of similar references, the same radius relation as for main sequence stars was used for subgiants. This method underestimates the stellar sizes significantly (by a factor $\gtrsim 2$), i.e., the given radii $r_\star$ and r_p should only be considered a very rough estimate.

Notes. Based on spectroscopic observations obtained with the AAOmega instrument in 2012 (see text). Candidate priorities $p_{\rm cand}$, instrumental magnitudes R_B, orbital periods p, and transit depths δF are repeated for information (see Table 8.2 for results from photometry). Spectral types, stellar effective temperatures $T_{\rm eff}$, and surface gravities $\log g$ were obtained through a comparison with template spectra (Gandolfi et al. 2008, see also Figure 8.13). Stellar radii $r_\star$ were calculated from the spectral types using a linear interpolation of tabulated data (Table 15.8, Cox 2000); the corresponding uncertainty is estimated to 10%. Candidate radii r_p were calculated using these more accurate estimates of $r_\star$ together with the ratio $r_p/r_\star$ from light curve modeling (Table 8.3).

and its FOV of 2° covers a BEST II field completely.

Since the target field F19 contains by far the most candidates, it was proposed for spectral characterization with AAOmega first. Observations have been obtained for a total integration time of 2.0 h (10×720 s) during the night of 16th February 2012 (proposal AO146). They comprise spectra for 329 interesting objects in the field (including eleven candidates of Table 8.2; for variable stars observed with AAOmega, see Section 9 and Appendix E.4), each covering the spectral range from 370 nm to 880 nm (gratings 385R and 580V) with a resolution of $R = 1{,}300$.

For the planetary candidates of priority 2 and 3, the observations were reduced in collaboration with Petr Kabath (ESO) and Davide Gandolfi (ESA). They were calibrated using bias and flat field reduction, a wavelength solution was obtained using arc frames, and individual scientific frames were combined. Finally, the resulting spectra were cross-matched with a set of suitable template spectra in order to obtain a first stellar classification (see example in Figure 8.13; for a detailed description of the procedure, see Gandolfi et al. 2008).

Five candidates in field F19 were classified as main sequence stars, two as subgiants, and three as giants; for the object F19_041059, the spectral resolution is insufficient to decide whether the target is a subgiant or at the main sequence. Table 8.4 shows the results of the spectroscopic characterization. In addition to the spectral types, it gives estimates on the effective temperature $T_{\rm eff}$ and the surface gravity $\log g$, which both are determined as an average of the corresponding parameters of matched template stars. For main sequence stars, $T_{\rm eff}$ and $\log g$ were compared to tabulated values (Cox 2000, Tables 7.6 and 15.8), which all agree within 5%.

Most importantly, the spectral classification now enables a much more robust estimate of stellar radii. Given the spectral types, stellar radii in Table 8.4 were obtained from a linear interpolation of Table 15.8 by Cox (2000). The three giants are transited by secondary objects of radii $r_p \gg 10\,r_J$, which can clearly be rejected as planetary candidates. For the five/six candidates around main sequence stars, the measurements yield planetary radii of 1.3–2.1 r_J, i.e., a very interesting range of planetary objects. For subgiants, the stellar radius is poorly constrained from the spectral type, and the planetary hypothesis cannot be rejected.

A direct comparison of the initial stellar radius estimations using 2MASS colors (Table 8.2) with the radii from spectroscopic data (Table 8.4) shows that the first method underestimated $r_\star$ for main sequence stars in average by 35%. The effect is most likely due to interstellar extinction, which has not been taken into account. For future transit searches, the method presented in Section 8.3.5 to obtain an initial stellar radius estimate should thus be complemented with a model to correct for the color excess. The stellar radii obtained spectroscopically for field F19 could be useful for its calibration.

8.4.3 Remaining Very Good Candidates

F17_064507

F17_064507 is the only candidate ranked with priority 2 in F17; it has a period of $p = 1.55220(2)$ days. However, its transit depth of 3.6% and the corresponding radius ratio of $r_p/r_\star = 0.186(1)$ place it at the upper limit for planetary objects. The first spectral class estimate from 2MASS colors yielded an inconclusive result for the $V = 15.2$ mag host star: They are compatible with types ranging from F8 to M5, so that the planetary radius can only be approximated to $(1.31 \pm 0.83)\, r_J$. Thus, a better spectroscopic classification is needed to clear if this candidate is a sub-stellar object or a brown dwarf.

However, the photometric quality of this candidate is good, and the ⋃-shaped transit feature can clearly be seen in five fully and one partially covered events. In addition, the less crowded field F17 yields a smaller probability for false alarms through blending compared to candidates in F19.

F19_010403

The host star of candidate F19_010403 is relatively faint ($V = 15.9$ mag), so that, although the signal itself is large ($\delta F = 5.3\%$), the transit is detected close to the photometric noise limit. The star itself is found to be solar-like (spectral type G0V, $r_\star = 1.1\, r_\odot$). The signal has a periodicity of 4.7317(4) days and corresponds to a secondary object with a radius of $r_p = (2.09 \pm 0.23)\, r_J$, i.e., if of planetary nature, it would be a highly inflated hot Jupiter.

Due to the faintness of the star, more accurate photometry is needed in order to constrain the system parameters better (in particular, the orbital period and the radius ratio).

F19_067715

Candidate F19_067715 features the smallest transit-like signal ($\delta F = 1.3\%$) found with BEST II so far. If confirmed, it would be placed among the fastest orbiting exoplanets with a period of only $p = 0.93668(5)$ days. The short period enabled an observational coverage of 16 full transits and 13 partial events, and allowed the detection of this small signal through binning.

The $V = 15.3$ mag host star has been classified as F5V ($r_\star = 1.3\, r_\odot$), which yields (together with the modeled radius ratio of $r_p/r_\star = 0.103(4)$) a radius estimate of $r_p = (1.30 \pm 0.14)\, r_J$ and puts the candidate into the range of Jupiter-class planets.

F19_083743

The star F19_083743 features $V = 14.2$ mag and is therefore the brightest target in the set of BEST II planetary candidates from F17–F19. Its 2.2% deep transit-like signal is clearly visible in 4 full and 3 partially covered events ($p = 2.4576(2)$ days). The host star is classified as F1V with a radius of $1.5\, r_\odot$, so that the transit signal

corresponds to an object of $r_p = (1.72 \pm 0.18)\, r_J$, i.e., a possibly inflated hot Jupiter planet.

F19_013266 and F19_108764

The two candidates F19_013266 and F19_108764 are very similar in their derived parameters, having periods of 1.76879(5) days and 1.91355(8) days, transit depths of 2.7% and 2.2%, and radii estimated to $r_p = (1.28 \pm 0.14)\, r_J$ and $(1.29 \pm 0.14)\, r_J$, respectively. Their G5V and G6V host stars are each $R_B = 14.3$ mag bright, but the candidates have been ranked priority 3 due to a significant amount ($\gtrsim 50\%$) of contaminating light within their respective aperture. High-resolution photometry is needed in order to separate the two candidates from their stellar neighborhood, and to determine the transit depth accurately. More photometric measurements, preferably at a higher SNR, would also allow to better constrain the system parameters as derived from light curve modeling (in particular, for F19_013266).

8.5 Summary and Outlook

Three target fields, F17–F19, have been selected and observed with BEST II for the purpose of transit search (Chapter 4). Within this work, 115,740 low-noise light curves have been analyzed for transit-like signals, and 6,605 of these have been analyzed visually. This analysis yielded an initial list of 41 planetary candidates in the fields F17 and F19, which have been checked for false alarm scenarios based upon the data at hand (i.e., BEST II photometry and star catalogs). Candidates were rejected that show stellar contamination, significant out-of-transit variation, different depths of odd and even transits, 2MASS colors indicating a giant or hot dwarf (OBA) host star, and/or an inconsistent stellar density as determined from the transit fit. These state-of-the-art procedures are applied in a very similar way by leading surveys (e.g., HATSouth, Bakos et al. 2013). After all tests, 14 candidates remained; these were given priorities from 1 to 3 for the follow-up process, and their parameters were obtained via light curve modeling. Furthermore, the detection yield of BEST II was found to be in agreement with expectations from simulations based on the field statistics (cf. Section 4.4).

Although many false positives could be identified through the described tests, the available information is yet not sufficient to confidently exclude all possible scenarios which are not of planetary origin. For that, further observations are required. The according strategy is adapted from the CoRoT follow-up procedure (Deeg et al. 2009; Moutou et al. 2009), which is largely standardized and was applied successfully to a large number of planets (e.g., CoRoT-11b; Gandolfi et al. 2010). It consists of three main steps:

First, **low-resolution spectroscopy** allows to obtain an initial classification of each candidate's host star. This is important in order to exclude giant and early-type stars, and to obtain an accurate radius estimate for the star (and, hence, the planetary radius). For the candidates in field F19, this part was concluded through AAOmega spectroscopy, which identified five main sequence stars, two subgiants, three giants, and one dwarf/subgiant star. For field F17 (in particular, the priority 2

candidate F17_064507), a spectral classification still needs to be obtained. However, the small number of candidates in this field does not justify the use of a multi-object spectrograph like AAOmega, and the faintness of the two candidates ($V \approx 15.5$ mag) requires long integration times and a large telescope. Since two candidates alone will probably not motivate an own observing proposal, it might be advantageous to merge the follow-up of these with other fields (e.g., candidates from ASTEP; cf. Chapter 10).

Second, several transit candidates presented here require **additional photometric observations** for two reasons. First, the target itself needs to be separated from contaminating neighbor stars with an angular resolution better than BEST II. Second, the transit signal itself must be measured at higher SNR in order to better constrain the system parameters from light curve modeling. Such observations are particularly necessary to improve the parameters of F17_006239, F19_010403, F19_013266, F19_057757, and F19_068690, and to limit the amount of third light leaking into the aperture of the targets F17_006239, F19_013266, F19_068690, and F19_108764. For field F19, additional observations have already been obtained with BEST II and ASTEP 400 recently, but not been reduced yet. Especially ASTEP is expected to contribute to the follow-up due to its larger aperture and better angular resolution, but the data will only be available in Europe in 2013.

Third, a stellar companion can only be excluded to have caused the transit-like signal through further spectroscopic observations, as some binaries are too close to be spatially resolved. **High-resolution spectroscopy** is used to either identify two distinct sets of stellar spectral lines (SB2), or a large periodic Doppler shift of the brighter component (SB1). The last step in the follow-up process of a transiting planet is the independent confirmation through accurate RV measurements (see Section 2.1), which also yield its true mass, and, hence, its density. However, because the candidates presented in this work are all found around relatively faint host stars, their confirmation will only be possible with the largest and most accurate RV facilities available today. The best two candidates presented in this work, F19_067715 and F19_083743, have recently been proposed to ESO for observations with the Ultraviolet and Visual Echelle Spectrograph (UVES; Dekker et al. 2000) at the 8 m Very Large Telescope (VLT) in Paranal, Chile. Approximately six hours of observations are required for each candidate in order to characterize it and to finally reject or confirm its planetary nature.

A general challenge for the follow-up process of the candidates presented within this work is their faintness ($V \simeq 14$–16 mag), which requires observations using the largest facilities in the world. Note that the possibilities to observe brighter targets are limited for a given telescope design, e.g., by its aperture and FOV. However, small adaptations are possible: Chapter 11 will present a discussion and an outlook on how the BEST II observing strategy could be adjusted based on the lessons learned from this thesis.

9 Stellar Variability in BEST II Fields

The improved method for variable star search (Chapter 7, see also Fruth et al. 2012) was applied to the BEST II data sets LRa02 and F17–F19 (see Table 4.1 for details on the observations). This chapter presents and discusses the scientific results.

Introduction

Since these target fields were monitored for different purposes, their analysis focuses on distinct aspects: Field LRa02 was observed in the follow-up process of CoRoT, and a first characterization of stellar variability based on BEST II data was presented by Kabath et al. (2009a). Through a *reanalysis* of the same data set, new detections could now be obtained within this work; they are presented in Section 9.1 and compared to the first BEST II publication and CoRoT classifications, which meanwhile have become available. The three fields F17–F19, however, have been selected and observed within the framework of this thesis (Section 4.2); as such, their analysis yields a *first* variability characterization, which is presented in Section 9.2.

Table 9.1: Summary of variable star search in BEST II target fields LRa02 and F17–F19.

Field	# Stars			# Variable Stars		
	$N_\star$	$J \geq 0.1$	$q \geq 10$	Known	New	Suspected
LRa02*a (v5)*	44,124	11,969[1] (27%)	799 (1.8%)	6[3]	281[3] (0.64%)	17 (0.04%)
LRa02*b (v4)*	76,466	19,117[1] (25%)	911 (1.2%)	6[3]	336[3] (0.44%)	35 (0.05%)
F17	68,317	20,965 (31%)	1,126 (1.7%)	2	646 (0.95%)	227 (0.33%)
F18	13,551	5,399[2] (40%)	176 (1.3%)	4	12 (0.09%)	9 (0.07%)
F19	127,202	89,123 (70%)	4,178 (3.3%)	11	1,861 (1.46%)	518 (0.41%)
Total	329,660	146,573 (44%)	7,190 (2.2%)	29[3]	3,136[3] (0.95%)	806 (0.24%)

1) — The variability search was optimized using this data set (see Section 7.3), and no star was excluded using any J limit; however, the number of stars with $J \geq 0.1$ is given here for comparison.
2) — Due the low number of stars in F18, the limit was lowered to $J \geq 0.05$ (see also Table D.1).
3) — Combined results from Kabath (2009) and this work (see Table 9.2 for details).

Notes. For each field, the table gives the total number of light curves $N_\star$, the number of light curves selected for variable star search (with $J \geq 0.1$, see also discussion in Section 7.5), the number of light curves that are finally analyzed visually (with quality parameter $q \equiv \delta\Theta(\omega^{(2)}_{\max}) \geq 10$, Equations (7.11) and (7.12)), and the number of known, new, and suspected variable stars. Numbers in brackets give the relative fraction compared to $N_\star$. For details on each data set and its observations, see Table 4.1.

In total, 329,660 light curves have been analyzed for stellar variability in this work. Table 9.1 gives an overview on how many variable stars could finally be identified in each target field. Details are discussed separately for LRa02 and F17–F19 in Section 9.1 and 9.2, respectively, while the overall detection yield is summarized and compared to other projects in Section 9.3.

The complete set of new variable star detections is listed for all four fields in Appendix E; for field LRa02, its content has already been published by Fruth et al. (2012) and is available at the Variable Star Index (VSX) database[1].

[1] http://www.aavso.org/vsx

Detrending

All variable star detections in this work are based on unfiltered data, i.e., without application of SysRem (Section 5.2.2). The algorithm provides significant advantages for transit search with BEST II (see Chapter 6), which aims at the detection of signals close to the photometric noise level. However, stellar variability spans much larger ranges of periods and amplitudes, and thus requires a different approach.

An initial variability analysis on detrended F17–F19 data sets revealed that SysRem had a negative effect on a number of light curves: A cross-check with unfiltered data showed that it over-corrected real variability in particular for variables with long periods and large amplitudes. It was thus decided not to use it prior to variability search. This minimizes the number of false negatives with large and long baseline variations. Despite this non-filtering, less than 1% of all new detections were missed, most of them having an SNR of ~ 1.

Classification of Variability

Detected variable stars are assigned variability types following Sterken and Jaschek (1996) and the classification scheme of the General Catalog of Variable Stars (GCVS; Samus et al. 2009). The identification is solely based on photometry, i.e., it depends on the shape, amplitude, and period of the brightness variation.

The following classes could be identified:

- **Eclipsing binary systems.** Light curves with clear eclipses and almost no variation in between are classified as Algol-type binaries (EA; prototype β Per). For systems with ellipsoidal components, phase variations are significant and hinder an exact determination of the beginning/end of eclipses (EB type; β Lyr). At orbital periods below one day, both objects are in contact, eclipses are of equal depth and are fully blended with the phase variation (EW type; W UMa).
- **Pulsating variable stars.** From photometry, the following pulsating types could be identified: δ Scuti variables (DSCT; periods $p \leq 0.2$ days), SX Phoenicis stars (SXPHE; similar to δ Scuti, but with several simultaneous periods), RR Lyrae (RR; $p = 0.2$–1 day, characteristic shape), Cepheids (CEP; $p > 1$ day, amplitudes 0.01–2 mag), Gamma Doradus stars (GDOR), and semi-regular variables (SR; $p \geq 20$ days with irregularities).
- **Rotating variable stars (ROT).** Stellar rotation can introduce flux variations due to stellar spots (SP), magnetic fields (ACV), or ellipsoidal components (ELL). (However, photometry alone often cannot distinguish these cases.)
- **Long periodic variables (LP).** Non-periodic variables or stars variable on timescales comparable to/larger than the observational coverage are named LP.
- **Inconclusive Cases (VAR).** Stars showing clear variability that cannot be assigned a type according to the classification scheme from photometry; further observations are needed to better constrain the physical origin of variability.

Known and Suspected Variability

Each variable star is searched by equatorial coordinates in the GCVS and the VSX. If it is found to match a previously *known* variable within 10″, it is marked in the catalog (Appendix E) with a "*k*" flag, and the corresponding catalog name is given for reference. Furthermore, classifications and periods from the catalog and BEST II, respectively, are compared in Sections 9.1 and 9.2.

Stars for which the variability, period, and/or classification cannot be determined without ambiguity are marked as *suspected* (indicated with an "*s*" flag). Predominantly, these show brightness variations close to the noise level of their light curve.

Ephemerides and Amplitudes

Ephemerides and amplitudes are given based on the results of the AoV algorithm (Chapter 7, Schwarzenberg-Czerny 1996). However, several periods were adjusted manually as a result of visual inspection (usually to multiples of the initial value). No ephemerides and amplitudes are given for long periodic (LP) classified variables.

Crowding

For some cases, the angular resolution of BEST II is not sufficient to fully separate the light of two adjacent stars, and the photometric apertures overlap. Thus, variability of the same shape and period can be detected in both light curves (with underestimated amplitudes, see Appendix C.1); such cases are marked as *contaminated* with a "*c*" flag. If the origin of variation can clearly be assigned to one of the overlapping stars due to a sufficient angular separation and/or brightness difference, only one object is presented in the catalog. Otherwise, both stars are presented as variables, and observations at higher angular resolution are needed to constrain the true origin of variability.

9.1 Field LRa02

The reanalysis of the LRa02 data set has already been described in detail in Sections 7.2 and 7.4 together with the optimization of the search method. This section focuses on new scientific results obtained with the improved method in field LRa02 and compares them to other projects; the results of this Section 9.1 have already been published by Fruth et al. (2012).

In addition to the 350 variables already published by Kabath et al. (2009a, Paper I in the following), 279 stars in LRa02 were identified with clear periodic variability (114 in LRa02*a* and 165 in LRa02*b*). Furthermore, 52 suspected periodic variable stars could be identified (17 in LRa02*a* and 35 in LRa02*b*). The total number of detections is given in Table 9.1, while Table 9.2 compares the corresponding quantities of this work with Paper I.

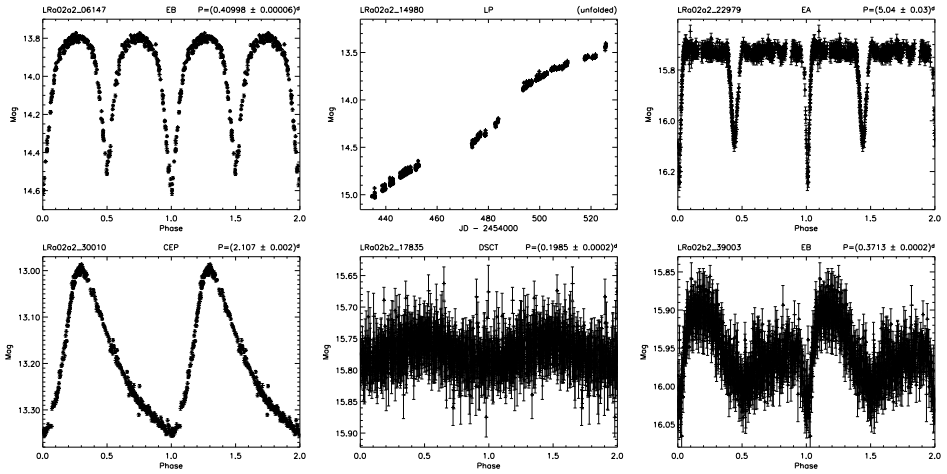

Figure 9.1: Phase-folded light curves of variable stars detected in field LRa02 after reanalysis of the data set. The complete figure set (331 images) is available in the electronic edition of the corresponding publication (Fruth et al. 2012).

Table 9.2: Variable star detections in BEST II data set LRa02 – summarized counts for Paper I (Kabath et al. 2009a) and this work.

	LRa02*a*	LRa02*b*	Total
Paper I	173 (4)	177 (1)	350 (5)
This work	114 (2)	165 (5)	279 (7)
This work (suspected)	17 (0)	35 (0)	52 (0)
Total	304 (6)	377 (6)	681 (12)

Note. The number of previously known variables in the field confirmed by BEST II is given in brackets (included in first number).

The newly identified variable stars of the BEST II data set LRa02 are listed in Table E.1 (Appendix E). Due to the reanalysis, the internal numbering is not consistent with Paper I, which is why IDs were given different prefixes (i.e., LRa02*a2* and LRa02*b2*, respectively). Furthermore, an improved data quality and search method allowed to refine the ephemerides and/or classification for 17 variables from Paper I in this work; they are presented in Table E.2.

Examples for phase-folded light curves of new detections and known variables with revised ephemerides can be found in Figure 9.1 and 9.2, respectively; the full set has been presented in an electronic format by Fruth et al. (2012).

9.1.1 Comparison with Known Variables

In addition to Paper I, seven known variables could be identified in field LRa02.

The three stars CoRoT 110742676, NSVS 12579155, and NSVS 12585233 have periods longer than 50 days. BEST II confirms their long-time periodicity, but the phase coverage of their cycles is insufficient to confirm the periods quantitatively. For the four eclipsing binaries ASAS J064835-0534.3, DY Mon, [KEE2007] 1318, and [KEE2007] 1334, both the classifications and periods have been confirmed.

The latter two have first been detected by Kabath et al. (2007) in the CoRoT IR01

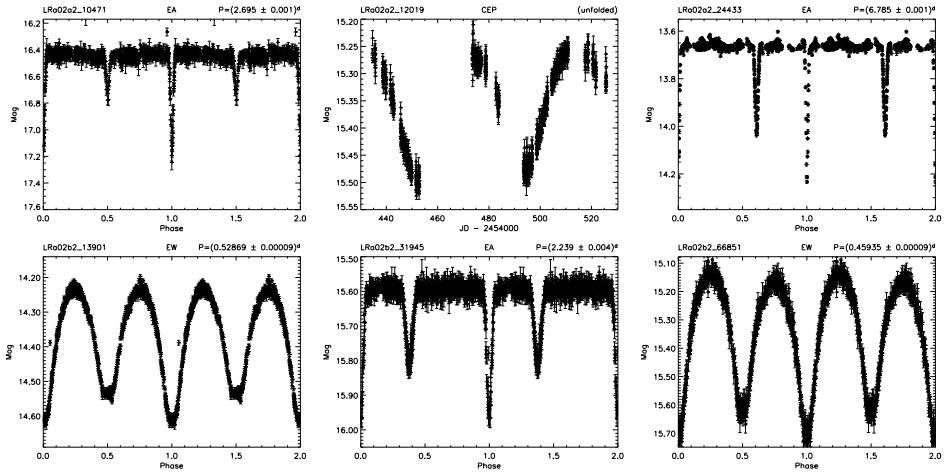

Figure 9.2: Phase-folded light curves of known variable stars in field LRa02 with revised parameters (examples). The complete set of 17 figures is shown in Fruth et al. (2012), Figure 11.

field with BEST, for which the chosen FOV shows a small overlap with the BEST II field LRa02*a*. However, the precision in the periods of these two binaries could be significantly improved because the LRa02 data set covers a much larger time period (41 compared to 12 nights) and the photometric quality of BEST II is better.

9.1.2 Comparison with CoRoT

The LRa02 data sets of BEST II and CoRoT are, except for the fact that they point to the same field, otherwise completely independent of each other and thus provide a valuable opportunity to compare the scientific results of the two surveys.

One step in the scientific analysis of CoRoT data consists of an automatic stellar variability classification (Debosscher et al. 2007, 2009). This method was also applied to the CoRoT observations of field LRa02, and the results are meanwhile – together with the full light curves – publicly available through the CoRoT archive.[2]

The CoRoT LRa02 data set contains 11,448 targets, from which 10,392 (91%) match a BEST II target within a maximum angular distance of 1″. Since LRa02 was not covered completely by BEST II (see Figure 7.1), 454 CoRoT targets are located outside of the BEST II FOV. Furthermore, the magnitude ranges do not overlap completely, so that 425 bright CoRoT stars are saturated on the BEST II CCD. The remaining 177 CoRoT targets are within the FOV and right magnitude range, but have no BEST II counterpart due to technical issues such as blooming. In the same way, BEST II observed a total of 93,943 stars in both pointings that have not been given a CoRoT mask or are located outside the CoRoT FOV.

From the 681 variable stars presented together in Paper I and this work, 262 variables (190 from Paper I, 72 from this work) match a CoRoT target. The corresponding CoRoT IDs are shown for the new detections in Tables E.1 and E.2.

CoRoT observed the LRa02 field about one year after BEST II, and the observing

[2]CoRoT data are available to the community from the CoRoT archive:
http://idoc-corot.ias.u-psud.fr/.

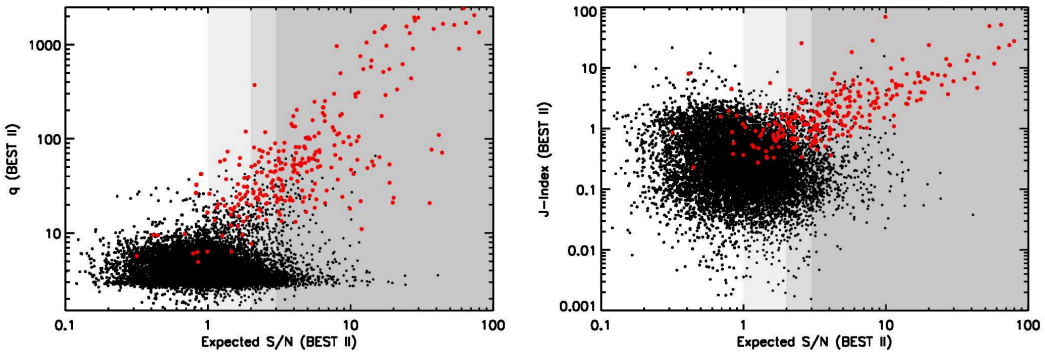

Figure 9.3: Detection efficiency of BEST II for the field LRa02. Shown are 10,392 stars that are measured by both BEST II and CoRoT. The expected BEST II S/N of CoRoT amplitudes is plotted on the x-axis (Equation (9.1)). On the y-axis, the left plot shows the suggested new quantity for variability ranking $q = \delta\Theta(\omega^{(2)}_{\max})$ (Equation (7.14)) and the right plot the Stetson J index for comparison. Variable stars detected in Paper I or this work are marked red. The area of possible BEST II detections is indicated in gray. *(Published as Figure 12 by Fruth et al. 2012.)*

times do not overlap. Because this work focuses on the improvement of variable star detection for ground-based telescopes, CoRoT and BEST II light curves have not been combined. However, it is noted that such a combination might yield improved ephemerides.

Detection Efficiency of BEST II and the New Search Algorithm

For stars both observed with CoRoT and BEST II, it is possible to investigate the performance of BEST II more in detail. The automatic classification (Debosscher et al. 2007) provides information about the amplitude of variation for CoRoT targets. Since the satellite has a much higher photometric precision, most of these amplitudes are well below the detection limit of BEST II. However, the knowledge of stellar variability with higher precision can be used to evaluate the detection efficiency of BEST II. Of particular interest are two questions: First, how many stars with sufficiently high variation in the CoRoT data set have been detected as variables from BEST II data? Second, are these clearly distinguished by the new detection algorithm from stars having variabilities below the threshold of BEST II?

The full amplitude A_C of variation was derived from the fit coefficients given in the CoRoT classification. As this contains each a low- and high-frequency entry for every CoRoT target, the amplitude was calculated as the maximum of both. The value A_C itself contains no information on whether the signal can be detected by BEST II or not, which strongly depends on the magnitude of a given star. Therefore, the quantity

$$\mathrm{S/N} = A_C/\sigma_B^{\min}(R_B) \tag{9.1}$$

is used to estimate the variability signal to noise (S/N). The noise $\sigma_B^{\min}(R_B)$ gives the photometric precision achievable with BEST II in the given data set for a star of magnitude R_B. It was determined by a fit to the σ-magnitude plot of the field (see Section 4.3; Equation (4.1) with parameters from Table 4.1).

Figure 9.3 shows the expected S/N for all stars that are contained in both data

sets. From 680 stars with CoRoT amplitudes that should be visible in the BEST II data (S/N > 3), 162 were detected as variable stars in Paper I and this work. 448 stars are expected to have a large S/N > 3, but show no significant variability in the BEST II data set ($q < 9$). 70 stars with both expected and measured variability (S/N > 3, $q > 9$) were not detected by BEST II.

Additionally, CoRoT light curves with significant variability in the CoRoT classification, but which were not variable in the BEST II data, were examined. Many of them show strong instrumental effects (hot pixels; Auvergne et al. 2009) which obviously mislead the automatic classification algorithm. However, from the 448 stars in this region, only 88 show a probability larger than 95% that they belong to any class, so most can be considered false alarms.

Stars that are expected to be variable (S/N > 3) and show variation in the BEST II light curve ($q > 9$), but were not detected as variable stars after visual inspection have been re-inspected. Such targets have been missed due to the smaller phase coverage of BEST II, or because the real noise of individual light curves is underestimated using $\sigma_B^{\min}$ (e.g., due to higher order extinction effects for very red stars).

Distinguishing between variable and non-variable stars works very well using the new ranking $q = \delta\Theta(\omega_{\max}^{(2)})$ (see Section 7.3). If the limit $q = 9$ is chosen to separate variables from the bulk of non-variable stars, 92% of all matched stars are found below the limit. Only seven variables have $q < 9$, but their light curves and low S/N indicate rather false detections than too low variability values. From all 780 stars with $q > 9$, one third belongs to the set of variable star detections. For comparison, Figure 9.3 also shows the J index vs. the expected S/N. The plot shows clearly that the separation between real and artifical variability is much weaker. The strength of the new ranking is particularly clear in the regime of $1 < \mathrm{S/N} < 3$, i.e., close to the detection limit of BEST II.

Comparison of Classifications

The variable star detections of BEST II were compared in detail with the automatic CoRoT classification for the 262 matched variables. The overall agreement between both methods is very good; details regarding the period and magnitude determination as well as the classifications obtained by BEST II and CoRoT are given in the remainder of this section. Figure 9.4 shows some instructive examples of variable stars in agreement (a) and with differences in the determined periods and/or classifications (b–f).

The mean magnitudes of matched stars are in reasonably good agreement (Figure 9.5). Only a few very long-term variables – like the example in Figure 9.4d – show differences in the order of 1 mag and above because BEST II and CoRoT observed during different phases; the remaining majority differs by only (0.059 ± 0.158) mag.

Periods determined by BEST II have been compared with the main frequency from the automatic CoRoT characterization. For 72.5% of the matched stars, the periods are equal or integral ($n = 1, \ldots, 5$) multiples of each other to a precision of at least 1%. The histogram of period ratios in Figure 9.6 shows that most detections have been identified in the CoRoT data with half the period compared to BEST II.

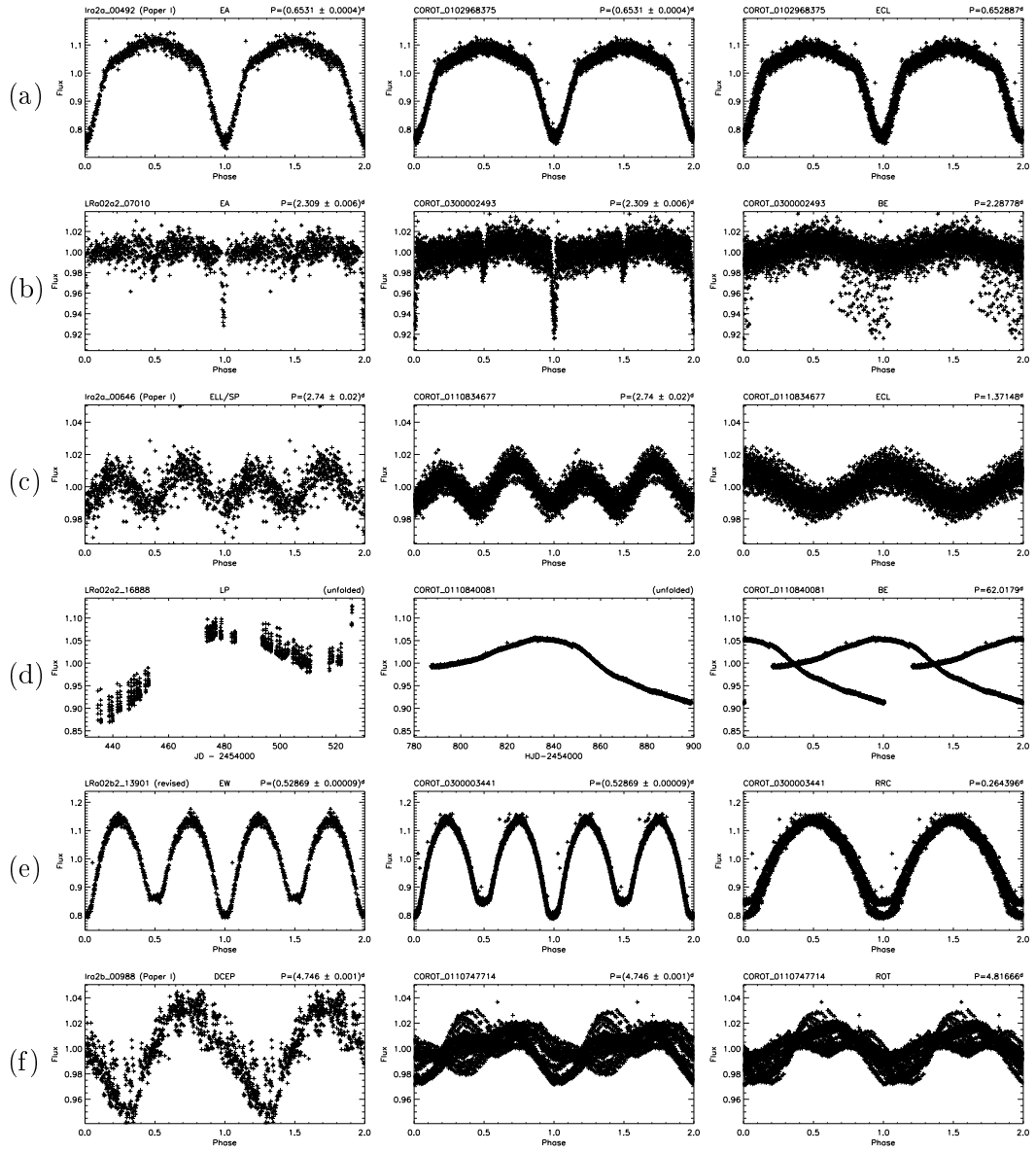

Figure 9.4: Examples of variable stars identified both by BEST II and CoRoT. Each row shows light curves of the same star: in the first column, the BEST II light curve is folded with the period from BEST II; in the second column, the CoRoT light curve folded with the BEST II period; and in the third column, the CoRoT light curve folded with the CoRoT period. Unfolded light curves are shown for long periodic variables. *(Published as Figure 13 by Fruth et al. 2012.)*

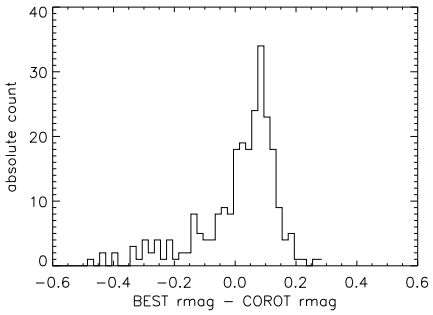

Figure 9.5: Histogram of differences between CoRoT and BEST II magnitudes (for matched detections, without very long periodic variables).
(Published as Figure 14 by Fruth et al. 2012.)

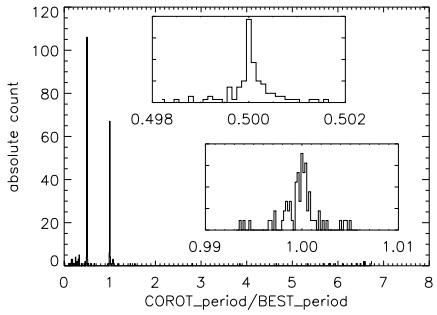

Figure 9.6: Histogram of CoRoT and BEST II period ratio for matched variable star detections. The insets show the two main peaks enlarged (normalized).
(Published as Figure 15 by Fruth et al. 2012.)

This is because many periods are doubled during the visual inspection of BEST II light curves in order to show full cycles (e.g., Figures 9.4c and 9.4e), in particular for W Ursae Majoris eclipsing binaries (EW).

The classes from visual inspection of BEST II light curves match the automatic classification of the CoRoT data set well. From the 262 variables present in both data sets, 196 stars have BEST II variability classes that are consistent with either the short- or long-periodic classification in the CoRoT data set. Note that the variability classes used by BEST II and CoRoT are slightly different: for example, BEST II distinguishes within the CoRoT class ECL between the eclipsing binary types EA, EB, and EW, while the CoRoT scheme includes, e.g., slowly pulsating B-stars, which are simply identified as VAR within the BEST II study. All such refinements are considered to represent a classification match.

The 64 stars with a clear disagreement in the variability classifications were checked carefully by reviewing the light curves from both BEST II and CoRoT. For 26 stars, the variability classes obtained by BEST II appear more realistic. Most of such cases are LP variable stars (e.g., Figure 9.4d) that have been identified as such in the BEST II data set by visual inspection. For these cases, even the longer CoRoT baseline does not cover a full cycle, so that the period and classification obtained from the CoRoT pipeline are not conclusive. Furthermore, some eclipsing binaries are clearly misclassified by the automatic CoRoT procedure. Figure 9.4e shows an example of a W Ursae Majoris type eclipsing binary that was identified as an RR Lyrae pulsator – most likely because it was detected with half of its physical period from the CoRoT data set. For three stars similar to the example in Figure 9.4b, narrow eclipse events were not detected by the CoRoT analysis. Most of the stars with implausible variability types were classified as BE by the automatic classification, which was described by Debosscher et al. (2009) as a "trash" class regarding its wide parameter spread. For 16 stars like the example in Figure 9.4f, the CoRoT classifications are in better agreement with the measurements. For most of these cases, this clearly results from the better photometric quality of the satellite data. For 22 cases, the photometric data itself are insufficient to choose between the CoRoT and BEST II classifications (e.g., EW/ELL). (Note that no automatic classification data were available for the two CoRoT targets 110833621 and 300001413.)

9.2 Fields F17–F19

The BEST II target fields F17–F19 were analyzed for stellar variability as described in Section 7.3.6: Out of all 209,070 light curves, 115,487 were analyzed with AoV, and 5,480 light curves with $q \equiv \delta\Theta(\omega^{(2)}_{\max}) \geq 10$ (Equations (7.11) and (7.12)) were finally inspected visually. The limit of $q = 10$ was selected following the comparison with CoRoT data in LRa02 (see Section 9.1.2) and the All Sky Automated Survey (ASAS, Pojmanski 2002), which also uses AoV statistics and $\Theta \geq 10$ as a criterion for visual inspection. This analysis yielded a total of 2,519 previously unknown variable stars, and 754 stars with suspected variability. Details on the numbers in each field are given in Table 9.1.

Table 9.3: Variable star detections in BEST II fields F17–F19, summarized per variability class.

	EA	EB	EW	EW/ DSCT	DSCT	RR	CEP	SX-PHE	GDOR	ROT	SR	LP	VAR
F17	92 (9)	28 (10)	133 (20)	33 (13)	45 (35)	38 (15)	30 (10)	2 (1)	1 (0)	67 (49)	14 (3)	154 (58)	11 (4)
F18	0 (3)	0 (1)	3 (0)	0 (0)	0 (0)	6 (0)	0 (0)	0 (0)	0 (0)	4 (4)	0 (0)	1 (0)	2 (1)
F19	287 (31)	139 (39)	374 (30)	83 (37)	126 (44)	57 (10)	56 (8)	0 (0)	0 (0)	114 (48)	144 (47)	199 (22)	293 (202)
Total	379 (43)	167 (50)	510 (50)	116 (50)	171 (79)	101 (25)	86 (18)	2 (1)	1 (0)	185 (101)	158 (50)	354 (80)	306 (207)

Notes. Given are the numbers of known and newly detected variable stars for each field and variability class (suspected variables in brackets).

Variability Characterization

The characterization of variability in fields F17–F19 is presented in large catalogs in Appendix E (Tables E.3–E.5). Details on how many stars have been found in each target field and variability class are given in Table 9.3. In total, 1,056 (plus 143 suspected) eclipsing binaries could be identified, 519 (173) pulsators, 185 (101) stars with rotational modulation, 354 (80) long periodic variables, and 422 (257) with other types of variability.

Figure 9.7 displays the period and amplitude of new detections for the most common variability classes (separated into binaries and others). It shows that BEST II is capable to characterize periodic stellar variability on timescales of less than an hour up to ~ 100 days (i.e., the length of a single observing season), and with amplitudes of a few mmag up to several magnitudes. Naturally, the sensitivity decreases with increasing periods of variation.

The large catalog of new BEST II variables includes a number of objects that are very interesting for astrophysical studies; Figure 9.8 shows some example light curves. Interesting cases include in particular:

- Eclipsing binaries with high SNR (e.g., F17_10421, F19_009645, F19_019884, F19_030794, F19_033571, F19_100160); if modeled, these light curves allow the determination of **stellar parameters** precisely. Such results improve the statistical basis and can help to solve open astrophysical questions, e.g., to decide between different proposed formation processes for W Ursae Majoris type binaries (Li et al. 2008).

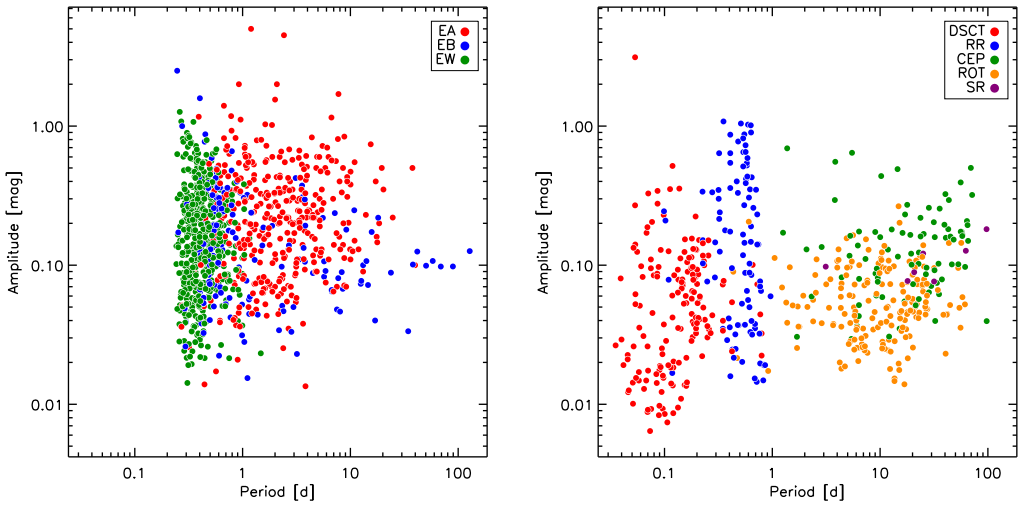

(a) Eclipsing binaries (b) Other variables

Figure 9.7: Variable stars in fields F17–F19. Shown are only new detections (i.e., without suspected and known variables) of the most common types, and only variables for which a period could be determined. (a) shows the eclipsing binary classes EA, EB, and EW, while (b) presents pulsators of types DSCT, RR, and CEP, as well as rotating (ROT) and semi-regular (SR) variables.

- For many eclipsing binaries presented here (e.g., F19_055270, F19_059739, F19_066533, F19_100160), their photometric time series enable very accurate eclipse timings. Future studies could, by studying timing *variations*, detect **additional bodies** in some of these systems (see, e.g., Borkovits and Hegedüs 1996).
- Likewise, an accurate timing of *eccentric* eclipsing binaries enables to measure their apsidal motion, which in turn enables to both test **stellar interior models** and the theory of **general relativity** (Giménez 2007). Several new detections of this work (e.g., F19_055270, F19_100956) are interesting for such investigations (cf. the criteria for selecting targets for apsidal motion studies as given in the catalog by Hegedüs et al. 2005).
- The detection of **cataclysmic binaries** like F19_022713 enables the improvement of knowledge about such objects and their accretion disks (for a recent review, see Giovannelli 2008).
- Amplitude modulation known as the **Blazhko-effect** (Blažko 1907) is found in the light curves of several RR Lyrae pulsators (e.g., F19_086712, F19_124221). Improved statistics through more detections can help to understand the physical nature of the effect, e.g., through correlations between its occurrence rate and the period and/or metallicity (Jurcsik et al. 2009).

Since the modeling of variable stars is not within the scope of this thesis, new detections are presented to the interested scientific community for further studies. In addition to the presentation within this work, the variables and their light curves will be published elsewhere.

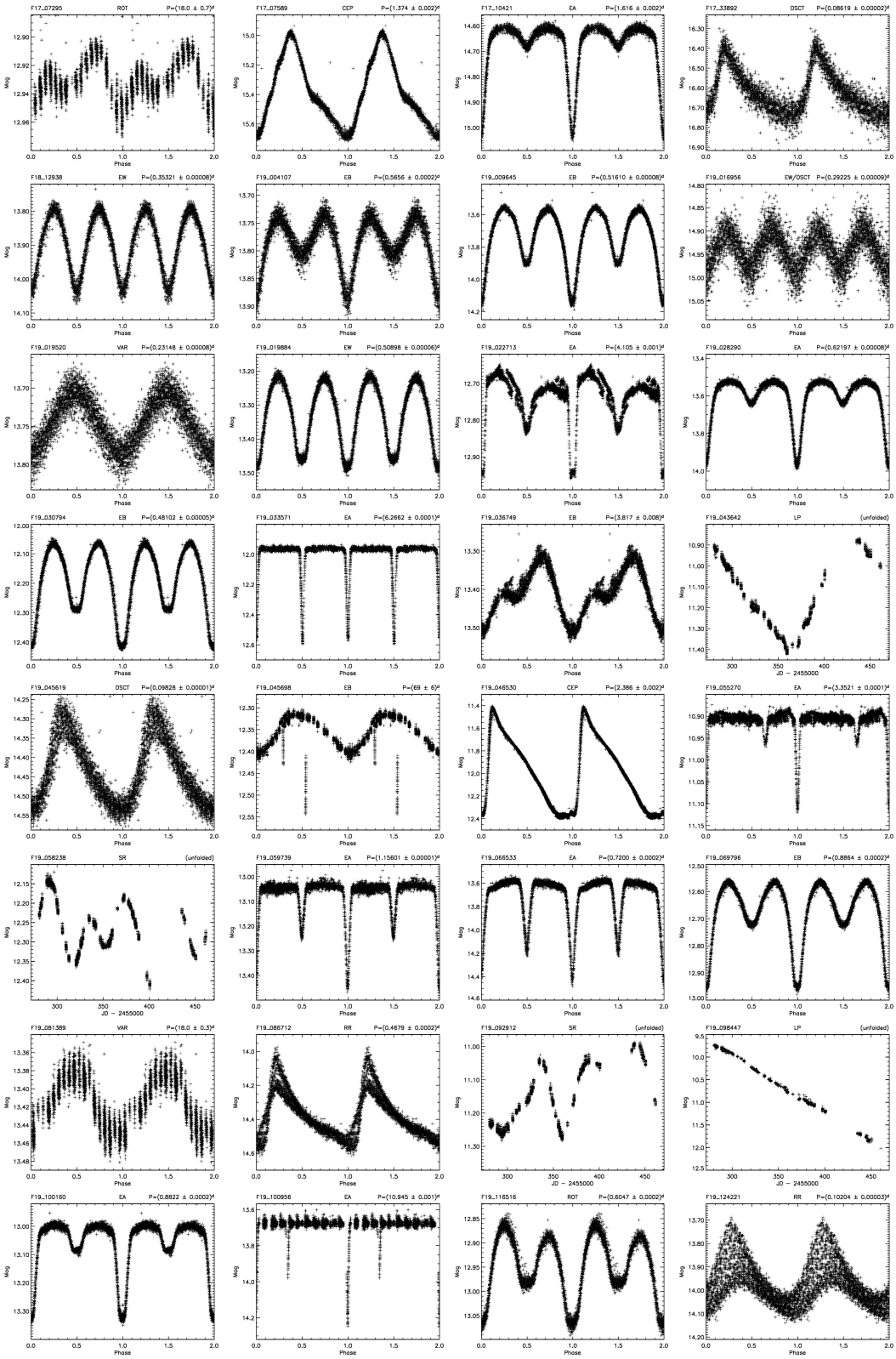

Figure 9.8: Light curves of variable stars detected in fields F17–F19 (examples). The light curves of all 3,273 variable and suspected variable stars within these fields will be published elsewhere in a machine-readable format.

Spectroscopic Characterization

For 318 interesting variable stars in target field F19, spectroscopic observations were obtained as part of the follow-up process of planetary candidates with the AAOmega instrument (see Section 8.4.2); these are marked with a "⋆" flag in Table E.5. Note, however, that the spectral classification of variable stars in the field has not been completed yet.

Comparison with Known Variables

A total number of 17 variable stars contained in the BEST II data sets F17–F19 were previously known. Table 9.4 gives their identifiers and compares periods and classifications with the corresponding reference values.

Table 9.4: Known variable stars in data sets F17–F19.

Identifier		R_B	Period p [d]		Classification		Reference
BEST II	Ref.	[mag]	BEST II	Ref.	BEST II	Ref.	
F17_03458	ASAS J142013-5339.9	11.6	3.329(4)	3.31	ROT	ROT	Kiraga (2012)
F17_32682	ASAS J142428-5416.0	12.5	–	323.7	LP	MISC	Pojmanski (2002)
F18_03793	YZ Gru	16.5	0.6976(7)	0.6974	RR	RRAB	Meinunger (1979)
F18_02074	ASAS J224935-4341.2	11.9	–	68.25	LP	MISC	Pojmanski (2002)
F18_05548	BE Gru	14.1	0.6055(2)	0.6054	RR	RRAB	Meinunger (1979)
F18_08895	AD Gru	15.5	0.7592(5)	0.7592	RR	RRAB	Meinunger (1979)
F19_000499	FV Nor	12.6	–	–	LP	LP?	Hoffleit (1931)
F19_045321	NU Nor†	11.7	–	–	LP	L	Meinunger (1970)
F19_046530	UX Nor	12.1	2.386(2)	2.38602	CEP	CWB	Petersen and Andreasen (1987)
F19_088903	KK Nor	14.0	0.45493(6)	–	RR	RR	Meinunger (1970)
F19_089192	EO Nor	11.3	0.8523(3)	0.8523(2)	EA	EA/SD:	Kruytbosch (1935)
F19_093711	IZ Nor	11.0	–	–	LP	L	Meinunger (1970)
F19_098447	NSV 7658	10.6	–	–	LP	–	Luyten (1936)
F19_104459	EM Nor	11.2	0.7383(2)	0.7384	EW	EW	Malkov et al. (2006)
F19_107786	IX Nor	10.6	–	–	LP	M	Meinunger (1970)
F19_111712	UV Nor	12.8	0.8742(2)	0.8741	EA	EA	Malkov et al. (2006)
F19_116322	PW Nor	12.1	–	–	LP	M:	Luyten (1936)

† Meinunger (1970) assigns the variability of NU Nor to the star 2MASS 16274939-5533450 (BEST II F19_045485). However, in BEST II data, the variability can clearly be assigned to the object 2MASS 16275033-5533400 (BEST II F19_045321), which is located at an angular distance of 9″ to the former.

Notes. Given are identifiers of this work and the GCVS and/or VSX, BEST II instrumental magnitudes R_B (cf. Section 5.2), and periods and classifications (if available) as obtained within this work and by previous surveys as referenced, respectively. The light curves of UX Nor (F19_046530) and NSV 7658 (F19_098447) are shown as examples in Figure 9.8.

For *all* stars that were classified and/or have periods determined by previous studies and this work, the results are in excellent agreement. For the RR Lyrae-type pulsator KK Nor, the period was first determined within this work.

9.3 Summary and Discussion

Within this work, five photometric data sets with 329,660 light curves have been analyzed for stellar variability. Using an improved detection method (see Chapter 7), a total of 2,791 previously unknown variable stars were found in the target fields LRa02, F17, F18, and F19. In addition to that, 806 stars are suspected to be variable, i.e., more and/or more precise measurements would be needed to better constrain their variability.

Kabath et al. (2009a) first analyzed BEST II observations on the CoRoT target field LRa02 for stellar variability and presented a catalog of 350 variable stars (of

which five were known previously). Now, using the same observational data, the improved data quality and methodology of this work yielded 279 *additional* (including seven known) and 52 suspected variables. A comparison of BEST II detections with CoRoT findings underlines the good performance of the new algorithm: The large majority of stars with CoRoT amplitudes that should be significant in the less precise time series of BEST II are given high rankings, and the number of false positives is remarkably low. Furthermore, the comparison shows again that the distinction between variable and non-variable stars is much more efficient than the previously used J index alone.

In addition to the previously known variable stars already confirmed by Kabath et al. (2009a), 24 known variables in the fields LRa02 and F17–F19 could be compared with BEST II time series as part of this thesis. For all of them, the ephemerides and classifications agree with the literature references. For 19 variables detected by Kabath et al. (2007, 2009a), the ephemerides and/or classification could be refined using the improved data set and analysis.

Furthermore, the BEST II search for stellar variability was validated by comparing the results with CoRoT. In the field LRa02, 262 variables have both been observed by BEST II and CoRoT (190 presented by Kabath et al. 2009a, and 72 from this work). Their classifications, periods, and magnitudes were compared on an individual basis and found to be overall in very good agreement. For 75% of all matched variables, the classifications are consistent, and for 73%, the derived periods agree within 1% tolerance. For the rest, divergences could be related to the different instrumental precision, observational time coverage, and degree of manual inspection.

Discussion

Table 9.5 summarizes the number of detections obtained within this work and compares them with previous BEST/BEST II findings and the results of other surveys. Although the results obtained by these projects are subject to various systematic differences (most importantly, concerning the photometric precision, monitored magnitude range and FOV, the time span and duty cycle of observations, and the applied analysis techniques and selection criteria; for a discussion, see also Tonry et al. 2005), the overall detection rate can be used to put the results of this work in context.

The following characteristics are noteworthy from Table 9.5:

- The detection yield of **BEST II** is significantly **larger than BEST** (0.28% for BEST, compared with 0.38%/0.98% for BEST II without/with this work). As already discussed by Kabath (2009), this is due to the increased duty cycle and better photometric quality of BEST II.
- The detection yield for the fields observed within **this work** varies from 0.1% to 1.5% for different reasons. F18 is the only BEST/BEST II field observed away from the galactic plane (latitude $b = -61°$); as such, it probes a different stellar population, which is generally expected to be less active (see, e.g., Huber et al. 2006; West et al. 2008; Ciardi et al. 2011). The large fraction for F19, however, can well be explained with the increased flux threshold (see Section 4.2.3 and Table D.1); if this threshold were to be chosen similar to

Table 9.5: Variable star detection yield with BEST and BEST II in comparison to other surveys.

Project	Field(s)	$N_\star$	$N_{\rm var}$	$N_{\rm var}/N_\star$	Reference
BEST	LRc01	29,426	92	0.31%	Karoff et al. (2007)
BEST	IRa01	30,426	54	0.18%	Kabath et al. (2007)
BEST	LRa01	29,830	44	0.15%	Kabath et al. (2008)
BEST	F2	32,129	145	0.45%	Pasternacki et al. (2011)
		121,811	**335**	**0.28%**	**Total for BEST**
BEST II	LRc02	98,219	426	0.43%	Kabath et al. (2009b)
BEST II	LRa02	104,335	350	0.34%	Kabath et al. (2009a)
		202,554	**776**	**0.38%**	**Total for BEST II (before this work)**
BEST II	LRa02	120,590	681	0.56%	Kabath et al. (2009a) and this work
BEST II	F17	68,317	648	0.97%	This work
BEST II	F18	13,551	16	0.12%	This work
BEST II	F19	127,202	1,872	1.47%	This work
		329,660	**3,217**	**0.98%**	**Total for BEST II (this work)**
ASAS	ASAS-1,2	140,000	3,800	2.71%	Pojmanski (2000)
ASAS	ASAS-3	17,000,000	50,099	0.29%	Pojmanski (2002)
OGLE	OGLE-II	16,502,826	68,194	0.41%	Zebrun et al. (2001)
OGLE	OGLE-III	200,000,000	193,000	0.10%	Soszyński et al. (2008, 2011)
EROS II		1,913,576	1,362	0.07%	Derue et al. (2002)
HATnet	HAT 199	98,000	1,617	1.65%	Hartman et al. (2004)
UNSW		87,000	850	0.98%	Christiansen et al. (2008)

Notes. The table gives the number of surveyed stars $N_\star$, the number of found variables $N_{\rm var}$, and the corresponding ratio $N_{\rm var}/N_\star$ for BEST/BEST II publications, this work, and selected references of important variable star surveys. If noted in the publication, $N_{\rm var}$ here includes known and new detections, i.e., the whole detection yield of a given survey. For comparison, the values for BEST and BEST II (before and within this work, respectively) are each summarized.

F17 and F18, the reduction would yield $\sim$200,000 stars and a corresponding detection ratio of $\sim$1% (assuming that the number of variables in the added high-noise light curves is negligible), i.e., a yield well comparable to F17.

- The detection yield of BEST II increases significantly for data analyzed within this work **compared to previous studies**. While Kabath et al. (2009a, b) found 0.4% of all surveyed stars to be variable, this work obtaines a mean fraction of 1.0%. For the reanalyzed data set LRa02, the yield can be compared directly: The number of detections increases by 95% (from 350 to 681).
- The **number of light curves** analyzed for stellar variability within this work (329,660 including the reanalyzed data set LRa02) exceeds the *total* number analyzed within the whole BEST/BEST II project so far (324,365). The **number of variable stars** identified with BEST/BEST II increases through this work from 1,111 to 3,978, i.e., by 258%.
- **Other surveys** that have analyzed large photometric data sets for stellar variability typically obtain detection yields in the range of 0.1–2.7%. Thus, BEST II yield results of 0.4–1.0% are comparable to the findings of other projects.

Conclusions

The results presented in this chapter show that BEST II can successfully detect and classify stellar variability. Its findings have been compared with results from CoRoT and previously known variables – they were found to be in very good agreement, thus validating the BEST II results. Furthermore, the overall detection is as efficient as large and successful photometric projects such as the *All Sky Automated Survey* (ASAS; Pojmanski 2002) or the *Optical Gravitational Lensing Experiment* (OGLE; Soszyński et al. 2008).

Previous studies (Kabath 2009; Kabath et al. 2009a, b) have already proven the capability of BEST II to search for stellar variability, which largely benefits from the excellent photometric quality and observational duty cycle encountered at its prime astronomical site in Chile. Within this work, it was possible to improve the observations and methodology further, so that the number of surveyed stars and the detection efficiency could both be increased significantly. In addition to the search for stellar variability itself (described in Chapter 7 and by Fruth et al. 2012), several other improvements that could be achieved within this thesis contribute to the results. Most importantly, they include an improved photometric data quality (See Section 4.3 and the discussion in Section 4.4), a target field selection optimized for BEST II (Section 4.2), and an improved pointing stability (Appendix A.2).

10 Transit Search from Antarctica

Antarctica is expected to provide a number of advantages for astronomy and therefore, Dome C is currently being considered as a site for future large-scale observatories (see Section 1.3). For transit search, the long polar night and low systematic noise are expected to be particularly advantageous.

First, the Antarctic winter allows an almost continuous time series to be obtained (Caldwell et al. 2004; Pont and Bouchy 2005), although the total amount of usable dark time is not increased compared to mid-latitude sites (Kenyon and Storey 2006). However, observations can cover large planetary orbits better than temperate sites with diurnal interruptions. Rauer et al. (2008b) showed that planets with periods of up to two weeks are covered well within one observing season at Dome C; in contrast, a similar performance with mid-latitude sites could only be achieved if three stations were combined into a network. While that study relied on observing times modeled from weather data and astronomical dark time, Crouzet et al. (2010) obtained statistics directly from the ASTEP-South telescope. They estimated the transit yield and compared it to an analogous instrumental setup at La Silla: The ASTEP-South 2008 campaign is expected to yield detections comparable to a modeled observing season at La Silla (1.08 and 1.04 planets, respectively). However, if the ASTEP-South observations were extended over the whole winter season, the expected yield would be larger at Dome C (1.62 planets).

Second, more and/or smaller planets are expected to be found at Dome C due to an increased photometric precision (Rauer and Deeg 2010). Two conditions are considered important in this respect: Less systematic noise due to stable environmental conditions (in particular, the lack of day/night temperature variations; Pont and Bouchy 2005), and less scintillation noise due to a low level of atmospheric turbulence. The latter is expected to be 2–4 times smaller at Dome C compared to temperate sites (Kenyon et al. 2006).

While these previous studies indicate an advantage for transit search at Dome C, they still need to be confirmed on the basis of photometric data. For example, the study of Kenyon et al. (2006) derived the scintillation noise from measurements of atmospheric turbulence profiles above Dome C; however, this will only yield an advantage if it forms the dominant component in the noise budget for bright stars, which yet remains to be investigated with real photometric time series. Crouzet et al. (2010) used observing statistics from Dome C, but modeled the photometric quality in Antarctica and Chile from instrument characteristics.

This study aims to address the open question – which transits can be detected with a real photometric survey at Antarctica? It uses first data from the ASTEP 400 telescope (Section 3.3), which performs a dedicated transit search at Dome C. In order to compare the performance of ASTEP 400 with real data from a mid-latitude site, parallel observations have been obtained with BEST II (Section 3.2) in Chile during a joint campaign in 2010. As Rauer et al. (2008b) showed, the combination

of these two sites can potentially extend the observational coverage significantly; in addition to the direct comparison of the photometric quality and expected detection yield, the data is thus combined and searched for transiting planets.

This chapter presents the results of observations obtained together with ASTEP and BEST II. The first Section 10.1 briefly compares photometric measurements of the known transiting planet WASP-18b, which are covered here as a test case for joint observations and their data reduction. Section 10.2 describes the search for transiting exoplanets in two target fields with both telescopes, which forms the basis for a comprehensive comparison of the detection yield between the two systems and observing sites in Sections 10.3 and 10.4. Finally, Section 10.5 discusses the results and summarizes this chapter.

10.1 Test Case WASP-18b

The two transiting hot Jupiters WASP-18b (Hellier et al. 2009) and WASP-19b (Hebb et al. 2010) were monitored intensively with ASTEP 400 during its first observing season to test the quality of the instrument. With depths $\delta F = 0.94\%$ (Southworth et al. 2009) and 2.1% (Hellier et al. 2011), and magnitudes of $V = 9.3$ and 12.6, respectively, the primary transits of both targets should be well visible. In addition, the targets were selected to test whether ASTEP can measure phase variations and secondary eclipses: With periods of 0.94 days (WASP-18b, Southworth et al. 2009) and 0.79 days (WASP-19b, Hellier et al. 2011), both are placed among the fastest orbiting exoplanets known, and thus are highly irradiated. In the optical, phase variations due to reflection are expected in the order of a few 100 ppm.[1]

Observations and Reduction

During the southern winter 2010, ASTEP 400 observed WASP-18b for 66 nights (including 34 contiguous nights from 8th June to 11th July), and WASP-19b for 30 nights (including 26 contiguous nights from 30th April to 25th May). In order to compare with measurements from a mid-latitude site, BEST II also monitored WASP-18b for 19 nights between 12th August and 7th December 2010.

The complete ASTEP 400 data sets have been reduced by the ASTEP team and are currently being analyzed scientifically. As part of this thesis, one night of ASTEP 400 data covering a WASP-18b transit was reduced to test the DLR photometric pipeline (Chapter 5) on time series from a project other than BEST/BEST II. In addition, all nights of BEST II observations on WASP-18b were reduced using the same routines. Pipeline parameters for each reduction are listed in Appendix D.

[1] Using the flux ratio $f_p/f_\star \propto A_g(r_p/a)^2$ (see, e.g., Kane and Gelino 2011), the planetary radius r_p and semi-major axis a for each planet, and a geometric albedo of $A_g \approx 0.3$.

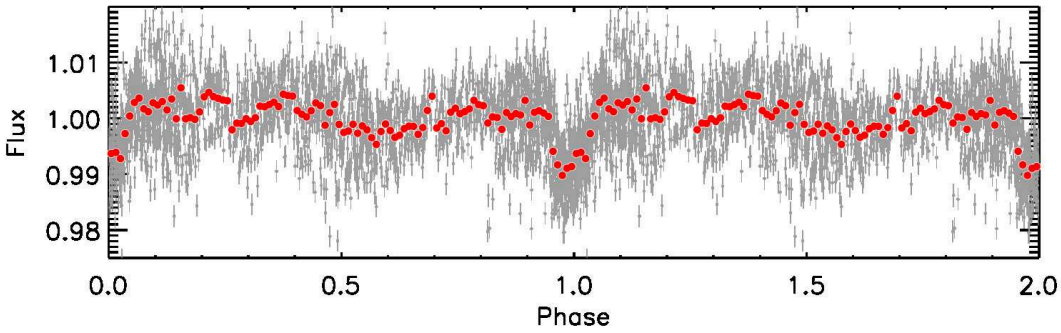

Figure 10.1: Phase-folded light curve of BEST II observations on WASP-18b in 2010 (ephemerides from Southworth et al. 2009). In addition to 2,011 individual measurements *(gray)*, the figure shows data binned within phase intervals of 0.01 *(red)*.

Table 10.1: Comparison of WASP-18b transits observed with ASTEP 400 and BEST II.

	Night	σ	σ_{bin}	$\langle \delta t \rangle$
ASTEP 400	4th July 2010	2.3 mmag	0.44 mmag	36 s
BEST II	28th August 2010	4.9 mmag	1.9 mmag	152 s

Notes. Standard deviations are calculated for each night and telescope from measurements *out of transit*; σ refers to original data (*gray* in Figure 10.2), and σ_{bin} to data binned within phase intervals of 0.01 (*red/blue* in Figure 10.2). The time sampling $\langle \delta t \rangle$ gives the typical span between two adjacent measurements.

Results

The BEST II observations contain 2,143 measurements, from which 2,011 form the final data set after all reduction steps. They cover six full and three partial transits of WASP-18b. The full phase-folded light curve is shown in Figure 10.1: For binned data, the transit is observed at a signal-to-noise ratio of 2.3. However, with an unbinned standard deviation of $\sigma = 6.8\,\mathrm{mmag}$ (outside the transit), the photometric quality of this data set is about a factor two worse than the large field surveys obtained as part of this thesis with BEST II (see Section 4.3). An analysis of individual nights shows that the photometric quality varies significantly; in fact, the data set only includes one good photometric night with a full transit event of WASP-18b.

Figure 10.2 shows a comparison of this night (28th August 2010) with a single ASTEP transit (4th July 2010). While the BEST II light curve is the best out of six with a full transit, the ASTEP night was selected without any requirement except for the planet to transit. Nevertheless, the photometric noise level in the ASTEP time series is more than a factor two lower (Table 10.1): Out of transit, ASTEP measurements show a standard deviation of $\sigma = 2.3\,\mathrm{mmag}$, while BEST II reaches 4.9 mmag. On binning to phase intervals of 0.01, the noise level in the ASTEP time series decreases by a factor of 5.2 to 0.44 mmag, and by 2.6 to 1.9 mmag for BEST II.[2]

[2]The fact that binning suppresses noise about two times more for ASTEP can be explained due to its shorter time sampling $\langle \delta t \rangle$ (Table 10.1): Under the assumption that the binning of N frames yields a noise level $\sigma_{\mathrm{bin}} \propto \sigma/\sqrt{N}$, one expects $\sigma_{\mathrm{bin,A}}/\sigma_{\mathrm{bin,B}} = \sqrt{\langle \delta t \rangle_A / \langle \delta t \rangle_B} \cdot \sigma_{\mathrm{A}}/\sigma_B = 0.49 \cdot \sigma_{\mathrm{A}}/\sigma_B$.

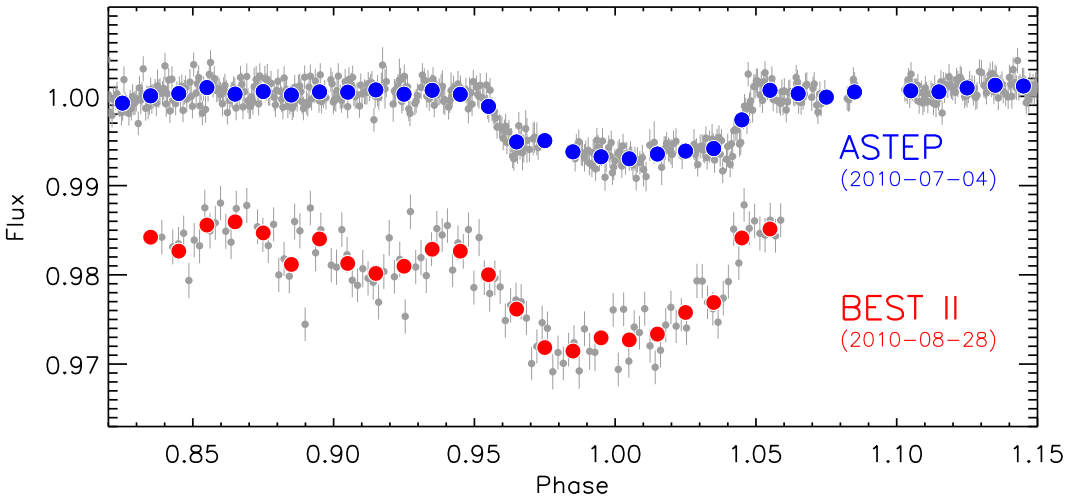

Figure 10.2: Phase-folded light curves of WASP-18b around transit (ephemerides from Southworth et al. 2009). Shown are two individual events, one observed with ASTEP 400 during the night of 4th July 2010 *(upper line)*, and one observed with BEST II during the night of 28th August 2010 *(lower line)*. In addition to individual measurements *(gray)*, data binned to phase intervals of 0.01 are shown in *red* (BEST II) and *blue* (ASTEP 400), respectively. For better visibility, the BEST II light curve was shifted in flux by −0.02.

Two conclusions can be drawn from this initial analysis: First, ASTEP data can successfully be reduced with the DLR pipeline in order to obtain high-precision photometry. This was achieved as part of this thesis through adaptations of the underlying procedures (see Chapter 5). Second, the photometric noise level of ASTEP for WASP-18b is more than four times smaller than for BEST II observations, if both are binned to the same phase interval. However, the data sets were only used as a test case here, i.e., they have only been compared for *one* target and a *single* night. A more quantitative comparison between the both sites can be drawn using the two large survey fields that have been observed together with ASTEP and BEST II; these are analyzed and discussed in detail in the next section.

10.2 Fields ASTEP-Exo2 and ASTEP-Exo3

Five fields, named ASTEP-Exo1–5, have been selected by the ASTEP team for transit search from Antarctica in 2010. While each pointing has been monitored for a period of about two weeks with ASTEP 400, BEST II joined the campaign for the fields ASTEP-Exo2 and ASTEP-Exo3. The observations, data reduction, analysis, and scientific results will be presented below.

10.2.1 Observations

The fields ASTEP-Exo2 and ASTEP-Exo3 have been observed during July/August 2010; Figure 10.3 shows the time series obtained with each telescope, and Table 10.2 compares the number of frames and nights.

Table 10.2: Number of frames, nights, and light curves obtained with ASTEP 400 and BEST II for the fields ASTEP-Exo2 and ASTEP-Exo3. (For BEST II observations, see also Table 4.1.)

	#Frames			#Nights		
	ASTEP	BEST2	total	ASTEP	BEST2	together
ASTEP-Exo2	5,895	391	6,286	17	6	19
ASTEP-Exo3	3,418	437*	3,855*	16	12	26
Σ (both fields)	9,313	828	10,141	26	18	38
	#Stars			#Stars ($\sigma \leq 0.01$ mag)		
	ASTEP	BEST2	both	ASTEP	BEST2	both
ASTEP-Exo2	37,619	90,330	9,124	2,318	8,229	745
ASTEP-Exo3	57,346	134,222	49,698	1,838	6,436	1,779
Σ (both fields)	94,965	224,552	58,822	4,156	14,665	2,524

* BEST II data set with 90 s exposure time

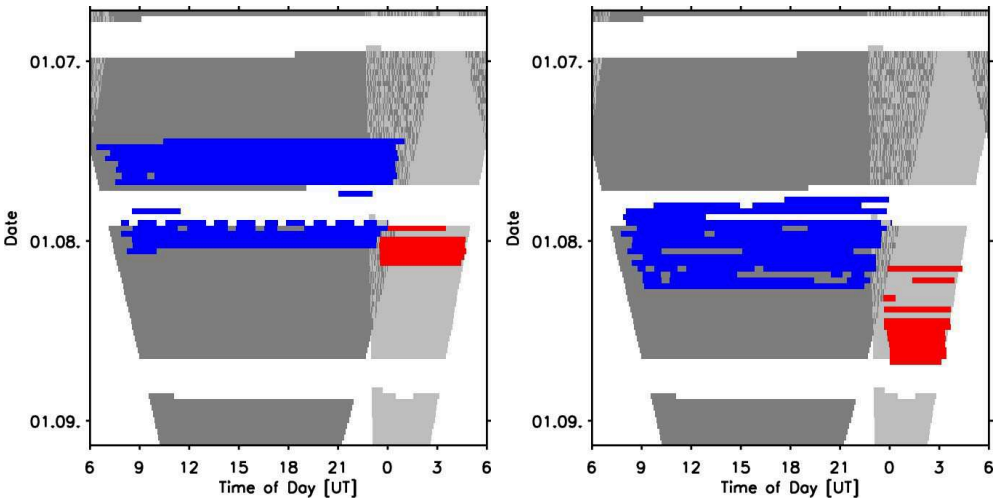

(a) ASTEP-Exo2 (b) ASTEP-Exo3

Figure 10.3: Joint BEST II/ASTEP field observations in 2010. Times of observations are shown for the fields (a) ASTEP-Exo2 and (b) ASTEP-Exo3. ASTEP time series are marked *blue*, BEST II observations *red*. For comparison, *gray* shaded areas indicate the maximum astronomical visibility b (Equation (B.3), i.e., target 30° above the horizon, Sun below −8°, etc.) of each respective field.

ASTEP-Exo2 was observed with ASTEP 400 from 14th July until 2nd August for a total of 17 nights, while BEST II pointed at the field for six nights between 29th July and 4th August. Observations with both telescopes have been obtained during four nights, but overlap only for 28 minutes on 29th July.

ASTEP-Exo3 was observed with a slightly larger timing offset between the two telescopes: ASTEP 400 observed the field for 16 nights between 24th July and 8th August, BEST II for 12 nights during 5th to 21st August. The data contain two nights with observations from both sites without overlap. BEST II obtained measurements at exposure times of $\Delta T = 10$ s and 90 s; the latter matches the ASTEP magnitude range better ($\Delta T = 70$ s for both fields), so that only the 90 s data set is presented in the following analysis.

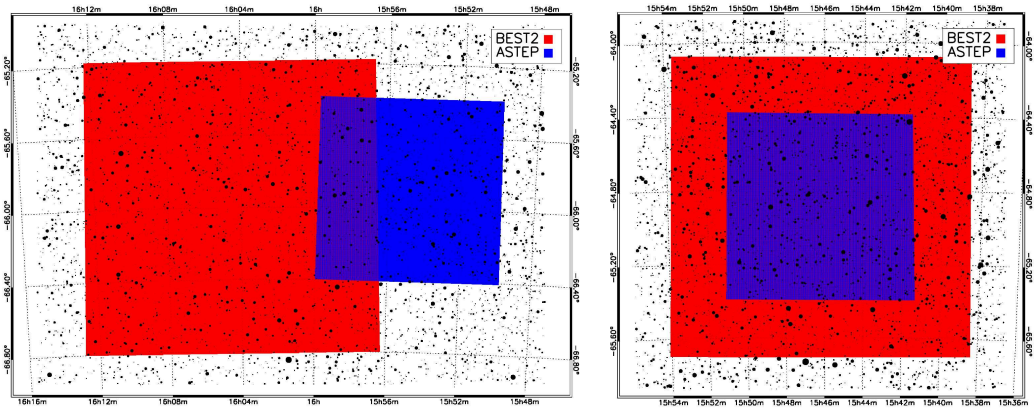

(a) ASTEP-Exo2 (b) ASTEP-Exo3

Figure 10.4: Sky positions of the fields (a) ASTEP-Exo2 and (b) ASTEP-Exo3. The FOV of BEST II ($1\overset{\circ}{.}7 \times 1\overset{\circ}{.}7$) is marked *red*, while the ASTEP FOV ($1\overset{\circ}{.}0 \times 1\overset{\circ}{.}0$) is shown in *blue*.

Pointings

BEST II can cover the FOV of ASTEP in a single pointing: Figure 10.4 shows a sky map with the relative positions and orientations of both fields for each telescope.

The ASTEP center coordinates for the target field ASTEP-Exo3,

$$(\alpha, \delta)_{\text{Exo3}} = (15^h 46^m 11\overset{s}{.}042, -64^\circ 53' 32\overset{''}{.}52) \ , \tag{10.1}$$

coincide with the BEST II observations. However, the ASTEP-Exo2 field was observed with ASTEP at a different pointing than initially announced. BEST II observed at the coordinates

$$(\alpha, \delta)^{\text{BEST II}}_{\text{Exo2}} = (16^h 04^m 32\overset{s}{.}414, -65^\circ 50' 35\overset{''}{.}31) \ , \tag{10.2a}$$

which are offset by $1\overset{\circ}{.}11$ from the final ASTEP pointing at

$$(\alpha, \delta)^{\text{ASTEP}}_{\text{Exo2}} = (15^h 54^m 48\overset{s}{.}499, -65^\circ 54' 04\overset{''}{.}35) \ , \tag{10.2b}$$

i.e., BEST II observations only cover $\sim$35% of the ASTEP-Exo2 field.

10.2.2 Photometric Data and Quality

Both data sets from each telescope have been calibrated and reduced using the DLR photometric pipeline (Chapter 5; pipeline parameters for each reduction are listed in Appendix D). After reduction, the light curves of each telescope have been analyzed *separately* and *in combination*. The remainder of this section first discusses the content and photometric quality of data from each telescope separately; the combination is described in the following Section 10.2.3, and the scientific analysis of both individual and combined light curves is covered in Section 10.2.4.

Table 10.3: Photometric noise levels and exposure times ΔT of joint BEST II/ASTEP observations. Values σ_r and Δf_{bg} are determined by fitting Equation (4.1) to each rms plot $(\widetilde{m}, \sigma)$.

Field	Data Set	ΔT	σ_r	Δf_{bg}
ASTEP-Exo2	ASTEP	70 s	2.7 mmag	14.6 ADU
	BEST II	120 s	2.4 mmag	12.6 ADU
ASTEP-Exo3	ASTEP	70 s	2.1 mmag	22.2 ADU
	BEST II	90 s	3.1 mmag	14.5 ADU

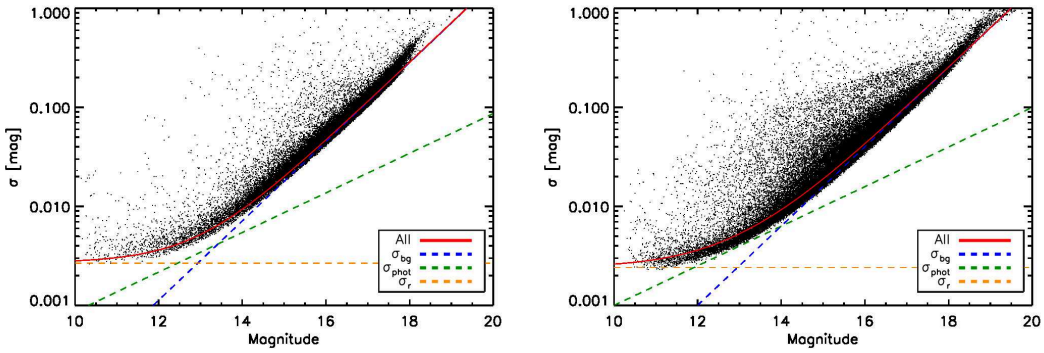

(a) ASTEP-Exo2

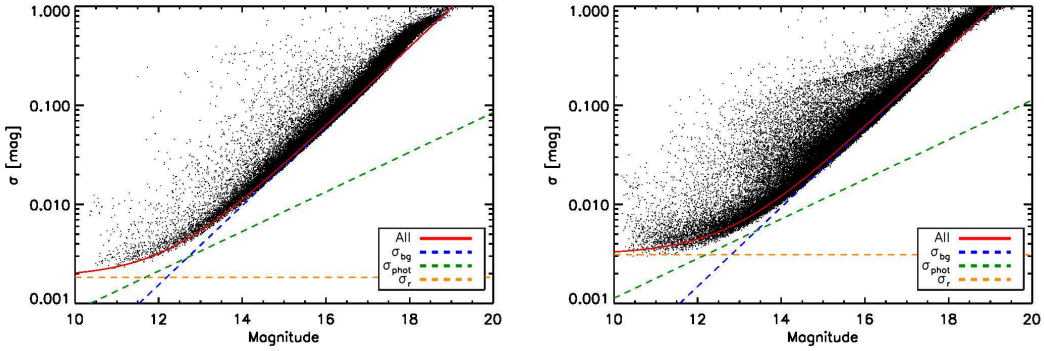

(b) ASTEP-Exo3

Figure 10.5: Photometric quality of observations on fields ASTEP-Exo2 and -Exo3. *Left* plots show median magnitudes and standard deviations for each ASTEP light curve (unbinned), *right* plots the same for BEST II. Lines indicate a fit of Equation (4.1) to the data (as in Figure 4.8).

Table 10.2 lists the number of light curves in each data set. The ASTEP 400 data set contains 57,346 light curves on ASTEP-Exo3, and 37,619 on ASTEP-Exo2. Due to the larger FOV, the BEST II data include more light curves than ASTEP: 134,222 for ASTEP-Exo3, and 90,330 for the (slightly different) ASTEP-Exo2 pointing.

The photometric quality of both fields is excellent: As the rms plots in Figure 10.5 show, a precision in the order of $\sim$2–3 mmag over the whole observing season is obtained with each telescope at the bright end of the magnitude range. Table 10.3 lists the limiting systematic noise component σ_r for each data set; it was obtained through fitting Equation (4.1) to each rms plot.

However, there are small differences between the fields and telescopes. For target field ASTEP-Exo2, ASTEP data show a minimum noise level of $\sigma_r = 2.7$ mmag, which is comparable to BEST II observations (2.4 mmag). For ASTEP-Exo3, ASTEP

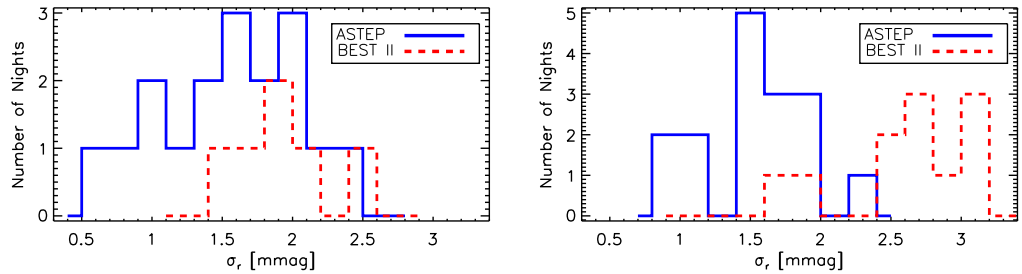

(a) ASTEP-Exo2 (b) ASTEP-Exo3

Figure 10.6: Histogram for nightly systematic noise components σ_r. Values have been obtained through fitting as in Figure 10.5, but for each night individually.

reaches with $\sigma_r = 2.1$ mmag an appreciably better noise level than BEST II in the same field (3.1 mmag).

In the same way as for the whole time series, σ_r was obtained for each night individually; the results are summarized in a histogram (Figure 10.6). Its distribution can be used to estimate the *best* and *average* nightly observing condition for each site: For BEST II, nights with a limiting noise of 2–3 mmag are regularly encountered, but values significantly below 2 mmag are rather exceptional. However, ASTEP nights are found *in average* at $\sigma_r \approx 1.5$–2.0 mmag, and sometimes well below: The best ASTEP night shows a minimum noise level of only 0.69 mmag, i.e., about a factor two less than the smallest value encountered by BEST II in either data set (1.6 mmag).

10.2.3 Light Curve Combination

Light curves from BEST II and ASTEP have been combined in order to extend the observational duty cycle. While the match itself can be obtained relatively easily using the stellar coordinates in each data set, a successful transit detection requires the stellar dimming to be measured consistently with both systems.

The details on the light curve combination, including a discussion on systematic differences between the two systems that might effect the transit detection, are described in the following.

Coordinate Match

The first step comprises a light curve match using the equatorial coordinates of each reduction. For each ASTEP light curve, the angular distance d to the nearest BEST II star has been calculated; it is plotted vs. the magnitude in Figure 10.7 for both fields. It shows a clear distinction between stars that are matched within $d \ll 2''$ and such that do not have a counterpart, i.e., with $d \gg 2''$. Therefore, the limit $d = 2''$ is used as the criterion for a successful match.

In target field ASTEP-Exo2, 9,124 stars meet this criterion (i.e., 10.1% of all BEST II, and 24.3% of all ASTEP stars; see Table 10.2). For field ASTEP-Exo3, the overlap is much better; here, 49,698 stars are matched (37.0% of BEST II, and 86.7% of all ASTEP stars). In total, joint observations are obtained for 58,822 stars.

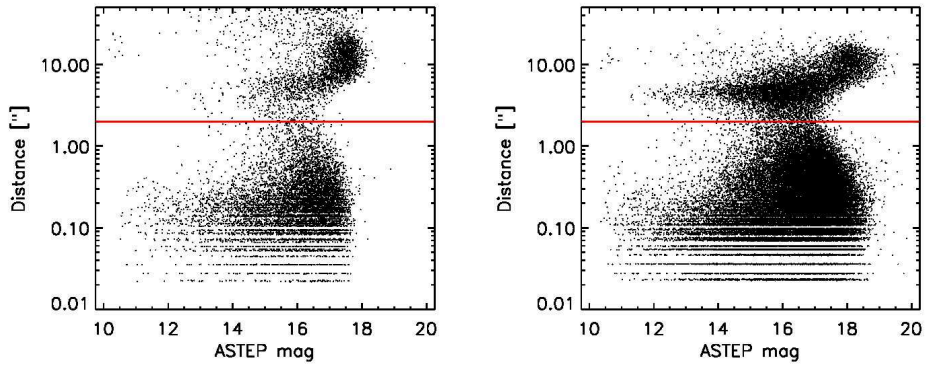

(a) ASTEP-Exo2 (b) ASTEP-Exo3

Figure 10.7: Distance d to nearest BEST II object for each star in the ASTEP data sets of (a) ASTEP-Exo2 and (b) ASTEP-Exo3. The *red line* denotes the limit of $2''$ that is used for matching.

Combination

Since the BEST II/ASTEP observing strategy does not aim at a precise calibration for *absolute* magnitudes (cf. Section 5.2.3), two light curves of the same star may show significantly different base levels in two reductions, i.e., much larger differences than their particular scatter. In order to sustain the relative precision, it is thus necessary to adjust the base levels. The left panels of Figure 10.8 compare mean magnitudes for matched stars in the ASTEP fields.

Individual light curves $\{(t_j^A, m_{ij}^A)\}$ from ASTEP (indicated with "A" in the following) are combined with BEST II ("B") measurements $\{(t_j^B, m_{ij}^B)\}$ for each matched star i as follows. First, the observing times are simply joined to

$$\left(t_j^C\right) = \left(t_1^A, \ldots, t_{N_A}^A, t_1^B, \ldots, t_{N_B}^B\right), \tag{10.3}$$

whereby N_A and N_B denote the number of frames in each data set, and "C" indicates the combined time series. Second, BEST II magnitudes m_{ij}^B are shifted by the difference between the mean magnitudes

$$\Delta m_i = \overline{m}_i^B - \overline{m}_i^A, \tag{10.4}$$

i.e.,

$$m_{ij}^C = \begin{cases} m_{ij}^A & \text{for } j \leq N_A \quad \text{(ASTEP)} \\ m_{i(j-N_A)}^B - \Delta m_i & \text{for } j > N_A \quad \text{(BEST II)} \,. \end{cases} \tag{10.5}$$

Comparison of Photometric Systems

BEST II and ASTEP use the same CCD (see Sections 3.2 and 3.3) and both observed the fields ASTEP-Exo2 and ASTEP-Exo3 in white light. Thus, the photometric systems are expected to be very similar. However, a dichroic mirror in the optical path of ASTEP 400 only reflects wavelengths longward of $\sim 550\,\mathrm{nm}$ to the scientific instrument, while the whole spectrum is used with BEST II. Thus, blue stars are expected to appear somewhat brighter when being observed with BEST II.

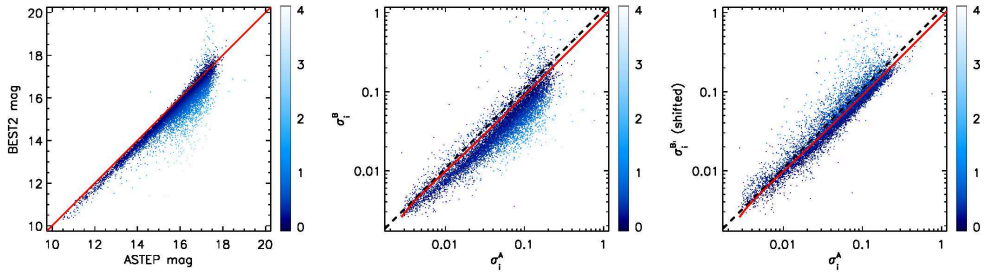

(a) ASTEP-Exo2

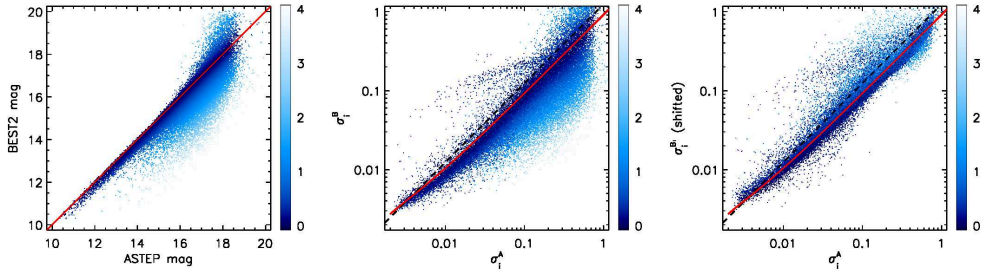

(b) ASTEP-Exo3

Figure 10.8: Direct comparison of ASTEP and BEST II photometry for each matched star i in data sets (a) ASTEP-Exo2 and (b) ASTEP-Exo3. *Left panels* show mean magnitudes $(\overline{m}_i^A, \overline{m}_i^B)$; the red line denotes $\overline{m}^A = \overline{m}^B$. Light curve standard deviations (σ_i^A, σ_i^B) are shown in the *middle*, while *right panels* compare the shifted BEST II noise level $\sigma_i^{B\prime} = \sigma_i^B \cdot 10^{-0.4 \cdot \Delta m_i}$ with σ_i^A. In the middle and right plots, the *red line* denotes the expected relationship between σ^A and σ^B for $\overline{m}^A = \overline{m}^B$ using the rms fits $\sigma^A(\overline{m}^A)$ and $\sigma^B(\overline{m}^B)$ (*red lines* in Figure 10.5). For comparison, the *black dashed line* shows the expected dependency from photon noise only (Equation (10.7)). The absolute magnitude difference $|\Delta m|$ (Equation (10.4)) is shown in *blue* as indicated in the color bar.

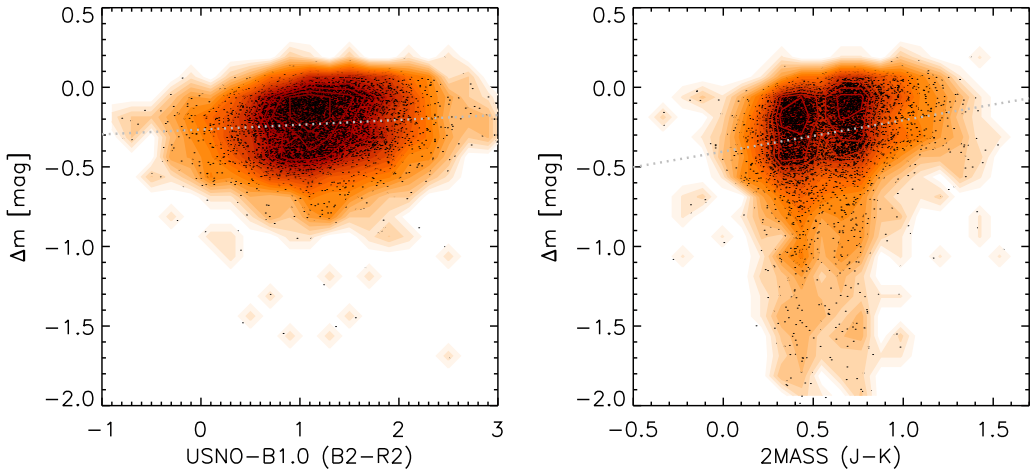

Figure 10.9: Magnitude difference Δm between BEST II and ASTEP 400 (Equation (10.4)) in field ASTEP-Exo3 as a function of stellar colors. The *left* plot uses $(B - R)$ from the USNO-B1.0 catalog (Monet et al. 2003), the *right* plot $(J - K)$ from 2MASS (Skrutskie et al. 2006). *Black* dots represent individual stars; the background color indicates their number density. A linear fit based on Equation (10.6) is shown by the *white dotted* line. (Only stars with $\overline{m}_i^A \leq 15$ mag are shown and used for the fit, since fainter stars exhibit large color uncertainties.)

In order to evaluate differences in both photometric systems quantitatively, catalog colors have been obtained for matched stars: $(B-R)$ from USNO-B1.0 (Monet et al. 2003) is used in the blue, and $(J-K)$ from 2MASS (Skrutskie et al. 2006) in the red part of the spectrum. For each star, they are compared with Δm (Equation (10.4)), which is expected to increase as a function of both. Figure 10.9 shows the analysis for the stars in target field ASTEP-Exo3. A linear fit to the data yields

$$\begin{aligned} \Delta m\,[(B-R)] &= (-0.266 \pm 0.006)\ \text{mag} + (B-R)\cdot(0.030 \pm 0.005) \\ \Delta m\,[(J-K)] &= (-0.404 \pm 0.011)\ \text{mag} + (J-K)\cdot(0.20 \pm 0.02)\ . \end{aligned} \tag{10.6}$$

The smaller number of matched stars in ASTEP-Exo2 show a very similar relation. The functional dependency of Equation (10.6) confirms the expected color dependency between both optical designs. However, because the differential amplitude is rather low, its influence upon the combined data is considered negligible.

Comparison of Photometric Precision for Each Star

The light curve combination allows the comparison of the photometric precision of ASTEP with BEST II for each matched star *individually*: The middle panel of Figure 10.8 shows both standard deviations, i.e., the pairs (σ_i^A, σ_i^B), and compares them to the respective σ-fits of Figure 10.5.

A large majority of stars in both fields shows significantly lower overall photometric noise levels in BEST II data compared to the respective ASTEP measurements. However, the deviation increases with the magnitude difference $|\Delta m|$ between BEST II and ASTEP, as the color coding of Figure 10.8 indicates. Different exposure times $\Delta T_{A/B}$ (Table 10.3) and telescope apertures $D_{A/B}$ (Chapter 3) alone cannot explain this effect, because that would yield

$$\frac{\sigma_i^B}{\sigma_i^A} = \frac{D_A}{D_B}\sqrt{\frac{g_B}{g_A}\cdot\frac{\Delta T_A}{\Delta T_B}} \quad \left(= 1.4065\cdot\sqrt{\frac{\Delta T_A}{\Delta T_B}}\ \text{for BEST II/ASTEP}\right) \tag{10.7}$$

for identical photometric systems (with gain factors $g_{A/B}$), i.e., a noise ratio that is *independent* of the stellar magnitude. Therefore, two alternative hypotheses have been investigated: Differences between the photometric systems or the angular resolution of both telescopes.

First, the magnitude difference Δm between both systems shows a slight color dependence. Hence, the noise level is also expected to vary with the stellar color: With the assumption of photon noise only, i.e., $\sigma = 1.0857\cdot\delta f \propto f^{-1/2}$, it follows that $\sigma_i^B/\sigma_i^A \propto 10^{0.2\Delta m_i}$. However, the derived color dependency of Δm (Equation (10.6)) is too small to explain differences up to an order of magnitude between σ_i^B and σ_i^A: With $\Delta m \gtrsim -0.5\,\text{mag}$, it follows that only $\sigma_i^B \gtrsim 0.8\cdot\sigma_i^A$.

Second, the BEST II pixel scale is larger ($1.5''$/Px compared to $0.9''$/Px for ASTEP 400). Therefore, BEST II fields are more affected by crowding, i.e., more stellar apertures overlap each other than in the ASTEP data. In turn, this yields a systematic magnitude difference $m_B < m_A$, and, hence, negative differences Δm for contaminated stars. In addition, overlapping apertures yield an underestimation of brightness variations (see Appendix C.3). To test the relevance of crowding in

the two data sets, a shifted value $\sigma_i^{B'}$ was calculated from the initial photometric noise σ_i^B of BEST II using Equation (C.10) and the assumption that magnitude differences Δm_i are *solely caused by contamination*. The right panel of Figure 10.8 compares $\sigma_i^{B'}$ with the corresponding (unshifted) ASTEP noise σ_i^A. It shows that the large majority of BEST II light curves with initial values of $\sigma_i^B \ll \sigma_i^A$ distribute smoothly around the noise dependency that is expected from the photometric quality of both data sets.

Thus, the analysis shows that crowding introduces significant systematic differences to absolute and relative brightness measurements, although the pixel scale of BEST II is only 1.7 times larger compared to ASTEP 400. This is particularly important for fainter stars ($m \gtrsim 15$ mag) in both fields, which are, however, less interesting for transit search. For bright stars, the photometric precision of both instruments compares well (see Figures 10.5 and 10.8).

Examples

Figures 10.10 and 10.11 give two examples of a joint ASTEP/BEST II light curve. Two variable stars have been selected in order to compare the variation: A short-periodic pulsator (δ Scuti type, Figure 10.10) and an eclipsing binary (EA type, Figure 10.11).

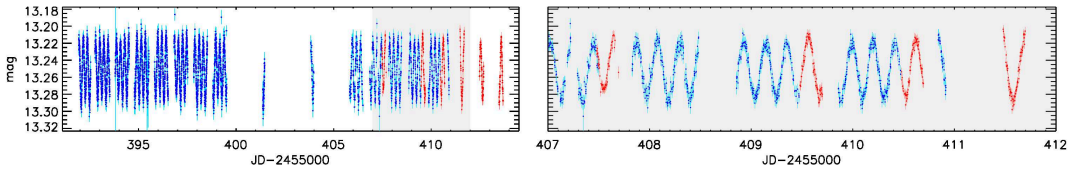

Figure 10.10: Example of a joint BEST II/ASTEP light curve – short periodic variable Exo2_026332. The *left* plot shows the whole light curve, while the *right* plot shows five days with the best overall time coverage. *Blue* points indicate ASTEP measurements, BEST II data appear in *red*.

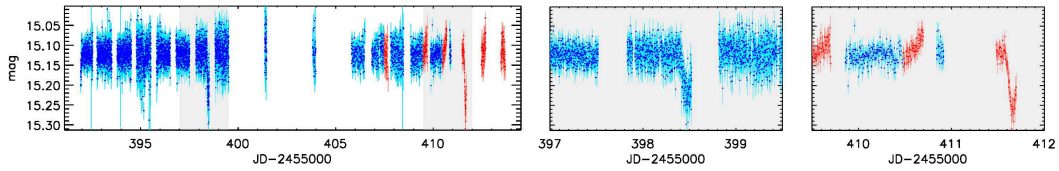

Figure 10.11: Example of a joint BEST II/ASTEP light curve – eclipsing binary Exo2_028863. The *left* plot shows the whole light curve, while the *right* panels enlarge the time series at 2.5 days around each of the two observed eclipses. Colors as in Figure 10.10.

The first case, Exo2_026332 (Figure 10.10), shows how BEST II time series can fill small gaps between two Antarctic nights and thus yield an almost continuous duty cycle. Furthermore, both the amplitude and photometric precision are in very good agreement.

The second case, Exo2_028863 (Figure 10.11), highlights an important and anticipated advantage of joint observations from Antarctica and a mid-latitude site: Since

only one eclipse event was observed with ASTEP 400, no period could be derived for this eclipsing binary from ASTEP time series alone. The additional BEST II observations, however, uncover a second event, so that the period can be constrained. Again, the amplitudes of both events are in good agreement. Therefore, just as this eclipsing binary could only be found in the joint time series, the chance of finding transiting planets should also be increased by combining the data.

10.2.4 Transit Search

Both ASTEP fields have been searched for planetary transits using the BLS algorithm as described in Chapter 6 (see Appendix D for BLS parameters). The analysis was performed on the two individual ASTEP 400 and BEST II data sets, as well as for the combined light curves. Table 10.4 shows the number of stars contained in each of these six data sets, the number of low-noise light curves analyzed with BLS, and the number of signals examined manually. For BEST II data alone, the noise limit was set to $\sigma_{\mathrm{bls}}^{\mathrm{min}} = 0.05\,\mathrm{mag}$ as for transit search in the fields F17–F19 (Chapter 8). Light curves with ASTEP measurements have a better time sampling and were thus analyzed up to a larger (unbinned) noise level of $\sigma_{\mathrm{bls}}^{\mathrm{min}} = 0.10\,\mathrm{mag}$. Out of these, the 20% most significant signals were examined visually in order to obtain a deep analysis of these first ASTEP data sets. For BEST II alone, the observational coverage only yields an insufficient detection efficiency (see also Section 10.3), so that only the 3% largest values of S_{bls} were investigated.

Table 10.4: Transit search in target fields ASTEP-Exo2 and ASTEP-Exo3.

Field	Data Set	Star Count			Limits	
		Total	$\sigma_i \leq \sigma_{\mathrm{bls}}^{\mathrm{min}}$	$S_{\mathrm{bls}} \geq S_{\mathrm{bls}}^{\mathrm{min}}$	$\sigma_{\mathrm{bls}}^{\mathrm{min}}$ [mag]	$S_{\mathrm{bls}}^{\mathrm{min}}$
ASTEP-Exo2	ASTEP	37,619	23,074	4,677 (20%)	0.10	3.37
	BEST II	90,330	47,201	1,431 (3%)	0.05	3.18
	combined	9,124	6,699	1,341 (20%)	0.10	3.62
ASTEP-Exo3	ASTEP	57,346	23,158	4,639 (20%)	0.10	3.52
	BEST II	134,222	46,853	1,441 (3%)	0.05	3.49
	combined	49,698	20,541	4,178 (20%)	0.10	3.98

Notes. Counts and parameters are given for ASTEP 400 and BEST II individually, as well as for combined data. Shown are the total number of stars in each data set, the number of low-noise ($\sigma_i \leq \sigma_{\mathrm{bls}}^{\mathrm{min}}$) light curves analyzed with BLS, and the number of light curves with $S_{\mathrm{bls}} \geq S_{\mathrm{bls}}^{\mathrm{min}}$ which have been inspected manually for transit signals. The latter is chosen such that a fixed percentage of low-noise light curves is inspected, as shown.

Similar to the BEST II data sets F17–F19, most light curves were already rejected through the visual inspection: Many signals with high SNR S_{bls} could be identified as eclipsing binaries due to their depth and/or clear $\bigvee$-shape, while the large majority of light curves close to the limit $S_{\mathrm{bls}}^{\mathrm{min}}$ showed no significant or systematic signals.

Overall, ten cases were identified as good candidates (seven in ASTEP-Exo2, three in ASTEP-Exo3) and analyzed carefully. They were matched with star catalogs to estimate the stellar type and density, transits were fitted with a trapezoid in order to improve their parameters and ephemerides, and several tests were applied to exclude false alarms from the information available; the procedures were adapted from BEST II transit search and are outlined in detail in Chapter 8.

Table 10.5: Transit candidates in target fields ASTEP-Exo2 and ASTEP-Exo3, sorted by priorities.

ID	Data	Magnitude					Color	Stellar Type		St. Density $[\rho_\odot]$		$S_{\rm bls}$		Ephemerides		Trapezoid Fit		
	A B C	R_B	V	R	J	K	J-K	H-K;J-H;J-K	$r_\star$ $[r_\odot]$	$\rho_{\rm SMO}$	$\rho_{\rm JK}$	A/B	C	T_0 [rHJD*]	p [d]	δF	T_{14}	T_{23}
priority 1																		
Exo2_17516	□ □ ⊛	15.3	15.4	···	14.9	14.5	0.43	–;K1-K2;G6	0.85 ± 0.06	1.30	1.02	3.3	3.8	392.354 ± 0.003	1.5730 ± 0.0004	1.7%	1.83^h	1.19^h
priority 3																		
Exo2_13865	⊛ – –	15.2	14.6	15.6	14.3	13.9	0.43	K6-M0;F7-G0;G6	0.9 ± 0.4	6.22	1.01	3.8	–	394.584 ± 0.002	3.342 ± 0.003	4.2%	2.45^h	2.06^h
Exo2_20735	⊛ – –	15.6	15.9	15.4	14.8	14.3	0.57	K3-K7;K0-K1;K1-K2	0.76 ± 0.09	1.73	1.23	6.6	–	395.412 ± 0.002	3.6728 ± 0.0008	3.4%	2.74^h	1.88^h
Exo2_23534	⊛ □ □	14.3	14.4	14.0	13.5	13.0	0.51	G9-K5;G8-G9;G9-K0	0.80 ± 0.08	1.42	1.13	3.6	3.4	392.366 ± 0.003	4.758 ± 0.004	0.8%	3.76^h	3.38^h
Exo2_27765	⊛ □ □	14.8	15.1	14.9	13.5	12.6	0.83	K8-M0;K7-M6;K8-M0	0.4 ± 0.3	1.57	3.34	4.1	3.5	392.295 ± 0.002	0.6720 ± 0.0002	0.9%	1.32^h	1.00^h
Exo3_35958	□ □ ⊛	15.0	15.2	14.2	14.6	14.1	0.52	M1-M2;G0-G4;G9-K0	0.8 ± 0.3	16.33	1.14	5.2	5.8	404.106 ± 0.004	2.629 ± 0.002	2.5%	1.49^h	1.27^h
rejected																		
Exo2_30301	□ □ ⊛	16.0	16.4	15.8	16.0	15.4	0.67	K6-K8;K3;K4	0.71 ± 0.07	0.57	1.54	<2	3.7	393.282 ± 0.006	3.841 ± 0.002	2.5%	3.79^h	2.62^h
Exo2_36240	⊛ – –	15.7	15.6	15.3	15.4	14.2	1.25	–;K3;–	0.772 ± 0.001	1.02	···	6.1	–	392.284 ± 0.003	1.7378 ± 0.0006	3.9%	2.08^h	0.77^h
Exo3_11454	⊛ □ □	13.0	13.2	13.0	12.5	12.3	0.25	B9-A4;F6;F4	2.0 ± 0.8	0.05	0.70	4.5	3.8	406.10 ± 0.04	5.67 ± 0.02	4.0%	8.01^h	2.52^h
Exo3_84704	– ⊛ –	14.1	···	16.8	···	···	···	···	···	0.13	···	4.9	–	414.499 ± 0.005	1.0982 ± 0.0006	5.0%	3.64^h	0.99^h

* rHJD = HJD − 2,455,000

Notes.

- Identifiers refer to the numbering in ASTEP and combined data sets (they are equal); only Exo3_84704 refers to the numbering within the BEST II data set.
- The *data* column indicates with the "□"-symbol that candidates are covered by ASTEP (A), BEST II (B), and/or the combined (C) time series. If a candidate was *found* in a data set, it is marked with an additional asterisk ("⊛") in the corresponding column. (*"Found"* in this respect means that the candidate is identified with the correct period and with $S_{\rm bls} \geq S_{\rm bls}^{\rm min}$.)
- Magnitudes are obtained by ASTEP (R_B) and coordinate matches to the NOMAD (V,R) and 2MASS (J,K) catalogs. Spectral type ranges and stellar radii $r_\star$ are estimated from 2MASS colors (Section 8.3.5).
- Quantities derived from photometry in this work (i.e., $\rho_{\rm SMO}$, ephemerides, trapezoid fit) are based on the combined time series for stars that have been observed with both telescopes. The BLS significance parameter $S_{\rm bls}$ is given for both the single telescope search (A/B) as well as the combined data set (C).
- The stellar densities $\rho_{\rm SMO}$ and $\rho_{\rm JK}$ are derived independently using the transit shape and the 2MASS $(J-K)$ color, respectively (Section 8.3.6).
- Ephemerides T_0 and p are the result of the mid-point fit to individual events (Section 8.2).
- The transit depth δF, the duration of the full transit T_{14}, and the main eclipse duration T_{23} are determined from a trapezoid fit to the folded light curve (Section 8.2).

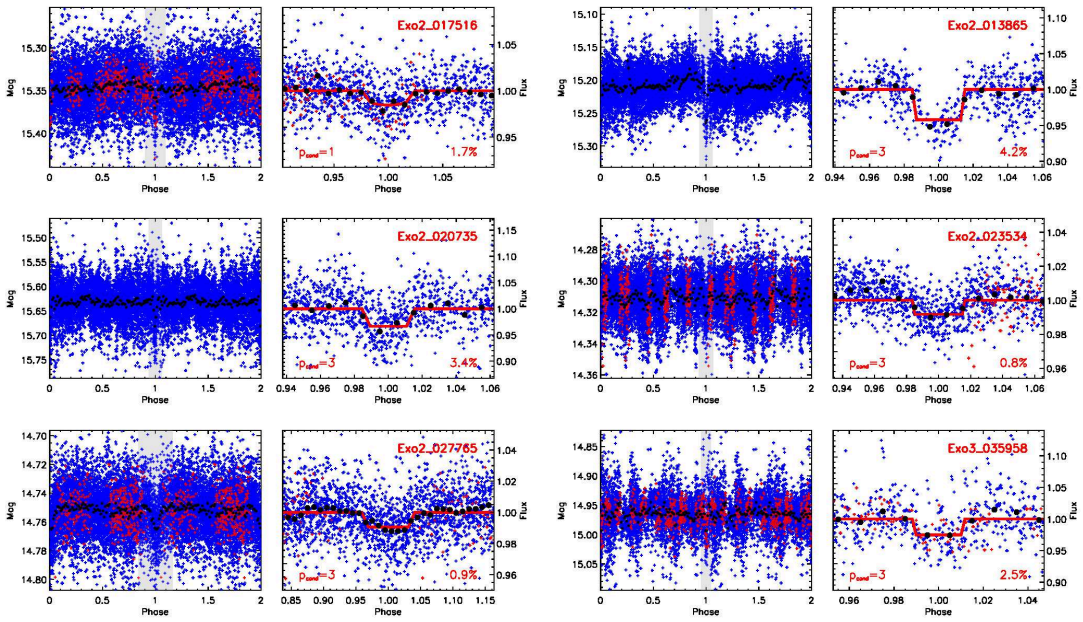

Figure 10.12: Folded light curves of transit candidates in fields ASTEP-Exo2 and ASTEP-Exo3. The left side of each panel shows the folded light curve in magnitudes. A phase range around the transit-like signal is marked *gray* and is also shown enlarged on the right plot of each panel, which plots measured fluxes together with the trapezoidal fit *(red line*; for Exo2_017516, the line shows the modeled transit fit – see text). ASTEP measurements are colored *blue*, BEST II data points *red*. In addition, black circles show values binned in intervals of $0.01\,p$, and candidate priorities p_{cand} and transit depths δF are given for information (see also Table 10.5).

The most important results and parameters are summarized for all candidates in Table 10.5. After all tests had been evaluated, each candidate was assigned a priority according to the scheme applied for BEST II detections (adapted from CoRoT, see page 99). One candidate was rated priority 1, five candidates were rated priority 3, and another four were rejected as false positives. Folded light curves of the six candidates with $p_{\mathrm{cand}} \leq 3$ are shown in Figure 10.12; periods of $p = 0.7$–$4.8\,\mathrm{days}$ and transit depths of $\delta F = 0.8$–4.2% place them in the parameter space of (possibly inflated) hot Jupiter planetary candidates.

Table 10.5 and Figure 10.12 also indicate whether a candidate is covered with ASTEP and/or BEST II observations, which depends on its position in the sky (see also Figure 10.4). Due to the very short time series of BEST II, only one candidate has been found outside the ASTEP FOV (Exo3_84704); however, its large depth of $\delta F = 5.0\%$ together with a clear $\bigvee$-shape caused it to be rejected. Out of the other nine candidates, three are located in the non-overlapping part of the ASTEP-Exo2 field, i.e., where no BEST II data is available. The remaining six candidates are covered by both data sets.

For the group of candidates contained in all three data sets (ASTEP, BEST II, and the combination), it is particularly interesting to note whether they were found successfully in each data set, or only in some of them. As Table 10.5 shows, none of these candidates was found with BEST II data alone, three candidates were *only* found in ASTEP data, and three could *only* be identified in the combined time

series. Qualitatively, this already shows the potential of network observations for transit search; Sections 10.3 and 10.4 will investigate this advantage quantitatively.

Exo2_17516

The group of candidates only found in combined time series includes the priority 1 candidate Exo2_17516. Although the BLS periods of ASTEP and the combined data set match, only the combination with BEST II data yields an SNR value above the applied threshold level $S_{\mathrm{bls}}^{\mathrm{min}}$: Due to an additional transit event recorded with BEST II, the significance S_{bls} is raised from 3.3 to 3.8.

The transit signal has a period of $p = 1.5730(4)$ days and a depth of $\delta F = 1.7\%$. Being the best candidate in these data sets, its light curve was modeled by Szilárd Csizmadia (DLR) using the TLCM package, i.e., in analogy to the candidates found in BEST II data (cf. Section 8.4.1). The modeling yields a radius ratio of $r_p/r_\star = 0.141 \pm 0.021$, but a relatively uncertain impact parameter of $b = 0.67 \pm 0.58$. More transits and/or observations with increased precision are needed in order to better constrain the planetary parameters, and to limit uncertainties in the ephemerides. Such observations have very recently been obtained with BEST II and ASTEP 400; they are currently being analyzed (BEST II) or transfered to Europe (ASTEP).

The candidate Exo2_17516 was found around a $V = 15.4$ mag star, for which 2MASS colors indicate G6–K2 spectral type. Combined with the modeling results, a first estimate would put the candidate at a radius of $r_p = (1.17 \pm 0.19)\, r_J$, if the planetary nature was confirmed. Altogether, the candidate is thus expected to be of hot Jupiter type similar to, e.g., CoRoT-1b (Barge et al. 2008).

In addition to the photometric observations, low-resolution spectroscopy is currently being planned in order to obtain a first spectral characterization of the candidates identified in the ASTEP-Exo2 and ASTEP-Exo3 fields.

10.3 Detection Yield I – Fields ASTEP-Exo2 and -Exo3

The candidates presented in the previous section *qualitatively* prove that ASTEP and combined ASTEP/BEST II data have a sufficient quality to find transits of hot Jupiters ($p \approx 1$–5 days, $\delta F \approx 1\%$). In the following, the detection yield is estimated *quantitatively* from basic characteristics such as the photometric noise budget and observational duty cycle of each data set. The aim of this approach is twofold:

- First, it can address whether the actual number of identified candidates meets the expectations in comparison to other surveys.
- Second, it allows a quantitative assessment of different factors which affect the detection yield.

This Section 10.3 first evaluates the detection yield of the two investigated data sets *as they are*, i.e., including systematic biases between the observations such as those related to the size of the FOV, photon noise level, time sampling, etc.. As such, it focuses on the first aim. The more general context of transit search in Antarctica will then be addressed in the next Section 10.4.

Model

The model used in Sections 10.3 and 10.4 to calculate the detection yield has already been applied to the BEST II fields F17–F19. As such, it is described in detail in Section 4.4 and only mentioned briefly here.

The calculation is based on a very general description of the detection yield (Equation (2.11)). However, by considering a single planetary radius r_{p0} and a small range $[p_0, p_1]$ of orbital periods p, the number of detections can be approximated as (Equation (4.4))

$$N_{\mathrm{det}} = N_{\mathrm{S/N}} \cdot f_{p0} \cdot f_t, \tag{10.8}$$

whereby $N_{\mathrm{S/N}}$ denotes the number of light curves with sufficient SNR to detect a transit in a given data set, and f_{p0} gives the fraction of stars that possess a planet of radius r_{p0} and period $p \in [p_0, p_1]$.

The parameter f_t defines a probability that is constrained by timing factors, i.e., it integrates the geometric transit probability $p_g(p)$ (Equation (2.13)) together with the observational window function p_{win} over $[p_0, p_1]$ (Equation (4.6)); the calculation of $p_g(p)$ is simplified (Equation (4.7)), and p_{win} is approximated by the phase coverage $p_{\mathrm{c3}}(p)$ of three or more transit events from real observing times (see also discussion in Section 6.3).

Since the two ASTEP fields have been monitored for only a relatively short period of time, the detection yield is being investigated for orbits of $p \in [1, 10]$ days. In this range, the probability for a star to host a Jupiter-sized planet is given in the literature: $f_{p0}^{(1)} = 0.10\%$ ($r_{p0} = 1.1\, r_J$, $p \in [1, 10]$ days; Bayliss and Sackett 2011) and $f_{p0}^{(2)} = 0.43\%$ ($M_p = M_J$, $p < 11.5$ days; Cumming et al. 2008) are taken as two representative examples for the current estimate of f_{p0}.

For the calculation of $N_{\mathrm{S/N}}$, the stellar population of each field is simulated using the Besançon model of the Galaxy (Robin et al. 2003), which allows the estimation of stellar radii $r_\star$. Hence, it yields a transit depth $\delta F = r_{\mathrm{p0}}^2 / r_\star^2$ for each simulated dwarf star. The depth is then compared to the noise level σ_i^{bin} (binned to 30 minutes) that is expected in the data set according to the brightness of star i. Following the results of tests with artificial transits in BEST II data (see Section 6.2.3), the criterion

$$\sigma_i^{\mathrm{bin}} \leq 0.64 \cdot \delta F \tag{10.9}$$

is used to decide whether a transit could be detected.

Finally, a Monte Carlo simulation calculates the fraction $f_{\mathrm{S/N}}$ of stars for which Equation (10.9) holds in a given set of $N_\star$ simulated stars; it immediately yields

$$N_{\mathrm{S/N}} = N_\star \cdot f_{\mathrm{S/N}} \ . \tag{10.10}$$

Simulation for Target Fields ASTEP-Exo2 and ASTEP-Exo3

The detection yield N_{det} of Jupiter-sized planets ($r_{\mathrm{p0}} \equiv r_J \Rightarrow \delta F \approx 1\%$) was calculated for both fields ASTEP-Exo2 and ASTEP-Exo3 using the characteristics of each data set at hand (i.e., ASTEP 400, BEST II, and the combination). Their respective observing times (Figure 10.3) and photometric quality (Figure 10.5) form,

Table 10.6: Expected number of hot Jupiter detections in ASTEP survey fields.

Field	Data Set	FOV [deg^2]	a_v [mag/kpc]	$N_\star$	$N_{\mathrm{S/N}}$	$f_{\mathrm{S/N}}$	f_t	$N_{\mathrm{det}}^{(1)}$	$N_{\mathrm{det}}^{(2)}$
ASTEP-Exo2	ASTEP	1.00	0.0	29,161	934	3.20%	0.0463	0.04	0.19
	BEST II	2.89	0.0	76,514	3,918	5.12%	0.0010	0.00	0.02
	overlap[1]	0.35	0.0	9,892	374	3.78%	0.0519	0.02	0.08
	combined[2]	1.00						0.05	0.20
ASTEP-Exo3	ASTEP	1.00	0.0	38,020	951	2.50%	0.0438	0.04	0.18
	BEST II	2.89	0.1	105,248	2,192	2.08%	0.0025	0.01	0.02
	overlap[1]	1.00	0.0	38,020	940	2.47%	0.0517	0.05	0.21

[1] Effective overlap area (Figure 10.4). The fact that not each star is matched is not taken into account.
[2] Combined detection yield, calculated as $N_{\mathrm{det}}^{\mathrm{combined}} = 0.65 \cdot N_{\mathrm{det}}^{\mathrm{ASTEP}} + N_{\mathrm{det}}^{\mathrm{overlap}}$

Notes. Stellar populations have been simulated using the Besançon model of the Galaxy. The interstellar extinction a_v has been adjusted for each field such that the star counts resample the observations (see example in Figure 4.9a). $N_\star$ gives the total count of modeled stars ($R \in [10, 16]$) within the FOV, while $f_{\mathrm{S/N}} = N_{\mathrm{S/N}}/N_\star$ refers to the fraction of stars with a sufficient SNR to detect Jupiter-like transits ($r_p \equiv r_J$, Equation (10.9)). The geometric probability is combined with the orbital coverage into the parameter f_t (Equation (4.6)). The expected detection yield N_{det} is given for $f_{p0}^{(1)} = 0.10\%$ (Bayliss and Sackett 2011) and $f_{p0}^{(2)} = 0.43\%$ (Cumming et al. 2008), respectively.

together with the field coordinates (Equations (10.1)–(10.2b)), the main input for the simulation. The results are summarized in Table 10.6 and discussed below.

Comparison with Transit Detections

The combined detection yield of both investigated fields is expected to be equal ($N_{\mathrm{det}} = 0.05$–0.20 for ASTEP-Exo2 and 0.05–0.21 for ASTEP-Exo3), although five candidates are found in field ASTEP-Exo2 and only one in ASTEP-Exo3. However, regarding the small numbers of candidates, the difference is not considered significant.

In total, the data of both fields and telescopes together are expected to yield 0.10–0.41 transit planet detections. Six candidates are actually found, which corresponds to a planet-to-candidate ratio of $\sim$1:15–1:60, i.e., it is comparable to field searches of BEST II and other ground-based surveys, which typically encounter ratios of $\sim$1:10–1:20 (see discussion and references in Section 8.4).

Photometric Precision (Observed Case)

In the ASTEP-Exo2 field, ASTEP provides a sufficient SNR to detect Jupiter-sized transiting planets for $N_{\mathrm{S/N}} = 934$ ($f_{\mathrm{S/N}} = 3.20\%$) of the $N_\star = 29{,}161$ simulated field stars. For BEST II, the detection criterion (Equation (10.9)) was met for 3,918 (5.12%) of 76,514 stars in the field. The combination of both data sets yields a slight increase in $f_{\mathrm{S/N}}$ compared to ASTEP alone (3.78%), but the corresponding absolute number (374) is rather low due to the small overlap.

For the ASTEP-Exo3 field, the differences in $f_{\mathrm{S/N}}$ are not as distinct: ASTEP yields a sufficient SNR for 951 (2.50%) of 38,020 light curves, and BEST II for 2,192 (2.08%) of 105,248 stars. The light curve combination decreases the number slightly to 940 (2.47%) in comparison to ASTEP alone.

While the discrepancy in absolute counts $N_{\mathrm{S/N}}$ is mostly due to the larger FOV

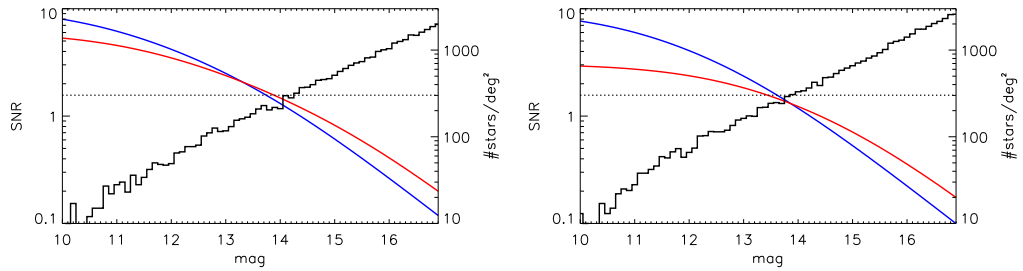

(a) ASTEP-Exo2 (b) ASTEP-Exo3

Figure 10.13: Signal-to-noise ratio (SNR) and number of stars in target fields ASTEP-Exo2 and ASTEP-Exo3 as a function of stellar magnitude. The *left* y-axis, the *solid blue* (ASTEP) and *solid red* (BEST II) lines give SNR $= \delta F/\sigma$ for a Jupiter-like transit signal of $\delta F = 1\%$ depth. For that, the limiting noise $\sigma(m)$ is obtained by fitting the standard deviation of data binned to 30 min (cf. Figures 4.8 and 10.5). The dashed line indicates the detection criterion used (Equation (10.9)). The right y-axis and the *solid black* line show the number of Besançon stars per deg^2 for comparison.

of BEST II, the difference in the fraction $f_{\mathrm{S/N}}$ is more surprising. It depends on the photometric precision and the number of stars in a field, which both largely depend on the stellar magnitude. Figure 10.13 compares them for both target fields and telescopes. Here, the SNR is calculated as $\delta F/\sigma$ using a Jupiter-like signal ($\delta F = 1\%$) and the limiting noise $\sigma(m)$ of data binned to intervals of 30 min. As the figure shows, ASTEP obtains a clearly better SNR on bright targets, whereas BEST II shows a slightly better SNR for $m \gtrsim 14$ mag (the latter effect being more pronounced for target field ASTEP-Exo2). Together with an exponentially increasing star count towards fainter magnitudes, it explains why BEST II yields a larger fraction $f_{\mathrm{S/N}}$ in this field. Note, however, that the improved SNR of ASTEP for bright stars is only marginally reflected in the results, as *both* BEST II and ASTEP provide a sufficient SNR to detect Jupiter-sized transiting planets for the majority of bright target stars. The detection of transiting planets of other sizes will be discussed in the next Section 10.4.

Duty Cycle (Observed Case)

Figure 10.14 displays the observational coverage $p_{\mathrm{c3}}(p)$ of three or more transits for both fields and projects. It shows that ASTEP data cover orbital periods up to 2–3 days completely, while BEST II observations alone are far too sparse to provide a reasonable phase coverage. However, if ASTEP observations are complemented with BEST II data, $p_{\mathrm{c3}}(p)$ is extended towards larger periods.

The detection yield is directly proportional to the timing probability f_t (Equation (10.8)). As such, it allows to assess the effect of additional BEST II observations *quantitatively*. The results for f_t are given in Table 10.6: With ASTEP time series, it yields 0.0463 for the field ASTEP-Exo2 and 0.0438 for ASTEP-Exo3. If BEST II data are added, the factor f_t (and, hence, the detection yield) **increases by 12%** to 0.0519 (ASTEP-Exo2), and **by 18%** to 0.0517 (ASTEP-Exo3), respectively.

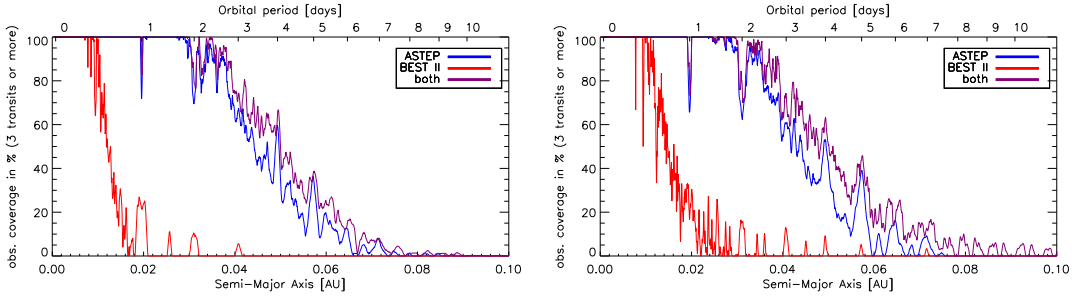

(a) ASTEP-Exo2 (b) ASTEP-Exo3

Figure 10.14: Phase coverage p_{c3} of three or more transits for the two ASTEP fields as a function of possible planetary orbits. The coverage is shown in *red* for the BEST II data, and in *blue* for ASTEP. The *violet* line gives the orbital coverage that is obtained using the joint time series. See Figure 10.3 for a graphical representation of the corresponding observational window functions.

10.4 Detection Yield II – Antarctica and Chile

In the previous section, the detection yield of ASTEP and BEST II has been analyzed and compared. However, the conclusions are strongly related to the underlying data sets ASTEP-Exo2 and ASTEP-Exo3 and the two telescopes that obtained them.

In order to compare the two sites in terms of their potential for transit search in a more general context, impacts on the detection yield should possibly be abstracted from the actual instrumental setup and observing strategy. In particular, this can include differences in the angular resolution and/or FOV, integration time, time sampling, target field characteristics, and observing strategy.

In this section, systematic differences that can be quantified are removed, and the yield analysis is repeated; in contrast to the previous section, this section rather aims at a comparison between the two sites than between the present setup of ASTEP 400 and BEST II.

Photometric Precision (General Case)

The photometric precision largely depends on the amount of light collected within a period of time. As such, it depends upon the exposure time, telescope aperture, CCD sensitivity, and cadence between two adjacent measurements. The resulting systematic difference in photometric precision is included in two scenarios, which are summarized in Table 10.7 and described in the following text.

Scenario 1. Each data set is binned into intervals of the same duration for both telescopes; the value was set to $\Delta t_{\mathrm{bin}}^{(1)} = 30\,\mathrm{min}$ in order to keep a reasonable sampling of $\gtrsim 3$ data points during a transit. Data binned at $\Delta t_{\mathrm{bin}}^{(1)}$ allows to study the detection yield of ASTEP 400 and BEST II on an equal time sampling that is typical for a transit.

Scenario 2. The systematic bias of ASTEP collecting more light than BEST II due to its larger aperture and smaller readout time is taken into account. The binning is adjusted such that ASTEP achieves the same photon noise level σ_{phot} as BEST II within $\Delta t_{\mathrm{bin}}^{(1)} = 30\,\mathrm{min}$, i.e., a changed binning interval $\Delta t_{\mathrm{bin}}^{(2)}$ is applied *only*

Table 10.7: Binning parameters for ASTEP-Exo2 and ASTEP-Exo3.

Binning	ASTEP-Exo2		ASTEP-Exo3	
	ASTEP	BEST II	ASTEP	BEST II
Scenario 1 – same $\Delta t_{\rm bin}$	30 min; 15.1	30 min; 6.1	30 min; 10.4	30 min; 4.8
Scenario 2 – same $\sigma_{\rm phot}$	9.0 min; 4.5	30 min; 6.1	6.1 min; 2.7	30 min; 4.8

Notes. The table gives the binning interval $\Delta t_{\rm bin}$ and the average number $\overline{n}_{\rm bin}$ of measurements per bin for each data set and investigated scenario (see text).

to ASTEP. It is calculated as follows: If $n_{\rm bin}$ data points are binned, the number of detected electrons is

$$N_e = n_{\rm bin} \cdot f \cdot g \ , \tag{10.11}$$

whereby g denotes the gain factor (in e^-/ADU) and f the flux of a single exposure measured in ADU. The value N_e determines the photon noise and is directly accessible from the photometry. Using Equations (5.8), (5.21), and $\sigma_{\rm phot} = 1/\sqrt{N_e}$, the condition $\sigma^A_{\rm phot} = \sigma^B_{\rm phot}$ is obtained, if

$$n^A_{\rm bin} = \frac{g_B}{g_A} \cdot 10^{0.4(\delta m_B - \delta m_A)} \cdot n^B_{\rm bin} \, , \tag{10.12}$$

whereby δm denotes the magnitude adjustment (Section 5.2.3) and the index A/B identifies ASTEP/BEST II parameters. They yield $n^A_{\rm bin} = 0.74\, n^B_{\rm bin}$ for field ASTEP-Exo2, and $n^A_{\rm bin} = 0.55\, n^B_{\rm bin}$ for ASTEP-Exo3, respectively. These ratios are realized using an ASTEP binning interval of $\Delta t^{(2)}_{\rm bin} = 9.0\,$min for ASTEP-Exo2, and 6.1 min for ASTEP-Exo3, respectively.[3]

For each scenario, the number $N_{\rm S/N}$ of light curves suitable for transit search is calculated as a function of planetary radius $r_{\rm p0}$. The results are compared based on the fraction $f_{\rm S/N} = N_{\rm S/N}/N_\star$, since the stellar count $N_\star$ itself depends on the size of the FOV; as such, it is driven by the project design and not a site characteristic. Furthermore, the two angular resolutions yield a different degree of contamination (Section 10.2.3); however, its influence on the results is largely reduced by excluding stars from the simulation that deviate by more than 0.5 mag from GSC2.2 (see Section 4.4).

Figure 10.15 displays the results in each target field and binning scenario. For ASTEP-Exo2 (Figure 10.15a), BEST II data binned to 30 min yield values of $f_{\rm S/N}$ that are 36–66% larger (for radii $r_{\rm p0} \geq 0.4\, r_J$) compared to ASTEP, whereas ASTEP yields 80–146% larger fractions for $r_{\rm p0} \leq 0.3\, r_J$. However, about 10^7 stars would have to be monitored in order to obtain a reasonable detection probability in this regime, i.e., the better performance of ASTEP is likely not to have any practical implication. If ASTEP data are binned to the same photon noise level, BEST II yields a better

[3] An alternative way to equalize the photon noise levels is to take the different characteristics (telescope size, exposure time, CCD gain) directly into account by using Equation (10.7). This approach yields comparable results ($n^A_{\rm bin} = 0.67\, n^B_{\rm bin}$ for field ASTEP-Exo2, and $n^A_{\rm bin} = 0.50\, n^B_{\rm bin}$ for ASTEP-Exo3, respectively). However, it does not reflect any additional instrumental effects (e.g., due to differences in the optics), whereas the chosen approach *directly relates to the photometric signal* and is thus considered to yield a more accurate comparison.

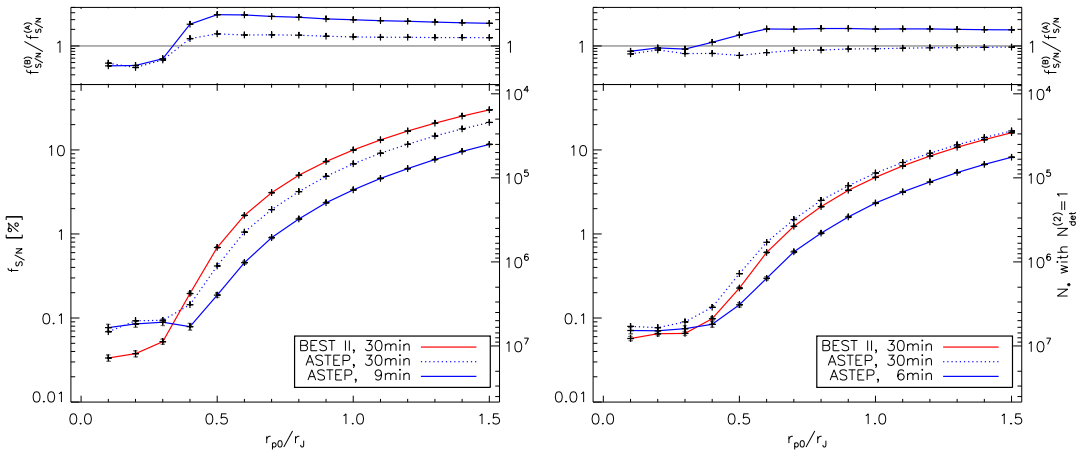

(a) ASTEP-Exo2 (b) ASTEP-Exo3

Figure 10.15: Fraction $f_{\mathrm{S/N}}(r_{\mathrm{p0}})$ in fields (a) ASTEP-Exo2 and (b) ASTEP-Exo3 of light curves that provide a photometric noise σ sufficient for the detection of a transit signal (Equation (10.9); for details on the simulation, see Section 4.4). The results are calculated as a function of the tested planetary radius r_{p0} and shown for the two binned scenarios, i.e., (1) ASTEP 400 *(blue, dotted)* and BEST II data *(red)* each binned to 30 min intervals, and (2) ASTEP 400 data *(blue, solid)* binned to the same photon noise level σ_{phot} as the corresponding BEST II data set *(red)*. The upper panels display the corresponding ratios $f^{B}_{\mathrm{S/N}}/f^{A}_{\mathrm{S/N}}$ for a direct comparison. In addition, $f_{\mathrm{S/N}}$ (*left* y-axis) is converted to the total number of stars $N_\star$ (*right* y-axis) that have to be observed for one detection (i.e., using Equations (10.8) and (10.10) with $N_{\mathrm{det}} = 1$, an average value of $f_t = 0.05$ and the more optimistic planet fraction $f^{(2)}_{p0} = 0.43\%$ (Cumming et al. 2008)).

fraction $f_{\mathrm{S/N}}$ than ASTEP for large planets (by 148–269% larger for $r_{\mathrm{p0}} \geq 0.4\,r_J$), while ASTEP still obtains better statistics for smaller planets ($f_{\mathrm{S/N}}$ by 70–130% larger than BEST II for $r_{\mathrm{p0}} \leq 0.3\,r_J$).

For ASTEP-Exo3 (Figure 10.15b), the ASTEP $f_{\mathrm{S/N}}$ is up to 48% better than BEST II if both data sets are binned to 30 min. However, if the comparison is made at the same photon noise level, the fraction $f_{\mathrm{S/N}}$ is up to 107% higher for BEST II, whereas ASTEP again only yields a larger fraction for very small radii (by 9–25% for $r_{\mathrm{p0}} \leq 0.3\,r_J$).

Duty Cycle (General Case)

In addition to the photometric precision, the transit detection efficiency is constrained by the observational duty cycle. Section 10.3 has already shown that the actual observing strategy of ASTEP and BEST II yields an increase of 12–18% in the estimated number of detections if the data sets of ASTEP-Exo2 and ASTEP-Exo3 are combined. In this section, the prospects of joint observations are examined further in a case study; its aim is to suggest an optimized observing strategy for future campaigns. As in Section 10.3, the timing parameter f_t (Equation (4.6)) is used to obtain a quantitative comparison.

The cases studied are shown in Figure 10.16 and indicated with letters (a)–(l) both in the figure and the text. They include four scenarios that are based on actual

Table 10.8: Impact of additional BEST II observations on the ASTEP planet detection yield.

Field	Real ASTEP time series			
	A	A & B	A & B (shifted)	A & B (max)
ASTEP-Exo2	**(a) 0.04630**	(b) 0.05189 (+12%)	(c) 0.05223 (+13%)	(d) 0.06144 (+33%)
ASTEP-Exo3	**(e) 0.04381**	(f) 0.05173 (+18%)	(g) 0.05207 (+19%)	(h) 0.05527 (+26%)
Month	**Maximal time series**			
		A (max)	A (max) & B (max)	
July		**(i) 0.08629**	(j) 0.09650 (+12%)	
August		**(k) 0.07198**	(l) 0.08563 (+19%)	

Notes. For each case studied, the table gives the timing fraction f_t (Equation (4.6)) that is proportional to the planet detection yield (Equation (4.4)). Cases include ASTEP 400 (A) and BEST II (B) time series; see the text for a detailed description. In addition, it shows the relative improvement of f_t compared to the reference case *(bold)* of ASTEP observations alone. Note that f_t could yield at most 0.10085 within the evaluated range of orbital periods (i.e., Equation (4.6) with $p_{c3}(p) = 1$, $p_0 = 1^d$, $p_1 = 10^d$).

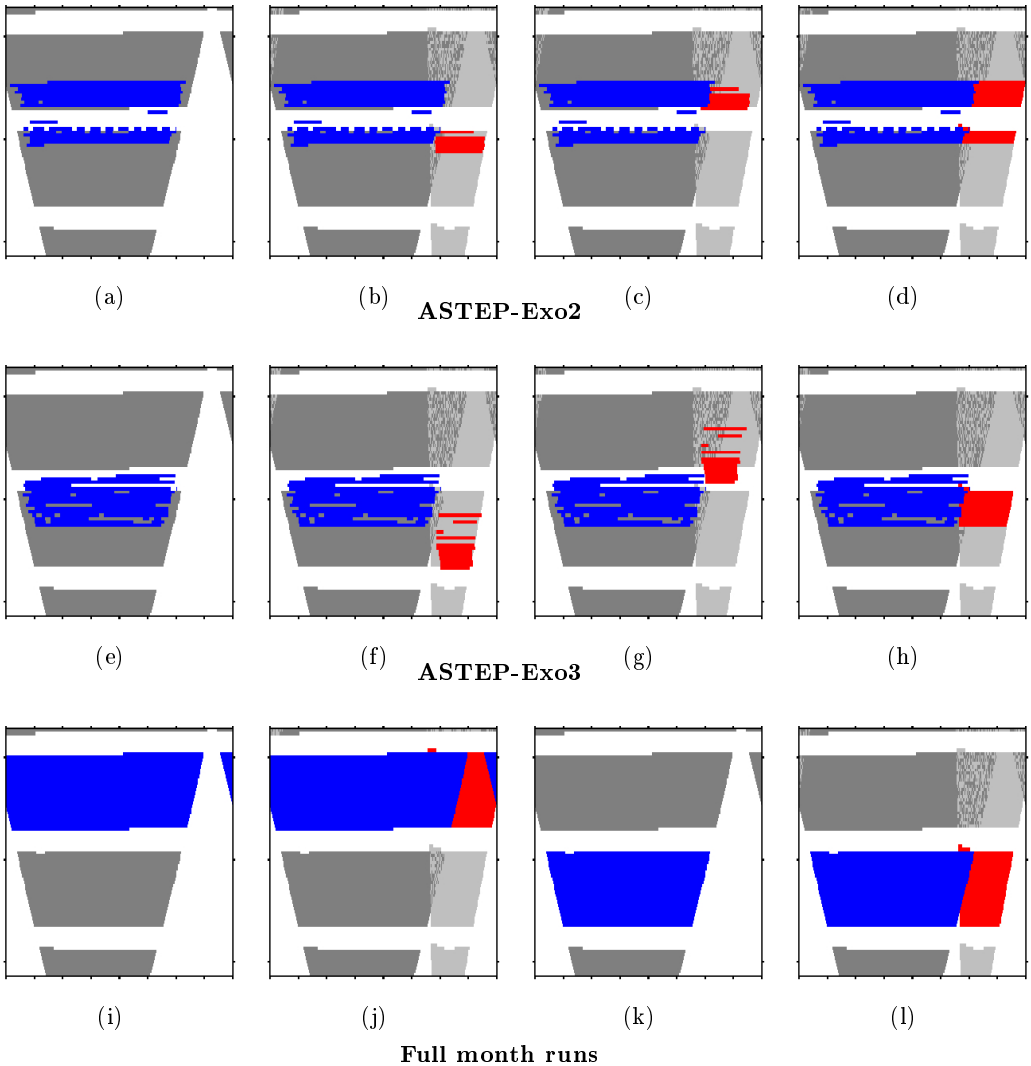

Figure 10.16: Case study for joint observations of ASTEP 400 and BEST II, based on actual observations of field ASTEP-Exo2 (a–d), ASTEP-Exo3 (e–h), and fully hypothetical time series (i–l). Axes and colors as in Figure 10.3. For case descriptions, see the text.

ASTEP observing dates of target field ASTEP-Exo2 (a–d), four on those of ASTEP-Exo3 (e–h), and four fully hypothetical scenarios (i–l). A brief description of all cases is given in the following list.

(a, e) First, they include the time series as obtained by ASTEP 400 in the 2010 season for the fields ASTEP-Exo2 (a) and ASTEP-Exo3 (e), which are used as a minimum reference for comparison.

(b, f) Second, joint observations of ASTEP 400 and BEST II are reviewed, i.e., as already discussed in Section 10.3.

(c, g) Third, BEST II time series have been shifted back in time by 1, 2, ... days in order to investigate how much could be gained from an improved scheduling of joint observations; the case with the largest value f_t is shown for each field.

(d, h) Fourth, the maximum increase that BEST II observations could possibly yield is evaluated by assuming an optimal duty cycle in Chile during nights with observations from Antarctica.

(i–l) Finally, ASTEP observations are also replaced by an optimal time series that could be obtained between two full Moons, i.e., about twice as long as the actual observations. Cases cover the months of July (i–j) and August 2010 (k–l), whereby (i) and (k) only include observations from Antarctica, and (j) and (l) complement these with an optimal duty cycle from Chile.

The impact of these different scenarios on the planet detection yield is quantified in Table 10.8. For each case, it gives the timing factor f_t and the relative increase of the ASTEP detection yield due to additional BEST II observations.

The actual ASTEP observations of fields ASTEP-Exo2 and ASTEP-Exo3 alone yield timing factors f_t of 0.044–0.046 (a and e). Comparable values are typically obtained from a mid-latitude site like Chile during a whole observing season covering 30–40 observing nights (cf. Section 4, in particular Tables 4.1 and 4.3). From Antarctica, however, the same performance was achieved within short runs of 2–3 weeks and only 16–17 nights (Table 10.2). If BEST II data are added, the factor f_t increases by 12–18% to 0.052 for both fields (b and f). The slight offset between ASTEP and BEST II time series seems to have a negligible impact, as a shift would at most have increased f_t by 0.00034 (c and g). However, if more observations were taken from Chile and scheduled optimally with ASTEP (d and h), f_t could be raised significantly up to 0.055-0.061, i.e., the detection yield could be increased by 26–33% compared to ASTEP alone.

A relative increase of 12–19% due to additional observations from Chile would even be encountered if ASTEP and BEST II observed the two fields continuously during one month (cases i and l): the factor f_t raises from 0.086 to 0.097 for July, and from 0.072 to 0.086 for August, respectively. As expected, the impact of complementary BEST II observations increases with the length of observing interruptions experienced during noon in Antarctica.

In addition, the two hypothetical scenarios allow to evaluate whether the ASTEP observing strategy to observe each field for approximately two weeks is advantageous, or, whether the duration should rather be extended. A comparison between cases (a) and (i) for ASTEP-Exo2, and between (e) and (k) for ASTEP-Exo3, respectively, shows, that a doubling of the time series only raises f_t by 64–86%. The smaller relative gain is due to the decreasing geometric probability for a transit geometry with increasing orbital period (Equation (4.7)). To maximize the detection yield in the evaluated period range of 1–10 days, it is thus better to double the number of surveyed stars by observing two fields, each yielding $f_t \approx 0.045$ within two weeks (or better, $f_t \approx 0.055$ together with BEST II).

10.5 Summary and Discussion

This chapter presented joint observations obtained with ASTEP 400 and BEST II in 2010. Their comparison aims at a first quantitative evaluation of the potential for transit search at Dome C that is solely based on real photometric time series. Particular attention was paid to the photometric precision and observational phase coverage, which are both expected to yield advantageous conditions for transit searches in Antarctica.

After the DLR photometric pipeline had been adapted for reduction of ASTEP data, joint observations of the known planet WASP-18b (Hellier et al. 2009) were reduced as a first test case. The transit event is clearly detected by both telescopes, but sampled at a much higher photometric precision with ASTEP (0.44 mmag compared to 1.9 mmag with BEST II during a single event). The whole data set on WASP-18b is currently being reduced and analyzed scientifically by the ASTEP team.

Out of five target fields observed for transit search with ASTEP 400 in its first year of operation, the two fields ASTEP-Exo2 and ASTEP-Exo3 were monitored together with BEST II during July and August 2010. For these, ASTEP measurements span 26 nights and include 94,965 stars, while BEST II obtained 224,552 light curves during 18 nights. Joint observations are available for 58,822 stars, the main limitation being that BEST II observations did not cover the ASTEP-Exo2 field optimally.

A first analysis of data from both fields and telescopes showed that the photometric quality is excellent, reaching mmag-precision for bright stars from both Antarctica and Chile over each respective observing campaign. A night-by-night analysis shows that the limiting noise component on average reaches 2–3 mmag in Chile, while 1.5–2.0 mmag are typically encountered at Dome C. The best night in Antarctica had an exceptionally good precision of 0.69 mmag.

In order to extend the observational duty cycle, light curves of ASTEP 400 and BEST II were combined. A case-by-case comparison showed that the photometric systems compare well, i.e., the brightness differences show only a small color dependence. More important is crowding, which can introduce systematic differences in

absolute and relative brightness measurements between the two systems. The effect becomes important for stars of $m \geq 15$ mag, while measurements for bright stars are generally in very good agreement.

Transit signals were searched for in each data set using BLS, yielding 9,902 transit-like signals that were inspected visually. Overall, ten planetary candidates could be identified. After a thorough analysis, one was rated priority 1, five were given priority 3, and four were rejected as false alarms. While no final candidate was found in BEST II data alone, the combination of ASTEP 400 and BEST II data significantly improved the findings compared to the results obtained with ASTEP data alone. If confirmed, all candidates would most likely belong to the class of hot Jupiters.

Using the photometric noise budget, observational coverage and a modeled stellar population, the detection yield was estimated for each field and data set. Depending on which literature value is used for the frequency of hot Jupiters, 0.10–0.41 findings are expected, which compares well with the number of identified candidates (assuming that one of 10–20 candidates is confirmed through follow-up observations).

Finally, the same model was applied to compare the transit search performance from Chile and Antarctica more generally and as a function of planetary radii, and to assess the potential of a combination of both sites.

If data are binned to equal time intervals of 30 min, ASTEP yields a larger fraction of light curves suitable for transit search for all tested radii in field ASTEP-Exo3, and slightly smaller values than BEST II in ASTEP-Exo2. Thus, the performance of the two telescopes is well comparable. However, if systematic biases due to different integration times, time samplings, and telescope apertures are taken into account, data from Chile show a significantly larger fraction of suitable light curves for almost all planetary radii tested.

The duty cycle obtained with ASTEP within approximately two weeks in each field yields a detection efficiency comparable to a typical whole observing season with BEST II. If BEST II observations are added, the yield increases by 12–18%. A case study has shown that a similar relative increase is even encountered if the duty cycle of ASTEP was extended further, and could be increased up to 26–33% if BEST II observations could be obtained in parallel to each night with observations from Antarctica.

Discussion

The main focus of this chapter are the prospects of Dome C for transit search. In particular, it addressed the question as to whether advantages expected by previous studies concerning the photometric quality and observational duty cycle can actually be confirmed in a transit survey using real photometric time series.

A comparison of WASP-18b transit observations and the minimum noise level encountered during individual nights for the fields ASTEP-Exo2 and ASTEP-Exo3

indicate exceptional photometric conditions at Dome C, and a significant advantage of ASTEP 400 over BEST II. However, if the data of individual nights are combined and binned, the overall noise budget for the two fields shows comparable or better detection statistics from Chile. Thus, given the data at hand, an advantage for transit search from Dome C due to a better photometric quality could not be confirmed.

However, although the comparison was set up as homogeneously as possible using the same routines for reduction and analysis, it still is influenced by systematic effects that could not be quantified and/or removed. For example, ASTEP light curves include about ten times more scientific frames and span significantly more nights, which might affect the photometric noise budget. Moreover, the two systems include different optical setups that might require further optimization of the data acquisition and/or reduction. For BEST II, this process has already advanced through several years of operation, while ASTEP has obtained these data sets in its first observing season. For example, Abe et al. (2012) recently found the sky-concentration effect (e.g., Andersen et al. 1995) to be of importance for ASTEP 400 flat fielding. A detailed comparison of each step in the data acquisition and reduction would thus be necessary to identify reasons for the difference in the final photometric quality, and to improve the detection efficiency further. The model used in this work is readily available to evaluate the effect on the detection yield quantitatively in any such new reduction.

In contrast to the photometric quality, the long polar night yields a *clear* advantage for transit search in Antarctica. Within two weeks of observations, ASTEP yields a detection for planets at short periods that can only be achieved during a whole season from Chile. In particular, the analysis in this chapter has shown that network observations can yield a significant increase in the detection yield compared to time series obtained from Antarctica alone. It has been proven that light curves of ASTEP and BEST II can be combined, and that a transit search yields more significant signals when using the combined data sets.

Outlook

In addition to the comparison between the two excellent sites in Chile and Antarctica, the recorded photometric data sets yield valuable astrophysical information. The scientific analysis is ongoing, and the next steps include in particular:

- A full analysis of the ASTEP WASP-18 and WASP-19 data sets for secondary eclipses and phase variations. This was not within the scope of this thesis and will be concluded shortly by the ASTEP team (Abe et al. 2012).

- Further observations of the planetary candidates presented in this thesis. This includes standard follow-up procedures in analogy to the BEST II candidates presented in this work (see Section 8.5), i.e., reconnaissance spectroscopy, high-resolution photometry, and radial velocity confirmation. The first step, however, includes photometric observations during predicted transit times in order to constrain the ephemerides (uncertainties have already grown to a few hours

due to the relatively short time range of observations in 2010), and to improve the parameters obtained from the light curve. Measurements have already been obtained with BEST II and ASTEP 400 in 2012, and spectroscopic observations are being planned.

- The excellent photometric quality of the ASTEP-Exo2 and ASTEP-Exo3 data sets allows for a precise characterization of stellar variability in these fields, which was not part of this work. However, the time series are expected to contain a large number of yet undetected variable stars, which should be searched for and analyzed in future studies.

11 Summary and Discussion

This work focuses on a field survey for transiting exoplanets, a quantitative comparison between photometric data from Chile and Antarctica, and an analysis of stellar variability in several target fields (cf. scientific objectives in Section 1.4.1).

This chapter concludes the thesis with a summary and discussion of its scientific results. First, Section 11.1 describes the method improvements that were necessary to achieve its objectives. Section 11.2 then focuses on the potential for transit searches from Dome C, Antarctica. Finally, Section 11.3 gives a résumé of the new planetary candidates and variable stars found by this work.

Each section briefly summarizes the results, discusses them in the relevant scientific context, and gives an outlook to future work.

11.1 Method Improvements

The scientific results of this work could not have been obtained without significant improvements regarding both the acquisition and scientific analysis of observational data, which are described in the following sections: Section 11.1.1 focuses on observations and their reduction, while Sections 11.1.2 and 11.1.3 present improvements regarding the search for transiting planets and stellar variability, respectively.

11.1.1 Observations and Data Reduction

All results of this work are related to data obtained with the Berlin Exoplanet Search Telescope II (BEST II), which is operated by the DLR Institute of Planetary Research and primarily used for follow-up observations of planetary candidates detected by the CoRoT satellite (Deeg et al. 2009).

The implementation phase of BEST II (Kabath 2009) had been concluded before this work began. Up to now, the system continues to work very reliably and autonomously, which enabled a large amount of photometric data to be collected with BEST II for this thesis. Concerning the hardware of the telescope, two major adjustments were performed during the course of this work: First, the **pointing accuracy** was increased from $\sim 7'$ to 10–15″, so that now significantly more stars in a given field can be fully covered with observations over a whole season. Second, a **new instrument** (CCD camera with filters and focus unit) was installed in Chile. However, since all scientific results presented here are based on observations obtained with the original instrument, only future studies will benefit from this second improvement (see outlook in Section 11.1.4).

In addition to that, the DLR photometric **pipeline** was significantly updated. The most important improvements are:

- The calibration procedures have been rebuilt completely for a more standardized calibration on a nightly basis that can also be executed on-site.
- The quality assessment has been improved at various steps through a condensed presentation of more and/or more objective selection criteria. For example, the most important properties of *every* recorded frame are easily reviewed by the observer during calibration, and images with the best seeing are automatically preselected for image subtraction.
- All parts of the pipeline have been reviewed to allow for flexible data reduction for projects other than BEST/BEST II. Three ASTEP data sets have been reduced, and the pipeline can quickly be adapted to any other project.
- Both an automatic rejection of bad frames and an adaptation of the SysRem detrending algorithm (Tamuz et al. 2005) to BEST II data yield a significant noise reduction, especially in the important range of $\sigma \lesssim 1\%$.

These improvements were a prerequisite for obtaining the scientific results presented here. In particular, they yield an improved photometric quality, which enhances the sensitivity for detecting transiting planets as well as stellar variability. However, the improved performance of BEST II also yields advantages beyond the immediate scientific focus of this thesis. For example, the new pipeline enhances the follow-up process of CoRoT candidates: Since the adjusted calibration is now able to work on-site and immediately after the observations, the response time within the follow-up procedure is reduced significantly. In particular, this enabled BEST II to contribute to the confirmation process of CoRoT-17b (Csizmadia et al. 2011) and CoRoT-24b (Alonso et al. 2012) on a short notice.

11.1.2 Scientific Analysis – Transit Search

During 2009/2010, the first BEST II transit survey was planned and executed: The three target fields F17, F18, and F19 have been observed for a total of 138 nights. They have been selected within this work based on a quantitative weighting of the field visibility, photometric quality due to varying airmass, and the number of suitable target stars. To select F17 and F18, only the first two criteria have been applied using existing procedures (Fruth 2008; Rauer et al. 2008a, b). The selection process for F19 was complemented as part of this thesis with a target count simulation based on the Besançon model of the Galaxy (Robin et al. 2003).

Using a simulation that assesses the detection yield based on the observational coverage, photometric quality, stellar content, and estimated fraction of transiting planets, an overall yield of 0.23–1.00 hot Jupiter detections is expected in F17–F19. More than half of these (i.e., 0.14–0.62 detections) are expected in target field F19. For comparison, the detection yield has also been estimated for a typical BEST II data set that was observed in support of the CoRoT mission and analyzed

for transiting planets before this work: In the two LRa02 fields (first reduction), the simulated yield was found to be as low as 0.01–0.06 planets per field.

For the first time within the BEST/BEST II project, the large observational data sets obtained for the selected fields (in particular F19) can be considered as providing a reasonable chance for finding a transiting extrasolar planet.

This improvement of the detection yield results from a consequent optimization of BEST II observations and its data pipeline for transit search. In particular, it can be assigned to the following improvements achieved:

- The three new target fields provide a **sufficient observational coverage** for transiting planets with short orbital periods (approx. 1–2 days). F17 and F18 have been monitored for a period of time comparable to earlier campaigns of BEST II (40 and 28 nights, respectively). However, F19 was observed for 70 nights, contains more data points than any other BEST/BEST II data set, and, hence, covers significantly longer orbital periods (up to 3–4 days).

- The inclusion of the stellar distribution significantly improved the **target field selection**: With 11,681 stars measured to at least 10 mmag precision, F19 includes far more high-precision light curves than any other BEST II data set recorded before, and 3.4 times more than F17 and F18 together. Thus, the target count simulation is considered an important and mandatory improvement for transit search with BEST II.

- All three data sets F17–F19 exhibit an **excellent photometric quality** ($\sigma \approx$ 3 mmag for the brightest stars over a whole season). For the observations of the CoRoT field LRa02 that were *reanalyzed* within this work, the detection yield could be compared directly with an earlier data reduction: It is estimated to increase by a factor of 2–4 due to the improved photometric precision.

- The **transit search** part of the pipeline, which is based on the *Box-Fitting Least Squares* algorithm (BLS; Kovács et al. 2002), was validated for BEST II. The analysis was based on artificial transits of varying depth, period, and phase that were inserted into the largest BEST II data set (F19) and subsequently attempted to be recovered using BLS. The results prove that BEST II time series and the corresponding transit search procedures yield a detection efficiency that is consistent with the system specifications. Furthermore, they show the clear need for detrending the data prior to transit search, which was implemented within this work through adapting the SysRem algorithm (Tamuz et al. 2005) to BEST II/ASTEP data.

Altogether, the optimized BEST II system, its excellent site, and a sophisticated reduction pipeline place its sensitivity among the best ground-based transit surveys: The estimated detection yield *per star* agrees well with that of the most successful transit survey, SuperWASP (Pollacco et al. 2006), which in average finds one planet in 430,000 light curves (Norton et al. 2011). Thus, the photometric quality, duty cycle, data reduction, and transit search procedures of this

study can be considered highly competitive for extrasolar planet searching. Large differences exist, however, in the number of stars surveyed. Together with the actual detections of this work, this issue will be put into perspective for future BEST II transit surveys in Section 11.3.1.

11.1.3 Scientific Analysis – Stellar Variability

Furthermore, the methods to analyze large photometric data sets for stellar variability were investigated in detail.

The Stetson J index (Stetson 1996) is used to select potentially variable stars within the BEST/BEST II (e.g., Pasternacki et al. 2011) and other projects (e.g., Zhang et al. 2003; Pepper and Burke 2006). However, this approach is highly affected by systematic variability: If the J index is used to (pre)select variable stars in BEST II data, it yields a very large ($\sim 98\%$) fraction of false positives. The analysis of variance statistic (AoV; Schwarzenberg-Czerny 1996), used within BEST/BEST II and many other projects (e.g., Bakos et al. 2004; Soszyński et al. 2008; Maciejewski et al. 2011) to search for periodic signals in astronomical time series, is also prone to systematic trends in the data; it is particularly biased to find periods of one day or multiples thereof.

Within this work, an in-depth analysis of stellar variability in the BEST II LRa02 data set was used to improve the search for stellar variability significantly. Together with the results of Kabath et al. (2009a), a visual inspection of all light curves in the field laid the basis to test and train different search methods. Best results were achieved using an average master power spectrum, which is used to flag systematic variability that is present in many light curves. The new method separates real variability from non-variable stars efficiently, i.e., using the new procedure, about ten times less light curves need to be inspected visually. It was applied successfully to five photometric data sets within this work, and has recently been published (Fruth et al. 2012).

The search for stellar variability has been validated through carefully comparing the scientific results with previous studies. In the CoRoT field LRa02, 262 variables from this work were compared to satellite data, and the results were found to comply: For 73% of them, the determined periods agree within 1%, and for 75% of them, the two classifications are consistent. After a visual inspection of light curves from both data sets, the BEST II classification was even found to be more realistic than the automatic CoRoT classification for 26 stars.

For 24 variable stars known from the literature within all investigated fields, the periods and classifications agree with the results of this work. For 19 variables identified with BEST/BEST II in previous studies (Kabath et al. 2007, 2009a), the ephemerides and/or classifications were improved.

Altogether, the findings of this work are in very good agreement with the results of other studies, thus confirming the integrity of the new detections presented here. In particular, the comparison with first-class data from

the CoRoT satellite reveals an excellent performance of BEST II within its magnitude range and photometric noise limit. **Thus, both BEST II and the new method for variable star search are efficient, state-of-the-art instruments to detect stellar variability from the ground.**

11.1.4 Outlook

Irrespective of the future observing strategy of BEST II, the methods used and/or improved within this thesis will be helpful for future work:

- A **new instrument** (consisting of an upgraded CCD camera, filter wheel, and focus unit) was installed in Chile. Current and future observations benefit from a significantly shorter readout time (yielding an improved photometric precision and/or time sampling), standard photometric filters, and an automatic focus. The new filters enable BEST II to obtain photometric measurements in standardized passbands, which has opened up a large range of new scientific applications. For example, BEST II has recently started to gather data for a study of active galactic nuclei using photometric reverberation mapping (Haas et al. 2011), which would not have been possible without the new filters.

- The **DLR photometric pipeline** was adjusted to the reduction of photometric data from projects other than BEST/BEST II, and it has already demonstrated its capability to reduce and analyze data from ASTEP, TEST, and VYSOS 6. Moreover, it is currently being merged with software from SuperWASP to a package for the new NGTS project (Chazelas et al. 2012). In the near future, some of the routines are thus expected to contribute to the next generation of transit search projects from ground.

- The **new method to search for stellar variability** presented in this study can be applied flexibly to any other photometric survey. As discussed in Chapter 7, the problem of false positives due to diurnal systematics is also encountered by several other ground-based projects. It may additionally yield an improvement for the analysis of satellite data for stellar variability, since the new method makes no preliminary assumption on the reason for systematic variation.

11.2 Transit Search from Antarctica

While the Chilean site of BEST II provides an excellent environment for transit search, the Antarctic continent has recently been identified as possibly providing even better observational conditions. In order to compare the potential of transit search between Chile and Antarctica, observations have been obtained by BEST II in parallel with ASTEP 400 (Dome C) as part of this work: In 2010, BEST II monitored the transiting planet WASP-18b for 19 nights (ASTEP for 66 nights), and the two fields ASTEP-Exo2 and ASTEP-Exo3 for a total of 18 nights (ASTEP for 26 nights).

Photometric time series from ASTEP were analyzed and compared with BEST II. As such, this thesis provides a first and direct comparison of the transit detection yield between Antarctica and an excellent mid-latitude site that is *solely based on real photometric time series*. The analysis was focused on the photometric quality and the observational duty cycle, which are both expected to be superior in Antarctica.

Concerning the **photometric quality**, it showed that ASTEP can reach sub-mmag precision ($\sim$0.5–1 mmag) during very good individual nights or when monitoring a particular event such as the transit of WASP-18b, while BEST II typically achieves $\sim$2–3 mmag. However, when all light curves of a whole observing season are compared and differences between the two systems are accounted for, no advantage could be identified for the Antarctic site. It is thus expected that systematic effects still make up the main limitation to the photometric precision during the first observing season of ASTEP 400. Whether these are intrinsic characteristics of the system or could be decreased further should be addressed in a future study through analyzing carefully each step in the data acquisition and calibration.

Concerning the **duty cycle**, it was shown that two weeks of ASTEP observations yield a comparable detection efficiency for short-period planets like BEST II during a whole season. In addition, the yield can further be increased significantly (up to $\sim$30%), if observations are obtained with both instruments. This work has shown that the combination of light curves from both surveys is feasible in practice: The photometric systems compare very well, and ASTEP time series were extended with BEST II data for 58,822 stars in the two fields ASTEP-Exo2 and ASTEP-Exo3.

A transit search in these fields yielded six planetary candidates. Some of these (including the most promising case) could only be identified by combining data from ASTEP and BEST II, which again underlines the potential of such a joint approach.

Outlook

Due to its excellent photometric quality and observational duty cycle, Antarctica provides an unique environment to search for transiting extrasolar planets. **Since the combination of photometric data of BEST II and ASTEP was proven to be both advantageous and feasible within the course of this study, further joint observational campaigns could be planned for the future.** For the detection of hot Jupiters, these would optimally include several target fields which are well observable from both Chile and Dome C, coordinated to be observed in parallel for about two weeks each. The procedures of this work are readily available for reducing and combining data from both projects.

11.3 New Detections

New planetary candidates and variable stars are the prime scientific results of this thesis. They are summarized in the following Sections 11.3.1 and 11.3.2, respectively.

11.3.1 Planetary Transits

The main objective of this thesis was to gain knowledge in the field of extrasolar planets through the detection of new systems. For that purpose, a dedicated transit search program was set up for BEST II, and new observational data has been analyzed for transiting extrasolar planets.

Within three target fields, 115,740 low-noise light curves ($\sigma \leq 0.05\,\mathrm{mag}$) were acquired and searched for transit-like signals. Out of these, 41 planetary candidates have been identified and analyzed in detail for causes other than a transiting planet. After these tests, 14 candidates have been selected as promising. Their parameters have been determined from light curve modeling, and they have been ranked with priorities for further observations.

For eleven candidates in target field F19, the host stars have been characterized via low resolution spectroscopy using the AAOmega instrument (Smith et al. 2004) in early 2012. Out of these, three are identified as giants (for which the transit is caused by a stellar companion), two are subgiants, one is either a subgiant or a dwarf star, and five are located at the main sequence. Thus, eight out of the eleven candidates in F19 remain good planetary candidates.

In addition, BEST II and ASTEP 400 together performed a transit survey in two target fields. It yielded a total 140,286 low-noise light curves (27,240 of them with measurements of both telescopes) that have been reduced and analyzed for transiting planets within this work. An initial list of ten planetary candidates was then subject to the same series of tests as for the BEST II survey, which finally left six good candidates remaining.

In total, 20 planetary candidates could be identified within this work (14 with BEST II, four with ASTEP 400 and BEST II, and two with ASTEP 400 data). These numbers are in good agreement with the detection yield estimated from the photometric quality of the data, the observational duty cycle, and the expected number of transiting hot Jupiters in each field. Moreover, the large number of identified candidates implies a significant chance of finding at least one planet, if one considers a typical candidate-to-planet-ratio as encountered in other surveys. However, further observations are needed in order to finally prove or disprove their planetary nature.

Current Status

Follow-up observations are complicated due to the faintness of the candidates, which requires large telescopes and/or long integration times, so that the process is prioritized depending on candidate rankings. While the host stars of eleven candidates in field F19 have already been characterized spectroscopically (yielding the rejection of three candidates around giant stars), such an analysis is still to be obtained for the remaining nine. Moreover, most candidates have been detected with a small SNR, so that additional photometry is required to confirm the signal, and to improve derived parameters. Follow-up photometry is also required to limit the uncertainties

in the ephemerides with proceeding time, and to confirm the signal on target with better angular resolution. Candidates within the two fields F19 and ASTEP-Exo2 have been re-observed with BEST II and ASTEP for this purpose in autumn 2012 and will be analyzed once the data arrive in Europe in spring 2013. Finally, high-resolution spectroscopy is required to exclude false alarm scenarios that could not be ruled out otherwise, and to finally confirm the planetary nature. The two most promising candidates of this work, F19_067715 and F19_083743, have recently been proposed for RV observations at the VLT in summer 2013 (ESO period 91).

Scientific Context

If confirmed, any of the candidates presented above will most likely be of the hot Jupiter type, and each new detection will improve the statistical sample. More planets are particularly useful to identify and/or refine correlations between planetary parameters (e.g., Enoch et al. 2012), such as, e.g., the relationship between planetary radii and their equilibrium temperature (Fortney et al. 2011; Laughlin et al. 2011; Enoch et al. 2012).

Depending on their detailed characterization (including, e.g., the density), which remains to be concluded via RV measurements, new detections can also help to understand a particular open scientific question, for example:

- The processes that account for the **low densities** of hot Jupiters such as CoRoT-5b (Rauer et al. 2009) are not well established yet. Explanations of their inflation usually include additional heating mechanisms, e.g., due to orbital circulization (Bodenheimer et al. 2001), transformation of incident radiation into kinetic energy in the planetary atmosphere (Guillot and Showman 2002), or Ohmic energy dissipation in the interior due to an interaction of the magnetic field with an ionized atmosphere (Batygin and Stevenson 2010). If a candidate of this work was found to be an inflated planet, its characteristics would help to constrain the most important mechanisms.

- Likewise, more hot Jupiters would help to identify the dominant processes that govern their **formation and evolution** (Morton and Johnson 2011), if their spin-orbit alignment could be determined through additional measurements of the Rossiter-McLaughlin effect.

- The list of candidates includes some very interesting host stars. In particular, the two most promising candidates are found around **intermediate-mass main sequence stars** (F1V and F5V, respectively), which are considered to host giant planets much more frequently than late-type stars (Johnson et al. 2007, 2010; Lovis and Mayor 2007; Kennedy and Kenyon 2008; Omiya et al. 2009). However, only six planetary systems with hot Jupiters around such stars are known to date.[1] The lack is largely attributed to a selection bias of the RV method against intermediate-mass dwarfs due to a small number of

[1] Extrasolar planets with $M_p \geq M_J$ and $p \leq 10^d$ around an early-type ($T_{\rm eff} \geq 6500\,{\rm K}$) main sequence star; based on *www.exoplanet.eu* (Schneider et al. 2011), state of 19th November 2012.

spectral lines, line broadening due to rotation, and stellar activity (see, e.g., Lagrange et al. 2009). Therefore, the detection of exoplanets around such stars *using the transit method* is crucial for extending our knowledge to all stellar types. A study of the detection yield within four CoRoT target fields recently also found indications for a lack of intermediate-mass planet hosts (Guenther et al. 2012), but the sample is still too small to draw robust conclusions. Thus, the candidates of this work can make a valuable contribution for testing the theoretical expectations on the frequency of hot Jupiters around such stars.

Outlook

While this work presented promising candidates for the first extrasolar planet of the BEST/BEST II project, follow-up observations need to continue in order to finally reject or confirm them. In addition, the search for yet unknown planets continues within the BEST/BEST II project and beyond.

However, the faintness of the candidates found in this study complicates the follow-up process significantly. Moreover, transiting planets around bright stars can be characterized much better through additional studies (e.g., their atmospheric composition through transit spectroscopy). **Based on improvements and lessons learned from this work, the BEST II observing strategy could be optimized for brighter targets.** A new target field, named F20, was chosen using the field selection method of this study and monitored during the observing season 2011/2012. Compared to F19, the exposure time was decreased from 300 s to 45 s in order to shift the photometric range by 2 mag towards brighter target stars (i.e., from $\sim$ 12–15 mag to 10–13 mag). Four sub-fields were observed alternately, so that the decreased number of bright stars was compensated by a four times larger FOV. For each sub-field, the time sampling could be kept approximately equal to F19 due to the shorter cadence of the new camera. These observations are currently being analyzed for transiting planets.

Given the specifications and latest results of BEST II and ASTEP, they meet the requirements to detect an extrasolar planet in the sense that they provide a sufficient observational coverage and photometric quality. However, their instrumental design only allows to monitor a few target fields per year at a sufficient time sampling and observational coverage, so that observations span a long time before a reasonable probability of detecting a transiting system is reached. In this respect, the multi-site and multi-telescope approach of highly successful projects is much more efficient. For example, the number of stars observed with SuperWASP, the most successful transit survey from ground, exceeds the BEST II survey presented here by almost two orders of magnitude. In the near future, the new NGTS project will follow the successful multi-telescope concept, and is expected to extend the ground-based detection limit down to Neptune-sized transiting planets and below (Chazelas et al. 2012). In this context, an extensive transit *search* for hot Jupiters using a single telescope like BEST II or ASTEP might not be considered competitive anymore; instead, these are likely to become more important for *dedicated* observations, e.g., to use the exquisite photometric quality for a follow-up of transit candidates from

the large surveys and further characterizations of already known planets.

11.3.2 Stellar Variability

Large photometric data sets acquired by surveys like BEST/BEST II not only allow to search for extrasolar planets, but also comprise a wealth of information about stellar variability in the target fields studied. Hence, they contribute to observational stellar astrophysics.

Within this work, data recorded within five target fields during 179 nights of BEST II observations were analyzed for stellar variability. In total, 329,660 stars have been investigated. Newly-discovered, clear stellar variability was identified in 2,791 cases, and an additional 806 stars are suspected to be variable. These new findings are presented in this work in a large catalog which comprises (where determinable), the period, amplitude, and classification of the variation. The new detections in the two LRa02 fields have already been presented to the scientific community by Fruth et al. (2012); a similar publication is currently being prepared for the findings in the fields F17–F19.

Scientific Context

More light curves have been analyzed for stellar variability within this work than within the whole BEST/BEST II project before, and the number of variable stars (known, new, and suspected) identified has increased significantly (from 1,111 to 3,979). Within this study, about 1% of all stars investigated were found to be variable, which compares well to the yield of photometric surveys such as ASAS (Pojmanski 2002) or OGLE (Soszyński et al. 2008). Compared to previous BEST II studies on stellar variability, the detection yield was increased significantly. For the data set LRa02, which was reanalyzed within this work, the number of detections increased by 95% (from 350 to 681). The enhanced perfomance is assigned to the methodological improvements achieved within this work, i.e., most importantly, the increased photometric quality and the new variable star search method.

The new detections make a significant contribution to the present knowledge of variable stars. Depending on how rigorously a catalog vets new findings before including them, the respective volume varies: GCVS, which only collects clear detections after a careful individual screening, encompasses 45,678 variables. VSX, which has less stringent criteria for selection, includes 213,228 variables (as of 6th November 2012). If all variable stars of this work were to be included into these catalogs (VSX already includes *all* detections in target field LRa02), **the number of presently known variables will increase by 2% (VSX), and by 8% (GCVS).**

A detailed characterization and modeling of the detected systems are beyond the scope of this thesis. However, the presented catalog includes a multitude of objects that are of interest for further astrophysical investigations:

- First, these are of interest from a **statistical** point of view: More known variable stars enable more robust analyses and/or to identify new correlations between characteristic parameters, which in turn can yield a better understanding of, e.g., the formation of close binaries (Li et al. 2008) or the Blazhko-effect (Jurcsik et al. 2009). The new detections of this work are of particular interest for these kinds of studies since they occupy a parameter space (e.g., magnitude range and/or sky position) that is largely unexplored to date: Within the data sets investigated in this study, the number of previously known objects is negligible compared to all variable objects (0.5% of all variable objects in F17–F19 were known before).

- Second, several **individual objects** are interesting targets for additional investigations in order to, e.g., search for additional bodies in eclipsing binary systems (e.g., Borkovits and Hegedüs 1996), test stellar interior models and general relativity (Giménez 2007), or to learn more about cataclysmic binaries and their accretion disks (Giovannelli 2008).

Outlook

While the data sets F17–F19 have both been analyzed for transits and stellar variability within this work, ASTEP data and the corresponding BEST II observations have only been investigated until now for transiting planets. In addition, these excellent data sets should be analyzed for stellar variability in a future study. Considering the large increase of variable star findings through the reanalysis of the LRa02 data set within this work, a reanalysis of other BEST/BEST II data sets using an improved methodology is also likely to yield many additional variable stars.

Final Note

In astronomy, observations provide the key to new insights, and an improved quality of the measurements has frequently triggered large advances such as the detection of extrasolar planets. Within this work, BEST II and ASTEP 400 were optimized and used as state-of-the-art instruments for studying stellar variability and detecting exoplanets via the transit method.

Future studies will build on our current knowledge about extrasolar planets and improve it further: An ever-increasing sample will enable a more detailed classification of their diversity and yield new insights into how they form and evolve. Most importantly, more precise measurements will gradually extend the realm of these analyses to the yet sparsely studied parameter space of small rocky planets, which will finally allow us to address the uniqueness of our Earth in a quantitative sense.

Without any doubt, both the quest for the best astronomical site and a continued optimization of the processes involved in the acquisition, reduction, and analysis of observational data will remain prime necessities for achieving this aim.

Appendix

Appendix A

BEST II Technical Improvements

A.1 New BEST II Instrument

The main instrument of BEST II, a 4k × 4k CCD by Finger Lakes Instrumentation, has been upgraded in the course of this work. The initial *"IMG series"* model was replaced with a *"ProLine"* camera with filters and an automatic focus unit in early August 2011 (see Section 3.2).

Technical Performance

The performance of the instrument has been tested at DLR Berlin. It was found to match the specifications of the manufacturer and confirmed by on-site tests after installation. The key results are written here.

The camera has two readout modes: The fast readout takes 14 s and yields an average biaslevel of 1644.4 ADU with a readout noise of 13.49 ADU, while the slow mode requires 31 s and yields a mean biaslevel of 2308.8 ADU with 7.08 ADU noise. Due to its significantly lower noise level, all observations are obtained with the slow readout. In general, the bias level was found to be very stable (mean changed less than ±1 ADU during a four hour test sequence taken at −20°C).

On being cooled at full power, the CCD can reach a temperature of 54.1°C below ambient. Below 0°C, bias variations with temperature were found to be negligible. The operating temperature has been set to −20°C, at which also the mean dark current is with

$$D(\Delta T) = -0.32\,\mathrm{ADU} + 0.0029\,\mathrm{ADU} \cdot \Delta T/s$$

very low.

The camera saturates at 2^{16} ADU = 65536 ADU, and its linearity breaks down above ∼ 42000 ADU. The gain was measured at $1.98\frac{\mathrm{e}^-}{\mathrm{ADU}}$.

Readout and Sampling

The original BEST II CCD had a readout time of 150 s. Therefore, the overhead is decreased by two minutes per frame. Since this additional time can be directly used

for more or longer exposures, this leads to an increase in the photometric precision and/or the time resolution with the new CCD.

For observations that are obtained at the same sampling, the available integration time is then raised by a factor

$$\delta n = \frac{\Delta T + 150\,\mathrm{s}}{\Delta T + 31\,\mathrm{s}} \ .$$

Depending on the exposure time ΔT, the number of frames can thus be increased by 36% (300 s) up to 370% (1 s) compared to the original CCD. If the additional measurements are binned, the photometric errors scale with a factor $1/\sqrt{\delta n}$ (assuming white noise only), i.e., the precision increases by 14% for long exposures (300 s) and up to 54% for very short exposures (1 s).

Filters

Observations in filters can be useful for various reasons. In the framework of BEST II in particular, they include the following advantages:

- An improved extinction correction can increase the photometric quality. Because atmospheric extinction is proportional to the airmass to first order (see Section 5.2.2, Equation (5.9)), it can be removed quite easily by averaging. However, the removal of higher order effects requires color information. A preliminary analysis has already shown that BEST II light curves of very blue or red stars can be dominated by residual extinction effects (Pasternacki, private communication), but how much the photometric precision can be increased by multicolor observations remains to be investigated quantitatively.

- Some scientific objectives – like the monitoring of very long ($\gtrsim 6\,\mathrm{h}$) planetary transits – require joint measurements of several ground-based observatories. The noise level in the combined data set can usually be decreased if all observations are obtained in a standardized photometric system.

- Stellar parameters can be assessed using multi-band photometry. These include the measurement of the effective temperature and bolometric correction (Flower 1996; Torres 2010), $\log g$, and metallicity (e.g., Worthey and Lee 2011), angular diameter (Barnes and Evans 1976) and reddening-free magnitudes (Madore 1982). Furthermore, an approximation of stellar radii and densities from colors can help to exclude giant and early-type stars in transit searches (see Section 8.3).

- Colors can be used to reject false positives in the follow-up process of transiting planets. When they pass the stellar disk, they occult regions of different colors and thus produce a *"characteristic colorimetric signature"* (Rosenblatt 1971). As Tingley (2004) has shown, this is distinctive from grazing binaries or blends, but the expected color differences are about an order of magnitude smaller than the transit depth. Although the method has been applied successfully

from ground (e.g., O'Donovan et al. 2006), it remains to be checked whether BEST II can provide a sufficient multiband precision for this purpose.

The filter wheel of the new CCD – a Finger Lakes Instrumentation CFW-4-5 – contains slots for five 50 mm square filters (see Figure A.1). Slots of number 1 to 4 are equipped with standard Bessell filters B, V, R and I, while slot number 0 is left empty to further allow for observations with a maximum photon yield. An additional U filter is present on-site, but not mounted.

The transmission curves of the available filter set are given by Bessell (1990) and repeated here in Figure A.2. In addition, the quantum efficiency of the CCD chip is shown in the figure. It can be seen that the overlap is largest with the R and V band, while the overall response is significantly smaller for observations in B or I. It is minimal for the U band, which is why this filter is currently not being used.

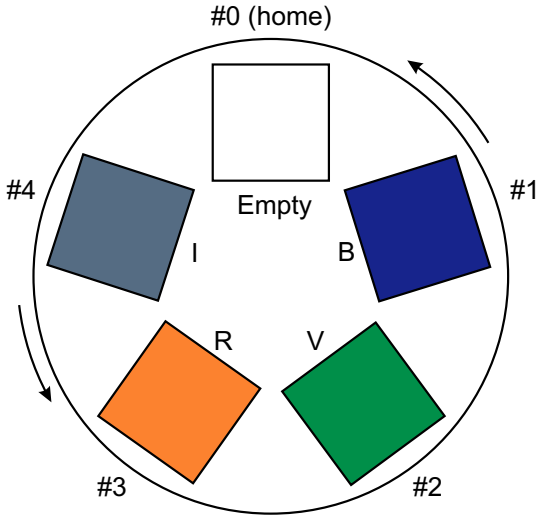

Figure A.1: BEST II filter wheel (schematical). The wheel rotates a selected filter into the optical path. It has been equipped with four Bessell filters ($BVRI$, slots #1–4), while slot #0 has been left empty for uncalibrated observations with a maximum photon yield.

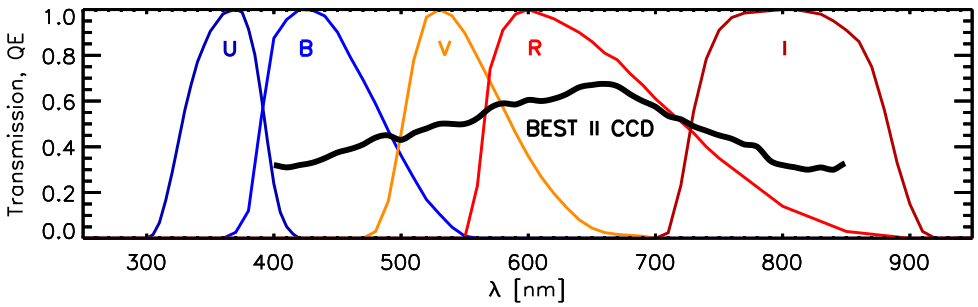

Figure A.2: BEST II CCD and filter sensitivity. Shown are the transmission curves for the five standard $UBVRI$ filters (from left to right, as given by Bessell 1990). In addition, the quantum efficiency (QE) of the BEST II CCD is shown in black (the same for both the original and the new CCD; data from KAF-16801 chip performance specifications, Kodak, 2000).

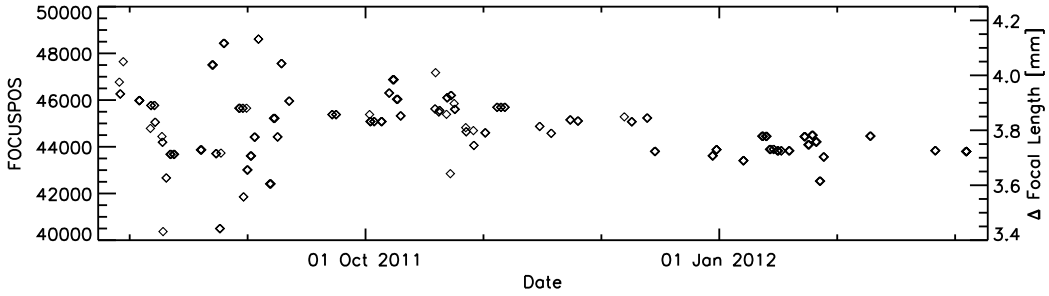

Figure A.3: Time dependence of BEST II focus since the implementation of the automatic focal unit. Positions are shown for the optical path without filters, i.e., they are subtracted by a fixed difference for observations obtained with filter. Values are given in travel steps that are recorded with every individual science frame. The right y-axis shows the corresponding focal length change in mm.

Focus

The usage of different filters together with an empty slot results in a difference of up to 1.8 mm in the focal length, which must be compensated by the focal unit. In addition, seasonal variations (e.g., due to thermal expansion) can now be compensated through a regular auto-focus procedure.

The first observations of BEST II with the new instrument and the implemented auto-focus routine allow to access focal variations quantitatively. Figure A.3 shows the focal positions that are stored in the header of each scientific frame for the first half year of operation. Although more data are required for analyzing the variations over long time scales, a small linear trend can already be observed. The variation is in the order of 2000 focus steps, which corresponds to 3–4 Px on the CCD. Similar shifts were encountered with the original setup. However, these were not corrected automatically, and thus occasionally yielded de-focused nights that had to be removed.

A.2 Pointing Stability

A precise pointing is important for long-term monitoring of target fields such as performed by BEST II. Small offsets of a few pixels between individual frames are common except for systems that are especially designed to provide a very high pointing stability. However, if there are large shifts, significant parts of the intended FOV are not covered and the time sampling decreases for many light curves.

During observations of the CoRoT field LRa02 between November 2008 and March 2009, the pointing stability of BEST II was found to vary significantly. Figure A.4 shows the midpoint position of all images with respect to a reference frame. The average deviation is 286 Px, and some frames were found to be more than 1000 Px away from the intended pointing, which means that up to a quarter of all stars are not covered.

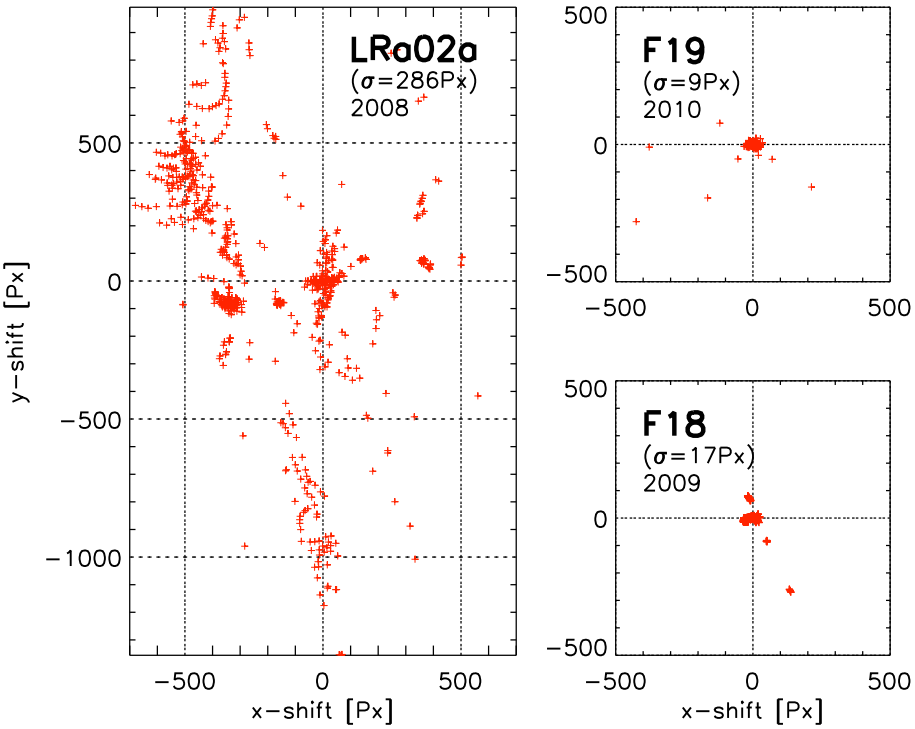

Figure A.4: Pointing stability of BEST II ($1\,\mathrm{Px} \equiv 1\farcs5$). The three plots show the displacements to the respective reference frame in CCD (x, y) coordinates for individual images in the data sets of LRa02a *(left)*, F18 *(lower right)* and F19 *(upper right)*. The axis scales are equal.

The problem was tackled and solved in a maintenance visit in March 2009 through a re-alignment of the telescope. An initial tilt of $29'21''$ between the equatorial axis of the telescope and the rotational axis of the Earth could be reduced by an iterative mechanical adjustment; the remaining small tilt of $5'16''$ has been measured and included into the pointing model of mount and software, so that the new pointing accuracy is typically well below $5'$.

The improvement can clearly be seen in subsequent observing runs (Figure A.4). Target field F18 (observed in August and September 2009) shows an average variation of only 17 Px, i.e., a very stable pointing. Through fine tuning of the pointing model and software parameters, it was possible to limit the differences further. For the F19 observations (March to September 2010), the average variation is only 9 Px.

Appendix B

Target Field Selection

This section describes the calculation of the total observing time, mean airmass, and the number of stars suitable for transit search. The parameters are calculated as a function of equatorial coordinates for a given period of time and observing site (Sections B.1 and B.2), and weighted against each other in order to obtain a quantitative criterion for target field selection (Section B.3).

B.1 Duty Cycle and Airmass Simulation

Both the visibility and the airmass of a target field depend on its celestial course during a given time period, so that they can be conveniently calculated together.

The simulation presented in this section is based upon procedures of a study on the potential of Dome C for transit search (Rauer et al. 2008a, b; Fruth 2008). The method is only outlined briefly here; technical details and its validation are described in depth by Fruth (2008).

Total Observing Time

If and at which airmass a given field is observable depends upon its position $(\alpha, \delta)_\star$ in the sky, the time of observation, and the geographical location of the observatory. Additional important constraints are the sky brightness due to the Sun and the Moon, as well as the separation between the Moon and the target. To decide if a target is observable or not at a given time t, one must calculate the local azimuth $A(t)$ and altitude $h(t)$ for Sun, Moon, and target, the Moon phase $\phi_{\leftmoon}(t)$, and restrict their ranges meaningfully. The calculation of these local coordinates was implemented using standard astronomical algorithms (Meeus 1998).

Since the movement of bodies in our Solar System is complex, accurate results for a whole time range $[t_a, t_e]$ can only be achieved through a numerical discretization into N_t equidistant steps. Local coordinates are therefore calculated for individual time points t_i, i.e.,

$$t_i = t_a + \delta t \cdot (i - 1/2) \qquad \text{with} \quad i \in \{1, \ldots, N_t\} \qquad \text{and} \quad \delta t = \frac{t_e - t_a}{N_t}. \tag{B.1}$$

A target field is considered observable in t_i, if

- the **Sun** stands no higher than $h_\odot^{\max}$ above the horizon,

$$h_\odot(t_i) \leq h_\odot^{\max} \tag{B.2a}$$

- the **Moon** stands no higher than $h_\leftmoon^{\max}$ above the horizon or has a phase of $\phi_\leftmoon^{\max}$ or less,

$$\left(h_\leftmoon(t_i) \leq h_\leftmoon^{\max}\right) \vee \left(\phi_\leftmoon(t_i) \leq \phi_\leftmoon^{\max}\right) \tag{B.2b}$$

- the **target** stands at least $h_\star^{\min}$ above the horizon,

$$h_\star(t_i) \geq h_\star^{\min} \tag{B.2c}$$

- and **target and Moon** are separated by at least $d_\leftmoon^{\min}$

$$d_\leftmoon(t_i) \geq d_\leftmoon^{\min} \; . \tag{B.2d}$$

For BEST II, the limits have been adapted from previous observational experience on similar locations. The sky brightness allows for good photometry if the Sun sets by more than eight degrees below the horizon (Patat et al. 2006; Fruth 2008), which corresponds to $h_\odot^{\max} = -8°$. The same limit is applied to the Moon, i.e., $h_\leftmoon^{\max} = -8°$, but only full Moon nights are excluded by setting $\phi_\leftmoon^{\max} = 0.9$. Frames obtained for airmasses $X > 2$ have been found not to be useful for high-precision photometry, so we apply $h_\star^{\min} = 30°$. Finally, the target-Moon distance is restricted to $d_\leftmoon^{\min} = 20°$.

In order to assess the duty cycle and airmass of a given field during a whole time range, it is useful to define a binary function

$$b_i : t_i \to \{0, 1\} \tag{B.3}$$

which yields a value of one if all criteria (*B*.2a)–(*B*.2d) are met, and zero otherwise. Using the sequence b_i, the total observing time T_1 within a given time range $[t_a, t_e]$ can easily be approximated by

$$T_1 := \delta t \cdot \sum_i b_i \; . \tag{B.4}$$

Mean Airmass

For each time point t_i, the airmass is defined by

$$X_i := \frac{1}{\sin h_\star(t_i)} \tag{B.5}$$

and can thus be readily derived from the target's altitude $h_\star(t_i)$. In order to access the potential photometric quality of a target field, it is useful to calculate its mean airmass $\overline{X}$ *during possible observations* within the time range $[t_a, t_e]$, i.e.,

$$\overline{X} = \frac{\sum_i b_i X_i}{\sum_i b_i} \; . \tag{B.6}$$

All-Sky Simulation

In order to obtain a quantitative comparison, a grid of points equidistant in right ascension and declination is used to sample the whole sky for possible target fields. The total observing time and mean airmass are calculated for each tested field coordinate set, thus providing a sky map of T_1 and $\overline{X}$ for any fixed time range $[t_a, t_e]$.

B.2 Target Count Simulation

The purpose of this second step of the simulation is to estimate the number of target stars within a given magnitude range and direction in the sky. In order to restrict the calculation to stars that are suitable for transit detection, two important factors must be accounted for. First, any input catalog used must allow for the exclusion of giants and early-type dwarf stars, which yield false positive detections for transit search (see Section 2.2). Second, the effect of contaminating background stars must be quantified with respect to the system's angular resolution.

Input Catalog

Although a large number of star catalogs are available from various surveys, only few provide spectral and luminosity classes that are needed to sort out stars with large radii. The largest sample of about 360,000 spectroscopically classified stars is provided by the Henry Draper catalog (HD; Cannon and Pickering 1918–1924) and its extensions (HDE; Cannon 1936; Cannon and Mayall 1949), which is almost complete for magnitudes $m \lesssim 9$. Given the small BEST II FOV, this magnitude limit is not faint enough to contain a sufficient number of target stars per field.

Alternatively, one can try to estimate stellar parameters using all-sky broad-band photometry for a large number of stars, e.g., from the Two Micron All Sky Survey (2MASS; Skrutskie et al. 2006). However, the problem is generally under-determined, so that additional assumptions or observations are required. Without such information, in particular the stellar radii cannot be determined without ambiguity (Belikov and Röser 2008). Space-based surveys such as CoRoT and Kepler therefore conduct extensive pre-mission observation programs for field characterization within their targeted sky regions (CoRoT Exo-Dat, Deleuil et al. 2009; Kepler Input Catalog, Brown et al. 2011).

The compilation of a broad-band catalog does not provide a reliable data input. Also an extensive observational campaign is not feasible for the BEST II field selection. Therefore, it was decided to use simulated star counts from a Galaxy model.

Besançon Model

The Besançon model (Robin et al. 2003) combines theories of galactic and stellar formation and evolution, constrained by observations, in order to provide a self-consistent model for the stellar population of the Milky Way. While being widely

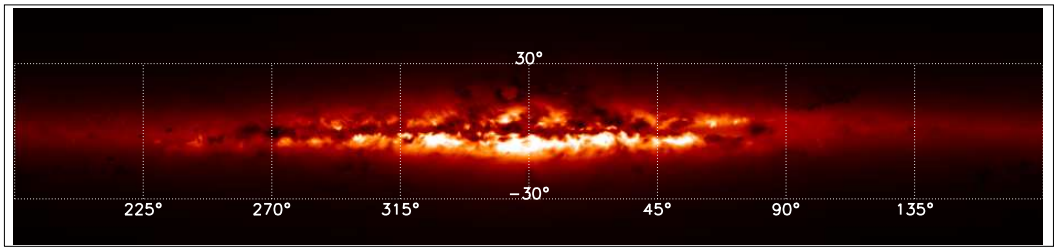

Figure B.1: Density of main sequence dwarf stars with $2 \leq V \leq 18$ from Besançon model as a function of galactic coordinates.

applied to studies of our Galaxy itself, the model is also useful for transit surveys. For example, it has been applied to evaluate their detection yield (e.g., Smith et al. 2006; Fressin et al. 2007, 2009) and for target field selection (e.g., Bayliss and Sackett 2007; Kane et al. 2007).

For the purpose of the BEST II field selection, the density of main sequence dwarf stars has been simulated using the Besançon model (Figure B.1). The resulting catalog provides star counts throughout the sky within bins of one square degree, one magnitude (from $V = 2$ to 18), and one spectral class (types O5, B5, ... , M5).

Crowding Simulation

The results from the Besançon model are used to simulate the crowding according to the specifications of BEST II (see Table B.1). For each coordinate in the catalog, the FOV is simulated in CCD dimensions (x, y) according to the pixel scale. Stars are distributed randomly throughout the field and each magnitude bin up to the counts determined by the Besançon model.

In a next step, the number of suitable targets within each direction is calculated. First, target stars are distinguished from non-targets by selecting stars of certain spectral types and within a certain magnitude range. Second, target stars with a significant amount of contaminating light within their PSF are excluded, because unresolvable background stars are the prime cause of false transit alarms. Therefore, the fraction γ_t of light actually originating from the target *itself* is calculated for every target star t. A target is considered *suitable* for transit search only if γ_t is larger than the threshold $\gamma_{\min}$. Otherwise, it is considered *contaminated*. The actual calculation of γ_t is adjusted to the aperture photometry as used by the BEST/BEST II data

Table B.1: Parameters used in the crowding simulation for BEST II.

PSF	Gaussian with $\sigma_{\text{fwhm}} = 3\,\text{Px}$ (Equation (C.5))
FOV= $1\overset{\circ}{.}7 \times 1\overset{\circ}{.}7$	BEST II FOV, with $4096 \times 4096\,\text{Px}$
$\text{FOV}_{\text{sim}} = 1^\circ \times 1^\circ$	Size of simulated FOV for each coordinate (results scaled to FOV)
$r_{\text{ap}} = 5\,\text{Px}$	Radius of aperture mask
$\gamma_{\min} = 99\%$	Minimum fraction of light from target
$12 \leq V \leq 15$	Target magnitude range
F5, G5, K5, M5	Spectral type bins of suitable targets
$n_{\text{cs}} = 100$	Number of Monte-Carlo simulations per coordinate

pipeline and detailed in Appendix C.1.

The respective numbers of suitable targets, $N_{\mathrm{st}}(\alpha, \delta)$, and contaminated targets, $N_{\mathrm{ct}}(\alpha, \delta)$, are calculated for each coordinate (α, δ) of the Besançon catalog. Since these are stochastic values (due to the random distribution of stars across magnitude bins and the FOV), the whole simulation is repeated n_{cs} times to provide robust count expectations.

B.3 Weighting of Target Field Parameters

The three main results of the simulations, i.e., the total observing time T_1, the mean airmass $\overline{X}$ and the number N_{st} of suitable targets, must finally be weighted against each other in order to compare different target fields in the sky. Quantitatively, this can be achieved by defining a single function $\Theta\left[T_1(\alpha, \delta), \overline{X}(\alpha, \delta), N_{\mathrm{st}}(\alpha, \delta)\right]$ that reaches its maximum for the direction (α, δ) that is best suited for transit search.

How should the above three quantities be combined? First, only a linear dependency of the weighting function on both the number of stars as well as the observing time is meaningful, i.e., $\Theta \propto T_1 N_{\mathrm{st}}$. Second, the weighting function should decrease monotonically in $\overline{X}$, as the photometric error can only increase with larger airmasses. For the actual dependency of Θ on $\overline{X}$, the approach of Rauer et al. (2008a, b) and Fruth (2008) is followed: An empirical relation is used to devalue Θ according to observational experience. Low airmasses are found not to affect the photometric signal-to-noise ratio, so that Θ stays almost constant for $1.0 \leq \overline{X} \leq 1.4$. Larger airmasses introduce an increasing photometric error, and observations usually cease for targets below an altitude of 30°. Thus, the function

$$\Theta\left(T_1, \overline{X}, N_{\mathrm{st}}\right) = \frac{T \cdot N_{\mathrm{st}}}{200^{\left(\overline{X}-1\right)^8}} \tag{B.7}$$

is used for weighting. It reproduces this dependency with an increasing devaluation of airmasses in the region $1.4 \leq \overline{X} \leq 2.0$ and a smooth transition $\Theta \to 0$ to non-observable targets with $\overline{X} \geq 2$ (Figure B.2).

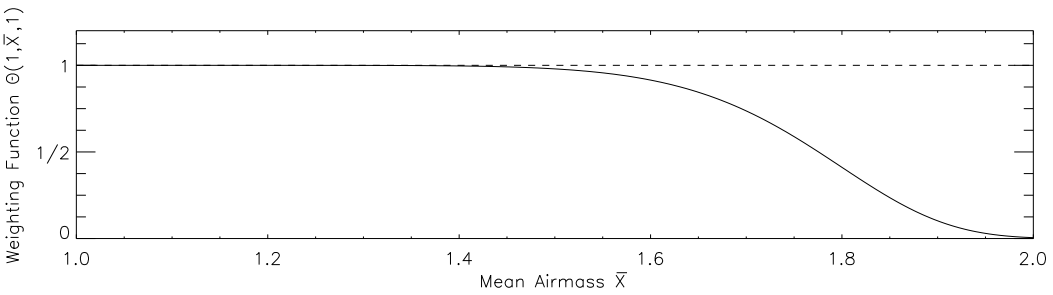

Figure B.2: Weighting of mean airmass $\overline{X}$ for target selection (Equation (B.7)).

Appendix C

Calculations

C.1 Fraction of Light in a Circular Aperture

How much light within a given aperture originates from a target source, and how much is contributed from other, contaminating objects? To address this question, it is first necessary to quantify the amount of light that falls within a given photometric aperture. Within the DLR pipeline, a circular aperture of radius r_{ap} is used (see Chapter 5.2.1).

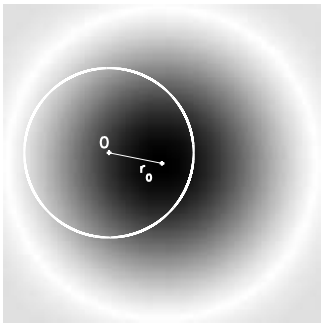

Figure C.1: Schematic view of the geometric problem of calculating the stellar flux within a radial aperture. The centroids of the PSF and the aperture are separated by r_0.

Let f_i be the total flux of a star with index $i \in \{1, \ldots, N_\star\}$, and $i = t$ be a source that is considered an interesting target. The flux of star i within the aperture of the target t can then be denoted by

$$F_t(i) = g \cdot f_i \ , \tag{C.1}$$

where g quantifies the geometrical overlap between the stellar PSF and the aperture (with $0 \leq g \leq 1$). For the target itself, the centroids of the aperture and the PSF $\psi(\vec{r})$ coincide in $\vec{r} = 0$, and the fraction of flux within the aperture $r \leq r_{\mathrm{ap}}$ is simply given by

$$g_0 = \int_0^{2\pi} \int_0^{r_{\mathrm{ap}}} \psi(\vec{r}) \, dr \, d\varphi \ . \tag{C.2}$$

In order to quantify the flux leaking from other stars into the aperture (Figure C.1), it is necessary to also consider PSFs with centroids shifted from the aperture's center by $\vec{r_0}$, i.e.

$$g(\vec{r_0}) = \int_0^{2\pi} \int_0^{r_{\mathrm{ap}}} \psi(\vec{r} - \vec{r_0}) \, dr \, d\varphi \ . \tag{C.3}$$

The contamination can then be calculated by comparing the flux from the target t with the total flux in the aperture, i.e. the fraction γ_t of light originating from the target t can be defined as

$$\gamma_t := \frac{F_t(t)}{\sum_i F_t(i)} = \frac{1}{1 + \frac{1}{g_0}\sum_{i \neq t} g(\vec{r}_i) f_i / f_t} \ . \tag{C.4}$$

Using the magnitude definition $f_i/f_t = 10^{0.4(m_t - m_i)}$, the value γ_t can be readily computed from the stellar magnitudes m_i and m_t.

Finally, a PSF function $\psi(\vec{r})$ must be chosen for the calculation of $g(\vec{r}_i)$. It is meaningful to use the same PSF shape for all stars, and to choose a radially symmetric function $\psi(\vec{r}) = \psi(r)$. The geometric overlap function $g(r_0)$ is then independent of the polar angle φ, and the only information needed in addition to the magnitudes are the distances r_i from the target to all other stars i.

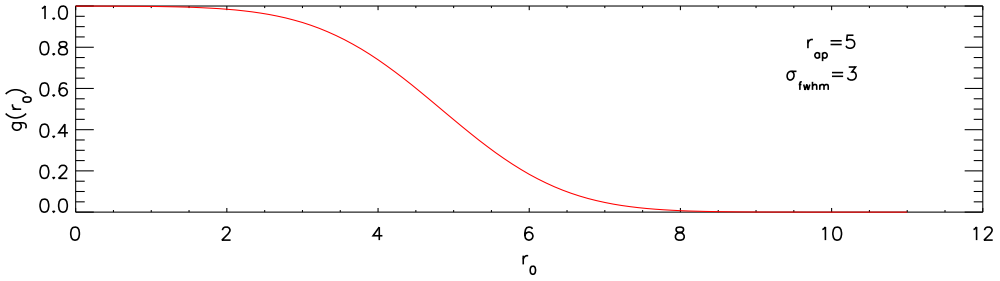

Figure C.2: Fraction of light that falls into a circular aperture of radius $r_{\mathrm{ap}} = 5$. The value $g(r_0)$ was calculated as a function of the distance r_0 from the aperture's center using Equation (C.6) and a Gaussian PSF of width $\sigma_{\mathrm{fwhm}} = 3$.

Example

A commonly used PSF function is the normalized Gaussian

$$\psi_g(\vec{r}) = \frac{1}{2\pi\sigma_g} \exp\left(-\frac{\vec{r}^{\,2}}{2\sigma_g^2}\right) \tag{C.5}$$

with the variance σ_g that is related to the full width at half maximum σ_{fwhm} through $\sigma_g = \frac{\sigma_{\mathrm{fwhm}}}{2\sqrt{2\ln 2}}$. For the calculation of $g(r_0)$, the center of the PSF $\psi_g(\vec{r})$ can simply be placed on the x-axis (using the symmetry $g(\vec{r}_0) = g(r_0)$). Inserting Equation (C.5) into Equation (C.3) yields

$$g(r_0) = \frac{1}{2\pi\sigma_g} \int_{-r_{\mathrm{ap}}}^{+r_{\mathrm{ap}}} \int_{-\sqrt{r_{\mathrm{ap}}^2 - x^2}}^{+\sqrt{r_{\mathrm{ap}}^2 - x^2}} \exp\left(-\frac{(x - r_0)^2 + y^2}{2\sigma_g^2}\right) dy\, dx \ , \tag{C.6}$$

which can be solved by numerical integration for all $r_0 \in \mathbb{R}_0^+$.

Figure C.2 shows the fraction $g(r_0)$ of flux leaking into an aperture of $r_{\mathrm{ap}} = 5$. The example shows $g(r_0)$ as a function of the distance r_0 between the centroids of the target's aperture and a second star, assuming Gaussian PSFs $\psi_g(\vec{r})$ with $\sigma_{\mathrm{fwhm}} = 3$ for both the target and its contaminant.

C.2 Sorting Parameter for Ranking Performance Evaluation

Let $X_\star = \{x_i\}$ with $i \in \{1, \ldots, N_\star\}$ be the group of all stars in a data set. The selection of variable stars – e.g., by sorting all stars according to a ranking quantity q – can then be considered a permutation $\widetilde{p}_v : X_\star \to X_\star$ that splits $X_\star$ into a part $X_v \subset X_\star$ containing all N_v variable stars and another part containing the rest:

$$\begin{aligned} \widetilde{p}_v(x_i) &\in X_v \quad \text{for} \quad i \leq N_v \\ \widetilde{p}_v(x_i) &\notin X_v \quad \text{for} \quad i > N_v \ . \end{aligned}$$

A check of the first N_v within $\{\widetilde{p}_v(x_i)\}$ would thus reveal all variable stars in the data set.

Unfortunately, such an *optimal* sorting $\widetilde{p}_v$ is usually unknown. In practice, a given permutation p_v aims at a similar splitting of variable and non-variable stars, but contaminates both groups with false positives. The number of identified variable stars $N'_v \leq N_v$ thus depends on the number of stars $N_{c\star} \leq N_\star$ that are actually checked:

$$\begin{aligned} N'_v\,(p_v,\, N_{c\star}) &= \sum_{i=1}^{N_{c\star}} \delta_v(p_v(x_i)) \\ \text{with} \quad \delta_v(x_i) &:= \begin{cases} 1 & x_i \in X_v \\ 0 & \text{otherwise} \end{cases} \ . \end{aligned}$$

A given variable star selection p_v can be compared directly with the optimal procedure $\widetilde{p}_v$. The number of missed variable stars is

$$\overline{N}'_v\,(p_v,\, N_{c\star}) = N'_v\,(\widetilde{p}_v,\, N_{c\star}) - N'_v\,(p_v,\, N_{c\star})\,,$$

whereby

$$N'_v\,(\widetilde{p}_v,\, N_{c\star}) = \min(N_{c\star},\ N_v).$$

For a comparison between different approaches, it is useful to evaluate the performance of p_v as a whole. For that, one can define the quality parameter

$$\xi = \frac{\sum_{N_{c\star}=1}^{N_\star} \overline{N}'_v\,(p_v,\, N_{c\star})}{N_v(N_\star - N_v)} \ .$$

The parameter ξ sums missed variable stars for all values of $N_{c\star}$. The denominator accounts for normalization such that $\xi = 0$ for $\widetilde{p}_v$ (best selection) and $\xi = 1$ for its counterpart (worst selection).

C.3 Photometric Variation with Crowding

Third light leaking into a stellar aperture not only yields an overestimation of the target flux, but also an underestimation of its photometric variation.

If a single target star is observed, relative brightness variations

$$\delta f_t = \frac{\Delta f_t}{f_t} \tag{C.7}$$

are only due to changes Δf_t in the target flux f_t. However, if more stars are enclosed in the aperture, the total flux f includes the target and contaminating light f_c, i.e.,

$$f = f_t + f_c. \tag{C.8}$$

If it varies again by Δf_t, the relative variation within the aperture yields

$$\delta f = \frac{\Delta f_t}{f} = \frac{f_t}{f} \cdot \delta f_t \tag{C.9}$$

and thus $\delta f \leq \delta f_t$ in case of any third light ($f_c > 0$). Using $\delta f = (0.4 \cdot \ln 10)\Delta m$, Equation (C.9) can be transformed to the magnitude range:

$$\Delta m = \frac{f_t}{f} \cdot \Delta m_t = \Delta m_t \cdot 10^{0.4(\overline{m} - \overline{m}_t)}, \tag{C.10}$$

whereby Δm and Δm_t denote differences from the mean magnitudes $\overline{m}$ and $\overline{m}_t$ of the contaminated aperture and the target due to the variation Δf_t.

Appendix D

Pipeline Parameters

Table D.1: Most important parameters for data reduction and analysis.

Parameter (Pipeline Name)	Symbol	BEST II								ASTEP 400		
		LRa02		F17	F18	F19	WASP	ASTEP-		WASP	ASTEP-	
		a_{v5}	b_{v4}				18b	Exo2	Exo3	18b	Exo2	Exo3
...Image Alignment												
SAMEXY_REF (im...)		00176	00144	00371	00054	02739	01025	00227	00000	00755	00397	02696
SAMEXY_NOBJ		20000	20000	20000	20000	20000	500	20000	20000	80	5000	5000
SAMEXY_ORDER		3	3	3	3	3	3	3	3	2	3	3
SAMEXY_INTERPMODE		2	2	2	2	2	2	2	2	2	2	2
SAMEXY_CUBICPARAM		-0.5	-0.5	-0.5	-0.5	-0.5	-0.5	-0.5	-0.5	-0.5	-0.5	-0.5
SAMEXY_MATCHLIMIT		50	50	50	50	50	50	50	50	50	50	50
SAMEXY_MAXRESIDUAL		10	10	10	10	10	10	10	10	1	10	10
...Image Subtraction (ISIS)												
nstamps_x=nstamps_y=10, half_mesh_size=9, half_stamp_size=15, deg_bg=2, ngauss=3 deg_gauss1=6, deg_gauss2=4, deg_gauss3=2, sigma_gauss1=0.7, sigma_gauss2=1, sigma_gauss3=1.2, deg_spatial=2												
sub_x, sub_y		2	1	1	1	1		1	1	1	1	1
saturation		55000	55000	55000	55000	55000	(*)	55000	55000	60000	55000	55000
pix_min		30	30	30	30	30	(*)	30	30	10	30	30
min_stamp_center		6000	6000	6000	6000	6000	(*)	6000	6000	1000	6000	6000
(*) ISIS applied, but records not kept.												
...Aperture Photometry												
PHOT_THRESHOLD	$f_{\min}$	150	60	140	18	600	20	120	80	50	80	80
PHOT_SATURATION		50000	48000	55000	55500	55000	55000	48000	48000	55000	55000	55000
PHOT_APSTAR	$r_{\rm ap}$	5 Px	5 Px	5 Px	7 Px	5 Px	7 Px	5 Px	5 Px	12 Px	5 Px	5 Px
PHOT_APSKY	$r_{\rm sky}$	14 Px	14 Px	20 Px	20 Px	20 Px	20 Px	20 Px	20 Px	30 Px	20 Px	20 Px
...Extinction Correction (zerooffset)												
ZOS_MAGCUT		200	200	300	100	200	2	200	200	2	200	200
ZOS_LOWRMS		9000	9000	2000	1000	5000	150	5000	5000	50	5000	5000
...Framequality												
FQ_STARFRACTION		0.10	0.10	0.10	0.10	0.05	0.10	0.10	0.10	–	0.03	0.03
FQ_LIMITTYPE		2	2	2	2	2	2	2	2	–	1	2
FQ_LIMIT1	$\gamma_{\max}$	(5)	(5)	(5)	(5)	(5)	(5)	(5)	(5)	–	2	(2)
FQ_LIMIT2	$\delta\sigma_{\rm limit}$	0.01	0.01	0.01	0.01	0.01	0.01	0.01	0.01	–	(0.01)	0.01
...Catalog Match (hatastrometry)												
HAT_ASTROCATALOG		USNO-A2		UCAC3			UCAC3			UCAC3		
HAT_CATKEYWORD		RMAG		R2MAG			R2MAG			R2MAG		
HAT_MATCHORDER		4	4	4	4	4	4	4	4	3	3	3
HAT_NOBJ		5000	5000	10000	10000	6000	5000	1000	1000	1000	3000	3000
HAT_MAXDISTANCE		0.002	0.0007	0.0007	0.0007	0.0007	0.0007	0.0007	0.0007	0.0007	0.0007	0.0007
...SysRem												
SR_MAGLIMIT	$m_{\rm sys}^{\max}$	–	–	20	20	15	18	20	20	18	20	20
SR_MAXRMS	$\sigma_{\rm sys}^{\max}$	–	–	2%	3%	1%	40%	1%	1%	10%	2%	2%
SR_NEFFECTS_FIND		–	–	20	20	20	20	10	10	20	20	20
SR_NEFFECTS_REM	$n_{\rm sys}$	–	–	4	5	5	3	6	5	1	3	5
Analysis of Variance (AoV)												
AOV_NH		7	7	7	7	7	–	–	–	–	–	–
AOV_JLIMIT		–	–	0.1	0.05	0.1	–	–	–	–	–	–
AOV_PERIODS(min)		0.1^d	0.1^d	0.05^d	0.05^d	0.05^d	–	–	–	–	–	–
AOV_PERIODS(max)		35^d	35^d	100^d	80^d	100^d	–	–	–	–	–	–
AOV_FSAMPL		5.0	5.0	3.0	7.0	3.0	–	–	–	–	–	–
AOV_FITMASTER_ORDER	N_Θ^c	7	7	4	3	3	–	–	–	–	–	–
AOV_FITMASTER_NSDEV	n_1	0.0	0.0	0.0	0.0	0.0	–	–	–	–	–	–
AOV_MAXEMPTY	n_2	10%	10%	10%	10%	10%	–	–	–	–	–	–
Transit Search (BLS)												
BLS_SNRLIMIT	$S_{\rm bls}^{\min}$	–	–	5.84	4.12	6.12	–	3.18	3.49	–	3.37	3.52
BLS_MINPOINTS		–	–	20	20	20	–	20	20	–	20	20
BLS_NPOINTS_BOX	$\widetilde{N}_K$	–	–	10	10	10	–	10	10	–	10	10
BLS_PER_MIN	$p_{\rm bls}^{\min}$	–	–	0.5^d	0.5^d	0.5^d	–	0.7^d	0.7^d	–	0.5^d	0.7^d
BLS_PER_MAX	$p_{\rm bls}^{\max}$	–	–	20^d	20^d	20^d	–	5^d	10^d	–	12^d	12^d
BLS_MIN_OCCBOXES	$n_{\rm box}^{\min}$	–	–	0.8	0.8	0.8	–	0.8	0.8	–	0.8	0.8
BLS_LENGTHBESTRUN	t_N-t_1	–	–	93^d	69^d	100^d	–	7^d	11^d	–	18^d	16^d
BLS_FINALERRORPERIOD	$\Delta E_{\rm lim}$	–	–	10^m	10^m	10^m	–	10^m	10^m	–	10^m	10^m
BLS_DPFACTOR		–	–	1	1	1	–	1	1	–	1	1
BLS_QMIN		–	–	$0.02p$	$0.02p$	$0.02p$	–	$0.02p$	$0.02p$	–	$0.02p$	$0.02p$
BLS_QMAX		–	–	$0.15p$	$0.15p$	$0.15p$	–	$0.15p$	$0.15p$	–	$0.15p$	$0.15p$
BLS_KMI		–	–	3	3	3	–	3	3	–	3	3
BLS_KKMI		–	–	50	50	50	–	50	50	–	50	50

Appendix E

Variable Star Catalogs

Table Format

- BEST II ID — Identifier within the BEST II project, consisting of field name and number saved in the `star.ID` field (see Fruth et al. 2011).
- Flag (F) — $c \equiv$ *contaminated*; the aperture of one or more neighboring stars overlaps with the target, and the variation can be seen in both light curves. (Note that multiple targets are listed in case the variability cannot clearly be assigned to a single star.)
  $s \equiv$ *suspected* variability; the quality of the light curves is not sufficient to fully exclude systematic errors as sources of variability, or the folded light curves are partly incomplete.
  $k \equiv$ *known* variable star (cross-matched with VSX and GCVS).
  $\star \equiv$ stellar spectrum obtained with AAOmega (only for F19).
- Coordinates — Equatorial coordinates (α, δ) for epoch J2000.0, derived by an astrometric match of CCD coordinates to the USNO-A2 (Monet 1998, for LRa02) or UCAC3 (Zacharias et al. 2010, for F17–F19) catalog.
- R_B — Instrumental BEST II magnitude (without filter).
- T_0 — Epoch of minimum brightness, given in rHJD = HJD − 2454400.
  (For LP variables, no epoch is given.)
- p — Period of variation. (For LP variables, no period is given.)
- A — Amplitude of variation. (For LP variables, no amplitude is given.)
- Type — Variability classification (see Chapter 9).
- Other Names — Names from other catalogs (VSX, GCVS, and CoRoT for LRa02), and/or of overlapping BEST II targets that show the same variability.

E.1 LRa02

The following Tables E.1 and E.2 show variable star catalogs produced or updated in the course of this thesis.

They are also available in machine-readable and Virtual Observatory (VO) forms in the online version of the corresponding publication (Fruth et al. 2012).

Table E.1: Variable stars in field LRa02 through reanalysis (see description on page 180).

BEST ID	F	α (J2000.0) h m s	δ ° ′ ″	R_B [mag]	T_0 [d] [rHJD]	p [d]	A [mag]	Type	Other Names
LRa02a2_00759		06 47 36.1	−03 52 26.6	18.11	34.638	0.828(2)	0.4(2)	EA	
LRa02a2_01976		06 48 38.3	−03 12 25.6	16.34	35.163	0.8348(6)	0.30(5)	EA/SP	
LRa02a2_03383		06 48 11.2	−03 46 30.4	17.13	35.097	1.294(4)	0.12(7)	CEP	
LRa02a2_04701		06 47 29.0	−04 32 17.2	15.25	38.772	8.6(2)	0.04(2)	ELL/SP	
LRa02a2_05225		06 48 39.9	−03 39 17.9	16.51	34.937	0.4350(4)	0.12(7)	ELL/SP	
LRa02a2_05867		06 47 59.9	−04 16 58.3	17.72	34.841	0.5255(5)	0.4(2)	EB	
LRa02a2_06108		06 47 52.7	−04 24 51.9	17.00	34.601	2.747(8)	0.22(7)	EA	
LRa02a2_06147		06 49 27.7	−03 08 05.2	13.87	34.711	0.40998(6)	0.73(3)	EB	
LRa02a2_06168		06 48 37.7	−03 48 47.3	16.15	35.256	0.8230(6)	0.16(3)	EA	
LRa02a2_06363	*s*	06 48 29.9	−03 56 40.3	15.80	35.944	1.646(7)	0.04(3)	ELL	
LRa02a2_06993		06 48 28.5	−04 03 24.8	13.82	34.705	0.4248(2)	0.106(8)	EW/ELL	CoRoT 300002950
LRa02a2_07010		06 48 16.7	−04 13 09.3	14.56	35.923	2.309(6)	0.04(2)	EA	CoRoT 300002493
LRa02a2_07056		06 48 46.6	−03 49 15.5	17.20	34.934	0.5425(5)	0.22(6)	EW	
LRa02a2_07090		06 49 33.8	−03 11 21.3	17.24	34.925	0.5427(7)	0.15(7)	EW	
LRa02a2_07148		06 48 00.7	−04 27 25.5	16.74	34.676	0.35786(8)	0.60(5)	EW	
LRa02a2_07282	*k*	06 49 38.7	−03 08 53.8	12.81	34.906	0.7766(2)	0.47(2)	EB	[KEE2007] 1334
LRa02a2_08275		06 49 08.9	−03 41 14.7	15.93	34.990	0.740(2)	0.04(3)	RR	CoRoT 110655930
LRa02a2_09051		06 48 28.3	−04 21 12.9	16.83	34.865	0.3138(5)	0.07(5)	RR	
LRa02a2_09234		06 48 13.4	−04 34 55.7	16.56	34.642	0.1687(1)	0.05(4)	DSCT	
LRa02a2_09414		06 49 47.6	−03 19 42.1	17.30	34.622	0.5960(4)	0.53(8)	EA	
LRa02a2_09533	*c*	06 49 18.8	−03 44 03.0	14.95	38.531	2.437(6)	0.04(1)	EA	CoRoT 110658519, LRa02a2_09557
LRa02a2_09557	*c*	06 49 19.0	−03 44 00.8	14.96	38.530	2.437(6)	0.05(1)	EA	LRa02a2_09533
LRa02a2_09670		06 49 14.0	−03 49 11.5	17.76	34.980	1.175(2)	0.5(2)	EA	
LRa02a2_10193		06 49 19.6	−03 49 08.9	16.65	35.129	2.71(2)	0.11(4)	EA	
LRa02a2_10249		06 49 40.5	−03 32 34.2	16.69	39.509	3.21(2)	0.18(6)	EA	
LRa02a2_10324	*s*	06 49 45.6	−03 29 02.4	14.40	35.185	2.428(8)	0.02(1)	EA	CoRoT 110830750
LRa02a2_10556	*s*	06 49 12.0	−03 58 03.3	17.05	73.795	0.9957(1)	0.7(1)	EA	
LRa02a2_10854		06 48 28.1	−04 36 18.2	16.95	34.714	0.3530(2)	0.37(5)	EW	
LRa02a2_11110		06 48 28.0	−04 38 19.5	14.45	34.627	0.07826(2)	0.03(2)	DSCT	CoRoT 300002930
LRa02a2_11345		06 49 25.1	−03 53 48.8	17.99	34.791	0.2630(2)	0.2(2)	ELL/SP	
LRa02a2_12346		06 48 54.1	−04 26 55.5	17.29	39.077	2.456(4)	0.54(8)	EA	
LRa02a2_12432		06 49 37.2	−03 52 30.8	14.36	34.865	0.4103(3)	0.030(8)	ELL	CoRoT 110743947
LRa02a2_12470		06 50 31.6	−03 08 42.6	12.86	···	···	···	LP	CoRoT 102994604
LRa02a2_12668	*s*	06 49 33.0	−03 57 54.5	14.68	···	···	···	LP	
LRa02a2_13104	*s*	06 50 32.6	−03 12 36.2	14.42	34.857	3.118(8)	0.77(5)	EA	CoRoT 102995371
LRa02a2_14061		06 49 46.6	−03 57 29.3	17.37	34.742	0.4039(4)	0.14(8)	EW	
LRa02a2_14200	*s*	06 49 27.8	−04 13 50.6	12.36	34.667	4.95(3)	0.053(7)	CV	CoRoT 110741479
LRa02a2_14296		06 50 36.9	−03 18 25.1	16.78	35.126	0.877(3)	0.09(5)	RR	
LRa02a2_14319		06 50 16.7	−03 35 03.1	16.73	34.829	0.905(3)	0.08(5)	RR	
LRa02a2_14696	*k*	06 50 51.8	−03 09 38.2	13.50	34.910	0.35752(8)	0.22(2)	EW	[KEE2007] 1318, CoRoT 103009726
LRa02a2_14980		06 49 38.7	−04 11 32.9	13.88	···	···	···	LP	CoRoT 300004000
LRa02a2_15143	*s*	06 50 56.4	−03 09 48.8	16.59	49.016	4.31(3)	0.22(5)	EA	
LRa02a2_15754		06 50 32.1	−03 34 28.5	18.23	34.767	1.781(4)	0.7(2)	EA	
LRa02a2_16236		06 49 57.0	−04 06 42.9	17.51	35.620	2.266(1)	···	EA	
LRa02a2_16514		06 49 23.9	−04 35 52.0	16.49	34.856	1.362(4)	0.08(3)	ELL	
LRa02a2_16888		06 50 54.9	−03 24 57.6	12.31	···	···	···	LP	CoRoT 110840081
LRa02a2_16999		06 50 12.7	−04 00 19.4	15.88	38.549	2.38(2)	0.03(3)	PULS	CoRoT 110663396
LRa02a2_17274		06 49 53.5	−04 18 07.4	16.52	34.998	0.632(3)	0.05(3)	RR	
LRa02a2_17294		06 50 43.6	−03 37 29.3	17.26	34.810	0.4385(6)	0.19(7)	RR	
LRa02a2_17440		06 50 19.3	−03 58 30.5	16.72	34.708	0.2901(3)	0.14(5)	RR	
LRa02a2_17795	*c*	06 50 50.5	−03 35 36.8	16.98	38.030	3.562(1)	0.3(1)	EA	LRa02a2_17820, LRa02a2_17853
LRa02a2_17820	*c*	06 50 50.6	−03 35 43.6	16.82	38.030	3.562(1)	0.4(1)	EA	LRa02a2_17795, LRa02a2_17853
LRa02a2_17853	*c*	06 50 51.0	−03 35 39.5	16.80	38.030	3.562(1)	0.1(1)	EA	LRa02a2_17795, LRa02a2_17820
LRa02a2_18179		06 50 49.8	−03 39 14.7	15.29	46.622	15.2(6)	0.04(2)	CEP	CoRoT 110838079
LRa02a2_18409		06 50 44.1	−03 45 33.0	17.69	34.860	0.732(2)	0.14(9)	ELL	
LRa02a2_18590		06 50 57.6	−03 35 54.3	12.30	···	···	···	LP	CoRoT 110665717
LRa02a2_18647		06 51 02.7	−03 32 10.1	17.36	35.865	2.53(3)	0.17(8)	CEP?	
LRa02a2_18850	*s*	06 49 56.8	−04 27 19.6	16.69	35.909	2.592(8)	0.15(5)	EA	
LRa02a2_19473		06 49 45.8	−04 40 27.3	15.61	34.813	0.41979(8)	0.32(2)	EW	CoRoT 110830830
LRa02a2_19935		06 51 00.0	−03 43 13.8	12.49	34.621	0.3582(2)	0.038(8)	EW	CoRoT 110666679
LRa02a2_20212	*c*	06 50 54.4	−03 49 41.1	15.79	35.310	4.087(1)	0.04(1)	EA	LRa02a2_20239
LRa02a2_20239	*c*	06 50 54.5	−03 49 45.1	15.84	35.310	4.087(1)	0.06(1)	EA	LRa02a2_20212
LRa02a2_20581		06 51 05.2	−03 43 32.7	16.24	35.157	1.422(3)	0.13(3)	EA	
LRa02a2_20799		06 51 28.3	−03 26 19.4	13.49	34.647	0.07167(2)	0.021(7)	DSCT	CoRoT 110756570
LRa02a2_21410	*s*	06 51 26.2	−03 32 27.4	16.98	35.330	3.88(2)	0.37(6)	EA	
LRa02a2_21828		06 50 26.8	−04 23 37.3	16.92	34.870	0.4286(4)	0.10(4)	EW/DSCT	

Table E.1: Variable stars in field LRa02 through reanalysis (continued).

BEST ID	F	α (J2000.0) h m s	δ ° ′ ″	R_B [mag]	T_0 [d] [rHJD]	p [d]	A [mag]	Type	Other Names
LRa02a2_22686		06 50 58.4	−04 04 15.4	17.85	35.177	0.697(2)	0.2(2)	RR	
LRa02a2_22747	*c*	06 50 22.6	−04 33 53.3	15.38	35.497	0.918(1)	0.05(2)	EA	LRa02a2_22772
LRa02a2_22772	*c*	06 50 22.9	−04 33 50.8	15.37	35.496	0.918(1)	0.04(2)	EA	CoRoT 110745836, LRa02a2_22747
LRa02a2_22979		06 51 14.3	−03 53 26.2	15.73	48.080	5.04(3)	0.36(6)	EA	CoRoT 110750519
LRa02a2_23000	*c*	06 50 38.6	−04 22 38.7	15.12	34.702	0.3641(3)	0.03(2)	EW	CoRoT 110750397, LRa02a2_23012
LRa02a2_23012	*c*	06 50 38.5	−04 22 46.2	15.73	34.882	0.3641(2)	0.13(2)	EW	LRa02a2_23000
LRa02a2_23212		06 50 40.2	−04 22 40.9	14.94	34.789	0.924(3)	0.02(1)	ELL	CoRoT 110835326
LRa02a2_24736	*cs*	06 51 59.4	−03 29 47.4	14.44	38.775	17.244(1)	0.35(1)	EA	LRa02a2_24784
LRa02a2_24784	*cs*	06 51 59.7	−03 29 47.5	14.12	38.775	17.244(1)	0.45(1)	EA	CoRoT 110676884, LRa02a2_24736
LRa02a2_26032		06 52 09.1	−03 30 59.9	14.94	34.889	0.879(3)	0.018(8)	ELL	CoRoT 110758472
LRa02a2_26057		06 52 10.4	−03 30 06.4	17.64	39.565	2.553(7)	0.31(9)	EA	
LRa02a2_26141	*s*	06 51 54.8	−03 43 20.2	18.20	34.739	0.5657(6)	0.3(2)	EA	
LRa02a2_26972		06 52 28.1	−03 22 38.4	16.32	35.074	0.5885(7)	0.20(3)	DSCT	
LRa02a2_27235		06 51 59.4	−03 47 58.8	15.79	94.231	14.4(9)	0.04(2)	CEP	CoRoT 110676724
LRa02a2_27669		06 52 17.9	−03 36 01.1	15.79	34.738	0.784(2)	0.05(3)	ELL	CoRoT 110762835
LRa02a2_27720		06 52 29.5	−03 26 52.2	17.25	34.621	0.3648(4)	0.15(7)	EW/DSCT	
LRa02a2_27851		06 51 23.0	−04 21 56.5	17.33	34.631	0.11388(5)	0.13(7)	DSCT	
LRa02a2_28413		06 52 06.2	−03 50 46.5	18.03	34.719	0.3796(3)	0.4(2)	EW	
LRa02a2_28472		06 51 29.1	−04 21 28.0	17.60	35.423	1.278(2)	0.5(1)	EA	
LRa02a2_28742		06 50 55.3	−04 50 40.1	17.26	38.385	6.31(1)	0.5(1)	EA	
LRa02a2_28913		06 52 49.4	−03 18 51.9	14.99	35.655	1.1752(9)	0.16(2)	EA	
LRa02a2_29296		06 52 45.6	−03 24 40.4	13.97	99.078	11.0(2)	0.125(8)	ACV	CoRoT 110857632
LRa02a2_29509		06 52 08.3	−03 56 48.8	14.15	35.540	3.119(7)	0.074(8)	EA	CoRoT 110681166
LRa02a2_30010		06 52 52.0	−03 24 42.1	13.24	35.108	2.107(2)	0.342(8)	CEP	
LRa02a2_30797		06 51 51.1	−04 20 00.6	17.13	76.148	10.7(3)	0.13(6)	VAR	
LRa02a2_31221		06 52 51.7	−03 33 25.2	15.33	35.078	1.424(7)	0.03(2)	ELL	CoRoT 110683920
LRa02a2_31497	*c*	06 52 55.3	−03 32 41.3	14.40	47.390	6.369(1)	0.05(1)	EA	LRa02a2_31542
LRa02a2_31542	*c*	06 52 55.6	−03 32 41.3	14.42	47.390	6.369(1)	0.06(1)	EA	LRa02a2_31497
LRa02a2_32046	*s*	06 52 02.3	−04 19 45.3	16.99	39.207	10.51(1)	0.4(1)	EA	
LRa02a2_32081		06 51 42.1	−04 36 31.2	17.48	34.707	0.14857(7)	0.2(1)	DSCT	
LRa02a2_32327	*c*	06 52 45.6	−03 46 15.2	17.22	35.333	0.909(2)	0.16(8)	EA	LRa02a2_32364
LRa02a2_32364	*c*	06 52 45.8	−03 46 20.1	17.24	35.328	0.909(1)	0.23(7)	EA	LRa02a2_32327
LRa02a2_32635	*s*	06 51 58.2	−04 27 01.8	14.21	51.176	35(3)	0.09(2)	LP	
LRa02a2_33180		06 52 03.7	−04 26 15.5	13.26	35.885	1.425(3)	0.04(1)	EA	
LRa02a2_33188		06 51 54.9	−04 33 30.3	16.33	35.409	0.971(3)	0.06(3)	ELL	
LRa02a2_33276		06 53 03.1	−03 38 31.6	16.21	34.786	1.393(3)	0.07(3)	EA	
LRa02a2_33392		06 53 07.1	−03 36 01.4	17.57	34.798	0.3313(2)	0.6(1)	EW	
LRa02a2_33543	*c*	06 52 35.5	−04 03 01.7	14.74	34.756	2.310(4)	0.06(2)	EA	CoRoT 110852861, LRa02a2_33564
LRa02a2_33564	*c*	06 52 35.7	−04 02 59.7	14.73	34.761	2.310(4)	0.06(2)	EA	LRa02a2_33543
LRa02a2_33777		06 51 55.9	−04 36 58.2	16.16	35.764	2.12(2)	0.06(3)	ELL	
LRa02a2_33819		06 52 13.7	−04 22 47.4	14.16	34.621	0.12691(7)	0.02(2)	DSCT	CoRoT 110760751
LRa02a2_33856		06 51 51.2	−04 41 22.8	16.49	35.128	0.7600(8)	0.12(4)	EA	
LRa02a2_34372		06 52 05.7	−04 33 17.1	17.60	46.365	3.07(2)	0.16(9)	EA	
LRa02a2_36084		06 53 16.8	−03 47 14.1	14.03	···	···	···	LP	
LRa02a2_36237		06 52 20.9	−04 34 00.6	17.10	37.493	2.837(1)	0.7(1)	EA	
LRa02a2_37194		06 53 36.2	−03 39 05.3	14.97	38.520	7.345(1)	0.18(1)	EA	
LRa02a2_37362		06 53 28.3	−03 46 37.9	14.31	34.976	1.480(7)	0.05(2)	ELL/SP	
LRa02a2_37585	*s*	06 53 35.1	−03 42 31.4	14.43	38.440	4.184(1)	0.06(1)	EA	
LRa02a2_38197		06 53 51.1	−03 33 41.6	16.03	34.673	0.11787(5)	0.09(3)	DSCT	
LRa02a2_38328	*c*	06 53 10.0	−04 08 22.2	16.26	34.844	0.3297(2)	0.13(4)	ELL/SP	LRa02a2_38363
LRa02a2_38363	*c*	06 53 10.2	−04 08 27.2	15.74	34.838	0.3297(2)	0.14(3)	ELL/SP	LRa02a2_38328
LRa02a2_38647		06 52 21.3	−04 50 15.3	17.36	35.333	1.592(3)	0.4(2)	EA	
LRa02a2_40108	*s*	06 54 19.2	−03 24 22.5	16.62	35.251	1.537(2)	0.36(4)	EA	
LRa02a2_40411		06 54 03.0	−03 39 49.1	16.87	35.508	2.783(7)	0.14(5)	EA	
LRa02a2_40819		06 53 58.9	−03 46 23.3	17.64	34.614	0.10502(3)	0.20(9)	DSCT	
LRa02a2_41299		06 53 58.4	−03 50 19.6	13.67	34.833	0.2593(2)	0.020(8)	EW	
LRa02a2_41729		06 53 06.9	−04 35 07.4	16.30	35.298	0.902(3)	0.08(4)	EW	
LRa02a2_42124		06 52 52.5	−04 49 29.6	15.63	34.694	0.1665(2)	0.08(2)	DSCT	CoRoT 110684342
LRa02a2_42551	*c*	06 54 32.2	−03 31 10.0	15.76	35.226	0.8121(5)	0.16(3)	EA	LRa02a2_42581
LRa02a2_42581	*c*	06 54 32.4	−03 31 07.4	15.71	35.222	0.8122(5)	0.17(3)	EA	LRa02a2_42551
LRa02a2_42662		06 53 24.5	−04 27 13.9	17.86	34.653	0.2809(2)	0.5(2)	EW	
LRa02a2_42943		06 54 17.2	−03 46 14.9	16.92	34.609	0.3610(2)	0.26(6)	EW	
LRa02a2_43814		06 53 30.2	−04 31 02.2	15.75	34.615	0.4079(2)	0.26(3)	EW	
LRa02a2_43959		06 54 09.5	−04 00 04.2	14.63	···	···	···	LP	
LRa02a2_44056	*s*	06 53 08.1	−04 50 46.2	15.33	35.691	1.470(3)	0.11(3)	EA	CoRoT 110768997
LRa02b2_00490		06 48 01.8	−05 14 25.9	16.97	34.599	0.15077(8)	0.09(5)	DSCT	
LRa02b2_00896		06 48 13.3	−05 07 04.1	18.44	34.795	0.2618(2)	0.4(2)	DSCT/EW	
LRa02b2_01881		06 48 40.1	−04 49 11.7	15.15	···	···	···	LP	
LRa02b2_02629		06 47 57.3	−05 27 17.4	13.45	···	···	···	LP	
LRa02b2_03217		06 48 04.9	−05 23 32.9	15.36	74.610	5.858(1)	0.2(1)	EA	
LRa02b2_03502		06 48 10.7	−05 20 00.0	14.76	35.862	3.63(3)	0.06(4)	ELL	
LRa02b2_03535		06 48 23.9	−05 09 23.6	15.61	34.629	0.845(3)	0.03(2)	ELL	
LRa02b2_03959		06 47 30.4	−05 54 44.7	15.52	39.914	3.41(5)	0.05(2)	EB	
LRa02b2_04183	*s*	06 47 32.8	−05 53 43.3	16.68	74.740	23.945(1)	0.5(1)	EA	
LRa02b2_04779		06 48 01.9	−05 32 22.0	12.68	34.920	0.576(1)	0.03(1)	DSCT	
LRa02b2_05187		06 48 53.0	−04 52 18.2	16.05	38.709	2.38(2)	0.06(3)	ELL/SP	
LRa02b2_05477		06 47 41.5	−05 51 56.3	16.33	35.602	1.054(2)	0.10(4)	EA	
LRa02b2_05842	*s*	06 48 52.6	−04 55 25.0	13.65	···	···	···	VAR	
LRa02b2_06804		06 48 38.4	−05 10 54.8	14.13	···	···	···	LP	
LRa02b2_07294		06 49 23.9	−04 35 51.9	16.46	34.805	0.681(3)	0.08(4)	DSCT	
LRa02b2_07981		06 48 36.1	−05 17 39.5	17.66	34.760	0.3738(4)	0.16(9)	DSCT/EW	
LRa02b2_08620	*s*	06 49 19.3	−04 45 11.4	18.76	34.597	0.343538(1)	···	EW	
LRa02b2_09107		06 48 50.0	−05 11 04.4	17.00	34.744	0.3677(3)	0.13(6)	EW	
LRa02b2_09439		06 48 09.1	−05 45 51.0	15.48	35.732	1.788(8)	0.03(2)	SP	

Table E.1: Variable stars in field LRa02 through reanalysis (continued).

BEST ID	F	α (J2000.0) h m s	δ ° ′ ″	R_B [mag]	T_0 [d] [rHJD]	p [d]	A [mag]	Type	Other Names
LRa02b2_09872		06 48 44.4	−05 18 46.2	16.86	34.838	0.2867(3)	0.09(5)	DSCT	
LRa02b2_10008		06 48 11.3	−05 46 33.4	12.71	...	...	...	LP	
LRa02b2_10224		06 48 49.3	−05 16 18.7	17.66	34.859	0.5627(5)	0.4(1)	EW	
LRa02b2_10728		06 48 59.5	−05 09 48.9	16.51	34.835	1.814(4)	0.21(4)	EA	
LRa02b2_11268		06 48 06.5	−05 55 19.7	15.67	35.444	1.88(2)	0.03(2)	ELL	
LRa02b2_11445		06 48 11.3	−05 52 14.7	17.47	34.648	0.5792(5)	0.46(9)	EB	
LRa02b2_11462		06 48 42.1	−05 27 01.9	14.38	35.093	1.104(2)	0.05(2)	EA	
LRa02b2_11806		06 49 19.8	−04 57 43.4	14.78	39.457	3.37(2)	0.04(2)	CEP	
LRa02b2_11813	*k*	06 48 35.2	−05 34 14.9	12.10	34.598	0.5401(1)	0.50(2)	EB	ASAS J064835-0534.3
LRa02b2_11844		06 49 23.8	−04 54 37.8	15.02	34.917	0.4198(1)	0.28(2)	EB	
LRa02b2_11899	*s*	06 49 09.4	−05 06 42.5	14.79	42.573	17.5(8)	0.03(1)	CEP	
LRa02b2_13396		06 49 36.6	−04 50 18.8	13.42	...	...	...	LP	
LRa02b2_13454		06 49 26.6	−04 58 36.7	17.41	34.804	0.989(3)	0.26(8)	EW	
LRa02b2_13466		06 48 19.9	−05 53 11.4	15.62	34.715	0.17730(9)	0.03(2)	DSCT	
LRa02b2_14283		06 48 41.4	−05 38 56.5	15.97	35.478	1.532(4)	0.07(3)	EA	
LRa02b2_14318		06 49 08.1	−05 17 13.9	15.49	35.448	0.958(2)	0.04(2)	ELL	
LRa02b2_15535		06 50 09.1	−04 32 20.1	15.69	47.832	3.62(2)	0.08(3)	EA	CoRoT 300003981
LRa02b2_15777		06 48 36.3	−05 49 06.9	15.57	41.406	7.8(2)	0.05(2)	CEP	
LRa02b2_16028		06 49 27.8	−05 08 03.1	18.66	34.726	0.2539(2)	0.5(3)	EW	
LRa02b2_16219	*c*	06 49 08.3	−05 24 50.9	17.51	34.715	0.178(2)	0.12(9)	EW/DSCT	LRa02b2_16291
LRa02b2_16291	*c*	06 49 08.5	−05 24 55.1	17.49	34.730	0.1783(8)	0.12(8)	EW/DSCT	LRa02b2_16219
LRa02b2_16607	*s*	06 50 06.5	−04 38 56.6	13.79	35.564	5.0255(1)	0.35(1)	EA	
LRa02b2_16823		06 48 52.7	−05 40 04.8	14.80	35.895	3.71(5)	0.04(2)	ELL/SP	
LRa02b2_16862		06 49 24.8	−05 13 57.3	17.57	41.850	4.771(1)	0.6(1)	EA	
LRa02b2_17083		06 49 19.5	−05 19 11.1	17.80	34.968	1.45283(1)	...	EA	
LRa02b2_17251		06 49 57.2	−04 49 06.5	15.43	38.128	11.7(3)	0.07(2)	ELL	
LRa02b2_17622		06 49 26.5	−05 15 49.8	16.33	34.757	0.759(2)	0.08(4)	SP	
LRa02b2_17835	*s*	06 49 11.1	−05 29 14.5	15.77	34.607	0.1985(2)	0.03(3)	DSCT	
LRa02b2_18245		06 49 42.9	−05 04 59.3	13.88	34.658	0.11989(6)	0.016(8)	DSCT	
LRa02b2_18699		06 49 59.4	−04 53 16.3	17.47	34.623	1.302(2)	0.5(2)	EA	
LRa02b2_18781		06 48 54.9	−05 46 25.1	18.06	34.628	0.1718(2)	0.3(2)	DSCT	
LRa02b2_18827	*k*	06 49 32.1	−05 16 13.6	13.94	...	...	...	LP	CoRoT 110742676
LRa02b2_19139		06 48 58.1	−05 45 13.8	15.25	34.669	1.298(2)	0.06(2)	EB	
LRa02b2_19818		06 48 48.7	−05 55 46.6	14.43	51.566	35(8)	0.026(8)	CEP	
LRa02b2_19857		06 49 19.0	−05 31 07.3	16.51	35.794	4.33(9)	0.08(4)	VAR	
LRa02b2_20460		06 49 51.1	−05 07 25.1	15.33	34.977	0.8460(6)	0.10(2)	EA	
LRa02b2_21184		06 49 34.8	−05 23 43.2	17.60	35.303	0.806(3)	0.17(8)	DSCT	
LRa02b2_21186		06 49 15.7	−05 39 20.6	16.35	35.037	0.4708(4)	0.21(6)	EW	
LRa02b2_21277		06 50 05.9	−04 58 41.5	15.58	35.142	0.717(2)	0.03(2)	EW	
LRa02b2_21509		06 50 12.3	−04 54 25.6	15.47	36.964	1.27295(1)	0.28(1)	EA	
LRa02b2_21824		06 50 12.1	−04 55 52.3	15.95	51.755	7.098(1)	0.3(1)	EA	
LRa02b2_23316	*k*	06 48 56.3	−06 03 54.6	13.55	48.957	8.66(3)	0.46(4)	EA	DY Mon
LRa02b2_23816		06 49 22.5	−05 44 36.6	13.50	34.779	2.2999(1)	0.08(1)	EA	
LRa02b2_24280		06 50 24.6	−04 55 45.3	17.60	39.585	1.7129(1)	0.8(1)	EA	
LRa02b2_24293		06 49 23.0	−05 46 10.5	16.27	35.060	0.853(3)	0.08(3)	RR	
LRa02b2_24373	*s*	06 49 49.9	−05 24 24.7	17.19	34.608	0.12668(6)	0.08(6)	DSCT	
LRa02b2_24494	*s*	06 50 01.6	−05 15 19.6	17.32	34.868	1.150(2)	0.12(7)	EB	
LRa02b2_26532		06 50 11.4	−05 15 45.5	16.59	35.002	0.596(2)	0.09(4)	RR	
LRa02b2_26557		06 49 45.3	−05 37 13.6	13.36	35.418	2.5459(1)	0.35(1)	EA	
LRa02b2_26591		06 50 02.8	−05 23 03.9	17.08	34.591	0.14469(8)	0.11(6)	DSCT	
LRa02b2_27353		06 50 24.3	−05 08 41.2	15.70	34.649	0.39638(6)	0.51(3)	EW	
LRa02b2_28132		06 50 35.5	−05 02 34.2	16.50	35.423	1.403(4)	0.08(4)	CEP	
LRa02b2_28179		06 49 35.1	−05 52 04.1	14.88	34.626	0.10260(3)	0.03(2)	DSCT	
LRa02b2_28230		06 50 35.1	−05 03 15.9	16.15	39.431	2.6279(1)	0.6(1)	EA	
LRa02b2_28322		06 49 31.9	−05 55 22.3	16.97	35.640	1.807(4)	0.20(7)	EA	
LRa02b2_28430	*k*	06 49 30.1	−05 57 16.2	12.28	...	...	...	LP	NSVS 12579155
LRa02b2_28475		06 49 27.4	−05 59 38.7	15.62	45.323	28(2)	0.12(3)	LP	
LRa02b2_28591		06 50 14.7	−05 21 18.2	16.45	35.156	0.892(3)	0.11(6)	DSCT	
LRa02b2_28638		06 49 50.6	−05 41 09.2	16.26	42.827	6.4(2)	0.06(3)	CEP	
LRa02b2_28688		06 49 52.7	−05 39 40.8	15.21	34.900	3.35(2)	0.05(2)	SP	
LRa02b2_28795	*c*	06 49 48.8	−05 43 13.5	16.28	34.688	0.3880(3)	0.11(4)	EA	LRa02b2_28796
LRa02b2_28796	*c*	06 49 48.7	−05 43 18.6	16.82	34.687	0.3880(3)	0.23(5)	EA	LRa02b2_28795
LRa02b2_29274		06 50 55.3	−04 50 40.0	17.24	82.560	6.308(1)	0.5(1)	EA	
LRa02b2_29970		06 50 13.3	−05 27 39.0	16.54	35.068	0.9481(9)	0.18(4)	EA	
LRa02b2_30226	*c*	06 49 58.4	−05 40 46.3	17.51	34.940	0.3770(2)	0.5(1)	EW	LRa02b2_30252
LRa02b2_30252	*c*	06 49 58.5	−05 40 49.7	17.41	34.939	0.3770(2)	0.5(1)	EW	LRa02b2_30226
LRa02b2_31232	*s*	06 49 33.5	−06 04 52.4	14.99	35.036	7.9(2)	0.06(2)	CEP	
LRa02b2_32093	*c*	06 50 23.8	−05 27 10.1	17.37	34.744	0.3599(2)	0.27(7)	EW	LRa02b2_32153
LRa02b2_32153	*c*	06 50 24.1	−05 27 08.6	17.33	34.744	0.3600(2)	0.33(7)	EW	LRa02b2_32093
LRa02b2_32404		06 50 25.9	−05 26 35.6	16.15	39.979	2.7165(1)	0.35(1)	EA	
LRa02b2_32696		06 49 49.3	−05 57 36.9	13.60	99.281	14.0(5)	0.021(7)	CEP	
LRa02b2_33330	*s*	06 50 55.1	−05 06 19.1	14.83	34.728	9.81022(1)	...	SP	
LRa02b2_34475	*s*	06 49 53.8	−06 01 02.4	17.17	34.808	0.2770(2)	0.13(6)	EW/DSCT	
LRa02b2_34505	*s*	06 50 33.8	−05 28 26.9	16.98	45.560	4.474(1)	0.4(1)	EA	
LRa02b2_34528		06 50 58.3	−05 08 26.1	13.28	...	...	...	LP	
LRa02b2_34908		06 49 48.8	−06 06 57.5	18.11	34.648	0.14926(7)	0.4(2)	DSCT	
LRa02b2_34984		06 50 08.0	−05 51 32.7	18.06	34.678	0.3689(3)	0.4(2)	EW	
LRa02b2_35262		06 51 15.7	−04 57 19.8	15.13	35.127	0.6518(9)	0.03(2)	ELL/SP	
LRa02b2_35307		06 51 28.5	−04 46 57.4	15.40	48.788	22(2)	0.03(2)	ELL	
LRa02b2_35605	*s*	06 49 56.6	−06 03 26.9	13.96	35.168	9.4(3)	0.02(1)	CEP	
LRa02b2_36290		06 50 42.3	−05 28 54.4	16.12	34.797	1.123(2)	0.20(6)	EA	
LRa02b2_36744		06 50 12.7	−05 54 49.8	13.40	34.633	0.08374(3)	0.014(8)	DSCT	
LRa02b2_37196	*s*	06 51 22.7	−04 59 23.8	16.12	49.680	6.539(1)	0.13(1)	EA	
LRa02b2_37922	*s*	06 50 43.4	−05 34 35.2	16.21	45.133	8.2(2)	0.05(3)	ELL	
LRa02b2_38440		06 51 51.2	−04 41 22.8	16.47	35.126	0.7601(9)	0.13(4)	EA	
LRa02b2_38758		06 50 36.8	−05 43 33.5	15.40	102.310	12.3(3)	0.05(2)	EB/SP	
LRa02b2_38894		06 50 59.9	−05 25 12.9	15.06	42.820	10.31(1)	0.09(1)	EA	
LRa02b2_39003		06 51 37.9	−04 54 36.4	15.96	34.707	0.3713(2)	0.12(3)	EB	

Table E.1: Variable stars in field LRa02 through reanalysis (continued).

BEST ID	F	α (J2000.0) h m s	δ ° ′ ″	R_B [mag]	T_0 [d] [rHJD]	p [d]	A [mag]	Type	Other Names
LRa02b2_39246		06 50 59.3	−05 27 20.2	16.42	38.936	5.2(2)	0.05(3)	ELL	
LRa02b2_39842		06 51 19.1	−05 13 40.2	16.40	34.939	1.081(4)	0.07(4)	RR	
LRa02b2_39902		06 51 38.1	−04 58 20.2	17.38	36.247	3.37757(1)	0.5(1)	EA	
LRa02b2_40298		06 50 36.5	−05 50 30.5	17.82	34.882	0.3163(2)	0.2(1)	EA	
LRa02b2_40925	*s*	06 51 31.2	−05 08 33.2	17.96	78.840	8.363(1)	0.9(1)	EA	
LRa02b2_41722		06 50 29.4	−06 02 25.8	17.57	34.677	0.2942(2)	0.3(1)	EW	
LRa02b2_41885		06 50 36.7	−05 57 10.8	13.71	82.439	14(2)	0.014(8)	ELL	
LRa02b2_42475		06 50 53.6	−05 45 55.0	16.98	34.950	0.3800(2)	0.22(5)	EW	
LRa02b2_43248		06 51 42.0	−05 09 42.6	12.66	35.107	0.880(2)	0.03(2)	ELL/SP	
LRa02b2_43415	*s*	06 50 29.8	−06 09 21.5	15.44	39.098	2.465(7)	0.06(2)	EA	
LRa02b2_43501		06 51 43.5	−05 09 29.5	17.82	34.627	0.1883(2)	0.3(2)	DSCT	
LRa02b2_43566	*cs*	06 51 57.0	−04 58 42.1	15.43	34.742	0.4152(4)	0.04(2)	EA	LRa02b2_43620
LRa02b2_43620	*cs*	06 51 57.2	−04 58 40.7	15.32	34.749	0.4151(4)	0.04(2)	EA	LRa02b2_43566
LRa02b2_43735		06 50 51.6	−05 52 55.0	16.71	34.799	0.2471(2)	0.15(5)	EW	
LRa02b2_44263		06 51 29.2	−05 24 25.3	17.39	34.608	0.1840(2)	0.12(7)	DSCT	
LRa02b2_44618		06 52 02.8	−04 58 38.7	17.39	35.434	1.131(2)	0.24(8)	EA	
LRa02b2_45559		06 52 17.4	−04 50 48.8	18.17	34.770	0.4054(4)	0.4(2)	EW	
LRa02b2_45714		06 50 46.2	−06 06 18.6	12.41	35.966	2.232(7)	0.13(2)	SP	
LRa02b2_45820		06 51 27.4	−05 33 00.8	16.66	34.687	0.3715(2)	0.27(4)	EW	
LRa02b2_46129	*c*	06 52 21.3	−04 50 15.1	17.28	35.335	0.7961(7)	0.45(8)	EA	LRa02b2_46220
LRa02b2_46220	*c*	06 52 21.7	−04 50 17.4	17.65	35.340	0.7961(9)	0.4(1)	EA	LRa02b2_46129
LRa02b2_46359		06 50 55.3	−06 01 45.8	17.36	35.230	5.29(1)	0.4(1)	EA	
LRa02b2_46361		06 50 49.7	−06 06 21.8	14.89	34.948	0.4335(4)	0.09(4)	ELL/SP	
LRa02b2_46392	*s*	06 51 43.4	−05 22 30.8	17.10	34.633	0.13991(4)	0.06(5)	DSCT	
LRa02b2_46419		06 50 50.0	−06 06 16.7	14.54	34.745	0.2168(2)	0.03(2)	DSCT	
LRa02b2_46972		06 51 29.2	−05 36 41.7	15.33	34.882	1.170(4)	0.02(2)	SP/ELL	
LRa02b2_48246	*s*	06 52 32.1	−04 50 48.3	15.53	···	···	···	EA	
LRa02b2_49690	*s*	06 51 07.4	−06 06 27.9	14.62	101.044	23.4(9)	0.04(2)	VAR	
LRa02b2_50400	*s*	06 52 03.8	−05 23 35.4	16.26	34.645	6.861(1)	0.12(1)	EA	
LRa02b2_50560	*s*	06 51 34.7	−05 48 09.7	15.66	···	···	···	EA	
LRa02b2_51022	*s*	06 52 31.7	−05 03 21.6	15.31	35.750	13.5(3)	0.04(2)	ELL	
LRa02b2_51885	*s*	06 51 21.2	−06 04 54.3	15.00	99.970	9.9(3)	0.02(2)	ELL	
LRa02b2_53367		06 51 18.6	−06 13 53.7	14.76	34.890	0.6290(3)	0.19(2)	EA	
LRa02b2_53725		06 52 34.7	−05 13 10.1	16.20	39.910	2.8325(1)	0.19(1)	EA	
LRa02b2_53805		06 52 59.2	−04 53 19.1	15.37	34.600	1.083(3)	0.03(2)	ELL/SP	
LRa02b2_54093		06 53 14.5	−04 42 08.2	14.30	39.090	2.548(1)	0.12(1)	EA	
LRa02b2_54271	*s*	06 51 43.4	−05 57 41.1	18.85	34.706	0.1514(2)	0.4(3)	EW/DSCT	
LRa02b2_54589		06 52 57.7	−04 58 05.8	14.44	34.656	0.4588(5)	0.03(2)	EA	
LRa02b2_55891		06 52 39.4	−05 19 21.4	12.25	95.983	18.4(8)	0.03(1)	ELL	
LRa02b2_56746		06 52 24.1	−05 35 55.2	17.63	38.210	4.09(6)	0.2(1)	EA	
LRa02b2_56904		06 51 43.9	−06 09 27.0	13.45	34.589	0.10280(4)	0.02(1)	DSCT	
LRa02b2_57256	*s*	06 53 20.6	−04 51 59.6	15.35	38.176	2.0765(1)	0.08(1)	EA	
LRa02b2_57394	*s*	06 52 51.1	−05 16 53.0	16.12	35.006	1.73(2)	0.05(5)	ELL/SP	
LRa02b2_58068		06 53 09.2	−05 05 03.7	16.19	34.765	0.5321(5)	0.12(3)	EW	
LRa02b2_58620		06 52 58.6	−05 16 21.5	13.19	75.963	38(3)	0.064(8)	CEP	
LRa02b2_59323		06 52 24.8	−05 47 27.3	15.77	34.637	0.12730(7)	0.04(3)	DSCT	
LRa02b2_59446	*c*	06 51 52.5	−06 14 24.3	14.81	35.003	0.5488(7)	0.03(2)	EW	LRa02b2_59484
LRa02b2_59484	*c*	06 51 52.6	−06 14 26.4	14.87	35.010	0.5488(7)	0.03(2)	EW	LRa02b2_59446
LRa02b2_59633		06 52 58.2	−05 21 31.2	17.15	35.800	0.3817(2)	0.55(9)	EB	
LRa02b2_60335	*k*	06 53 34.3	−04 55 30.3	12.41	···	···	···	LP	NSVS 12585233
LRa02b2_60381	*c*	06 53 41.6	−04 49 47.8	17.72	34.598	0.1730(2)	0.2(2)	EW/DSCT	LRa02b2_60435
LRa02b2_60435	*c*	06 53 41.6	−04 49 55.5	16.72	34.611	0.17306(9)	0.20(5)	EW/DSCT	LRa02b2_60381
LRa02b2_60453	*c*	06 53 24.6	−05 04 02.5	16.94	34.749	0.3951(5)	0.11(5)	DSCT	LRa02b2_60497
LRa02b2_60497	*c*	06 53 24.9	−05 03 59.1	17.04	34.766	0.3952(6)	0.08(5)	DSCT	LRa02b2_60453
LRa02b2_60827		06 52 24.7	−05 54 59.8	15.12	34.895	0.3254(2)	0.03(2)	EA	
LRa02b2_61566		06 52 02.4	−06 16 47.2	16.04	35.105	0.5500(8)	0.06(3)	EW	
LRa02b2_62025		06 53 48.3	−04 52 15.2	14.19	34.659	0.08150(3)	0.02(2)	DSCT	
LRa02b2_62405		06 53 00.8	−05 33 19.8	17.47	34.655	0.14175(7)	0.18(8)	DSCT	
LRa02b2_62434		06 53 22.4	−05 15 41.5	16.50	41.565	1.2902(1)	0.4(1)	EA	
LRa02b2_62631	*s*	06 53 05.8	−05 30 17.1	16.31	34.917	1.83(2)	0.06(3)	SP	
LRa02b2_62679		06 53 43.0	−04 59 55.9	13.92	35.550	1.060(3)	0.019(8)	EB	
LRa02b2_62795		06 54 01.2	−04 45 24.3	17.68	34.633	0.12246(5)	0.4(2)	DSCT	
LRa02b2_63427		06 53 02.8	−05 36 44.4	17.93	35.069	0.811(2)	0.2(1)	EW	
LRa02b2_63696		06 52 53.4	−05 46 00.4	16.49	70.493	39.2706(1)	···	CEP	
LRa02b2_63716		06 52 19.4	−06 13 49.5	12.62	···	···	···	LP	
LRa02b2_63848		06 52 33.1	−06 03 22.0	18.90	34.856	0.4155(3)	1.0(4)	EW	
LRa02b2_64557		06 53 04.2	−05 41 25.6	15.72	34.993	1.73(2)	0.05(3)	SP	
LRa02b2_65044		06 52 27.3	−06 14 04.6	14.32	34.696	3.65307(1)	···	ELL/SP	
LRa02b2_65892		06 53 29.5	−05 27 36.8	16.28	34.642	0.9269(9)	0.15(3)	EA	
LRa02b2_67207	*s*	06 53 59.0	−05 10 19.2	16.78	34.695	0.1521(2)	0.07(5)	EW/DSCT	
LRa02b2_67578	*s*	06 53 51.0	−05 18 46.2	18.61	34.587	0.13967(7)	0.6(4)	DSCT	
LRa02b2_67689		06 53 08.6	−05 54 06.0	16.64	35.065	1.1468(1)	0.2(1)	EA	
LRa02b2_68447		06 53 34.5	−05 36 41.6	14.46	35.481	3.06(2)	0.05(2)	ELL/SP	
LRa02b2_68479		06 53 34.7	−05 36 37.6	14.38	35.506	3.06(2)	0.05(2)	ELL/SP	
LRa02b2_70266		06 54 11.6	−05 15 21.8	16.27	34.832	0.3779(2)	0.20(3)	EW	
LRa02b2_70360		06 53 11.2	−06 05 18.3	16.34	34.755	0.6076(5)	0.16(4)	EA	
LRa02b2_70715	*c*	06 54 06.1	−05 22 12.3	18.01	34.791	1.545(4)	0.3(2)	EA	LRa02b2_70769
LRa02b2_70769	*c*	06 54 06.3	−05 22 16.7	17.95	34.790	1.544(4)	0.4(2)	EA	LRa02b2_70715
LRa02b2_71171		06 54 30.6	−05 04 15.1	16.38	35.823	1.4336(1)	0.3(1)	EA	
LRa02b2_71734	*s*	06 53 46.5	−05 43 20.7	15.80	51.029	7.4(2)	0.05(2)	ELL	
LRa02b2_71766		06 53 31.8	−05 55 35.7	15.57	45.881	8.1(2)	0.05(2)	ELL	
LRa02b2_71833		06 53 30.7	−05 56 43.7	15.18	39.502	2.57(2)	0.04(2)	EB	
LRa02b2_72028		06 53 52.6	−05 39 49.7	14.33	104.975	16.1(3)	0.06(1)	SP	
LRa02b2_72229		06 54 28.1	−05 11 31.7	17.08	34.772	0.3202(5)	0.13(6)	EW/DSCT	
LRa02b2_72506		06 53 41.2	−05 51 30.1	17.65	34.727	0.5563(6)	0.4(2)	EB	
LRa02b2_72792	*s*	06 54 07.8	−05 31 16.6	15.87	39.815	8.595(1)	0.1(1)	EA	
LRa02b2_73086		06 53 24.0	−06 08 41.7	15.28	78.205	8.4(2)	0.09(2)	CEP	
LRa02b2_73250		06 53 14.7	−06 17 04.7	16.22	34.615	0.4629(6)	0.10(4)	DSCT	

Table E.1: Variable stars in field LRa02 through reanalysis (continued).

BEST ID	F	α (J2000.0) h m s	δ ° ′ ″	R_B [mag]	T_0 [d] [rHJD]	p [d]	A [mag]	Type	Other Names
LRa02b2_74274		06 53 49.7	−05 53 48.5	16.83	34.790	0.2840(2)	0.20(5)	EW	
LRa02b2_74768		06 53 24.9	−06 16 26.4	17.31	34.962	1.121(2)	0.5(1)	EA	
LRa02b2_75238		06 54 12.7	−05 39 49.7	15.37	48.996	5.75(9)	0.05(2)	SP	
LRa02b2_75988	*s*	06 54 53.0	−05 10 19.1	18.66	35.219	1.146(2)	0.8(3)	EA	
LRa02b2_76168		06 55 09.0	−04 58 01.3	16.66	34.842	2.38(7)	0.11(4)	CEP	

Table E.2: Variable stars in field LRa02 with revised parameters (see description on page 180).

BEST ID	F	α (J2000.0) h m s	δ ° ′ ″	R_B [mag]	T_0 [d] [rHJD]	p [d]	A [mag]	Type	Other Names
LRa02a2_04976	*k*	06 47 31.2	−04 32 56.9	15.05	···	···	···	EA	lra2a_00269
LRa02a2_07847	*k*	06 48 31.9	−04 07 57.9	16.45	39.649	1.5015(1)	1.3(1)	EA	lra2a_00416
LRa02a2_08694	*k*	06 49 11.9	−03 42 33.8	16.14	34.694	0.31415(5)	0.46(3)	EW	lra2a_00450
LRa02a2_10471	*k*	06 50 03.3	−03 15 47.4	16.44	35.159	2.695(1)	0.8(1)	EA	lra2a_00531
LRa02a2_12019	*k*	06 48 55.1	−04 23 38.1	15.33	···	···	···	CEP	CoRoT 110826631, lra2a_00601
LRa02a2_24433	*ck*	06 52 00.5	−03 26 32.8	13.66	98.695	6.785(1)	0.6(1)	EA	CoRoT 110677259, lra2a_01126, LRa02a2_24442
LRa02a2_24442	*ck*	06 52 00.8	−03 26 25.7	14.32	98.695	6.785(1)	0.26(1)	EA	lra2a_01127, LRa02a2_24433
LRa02b2_03306	*k*	06 47 43.8	−05 41 12.7	12.57	···	···	···	LP	lra2b_01648
LRa02b2_05167	*k*	06 48 45.4	−04 58 26.2	15.69	34.740	0.7749(4)	0.43(4)	EA	lra2b_01600
LRa02b2_13901	*k*	06 48 40.7	−05 37 53.6	14.33	35.085	0.52869(9)	0.39(2)	EW	lra2b_01437
LRa02b2_23935	*k*	06 49 15.7	−05 50 38.9	14.06	35.241	2.966(8)	0.16(2)	EA	lra2b_01257
LRa02b2_31945	*k*	06 50 23.9	−05 26 29.5	15.60	34.697	2.239(4)	0.24(4)	EA	lra2b_01080
LRa02b2_38262	*k*	06 50 53.6	−05 27 40.8	12.43	41.500	41(1)	0.18(1)	SR	lra2b_00968
LRa02b2_48861	*k*	06 51 23.9	−05 49 23.6	13.58	···	···	···	LP	lra2b_00738
LRa02b2_51632	*k*	06 51 19.7	−06 05 02.2	15.92	35.282	1.388(4)	0.08(5)	ELL/SP	lra2b_00687
LRa02b2_59423	*k*	06 52 27.3	−05 45 51.8	13.41	34.730	1.8214(1)	0.62(1)	EA	lra2b_00469
LRa02b2_66851	*k*	06 53 19.6	−05 40 49.6	15.29	34.760	0.45935(9)	0.57(3)	EW	lra2b_00323

E.2 F17

Table E.3: Variable stars in field F17 (see description on page 180).

BEST ID	F	α (J2000.0) h m s	δ ° ′ ″	R_B [mag]	T_0 [d] [rHJD]	p [d]	A [mag]	Type	Other Names
F17_00273		14 19 05.6	−53 57 06.4	14.12	54.014	12.0(3)	0.024(8)	ROT	
F17_00277		14 18 42.1	−54 10 59.8	14.40	47.292	19(2)	0.03(2)	ROT	
F17_00346	*s*	14 19 48.1	−53 32 20.4	14.59	···	···	···	LP	
F17_00411	*s*	14 18 47.8	−54 08 33.7	12.77	64.080	13.5(3)	0.03(2)	ROT	
F17_00448		14 19 52.8	−53 30 18.6	16.66	42.634	0.3055(2)	0.21(7)	EW	
F17_00521		14 19 47.2	−53 34 10.9	14.39	···	···	···	SR	
F17_00592	*s*	14 19 41.2	−53 38 22.9	13.42	67.176	26(2)	0.030(7)	CEP	
F17_00606	*c*	14 20 24.9	−53 12 11.8	13.98	44.059	4.8239(1)	0.13(1)	EA	
F17_00651		14 20 02.0	−53 26 19.9	17.89	42.686	0.4451(4)	0.8(2)	EB	
F17_00709	*cs*	14 20 26.1	−53 12 09.9	14.89	42.563	2.62(2)	0.29(5)	EA	
F17_00717		14 19 17.3	−53 53 27.2	16.44	42.551	0.09229(4)	0.13(4)	DSCT	
F17_00894	*s*	14 18 08.8	−54 34 51.0	14.27	62.361	12.3(3)	0.02(2)	ROT	
F17_00965		14 17 57.2	−54 42 01.4	14.47	···	···	···	LP	
F17_01116	*c*	14 18 48.9	−54 13 00.8	17.58	53.133	9.8(5)	0.2(2)	VAR	F17_01153
F17_01117	*s*	14 18 43.8	−54 16 03.5	14.61	52.338	15.5(7)	0.02(2)	ROT	
F17_01144		14 18 01.4	−54 40 57.5	14.77	42.961	0.5445(3)	0.07(2)	EA	
F17_01153	*c*	14 18 49.2	−54 13 05.8	17.57	52.896	9.8(5)	0.3(2)	VAR	F17_01116
F17_01210	*c*	14 18 47.4	−54 14 38.7	16.28	42.831	0.3696(3)	0.13(4)	EW	F17_01262
F17_01262	*c*	14 18 48.1	−54 14 35.6	15.74	42.834	0.3696(4)	0.04(3)	EW	F17_01210
F17_01265		14 18 16.9	−54 32 51.3	12.88	119.905	27(3)	0.05(1)	ROT	
F17_01433		14 18 08.1	−54 39 06.0	13.37	···	···	···	LP	
F17_01443	*c*	14 20 18.8	−53 21 48.4	14.31	63.761	26(2)	0.10(2)	ROT	
F17_01490	*c*	14 19 51.7	−53 38 29.1	17.71	42.505	0.3253(3)	0.3(2)	EW/DSCT	
F17_01546		14 20 29.5	−53 16 01.7	12.99	51.327	22(2)	0.04(2)	ROT	
F17_01613		14 19 42.2	−53 44 54.7	13.40	42.861	0.4261(9)	0.02(2)	RR	
F17_01801	*c*	14 19 51.7	−53 40 33.0	14.30	44.723	3.6355(1)	0.29(1)	EA	
F17_01804		14 19 31.3	−53 52 48.9	15.20	···	···	···	LP	
F17_01813		14 19 34.2	−53 51 06.3	15.84	42.614	0.38048(9)	0.53(3)	EW	
F17_01848		14 19 42.1	−53 46 46.4	12.64	···	···	···	LP	
F17_01935		14 18 18.9	−54 36 16.6	12.63	···	···	···	LP	
F17_01960		14 20 07.7	−53 32 09.1	15.50	44.630	19.55(1)	0.5(1)	EA	
F17_02004	*c*	14 18 18.5	−54 36 52.6	16.53	42.494	0.28722(9)	0.38(5)	EW	
F17_02036	*s*	14 18 10.0	−54 42 05.9	16.88	42.507	0.15324(9)	0.05(6)	DSCT	
F17_02052		14 20 35.6	−53 15 51.3	13.92	42.527	0.4566(8)	0.03(2)	RR	
F17_02104		14 20 12.3	−53 30 12.5	16.90	42.532	0.7518(5)	0.63(8)	EA	
F17_02108	*c*	14 19 33.6	−53 53 27.3	14.31	42.775	0.4374(3)	0.09(2)	EW	
F17_02333		14 20 31.9	−53 19 57.0	13.37	42.932	0.5038(5)	0.050(8)	EW	
F17_02613		14 19 21.0	−54 04 19.6	13.15	···	···	···	LP	
F17_02614		14 19 19.6	−54 05 09.3	17.45	42.498	0.5734(7)	0.2(1)	EW	

Table E.3: Variable stars in field F17 (continued).

BEST ID	F	α (J2000.0) h m s	δ ° ′ ″	R_B [mag]	T_0 [d] [rHJD]	p [d]	A [mag]	Type	Other Names
F17_02646		14 18 46.4	−54 24 54.3	12.89	...	...	...	SR	
F17_02928		14 19 33.6	−53 59 11.2	14.31	...	...	...	LP	
F17_02983		14 19 42.5	−53 54 19.2	12.65	42.599	2.0162(1)	0.11(1)	EA	
F17_03214	*s*	14 20 10.5	−53 38 53.9	13.40	...	...	...	LP	
F17_03232	*s*	14 19 49.9	−53 51 21.7	14.57	49.099	10.2(4)	0.03(2)	ROT	
F17_03286	*s*	14 19 14.1	−54 13 04.3	14.86	44.103	0.843(3)	0.02(2)	RR	
F17_03290	*c*	14 18 22.9	−54 43 08.0	14.91	42.990	0.5038(2)	0.48(3)	EA	
F17_03306		14 20 53.4	−53 13 34.9	14.63	42.756	0.3813(1)	0.24(2)	EW	
F17_03340	*s*	14 20 24.0	−53 31 41.8	13.58	60.601	17.1(4)	0.04(1)	VAR	
F17_03381		14 19 08.3	−54 17 19.9	17.87	49.065	3.80(9)	0.3(2)	CEP	
F17_03395	*s*	14 19 05.9	−54 18 51.7	14.60	...	...	...	SR	
F17_03416	*c*	14 18 23.9	−54 43 33.4	16.61	42.649	0.3729(3)	0.13(5)	EW/DSCT	F17_03487
F17_03458	*k*	14 20 12.0	−53 39 53.9	11.61	60.675	3.3266(1)	...	ROT	ASAS J142013-5339.9
F17_03487	*c*	14 18 24.5	−54 43 35.9	17.15	42.646	0.3729(4)	0.12(8)	EW/DSCT	F17_03416
F17_03675	*s*	14 18 52.8	−54 28 29.8	13.53	53.172	8.12(6)	0.042(8)	ROT	
F17_04001		14 20 15.9	−53 41 10.4	12.95	...	...	...	SR	
F17_04009		14 20 26.5	−53 34 49.0	14.88	46.773	1.467(2)	0.28(2)	EA	
F17_04082		14 19 13.8	−54 18 45.0	15.62	42.747	0.4485(2)	0.39(3)	EW	
F17_04137		14 20 47.6	−53 22 58.5	13.44	...	...	...	SR	
F17_04206		14 20 19.0	−53 40 41.5	17.62	42.548	0.4757(6)	0.2(2)	EW	
F17_04243		14 20 05.4	−53 49 04.6	16.08	42.884	0.4813(4)	0.07(4)	EA	
F17_04294		14 18 36.5	−54 42 02.7	13.52	44.555	14.5(3)	0.49(4)	CEP	
F17_04425		14 20 57.6	−53 18 52.3	14.64	...	...	...	LP	
F17_04458	*s*	14 19 54.6	−53 57 13.1	13.64	62.879	34(2)	0.060(8)	ROT	
F17_04659		14 18 39.3	−54 43 08.3	18.29	42.555	0.2698(2)	1.1(3)	EW	
F17_04858		14 18 52.5	−54 36 52.9	17.98	42.628	0.3358(2)	0.6(2)	EW	
F17_05185	*s*	14 19 58.5	−54 00 17.0	14.98	42.492	0.030991(4)	0.01(2)	SXPHE	
F17_05238		14 18 49.1	−54 41 40.8	13.71	...	...	...	LP	
F17_05265		14 19 23.4	−54 21 40.5	14.75	48.836	2.87(3)	0.04(2)	ROT	
F17_05282		14 19 31.3	−54 17 15.7	13.40	42.673	0.4022(3)	0.029(4)	EW	
F17_05350		14 19 10.8	−54 29 52.3	15.03	42.507	0.12115(7)	0.02(2)	DSCT	
F17_05423		14 19 51.2	−54 06 13.2	14.45	...	...	...	LP	
F17_05429		14 18 47.5	−54 43 51.1	12.60	...	...	...	LP	
F17_05600	*s*	14 19 24.9	−54 23 14.6	13.90	46.954	3.7(2)	0.015(7)	ROT	
F17_05608		14 20 35.9	−53 40 47.2	13.39	...	...	...	LP	
F17_05677	*c*	14 19 39.8	−54 14 53.5	13.67	44.435	12.5(5)	0.04(2)	ROT	
F17_05696		14 19 24.4	−54 24 08.1	13.10	42.493	0.07347(3)	0.006(7)	DSCT	
F17_05740		14 18 56.0	−54 41 07.8	15.11	44.586	0.7909(3)	0.48(2)	EB	
F17_05786	*s*	14 19 32.2	−54 20 07.6	13.35	46.681	5.8(2)	0.021(6)	ROT	
F17_05999		14 18 52.4	−54 44 58.9	16.03	47.351	5.51(2)	0.72(6)	EA	
F17_06088	*s*	14 20 41.5	−53 40 34.1	13.98	...	...	...	LP	
F17_06287	*s*	14 19 40.0	−54 18 50.8	13.17	...	...	...	LP	
F17_06360		14 20 11.6	−54 00 28.2	15.58	42.818	0.8598(4)	0.45(3)	EA	
F17_06423	*c*	14 19 08.6	−54 38 21.5	14.93	42.587	0.796(3)	0.02(2)	DSCT	F17_06491
F17_06491	*c*	14 19 09.2	−54 38 21.6	14.94	42.691	0.796(2)	0.03(2)	DSCT	F17_06423
F17_06502		14 20 48.2	−53 39 12.3	16.25	42.588	0.1863(2)	0.09(4)	DSCT	
F17_06560	*s*	14 19 23.6	−54 30 18.3	12.92	...	...	...	LP	
F17_06571		14 21 16.5	−53 22 21.4	14.39	...	...	...	LP	
F17_06654		14 19 36.9	−54 23 04.6	15.21	42.795	0.4443(5)	0.02(2)	EW	
F17_06662		14 20 43.9	−53 42 56.4	14.64	42.623	0.4114(4)	0.03(2)	EW	
F17_06674		14 20 23.2	−53 55 31.3	12.34	...	...	...	LP	
F17_06731		14 20 25.6	−53 54 31.3	12.82	...	...	...	LP	
F17_06794	*s*	14 20 04.0	−54 07 50.6	16.02	...	...	...	LP	
F17_06858		14 20 48.8	−53 41 13.3	15.58	44.763	2.723(6)	0.29(4)	EA	
F17_06893		14 19 47.9	−54 18 06.1	14.08	...	...	...	LP	
F17_06935	*s*	14 19 57.0	−54 13 01.9	14.03	75.636	16.1(8)	0.05(1)	ROT	
F17_06998	*cs*	14 20 19.1	−54 00 10.4	16.86	48.247	9.6(3)	0.17(7)	ROT	F17_07049
F17_07042	*c*	14 21 02.7	−53 33 59.2	15.19	42.681	0.423(1)	0.02(2)	DSCT	F17_07122
F17_07049	*cs*	14 20 19.4	−54 00 13.0	16.93	48.305	9.6(2)	0.17(7)	ROT	F17_06998
F17_07053	*s*	14 19 26.8	−54 31 41.7	17.33	42.931	0.613(1)	0.11(9)	EB	
F17_07082		14 19 33.8	−54 27 39.3	13.99	51.312	17.5(7)	0.035(8)	ROT	
F17_07090	*s*	14 21 21.2	−53 22 57.6	16.21	55.850	2.5373(1)	0.2(1)	EA	
F17_07122	*c*	14 21 03.3	−53 34 02.7	15.37	42.724	0.4229(8)	0.05(3)	DSCT	F17_07042
F17_07270	*c*	14 21 04.7	−53 34 25.8	16.06	153.311	23(2)	0.11(3)	ROT	
F17_07295		14 21 22.8	−53 23 31.9	12.93	42.815	18.0(7)	0.05(1)	ROT	
F17_07331		14 21 15.6	−53 28 07.7	15.08	...	...	...	LP	
F17_07411		14 19 50.6	−54 20 08.0	13.47	...	...	...	LP	
F17_07452		14 21 36.2	−53 16 19.1	13.55	...	...	...	LP	
F17_07538		14 20 36.6	−53 53 21.9	14.57	...	...	...	LP	
F17_07553		14 20 37.9	−53 52 43.4	17.50	42.536	0.3696(4)	0.2(2)	EW/DSCT	
F17_07589		14 19 21.2	−54 38 40.3	15.43	46.585	1.374(2)	0.69(3)	CEP	
F17_07664		14 20 36.6	−53 54 10.0	14.04	42.838	0.839(4)	0.02(1)	RR	
F17_07698		14 20 28.8	−53 59 06.5	13.05	149.451	55(3)	0.23(2)	VAR	
F17_07729		14 19 14.3	−54 43 42.3	12.79	...	...	...	LP	
F17_07741	*cs*	14 20 34.1	−53 56 13.4	14.66	42.528	0.05080(2)	0.01(2)	DSCT	F17_07786
F17_07786	*cs*	14 20 34.5	−53 56 09.6	14.72	42.528	0.05080(2)	0.01(2)	DSCT	F17_07741
F17_07829	*s*	14 21 20.9	−53 28 17.2	14.94	...	...	...	LP	
F17_07888		14 21 31.8	−53 21 53.0	12.40	...	...	...	LP	
F17_07973		14 21 16.2	−53 32 12.8	14.28	...	...	...	LP	
F17_08103		14 21 11.9	−53 35 47.5	14.77	42.837	1.147(4)	0.06(2)	EB	
F17_08132		14 21 36.6	−53 20 49.8	15.97	42.562	0.2290(3)	0.05(5)	DSCT	
F17_08136		14 21 17.9	−53 32 16.2	16.44	42.756	0.3443(2)	0.37(5)	EW	
F17_08318		14 20 28.4	−54 03 30.4	13.61	...	...	...	LP	
F17_08408		14 20 08.8	−54 15 52.5	14.19	53.277	21.6(5)	0.108(8)	ROT	
F17_08559		14 20 14.3	−54 13 34.4	16.79	44.136	1.099(2)	0.31(6)	EA	
F17_08626	*c*	14 19 27.9	−54 41 34.8	11.75	...	...	...	LP	F17_08686
F17_08668		14 19 35.4	−54 37 24.0	13.35	...	...	...	LP	
F17_08686	*c*	14 19 28.3	−54 41 41.7	12.16	...	...	...	LP	F17_08626

Table E.3: Variable stars in field F17 (continued).

BEST ID	F	α (J2000.0) h m s	δ ° ′ ″	R_B [mag]	T_0 [d] [rHJD]	p [d]	A [mag]	Type	Other Names
F17_08708	*c*	14 21 44.0	−53 19 55.3	14.79	···	···	···	LP	
F17_08727	*s*	14 21 15.7	−53 37 28.8	14.92	42.674	0.4404(9)	0.02(2)	RR	
F17_08837		14 19 57.8	−54 25 13.5	14.10	···	···	···	LP	
F17_08982	*c*	14 20 11.0	−54 18 21.1	12.67	42.505	0.07023(3)	0.009(7)	DSCT	
F17_09074		14 20 13.5	−54 17 25.6	12.19	···	···	···	LP	
F17_09094		14 19 54.1	−54 29 02.0	15.73	42.671	10.5(3)	0.10(3)	ROT	
F17_09183		14 21 44.1	−53 23 01.3	14.17	42.814	0.4663(2)	0.12(2)	EW	
F17_09194		14 21 50.2	−53 19 18.3	14.90	···	···	···	LP	
F17_09205	*s*	14 20 28.3	−54 09 24.5	12.18	···	···	···	EB	
F17_09217		14 21 07.3	−53 45 51.6	14.58	···	···	···	LP	
F17_09272		14 20 35.3	−54 05 37.8	13.68	44.426	23.8(5)	0.088(8)	EB	
F17_09279		14 19 29.4	−54 45 01.3	16.64	42.627	0.3500(3)	0.20(6)	EW	
F17_09386	*c*	14 21 11.6	−53 44 32.1	13.17	42.587	0.7047(3)	0.35(2)	EB	
F17_09418		14 21 13.4	−53 43 40.2	18.31	42.636	0.3949(4)	0.4(3)	EW	
F17_09506		14 20 07.1	−54 24 18.1	13.39	42.693	0.2529(2)	0.019(8)	EW/DSCT	
F17_09524		14 20 28.7	−54 11 24.2	12.83	···	···	···	SR	
F17_09602		14 21 21.7	−53 39 50.1	16.00	42.621	0.763(2)	0.14(7)	EW	
F17_09622		14 20 56.5	−53 55 23.4	12.13	···	···	···	LP	
F17_09624	*c*	14 20 29.6	−54 11 39.7	14.07	47.205	3.69(7)	0.04(2)	ROT	F17_09661
F17_09625		14 20 14.7	−54 20 34.6	11.94	···	···	···	LP	
F17_09661	*c*	14 20 30.0	−54 11 34.6	13.75	47.353	3.66(5)	0.04(1)	ROT	F17_09624
F17_09664		14 20 12.2	−54 22 14.9	17.02	42.906	0.649(1)	0.17(7)	EW	
F17_09750		14 19 54.1	−54 33 33.3	16.02	42.527	0.05904(2)	0.05(3)	DSCT	
F17_09751	*s*	14 19 37.6	−54 43 18.1	16.82	42.551	0.14929(7)	0.05(6)	DSCT	
F17_09753	*c*	14 19 34.5	−54 45 07.2	15.12	···	···	···	LP	
F17_09775		14 21 48.8	−53 24 06.5	12.91	103.997	15.2(5)	0.03(1)	CEP	
F17_09946	*c*	14 20 11.4	−54 24 43.1	15.46	42.681	0.3078(3)	0.06(3)	EW	F17_10010
F17_09960		14 20 24.5	−54 16 48.1	17.14	42.875	0.4156(5)	0.13(7)	EW/DSCT	
F17_09966	*c*	14 21 29.4	−53 37 29.4	16.55	42.641	0.2906(2)	0.24(5)	EW	F17_10007
F17_10007	*c*	14 21 29.7	−53 37 32.6	16.51	42.641	0.2906(2)	0.28(5)	EW	F17_09966
F17_10010	*c*	14 20 12.0	−54 24 44.2	15.07	42.685	0.3078(2)	0.06(2)	EW	F17_09946
F17_10150		14 22 05.8	−53 16 16.2	12.87	44.183	22(2)	0.07(2)	ROT	
F17_10179		14 20 41.1	−54 08 26.2	17.74	42.707	0.4526(5)	0.2(2)	EW/DSCT	
F17_10212		14 20 49.6	−54 03 25.9	15.24	142.416	17(2)	0.05(2)	CEP	
F17_10230	*s*	14 19 56.7	−54 35 18.9	14.51	···	···	···	LP	
F17_10234	*cs*	14 21 47.3	−53 28 18.5	16.66	42.556	0.647(2)	0.06(5)	EW/DSCT	F17_10254
F17_10254	*cs*	14 21 47.5	−53 28 15.3	16.81	42.557	0.647(2)	0.07(6)	EW/DSCT	F17_10234
F17_10421		14 21 15.2	−53 49 25.1	14.64	46.884	1.616(2)	0.41(2)	EA	
F17_10529	*s*	14 20 22.4	−54 22 04.4	13.06	···	···	···	LP	
F17_10593	*s*	14 20 29.5	−54 18 23.0	16.22	···	···	···	LP	
F17_10765		14 19 48.0	−54 44 14.7	14.50	···	···	···	LP	
F17_10844	*c*	14 21 49.4	−53 31 21.0	11.52	42.600	2.2743	0.048	EA	
F17_10863		14 21 50.7	−53 30 41.2	14.96	118.122	25(2)	0.06(2)	ROT	
F17_10918		14 20 19.1	−54 26 45.8	17.07	42.572	0.3249(3)	0.12(7)	EW/DSCT	
F17_10945	*c*	14 19 52.5	−54 42 44.6	15.63	42.819	0.5845(3)	0.40(3)	EW	
F17_10957		14 20 23.9	−54 24 10.1	18.08	42.591	0.2785(2)	0.8(3)	EW	
F17_11288		14 21 15.0	−53 55 24.6	17.33	42.729	0.3252(3)	0.25(8)	EW	
F17_11416	*c*	14 20 09.8	−54 35 36.0	15.37	42.747	0.4043(3)	0.10(3)	EW	F17_11417
F17_11417	*c*	14 20 09.7	−54 35 38.6	16.02	42.748	0.4043(2)	0.20(4)	EW	F17_11416
F17_11612		14 20 57.7	−54 08 00.6	16.25	42.715	1.664(2)	0.57(5)	EA	
F17_11632	*s*	14 20 49.7	−54 12 55.6	18.29	42.616	0.4074(5)	0.2(2)	EW/DSCT	
F17_11814	*s*	14 21 42.2	−53 42 08.6	13.78	42.536	0.05614(2)	0.013(7)	DSCT	
F17_11947		14 22 25.2	−53 16 22.0	16.69	42.720	0.5089(7)	0.09(5)	EW	
F17_12085		14 20 57.0	−54 11 37.1	15.50	···	···	···	LP	
F17_12090		14 20 36.2	−54 24 08.9	16.09	···	···	···	LP	
F17_12218		14 20 25.6	−54 31 26.9	16.07	44.567	0.7594(6)	0.25(3)	EW	
F17_12234		14 20 54.3	−54 14 14.8	17.74	42.625	0.4115(6)	0.2(2)	EW/DSCT	
F17_12247	*s*	14 22 14.5	−53 25 03.5	18.10	42.981	0.5065(7)	0.2(2)	EW	
F17_12396		14 20 35.4	−54 26 36.5	15.60	···	···	···	LP	
F17_12419	*s*	14 20 00.4	−54 47 30.2	13.69	···	···	···	LP	
F17_12548		14 22 33.4	−53 15 08.0	15.70	42.816	0.6002(8)	0.08(3)	EW	
F17_12564		14 22 09.4	−53 30 15.5	13.76	···	···	···	LP	
F17_12690		14 22 32.2	−53 16 50.8	13.18	···	···	···	LP	
F17_12734	*c*	14 21 20.3	−54 01 37.7	15.70	42.922	0.5614(3)	0.29(3)	EW	
F17_13119		14 22 33.0	−53 19 22.1	17.27	42.633	0.1532(2)	0.12(9)	DSCT	
F17_13201		14 21 24.6	−54 02 22.6	15.41	···	···	···	LP	
F17_13303		14 20 44.5	−54 27 20.6	17.77	44.490	1.0935(1)	0.5(1)	EA	
F17_13447		14 20 20.3	−54 42 44.0	14.77	42.735	0.5612(2)	0.26(2)	EW	
F17_13626	*c*	14 20 59.9	−54 20 05.1	15.08	42.959	0.5737(8)	0.07(3)	EB	F17_13644
F17_13644	*c*	14 20 59.9	−54 20 11.8	14.67	42.955	0.5737(4)	0.10(1)	EB	F17_13626
F17_13656		14 22 02.8	−53 41 45.0	12.15	···	···	···	LP	
F17_13675	*s*	14 21 32.3	−54 00 41.5	18.48	42.563	0.09026(4)	0.2(3)	DSCT	
F17_13692		14 20 36.4	−54 34 42.1	15.45	42.522	0.09461(5)	0.03(2)	DSCT	
F17_13818		14 21 38.8	−53 57 38.2	13.02	···	···	···	SR	
F17_13950		14 21 36.5	−53 59 53.3	17.11	42.743	0.4072(4)	0.20(7)	EW	
F17_13977		14 21 20.2	−54 09 56.3	18.64	42.550	0.6711(1)	1.4(1)	EA	
F17_14061	*c*	14 22 49.1	−53 15 10.6	12.94	···	···	···	LP	
F17_14141		14 22 18.2	−53 35 01.9	17.57	42.737	0.3058(2)	0.2(1)	EW/DSCT	
F17_14321	*s*	14 20 24.0	−54 45 55.8	13.55	51.072	10.3(2)	0.031(8)	ROT	
F17_14352		14 21 41.8	−53 59 02.1	13.42	···	···	···	LP	
F17_14373		14 20 59.7	−54 24 47.1	14.80	42.692	0.5266(2)	0.37(2)	EA	
F17_14585	*s*	14 21 45.2	−53 58 22.3	13.11	51.187	9.9(4)	0.020(7)	ROT	
F17_14619	*s*	14 22 38.6	−53 25 26.7	13.64	53.388	13.0(7)	0.03(1)	ROT	
F17_14642		14 21 34.0	−54 05 43.4	17.82	42.761	0.3306(5)	0.1(2)	EW/DSCT	
F17_14714		14 22 00.1	−53 50 08.1	15.95	42.531	0.4853(6)	0.06(4)	EW	
F17_14958		14 21 41.3	−54 03 21.7	16.65	46.546	1.474(4)	0.13(5)	EA	
F17_15138		14 21 07.6	−54 25 03.0	16.55	42.538	0.08817(4)	0.10(5)	DSCT	
F17_15184	*c*	14 20 34.9	−54 45 06.8	17.10	42.633	0.3457(2)	0.27(8)	EW	

Table E.3: Variable stars in field F17 (continued).

BEST ID	F	α (J2000.0) h m s	δ ° ′ ″	R_B [mag]	T_0 [d] [rHJD]	p [d]	A [mag]	Type	Other Names
F17_15203	*c*	14 21 20.0	−54 18 09.1	15.11	61.117	27(3)	0.05(2)	ROT	
F17_15278	*c*	14 22 40.8	−53 28 39.6	16.44	42.580	0.4074(2)	0.54(6)	RR	F17_15316, F17_15395
F17_15285	*c*	14 21 20.7	−54 18 10.1	15.03	62.106	26(3)	0.05(2)	ROT	
F17_15316	*c*	14 22 41.3	−53 28 33.4	16.71	42.580	0.4074(3)	0.36(6)	RR	F17_15278, F17_15395, F17_15455
F17_15395	*c*	14 22 41.8	−53 28 42.0	15.63	42.580	0.40738(9)	0.87(4)	RR	F17_15278, F17_15316, F17_15455
F17_15455	*c*	14 22 42.5	−53 28 40.3	15.89	42.581	0.4074(2)	0.64(4)	RR	F17_15316, F17_15395
F17_15528		14 21 06.6	−54 28 17.9	15.77	51.457	23(2)	0.10(3)	CEP	
F17_15651		14 22 04.8	−53 53 32.4	13.44	...	...	...	LP	
F17_15719		14 23 01.3	−53 18 36.7	17.88	42.596	0.3605(2)	0.6(2)	EW	
F17_15775		14 21 17.7	−54 23 14.5	13.78	54.651	20(1)	0.05(2)	ROT	
F17_16055	*s*	14 20 58.5	−54 36 41.3	12.27	56.938	42(4)	0.056(8)	VAR	
F17_16062	*cs*	14 20 42.3	−54 46 25.3	17.82	42.576	0.13849(7)	0.3(2)	DSCT	F17_16121
F17_16118		14 20 52.2	−54 40 50.4	17.21	44.763	0.829(2)	0.25(9)	EA	
F17_16121	*cs*	14 20 43.0	−54 46 21.8	17.72	42.554	0.13848(7)	0.2(2)	DSCT	F17_16062
F17_16253		14 22 08.8	−53 55 04.1	16.06	46.335	4.40(7)	0.08(4)	CEP	
F17_16316		14 21 55.1	−54 03 58.6	11.13	...	...	...	LP	
F17_16496	*s*	14 22 53.0	−53 29 11.3	11.56	48.290	10.4(3)	0.026(6)	CEP	
F17_16551		14 21 51.1	−54 08 08.0	14.17	...	...	...	LP	
F17_16630	*s*	14 22 52.2	−53 30 38.5	12.43	...	...	...	LP	
F17_16823	*s*	14 22 10.0	−53 58 08.4	14.47	53.280	14(5)	0.03(2)	ROT	
F17_16849		14 21 16.2	−54 31 26.8	14.19	57.094	15(2)	0.020(7)	ROT	
F17_17020	*c*	14 22 44.4	−53 38 08.0	15.79	46.640	10.036(1)	0.47(1)	EA	F17_17034
F17_17034	*c*	14 22 44.3	−53 38 13.8	16.04	46.640	10.036(1)	0.38(1)	EA	F17_17020
F17_17051	*s*	14 21 25.2	−54 27 18.5	12.02	...	...	...	LP	
F17_17118	*s*	14 22 34.9	−53 44 42.0	12.52	42.509	0.07137(3)	0.01(2)	DSCT	
F17_17138		14 21 23.3	−54 28 57.8	16.46	...	...	...	LP	
F17_17177		14 22 25.5	−53 51 01.0	13.35	57.946	16.9(6)	0.05(2)	ROT	
F17_17195	*s*	14 21 35.1	−54 22 10.2	14.88	44.468	0.717(2)	0.01(2)	DSCT	
F17_17260		14 22 24.3	−53 52 22.7	16.85	42.934	0.5848(6)	0.17(6)	EA	
F17_17281		14 21 08.0	−54 39 14.2	15.90	42.625	0.4142(5)	0.04(3)	EB	
F17_17451		14 21 10.9	−54 38 34.8	15.94	42.976	0.7139(5)	0.26(3)	EA	
F17_17457		14 23 13.7	−53 22 32.3	13.90	...	...	...	LP	
F17_17659	*c*	14 21 46.5	−54 18 21.0	14.51	...	...	...	LP	F17_17697
F17_17697	*c*	14 21 46.8	−54 18 19.7	14.51	...	...	...	LP	F17_17659
F17_17699		14 21 31.7	−54 27 33.9	16.72	44.850	1.651(4)	0.16(6)	EA	
F17_17840	*s*	14 22 36.9	−53 48 18.0	14.54	...	...	...	LP	
F17_17847	*s*	14 21 17.9	−54 36 58.6	15.39	...	...	...	LP	
F17_17857	*s*	14 22 46.9	−53 42 09.7	14.99	42.532	0.09893(5)	0.02(2)	DSCT	
F17_17937		14 21 19.4	−54 36 38.4	13.91	...	...	...	LP	
F17_18152	*s*	14 21 26.1	−54 34 00.8	14.26	53.334	12.2(4)	0.04(2)	ROT	
F17_18287	*s*	14 21 16.3	−54 40 49.4	13.76	98.241	29(2)	0.05(2)	ROT	
F17_18348		14 22 45.5	−53 46 26.1	12.08	...	...	...	LP	
F17_18573	*s*	14 22 32.8	−53 55 59.2	17.14	42.721	0.718(3)	0.09(7)	RR	
F17_18806		14 22 12.5	−54 10 08.6	16.32	42.824	0.726(3)	0.07(4)	DSCT	
F17_18946	*s*	14 21 11.9	−54 47 57.9	16.30	42.677	0.4917(9)	0.09(4)	RR	
F17_18991		14 22 18.2	−54 07 51.2	14.17	42.575	0.7848(3)	0.347(8)	EW	
F17_19008	*s*	14 22 02.9	−54 17 22.1	14.59	46.003	22(3)	0.04(2)	CEP	
F17_19012		14 21 26.2	−54 39 45.2	12.56	...	...	...	SR	
F17_19063	*s*	14 22 50.1	−53 48 18.9	12.71	48.941	15(3)	0.032(8)	ROT	
F17_19103		14 23 02.8	−53 40 36.0	14.40	42.649	0.835(3)	0.02(1)	RR	
F17_19137		14 21 45.0	−54 29 04.1	12.11	...	...	...	SR	
F17_19206	*cs*	14 22 04.6	−54 17 37.8	14.56	42.519	0.034874(5)	0.01(1)	DSCT	
F17_19298		14 23 41.8	−53 17 05.4	13.65	...	...	...	LP	
F17_19450		14 21 21.0	−54 45 40.6	13.42	...	...	...	LP	
F17_19455		14 22 56.0	−53 47 19.0	15.28	47.052	11.2(4)	0.09(2)	ROT	
F17_19461		14 21 24.0	−54 44 00.8	15.19	44.655	0.774(3)	0.04(3)	DSCT	
F17_19549	*s*	14 22 45.0	−53 54 48.7	15.36	...	...	...	LP	
F17_19624	*s*	14 23 04.8	−53 42 54.9	13.39	...	...	...	LP	
F17_19626	*s*	14 22 32.9	−54 02 49.4	17.97	42.640	0.2617(2)	0.2(2)	EW	
F17_19682		14 23 46.0	−53 17 06.4	14.28	75.316	25(2)	0.07(2)	ROT	
F17_19788	*s*	14 22 11.1	−54 17 19.5	13.24	49.266	13.2(5)	0.044(8)	EB	
F17_19792	*s*	14 21 57.6	−54 25 40.7	14.54	42.565	0.446(1)	0.01(1)	RR	
F17_19872		14 23 34.4	−53 25 41.3	16.85	42.946	0.6697(6)	0.31(6)	EB	
F17_19874	*s*	14 23 23.3	−53 32 43.5	17.22	42.743	0.694(3)	0.14(8)	EW	
F17_19958		14 23 23.8	−53 33 03.0	16.84	42.921	0.6545(8)	0.12(6)	EW	
F17_19966		14 21 25.8	−54 46 11.6	16.74	42.929	0.560(1)	0.09(5)	RR	
F17_19990	*s*	14 21 21.6	−54 48 45.0	14.24	46.989	10.1(4)	0.03(2)	ROT	
F17_20016		14 21 45.0	−54 34 52.7	14.10	...	...	...	LP	
F17_20105		14 22 41.5	−54 00 35.3	14.45	42.869	8.6(2)	0.034(8)	ROT	
F17_20210	*s*	14 23 19.8	−53 37 16.6	15.22	...	...	...	LP	
F17_20367		14 21 56.4	−54 30 16.6	14.83	51.825	6.3(1)	0.03(2)	ROT	
F17_20503	*c*	14 22 00.7	−54 28 36.5	15.76	42.686	0.3410(2)	0.10(3)	EW	F17_20554
F17_20512		14 23 18.1	−53 40 31.5	13.91	...	...	...	LP	
F17_20520		14 22 06.4	−54 25 14.8	15.25	53.167	19.9(9)	0.09(2)	ROT	
F17_20524		14 21 39.2	−54 41 52.7	17.01	44.482	1.054(2)	0.21(7)	EA	
F17_20554	*c*	14 22 01.2	−54 28 38.7	15.78	42.685	0.3410(3)	0.08(3)	EW	F17_20503
F17_20555		14 21 57.8	−54 30 50.4	14.87	42.590	24.705(1)	0.22(1)	EA	
F17_20694		14 22 21.0	−54 17 28.5	17.74	44.839	1.278(4)	0.2(2)	EA	
F17_20768		14 23 27.3	−53 36 32.6	17.10	42.927	0.743(3)	0.14(8)	RR	
F17_20903		14 22 21.3	−54 18 53.4	14.01	47.079	1.674(4)	0.04(2)	EA	
F17_21074		14 22 51.3	−54 01 19.5	13.61	44.391	1.038(3)	0.028(6)	EB	
F17_21195	*s*	14 21 38.4	−54 46 48.3	15.12	47.012	30(2)	0.10(2)	CEP	
F17_21316		14 23 16.9	−53 46 41.5	17.25	42.799	0.4176(4)	0.24(8)	EW	
F17_21422		14 22 09.6	−54 29 13.1	14.07	42.982	0.771(3)	0.020(8)	RR	
F17_21455		14 24 06.0	−53 16 07.1	16.74	42.669	0.2757(3)	0.10(6)	EW/DSCT	
F17_21518		14 22 15.1	−54 26 25.9	16.65	42.939	0.4596(3)	0.33(5)	EB	

Table E.3: Variable stars in field F17 (continued).

BEST ID	F	α (J2000.0) δ	R_B	T_0 [d]	p [d]	A	Type	Other Names
		h m s ° ′ ″	[mag]	[rHJD]		[mag]		
F17_21539		14 22 57.3 −54 00 23.4	18.15	42.727	2.2065(1)	0.6(1)	EA	
F17_21583	*s*	14 22 39.1 −54 12 05.7	14.80	···	···	···	LP	
F17_21674		14 22 56.2 −54 02 05.3	13.65	42.607	0.751(2)	0.021(7)	EW	
F17_21715		14 24 01.7 −53 20 42.6	13.01	42.892	0.4431(3)	0.014(6)	EA	
F17_21771	*s*	14 21 41.1 −54 48 53.0	15.84	42.502	0.14852(8)	0.02(3)	DSCT	
F17_21787		14 22 20.3 −54 25 00.8	12.45	···	···	···	LP	
F17_21789		14 22 15.9 −54 27 42.0	13.92	···	···	···	SR	
F17_21798	*c*	14 23 30.0 −53 41 31.3	16.08	42.728	0.3513(3)	0.04(3)	EW	
F17_21799	*c*	14 23 29.8 −53 41 36.7	16.28	42.723	0.4263(4)	0.07(4)	EA	
F17_21849	*s*	14 22 43.0 −54 11 21.9	16.22	42.658	0.4092(4)	0.03(3)	EW	
F17_21948		14 23 29.3 −53 42 49.6	13.94	42.734	0.6669(2)	0.258(8)	RR	
F17_22003		14 23 09.8 −53 55 33.8	13.79	···	···	···	LP	
F17_22148		14 22 55.1 −54 05 45.1	14.42	···	···	···	LP	
F17_22358	*c*	14 23 23.9 −53 49 03.1	15.35	46.059	2.39(2)	0.06(2)	ROT	F17_22388
F17_22388	*c*	14 23 24.0 −53 49 08.4	15.36	46.043	2.39(2)	0.04(2)	ROT	F17_22358
F17_22468		14 22 07.9 −54 37 00.1	14.95	···	···	···	LP	
F17_22558		14 23 56.4 −53 29 30.2	14.29	42.526	0.825(4)	0.01(1)	RR	
F17_22581	*s*	14 22 42.8 −54 16 15.4	14.71	52.310	16(2)	0.03(2)	ROT	
F17_22673		14 22 03.6 −54 40 55.7	14.74	···	···	···	LP	
F17_22760		14 23 25.8 −53 50 33.5	17.61	42.798	0.4531(4)	0.2(2)	EA	
F17_22889		14 22 18.1 −54 33 35.9	17.32	42.718	0.7087(5)	0.67(9)	EA	
F17_23038		14 23 14.5 −53 59 22.6	14.64	42.537	0.2235(4)	0.02(2)	DSCT	
F17_23050	*c*	14 23 42.4 −53 41 46.3	16.49	42.503	0.32838(9)	0.48(5)	EW	
F17_23054	*s*	14 22 26.5 −54 29 22.0	13.76	46.297	22(2)	0.031(8)	CEP	
F17_23097		14 23 32.6 −53 48 19.7	13.93	···	···	···	LP	
F17_23115		14 23 27.1 −53 51 59.2	14.59	44.101	2.50(2)	0.09(2)	ROT	
F17_23135		14 21 53.5 −54 50 07.1	14.64	···	···	···	LP	
F17_23189	*s*	14 22 59.0 −54 10 09.7	14.02	55.171	9.9(2)	0.03(1)	ROT	
F17_23499		14 24 06.2 −53 29 34.9	13.94	42.727	0.2992(2)	0.042(7)	EW	
F17_23868	*s*	14 22 46.7 −54 22 15.5	17.89	44.430	4.38(5)	0.5(2)	EA	
F17_24022		14 23 38.7 −53 50 40.6	14.29	44.390	4.91(2)	0.60(4)	EA	
F17_24064		14 24 16.8 −53 26 32.7	15.42	117.710	26(2)	0.08(3)	ROT	
F17_24078		14 22 52.8 −54 19 53.5	15.90	54.198	20(3)	0.09(3)	ROT	
F17_24143		14 24 15.2 −53 28 10.9	12.56	···	···	···	SR	
F17_24151	*s*	14 23 06.4 −54 11 53.3	15.20	42.522	0.07388(3)	0.01(2)	DSCT	
F17_24221		14 23 50.6 −53 44 30.5	16.62	42.739	0.3648(2)	0.18(5)	EW	
F17_24311		14 23 17.8 −54 06 00.3	13.19	53.130	7.51(7)	0.048(6)	EB	
F17_24349		14 22 19.3 −54 42 27.6	13.20	42.530	0.10618(6)	0.007(7)	DSCT	
F17_24374		14 23 00.8 −54 17 04.2	14.96	52.248	32(4)	0.04(2)	CEP	
F17_24395	*c*	14 22 14.8 −54 45 30.4	16.80	42.892	0.4573(4)	0.22(7)	EW	
F17_24440	*s*	14 23 43.5 −53 50 43.2	14.66	51.000	10.0(3)	0.02(1)	ROT	
F17_24447	*s*	14 22 54.9 −54 21 17.7	12.57	44.849	1.456(8)	0.009(6)	ROT	
F17_24452	*s*	14 24 26.7 −53 22 58.0	17.77	42.592	0.2689(2)	0.2(2)	EW/DSCT	
F17_24482		14 23 14.3 −54 09 22.1	14.93	···	···	···	LP	
F17_24654		14 22 16.0 −54 46 31.7	15.03	48.371	3.359(8)	0.20(2)	EA	
F17_24848		14 23 13.0 −54 12 25.9	14.25	42.497	1.830(3)	0.22(2)	EA	
F17_24857		14 24 12.2 −53 34 47.3	17.70	42.716	0.3579(4)	0.2(2)	EW/DSCT	
F17_24899		14 24 25.0 −53 26 52.8	11.41	···	···	···	LP	
F17_25088		14 24 15.4 −53 34 19.4	16.06	95.906	23(2)	0.12(4)	CEP	
F17_25134	*c*	14 23 10.4 −54 15 55.1	17.05	42.815	0.6372(6)	0.25(7)	EA	F17_25135
F17_25135	*c*	14 23 10.2 −54 16 00.7	17.24	42.815	0.6372(6)	0.22(8)	EA	F17_25134
F17_25235	*s*	14 23 33.0 −54 02 19.5	13.40	98.490	16(2)	0.027(8)	EB	
F17_25276	*s*	14 24 19.0 −53 33 14.2	12.49	···	···	···	LP	
F17_25311		14 23 47.6 −53 53 32.9	16.87	42.961	1.085(2)	0.37(7)	EA	
F17_25360		14 23 36.6 −54 00 55.1	13.90	···	···	···	LP	
F17_25597	*s*	14 24 34.6 −53 25 17.5	13.94	42.521	0.05376(2)	0.007(8)	DSCT	
F17_25598		14 24 30.3 −53 28 03.3	14.28	42.555	0.08971(4)	0.02(1)	DSCT	
F17_25723		14 23 07.9 −54 21 16.4	12.36	42.605	0.1334(1)	0.009(8)	DSCT	
F17_25730		14 23 58.4 −53 49 25.7	14.08	42.861	0.4881(8)	0.037(8)	RR	
F17_25773	*s*	14 23 24.1 −54 11 24.2	11.72	···	···	···	LP	
F17_26044	*s*	14 23 01.7 −54 27 18.2	14.31	···	···	···	SR	
F17_26094		14 24 33.3 −53 29 27.5	11.78	···	···	···	LP	
F17_26174	*c*	14 23 33.7 −54 08 10.9	17.49	42.870	0.3863(3)	0.3(1)	EW	F17_26236
F17_26236	*c*	14 23 34.3 −54 08 14.9	17.51	42.867	0.3863(4)	0.2(1)	EW	F17_26174
F17_26346		14 24 10.5 −53 46 03.9	14.96	47.047	22(2)	0.08(2)	ROT	
F17_26360		14 22 25.7 −54 51 46.1	13.89	···	···	···	LP	
F17_26384	*c*	14 22 35.9 −54 45 40.3	14.98	53.015	43(4)	0.18(2)	CEP	
F17_26419		14 22 53.6 −54 34 59.5	11.87	···	···	···	LP	
F17_26423		14 24 45.8 −53 23 45.2	13.41	···	···	···	LP	
F17_26432		14 22 45.5 −54 40 05.6	14.76	57.063	20(2)	0.06(2)	ROT	
F17_26606		14 24 37.1 −53 30 35.3	16.95	42.867	0.4477(5)	0.14(6)	EW/DSCT	
F17_26762	*s*	14 23 32.5 −54 13 03.5	17.41	42.817	0.3431(4)	0.11(8)	EW/DSCT	
F17_26773	*s*	14 22 47.7 −54 41 01.0	15.21	53.419	15.3(5)	0.04(2)	CEP	
F17_26804	*c*	14 24 44.6 −53 27 11.6	15.55	42.998	0.5402(2)	0.39(3)	EB	F17_26896
F17_26855		14 22 56.6 −54 36 05.2	17.81	44.874	1.331(4)	0.3(2)	EA	
F17_26871		14 23 34.3 −54 12 33.4	16.29	42.639	3.23(1)	0.29(1)	EA	
F17_26880		14 24 51.4 −53 23 03.2	11.51	···	···	···	LP	
F17_26896	*c*	14 24 45.4 −53 27 08.4	16.44	42.998	0.5402(5)	0.27(5)	EB	F17_26804
F17_26925	*s*	14 22 35.3 −54 49 33.3	13.27	···	···	···	LP	
F17_26986		14 24 40.8 −53 30 51.8	11.72	···	···	···	LP	
F17_27039		14 23 47.2 −54 05 29.4	17.80	44.342	2.157(7)	0.4(2)	EA	
F17_27103	*c*	14 23 52.5 −54 02 32.2	16.83	42.555	0.3258(5)	0.13(6)	RR	F17_27171
F17_27148		14 23 58.5 −53 58 56.6	14.33	47.316	5.4(1)	0.029(8)	CEP	
F17_27171	*c*	14 23 52.9 −54 02 39.1	16.91	42.551	0.3258(4)	0.24(7)	RR	F17_27103
F17_27196	*s*	14 22 47.8 −54 43 30.9	15.92	42.545	0.09848(5)	0.02(3)	DSCT	
F17_27207	*cs*	14 23 37.2 −54 12 52.3	16.04	42.672	0.988(4)	0.10(3)	EW	F17_27252
F17_27252	*cs*	14 23 37.7 −54 12 49.3	15.99	42.673	0.988(4)	0.11(3)	EW	F17_27207
F17_27279		14 24 45.7 −53 29 23.3	13.34	···	···	···	LP	

Table E.3: Variable stars in field F17 (continued).

BEST ID	F	α (J2000.0) h m s	δ ° ′ ″	R_B [mag]	T_0 [d] [rHJD]	p [d]	A [mag]	Type	Other Names
F17_27301		14 24 17.0	−53 48 06.3	14.11	...	...	...	LP	
F17_27363		14 24 07.3	−53 54 44.4	15.20	161.204	74(7)	0.34(4)	VAR	
F17_27475	*c*	14 24 07.8	−53 55 12.4	17.06	42.799	0.3454(3)	0.09(7)	EW	
F17_27920	*s*	14 23 24.2	−54 25 44.9	14.86	47.590	4.3(2)	0.03(2)	CEP	
F17_27986		14 24 43.6	−53 35 36.7	14.34	42.809	0.9003(9)	0.021(8)	EA	
F17_28011	*s*	14 23 55.7	−54 06 28.0	16.06	...	...	...	LP	
F17_28176		14 24 22.4	−53 50 19.9	15.81	42.562	0.1938(2)	0.08(3)	DSCT	
F17_28197	*c*	14 24 48.5	−53 33 34.3	13.43	46.068	5.3(3)	0.038(8)	ROT	
F17_28210	*c*	14 24 44.9	−53 36 00.7	16.01	42.741	0.3915(3)	0.14(3)	EW	
F17_28263		14 22 44.9	−54 52 11.5	13.85	42.514	0.3478(5)	0.03(2)	RR	
F17_28278	*s*	14 23 11.5	−54 35 49.1	15.99	42.516	0.06176(2)	0.02(3)	DSCT	
F17_28309		14 23 57.9	−54 06 56.9	16.36	42.767	0.4648(4)	0.15(4)	EW	
F17_28464		14 23 26.3	−54 27 57.6	15.05	...	...	...	LP	
F17_28567		14 24 56.4	−53 31 11.6	13.63	...	...	...	LP	
F17_28568		14 24 56.0	−53 31 24.9	14.41	44.504	3.16(3)	0.07(2)	ROT	
F17_28593		14 24 11.9	−54 00 03.8	17.60	46.148	3.84(5)	0.6(2)	CEP	
F17_28659		14 23 44.1	−54 18 11.2	15.52	55.223	15(2)	0.05(2)	ROT	
F17_28763		14 25 13.3	−53 21 20.3	15.50	42.608	0.3627(2)	0.14(2)	EW	
F17_28798	*s*	14 24 08.5	−54 03 40.5	13.30	48.108	2.41(3)	0.023(8)	CEP	
F17_28815		14 23 44.0	−54 19 21.2	15.18	...	...	...	LP	
F17_28867		14 23 15.0	−54 37 49.0	15.04	...	...	...	LP	
F17_29058		14 22 59.7	−54 48 27.5	15.37	52.643	7.0(2)	0.06(2)	VAR	
F17_29097	*s*	14 24 25.1	−53 54 58.6	15.53	...	...	...	LP	
F17_29185		14 25 13.4	−53 24 17.7	16.34	42.716	0.3166(2)	0.18(4)	EW	
F17_29198	*s*	14 24 56.6	−53 35 28.4	13.69	48.279	10.1(3)	0.029(7)	ROT	
F17_29252	*s*	14 23 02.7	−54 47 57.8	15.07	104.800	15.367(1)	0.3(1)	EA	
F17_29293	*s*	14 23 10.8	−54 43 14.5	13.32	...	...	...	LP	
F17_29374	*c*	14 23 52.0	−54 17 51.3	17.15	44.772	0.800(2)	0.29(7)	EW	F17_29375
F17_29375	*c*	14 23 51.9	−54 17 55.1	17.25	44.774	0.800(2)	0.35(8)	EW	F17_29374
F17_29506		14 24 35.4	−53 50 57.0	13.85	...	...	...	LP	
F17_29519		14 25 22.6	−53 20 13.2	13.17	...	...	...	LP	
F17_29533		14 23 19.8	−54 38 55.2	14.80	42.513	0.13446(6)	0.08(3)	DSCT	
F17_29540	*s*	14 24 29.5	−53 55 00.2	15.77	42.563	0.11498(4)	0.02(3)	DSCT	
F17_29786		14 24 48.9	−53 44 13.3	11.83	...	...	...	LP	
F17_29794	*s*	14 23 27.6	−54 36 00.4	13.07	42.508	0.06077(2)	0.006(8)	DSCT	
F17_29885	*c*	14 25 05.6	−53 33 56.5	15.96	42.945	0.5015(4)	0.31(3)	EA	F17_29947
F17_29947	*c*	14 25 06.3	−53 33 56.9	15.59	42.946	0.5015(2)	0.36(2)	EA	F17_29885
F17_30042		14 23 18.4	−54 43 28.7	15.29	57.047	6.72(8)	0.06(2)	EB	
F17_30048		14 24 52.8	−53 43 33.5	16.58	42.547	0.1805(2)	0.07(4)	DSCT	
F17_30217		14 24 09.2	−54 12 35.3	13.24	...	...	...	LP	
F17_30278		14 24 52.8	−53 45 03.0	18.01	44.822	1.663(4)	0.7(2)	EA	
F17_30292		14 23 07.3	−54 51 52.2	17.68	42.621	0.2718(2)	0.3(2)	EW	
F17_30311		14 25 06.4	−53 36 23.5	17.14	49.141	12.8(8)	0.18(7)	CEP	
F17_30419	*s*	14 24 16.5	−54 09 18.2	14.30	44.712	8.1(2)	0.02(1)	ROT	
F17_30424		14 23 23.2	−54 42 50.1	16.42	42.699	0.3551(2)	0.20(4)	EW	
F17_30518		14 25 27.5	−53 23 39.5	16.58	62.105	28(2)	0.27(5)	VAR	
F17_30625		14 23 43.0	−54 31 38.5	15.70	...	...	...	LP	
F17_30654	*s*	14 24 40.2	−53 55 30.3	15.33	...	...	...	LP	
F17_30717		14 23 45.4	−54 30 40.0	14.09	48.843	5.201(1)	0.19(1)	EA	
F17_30719	*s*	14 23 12.9	−54 50 52.2	16.61	42.777	0.3575(4)	0.06(5)	EW/DSCT	
F17_30946	*s*	14 23 14.1	−54 51 30.5	14.71	42.638	2.43(3)	0.05(2)	ROT	
F17_30977	*s*	14 24 03.7	−54 20 44.7	15.85	42.958	0.5726(5)	0.05(3)	EA	
F17_30990		14 24 11.1	−54 16 10.7	16.99	42.773	0.3657(4)	0.09(6)	EW	
F17_31197		14 23 52.1	−54 29 27.0	11.83	75.080	15.8(8)	0.034(8)	ROT	
F17_31309		14 24 28.7	−54 06 55.6	17.98	42.745	0.3499(2)	1.1(2)	EW	
F17_31343		14 24 37.4	−54 01 27.3	17.40	42.779	0.5734(6)	0.16(8)	EA	
F17_31454		14 25 42.3	−53 19 43.8	14.88	57.224	16(3)	0.07(3)	ROT	
F17_31470	*cs*	14 24 49.8	−53 54 22.6	17.14	42.549	0.1706(2)	0.06(7)	DSCT	F17_31484
F17_31484	*cs*	14 24 50.1	−53 54 17.9	17.13	42.561	0.1706(2)	0.08(8)	DSCT	F17_31470
F17_31585		14 24 22.9	−54 12 18.9	16.03	42.557	0.5045(5)	0.13(3)	EW	
F17_31620	*c*	14 24 10.2	−54 20 38.7	16.69	42.726	0.4145(2)	0.37(5)	EW	
F17_31650		14 23 54.2	−54 30 56.9	15.44	47.450	1.78(2)	0.04(2)	ROT	
F17_31659		14 24 44.1	−53 59 15.5	14.55	57.865	32(9)	0.10(2)	ROT	
F17_31762	*s*	14 24 36.2	−54 05 02.5	14.20	48.390	15(2)	0.024(8)	ROT	
F17_31802	*s*	14 24 24.6	−54 12 39.4	18.66	42.663	0.3936(5)	0.4(3)	EW	
F17_31884		14 24 07.2	−54 24 17.1	16.91	54.100	17(1)	0.23(6)	CEP	
F17_31913		14 25 33.6	−53 28 32.9	13.20	42.540	0.05100(2)	0.010(8)	DSCT	
F17_32033		14 23 43.3	−54 40 13.4	16.48	42.710	0.2504(2)	0.17(5)	EW	
F17_32068		14 24 57.7	−53 53 06.2	16.29	42.500	0.2319(3)	0.11(4)	DSCT	
F17_32184		14 24 27.9	−54 13 04.8	16.80	42.618	0.4689(4)	0.15(5)	EW/DSCT	
F17_32332	*s*	14 24 50.2	−53 59 42.8	16.86	42.533	0.3136(3)	0.08(6)	EW/DSCT	
F17_32392	*s*	14 23 38.9	−54 45 11.1	14.54	44.105	0.833(3)	0.02(2)	RR	
F17_32401	*s*	14 24 47.4	−54 01 49.9	15.18	...	...	...	LP	
F17_32431	*s*	14 25 40.1	−53 27 33.4	12.15	...	...	...	LP	
F17_32493	*s*	14 24 48.6	−54 01 40.4	13.78	...	...	...	LP	
F17_32498		14 23 38.2	−54 46 15.7	18.32	42.516	0.3219(3)	0.3(3)	EW/DSCT	
F17_32517		14 24 05.7	−54 29 10.3	14.27	...	...	...	LP	
F17_32567		14 23 59.9	−54 33 9.9	16.43	61.656	19(2)	0.12(5)	CEP	
F17_32682	*k*	14 24 28.3	−54 15 54.6	12.69	...	...	...	LP	ASAS J142428-5416.0
F17_32825		14 25 44.9	−53 26 48.6	16.66	42.629	1.257(4)	0.17(8)	CEP	
F17_32838		14 25 41.2	−53 29 22.9	17.13	42.584	0.1623(2)	0.11(8)	DSCT	
F17_33305	*s*	14 24 23.5	−54 22 48.1	12.39	42.496	0.06246(2)	0.005(6)	DSCT	
F17_33320		14 24 35.8	−54 15 03.7	17.25	42.763	0.3448(2)	0.28(8)	EW	
F17_33337		14 24 59.4	−53 59 53.8	13.35	...	...	...	SR	
F17_33429		14 24 52.0	−54 05 19.5	15.79	42.587	0.30529(7)	0.34(3)	EW	
F17_33471	*s*	14 24 48.1	−54 08 01.8	17.24	42.595	0.5539(7)	0.12(8)	EW	
F17_33582	*c*	14 25 06.3	−53 56 59.7	17.29	42.658	0.3700(2)	0.38(8)	EW	
F17_33628		14 24 43.7	−54 11 51.1	13.18	...	...	...	LP	

Table E.3: Variable stars in field F17 (continued).

BEST ID	F	α (J2000.0) δ	R_B	T_0 [d]	p [d]	A	Type	Other Names
		h m s ° ′ ″	[mag]	[rHJD]		[mag]		
F17_33891	*c*	14 24 15.0 −54 31 43.8	16.72	42.527	0.08619(2)	0.28(5)	DSCT	F17_33892
F17_33892	*c*	14 24 14.9 −54 31 49.0	16.64	42.529	0.08619(2)	0.34(5)	DSCT	F17_33891
F17_33904	*s*	14 25 24.3 −53 47 13.5	14.95	44.231	0.883(4)	0.03(2)	RR	
F17_33981		14 24 39.2 −54 16 55.5	15.42	44.141	2.282(3)	0.66(5)	EA	
F17_33990		14 23 52.7 −54 46 18.4	11.92	...	...	...	LP	
F17_33993	*s*	14 23 45.6 −54 50 42.2	14.61	96.568	38(6)	0.04(1)	CEP	
F17_34186		14 25 20.6 −53 51 27.6	18.03	44.522	1.471(4)	0.3(2)	EA	
F17_34199		14 24 30.0 −54 24 07.4	16.88	42.769	0.4630(6)	0.15(6)	EW	
F17_34261		14 25 47.0 −53 34 26.5	14.05	...	...	...	LP	
F17_34396		14 24 09.2 −54 38 29.4	17.05	42.892	0.949(2)	0.33(7)	EB	
F17_34649		14 25 18.1 −53 55 54.7	15.57	47.820	6.38(6)	0.17(2)	CEP	
F17_34673	*s*	14 25 01.0 −54 07 08.9	13.63	48.352	16(8)	0.03(2)	ROT	
F17_34677		14 24 49.4 −54 14 36.7	15.46	55.641	4.89(4)	0.16(2)	ROT	
F17_34723	*s*	14 25 47.9 −53 36 49.3	13.69	42.565	1.225(4)	0.010(7)	VAR	
F17_35145		14 25 47.9 −53 39 26.3	15.46	42.523	0.2367(3)	0.04(2)	DSCT	
F17_35156		14 24 25.3 −54 32 55.9	14.58	46.759	13.3(7)	0.06(2)	ROT	
F17_35238		14 25 56.3 −53 34 30.7	12.83	...	...	...	LP	
F17_35247		14 24 43.5 −54 22 03.6	17.24	42.499	0.12300(9)	0.08(9)	DSCT	
F17_35307	*s*	14 26 04.6 −53 29 28.5	14.92	...	...	...	LP	
F17_35342		14 26 10.2 −53 25 59.4	17.64	42.609	0.2820(2)	0.6(2)	EW	
F17_35362	*s*	14 26 13.3 −53 23 58.4	12.24	...	...	...	LP	
F17_35490	*s*	14 24 22.0 −54 37 11.3	17.12	42.508	0.05665(2)	0.07(8)	DSCT	
F17_35552		14 25 52.2 −53 39 12.4	18.12	42.844	0.3663(4)	0.2(2)	EW/DSCT	
F17_35555		14 25 36.6 −53 49 27.6	17.37	42.673	0.3491(3)	0.3(2)	EW	
F17_35640	*c*	14 24 46.6 −54 22 21.1	16.83	42.529	0.749(2)	0.20(7)	EW	
F17_35714		14 24 28.9 −54 34 01.6	15.99	42.967	4.49(5)	0.09(4)	EB	
F17_35730		14 24 32.9 −54 31 35.2	17.03	42.510	0.2452(2)	0.10(6)	EW/DSCT	
F17_35873		14 25 13.3 −54 06 37.1	17.66	42.747	0.3342(2)	0.8(2)	EW	
F17_36114		14 25 30.9 −53 56 31.9	17.78	42.937	0.4795(6)	0.2(2)	EW	
F17_36155		14 24 44.4 −54 26 48.2	14.32	42.542	0.4082(6)	0.02(1)	RR	
F17_36205	*s*	14 25 54.4 −53 41 36.3	13.00	44.584	12.6(3)	0.028(7)	ROT	
F17_36438		14 25 55.0 −53 42 23.7	15.04	...	...	...	LP	
F17_36477		14 25 18.8 −54 06 26.4	15.81	42.825	0.3579(3)	0.12(4)	EW/DSCT	
F17_36613		14 26 12.7 −53 31 41.3	17.06	42.987	0.5919(7)	0.20(7)	EW	
F17_36783	*s*	14 25 58.3 −53 42 16.5	16.15	43.197	8.4406	0.11	EA	
F17_36834	*s*	14 25 13.0 −54 12 21.9	18.18	44.234	0.591(1)	0.3(2)	EW	
F17_36859		14 24 50.6 −54 26 50.0	12.37	...	...	...	LP	
F17_37254		14 25 35.4 −53 59 59.2	12.36	...	...	...	SR	
F17_37293		14 25 42.0 −53 55 59.0	14.65	42.495	0.2466(2)	0.02(1)	EW/DSCT	
F17_37302		14 25 00.7 −54 22 48.9	12.57	51.932	6.11(9)	0.037(7)	CEP	
F17_37423		14 24 31.3 −54 42 9.9	17.05	46.094	28(4)	0.26(7)	CEP	
F17_37649	*c*	14 25 01.5 −54 24 19.2	14.03	96.573	3.951(1)	0.51(1)	EA	
F17_37659		14 26 30.8 −53 25 29.2	12.00	...	...	...	LP	
F17_37673	*c*	14 25 07.4 −54 20 35.2	15.45	42.774	0.4733(3)	0.10(2)	EW	F17_37722
F17_37722	*c*	14 25 08.0 −54 20 29.1	16.16	42.776	0.4733(4)	0.15(5)	EW	F17_37673
F17_37742	*s*	14 25 35.4 −54 02 47.6	15.23	...	...	...	LP	
F17_37944		14 25 17.6 −54 15 33.8	13.33	47.722	1.3545(1)	0.79(1)	EA	
F17_38115		14 24 44.2 −54 37 49.9	17.17	42.547	0.3694(4)	0.12(8)	EW/DSCT	
F17_38143		14 25 38.9 −54 02 48.8	13.78	...	...	...	LP	
F17_38200	*c*	14 24 59.5 −54 28 39.2	15.45	47.024	3.562(8)	0.37(2)	EB	F17_38201
F17_38201	*c*	14 24 59.3 −54 28 45.0	15.53	47.010	3.56(2)	0.31(3)	EB	F17_38200
F17_38221	*s*	14 24 39.3 −54 41 36.3	12.60	42.523	0.5442(7)	0.011(8)	EW	
F17_38296		14 24 28.8 −54 48 38.8	16.80	42.755	0.7040(7)	0.29(6)	EW	
F17_38337	*s*	14 26 29.3 −53 30 27.7	15.24	42.859	9.4(6)	0.03(2)	VAR	
F17_38462	*s*	14 26 23.9 −53 34 47.5	12.11	...	...	...	LP	
F17_38463	*c*	14 26 13.4 −53 41 52.8	17.84	44.524	1.051(3)	0.6(2)	EA	F17_38464
F17_38464	*c*	14 26 13.2 −53 42 00.1	16.80	44.525	1.051(2)	0.72(7)	EA	F17_38463
F17_38503	*c*	14 24 22.3 −54 53 54.1	16.74	42.886	0.535(2)	0.12(6)	RR	F17_38582
F17_38582	*c*	14 24 22.9 −54 53 55.3	16.71	42.885	0.5348(8)	0.17(5)	RR	F17_38503
F17_38671	*s*	14 24 30.6 −54 49 30.5	12.90	...	...	...	LP	
F17_38757		14 25 46.9 −54 01 03.8	13.14	52.007	13.6(7)	0.015(6)	ROT	
F17_38828	*s*	14 24 27.6 −54 52 14.6	13.36	46.072	4.2(4)	0.032(8)	ROT	
F17_38922	*c*	14 26 32.5 −53 31 36.4	12.77	55.413	7.024(1)	0.14(1)	EA	
F17_38947		14 25 53.2 −53 58 00.9	13.67	...	...	...	LP	
F17_39224	*s*	14 24 35.3 −54 49 43.4	18.49	42.649	0.3416(3)	0.5(3)	EW	
F17_39265	*s*	14 24 59.4 −54 34 36.9	13.29	53.188	11.8(3)	0.025(8)	ROT	
F17_39280		14 25 12.4 −54 26 24.2	17.79	42.980	1.281(3)	0.4(2)	EA	
F17_39580	*c*	14 25 09.1 −54 30 08.8	15.63	42.544	0.37476(6)	0.61(3)	EW	
F17_39596		14 25 06.5 −54 31 57.5	14.45	42.520	1.475(4)	0.02(1)	EW	
F17_39624	*c*	14 24 44.4 −54 46 12.5	14.22	...	...	...	LP	
F17_39747	*s*	14 25 52.7 −54 02 55.2	13.52	...	...	...	SR	
F17_39752	*s*	14 24 34.3 −54 53 20.2	16.39	54.710	14.1(5)	0.12(5)	EB	
F17_39865	*s*	14 24 34.1 −54 53 55.7	17.37	44.258	0.611(2)	0.1(1)	RR	
F17_39896	*s*	14 26 24.0 −53 42 50.1	13.06	...	...	...	LP	
F17_39955		14 25 46.3 −54 08 02.5	15.09	46.443	6.39(9)	0.08(2)	CEP	
F17_40016	*s*	14 24 54.7 −54 41 41.2	14.96	...	...	...	LP	
F17_40239	*s*	14 24 50.9 −54 45 20.8	16.71	42.609	0.2128(2)	0.05(6)	DSCT	
F17_40266		14 25 28.2 −54 21 35.6	13.71	52.845	9.5(3)	0.04(1)	ROT	
F17_40330	*s*	14 26 47.2 −53 29 44.5	18.62	42.770	0.3092(5)	0.5(3)	DSCT	
F17_40340		14 25 17.6 −54 28 58.5	16.64	42.742	0.4009(4)	0.11(5)	EW/DSCT	
F17_40399		14 25 21.6 −54 26 42.5	13.15	42.510	0.034315(7)	0.007(7)	SXPHE	
F17_40435		14 24 52.2 −54 45 43.2	11.72	...	...	...	LP	
F17_40462		14 26 14.1 −53 52 43.2	14.91	...	...	...	LP	
F17_40563	*s*	14 26 57.8 −53 23 55.5	11.94	42.622	0.2248(2)	0.010(8)	EW/DSCT	
F17_40593		14 25 10.4 −54 34 58.5	13.80	53.499	27(2)	0.054(8)	ROT	
F17_40746		14 25 44.1 −54 14 08.1	15.56	42.690	0.2901(2)	0.08(2)	EW/DSCT	
F17_40870	*s*	14 26 54.7 −53 27 45.9	16.97	42.562	0.1720(2)	0.05(6)	DSCT	
F17_40930		14 24 42.4 −54 54 29.9	17.34	42.544	0.06269(2)	0.08(9)	DSCT	

Table E.3: Variable stars in field F17 (continued).

BEST ID	F	α (J2000.0) h m s	δ ° ′ ″	R_B [mag]	T_0 [d] [rHJD]	p [d]	A [mag]	Type	Other Names
F17_40991		14 24 57.4	−54 45 20.4	16.88	42.557	0.2804(2)	0.21(6)	EW	
F17_41056		14 25 29.7	−54 25 07.5	14.74	42.767	0.42208(9)	0.30(2)	EW	
F17_41293	*s*	14 26 19.6	−53 53 46.1	15.83	48.367	3.26(2)	0.06(3)	EA	
F17_41346		14 25 37.2	−54 21 57.2	16.28	42.769	0.3025(3)	0.06(4)	EW	
F17_41419		14 24 51.6	−54 51 29.1	16.82	42.606	0.3089(2)	0.21(6)	EW	
F17_41441		14 25 00.4	−54 46 01.8	13.54	42.514	0.08403(4)	0.02(2)	DSCT	
F17_41483	*c*	14 26 38.0	−53 42 35.4	14.25	42.606	0.3799(3)	0.03(1)	EW	
F17_41750	*s*	14 26 58.0	−53 30 25.7	13.94	...	...	...	LP	
F17_41776		14 26 07.8	−54 04 14.4	16.76	42.867	0.4968(3)	0.50(6)	EW	
F17_41958		14 24 47.3	−54 56 57.3	16.65	42.924	0.5817(5)	0.37(6)	EB	
F17_41972		14 25 27.2	−54 31 34.6	15.96	46.889	2.940(6)	0.31(3)	EA	
F17_42006	*s*	14 25 37.1	−54 25 21.9	13.81	44.963	14.2(5)	0.03(1)	ROT	
F17_42098		14 26 34.9	−53 47 52.7	13.50	46.107	6.03(6)	0.040(7)	ROT	
F17_42164		14 25 31.0	−54 30 14.3	17.58	42.847	0.5502(5)	0.9(2)	RR	
F17_42206		14 26 26.9	−53 53 51.5	16.59	44.209	0.5982(4)	0.52(5)	EA	
F17_42313		14 25 47.2	−54 20 38.8	15.97	51.820	9.938(1)	0.13(1)	EA	
F17_42416		14 26 31.8	−53 51 50.8	13.94	42.512	0.043829(9)	0.012(7)	SXPHE	
F17_42557	*s*	14 26 54.7	−53 37 15.0	13.17	49.357	13.4(6)	0.019(6)	ROT	
F17_42620	*c*	14 26 12.9	−54 05 34.7	15.78	42.986	1.0723(7)	0.52(3)	EA	
F17_42661	*c*	14 26 14.6	−54 04 44.5	14.73	44.537	0.691(2)	0.04(2)	RR	F17_42738
F17_42674	*s*	14 24 52.8	−54 57 30.0	14.20	...	...	...	LP	
F17_42737	*s*	14 26 18.9	−54 02 18.5	16.41	42.824	0.3965(4)	0.05(5)	EW/DSCT	
F17_42738	*c*	14 26 15.0	−54 04 49.4	14.89	44.543	0.691(3)	0.04(2)	RR	F17_42661
F17_42752		14 25 57.5	−54 16 30.9	12.99	44.630	0.717(3)	0.014(8)	RR	
F17_42958		14 26 11.7	−54 08 21.9	13.59	48.133	6.3(1)	0.020(7)	ROT	
F17_43044	*s*	14 24 56.0	−54 57 23.9	17.74	42.526	0.4889(6)	0.2(2)	EW	
F17_43118		14 25 12.8	−54 47 13.1	14.37	42.603	0.471(1)	0.021(8)	ROT	
F17_43287	*c*	14 26 57.1	−53 39 47.0	16.90	42.551	0.07476(3)	0.10(6)	DSCT	F17_43333
F17_43291		14 26 42.9	−53 49 20.4	16.99	42.661	0.3669(3)	0.4(2)	EW	
F17_43333	*c*	14 26 57.6	−53 39 42.5	17.19	42.547	0.07476(3)	0.11(8)	DSCT	F17_43287
F17_43363		14 25 12.7	−54 48 40.1	13.91	...	...	...	LP	
F17_43436		14 27 22.2	−53 23 26.6	15.72	44.536	1.151(3)	0.04(3)	EB	
F17_43454	*c*	14 25 08.1	−54 52 00.8	16.79	42.901	0.4349(5)	0.11(6)	EA	F17_43496
F17_43496	*c*	14 25 08.7	−54 51 50.6	15.53	42.901	0.4348(3)	0.09(2)	EA	F17_43454
F17_43523	*c*	14 25 13.2	−54 49 02.4	16.10	42.655	0.3503(3)	0.06(4)	EW	
F17_43617		14 25 26.6	−54 41 03.8	13.47	...	...	...	LP	
F17_43632		14 27 17.2	−53 27 59.5	14.45	...	...	...	LP	
F17_43723	*s*	14 25 35.2	−54 36 22.7	16.23	...	...	...	LP	
F17_43785		14 25 50.3	−54 26 52.1	15.07	42.523	0.3507(3)	0.05(2)	EW	
F17_44016	*c*	14 26 55.4	−53 45 05.6	16.79	42.582	0.11259(3)	0.35(5)	DSCT	
F17_44017		14 26 49.2	−53 49 20.0	15.03	...	...	...	LP	
F17_44059	*s*	14 26 51.9	−53 47 40.3	15.59	49.878	4.4(2)	0.04(2)	ROT	
F17_44227		14 25 57.8	−54 24 25.9	15.30	112.153	17.9(8)	0.08(2)	ROT	
F17_44523		14 25 42.4	−54 36 12.1	16.30	42.567	0.3413(3)	0.08(5)	EW	
F17_44525	*s*	14 25 37.7	−54 39 15.4	15.35	118.919	25(2)	0.06(2)	ROT	
F17_44774	*s*	14 27 21.3	−53 31 55.8	14.73	...	...	...	LP	
F17_44781		14 26 07.0	−54 21 41.9	17.40	55.700	4.822(1)	0.5(1)	EA	
F17_45102		14 25 39.6	−54 41 04.5	13.11	42.898	0.6313(6)	0.027(6)	EW	
F17_45164		14 27 27.8	−53 29 37.9	17.95	42.833	0.4264(4)	0.3(2)	EW/DSCT	
F17_45361		14 27 12.5	−53 41 05.3	14.42	...	...	...	LP	
F17_45363		14 26 47.2	−53 58 09.8	15.85	103.184	32(2)	0.20(3)	CEP	
F17_45374	*s*	14 26 01.7	−54 28 12.7	16.81	42.511	0.04341(1)	0.04(6)	DSCT	
F17_45553	*s*	14 26 16.9	−54 19 13.7	16.81	42.663	0.1806(2)	0.05(5)	DSCT	
F17_45607		14 27 23.1	−53 35 11.5	11.97	...	...	...	LP	
F17_45629		14 26 46.1	−54 00 22.7	14.83	51.334	12.1(5)	0.03(2)	ROT	
F17_45758		14 26 32.7	−54 09 56.7	14.14	...	...	...	LP	
F17_45798		14 26 50.9	−53 58 05.2	15.46	...	...	...	LP	
F17_46083		14 26 36.7	−54 09 12.8	15.10	96.129	26(2)	0.04(2)	ROT	
F17_46100		14 27 11.2	−53 46 10.8	16.17	42.911	1.231(8)	0.07(3)	ROT	
F17_46285		14 26 56.0	−53 57 30.8	15.93	52.678	14.8(5)	0.27(3)	ROT	
F17_46362		14 27 46.7	−53 23 19.4	15.85	49.010	3.901(1)	0.22(1)	EA	
F17_46400		14 26 08.8	−54 29 15.0	13.54	...	...	...	LP	
F17_46404		14 27 43.7	−53 25 40.9	18.16	42.599	0.3889(4)	0.3(2)	EW	
F17_46408		14 27 11.5	−53 47 44.1	16.83	42.564	0.2458(2)	0.09(5)	EW/DSCT	
F17_46706		14 26 07.9	−54 31 40.8	14.72	42.853	0.858(4)	0.02(2)	RR	
F17_46768		14 27 47.4	−53 25 17.2	16.57	44.231	2.898(7)	0.57(7)	EA	
F17_46811		14 27 07.4	−53 52 52.6	17.21	42.584	0.2643(2)	0.14(8)	EW/DSCT	
F17_47183		14 27 06.2	−53 55 48.4	14.90	46.490	40(2)	0.32(2)	CEP	
F17_47224	*s*	14 27 49.4	−53 26 33.0	14.67	...	...	...	LP	
F17_47283		14 26 38.3	−54 14 57.6	12.67	...	...	...	LP	
F17_47363		14 26 37.2	−54 16 05.3	13.66	...	...	...	LP	
F17_47367	*c*	14 26 03.8	−54 38 01.8	15.81	42.709	0.38991(9)	0.38(3)	EW	
F17_47438		14 27 29.8	−53 41 10.9	13.49	...	...	...	LP	
F17_47476	*s*	14 26 20.0	−54 28 03.1	15.43	44.799	0.805(3)	0.04(2)	RR	
F17_47674		14 25 38.6	−54 55 48.1	11.74	...	...	...	LP	
F17_48165		14 27 17.3	−53 54 02.4	17.23	42.570	5.147(1)	0.6(1)	EA	
F17_48222	*c*	14 27 07.0	−54 01 16.0	16.04	42.650	0.24309(9)	0.14(3)	EW	F17_48246
F17_48229		14 26 42.4	−54 17 44.5	16.42	42.731	0.4794(3)	0.33(5)	RR	
F17_48246	*c*	14 27 06.9	−54 01 21.5	16.21	42.649	0.2431(2)	0.10(3)	EW	F17_48222
F17_48249		14 26 50.8	−54 12 12.3	15.37	...	...	...	LP	
F17_48297	*s*	14 25 56.3	−54 48 04.1	17.30	42.737	0.788(2)	0.2(1)	EW	
F17_48438		14 25 53.1	−54 50 58.7	17.30	42.542	0.1404(2)	0.11(9)	DSCT	
F17_48456		14 25 57.3	−54 48 18.4	17.45	42.653	0.3211(3)	0.6(2)	RR	
F17_48566		14 26 25.0	−54 30 54.9	15.61	42.601	0.3663(1)	0.30(3)	EB	
F17_48883		14 26 09.0	−54 43 06.9	13.11	...	...	...	SR	
F17_48924	*s*	14 27 35.9	−53 45 40.0	13.69	42.499	0.029493(3)	0.006(7)	DSCT	
F17_48927	*s*	14 26 27.8	−54 31 09.7	16.52	42.787	0.3269(3)	0.09(5)	EW	
F17_48953		14 25 51.1	−54 55 06.2	17.00	42.814	0.3446(2)	0.37(7)	EW	

Table E.3: Variable stars in field F17 (continued).

BEST ID	F	α (J2000.0) h m s	δ ° ′ ″	R_B [mag]	T_0 [d] [rHJD]	p [d]	A [mag]	Type	Other Names
F17_49003		14 27 55.4	−53 32 43.0	17.39	44.135	0.898(2)	0.2(1)	EA	
F17_49243	*s*	14 26 44.6	−54 22 02.1	16.34	42.530	0.3717(5)	0.04(4)	EW/DSCT	
F17_49481		14 26 31.7	−54 31 49.8	16.27	42.520	0.5826(4)	0.23(4)	EB	
F17_49497	*s*	14 27 00.1	−54 13 06.3	13.18	42.653	0.2973(3)	0.007(6)	EW	
F17_49503		14 26 22.8	−54 37 45.2	17.21	42.594	0.3765(2)	0.50(9)	EW	
F17_49564		14 27 40.7	−53 46 13.5	16.81	47.825	6.914(1)	0.3(1)	EA	
F17_49861	*s*	14 26 17.7	−54 43 19.6	15.30	98.312	13.3(3)	0.08(2)	EB	
F17_49926		14 27 23.3	−54 00 17.3	16.35	44.397	0.639(3)	0.09(4)	RR	
F17_50058		14 26 54.3	−54 20 35.2	11.30	52.100	28(2)	0.064(8)	CEP	
F17_50061		14 26 40.3	−54 29 47.2	17.10	42.994	0.5907(5)	0.17(8)	EA	
F17_50141	*s*	14 28 01.4	−53 35 30.5	13.85	42.826	0.841(3)	0.006(6)	RR	
F17_50235		14 27 15.6	−54 07 11.9	16.03	95.196	7.4(2)	0.15(3)	ROT	
F17_50244		14 27 48.0	−53 45 21.2	12.81	42.496	2.574(7)	0.110(7)	ROT	
F17_50255	*s*	14 26 20.4	−54 43 44.8	16.24	42.950	0.692(2)	0.06(4)	RR	
F17_50290		14 26 26.2	−54 40 17.4	17.91	42.698	0.3970(4)	0.2(2)	EW/DSCT	
F17_50494		14 26 54.9	−54 22 37.2	17.00	42.897	0.657(3)	0.10(7)	DSCT	
F17_50626		14 27 19.9	−54 06 50.3	13.82	...	...	...	LP	
F17_50819		14 26 57.9	−54 22 31.4	15.16	42.666	0.3830(4)	0.06(2)	EW	
F17_50977		14 27 28.5	−54 03 10.7	16.65	42.664	0.3721(2)	0.22(5)	EW	
F17_51408		14 27 38.3	−53 59 11.8	17.33	42.711	0.4043(4)	0.14(8)	EW	
F17_51413	*s*	14 26 55.2	−54 28 05.6	16.27	42.690	0.648(2)	0.06(4)	EW	
F17_51429	*s*	14 26 45.3	−54 34 47.0	15.28	42.717	7.1(2)	0.04(2)	ROT	
F17_51686		14 27 35.3	−54 02 47.7	17.10	42.595	0.4125(4)	0.18(7)	EW/DSCT	
F17_51768		14 26 32.8	−54 44 46.8	15.25	44.289	1.154(2)	0.20(5)	EA	
F17_51770		14 26 15.0	−54 56 15.3	12.00	...	...	...	LP	
F17_51793		14 28 14.1	−53 36 55.6	16.00	44.197	0.5786(6)	0.14(3)	EB	
F17_51833	*s*	14 28 24.0	−53 30 16.6	15.17	...	...	...	LP	
F17_51872		14 26 33.7	−54 44 49.3	14.46	42.558	0.5768(2)	0.27(2)	EA	
F17_51888	*c*	14 27 05.6	−54 23 55.4	16.74	42.539	0.2759(3)	0.09(6)	EW	F17_51944
F17_51921		14 26 57.1	−54 29 49.7	15.70	42.534	0.5547(7)	0.07(3)	EW	
F17_51944	*c*	14 27 06.0	−54 23 58.1	16.76	42.535	0.2759(2)	0.10(6)	EW	F17_51888
F17_52283	*s*	14 26 37.0	−54 45 20.9	13.51	44.495	0.672(2)	0.02(2)	RR	
F17_52295		14 27 28.2	−54 11 32.4	15.21	...	...	...	LP	
F17_52431		14 27 42.2	−54 02 56.1	15.76	42.533	0.06376(2)	0.03(3)	DSCT	
F17_52492	*c*	14 28 21.0	−53 36 36.4	14.44	...	...	...	LP	
F17_52528	*s*	14 26 23.8	−54 55 17.0	15.87	44.122	0.973(3)	0.11(3)	EB	
F17_52621	*s*	14 26 17.9	−54 59 34.3	13.20	...	...	...	LP	
F17_52674		14 26 32.8	−54 50 19.0	12.25	42.513	1.69(2)	0.031(8)	CEP	
F17_52687	*c*	14 27 01.1	−54 31 56.3	15.65	49.019	3.320(7)	0.59(5)	EA	
F17_52807		14 28 24.3	−53 36 23.3	15.99	42.505	17.8(5)	0.27(4)	CEP	
F17_52841	*s*	14 27 45.7	−54 03 09.5	13.85	...	...	...	LP	
F17_52955	*s*	14 27 24.6	−54 18 08.3	18.16	42.838	0.585(2)	0.2(2)	EW/DSCT	
F17_52965	*s*	14 26 35.9	−54 50 11.1	13.49	...	...	...	LP	
F17_53106		14 27 35.2	−54 11 46.7	14.82	42.596	0.4035(4)	0.06(2)	EB	
F17_53128	*s*	14 27 09.4	−54 29 05.9	14.51	...	...	...	LP	
F17_53294	*s*	14 28 28.7	−53 36 12.8	18.47	42.763	0.2790(2)	0.4(3)	EW	
F17_53418		14 27 54.6	−54 00 29.8	15.50	...	...	...	LP	
F17_53471		14 28 06.8	−53 52 26.7	14.83	...	...	...	LP	
F17_53481	*s*	14 26 42.5	−54 48 50.6	13.14	42.528	0.03860(3)	0.007(8)	DSCT	
F17_53572		14 27 39.2	−54 11 59.2	14.89	113.656	21(3)	0.10(2)	ROT	
F17_53792		14 27 38.3	−54 14 00.9	14.93	...	...	...	LP	
F17_53859		14 28 10.1	−53 52 50.4	13.16	...	...	...	LP	
F17_53869	*s*	14 27 04.0	−54 37 18.2	17.36	42.920	0.650(2)	0.11(9)	EW	
F17_53911		14 27 58.3	−54 01 17.9	17.58	44.435	0.6764(9)	0.2(2)	EA	
F17_53936		14 28 05.7	−53 56 20.2	11.78	48.890	7.6(3)	0.023(6)	ROT	
F17_53979	*s*	14 27 00.5	−54 40 22.1	13.22	...	...	...	LP	
F17_54088	*s*	14 27 09.7	−54 34 54.6	16.87	42.588	1.61(2)	0.10(6)	ROT	
F17_54170		14 27 16.1	−54 31 18.3	14.82	...	...	...	LP	
F17_54385		14 28 18.3	−53 50 33.4	15.62	...	...	...	LP	
F17_54518		14 27 47.7	−54 12 28.3	15.35	48.800	3.556(1)	0.22(1)	EA	
F17_54647		14 26 54.9	−54 48 20.3	11.85	42.680	0.3811(6)	0.029(8)	RR	
F17_54692		14 26 42.0	−54 56 54.2	14.10	...	...	...	SR	
F17_54750	*s*	14 27 53.2	−54 10 11.2	13.65	...	...	...	LP	
F17_54827	*s*	14 28 24.8	−53 49 04.0	15.46	42.555	0.718(2)	0.03(3)	RR	
F17_54921		14 27 20.5	−54 33 16.3	17.30	42.538	0.07939(3)	0.1(1)	DSCT	
F17_55027		14 28 28.6	−53 47 52.4	18.22	42.816	1.489(4)	0.8(2)	EA	
F17_55040	*s*	14 28 20.1	−53 53 51.9	15.08	...	...	...	LP	
F17_55108		14 27 00.9	−54 47 26.8	15.28	...	...	...	LP	
F17_55134		14 27 43.0	−54 19 47.9	14.60	49.296	16.2(9)	0.04(2)	ROT	
F17_55497	*s*	14 27 22.7	−54 35 29.8	12.50	42.647	0.4304(6)	0.014(8)	EW/DSCT	
F17_55538		14 27 14.6	−54 41 06.8	12.99	...	...	...	LP	
F17_55539	*c*	14 28 55.4	−53 32 22.3	14.19	...	...	...	VAR	
F17_55609	*s*	14 27 02.8	−54 49 16.9	16.20	44.127	0.546(2)	0.06(4)	RR	
F17_55618	*c*	14 28 24.7	−53 54 23.1	15.47	42.697	0.3697(2)	0.17(2)	EW	F17_55672
F17_55672	*c*	14 28 25.1	−53 54 22.6	15.48	42.697	0.3698(2)	0.14(2)	EW	F17_55618
F17_55682	*c*	14 27 20.9	−54 37 48.3	16.84	42.799	0.3587(2)	0.43(6)	EW	
F17_55849		14 27 03.7	−54 50 04.3	14.27	42.536	0.05169(2)	0.03(2)	DSCT	
F17_55938		14 27 22.5	−54 38 23.5	14.89	42.623	0.5061(3)	0.06(2)	EA	
F17_56006		14 28 07.9	−54 08 13.5	12.46	42.548	2.668(1)	0.035(1)	EA	
F17_56194		14 28 47.7	−53 42 02.5	14.27	42.498	0.05520(2)	0.02(1)	DSCT	
F17_56272		14 28 20.9	−54 01 09.3	17.20	42.782	0.5114(3)	1.04(8)	RR	
F17_56304		14 28 51.7	−53 39 59.6	14.39	...	...	...	LP	
F17_56366		14 27 15.0	−54 45 59.8	13.91	...	...	...	LP	
F17_56413		14 27 10.5	−54 49 15.6	14.25	53.557	28(2)	0.026(8)	VAR	
F17_56480		14 29 00.7	−53 34 49.3	16.00	47.514	2.08(2)	0.13(4)	CEP	
F17_56649		14 27 31.8	−54 36 53.5	15.60	42.753	1.050(4)	0.11(3)	ROT	
F17_56655		14 27 04.8	−54 54 36.6	12.15	...	...	...	LP	
F17_56693		14 28 46.4	−53 46 20.4	13.55	48.697	17.3(9)	0.030(6)	ROT	

Table E.3: Variable stars in field F17 (continued).

BEST ID	F	α (J2000.0) h m s	δ ° ′ ″	R_B [mag]	T_0 [d] [rHJD]	p [d]	A [mag]	Type	Other Names
F17_56742		14 28 25.4	−54 01 09.5	18.02	42.646	0.2772(3)	0.3(2)	RR	
F17_57009		14 29 09.9	−53 31 59.1	13.79	47.334	10.5(3)	0.028(6)	ROT	
F17_57202	*c*	14 29 03.9	−53 37 18.8	17.01	42.706	0.2632(2)	0.19(6)	EW	F17_57237
F17_57237	*c*	14 29 04.3	−53 37 13.4	17.53	42.573	0.2632(2)	0.2(1)	EW	F17_57202
F17_57255		14 28 35.0	−53 57 46.4	13.92	...	...	...	LP	
F17_57526		14 27 38.9	−54 37 40.3	12.68	...	...	...	LP	
F17_57642		14 27 46.7	−54 33 15.5	17.29	42.554	0.635(2)	0.19(8)	RR	
F17_57719		14 27 29.6	−54 45 09.1	18.24	42.779	2.464(8)	0.5(3)	EA	
F17_57774	*s*	14 27 22.3	−54 50 18.4	14.95	44.855	9.03(9)	0.20(2)	ROT	
F17_57796		14 28 12.7	−54 16 50.2	14.59	...	...	...	LP	
F17_57954		14 29 21.0	−53 30 30.8	15.39	44.486	8.79(8)	0.84(8)	EA	
F17_58040		14 28 59.7	−53 46 07.6	18.21	42.668	1.630(4)	0.6(3)	EA	
F17_58136	*s*	14 29 02.5	−53 44 54.6	15.67	46.542	19(5)	0.05(3)	CEP	
F17_58277	*s*	14 27 17.5	−54 56 51.3	15.16	119.335	26(2)	0.05(2)	ROT	
F17_58331		14 28 35.9	−54 04 45.5	13.25	...	...	...	LP	
F17_58368	*s*	14 28 40.9	−54 01 29.4	14.96	57.033	18.8(6)	0.07(2)	ROT	
F17_58425		14 27 59.8	−54 29 55.0	16.34	42.790	0.3291(3)	0.08(4)	EW	
F17_58524		14 27 42.9	−54 41 49.7	14.51	52.758	17(2)	0.04(2)	ROT	
F17_58712	*s*	14 28 48.2	−53 58 45.9	14.63	...	...	...	LP	
F17_58812	*s*	14 27 52.3	−54 37 28.0	13.72	...	...	...	LP	
F17_59125		14 27 21.1	−55 00 05.6	11.59	47.793	2.32(2)	0.06(2)	CEP	
F17_59212	*c*	14 27 23.1	−54 59 14.5	15.28	...	...	...	LP	F17_59308
F17_59220		14 29 01.3	−53 53 01.2	12.20	44.412	0.687(2)	0.015(4)	RR	
F17_59243		14 28 24.9	−54 18 15.4	12.53	...	...	...	LP	
F17_59308	*c*	14 27 23.6	−54 59 18.7	15.40	...	...	...	LP	F17_59212
F17_59419	*c*	14 27 59.1	−54 36 48.3	13.64	44.947	1.288(3)	0.07(2)	EA	
F17_59540	*s*	14 27 52.4	−54 42 02.0	12.48	101.518	21.4(9)	0.07(2)	ROT	
F17_59770	*s*	14 29 17.2	−53 45 36.4	14.84	42.541	0.10184(6)	0.01(2)	DSCT	
F17_59934		14 27 50.3	−54 46 16.3	12.49	...	...	...	LP	
F17_60076	*s*	14 28 50.3	−54 06 42.1	15.03	44.745	11.9(5)	0.03(2)	EB	
F17_60188		14 28 25.9	−54 24 07.1	13.86	42.764	0.4319(2)	0.118(8)	EW	
F17_60193		14 28 00.7	−54 41 03.6	15.87	42.811	0.3550(3)	0.09(3)	EA	
F17_60240		14 28 15.8	−54 31 16.2	14.95	44.114	0.5412(2)	0.23(2)	EB	
F17_60288		14 29 12.1	−53 52 52.7	17.00	42.528	0.3193(2)	0.18(9)	EW	
F17_60594		14 28 15.7	−54 33 32.3	13.48	...	...	...	LP	
F17_60652	*c*	14 27 48.2	−54 52 13.4	17.32	42.535	0.3432(3)	0.1(1)	EW	F17_60686, F17_60729
F17_60659	*s*	14 29 14.7	−53 53 26.7	15.63	42.587	0.703(1)	0.02(3)	EW	
F17_60668		14 28 14.0	−54 35 05.9	12.63	...	...	...	LP	
F17_60677		14 28 43.7	−54 15 00.9	15.82	42.679	0.4085(3)	0.13(3)	EW	
F17_60686	*c*	14 27 48.7	−54 52 08.3	16.85	42.533	0.3432(3)	0.17(6)	EW	F17_60652, F17_60729
F17_60697	*s*	14 28 28.4	−54 25 38.8	15.45	44.076	1.022(4)	0.03(2)	ROT	
F17_60729	*c*	14 27 49.0	−54 52 13.6	16.87	42.534	0.3432(3)	0.13(6)	EW	F17_60652, F17_60686
F17_60864	*c*	14 28 46.5	−54 14 44.7	16.66	42.749	0.3940(2)	0.25(5)	EW	
F17_60886		14 28 52.4	−54 10 40.5	16.05	42.548	0.4158(2)	0.28(3)	EW	
F17_60994	*s*	14 28 55.7	−54 09 10.6	11.52	44.920	4.9903(1)	0.3(1)	EA	
F17_61057	*s*	14 29 20.8	−53 51 58.1	16.11	42.592	0.2226(4)	0.03(3)	DSCT	
F17_61239	*s*	14 28 24.0	−54 32 10.6	14.94	57.766	17(2)	0.07(2)	ROT	
F17_61292		14 29 54.0	−53 29 53.7	17.67	44.815	0.92395(1)	2(1)	EA	
F17_61514		14 27 54.6	−54 53 41.2	18.40	42.704	0.5126(6)	0.6(3)	EW	
F17_61523		14 29 40.9	−53 40 52.5	14.39	...	...	...	LP	
F17_61566		14 27 53.1	−54 55 03.2	15.92	42.749	0.3940(8)	0.04(3)	RR	
F17_61619	*s*	14 28 13.8	−54 41 33.3	14.62	...	...	...	LP	
F17_61633		14 28 36.2	−54 26 33.0	15.00	44.655	1.553(4)	0.06(2)	EA	
F17_61885	*s*	14 28 14.7	−54 42 49.1	15.24	42.496	0.696(3)	0.03(3)	RR	
F17_61939		14 27 54.1	−54 56 46.1	15.65	139.900	60(2)	0.21(5)	VAR	
F17_62237		14 28 42.9	−54 26 05.3	12.24	42.525	0.07524(3)	0.009(7)	DSCT	
F17_62463		14 28 46.8	−54 24 58.9	13.84	55.076	15.3(4)	0.04(2)	ROT	
F17_62475		14 28 29.8	−54 36 39.0	14.92	...	...	...	LP	
F17_62525	*s*	14 29 54.9	−53 37 42.4	11.54	...	...	...	LP	
F17_62547	*s*	14 28 30.8	−54 36 18.8	14.15	54.047	13.4(3)	0.05(2)	ROT	
F17_62669		14 29 22.2	−54 01 44.3	17.09	42.769	0.3022(2)	0.13(7)	EW	
F17_62754	*s*	14 28 54.7	−54 21 22.4	13.06	42.557	0.1946(2)	0.009(7)	DSCT	
F17_62759	*s*	14 28 39.8	−54 31 31.1	14.11	47.192	15.5(8)	0.017(8)	ROT	
F17_62994		14 28 46.8	−54 28 19.2	14.90	57.183	12.1(8)	0.03(2)	CEP	
F17_63072		14 28 37.7	−54 35 05.5	15.34	44.693	1.108(3)	0.04(2)	GDOR	
F17_63085	*s*	14 28 45.5	−54 29 54.9	19.00	42.552	0.3658(3)	1.0(6)	EW	
F17_63202		14 29 42.4	−53 51 09.2	13.42	...	...	...	LP	
F17_63334		14 30 03.5	−53 36 57.8	15.95	44.115	2.87(3)	0.14(4)	CEP	
F17_63376		14 29 17.4	−54 09 51.5	15.56	...	...	...	LP	
F17_63554		14 28 43.8	−54 34 01.8	16.61	44.700	1.289(2)	0.18(6)	EA	
F17_63609	*s*	14 30 06.3	−53 36 45.1	14.47	42.823	1.340(4)	0.03(2)	ROT	
F17_63751		14 28 31.9	−54 43 17.9	15.60	...	...	...	LP	
F17_63971		14 28 38.9	−54 39 58.4	17.13	57.427	11.8(8)	0.13(8)	CEP	
F17_63973	*c*	14 28 26.8	−54 48 07.7	16.35	42.521	0.6010(8)	0.11(5)	EW	
F17_64038		14 29 25.5	−54 08 32.2	13.70	...	...	...	LP	
F17_64073	*c*	14 28 47.1	−54 35 14.5	14.36	51.740	23(2)	0.08(2)	VAR	F17_64133
F17_64081	*s*	14 30 20.6	−53 29 32.0	14.42	42.552	0.07212(3)	0.01(1)	DSCT	
F17_64101		14 28 20.8	−54 53 05.2	14.33	42.643	0.2483(2)	0.01(2)	EW/DSCT	
F17_64133	*c*	14 28 47.5	−54 35 20.4	14.51	54.712	23(9)	0.06(3)	VAR	F17_64073
F17_64289		14 29 05.1	−54 24 21.4	17.11	42.611	0.2532(2)	0.17(8)	EB	
F17_64323		14 29 45.7	−53 56 17.3	17.85	42.703	0.2492(2)	0.3(2)	EW	
F17_64390	*s*	14 28 17.2	−54 57 18.6	14.53	...	...	...	LP	
F17_64501		14 29 54.8	−53 50 51.1	11.32	...	...	...	LP	
F17_64607	*s*	14 28 45.0	−54 40 05.9	13.25	...	...	...	LP	
F17_64719		14 29 06.8	−54 26 02.3	15.07	42.889	0.626(2)	0.03(3)	RR	
F17_64841	*s*	14 28 14.5	−55 02 03.7	11.88	...	...	...	LP	
F17_64891		14 28 41.5	−54 44 30.7	15.89	42.681	0.4524(3)	0.19(3)	EW	
F17_65059	*s*	14 28 40.7	−54 46 07.0	13.42	98.424	27(3)	0.04(2)	EB	

Table E.3: Variable stars in field F17 (continued).

BEST ID	F	α (J2000.0) δ	R_B	T_0 [d]	p [d]	A	Type	Other Names
		h m s ° ′ ″	[mag]	[rHJD]		[mag]		
F17_65073		14 29 19.5 −54 19 45.1	14.06	...	...	...	LP	
F17_65237	*c*	14 28 23.2 −54 58 48.5	16.93	42.841	0.5287(6)	0.22(8)	EW	F17_65311
F17_65243		14 30 08.3 −53 46 22.4	18.75	42.626	0.595(1)	1.0(5)	RR	
F17_65270		14 29 45.1 −54 03 02.7	16.84	44.319	1.034(2)	0.25(5)	EW	
F17_65311	*c*	14 28 24.0 −54 58 46.1	16.74	42.839	0.5288(6)	0.13(7)	EW	F17_65237
F17_65315	*s*	14 30 04.1 −53 49 52.3	14.03	56.942	20(2)	0.026(8)	ROT	
F17_65430		14 29 06.1 −54 31 11.8	14.53	...	...	...	LP	
F17_65457		14 28 25.0 −54 58 58.4	15.58	42.662	3.46(7)	0.08(3)	ROT	
F17_65535	*c*	14 29 23.8 −54 19 46.5	15.56	42.867	1.222(2)	0.24(3)	EA	F17_65557, F17_65619
F17_65557	*c*	14 29 23.8 −54 19 51.6	15.54	42.867	1.222(2)	0.19(2)	EA	F17_65535, F17_65619
F17_65619	*c*	14 29 24.5 −54 19 50.0	15.64	42.871	1.222(2)	0.12(3)	EA	F17_65535, F17_65557
F17_65709		14 29 27.4 −54 18 21.1	17.65	42.792	0.781(2)	0.2(2)	EA	
F17_65758	*s*	14 30 14.4 −53 45 27.7	13.88	42.741	1.069(3)	0.02(1)	EB	
F17_65759		14 30 12.1 −53 47 10.1	15.57	42.639	0.5734(3)	0.31(3)	EW	
F17_65768		14 28 35.6 −54 53 56.4	14.99	...	...	...	LP	
F17_65787		14 30 07.1 −53 51 00.4	13.52	42.507	0.06956(3)	0.009(8)	DSCT	
F17_65825		14 29 57.3 −53 58 12.7	13.43	...	...	...	LP	
F17_65843		14 29 18.1 −54 25 45.0	14.95	...	...	...	LP	
F17_65881	*s*	14 28 58.0 −54 39 44.4	16.92	42.857	0.4816(7)	0.08(7)	EA	
F17_65991		14 29 23.2 −54 23 16.3	13.18	42.639	0.2659(2)	0.006(6)	EW/DSCT	
F17_66189		14 30 36.9 −53 32 21.8	15.72	44.748	0.786(3)	0.07(3)	RR	
F17_66255		14 29 26.1 −54 23 13.4	15.19	42.502	0.5930(7)	0.06(2)	EW	
F17_66266		14 29 24.0 −54 24 46.2	14.86	...	...	...	LP	
F17_66302		14 28 35.6 −54 57 43.9	13.44	...	...	...	LP	
F17_66350		14 30 42.8 −53 29 21.7	17.51	42.803	0.3489(3)	0.2(2)	EW/DSCT	
F17_66404		14 29 46.4 −54 10 17.2	15.11	44.775	5.407(1)	0.13(1)	EA	
F17_66570	*s*	14 28 45.4 −54 53 05.1	13.74	52.049	18.4(6)	0.06(2)	ROT	
F17_66706	*s*	14 28 36.3 −55 00 14.4	13.42	51.094	24(2)	0.10(3)	ROT	
F17_66837	*c*	14 30 33.1 −53 40 03.2	17.10	42.528	0.3751(2)	0.55(9)	EW	
F17_66884		14 30 46.9 −53 30 20.3	18.50	42.810	0.3874(3)	0.6(3)	EW	
F17_66978		14 28 59.2 −54 46 47.8	15.10	...	...	...	LP	
F17_67069	*s*	14 29 38.9 −54 20 23.5	14.45	42.683	0.2881(2)	0.01(2)	EW/DSCT	
F17_67152		14 28 56.3 −54 50 09.5	16.70	49.245	7.2(2)	0.24(6)	EB	
F17_67218	*c*	14 29 41.6 −54 19 41.9	15.72	42.804	0.4023(4)	0.03(3)	EW/DSCT	
F17_67219	*c*	14 29 41.6 −54 19 49.3	16.05	42.826	0.5038(7)	0.06(3)	EW/DSCT	
F17_67344	*s*	14 29 34.3 −54 25 48.3	13.54	42.518	0.032370(5)	0.008(8)	DSCT	
F17_67359		14 30 23.8 −53 50 59.2	13.70	101.989	21.3(9)	0.05(2)	ROT	
F17_67392		14 29 42.5 −54 20 21.5	17.69	42.559	0.3105(2)	0.7(2)	EW	
F17_67475		14 29 04.8 −54 46 54.6	12.53	56.783	17.8(6)	0.045(8)	ROT	
F17_67547		14 29 26.4 −54 32 44.9	16.82	42.545	0.10908(5)	0.13(7)	DSCT	
F17_67612	*s*	14 28 42.4 −55 02 53.0	15.28	...	...	...	LP	
F17_67675		14 29 24.7 −54 34 49.4	13.23	...	...	...	LP	
F17_67883		14 30 29.3 −53 50 50.2	17.22	44.168	0.5703(7)	0.42(8)	RR	
F17_68100	*s*	14 30 17.2 −54 01 13.1	15.12	...	...	...	LP	
F17_68144		14 29 26.9 −54 36 36.6	16.61	42.533	0.1877(3)	0.06(5)	DSCT	
F17_68159		14 29 26.4 −54 37 03.9	17.87	42.624	0.6221(9)	0.3(2)	EW	

E.3 F18

Table E.4: Variable stars in field F18 (see description on page 180).

BEST ID	F	α (J2000.0) δ	R_B	T_0 [d]	p [d]	A	Type	Other Names
		h m s ° ′ ″	[mag]	[rHJD]		[mag]		
F18_00214		22 47 17.7 −44 20 58.6	13.26	72.444	12.8(4)	0.032(8)	VAR	
F18_00889	*s*	22 48 32.1 −43 48 29.9	12.23	70.114	11.1(2)	0.044(7)	EA	
F18_01367	*s*	22 47 43.6 −44 41 15.9	14.25	132.182	14.0(4)	0.03(2)	ROT	
F18_01676	*s*	22 48 23.7 −44 22 14.0	13.67	...	...	...	EA	
F18_02074	*k*	22 49 35.0 −43 41 09.3	11.86	...	...	...	LP	ASAS J224935-4341.2
F18_03150		22 49 07.0 −44 34 34.6	13.57	68.437	5.72(9)	0.05(2)	ROT	
F18_03440		22 49 14.8 −44 36 26.7	11.77	88.749	11.1(3)	0.025(4)	ROT	
F18_03793	*k*	22 49 06.2 −44 54 04.9	16.54	63.945	0.6976(7)	0.95(9)	RR	YZ Gru
F18_05505	*s*	22 52 14.5 −43 24 20.6	14.05	69.335	15.7(8)	0.02(2)	ROT	
F18_05548	*k*	22 50 40.2 −44 39 46.6	14.13	63.848	0.6055(2)	1.04(2)	RR	BE Gru
F18_06111		22 52 07.2 −43 48 43.8	17.45	64.150	0.644(2)	0.4(2)	RR	
F18_06765		22 52 21.9 −43 57 23.1	13.49	63.800	0.4033(5)	0.036(8)	RR	
F18_07603		22 52 53.7 −43 58 11.6	16.33	63.636	0.2476(2)	0.63(9)	EW	
F18_08267	*s*	22 53 35.7 −43 46 34.3	15.25	63.740	1.565(7)	0.03(3)	EA	
F18_08585		22 53 47.1 −43 47 28.8	11.85	70.519	12.5(5)	0.024(4)	ROT	
F18_08723		22 53 16.2 −44 15 50.4	12.13	64.664	7.2(2)	0.024(7)	ROT	
F18_08895	*k*	22 53 01.7 −44 32 39.0	15.53	63.639	0.7592(5)	0.73(4)	RR	AD Gru
F18_08981		22 53 38.2 −44 05 58.4	14.22	69.308	13.4(3)	0.03(2)	VAR	
F18_10427		22 54 17.2 −44 17 40.3	16.55	63.657	0.28227(8)	0.8(1)	EW	
F18_10917		22 54 34.8 −44 18 01.4	14.02	63.543	0.642(3)	0.04(3)	RR	
F18_10951	*s*	22 55 33.4 −43 30 11.1	12.25	88.672	14.0(4)	0.023(6)	ROT	
F18_11994	*s*	22 54 58.1 −44 36 06.2	14.15	78.260	12.2(4)	0.04(2)	ROT	
F18_12932	*s*	22 55 12.0 −45 00 20.4	12.63	65.982	4.17(5)	0.029(8)	VAR	
F18_12938		22 55 01.9 −45 08 41.9	13.88	63.622	0.35321(8)	0.24(2)	EW	
F18_13265	*s*	22 56 24.0 −44 14 17.2	16.27	63.535	0.5314(7)	0.11(7)	EB	

E.4 F19

Table E.5: Variable stars in field F19 (see description on page 180).

BEST ID	F	α (J2000.0) h m s	δ ° ′ ″	R_B [mag]	T_0 [d] [rHJD]	p [d]	A [mag]	Type	Other Names
F19_000002	*c*	16 31 57.2	−56 46 40.0	14.24	81.119	0.51944(9)	0.59(3)	EB	
F19_000271		16 31 51.7	−56 07 31.1	14.35	99.145	64(7)	0.08(2)	VAR	
F19_000396		16 31 53.9	−56 36 04.7	12.79	93.912	7.8905(1)	0.16(1)	EA	
F19_000433	*c*	16 31 53.2	−56 31 22.7	12.31	275.611	69(4)	0.50(5)	CEP	
F19_000441		16 31 50.8	−56 08 42.8	13.42	90.725	20.2(8)	0.03(2)	ROT	
F19_000499	*ck*	16 31 51.0	−56 14 57.9	12.60	...	...	...	LP	FV Nor
F19_000546		16 31 44.9	−55 27 07.0	15.52	80.778	0.24814(7)	0.3(2)	EW/DSCT	
F19_000678	*c*	16 31 48.8	−56 04 22.5	13.80	81.173	0.9057(9)	0.04(2)	EW	
F19_000695		16 31 52.3	−56 38 21.8	12.94	92.655	30(2)	0.07(2)	VAR	
F19_000944		16 31 44.9	−55 44 46.8	15.47	80.712	0.5124(4)	0.07(5)	EA	
F19_000997	*c*	16 31 48.4	−56 17 44.6	15.14	80.754	0.11164(2)	0.19(6)	VAR	
F19_001099		16 31 43.2	−55 38 56.7	15.58	81.222	0.7048(5)	0.09(6)	EA	
F19_001106	*s*	16 31 51.2	−56 52 58.6	13.31	...	...	...	SR	
F19_001251	*c*	16 31 45.1	−56 01 15.2	13.85	80.714	0.41449(9)	0.13(2)	EW	F19_001310
F19_001310	*c*	16 31 44.8	−56 01 11.9	13.45	80.714	0.4145(2)	0.07(2)	EW	F19_001251
F19_001376		16 31 43.2	−55 50 17.4	15.41	99.245	25(1)	0.17(5)	CEP	
F19_001412		16 31 41.6	−55 39 09.3	13.89	94.655	7.66(8)	0.03(2)	VAR	
F19_001423		16 31 48.8	−56 45 40.7	16.42	82.816	5.8489(1)	0.5(1)	EA	
F19_001478		16 31 44.3	−56 05 49.0	13.72	81.162	0.793(2)	0.04(3)	VAR	
F19_001502		16 31 45.6	−56 19 25.0	17.37	80.747	0.2883(1)	0.4(3)	EW	
F19_001534	*c*	16 31 48.4	−56 51 42.6	13.02	...	...	...	LP	
F19_001572	⋆	16 31 46.8	−56 35 14.4	12.56	81.076	4.7539(1)	0.32(1)	EA	
F19_001807	*s*	16 31 46.0	−56 44 02.5	11.94	...	...	...	SR	
F19_001848	*c*	16 31 41.3	−56 00 52.7	14.31	80.812	0.38796(6)	0.26(3)	EW	
F19_001979		16 31 44.8	−56 42 03.2	14.81	80.837	0.2542(1)	0.03(3)	EW/DSCT	
F19_002000	*s*	16 31 37.5	−55 37 04.0	14.77	128.278	80(2)	0.10(3)	CEP	
F19_002100		16 31 38.2	−55 46 50.1	15.29	83.534	3.76(2)	0.18(5)	EA	
F19_002108		16 31 45.0	−56 54 26.5	14.80	80.926	0.2968(2)	0.04(3)	EW	
F19_002120	*s*	16 31 40.7	−56 09 20.4	12.79	88.085	10.9(4)	0.012(6)	VAR	
F19_002173		16 31 44.0	−56 46 24.7	10.85	...	...	...	LP	
F19_002254		16 31 40.7	−56 14 54.6	13.74	80.907	0.3300(2)	0.02(2)	EW/DSCT	
F19_002335	*s*	16 31 42.8	−56 41 00.5	15.03	81.408	6.3(1)	0.04(3)	ROT	
F19_002380		16 31 40.8	−56 22 54.3	13.87	...	...	...	LP	
F19_002425	*s*	16 31 37.8	−55 57 20.9	15.77	80.700	0.3896(3)	0.2(2)	EW	
F19_002507		16 31 36.7	−55 52 05.4	14.26	80.819	0.31849(9)	0.03(3)	EA	
F19_002522		16 31 41.9	−56 44 02.1	13.33	80.744	0.09566(3)	0.02(2)	DSCT	
F19_002564	*c*	16 31 37.8	−56 05 13.5	13.84	80.679	0.2873(2)	0.02(2)	EW	F19_002592
F19_002592	*c*	16 31 37.7	−56 05 20.4	14.11	80.956	0.2873(2)	0.03(3)	EW	F19_002564
F19_002596	*s*	16 31 35.3	−55 45 32.8	15.62	80.889	0.2919(2)	0.05(6)	EW	
F19_002651	⋆	16 31 37.9	−56 11 05.4	13.08	81.119	0.831(1)	0.015(7)	VAR	
F19_002685	*c*	16 31 36.2	−55 56 57.6	14.23	81.618	1.696(7)	0.04(2)	VAR	
F19_002874		16 31 41.2	−56 59 43.5	12.51	95.513	9.06(8)	0.09(2)	CEP	
F19_002933	*c*	16 31 37.1	−56 17 29.1	15.71	81.021	0.9483(9)	0.15(6)	EA	
F19_003055	⋆	16 31 35.3	−56 07 44.7	14.22	105.675	18.49(1)	0.2(1)	EA	
F19_003165		16 31 39.3	−56 56 17.6	14.28	135.341	37(8)	0.07(4)	VAR	
F19_003167	*c*	16 31 38.9	−56 51 32.3	14.97	81.011	0.3479(2)	0.06(4)	EW/DSCT	
F19_003207		16 31 38.1	−56 45 39.4	11.61	...	...	...	SR	
F19_003231	*c*	16 31 29.2	−55 23 44.7	14.15	80.675	0.38605(8)	0.33(5)	EW	
F19_003288		16 31 33.7	−56 05 00.5	12.87	291.072	87(6)	0.06(1)	VAR	
F19_003320	*c*⋆	16 31 33.7	−56 06 18.4	13.78	80.849	0.40916(9)	0.11(2)	EW	
F19_003412		16 31 29.7	−55 36 28.2	15.54	80.912	0.3922(2)	0.26(5)	EW/DSCT	
F19_003536	*c*	16 31 31.8	−55 59 40.7	14.98	81.429	0.8312(6)	0.11(4)	EA	F19_003603
F19_003603	*c*	16 31 31.5	−55 59 35.9	14.94	81.427	0.8312(7)	0.07(4)	EA	F19_003536
F19_003709	*s*	16 31 35.7	−56 50 51.1	11.16	...	...	...	SR	
F19_003813	*s*	16 31 32.0	−56 16 24.4	13.35	83.618	21(3)	0.03(2)	VAR	
F19_004107		16 31 32.2	−56 34 04.0	13.78	80.750	0.5656(2)	0.15(2)	EB	
F19_004133	*c*	16 31 32.2	−56 35 01.1	14.15	81.103	0.9193	0.045	EA	
F19_004143		16 31 27.7	−55 52 04.8	11.26	...	...	...	SR	
F19_004328	*s*	16 31 30.5	−56 30 55.0	12.00	80.678	0.07170(2)	0.01(2)	DSCT	
F19_004339		16 31 26.5	−55 52 59.2	15.59	89.618	4.51(2)	0.12(5)	EA	
F19_004442	*c*	16 31 28.0	−56 12 40.2	13.24	80.770	0.4592(3)	0.4(2)	EB	
F19_004458		16 31 32.0	−56 59 32.9	13.64	80.681	0.42570(5)	0.37(2)	EW	
F19_004499		16 31 28.4	−56 19 27.0	12.11	...	...	...	LP	
F19_004554	*c*	16 31 30.4	−56 46 38.7	13.36	121.684	48(3)	0.07(2)	VAR	F19_004673
F19_004641	*s*	16 31 30.9	−56 58 02.3	13.81	80.917	0.4130(4)	0.01(2)	VAR	
F19_004663		16 31 26.5	−56 09 43.0	11.83	80.694	0.09622(3)	0.009(8)	DSCT	
F19_004673	*c*	16 31 29.9	−56 46 38.6	13.64	121.591	48(3)	0.08(2)	VAR	F19_004554
F19_004933	*c*	16 31 20.1	−55 26 43.0	15.01	81.724	2.75513(1)	0.4(1)	EA	
F19_004967	⋆	16 31 27.6	−56 38 51.1	16.38	80.883	0.30495(5)	0.9(2)	EW	
F19_005012	*s*	16 31 26.4	−56 28 07.8	13.53	83.191	10.0(2)	0.03(2)	VAR	
F19_005038		16 31 24.9	−56 14 53.5	14.83	80.685	0.30340(4)	0.34(3)	EW	
F19_005045		16 31 23.6	−56 02 27.2	15.34	90.009	11.7(3)	0.07(4)	VAR	
F19_005071		16 31 24.6	−56 13 02.1	14.54	80.727	0.37945(9)	0.14(2)	EW	
F19_005137		16 31 21.8	−55 50 40.7	12.67	80.950	5.89(6)	0.05(3)	ROT	
F19_005140		16 31 21.1	−55 44 01.4	14.82	80.980	0.4196(2)	0.24(7)	EW	
F19_005175		16 31 20.4	−55 40 31.1	11.58	...	...	...	LP	
F19_005186		16 31 27.0	−56 47 57.9	13.27	81.135	1.3364	0.048	EA	
F19_005209		16 31 27.5	−56 55 50.5	15.66	80.766	0.22521(6)	0.34(6)	RR	
F19_005215	*c*⋆	16 31 26.4	−56 40 37.8	14.27	80.734	0.4569(2)	0.11(2)	EB	
F19_005216	*c*⋆	16 31 25.5	−56 31 56.4	12.13	81.003	0.37956(4)	0.37(2)	EW	
F19_005332	*c*	16 31 23.5	−56 19 22.6	13.21	80.944	0.4507(1)	0.106(8)	EB	
F19_005336	*s*	16 31 22.7	−56 11 21.8	14.73	91.589	6.32(4)	0.10(3)	EB	
F19_005344		16 31 20.9	−55 54 11.4	10.78	...	...	...	LP	
F19_005508	*c*	16 31 19.1	−55 44 54.1	13.61	80.697	0.4273(3)	0.05(3)	EW	F19_005544

Table E.5: Variable stars in field F19 (continued).

BEST ID	F	α (J2000.0) h m s	δ ° ′ ″	R_B [mag]	T_0 [d] [rHJD]	p [d]	A [mag]	Type	Other Names
F19_005544	c	16 31 18.8	−55 44 47.9	13.79	80.698	0.4274(3)	0.05(3)	EW	F19_005508
F19_005595	c	16 31 24.8	−56 48 49.0	12.96	80.670	0.4117(2)	0.025(8)	EW/DSCT	
F19_005696	c	16 31 18.3	−55 47 50.1	11.43	184.896	100(3)	0.19(4)	VAR	
F19_005745	s	16 31 23.8	−56 45 23.7	13.39	95.441	62(6)	0.02(1)	VAR	
F19_005774		16 31 23.7	−56 47 41.6	14.37	93.816	9.01(8)	0.17(3)	CEP	
F19_005941		16 31 20.4	−56 20 42.3	14.43	80.945	0.5495(4)	0.07(3)	EB	
F19_006037		16 31 18.5	−56 06 51.5	14.27	317.842	58(4)	0.06(2)	ROT	
F19_006104		16 31 18.7	−56 12 38.7	13.23	93.028	6.35(6)	0.043(8)	CEP	
F19_006250		16 31 20.5	−56 40 33.6	14.38	80.960	0.36069(8)	0.13(2)	EW	
F19_006251	s	16 31 20.4	−56 39 08.9	17.60	80.698	0.3181(2)	0.3(4)	EB	
F19_006375	s	16 31 12.2	−55 25 44.8	11.34	270.605	56(4)	0.12(5)	VAR	
F19_006450		16 31 16.6	−56 10 30.3	12.37	96.355	20.7(7)	0.09(3)	SR	
F19_006547		16 31 12.4	−55 35 48.2	14.94	80.820	0.3397(2)	0.06(4)	EW	
F19_006679	s	16 31 18.7	−56 50 09.6	13.19	81.182	0.5374(6)	0.01(2)	VAR	
F19_006742	c	16 31 18.6	−56 54 37.8	13.51	83.440	3.860(4)	0.41(3)	EA	
F19_006823	$\star$	16 31 13.9	−56 04 33.9	13.81	82.895	3.3598(1)	0.11(1)	EB	
F19_006912	s	16 31 16.1	−56 33 15.2	13.32	80.672	0.3807(3)	0.04(3)	EW/DSCT	
F19_006916	s	16 31 14.3	−56 13 21.0	16.38	83.944	9.0(2)	0.2(1)	ROT	
F19_007005	$c\star$	16 31 16.3	−56 42 11.7	13.54	81.539	1.1038(4)	0.32(2)	EB	
F19_007108	c	16 31 14.1	−56 24 53.2	15.05	80.848	0.30253(5)	0.24(3)	EW	F19_007203
F19_007110		16 31 13.4	−56 15 11.8	12.33	81.567	0.963(2)	0.027(8)	VAR	
F19_007203	c	16 31 13.9	−56 24 55.8	14.90	80.847	0.30253(5)	0.22(3)	EW	F19_007108
F19_007278	c	16 31 10.7	−55 56 55.3	13.50	81.102	0.4610(3)	0.04(2)	EW	F19_007409
F19_007282	c	16 31 09.4	−55 44 16.4	15.10	80.969	0.6113(4)	0.12(4)	EW	
F19_007287		16 31 15.7	−56 54 42.0	14.07	81.061	0.3921(3)	0.06(2)	EB	
F19_007333	c	16 31 13.6	−56 31 02.3	13.74	81.107	0.48570(8)	0.19(2)	EW	
F19_007397		16 31 13.3	−56 30 43.6	13.01	185.288	70(2)	0.015(7)	VAR	
F19_007409	c	16 31 10.0	−55 56 56.9	13.95	81.101	0.4610(3)	0.09(5)	EW	F19_007278
F19_007431	$\star$	16 31 10.9	−56 06 53.0	11.34	80.697	1.0289(5)	0.13(2)	EA	
F19_007486	c	16 31 13.0	−56 34 27.0	14.25	82.273	5.70(2)	0.11(2)	EB	F19_007519
F19_007519	c	16 31 13.0	−56 34 20.1	14.46	82.277	5.70(3)	0.08(2)	EB	F19_007486
F19_007592		16 31 06.1	−55 30 49.5	12.44	...	...	...	LP	
F19_007664		16 31 11.7	−56 31 07.3	13.28	82.434	53(3)	0.10(2)	ROT	
F19_007757		16 31 12.7	−56 50 37.5	15.00	80.894	0.3531(2)	0.05(3)	EW/DSCT	
F19_007860		16 31 10.3	−56 27 01.6	11.50	...	...	...	SR	
F19_008001	s	16 31 11.6	−56 55 14.8	14.38	187.086	16.9(6)	0.06(2)	EB	
F19_008006		16 31 10.3	−56 37 33.8	15.29	80.925	0.2891(2)	0.04(4)	EW	
F19_008009		16 31 09.5	−56 28 05.9	14.54	80.979	0.8394(4)	0.39(4)	EW	
F19_008149		16 31 09.7	−56 40 06.9	13.07	83.061	19.2(7)	0.08(2)	VAR	
F19_008164		16 31 05.5	−55 56 03.5	15.21	81.093	0.45282(8)	0.55(4)	EW	
F19_008217		16 31 09.2	−56 39 57.9	14.67	80.832	0.4346(4)	0.08(5)	VAR	
F19_008230		16 31 05.8	−56 02 06.7	11.00	...	...	...	LP	
F19_008231		16 31 05.6	−55 59 32.2	13.83	82.036	2.89(2)	0.04(2)	VAR	
F19_008382	c	16 31 07.7	−56 31 15.1	14.65	80.886	0.4271(2)	0.07(3)	EW	F19_008471
F19_008471	c	16 31 07.2	−56 31 11.1	15.11	80.885	0.4271(2)	0.15(4)	EW	F19_008382
F19_008530	s	16 31 08.4	−56 50 49.6	13.80	80.999	1.016(4)	0.02(2)	VAR	
F19_008548		16 31 03.6	−55 57 32.2	13.27	80.700	0.050817(8)	0.01(1)	DSCT	
F19_008683	s	16 31 01.5	−55 44 06.5	13.79	80.730	0.15146(6)	0.01(2)	DSCT	
F19_008961		16 31 02.7	−56 11 09.0	15.19	80.954	0.4107(2)	0.22(4)	EW	
F19_009018		16 31 01.1	−55 58 21.0	12.84	81.561	8.50(7)	0.07(1)	EB	
F19_009081	s	16 31 00.4	−55 55 13.0	13.71	88.431	8.5(2)	0.02(1)	ROT	
F19_009171	cs	16 31 02.2	−56 19 37.3	11.08	...	...	...	SR	
F19_009224	s	16 31 03.5	−56 37 08.4	14.86	95.700	10.7(3)	0.07(3)	VAR	
F19_009329	s	16 31 01.7	−56 23 40.5	12.75	80.830	0.3914(2)	0.008(6)	EW/DSCT	
F19_009385		16 31 02.7	−56 39 31.1	11.30	...	...	...	SR	
F19_009524	c	16 31 01.1	−56 27 47.7	13.64	273.593	68(9)	0.05(2)	VAR	F19_009559
F19_009559	c	16 31 01.0	−56 27 52.3	13.79	265.877	68(9)	0.04(1)	VAR	F19_009524
F19_009570	c	16 30 58.2	−55 59 05.6	12.23	...	...	...	LP	
F19_009585		16 30 54.7	−55 26 09.6	14.54	80.944	0.2787(1)	0.05(4)	EW/DSCT	
F19_009622	c	16 31 02.4	−56 51 14.1	12.29	152.735	42(3)	0.045(8)	ROT	F19_009713
F19_009631	s	16 30 58.5	−56 05 10.0	14.30	80.936	0.3047(3)	0.02(2)	VAR	
F19_009645	$\star$	16 30 55.5	−55 35 57.7	13.70	80.937	0.51610(8)	0.59(4)	EB	
F19_009713	c	16 31 02.1	−56 51 18.2	12.32	152.942	42(3)	0.04(1)	ROT	F19_009622
F19_009838	$c\star$	16 31 01.2	−56 53 29.0	12.37	88.999	12.48(8)	0.07(2)	EB	
F19_009868	$s\star$	16 31 01.2	−56 55 03.6	11.79	81.120	0.5717	0.0064	EA	
F19_009937		16 31 00.0	−56 42 23.7	15.19	93.106	24.8(7)	0.07(4)	ROT	
F19_009995	c	16 30 55.1	−55 50 54.6	14.73	80.943	0.4851(2)	0.19(4)	EB	
F19_010018	c	16 30 58.9	−56 33 39.1	14.16	80.822	0.6352(2)	0.90(3)	RR	
F19_010096	c	16 30 55.7	−56 01 28.7	15.60	80.764	0.5807(3)	0.52(6)	RR	F19_010097
F19_010097	c	16 30 55.7	−56 01 23.4	15.34	80.765	0.5807(2)	0.54(4)	RR	F19_010096
F19_010216	$\star$	16 30 52.9	−55 39 05.9	17.00	80.706	0.6723(5)	0.8(3)	EA	
F19_010299	c	16 30 55.5	−56 09 26.5	14.86	80.978	0.4900(2)	0.13(3)	EW	
F19_010339	s	16 30 59.0	−56 58 22.9	15.91	81.721	1.364(3)	0.16(7)	EB	
F19_010349		16 30 55.5	−56 13 32.4	15.29	80.703	1.455(7)	0.07(4)	VAR	
F19_010547		16 30 51.3	−55 44 05.8	15.40	80.956	0.3219(2)	0.06(5)	EW/DSCT	
F19_010599	s	16 30 55.6	−56 35 25.0	12.32	...	...	...	SR	
F19_010667	s	16 30 54.6	−56 26 35.7	14.86	80.798	0.15925(6)	0.03(3)	VAR	
F19_010747	c	16 30 51.3	−55 54 25.6	11.87	...	...	...	LP	
F19_010892	s	16 30 53.1	−56 23 12.3	14.11	81.475	0.880(2)	0.03(2)	VAR	
F19_010893	$c\star$	16 30 53.0	−56 21 32.9	13.71	139.885	3.962(1)	0.44(1)	EA	
F19_010985	$\star$	16 30 52.1	−56 17 51.3	14.78	81.483	1.6234(8)	1.03(7)	EA	
F19_011285	$c\star$	16 30 53.0	−56 51 18.7	13.98	81.456	1.6119(8)	0.32(3)	EA	
F19_011349	s	16 30 50.8	−56 27 30.1	13.83	83.043	13.8(4)	0.03(2)	ROT	
F19_011380	$\star$	16 30 51.7	−56 38 55.0	13.45	80.738	0.37636(5)	0.13(1)	EW	
F19_011426		16 30 47.4	−55 52 37.6	13.23	90.858	40.7(7)	0.16(1)	CEP	
F19_011444	c	16 30 52.3	−56 54 45.3	15.41	92.022	22.7(8)	0.15(5)	VAR	
F19_011491		16 30 46.8	−55 51 16.4	13.48	81.752	1.821(2)	0.07(3)	EA	
F19_011521		16 30 45.3	−55 38 11.2	15.07	80.904	0.4160(2)	0.15(5)	EW	

Table E.5: Variable stars in field F19 (continued).

BEST ID	F	α (J2000.0) h m s	δ ° ′ ″	R_B [mag]	T_0 [d] [rHJD]	p [d]	A [mag]	Type	Other Names
F19_011528		16 30 51.8	−56 55 06.8	15.45	146.009	43(4)	0.14(5)	ROT	
F19_011556		16 30 46.1	−55 46 37.2	12.07	...	...	...	SR	
F19_011581	*c*	16 30 48.7	−56 16 36.7	13.74	81.667	5.35(8)	0.03(2)	VAR	F19_011666
F19_011638		16 30 47.5	−56 07 34.3	14.00	88.336	10.2(2)	0.04(2)	ROT	
F19_011641	⋆	16 30 46.9	−56 00 08.5	14.87	80.760	0.5750(2)	0.46(3)	EB	
F19_011666	*c*	16 30 48.2	−56 16 32.4	13.90	81.523	5.4(2)	0.03(2)	VAR	F19_011581
F19_011715	*c*⋆	16 30 43.5	−55 30 22.2	13.55	80.943	0.5773(4)	0.10(5)	EB	
F19_011733		16 30 47.3	−56 11 18.5	14.41	83.875	5.30(7)	0.03(2)	ROT	
F19_011765		16 30 48.2	−56 22 15.6	12.02	172.155	32(2)	0.13(3)	VAR	
F19_011829	⋆	16 30 43.1	−55 32 46.3	14.30	81.260	0.7507(2)	0.33(2)	EB	
F19_011909	*s*	16 30 48.6	−56 39 18.3	14.20	96.581	10.2(2)	0.02(2)	ROT	
F19_011917	⋆	16 30 46.0	−56 07 22.5	12.70	81.023	0.5008(2)	0.23(4)	EW	
F19_011988	*c*	16 30 48.2	−56 38 05.0	12.31	105.995	76(5)	0.23(3)	VAR	
F19_012012		16 30 45.5	−56 07 54.3	12.57	...	...	...	SR	
F19_012037	*s*	16 30 46.7	−56 23 01.6	14.11	122.950	115.14(1)	0.5(1)	EA	
F19_012145	*s*	16 30 44.8	−56 08 45.3	13.77	139.760	27.65(1)	0.08(1)	EA	
F19_012244	⋆	16 30 42.8	−55 52 39.3	15.57	120.840	7.346(1)	0.56(1)	EA	
F19_012305		16 30 44.2	−56 10 35.0	15.37	80.840	0.2970(1)	0.07(4)	EW	
F19_012402	*c*	16 30 46.3	−56 44 19.0	15.90	80.718	0.3187(2)	0.08(6)	EW	
F19_012443	*s*	16 30 42.3	−55 57 05.9	12.74	...	...	...	LP	
F19_012452	*c*	16 30 46.2	−56 48 09.8	12.95	88.006	31(2)	0.032(8)	VAR	
F19_012523		16 30 44.5	−56 28 33.6	15.07	80.802	1.086(2)	0.08(3)	EB	
F19_012566		16 30 41.0	−55 52 16.9	12.34	172.812	17.5288(1)	0.16(1)	EA	
F19_012736	⋆	16 30 40.7	−55 58 17.5	13.72	123.910	7.4396(1)	0.17(1)	EA	
F19_012835	*s*	16 30 37.9	−55 33 01.0	12.70	82.383	13.7(2)	0.04(2)	VAR	
F19_012933	*s*	16 30 43.9	−56 52 08.0	11.18	128.703	20.5(5)	0.06(2)	VAR	
F19_012966		16 30 38.3	−55 45 12.9	11.53	...	...	...	LP	
F19_012982	*c*	16 30 41.4	−56 22 21.3	14.78	80.736	0.17881(8)	0.04(3)	DSCT	
F19_013128		16 30 40.3	−56 16 52.9	14.15	88.275	48(5)	0.03(2)	VAR	
F19_013171	*c*	16 30 37.7	−55 50 29.9	13.01	...	...	...	LP	
F19_013176	⋆	16 30 36.4	−55 36 30.1	14.60	82.512	2.019(2)	0.28(3)	EA	
F19_013215		16 30 40.5	−56 25 14.9	14.93	80.718	0.4554(2)	0.17(4)	EW	
F19_013220		16 30 37.9	−55 55 06.5	13.12	80.722	0.09062(2)	0.019(8)	DSCT	
F19_013309	⋆	16 30 40.1	−56 27 18.1	16.66	80.677	0.27505(5)	1.0(2)	EB	
F19_013339	*s*	16 30 40.0	−56 28 40.9	11.29	88.850	11.7(2)	0.03(1)	SR	
F19_013419	*s*	16 30 41.3	−56 54 37.9	12.78	...	...	...	LP	
F19_013528	*s*	16 30 35.0	−55 42 59.5	15.82	80.701	0.4816(6)	0.09(8)	VAR	
F19_013551		16 30 37.1	−56 07 47.8	14.28	83.828	10.6(3)	0.03(2)	ROT	
F19_013663		16 30 36.3	−56 03 32.8	13.21	80.839	0.4623(6)	0.02(1)	VAR	
F19_013707		16 30 39.3	−56 48 29.9	13.77	81.104	1.722(6)	0.05(2)	ROT	
F19_013804		16 30 38.3	−56 39 42.6	12.95	88.853	8.7688	0.071	EA	
F19_013819	*c*⋆	16 30 35.3	−56 03 05.1	14.72	80.958	0.7425(3)	0.18(3)	EB	
F19_013864	*c*	16 30 38.5	−56 51 11.1	13.67	80.692	0.3623(2)	0.08(3)	EW	F19_013998
F19_013878	*c*	16 30 35.3	−56 08 07.9	15.39	81.031	0.4193(2)	0.25(6)	EW	
F19_013904	*cs*	16 30 38.1	−56 45 45.7	13.18	80.861	0.2206(1)	0.010(8)	VAR	F19_013965
F19_013916		16 30 36.0	−56 18 00.1	12.19	...	...	...	LP	
F19_013926		16 30 34.0	−55 54 18.0	12.52	...	...	...	LP	
F19_013965	*cs*	16 30 37.7	−56 45 52.5	13.39	80.860	0.22060(9)	0.01(2)	VAR	F19_013904
F19_013994		16 30 38.4	−56 58 58.0	11.48	80.888	0.4015(2)	0.029(8)	EW	
F19_013998	*c*	16 30 37.9	−56 51 10.6	13.66	80.692	0.3623(2)	0.10(3)	EW	F19_013864
F19_014276	*c*	16 30 32.3	−55 57 03.4	15.20	81.200	0.5848(4)	0.08(4)	EA	
F19_014469		16 30 35.3	−56 49 25.4	14.51	80.778	0.4332(3)	0.03(2)	EW	
F19_014496		16 30 28.6	−55 28 36.2	14.35	83.310	2.947(6)	0.15(5)	EA	
F19_014531	*c*	16 30 33.8	−56 34 35.7	13.59	97.630	65(6)	0.03(2)	VAR	F19_014695
F19_014565	*c*	16 30 33.8	−56 34 31.8	13.63	282.210	60(2)	0.02(2)	VAR	
F19_014598		16 30 34.1	−56 41 38.9	15.10	80.701	0.039207(4)	0.08(4)	DSCT	
F19_014642		16 30 32.7	−56 23 05.3	13.28	91.394	19.2(5)	0.04(2)	VAR	
F19_014695	*c*	16 30 33.2	−56 34 31.3	13.76	97.213	60(2)	0.03(2)	VAR	F19_014531
F19_014709		16 30 30.4	−56 00 23.0	12.77	...	...	...	LP	
F19_014755		16 30 31.9	−56 24 27.6	16.30	81.026	0.36993(8)	0.72(9)	EW	
F19_014864	*c*	16 30 30.7	−56 14 51.2	15.05	80.805	0.3347(2)	0.05(4)	EW	F19_015025
F19_014892		16 30 31.0	−56 19 51.7	14.04	83.903	42(4)	0.04(2)	VAR	
F19_014969		16 30 29.3	−56 05 20.1	15.47	80.730	0.3041(2)	0.06(4)	EW	
F19_015015	*c*	16 30 32.0	−56 43 09.0	14.01	80.815	0.15947(6)	0.05(2)	DSCT	F19_015137
F19_015025	*c*	16 30 29.8	−56 14 49.3	15.19	80.805	0.3347(2)	0.08(4)	EW	F19_014864
F19_015056	*c*	16 30 29.5	−56 13 48.0	14.40	80.686	0.26185(7)	0.05(2)	EW	F19_015143
F19_015137	*c*	16 30 31.1	−56 43 11.8	13.65	80.814	0.15947(7)	0.02(1)	DSCT	F19_015015
F19_015143	*c*	16 30 29.1	−56 13 43.1	14.54	80.686	0.26185(8)	0.05(2)	EW	F19_015056
F19_015170		16 30 30.3	−56 33 51.0	16.39	81.473	1.172(4)	0.2(1)	VAR	
F19_015235		16 30 31.6	−57 00 29.7	13.35	81.186	1.204(2)	0.08(2)	VAR	
F19_015275		16 30 29.6	−56 31 41.0	15.32	94.957	16.4(6)	0.06(4)	ROT	
F19_015291		16 30 26.5	−55 50 53.9	13.45	81.025	18.6(5)	0.06(2)	VAR	
F19_015386		16 30 27.8	−56 13 21.9	15.99	80.799	0.5220(4)	0.10(7)	EW/DSCT	
F19_015412		16 30 29.7	−56 42 23.3	14.21	81.630	2.54(1)	0.06(2)	ROT	
F19_015595		16 30 23.5	−55 35 39.7	16.00	80.794	0.17711(8)	0.10(7)	DSCT	
F19_015601		16 30 28.5	−56 38 00.1	11.23	334.647	85(5)	0.27(2)	VAR	
F19_015605		16 30 27.3	−56 23 05.8	14.97	80.728	0.2230(2)	0.04(4)	VAR	
F19_015608		16 30 26.2	−56 09 16.8	15.46	274.648	35(2)	0.13(5)	VAR	
F19_015683	*c*⋆	16 30 24.4	−55 51 51.4	14.93	81.205	0.6211(3)	0.35(3)	RR	
F19_015711	*c*	16 30 26.0	−56 12 30.5	14.42	80.779	0.4780(2)	0.14(2)	EW	F19_015811
F19_015734	*c*	16 30 28.6	−56 51 31.2	13.71	80.887	0.6166(2)	0.36(2)	EB	
F19_015746		16 30 25.3	−56 06 52.1	11.44	80.721	0.08475(2)	0.014(7)	DSCT	
F19_015793		16 30 28.2	−56 53 57.1	13.39	291.699	59(4)	0.26(4)	VAR	
F19_015811	*c*	16 30 25.5	−56 12 34.4	14.29	80.780	0.4780(2)	0.09(2)	EW	F19_015711
F19_015927		16 30 26.9	−56 41 37.3	10.72	...	...	...	SR	
F19_015981	⋆	16 30 24.8	−56 14 27.7	14.35	80.734	0.9247(8)	0.10(3)	EB	
F19_016094		16 30 26.1	−56 42 45.8	12.60	285.700	61(4)	0.052(8)	ROT	
F19_016100		16 30 24.4	−56 19 30.7	14.18	92.412	6.96(5)	0.04(2)	ROT	

Table E.5: Variable stars in field F19 (continued).

BEST ID	F	α (J2000.0) h m s	δ ° ′ ″	R_B [mag]	T_0 [d] [rHJD]	p [d]	A [mag]	Type	Other Names
F19_016151	*c*	16 30 20.7	−55 37 43.6	14.29	80.963	0.6325(3)	0.15(2)	RR	
F19_016211	*c*	16 30 23.0	−56 08 39.9	12.36	...	...	...	LP	
F19_016279	*c*	16 30 22.9	−56 11 21.6	15.38	80.738	0.2081(1)	0.04(4)	VAR	
F19_016287	*s*	16 30 20.8	−55 45 43.9	15.86	80.671	0.13137(4)	0.05(6)	DSCT	
F19_016307	*c*	16 30 24.0	−56 27 16.0	10.85	159.542	57(3)	0.25(3)	VAR	
F19_016342	*cs*	16 30 25.0	−56 45 00.9	14.07	81.021	0.858(2)	0.02(2)	VAR	F19_016368
F19_016368	*cs*	16 30 24.8	−56 44 54.7	13.89	81.008	0.858(3)	0.01(2)	VAR	F19_016342
F19_016443	*c*	16 30 22.0	−56 10 31.0	14.47	81.010	0.4472(2)	0.14(2)	EW	
F19_016472		16 30 22.2	−56 15 20.1	15.87	80.705	0.14646(7)	0.08(6)	DSCT	
F19_016499		16 30 24.6	−56 55 29.7	14.08	319.618	86(7)	0.17(2)	VAR	
F19_016552		16 30 19.2	−55 44 11.7	13.72	80.699	0.039914(4)	0.03(3)	DSCT	
F19_016634		16 30 23.5	−56 49 07.8	16.19	92.175	15.2(6)	0.20(9)	ROT	
F19_016640	*c*	16 30 22.1	−56 25 51.4	11.02	...	...	...	LP	
F19_016677	*c*	16 30 22.0	−56 25 54.7	11.01	...	...	...	LP	
F19_016735		16 30 21.9	−56 31 03.3	10.71	...	...	...	LP	
F19_016758	*c*	16 30 23.5	−57 00 53.5	14.04	81.169	0.5959(7)	0.06(2)	RR	
F19_016831		16 30 16.9	−55 33 06.7	13.30	...	...	...	SR	
F19_016846		16 30 19.8	−56 09 18.6	12.05	...	...	...	SR	
F19_016883	*c*	16 30 16.6	−55 34 03.2	14.83	80.820	0.2923(2)	0.07(4)	EW/DSCT	F19_016956, F19_017003
F19_016956	*c*	16 30 16.4	−55 34 07.4	14.94	80.825	0.29225(9)	0.09(4)	EW/DSCT	F19_016883, F19_017003
F19_017003	*c*	16 30 16.2	−55 34 03.8	14.85	80.818	0.2923(2)	0.1(1)	EW/DSCT	F19_016883, F19_016956
F19_017026	*s*	16 30 16.1	−55 35 11.5	13.21	80.772	0.17892(9)	0.01(2)	DSCT	
F19_017064	⋆	16 30 15.2	−55 27 02.1	16.52	80.796	0.39185(8)	1.2(2)	EA	
F19_017146	*c*	16 30 19.8	−56 32 19.5	14.29	80.766	0.33107(5)	0.28(2)	EW	
F19_017157	*c*	16 30 16.3	−55 47 22.0	14.06	81.021	0.4045(2)	0.05(2)	EW	F19_017192
F19_017192	*c*	16 30 16.3	−55 47 26.5	13.93	81.019	0.4045(2)	0.05(2)	EW	F19_017157
F19_017213		16 30 18.4	−56 17 51.9	14.31	81.018	0.6768(2)	0.33(2)	EB	
F19_017259	*c*	16 30 16.2	−55 51 01.5	12.03	...	...	...	LP	
F19_017282	*c*	16 30 19.0	−56 29 01.7	11.01	...	...	...	LP	
F19_017375	*s*	16 30 17.5	−56 16 46.7	13.49	92.306	6.40(4)	0.02(1)	VAR	
F19_017383	*c*	16 30 14.3	−55 37 03.4	14.23	80.740	0.30309(7)	0.10(2)	EW	
F19_017413	*s*	16 30 17.0	−56 12 12.4	15.81	80.948	0.2932(2)	0.05(6)	EW/DSCT	
F19_017442	*c*	16 30 16.4	−56 06 02.0	14.46	80.889	0.4966(3)	0.06(2)	EW	F19_017475
F19_017460	*s*	16 30 13.3	−55 29 31.6	16.39	80.757	0.2530(2)	0.1(2)	VAR	
F19_017475	*c*	16 30 16.2	−56 06 06.1	14.88	80.888	0.4966(3)	0.11(3)	EW	F19_017442
F19_017648	*s*	16 30 14.2	−55 52 02.3	10.97	80.762	0.09986(3)	0.008(7)	DSCT	
F19_017671	*c*	16 30 16.8	−56 29 46.7	15.08	88.149	4.01(4)	0.11(4)	ROT	F19_017797
F19_017797	*c*	16 30 16.2	−56 29 45.8	14.79	88.093	4.01(3)	0.10(3)	ROT	F19_017671
F19_017853	*c*	16 30 12.4	−55 41 33.5	12.27	81.215	0.7721(5)	0.042(7)	EB	
F19_017946	*s*	16 30 17.0	−56 55 54.1	15.10	80.740	0.16919(7)	0.04(5)	VAR	
F19_017986	⋆	16 30 13.4	−56 05 40.1	12.36	80.659	3.0149(1)	0.2(1)	EA	
F19_018000		16 30 10.2	−55 27 29.1	14.74	80.723	0.4510(3)	0.18(8)	EA	
F19_018116	⋆	16 30 11.1	−55 45 26.8	13.37	81.424	0.8693	0.037	EA	
F19_018304	*s*	16 30 09.9	−55 42 43.4	14.28	83.252	4.20(5)	0.03(3)	VAR	
F19_018346	⋆	16 30 14.3	−56 50 44.9	12.50	81.505	1.110(2)	0.015(6)	EB	
F19_018371	*c*	16 30 08.7	−55 34 56.3	13.60	...	...	...	LP	
F19_018401	*s*	16 30 09.2	−55 41 21.6	15.93	80.675	0.20021(9)	0.2(2)	VAR	
F19_018468		16 30 07.6	−55 27 11.5	15.66	81.062	5.29(2)	0.5(2)	EA	
F19_018527		16 30 13.1	−56 50 18.1	14.02	80.706	0.3573(2)	0.04(2)	EW	
F19_018532		16 30 10.3	−56 05 42.0	13.03	171.942	28(2)	0.035(8)	VAR	
F19_018637	*c*	16 30 07.7	−55 39 36.7	13.51	80.904	0.4058(2)	0.22(5)	EW	
F19_018666	*s*	16 30 08.7	−55 53 32.4	12.06	95.270	15.4(2)	0.05(2)	VAR	
F19_018765		16 30 11.3	−56 42 16.5	12.09	...	...	...	LP	
F19_018814	*cs*	16 30 09.3	−56 15 01.5	15.79	80.748	0.4406(2)	0.12(7)	EA	F19_018886
F19_018886	*cs*	16 30 09.0	−56 14 53.9	15.33	80.748	0.4406(3)	0.04(4)	EA	F19_018814
F19_018913		16 30 10.8	−56 43 29.1	12.41	...	...	...	SR	
F19_018915	*c*	16 30 10.3	−56 37 21.8	14.33	80.671	0.5660(4)	0.10(3)	EW	F19_019003
F19_018931		16 30 07.3	−55 55 07.9	12.95	...	...	...	LP	
F19_019001	*cs*	16 30 10.4	−56 46 35.3	14.44	80.694	0.3048(2)	0.02(2)	VAR	F19_019095
F19_019003	*c*	16 30 09.8	−56 37 18.9	14.42	80.672	0.5660(3)	0.10(2)	EW	F19_018915
F19_019019		16 30 04.5	−55 26 21.1	15.52	83.573	10.4(2)	0.07(5)	ROT	
F19_019032	*s*	16 30 08.6	−56 21 00.7	13.40	...	...	...	VAR	
F19_019036	⋆	16 30 08.0	−56 12 11.9	12.72	80.764	0.23373(4)	0.100(8)	DSCT	
F19_019084	*c*	16 30 05.2	−55 39 09.2	15.03	128.558	4.021(1)	0.17(1)	EA	
F19_019095	*cs*	16 30 09.8	−56 46 36.8	14.43	80.701	0.3048(2)	0.02(2)	VAR	F19_019001
F19_019117		16 30 05.8	−55 47 52.4	15.22	88.128	4.12(5)	0.11(5)	ROT	
F19_019124	*c*	16 30 04.2	−55 28 39.2	13.62	81.096	0.6150(6)	0.09(3)	RR	F19_019244
F19_019152		16 30 04.5	−55 34 9.9	13.76	83.790	4.39(6)	0.07(6)	ROT	
F19_019173		16 30 05.9	−55 55 36.8	11.76	308.437	97(5)	0.18(2)	SR	
F19_019244	*c*	16 30 03.6	−55 28 37.8	13.71	81.095	0.6150(7)	0.10(4)	RR	F19_019124
F19_019290	*c*	16 30 08.2	−56 36 05.4	12.16	...	...	...	LP	
F19_019309		16 30 04.4	−55 44 10.9	12.70	95.379	10.4(3)	0.02(2)	VAR	
F19_019322		16 30 07.6	−56 29 43.8	13.96	95.103	16.8(7)	0.10(3)	VAR	
F19_019409	⋆	16 30 03.9	−55 44 58.0	12.39	82.790	3.069(8)	0.08(3)	EA	
F19_019426		16 30 07.5	−56 37 47.5	14.82	83.273	3.6378	0.038	EA	
F19_019455		16 30 07.4	−56 36 37.7	13.38	80.989	0.7036(4)	0.056(8)	EW	
F19_019481	*c*	16 30 02.0	−55 24 07.2	14.17	91.717	18.7(6)	0.11(2)	ROT	
F19_019520	*c*	16 30 06.9	−56 35 24.4	13.74	80.767	0.23148(8)	0.08(2)	VAR	
F19_019550		16 30 07.5	−56 49 39.7	13.21	...	...	...	LP	
F19_019577		16 30 07.3	−56 49 16.9	16.01	81.236	4.11(4)	0.13(7)	ROT	
F19_019695		16 30 02.0	−55 39 25.9	12.11	...	...	...	SR	
F19_019716		16 30 04.3	−56 11 50.5	12.68	81.236	0.916(2)	0.017(7)	ROT	
F19_019742	*c*	16 30 05.8	−56 35 58.2	15.47	80.859	0.27987(6)	0.27(5)	EW	
F19_019826	*c*	16 30 03.0	−56 01 34.3	15.12	80.698	0.3679(2)	0.10(5)	EW	F19_019954, F19_019955
F19_019884	⋆	16 30 05.4	−56 43 07.6	13.30	81.068	0.50898(6)	0.28(2)	EW	
F19_019922		16 30 03.2	−56 11 38.1	12.41	128.221	13.6(3)	0.015(6)	ROT	
F19_019934	⋆	16 29 59.5	−55 23 35.2	14.93	81.200	0.6034(4)	0.13(3)	EB	
F19_019954	*c*	16 30 02.2	−56 01 34.6	15.17	80.697	0.3679(2)	0.11(4)	EW	F19_019826, F19_019955

Table E.5: Variable stars in field F19 (continued).

BEST ID	F	α (J2000.0) h m s	δ ° ′ ″	R_B [mag]	T_0 [d] [rHJD]	p [d]	A [mag]	Type	Other Names
F19_019955	*c*	16 30 02.3	−56 01 28.5	15.44	80.695	0.3679(2)	0.13(5)	EW	F19_019826, F19_019954
F19_020020	*cs*	16 30 01.1	−55 51 01.6	13.77	80.875	0.3032(2)	0.02(2)	EW/DSCT	F19_020159
F19_020057	*c*⋆	16 30 01.0	−55 52 44.8	12.89	91.441	5.88(3)	0.09(3)	EB	
F19_020062		16 30 00.3	−55 43 00.6	11.64	...	...	...	SR	
F19_020076		16 30 03.8	−56 33 17.9	13.00	81.867	3.12(3)	0.04(2)	VAR	
F19_020106	⋆	16 30 03.6	−56 33 29.2	13.71	81.267	0.9890(8)	0.05(2)	EB	
F19_020117		16 30 02.2	−56 12 25.0	11.66	...	...	...	SR	
F19_020159	*cs*	16 30 00.4	−55 50 59.1	13.61	80.863	0.3032(2)	0.01(2)	EW/DSCT	F19_020020
F19_020250		16 30 00.6	−55 59 20.2	11.31	...	...	...	LP	
F19_020284	*s*	16 30 00.2	−55 56 41.1	11.50	91.009	11.4(4)	0.021(8)	ROT	
F19_020381	*s*	16 30 01.6	−56 23 33.4	14.20	83.179	3.4905(1)	0.14(1)	EA	
F19_020433		16 29 59.1	−55 50 32.0	14.84	80.790	0.14134(5)	0.03(3)	DSCT	
F19_020484		16 30 01.0	−56 23 43.1	13.16	91.705	6.23(7)	0.033(8)	VAR	
F19_020550	*c*	16 30 02.6	−56 58 19.7	14.52	80.931	0.3871(2)	0.06(3)	EW	F19_020634
F19_020634	*c*	16 30 02.2	−56 58 13.2	15.07	80.929	0.3871(1)	0.23(4)	EW	F19_020550
F19_020861	⋆	16 29 55.3	−55 31 38.8	13.90	81.011	1.790(2)	0.26(5)	EA	
F19_020941	*c*	16 29 56.4	−55 53 20.7	15.12	80.947	0.42695(8)	0.36(4)	EW	
F19_021043		16 29 57.8	−56 21 25.8	11.54	128.179	27(1)	0.09(3)	VAR	
F19_021116	*c*	16 29 58.4	−56 36 17.2	14.28	80.862	0.25313(5)	0.14(2)	EW	F19_021205
F19_021205	*c*	16 29 58.0	−56 36 17.9	14.33	80.862	0.25313(4)	0.13(2)	EW	F19_021116
F19_021215	⋆	16 29 56.8	−56 18 17.6	13.45	80.600	39.8(1)	0.1(1)	EA	
F19_021221		16 29 55.4	−55 56 53.4	15.39	80.712	0.17940(8)	0.16(7)	DSCT	
F19_021253	*s*	16 29 54.8	−55 51 09.4	15.17	80.677	0.16861(6)	0.02(3)	VAR	
F19_021557	*c*⋆	16 29 56.9	−56 52 37.9	13.03	81.461	1.1564(4)	0.156(8)	EW	
F19_021790		16 29 53.0	−56 06 48.7	14.74	81.503	57(6)	0.09(2)	VAR	
F19_021974		16 29 54.5	−56 54 08.1	14.89	80.926	0.26724(8)	0.06(3)	EW	
F19_022114		16 29 52.7	−56 31 57.4	12.56	112.806	47(3)	0.034(8)	VAR	
F19_022183		16 29 48.4	−55 31 01.8	14.42	81.322	0.6557(5)	0.08(3)	EW	
F19_022251		16 29 51.3	−56 18 58.2	14.10	96.130	32(2)	0.07(2)	VAR	
F19_022297	*c*	16 29 50.8	−56 14 16.7	14.74	105.004	18.4(5)	0.06(3)	VAR	
F19_022390	*c*	16 29 50.6	−56 18 05.6	15.44	80.935	0.30940(8)	0.23(5)	EW	
F19_022480	*c*⋆	16 29 50.1	−56 20 02.9	15.38	81.160	0.52835(9)	0.63(5)	EW	
F19_022502	*c*	16 29 51.2	−56 44 33.3	11.48	...	...	...	LP	
F19_022535		16 29 51.5	−56 54 26.6	12.94	...	...	...	SR	
F19_022593	*c*⋆	16 29 48.6	−56 05 38.1	13.54	80.742	1.696(4)	0.025(8)	ROT	
F19_022650	*c*	16 29 49.2	−56 21 35.3	14.23	80.753	0.18256(9)	0.03(2)	DSCT	F19_022789
F19_022651	⋆	16 29 49.1	−56 19 26.8	13.79	80.735	0.4582(2)	0.12(3)	EB	
F19_022668		16 29 45.4	−55 24 11.3	15.26	80.727	0.3928(2)	0.30(5)	EW	
F19_022713	*c*⋆	16 29 49.2	−56 25 11.3	12.72	82.060	4.105(1)	0.25(1)	EA	
F19_022789	*c*	16 29 48.7	−56 21 36.0	14.16	80.746	0.18256(8)	0.04(2)	DSCT	F19_022650
F19_022845	*s*	16 29 49.9	−56 54 33.9	15.10	81.937	2.498(6)	0.12(3)	EB	
F19_022893		16 29 48.6	−56 32 55.5	14.56	81.532	4.37(4)	0.04(3)	ROT	
F19_022925		16 29 49.9	−57 00 08.3	13.58	...	...	...	SR	
F19_022949		16 29 45.0	−55 39 51.3	11.11	...	...	...	LP	
F19_022959	*s*	16 29 49.2	−56 48 43.0	14.61	80.737	0.2685(1)	0.03(3)	EW	
F19_022970	*c*	16 29 47.7	−56 20 46.5	12.69	...	...	...	LP	
F19_023035	*c*	16 29 46.5	−56 08 24.2	12.56	...	...	...	LP	
F19_023053		16 29 49.0	−56 55 56.2	11.91	...	...	...	LP	
F19_023137		16 29 47.4	−56 31 08.7	13.64	83.871	8.7(2)	0.02(2)	VAR	
F19_023138		16 29 46.9	−56 21 43.7	14.68	91.617	14.5(4)	0.13(3)	VAR	
F19_023154		16 29 48.5	−56 58 33.8	12.74	...	...	...	SR	
F19_023343		16 29 46.2	−56 28 52.7	11.68	...	...	...	LP	
F19_023370	*cs*	16 29 46.9	−56 43 44.2	13.51	81.851	1.393(6)	0.02(2)	VAR	F19_023445
F19_023401		16 29 47.0	−56 48 50.4	12.61	89.633	5.56(5)	0.06(1)	ROT	
F19_023428		16 29 43.5	−55 52 14.2	13.13	82.067	2.84(2)	0.04(3)	VAR	
F19_023445	*cs*	16 29 46.4	−56 43 47.2	13.49	81.838	1.393(4)	0.02(2)	VAR	F19_023370
F19_023516		16 29 45.3	−56 30 07.3	12.64	...	...	...	SR	
F19_023521	*s*	16 29 44.8	−56 18 34.7	14.90	94.368	18.3(9)	0.03(3)	VAR	
F19_023614	*s*	16 29 46.1	−56 54 46.6	12.36	81.288	0.6560(5)	0.011(7)	EB	
F19_023721	*c*	16 29 45.2	−56 45 21.2	15.32	81.041	0.5671(2)	0.39(4)	RR	
F19_023733	*s*	16 29 43.6	−56 16 04.8	12.94	94.493	18.1(5)	0.012(6)	VAR	
F19_023821	*s*	16 29 45.0	−56 57 15.1	10.89	...	...	...	SR	
F19_023823		16 29 44.5	−56 43 37.1	13.89	83.477	3.61(3)	0.03(2)	VAR	
F19_023833	*c*⋆	16 29 41.8	−55 52 51.6	13.72	82.756	3.262(4)	0.25(3)	EA	
F19_023846	*s*	16 29 44.9	−56 55 42.2	11.33	81.315	13.4(4)	0.04(1)	VAR	
F19_024025	*s*	16 29 41.4	−56 05 41.0	13.08	85.070	11.8891	0.11	EA	
F19_024064	*c*	16 29 41.2	−56 07 17.3	14.69	80.720	0.2903(1)	0.05(3)	EB	
F19_024091		16 29 40.6	−55 58 29.5	10.69	...	...	...	LP	
F19_024092	*s*⋆	16 29 40.4	−55 57 47.9	12.30	100.700	81.86(1)	0.035(1)	EA	
F19_024094	*c*	16 29 39.8	−55 48 54.9	15.78	81.197	0.6200(5)	0.10(6)	EB	F19_024240
F19_024240	*c*	16 29 39.1	−55 48 57.3	14.65	81.193	0.6201(4)	0.07(3)	EB	F19_024094
F19_024337		16 29 38.2	−55 42 09.4	15.81	81.537	1.526(3)	0.18(9)	EA	
F19_024382	*s*	16 29 41.7	−56 49 25.3	12.34	...	...	...	LP	
F19_024438	*c*	16 29 38.7	−55 56 47.4	15.19	80.672	0.08558(2)	0.09(4)	DSCT	F19_024439
F19_024439	*c*	16 29 38.7	−55 56 43.4	15.15	80.672	0.08558(2)	0.08(4)	DSCT	F19_024438
F19_024448	*s*	16 29 36.4	−55 23 37.7	11.00	95.147	16(2)	0.05(2)	VAR	
F19_024453		16 29 41.1	−56 42 34.8	12.91	...	...	...	LP	
F19_024469		16 29 38.9	−56 03 21.2	15.25	82.583	2.150(4)	0.20(7)	EA	
F19_024560	*s*	16 29 39.8	−56 27 28.2	15.75	80.678	0.05749(2)	0.06(7)	DSCT	
F19_024612		16 29 36.3	−55 34 53.3	16.16	80.729	0.2093(2)	0.15(8)	DSCT	
F19_024618	*s*	16 29 40.8	−56 59 39.9	12.67	83.372	16.2(5)	0.03(2)	VAR	
F19_024623		16 29 40.3	−56 44 25.4	14.27	80.776	0.3413(2)	0.02(2)	EW/DSCT	
F19_024762	*c*	16 29 38.6	−56 27 21.5	14.96	80.902	0.3966(2)	0.06(4)	EW/DSCT	
F19_024773	*s*	16 29 36.0	−55 45 01.3	13.77	80.739	0.2772(1)	0.01(1)	EW/DSCT	
F19_024846	*s*	16 29 38.0	−56 28 32.3	12.79	81.449	1.578(4)	0.03(2)	VAR	
F19_024854	*s*	16 29 36.4	−55 58 53.7	14.93	262.670	23(2)	0.04(3)	VAR	
F19_025020	*s*	16 29 38.5	−56 57 13.8	16.26	88.596	11.4(3)	0.16(9)	VAR	
F19_025160	⋆	16 29 35.2	−56 04 40.4	15.52	82.428	2.218(2)	0.44(5)	EA	

Table E.5: Variable stars in field F19 (continued).

BEST ID	F	α (J2000.0) h m s	δ ° ′ ″	R_B [mag]	T_0 [d] [rHJD]	p [d]	A [mag]	Type	Other Names
F19_025246		16 29 37.0	−56 48 41.9	11.16	100.683	22.5(8)	0.08(2)	VAR	
F19_025400	⋆	16 29 35.2	−56 28 10.8	13.95	82.824	2.306(4)	0.10(3)	EB	
F19_025481		16 29 32.3	−55 45 20.0	12.84	82.513	4.38(9)	0.018(8)	ROT	
F19_025496	*c*	16 29 34.4	−56 21 04.5	12.01	···	···	···	LP	
F19_025508		16 29 32.2	−55 46 20.8	13.01	···	···	···	LP	
F19_025546	*c*	16 29 32.5	−55 52 01.7	11.73	···	···	···	SR	
F19_025547		16 29 32.3	−55 49 49.8	12.21	125.826	59(4)	0.025(6)	VAR	
F19_025549		16 29 31.8	−55 43 21.5	13.44	80.751	0.14235(5)	0.01(1)	DSCT	
F19_025701		16 29 33.1	−56 16 02.2	11.79	93.801	80(3)	0.014(4)	VAR	
F19_025766	*c*	16 29 32.7	−56 17 24.5	15.12	80.788	0.4251(2)	0.20(4)	EW	
F19_025793	*s*	16 29 32.7	−56 18 38.1	15.51	81.178	0.6429(6)	0.15(8)	EA	
F19_025827	*s*	16 29 31.3	−55 56 42.1	15.13	80.670	0.3087(2)	0.05(4)	EW	
F19_025841		16 29 34.1	−57 00 34.0	12.24	81.006	45(2)	0.16(2)	VAR	
F19_026064		16 29 31.1	−56 16 09.2	11.91	88.965	10.5(2)	0.059(8)	CEP	
F19_026184	*s*	16 29 31.4	−56 36 19.9	14.88	80.858	0.2673(2)	0.03(3)	DSCT	
F19_026234	*s*	16 29 28.4	−55 45 38.1	13.46	···	···	···	SR	
F19_026247		16 29 31.7	−56 52 49.5	11.46	···	···	···	SR	
F19_026272	⋆	16 29 27.2	−55 30 52.1	15.74	81.043	0.3990(1)	0.42(6)	EW	
F19_026392		16 29 30.2	−56 37 20.4	16.01	81.023	0.6367(4)	0.14(7)	EA	
F19_026420	*s*	16 29 30.9	−56 57 57.6	13.10	88.953	4.42(3)	0.018(8)	VAR	
F19_026515		16 29 29.4	−56 33 45.0	15.61	80.777	0.2913(1)	0.10(5)	EW	
F19_026610		16 29 29.7	−56 56 11.9	15.58	80.799	0.2749(1)	0.05(5)	EA	
F19_026652	*s*	16 29 24.7	−55 24 13.5	12.91	93.351	38(2)	0.10(4)	VAR	
F19_026689		16 29 28.6	−56 34 08.4	15.91	80.987	0.4711(3)	0.13(6)	EW	
F19_026720		16 29 28.4	−56 36 15.8	14.88	81.710	2.6639(1)	0.13(1)	EA	
F19_026753	*s*	16 29 28.0	−56 31 41.8	13.00	246.296	34(2)	0.025(8)	ROT	
F19_026808	*s*	16 29 25.3	−55 46 22.0	11.85	276.038	60(2)	0.012(4)	VAR	
F19_026809		16 29 24.8	−55 36 01.1	12.92	···	···	···	LP	
F19_026873	*s*	16 29 25.2	−55 50 56.4	12.38	309.715	90(2)	0.024(6)	VAR	
F19_026922	*s*	16 29 27.8	−56 47 09.6	12.46	81.217	2.86(2)	0.06(2)	VAR	
F19_026976	*c*	16 29 25.5	−56 02 29.6	11.15	80.714	0.11801(4)	0.018(8)	RR	F19_026977
F19_026977	*c*	16 29 25.4	−56 02 26.3	11.15	80.722	0.11800(4)	0.017(8)	RR	F19_026976
F19_027007	*c*	16 29 25.0	−55 57 57.2	14.59	81.098	0.732(2)	0.05(2)	VAR	F19_027058
F19_027041	⋆	16 29 26.2	−56 26 43.1	14.62	82.750	8.548(1)	0.14(1)	EA	
F19_027058	*c*	16 29 24.6	−55 58 03.4	14.58	81.159	0.732(2)	0.04(2)	VAR	F19_027007
F19_027181	*c*	16 29 25.8	−56 31 36.1	14.34	80.975	0.30605(5)	0.18(2)	EW	
F19_027188	*c*	16 29 25.1	−56 20 39.0	12.03	···	···	···	SR	
F19_027196	*s*	16 29 24.6	−56 10 17.7	14.74	83.014	2.65(2)	0.09(4)	VAR	
F19_027245		16 29 22.3	−55 31 51.1	15.30	80.688	0.19782(8)	0.13(5)	DSCT	
F19_027252	*c*	16 29 25.9	−56 41 15.4	11.40	···	···	···	LP	
F19_027266		16 29 23.7	−55 59 53.8	13.47	100.643	39(5)	0.04(1)	ROT	
F19_027369	*c*⋆	16 29 22.2	−55 44 02.9	13.18	80.845	1.0248(3)	0.305(8)	EB	
F19_027397		16 29 22.5	−55 51 40.6	13.31	81.643	5.12(4)	0.027(8)	ROT	
F19_027400	*c*⋆	16 29 22.0	−55 41 44.1	13.87	80.962	0.41980(8)	0.23(2)	EW	
F19_027433		16 29 25.3	−56 52 29.1	12.98	80.698	0.09212(2)	0.02(1)	DSCT	
F19_027460	*c*	16 29 21.6	−55 42 03.4	13.33	80.895	2.0025(1)	0.12(1)	EA	
F19_027496		16 29 25.0	−57 01 02.5	16.15	80.968	0.5125(3)	0.3(2)	EW	
F19_027580	*cs*	16 29 24.3	−56 53 30.3	14.61	122.732	18.1(5)	0.12(3)	EB	
F19_027690	*c*⋆	16 29 21.3	−55 58 06.7	14.18	80.886	1.2709(4)	0.41(2)	EA	
F19_027754		16 29 20.6	−55 55 08.7	15.15	80.813	0.26237(5)	0.32(5)	EW	
F19_027934	*s*	16 29 18.9	−55 39 54.6	15.56	91.791	12.7(2)	0.16(5)	EB	
F19_027943	*c*	16 29 22.0	−56 45 19.3	12.75	235.177	100(5)	0.040(7)	CEP	
F19_027960		16 29 18.9	−55 45 11.7	16.04	81.004	0.3940(3)	0.11(7)	EW/DSCT	
F19_027976	*c*	16 29 21.3	−56 30 23.0	13.25	···	···	···	LP	
F19_028087		16 29 18.1	−55 40 45.6	12.00	···	···	···	LP	
F19_028097	*c*	16 29 21.2	−56 44 49.9	14.81	82.542	32(2)	0.16(3)	CEP	
F19_028151	*s*	16 29 21.2	−56 53 48.1	14.31	81.413	2.68(2)	0.03(2)	VAR	
F19_028163		16 29 19.4	−56 14 17.5	13.42	99.696	76(8)	0.046(8)	VAR	
F19_028189		16 29 20.2	−56 37 04.4	11.88	···	···	···	SR	
F19_028201		16 29 17.9	−55 48 19.3	14.12	80.744	0.18749(7)	0.04(2)	DSCT	
F19_028223		16 29 20.3	−56 40 53.8	12.66	300.699	93(5)	0.36(3)	VAR	
F19_028268	⋆	16 29 20.0	−56 35 23.6	13.62	82.114	3.8323	0.013	EA	
F19_028290	*c*⋆	16 29 20.4	−56 53 19.9	13.55	80.776	0.62197(8)	0.44(2)	EA	
F19_028322	*cs*⋆	16 29 19.4	−56 32 21.0	14.96	82.266	7.5218	0.054	EA	
F19_028347		16 29 16.0	−55 27 44.0	16.33	80.890	0.24627(6)	0.4(1)	EW/DSCT	
F19_028393		16 29 20.0	−56 54 17.9	15.17	81.013	0.3552(2)	0.09(4)	EW/DSCT	
F19_028454	*s*	16 29 15.5	−55 30 03.8	14.97	80.685	0.2425(1)	0.04(5)	EW/DSCT	
F19_028539		16 29 16.2	−55 49 26.4	12.82	80.777	0.12058(4)	0.009(7)	DSCT	
F19_028570		16 29 17.3	−56 12 37.5	14.21	80.994	0.3472(2)	0.07(2)	DSCT	
F19_028602		16 29 17.5	−56 21 39.5	16.55	81.094	0.5557(2)	0.6(2)	EW	
F19_028637		16 29 16.6	−56 08 19.2	12.11	···	···	···	SR	
F19_028646	*s*	16 29 15.0	−55 37 25.2	15.19	81.102	0.4389(3)	0.03(4)	EW/DSCT	
F19_028870	*s*	16 29 16.2	−56 23 35.5	11.22	80.738	0.10348(3)	0.03(3)	VAR	
F19_028873	*c*⋆	16 29 15.3	−56 07 31.8	14.02	95.745	6.2814(1)	0.11(1)	EA	
F19_028901		16 29 14.6	−55 54 30.5	13.11	···	···	···	SR	
F19_028915	*s*	16 29 17.1	−56 54 14.4	13.67	269.650	26(2)	0.03(2)	VAR	
F19_029002		16 29 15.0	−56 13 01.0	15.56	80.716	0.5043(2)	0.36(6)	EW	
F19_029043	*cs*	16 29 14.9	−56 14 38.9	15.06	80.763	0.3839(2)	0.08(4)	EW	
F19_029063		16 29 16.2	−56 48 16.1	15.76	80.962	0.3193(2)	0.2(2)	EW	
F19_029110	*cs*	16 29 14.5	−56 14 53.7	12.12	80.958	0.3839(2)	0.010(4)	EW	
F19_029176		16 29 12.7	−55 46 16.6	15.02	81.086	0.5068(4)	0.09(4)	EB	
F19_029182	*c*	16 29 12.0	−55 33 02.3	13.29	80.728	0.7343(5)	0.09(2)	EW	
F19_029189		16 29 11.5	−55 23 55.2	12.03	···	···	···	SR	
F19_029558	*s*	16 29 10.3	−55 41 39.9	12.79	100.902	26(2)	0.05(3)	VAR	
F19_029716		16 29 11.2	−56 14 43.9	12.01	82.100	2.177(4)	0.034(6)	EB	
F19_029741		16 29 12.5	−56 52 46.4	13.48	93.874	6.77(9)	0.03(2)	ROT	
F19_029799	*c*	16 29 09.1	−55 40 04.7	15.94	80.928	0.4523(2)	0.42(8)	EW	
F19_029834		16 29 10.1	−56 04 40.7	15.35	80.825	0.28581(4)	0.48(5)	EW	

Table E.5: Variable stars in field F19 (continued).

BEST ID	F	α (J2000.0) h m s	δ ° ′ ″	R_B [mag]	T_0 [d] [rHJD]	p [d]	A [mag]	Type	Other Names
F19_029926	*cs*	16 29 09.9	−56 09 16.8	14.96	89.830	3.3599(1)	0.3(1)	EA	
F19_029929	*s*	16 29 09.8	−56 06 32.5	15.07	80.695	0.14446(6)	0.03(3)	VAR	
F19_029951		16 29 11.3	−56 45 43.8	14.38	81.129	0.5886(3)	0.59(9)	RR	
F19_030083		16 29 07.8	−55 42 00.2	12.43	...	...	...	SR	
F19_030226		16 29 08.6	−56 13 13.0	13.36	81.571	6.37(5)	0.052(8)	CEP	
F19_030314	*cs*	16 29 05.9	−55 28 52.4	14.81	81.315	6.28(4)	0.08(4)	ROT	F19_030421
F19_030387	*s*	16 29 05.8	−55 32 25.3	13.45	90.354	9.7(2)	0.012(8)	VAR	
F19_030421	*cs*	16 29 05.3	−55 28 47.9	14.88	81.352	6.28(4)	0.07(4)	ROT	F19_030314
F19_030465	*cs*	16 29 07.7	−56 21 44.9	13.08	83.544	4.66(4)	0.014(8)	VAR	
F19_030509		16 29 04.8	−55 27 58.7	15.88	81.007	0.34055(9)	0.32(6)	EW	
F19_030642		16 29 07.0	−56 28 14.1	13.69	96.836	8.9(2)	0.05(2)	ROT	
F19_030794	⋆	16 29 07.0	−56 52 44.7	12.16	81.110	0.48102(5)	0.359(8)	EB	
F19_030850		16 29 03.6	−55 38 05.5	11.69	...	...	...	LP	
F19_030904		16 29 05.3	−56 18 07.7	14.09	172.256	21(1)	0.09(3)	VAR	
F19_030914	⋆	16 29 02.9	−55 29 54.9	13.90	81.767	2.3352(1)	0.08(1)	EA	
F19_030922		16 29 06.1	−56 45 27.1	11.65	...	...	...	LP	
F19_030984	*cs*	16 29 05.4	−56 37 54.7	13.98	81.573	1.260(4)	0.02(2)	VAR	F19_031071
F19_031025	⋆	16 29 02.6	−55 38 55.0	13.99	81.046	0.6763(3)	0.47(7)	EA	
F19_031051		16 29 03.1	−55 49 49.9	15.75	80.848	0.3182(2)	0.30(6)	RR	
F19_031071	*cs*	16 29 05.1	−56 37 53.2	13.92	81.520	1.260(3)	0.01(2)	VAR	F19_030984
F19_031085		16 29 03.0	−55 53 32.9	13.53	80.725	0.06458(2)	0.013(8)	DSCT	
F19_031197	⋆	16 29 04.6	−56 48 31.8	15.04	80.771	0.7953(2)	0.66(4)	EB	
F19_031213		16 29 03.5	−56 18 53.9	16.50	80.706	0.3999(2)	0.4(2)	EW	
F19_031254	*s*	16 29 02.8	−56 06 58.2	14.45	80.702	70(5)	0.13(2)	EB	
F19_031257		16 29 02.1	−55 52 34.3	15.06	89.436	11.9(2)	0.10(3)	VAR	
F19_031317		16 29 02.9	−56 17 26.1	16.12	80.899	0.2852(2)	0.10(7)	VAR	
F19_031402		16 29 02.1	−56 09 42.2	16.14	80.897	0.3535(3)	0.14(8)	VAR	
F19_031417	*s*	16 29 03.4	−56 41 41.5	15.94	80.672	0.16302(6)	0.07(9)	VAR	
F19_031474	*cs*	16 29 03.5	−56 59 21.7	14.52	122.043	60(6)	0.08(3)	VAR	
F19_031528		16 29 00.5	−55 48 44.1	13.94	89.183	9.2(2)	0.06(2)	CEP	
F19_031884	*c*	16 28 59.5	−56 06 35.5	13.04	81.123	0.4956(2)	0.100(8)	EB	
F19_031885	*s*	16 28 59.3	−56 01 21.0	15.15	80.830	0.3863(4)	0.04(3)	RR	
F19_032009		16 29 00.1	−56 43 05.2	12.30	81.632	1.243(4)	0.04(2)	VAR	
F19_032050	*cs*	16 28 59.0	−56 16 41.1	13.86	155.237	53(5)	0.04(2)	VAR	F19_032086
F19_032086	*cs*	16 28 58.9	−56 16 38.3	13.83	262.068	54(6)	0.03(2)	VAR	F19_032050
F19_032221		16 28 57.8	−56 07 11.4	14.17	81.035	0.5126(2)	0.08(2)	EW	
F19_032268	*c*	16 28 55.8	−55 27 42.7	13.95	83.183	7.32(7)	0.11(2)	CEP	
F19_032282	*s*	16 28 58.2	−56 22 54.3	13.47	81.174	0.912(3)	0.01(2)	VAR	
F19_032349		16 28 58.1	−56 31 02.8	12.43	197.466	30(5)	0.07(2)	CEP	
F19_032422		16 28 56.9	−56 14 15.7	13.93	81.005	0.6495(3)	0.13(2)	EB	
F19_032476	*c*	16 28 57.5	−56 39 26.5	14.05	80.751	1.325(2)	0.07(2)	EA	F19_032563
F19_032563	*c*⋆	16 28 57.1	−56 39 20.5	14.45	80.754	1.325(1)	0.20(3)	EA	F19_032476
F19_032724	*s*	16 28 53.9	−55 41 16.1	11.68	105.194	28(1)	0.05(2)	VAR	
F19_032729	*c*	16 28 56.5	−56 52 17.8	14.00	81.017	0.5456(2)	0.12(2)	EW	
F19_032857	⋆	16 28 54.5	−56 08 19.0	12.90	81.165	2.332(4)	0.051(7)	EB	
F19_032876	⋆	16 28 52.8	−55 30 06.2	14.74	83.754	2.3869(1)	0.34(1)	EA	
F19_032904		16 28 54.1	−56 04 25.6	13.74	100.892	21(2)	0.02(1)	VAR	
F19_032978	*c*⋆	16 28 53.9	−56 06 30.1	12.37	80.654	4.5973(1)	0.105(1)	EA	
F19_033040	*s*⋆	16 28 53.6	−56 07 18.9	15.14	89.710	16.875(1)	0.4(1)	EA	
F19_033108	*c*	16 28 52.5	−55 55 02.8	14.09	80.939	0.4357(2)	0.07(3)	EW	F19_033203, F19_033240
F19_033203	*c*	16 28 52.2	−55 54 57.7	14.00	80.730	0.4357(3)	0.04(2)	EW	F19_033108, F19_033240
F19_033221		16 28 50.8	−55 25 00.4	13.02	80.787	0.1903(1)	0.02(3)	VAR	
F19_033224		16 28 53.9	−56 43 22.8	16.53	81.840	1.434(2)	0.2(2)	EA	
F19_033236	⋆	16 28 52.3	−56 00 24.0	15.70	80.498	7.7515(1)	1.7(1)	EA	
F19_033240	*c*	16 28 52.0	−55 55 01.5	13.90	80.725	0.4357(2)	0.07(2)	EW	F19_033108, F19_033203
F19_033376	*c*	16 28 49.9	−55 26 10.9	14.93	80.823	0.37712(9)	0.26(4)	EW	F19_033517
F19_033451	*s*	16 28 52.7	−56 46 55.8	14.59	80.711	0.13266(4)	0.02(2)	DSCT	
F19_033508	*s*	16 28 50.4	−55 52 29.4	14.04	271.524	43(3)	0.03(2)	VAR	
F19_033517	*c*	16 28 49.3	−55 26 07.5	14.89	80.822	0.37712(6)	0.34(3)	EW	F19_033376
F19_033547	*s*	16 28 49.0	−55 24 35.8	14.59	80.796	0.1602(2)	0.02(3)	VAR	
F19_033571	*c*⋆	16 28 50.5	−55 59 40.6	11.97	81.645	6.2662(1)	0.6(1)	EA	
F19_033774		16 28 50.5	−56 26 55.2	15.05	80.825	0.41895(8)	0.33(4)	EW	
F19_033823		16 28 48.7	−55 49 33.2	12.40	80.746	0.4539(5)	0.03(2)	RR	
F19_033825		16 28 48.6	−55 45 04.1	14.21	80.689	0.09769(4)	0.02(2)	DSCT	
F19_033836	*c*	16 28 50.6	−56 39 05.5	13.80	80.960	0.32037(6)	0.09(2)	EW	
F19_033986	*c*	16 28 47.1	−55 32 53.2	11.70	...	...	...	LP	
F19_034021	⋆	16 28 46.8	−55 28 13.9	14.36	81.137	0.8561(3)	0.35(3)	EA	
F19_034040	⋆	16 28 48.6	−56 15 43.4	14.16	81.945	8.5411(1)	0.5(1)	EA	
F19_034107		16 28 48.6	−56 24 23.0	13.02	100.679	41(3)	0.023(7)	ROT	
F19_034114	*c*⋆	16 28 47.5	−55 58 46.5	12.56	80.870	1.784(2)	0.07(2)	EA	
F19_034169	*c*⋆	16 28 48.1	−56 20 37.4	13.08	81.452	1.1710(5)	0.14(2)	EA	
F19_034180		16 28 46.6	−55 43 42.7	15.40	80.745	0.18006(8)	0.06(4)	DSCT	
F19_034210	*s*	16 28 47.6	−56 11 02.6	15.33	80.718	0.4334(3)	0.05(5)	EW	
F19_034240	*c*	16 28 47.9	−56 23 39.7	14.57	91.921	50(4)	0.06(3)	VAR	
F19_034441	⋆	16 28 46.8	−56 25 04.4	16.98	80.779	0.4016(2)	1.6(3)	EB	
F19_034516	⋆	16 28 45.5	−55 56 38.5	15.35	82.420	3.108(6)	0.42(4)	EB	
F19_034543		16 28 45.7	−56 10 45.4	14.93	80.937	0.8468(8)	0.07(4)	EA	
F19_034606		16 28 46.8	−56 54 39.8	13.65	89.163	9.1(2)	0.02(2)	VAR	
F19_034614		16 28 46.4	−56 34 17.1	13.04	99.910	12.8(4)	0.014(7)	VAR	
F19_034686	*c*	16 28 45.8	−56 30 14.8	14.84	80.899	0.864(1)	0.14(4)	EB	
F19_034778		16 28 44.8	−56 17 39.8	12.45	92.224	6.12(3)	0.025(8)	ROT	
F19_034789	*c*	16 28 43.8	−55 51 01.7	12.84	93.182	25.1(7)	0.12(3)	SR	
F19_034825	*c*	16 28 43.3	−55 43 47.4	13.31	81.012	0.4109(2)	0.07(2)	EW	F19_034855
F19_034830		16 28 42.8	−55 32 12.0	11.34	...	...	...	LP	
F19_034849		16 28 43.8	−55 59 03.0	14.02	81.054	0.40595(8)	0.22(3)	EW	
F19_034855	*c*	16 28 43.1	−55 43 42.9	13.25	81.012	0.4109(1)	0.058(8)	EW	F19_034825
F19_034860	*c*	16 28 42.8	−55 35 53.2	14.86	80.840	0.4523(2)	0.18(5)	EW	F19_035012
F19_034970	*c*	16 28 43.0	−55 51 41.5	11.85	...	...	...	SR	

Table E.5: Variable stars in field F19 (continued).

BEST ID	F	α (J2000.0) h m s	δ ° ′ ″	R_B [mag]	T_0 [d] [rHJD]	p [d]	A [mag]	Type	Other Names
F19_035012	*c*	16 28 42.1	−55 35 58.5	14.34	80.840	0.4523(1)	0.32(4)	EW	F19_034860
F19_035102	*c⋆*	16 28 43.4	−56 22 16.0	14.69	81.172	0.6523(2)	0.30(3)	EA	
F19_035119		16 28 42.0	−55 43 48.9	14.61	80.774	0.9147(5)	0.28(4)	EA	
F19_035139	*c*	16 28 43.2	−56 20 31.5	12.30	···	···	···	LP	
F19_035203	*c*	16 28 43.7	−56 55 34.0	12.37	···	···	···	SR	
F19_035298	*cs*	16 28 40.7	−55 33 45.6	15.41	80.775	0.4278(3)	0.10(5)	EW	
F19_035320		16 28 42.1	−56 14 22.5	15.69	125.675	24(2)	0.16(5)	CEP	
F19_035327		16 28 41.0	−55 45 09.3	15.68	80.702	0.18495(9)	0.07(6)	VAR	
F19_035365	*s*	16 28 42.5	−56 36 18.4	12.18	···	···	···	LP	
F19_035367		16 28 42.3	−56 31 42.6	14.01	90.474	10.4(3)	0.03(2)	ROT	
F19_035380	*c*	16 28 41.0	−55 54 20.4	14.77	80.952	0.39471(8)	0.23(3)	EW	
F19_035414		16 28 41.2	−56 05 32.0	14.05	123.643	80(2)	0.06(2)	VAR	
F19_035606		16 28 41.4	−56 42 13.3	16.06	80.813	0.3073(1)	0.17(7)	EW	
F19_035695	*s*	16 28 39.1	−55 46 45.0	14.81	81.511	2.3501(1)	0.09(1)	EA	
F19_035894	*s*	16 28 40.1	−56 49 44.0	14.69	80.937	0.4972(3)	0.03(3)	EB	
F19_035907	*c*	16 28 39.2	−56 16 09.2	13.20	80.785	0.3370(2)	0.03(2)	EW	F19_035943
F19_035943	*c*	16 28 38.9	−56 16 03.7	13.18	80.788	0.3370(2)	0.019(8)	EW	F19_035907
F19_035953	*c*	16 28 38.1	−55 53 11.7	15.12	80.766	0.4605(2)	0.12(4)	EW	F19_036063
F19_036039	⋆	16 28 36.9	−55 30 17.5	13.06	81.428	0.8291(9)	0.12(6)	EW	
F19_036049	*c⋆*	16 28 39.0	−56 36 12.3	14.41	82.704	4.5421(1)	0.27(1)	EA	
F19_036050	*c*	16 28 38.9	−56 30 31.8	11.27	90.137	10.5003	0.13	EA	
F19_036063	*c*	16 28 37.7	−55 53 10.5	14.93	80.989	0.4605(3)	0.11(4)	EW	F19_035953
F19_036086	*c*	16 28 38.3	−56 17 31.8	12.86	···	···	···	SR	
F19_036173		16 28 38.9	−56 54 02.4	12.61	···	···	···	LP	
F19_036183	*s*	16 28 38.0	−56 24 36.0	11.49	···	···	···	SR	
F19_036292		16 28 37.9	−56 35 30.7	10.73	···	···	···	LP	
F19_036480		16 28 35.2	−55 43 33.8	15.32	109.289	11.0(5)	0.07(4)	VAR	
F19_036611	*s*	16 28 34.6	−55 45 19.5	15.88	80.753	0.13610(4)	0.05(7)	DSCT	
F19_036669		16 28 35.8	−56 30 30.9	15.70	80.672	0.3885(2)	0.17(6)	EW/DSCT	
F19_036749	*c⋆*	16 28 34.3	−55 56 57.2	13.41	83.190	3.817(8)	0.19(2)	EB	
F19_036981	*s*	16 28 32.4	−55 34 00.8	11.78	122.309	24.1(9)	0.11(5)	VAR	
F19_037017	*c⋆*	16 28 34.4	−56 48 51.7	13.79	80.850	1.6773(9)	0.33(3)	EA	
F19_037026		16 28 33.7	−56 21 20.6	11.99	89.555	18.9(4)	0.04(1)	VAR	
F19_037081		16 28 34.0	−56 47 31.7	13.98	146.804	81(7)	0.10(2)	VAR	
F19_037090	*c*	16 28 33.2	−56 17 56.5	14.58	81.302	1.449(2)	0.10(3)	EA	
F19_037105	*c*	16 28 32.0	−55 39 21.4	11.10	···	···	···	LP	
F19_037129		16 28 32.9	−56 12 56.8	12.77	109.726	46(2)	0.10(2)	CEP	
F19_037276		16 28 31.3	−55 45 54.4	16.12	81.271	1.355(2)	0.3(2)	EA	
F19_037493		16 28 31.8	−56 43 22.9	16.08	83.215	2.773(4)	0.20(8)	EA	
F19_037554	*c*	16 28 31.6	−56 44 08.5	13.86	81.408	4.32(3)	0.06(2)	ROT	F19_037620
F19_037620	*c*	16 28 31.1	−56 44 03.4	13.96	81.355	4.32(4)	0.05(2)	ROT	F19_037554
F19_037662	*c⋆*	16 28 30.7	−56 32 51.1	13.60	83.011	3.533(4)	0.30(3)	EA	
F19_037825		16 28 28.3	−55 38 29.1	14.81	80.717	0.2822(1)	0.08(4)	EW	
F19_037905	*cs*	16 28 29.4	−56 33 46.5	12.44	82.337	12.1(2)	0.04(2)	VAR	
F19_037972		16 28 27.1	−55 30 12.5	17.11	80.896	0.24725(4)	2.5(4)	EB	
F19_037995		16 28 28.6	−56 19 46.7	15.18	80.686	0.25972(9)	0.06(5)	EW/DSCT	
F19_038150	⋆	16 28 28.5	−56 54 40.5	14.18	80.706	0.068140(6)	0.17(2)	DSCT	
F19_038168	*c*	16 28 27.8	−56 20 13.6	12.67	···	···	···	VAR	
F19_038176		16 28 27.0	−55 56 44.0	13.35	94.177	57(4)	0.17(3)	CEP	
F19_038187		16 28 28.3	−56 53 42.8	14.42	80.974	0.5784(3)	0.14(2)	EB	
F19_038196	*s*	16 28 27.7	−56 27 27.2	12.92	81.086	0.5099(4)	0.011(8)	EB	
F19_038216	*s*	16 28 26.2	−55 38 39.4	12.06	92.861	41(2)	0.03(2)	EB	
F19_038269	*s*	16 28 27.7	−56 38 20.1	14.27	149.311	16(5)	0.03(2)	EB	
F19_038274		16 28 27.2	−56 20 55.1	12.81	91.388	22(3)	0.06(2)	VAR	
F19_038307	*s*	16 28 27.8	−56 52 54.3	16.09	81.792	1.625(4)	0.14(8)	EB	
F19_038325	⋆	16 28 26.5	−56 03 54.8	16.35	81.168	0.7829(3)	1.2(2)	EA	
F19_038332	*s*	16 28 25.9	−55 45 32.6	14.31	80.948	0.3219(2)	0.02(2)	EW/DSCT	
F19_038349	*s*	16 28 27.3	−56 36 50.8	11.79	95.972	17.6(4)	0.04(2)	VAR	
F19_038408		16 28 27.0	−56 38 57.0	12.70	···	···	···	LP	
F19_038417		16 28 26.7	−56 24 48.0	12.86	300.293	65(4)	0.08(2)	VAR	
F19_038532	*c*	16 28 26.4	−56 35 46.0	14.16	81.851	5.79(6)	0.04(2)	ROT	F19_038673
F19_038581		16 28 25.3	−56 02 32.6	14.86	89.080	4.69(5)	0.04(3)	ROT	
F19_038634		16 28 26.1	−56 48 00.7	12.82	80.702	0.05784(2)	0.02(2)	DSCT	
F19_038647		16 28 25.2	−56 10 25.3	14.55	82.964	2.471(4)	0.12(6)	EA	
F19_038673	*c*	16 28 25.8	−56 35 48.9	13.84	81.370	5.79(5)	0.03(2)	ROT	F19_038532
F19_038674		16 28 25.6	−56 31 47.1	13.21	80.826	0.34103(9)	0.050(8)	EW	
F19_038683	*c⋆*	16 28 24.8	−56 01 36.7	13.34	80.914	0.5328(4)	0.12(6)	EB	
F19_038995		16 28 23.8	−56 32 36.7	13.42	···	···	···	LP	
F19_039042		16 28 22.5	−55 52 12.2	11.89	95.741	19.0(6)	0.06(2)	VAR	
F19_039046		16 28 22.3	−55 46 55.3	14.56	80.835	0.4423(3)	0.04(2)	EW	
F19_039138	*cs*	16 28 22.1	−56 05 20.8	11.90	96.946	19.7(7)	0.05(2)	VAR	F19_039170, F19_039311
F19_039170	*cs*	16 28 22.1	−56 05 18.9	11.90	97.009	19.7(6)	0.05(2)	VAR	F19_039138, F19_039311
F19_039184		16 28 23.1	−56 58 29.5	14.19	80.934	0.3424(2)	0.02(2)	EW	
F19_039187	⋆	16 28 23.2	−56 51 04.3	14.17	82.686	3.546(4)	0.53(6)	EA	
F19_039202		16 28 22.4	−56 16 53.0	12.77	80.689	0.3646(4)	0.009(6)	VAR	
F19_039268	*c*	16 28 22.0	−56 15 50.6	13.05	···	···	···	LP	
F19_039311	*cs*	16 28 21.6	−56 05 19.9	11.85	96.905	19.7(7)	0.05(2)	VAR	F19_039138, F19_039170
F19_039437	*s*	16 28 20.3	−55 39 26.0	17.04	82.227	1.899(3)	0.4(2)	EA	
F19_039471	*c*	16 28 19.6	−55 25 18.1	13.06	···	···	···	LP	
F19_039486		16 28 20.9	−56 12 43.5	14.27	81.380	0.9083(6)	0.09(2)	EW	
F19_039579		16 28 20.4	−56 15 52.7	11.97	94.073	45(3)	0.052(8)	ROT	
F19_039615	*s*	16 28 19.9	−56 02 14.0	11.70	···	···	···	LP	
F19_039616		16 28 19.8	−56 00 48.3	14.67	81.642	6.40(8)	0.10(4)	ROT	
F19_039643		16 28 20.3	−56 25 07.9	15.48	82.750	2.423(4)	0.11(5)	EA	
F19_039806	*s*	16 28 19.7	−56 37 55.2	14.23	81.312	5.53(4)	0.04(2)	ROT	
F19_039863	⋆	16 28 17.5	−55 24 27.8	12.54	82.110	2.3648(1)	0.085(1)	EA	
F19_040047	*s*	16 28 18.5	−56 37 09.4	15.69	81.027	0.4063(2)	0.08(8)	EB	
F19_040073		16 28 16.5	−55 25 26.6	13.92	···	···	···	LP	

Table E.5: Variable stars in field F19 (continued).

BEST ID	F	α (J2000.0) h m s	δ ° ′ ″	R_B [mag]	T_0 [d] [rHJD]	p [d]	A [mag]	Type	Other Names
F19_040095	*c*	16 28 17.6	−56 09 30.6	14.72	80.787	0.4135(2)	0.10(3)	EW/DSCT	F19_040160
F19_040114	*s*	16 28 18.3	−56 49 52.8	12.00	...	...	...	SR	
F19_040160	*c*	16 28 17.3	−56 09 25.6	14.68	80.783	0.4135(2)	0.12(3)	EW/DSCT	F19_040095
F19_040193	*c*	16 28 17.1	−56 07 31.9	13.39	80.754	0.36478(8)	0.18(2)	RR	
F19_040214		16 28 17.8	−56 54 12.8	16.25	80.797	0.26917(9)	0.20(8)	EW/DSCT	
F19_040254	*s*	16 28 17.5	−56 43 41.5	15.14	81.051	0.634(2)	0.05(5)	RR	
F19_040352		16 28 15.1	−55 26 58.4	16.37	81.123	0.4808(2)	0.4(1)	EW	
F19_040409		16 28 15.9	−56 02 34.1	16.56	81.455	0.824(2)	0.2(2)	VAR	
F19_040459	*c*	16 28 16.2	−56 35 37.1	14.36	80.926	0.38511(6)	0.25(2)	EW	
F19_040501		16 28 15.1	−55 53 55.6	11.90	149.129	64(5)	0.21(3)	CEP	
F19_040623		16 28 14.9	−56 11 16.2	12.00	...	...	...	SR	
F19_040696		16 28 14.4	−56 08 25.2	12.47	80.784	0.34424(9)	0.046(8)	EW	
F19_041118	*s*	16 28 12.3	−56 12 54.2	12.78	80.766	0.2935(2)	0.006(6)	EW/DSCT	
F19_041253	*c*⋆	16 28 11.8	−56 17 55.4	13.43	81.058	0.7564(6)	0.06(2)	EB	
F19_041295		16 28 11.7	−56 26 30.0	11.65	81.059	0.4789(5)	0.04(2)	RR	
F19_041304		16 28 11.0	−55 59 09.0	15.33	82.183	8.8(2)	0.13(5)	VAR	
F19_041326		16 28 11.8	−56 38 26.8	12.11	250.598	38.0(6)	0.101(7)	EB	
F19_041341	*c*	16 28 10.8	−55 54 36.7	14.54	80.956	0.5623(3)	0.06(3)	EB	
F19_041442		16 28 10.4	−56 01 40.8	11.52	92.191	19.6(5)	0.06(2)	VAR	
F19_041457		16 28 09.7	−55 32 31.2	11.73	...	...	...	LP	
F19_041563	*c*	16 28 10.5	−56 47 44.4	14.58	261.322	51(6)	0.04(3)	VAR	F19_041711
F19_041566		16 28 10.5	−56 37 29.3	16.10	81.164	0.5384(3)	0.6(2)	RR	
F19_041665	*s*	16 28 10.2	−56 52 40.3	16.29	80.734	0.2791(1)	0.08(9)	EW/DSCT	
F19_041682		16 28 09.2	−56 01 28.3	15.63	80.706	0.3813(2)	0.35(6)	EW	
F19_041697	*c*	16 28 08.6	−55 34 20.2	11.63	...	...	...	SR	
F19_041711	*c*	16 28 09.9	−56 47 44.1	14.36	262.074	52(7)	0.03(2)	VAR	F19_041563
F19_041741		16 28 08.4	−55 35 56.4	14.24	81.345	0.9223(7)	0.08(3)	EA	
F19_041783	*c*	16 28 07.8	−55 24 44.3	15.07	81.033	0.3947(2)	0.08(5)	EW	F19_041855
F19_041855	*c*	16 28 07.6	−55 24 50.9	15.12	81.029	0.3947(3)	0.07(4)	EW	F19_041783
F19_041986	*c*	16 28 07.5	−55 47 30.3	14.95	81.061	0.6696(4)	0.19(4)	EW	F19_042114
F19_042011	⋆	16 28 07.8	−56 08 10.0	13.49	91.690	6.13(2)	0.46(5)	EA	
F19_042114	*c*	16 28 06.7	−55 47 31.1	14.76	80.727	0.6695(5)	0.10(3)	EW	F19_041986
F19_042132	*c*	16 28 07.7	−56 44 27.9	13.25	92.212	7.71(5)	0.08(1)	EB	
F19_042205	*c*⋆	16 28 06.7	−56 04 10.5	14.67	80.681	0.29621(5)	0.18(2)	EW	
F19_042321	*c*	16 28 05.2	−55 26 29.7	14.91	80.714	0.6073(5)	0.31(8)	RR	
F19_042419		16 28 05.9	−56 22 53.5	11.82	80.770	0.13375(4)	0.04(2)	DSCT	
F19_042514		16 28 05.0	−56 01 07.3	13.60	100.595	26(1)	0.06(2)	VAR	
F19_042523	*c*	16 28 04.2	−55 26 10.1	11.99	80.897	0.2589(2)	0.03(1)	DSCT	F19_042559
F19_042559	*c*	16 28 04.0	−55 26 05.4	11.95	80.905	0.2588(2)	0.03(5)	DSCT	F19_042523
F19_042578	*c*	16 28 04.8	−56 08 12.0	15.25	80.732	0.4047(2)	0.11(4)	EW	
F19_042635		16 28 05.3	−56 57 10.2	17.35	159.206	28(2)	0.5(3)	VAR	
F19_042675		16 28 04.7	−56 28 12.0	13.43	80.757	0.5228(3)	0.05(2)	RR	
F19_042818	⋆	16 28 04.2	−56 43 27.6	14.94	81.496	1.350(2)	0.06(3)	EA	
F19_042834		16 28 03.2	−55 52 38.2	12.78	...	...	...	SR	
F19_042974	*c*⋆	16 28 03.1	−56 22 58.2	14.63	80.886	0.6316(2)	1.01(3)	RR	
F19_043029		16 28 03.1	−56 41 21.2	14.29	120.953	33(2)	0.05(2)	VAR	
F19_043079		16 28 02.3	−56 03 40.2	15.53	80.859	0.2574(2)	0.07(5)	VAR	
F19_043153	*cs*⋆	16 28 02.3	−56 21 04.9	13.46	80.974	1.208(2)	0.023(8)	EA	
F19_043221	*s*	16 28 01.9	−56 13 30.0	14.93	81.158	1.124(4)	0.03(3)	VAR	
F19_043298	⋆	16 28 01.0	−55 50 16.9	14.14	90.900	5.183(1)	0.3(1)	EA	
F19_043457		16 28 00.8	−56 31 56.6	13.62	80.855	1.303(4)	0.02(2)	VAR	
F19_043462		16 28 00.6	−56 12 21.0	13.77	80.741	0.2823(2)	0.01(2)	EW/DSCT	
F19_043467	*s*	16 28 00.3	−56 02 55.3	15.07	80.693	0.1890(2)	0.03(4)	DSCT	
F19_043539	*s*	16 27 59.7	−55 45 09.7	14.07	...	...	...	LP	
F19_043616	*s*	16 27 59.1	−55 36 15.4	11.04	...	...	...	VAR	
F19_043642	*c*	16 27 59.5	−55 58 23.9	11.20	...	...	...	LP	
F19_043739	*s*	16 27 58.6	−55 40 43.5	14.23	93.549	17.5(5)	0.04(2)	VAR	
F19_043750		16 27 59.4	−56 44 28.8	15.18	81.183	0.8085(6)	0.17(4)	EB	
F19_043752	*c*	16 27 59.1	−56 38 21.1	13.18	80.926	0.36656(8)	0.10(2)	EW	F19_043859
F19_043859	*c*	16 27 58.9	−56 38 16.6	13.07	80.926	0.36656(8)	0.064(8)	EW	F19_043752
F19_043864		16 27 58.8	−56 32 26.0	13.80	121.540	2.0001(1)	0.07(1)	EA	
F19_043870		16 27 58.5	−56 12 37.0	14.77	83.676	4.61(4)	0.09(3)	VAR	
F19_043902		16 27 58.6	−56 33 24.6	14.30	80.740	0.32161(7)	0.22(2)	RR	
F19_043910		16 27 58.2	−56 11 33.6	11.83	...	...	...	SR	
F19_043998	*c*	16 27 58.2	−56 40 05.8	13.85	80.900	0.3884(2)	0.06(2)	EW	F19_043999
F19_043999	*c*	16 27 58.1	−56 40 00.6	13.71	80.898	0.3884(2)	0.03(1)	EW	F19_043998
F19_044093		16 27 56.8	−55 41 41.6	15.11	82.849	7.1(1)	0.07(3)	ROT	
F19_044294	*c*	16 27 55.8	−55 47 47.9	14.47	91.491	11.7(1)	0.29(3)	VAR	
F19_044352	⋆	16 27 55.8	−56 03 39.2	14.72	80.887	0.5866(2)	0.43(4)	RR	
F19_044457		16 27 55.3	−56 05 07.9	12.86	94.664	35(3)	0.029(8)	VAR	
F19_044552	*cs*	16 27 54.8	−56 07 34.4	14.36	80.692	0.4300(3)	0.05(3)	EW	
F19_044614	*s*	16 27 54.2	−55 53 40.5	12.58	...	...	...	SR	
F19_044624	*c*⋆	16 27 53.7	−55 23 38.9	13.66	81.385	2.2301(1)	0.08(1)	EA	
F19_044646	⋆	16 27 54.3	−56 07 20.7	13.14	80.899	2.271(4)	0.06(1)	EA	
F19_044808	⋆	16 27 53.3	−55 54 04.8	12.84	80.698	1.27111(1)	0.53(1)	EA	
F19_044823	*s*	16 27 53.8	−56 52 05.9	12.93	88.312	8.01(6)	0.025(8)	ROT	
F19_044842		16 27 53.1	−56 00 47.8	14.48	80.759	0.2776(2)	0.04(2)	DSCT	
F19_044908	*s*	16 27 52.7	−55 57 51.1	14.01	80.987	0.4151(3)	0.02(2)	EW	
F19_044916		16 27 52.5	−55 43 25.7	11.98	...	...	...	LP	
F19_044986	*c*⋆	16 27 52.6	−56 02 55.4	14.96	81.258	2.6436	0.071	EA	
F19_045024		16 27 51.9	−55 37 50.9	15.67	80.674	0.19430(6)	0.22(5)	DSCT	
F19_045041	*cs*	16 27 52.6	−56 37 07.5	13.82	80.699	0.2264(2)	0.06(4)	VAR	F19_045173
F19_045090		16 27 52.1	−56 11 36.7	12.82	99.140	13.6(5)	0.017(7)	VAR	
F19_045173	*cs*	16 27 51.8	−56 37 10.7	13.36	80.681	0.2264(2)	0.02(2)	VAR	F19_045041
F19_045214		16 27 51.2	−55 54 51.1	10.79	80.706	0.09402(3)	0.01(1)	DSCT	
F19_045226	*cs*	16 27 51.5	−56 54 51.1	13.49	90.691	6.05(4)	0.03(2)	ROT	F19_045394
F19_045246		16 27 50.8	−55 47 04.3	12.66	...	...	...	LP	
F19_045321	*ck*	16 27 50.3	−55 33 40.0	11.69	...	...	...	LP	NU Nor

Table E.5: Variable stars in field F19 (continued).

BEST ID	F	α (J2000.0) h m s	δ ° ′ ″	R_B [mag]	T_0 [d] [rHJD]	p [d]	A [mag]	Type	Other Names
F19_045346	$c\star$	16 27 50.7	−56 12 32.9	14.76	81.141	4.389(7)	0.83(6)	EA	
F19_045394	cs	16 27 50.8	−56 54 49.4	13.34	90.802	6.11(4)	0.03(2)	ROT	F19_045226
F19_045570		16 27 49.2	−55 54 01.0	12.43	81.978	12.0(7)	0.029(8)	VAR	
F19_045619		16 27 48.8	−55 39 32.6	14.45	80.713	0.09828(1)	0.23(3)	DSCT	
F19_045698	$\star$	16 27 48.7	−55 53 13.6	12.36	88.484	69(6)	0.10(3)	EB	
F19_045795	$c\star$	16 27 48.0	−55 43 10.1	14.15	81.471	1.666(2)	0.30(4)	EA	
F19_045901		16 27 47.7	−55 50 15.6	14.36	80.677	0.13296(3)	0.09(2)	DSCT	
F19_045993	c	16 27 47.4	−56 20 42.4	14.47	···	···	···	LP	
F19_046038	$c\star$	16 27 47.3	−56 16 03.5	13.52	95.228	9.62(4)	0.20(3)	EA	
F19_046119	c	16 27 46.4	−55 41 15.7	14.68	121.710	2.7701(1)	0.07(1)	EA	
F19_046148		16 27 46.4	−55 53 42.8	11.14	···	···	···	LP	
F19_046171		16 27 46.4	−56 05 33.4	16.38	83.034	2.707(4)	0.7(2)	EA	
F19_046235	s	16 27 46.0	−56 04 37.8	15.07	80.697	0.05047(2)	0.03(4)	DSCT	
F19_046265	$\star$	16 27 45.6	−55 50 02.4	14.86	82.029	4.156(7)	0.25(3)	EA	
F19_046276	$\star$	16 27 46.0	−56 42 47.2	14.90	82.316	1.888(3)	0.06(3)	EA	
F19_046413	$c\star$	16 27 45.1	−56 07 51.9	13.26	80.803	0.20280(8)	0.05(2)	DSCT	
F19_046424	s	16 27 44.5	−55 28 37.1	14.94	177.589	13.2(2)	0.12(3)	EA	
F19_046530	$ck\star$	16 27 44.7	−56 47 08.3	12.05	82.115	2.386(2)	0.99(3)	CEP	UX Nor
F19_046686	$\star$	16 27 43.3	−55 46 11.2	13.01	88.680	15.4375(1)	0.74(1)	EA	
F19_046704		16 27 43.7	−56 30 18.2	15.70	83.794	3.64(3)	0.11(5)	VAR	
F19_046856	c	16 27 42.4	−55 34 20.3	15.47	80.767	0.09890(2)	0.24(6)	RR	
F19_046867		16 27 42.9	−56 25 24.6	14.85	81.374	0.901(3)	0.06(4)	VAR	
F19_046916	$c\star$	16 27 42.4	−55 57 49.1	13.16	81.121	0.6360(2)	0.141(8)	EB	
F19_046923	s	16 27 41.9	−55 36 40.0	12.89	···	···	···	SR	
F19_046930	cs	16 27 42.5	−56 53 41.5	14.42	···	···	···	LP	
F19_046998	cs	16 27 42.2	−56 53 44.4	14.39	···	···	···	LP	
F19_047089	s	16 27 41.4	−55 53 52.9	13.04	80.670	0.3682(2)	0.012(7)	EW/DSCT	
F19_047137		16 27 41.1	−55 40 03.0	15.45	80.886	1.2114(9)	0.31(6)	EA	
F19_047252	c	16 27 40.7	−56 17 32.4	12.83	···	···	···	LP	
F19_047325		16 27 40.4	−56 26 08.6	12.89	91.010	21.0(8)	0.012(6)	VAR	
F19_047380	c	16 27 39.9	−55 49 32.9	15.78	81.511	5.49(3)	0.64(9)	CEP	
F19_047403	c	16 27 40.2	−56 17 34.5	12.89	···	···	···	LP	
F19_047468	s	16 27 39.8	−56 40 12.5	13.03	80.788	0.972(2)	0.10(5)	EB	
F19_047489		16 27 39.3	−55 39 07.6	11.92	···	···	···	LP	
F19_047559		16 27 38.8	−55 28 59.7	15.50	80.704	0.8642(9)	0.14(7)	EW	
F19_047631		16 27 39.0	−56 57 19.5	12.26	···	···	···	LP	
F19_047638	$\star$	16 27 38.9	−56 37 25.9	13.77	81.099	0.6420(2)	0.24(2)	EW	
F19_047724		16 27 38.6	−56 28 40.2	10.31	···	···	···	LP	
F19_047898		16 27 37.6	−56 15 01.0	16.17	80.773	0.3527(2)	0.2(2)	EW/DSCT	
F19_048083	c	16 27 36.7	−56 12 04.0	11.45	···	···	···	LP	
F19_048172		16 27 36.4	−56 50 29.9	15.33	80.729	0.2730(1)	0.2(2)	EW	
F19_048261	$\star$	16 27 35.4	−55 27 09.4	13.00	81.627	3.7098(1)	0.49(1)	EA	
F19_048338	s	16 27 35.4	−56 36 05.5	14.26	89.847	5.32(3)	0.06(2)	ROT	
F19_048467		16 27 34.4	−55 23 35.4	15.59	80.956	0.3032(2)	0.08(5)	EW	
F19_048489	c	16 27 34.7	−56 10 59.4	10.90	···	···	···	SR	
F19_048532	$\star$	16 27 34.2	−55 55 06.9	14.73	81.891	7.66(2)	0.81(9)	EA	
F19_048570	$\star$	16 27 34.2	−56 12 33.8	15.29	81.376	1.582(2)	0.15(6)	EA	
F19_048639	c	16 27 33.8	−56 20 14.9	12.75	97.800	24(2)	0.07(2)	VAR	F19_048753
F19_048654		16 27 33.9	−56 40 18.4	14.94	270.548	16.8(7)	0.05(3)	VAR	
F19_048730	s	16 27 33.3	−56 00 43.6	16.57	80.783	0.702(2)	0.1(2)	VAR	
F19_048753	c	16 27 33.2	−56 20 17.4	12.60	122.487	24(1)	0.05(2)	VAR	F19_048639
F19_048958	s	16 27 32.3	−56 36 06.0	11.08	···	···	···	SR	
F19_048967		16 27 32.2	−56 08 55.7	15.31	80.680	0.3391(1)	0.13(4)	EW	
F19_048998	c	16 27 32.0	−56 11 10.2	12.58	···	···	···	LP	
F19_049036	c	16 27 31.8	−56 08 20.9	13.55	81.575	0.994(3)	0.09(2)	EW	F19_049037, F19_049132
F19_049037	c	16 27 31.8	−56 08 14.3	14.40	81.557	0.995(2)	0.11(3)	EW	F19_049036, F19_049132
F19_049084		16 27 31.4	−55 41 26.8	15.59	80.731	0.3135(2)	0.10(7)	EW/DSCT	
F19_049132	c	16 27 31.4	−56 08 27.3	13.24	81.558	0.995(3)	0.04(1)	EW	F19_049036, F19_049037
F19_049213	s	16 27 30.8	−55 59 08.3	13.77	81.006	0.4152(3)	0.01(2)	EW/DSCT	
F19_049225	s	16 27 30.6	−55 29 39.0	15.90	81.816	1.562(8)	0.10(7)	VAR	
F19_049235	$\star$	16 27 30.8	−56 30 48.5	15.11	81.301	0.7900(2)	0.93(4)	EA	
F19_049246		16 27 30.6	−55 47 40.9	12.26	···	···	···	SR	
F19_049265	$\star$	16 27 30.6	−56 27 00.7	14.41	81.404	0.8457(5)	0.04(2)	EA	
F19_049338		16 27 30.1	−56 10 22.3	12.22	···	···	···	LP	
F19_049491		16 27 29.3	−55 42 22.3	16.18	82.300	1.802(8)	0.14(9)	VAR	
F19_049528	s	16 27 29.1	−55 36 57.6	13.48	···	···	···	SR	
F19_049529	cs	16 27 29.0	−55 35 54.9	14.70	80.693	0.3210(3)	0.02(3)	VAR	F19_049616
F19_049549		16 27 29.2	−56 08 56.7	11.80	···	···	···	LP	
F19_049569	c	16 27 29.0	−56 23 05.2	10.77	···	···	···	SR	
F19_049585	c	16 27 28.9	−55 45 17.7	17.68	80.687	0.053331(6)	3.1(7)	DSCT	F19_049787
F19_049616	cs	16 27 28.6	−55 35 51.9	14.82	80.975	0.3210(3)	0.03(3)	VAR	F19_049529
F19_049699	$c\star$	16 27 28.3	−56 13 12.9	12.69	91.300	13.13(1)	0.1(1)	EB	
F19_049704	c	16 27 28.2	−56 02 25.6	15.73	81.578	0.9121(6)	0.18(6)	EA	
F19_049778	c	16 27 27.9	−56 05 11.1	15.59	80.852	0.37558(6)	0.58(5)	EW	
F19_049787	c	16 27 27.8	−55 45 09.3	16.24	80.688	0.053330(6)	0.3(1)	DSCT	F19_049585
F19_049816		16 27 27.7	−56 03 09.3	15.10	89.359	43(2)	0.29(3)	CEP	
F19_049834		16 27 27.6	−56 44 35.2	12.78	···	···	···	LP	
F19_049849	$c\star$	16 27 27.6	−55 56 06.1	12.76	80.978	0.5061(2)	0.30(3)	EW	
F19_049861		16 27 27.3	−55 30 40.8	12.21	···	···	···	LP	
F19_049872	s	16 27 27.4	−56 36 02.6	13.80	81.318	10.9(2)	0.02(2)	VAR	
F19_049986	s	16 27 27.0	−56 40 17.8	12.48	···	···	···	VAR	
F19_050107	$s\star$	16 27 26.3	−56 08 23.8	12.82	81.896	2.0745(1)	0.07(1)	EA	
F19_050149		16 27 26.1	−56 03 49.6	12.38	···	···	···	LP	
F19_050175	c	16 27 26.1	−56 39 35.3	15.12	80.993	0.6447(7)	0.05(3)	EB	
F19_050297		16 27 25.4	−56 48 06.9	13.33	81.123	0.5577(5)	0.037(8)	RR	
F19_050321	c	16 27 25.3	−55 49 18.0	14.22	80.850	0.6278(2)	0.19(2)	EW	
F19_050354		16 27 25.0	−56 50 40.2	15.04	93.259	15.8(5)	0.05(3)	ROT	
F19_050360		16 27 25.0	−56 27 54.1	16.86	94.541	7.8(2)	0.5(2)	VAR	

Table E.5: Variable stars in field F19 (continued).

BEST ID	F	α (J2000.0) h m s	δ ° ′ ″	R_B [mag]	T_0 [d] [rHJD]	p [d]	A [mag]	Type	Other Names
F19_050410		16 27 24.5	−55 25 23.8	12.51	81.692	1.187(4)	0.05(4)	VAR	
F19_050478	*c*	16 27 24.2	−56 57 13.8	13.90	80.773	0.3137(2)	0.02(2)	EW	
F19_050521	*c*	16 27 24.2	−56 31 07.5	15.36	80.751	0.5487(4)	0.27(6)	RR	
F19_050523	*s*	16 27 24.1	−56 23 46.4	12.72	81.313	0.648(1)	0.02(2)	RR	
F19_050687		16 27 23.3	−56 20 52.6	12.39	122.031	62(3)	0.13(2)	SR	
F19_050797		16 27 22.5	−55 49 46.7	15.57	80.879	0.3375(2)	0.08(7)	EW/DSCT	
F19_050806	*s*	16 27 22.4	−56 51 25.8	16.43	80.876	0.2945(2)	0.08(9)	EW/DSCT	
F19_050808	*c*	16 27 22.4	−56 49 51.2	12.13	...	...	...	SR	
F19_050862	*s*	16 27 22.2	−55 54 11.7	13.82	81.202	0.6265(5)	0.03(2)	EW	
F19_050875		16 27 22.2	−55 28 41.1	12.39	...	...	...	LP	
F19_050931	*c*	16 27 22.1	−56 16 29.7	12.06	...	...	...	SR	
F19_050947	*c*	16 27 21.8	−55 47 39.0	15.04	81.174	0.6994(6)	0.05(3)	EW	F19_050948
F19_050948	*c*	16 27 21.9	−55 47 32.7	15.51	81.181	0.6994(5)	0.15(5)	EW	F19_050947
F19_051007		16 27 21.6	−55 42 42.0	15.98	80.676	0.16401(7)	0.09(7)	DSCT	
F19_051010	*c*⋆	16 27 21.5	−55 33 33.1	14.17	188.580	4.961(1)	0.24(1)	EA	
F19_051043	*s*	16 27 21.5	−55 44 35.2	12.36	80.749	0.1856(1)	0.009(8)	DSCT	
F19_051090		16 27 21.1	−56 42 30.6	14.33	80.773	0.32279(5)	0.21(2)	EW	
F19_051093	*c*	16 27 21.0	−56 25 56.7	15.12	81.013	0.4746(3)	0.20(6)	EW	
F19_051153		16 27 20.7	−56 48 03.8	13.23	80.909	0.3786(1)	0.07(1)	EW	
F19_051220		16 27 20.4	−56 43 17.9	14.89	80.895	0.5066(2)	0.32(3)	EW	
F19_051237		16 27 20.3	−55 59 15.5	15.39	81.540	1.5907	0.080	EA	
F19_051265		16 27 20.1	−56 02 10.4	15.20	80.965	0.3151(2)	0.06(5)	EW/DSCT	
F19_051300		16 27 20.0	−56 17 03.7	14.81	80.759	0.2854(2)	0.10(3)	VAR	
F19_051315	*s*	16 27 20.1	−55 39 00.7	13.90	250.771	29(2)	0.03(2)	VAR	
F19_051324	*c*⋆	16 27 19.8	−56 50 20.9	12.53	96.505	9.3398(1)	0.43(1)	EA	
F19_051353		16 27 19.7	−55 32 35.0	11.67	80.716	0.3905(2)	0.016(7)	EW/DSCT	
F19_051454	*c*	16 27 19.3	−55 43 18.4	14.86	81.188	0.7295(5)	0.12(4)	EW	F19_051524, F19_051670
F19_051460		16 27 19.2	−55 23 45.8	13.08	...	...	...	SR	
F19_051524	*c*	16 27 18.9	−55 43 22.2	14.30	81.184	0.7295(6)	0.08(3)	EW	F19_051454, F19_051670
F19_051622	*s*	16 27 18.5	−56 24 50.1	10.89	171.430	42(4)	0.010(4)	VAR	
F19_051643		16 27 18.1	−56 50 31.7	14.11	...	...	...	VAR	
F19_051670	*c*	16 27 18.3	−55 43 24.6	14.50	81.193	0.7295(6)	0.08(3)	EW	F19_051454, F19_051524
F19_051744		16 27 17.9	−55 28 31.1	15.77	80.828	0.3937(2)	0.28(7)	EW	
F19_051970		16 27 16.8	−56 02 03.5	12.19	93.794	49(3)	0.08(2)	VAR	
F19_052020	*s*	16 27 16.5	−55 25 49.5	14.79	80.732	0.16197(7)	0.03(3)	DSCT	
F19_052028		16 27 16.3	−56 48 00.0	15.81	80.676	0.31242(6)	0.49(6)	EW	
F19_052039		16 27 16.4	−56 31 47.6	16.08	100.986	47(3)	0.33(7)	VAR	
F19_052162		16 27 15.8	−55 27 51.5	12.78	80.728	0.10345(4)	0.03(4)	DSCT	
F19_052165	*c*	16 27 15.8	−55 25 20.8	13.98	80.980	0.4204(3)	0.09(4)	EW/DSCT	
F19_052203	*c*	16 27 15.5	−55 47 40.7	14.60	81.257	0.6168(4)	0.04(3)	EA	F19_052298
F19_052245	*cs*	16 27 15.2	−56 25 35.4	13.59	80.851	0.4391(5)	0.05(3)	VAR	
F19_052257	*c*	16 27 15.4	−55 54 06.1	14.29	81.064	0.4562(2)	0.21(2)	EB	
F19_052298	*c*	16 27 15.2	−55 47 44.7	14.66	81.256	0.6168(4)	0.04(2)	EA	F19_052203
F19_052322		16 27 15.1	−56 00 57.7	12.90	93.154	20.2(6)	0.07(2)	CEP	
F19_052378	*s*	16 27 14.6	−56 25 46.9	13.71	83.688	6.06(4)	0.04(2)	VAR	
F19_052461		16 27 14.3	−55 44 05.8	14.10	83.420	2.84(2)	0.03(2)	EB	
F19_052543	*c*	16 27 13.7	−56 28 37.7	11.51	...	...	...	LP	
F19_052568	*cs*	16 27 13.7	−55 30 46.6	15.35	81.001	0.4935(4)	0.06(5)	EW	F19_052633
F19_052617		16 27 13.4	−56 19 07.7	13.09	83.285	4.7(2)	0.02(1)	VAR	
F19_052633	*cs*	16 27 13.5	−55 30 50.9	15.27	80.993	0.4936(4)	0.07(5)	EW	F19_052568
F19_052667	*c*⋆	16 27 12.9	−56 53 23.2	13.00	80.759	0.19416(5)	0.09(2)	DSCT	
F19_052801		16 27 12.4	−56 20 23.1	15.57	81.696	5.4035(1)	0.25(1)	EA	
F19_052812		16 27 12.4	−55 31 32.7	13.57	...	...	...	LP	
F19_052873	*s*	16 27 12.1	−56 01 37.4	11.03	...	...	...	SR	
F19_053087		16 27 10.8	−55 52 49.3	12.64	267.702	65(7)	0.016(7)	VAR	
F19_053142	*c*	16 27 10.4	−56 13 11.5	13.32	80.819	0.3673(2)	0.10(3)	EW	
F19_053170	*cs*⋆	16 27 10.1	−56 32 20.7	12.65	...	...	...	EA	
F19_053218	*c*	16 27 10.2	−55 51 01.8	12.51	121.760	60(3)	0.14(2)	VAR	
F19_053263	*s*	16 27 09.4	−56 52 12.0	12.75	97.374	19(2)	0.05(2)	ROT	
F19_053335	⋆	16 27 09.6	−55 46 27.5	14.55	92.675	7.935(1)	0.4(1)	EA	
F19_053425	⋆	16 27 09.0	−56 17 38.7	14.60	80.960	0.30500(5)	0.27(3)	EB	
F19_053473	*c*⋆	16 27 08.3	−57 00 27.7	13.02	80.809	0.15743(3)	0.060(8)	DSCT	
F19_053491	*c*	16 27 08.6	−56 25 18.7	12.65	...	...	...	LP	
F19_053498		16 27 08.7	−55 55 42.8	15.94	81.463	0.8023(4)	0.34(7)	EA	
F19_053523	*s*	16 27 08.3	−56 40 37.0	14.27	92.237	67(9)	0.04(2)	VAR	
F19_053534		16 27 08.4	−56 17 09.1	11.94	...	...	...	LP	
F19_053536	*c*	16 27 08.4	−56 15 35.9	14.66	80.794	0.19151(8)	0.06(3)	VAR	F19_053598, F19_053772
F19_053598	*c*	16 27 08.1	−56 15 40.9	14.25	80.790	0.19151(8)	0.07(4)	VAR	F19_053536, F19_053772
F19_053618		16 27 07.7	−56 57 40.0	14.67	80.933	0.27129(7)	0.10(3)	EW	
F19_053633	*s*	16 27 08.0	−56 15 17.9	15.35	81.001	1.113(3)	0.07(4)	EB	
F19_053769	*s*	16 27 07.2	−56 23 15.1	14.62	81.016	0.3880(2)	0.04(3)	EW	
F19_053772	*c*	16 27 07.2	−56 15 41.4	13.64	80.784	0.19151(9)	0.02(1)	VAR	F19_053536, F19_053598
F19_053822	*s*	16 27 07.2	−55 37 34.6	15.99	80.926	0.2611(2)	0.07(8)	EW/DSCT	
F19_053849		16 27 07.0	−56 10 15.7	15.50	90.862	17.2(6)	0.10(5)	VAR	
F19_053865	⋆	16 27 06.3	−56 58 58.3	14.21	94.767	5.6378(1)	0.28(1)	EA	
F19_053911	*c*	16 27 06.3	−56 24 36.2	12.75	80.966	0.3856(2)	0.08(3)	EW	F19_054039
F19_053927	*s*	16 27 06.6	−55 42 05.3	12.55	135.450	139(6)	0.22(2)	EB	
F19_053952	*c*	16 27 06.4	−56 02 44.0	14.78	81.218	0.5873(3)	0.14(3)	EW	F19_053953
F19_053953	*c*	16 27 06.4	−56 02 38.3	14.73	81.217	0.5873(2)	0.18(3)	EW	F19_053952
F19_053968	*c*	16 27 05.7	−56 59 17.0	13.88	81.164	0.6691(6)	0.02(2)	EW/DSCT	F19_054099
F19_054039	*c*	16 27 05.7	−56 24 38.2	12.67	80.968	0.3856(1)	0.054(8)	EW	F19_053911
F19_054047		16 27 05.9	−56 06 44.9	15.73	283.130	70(2)	0.11(5)	VAR	
F19_054099	*c*	16 27 05.1	−56 59 17.3	13.84	81.169	0.6690(5)	0.02(2)	EW/DSCT	F19_053968
F19_054172		16 27 05.0	−56 46 20.3	12.81	...	...	...	LP	
F19_054379		16 27 04.0	−56 28 21.4	16.67	81.322	0.7038(3)	0.7(2)	EA	
F19_054400	*c*	16 27 04.3	−55 25 09.7	12.50	313.301	57(5)	0.15(3)	VAR	
F19_054561		16 27 03.4	−55 47 41.2	12.28	...	...	...	LP	
F19_054570	*c*	16 27 03.4	−55 28 34.4	13.97	80.950	0.5422(1)	0.34(3)	EW	

Table E.5: Variable stars in field F19 (continued).

BEST ID	F	α (J2000.0) δ	R_B	T_0 [d]	p [d]	A	Type	Other Names
		h m s ° ′ ″	[mag]	[rHJD]		[mag]		
F19_054611		16 27 02.9 −56 25 20.4	16.06	81.046	0.5736(4)	0.3(2)	EB	
F19_054700		16 27 02.3 −56 12 56.5	13.94	80.672	0.035193(3)	0.03(2)	DSCT	
F19_054729		16 27 02.0 −56 26 03.4	15.53	80.936	0.4459(2)	0.15(5)	EW	
F19_054737	*s*	16 27 02.3 −55 52 50.2	13.75	81.687	1.042(3)	0.01(2)	ROT	
F19_054775	*s*	16 27 01.4 −56 49 56.4	15.21	80.789	0.2793(1)	0.04(4)	EW/DSCT	
F19_054803	*s*	16 27 01.9 −55 58 23.0	13.88	81.190	0.685(2)	0.01(2)	VAR	
F19_054899	⋆	16 27 01.3 −56 08 12.9	14.69	82.803	2.8035(1)	0.07(1)	EA	
F19_055055	*c*⋆	16 27 00.8 −55 33 23.7	15.15	83.056	2.919(6)	0.20(5)	EA	
F19_055092		16 26 59.8 −57 01 19.0	14.81	80.922	0.2981(2)	0.04(3)	EB	
F19_055102		16 26 60.0 −56 44 53.9	15.36	80.845	0.2952(2)	0.15(4)	RR	
F19_055219	*c*	16 26 59.7 −56 09 57.4	13.23	···	···	···	LP	
F19_055270	⋆	16 26 59.9 −55 28 47.6	10.91	94.775	3.3521(1)	0.21(1)	EA	
F19_055279	*s*	16 26 59.2 −56 31 40.3	15.06	80.760	0.18418(9)	0.03(3)	VAR	
F19_055306	*c*⋆	16 26 58.9 −56 41 48.3	13.07	91.590	3.1997(1)	0.11(1)	EA	
F19_055331	*c*	16 26 59.4 −55 42 15.6	11.09	···	···	···	SR	
F19_055387	⋆	16 26 58.5 −56 47 13.7	14.75	81.783	1.699(3)	0.08(3)	EA	
F19_055573		16 26 58.3 −55 40 38.0	14.04	···	···	···	SR	
F19_055618		16 26 57.6 −56 14 38.7	13.76	95.556	8.8(2)	0.04(2)	VAR	
F19_055698	*c*	16 26 56.9 −56 26 27.3	11.44	···	···	···	LP	
F19_055712	*c*	16 26 57.3 −55 44 29.5	14.58	139.686	37(2)	0.11(3)	VAR	
F19_055818	*s*	16 26 56.7 −55 59 31.9	14.87	···	···	···	VAR	
F19_055959		16 26 56.1 −55 39 38.6	15.70	80.901	0.2475(2)	0.14(6)	VAR	
F19_055975		16 26 55.3 −56 37 47.7	11.44	97.127	9.6(2)	0.020(7)	VAR	
F19_055991	*c*	16 26 55.9 −55 44 40.7	14.55	200.197	32(2)	0.10(3)	VAR	
F19_056045	*s*	16 26 55.1 −56 29 26.4	12.82	309.008	80(2)	0.014(6)	VAR	
F19_056204		16 26 54.3 −56 27 10.6	12.77	80.745	4.22(4)	0.020(8)	ROT	
F19_056266		16 26 54.1 −56 16 09.1	14.06	81.485	0.8493(5)	0.20(4)	EW	
F19_056280	*c*	16 26 54.6 −55 27 23.4	15.40	80.792	0.14718(5)	0.07(5)	DSCT	F19_056365
F19_056365	*c*	16 26 54.1 −55 27 28.5	15.11	80.785	0.14718(6)	0.07(5)	DSCT	F19_056280
F19_056394	*s*	16 26 53.9 −55 50 13.7	12.39	94.598	34(2)	0.020(6)	CEP	
F19_056497	*c*	16 26 52.2 −56 59 29.4	11.09	···	···	···	LP	
F19_056692		16 26 51.6 −56 31 40.3	14.76	80.761	0.19524(6)	0.13(3)	DSCT	
F19_056726	*s*	16 26 51.6 −56 24 43.3	12.61	93.289	23.6(6)	0.032(8)	EB	
F19_056742	*c*⋆	16 26 52.1 −55 35 36.3	13.24	80.717	0.33918(4)	0.137(8)	EW	
F19_056794		16 26 51.3 −56 15 49.7	12.50	···	···	···	LP	
F19_056859	*s*	16 26 50.8 −56 22 04.5	12.32	109.351	39(3)	0.025(7)	VAR	
F19_056861		16 26 50.9 −56 15 41.0	12.06	···	···	···	LP	
F19_056943	*s*	16 26 51.0 −55 34 15.7	12.98	···	···	···	SR	
F19_056975		16 26 50.9 −55 29 10.2	11.00	···	···	···	SR	
F19_056983		16 26 49.7 −56 49 50.7	11.95	···	···	···	SR	
F19_057110	*c*	16 26 50.0 −55 52 42.6	15.37	80.930	0.3249(2)	0.08(4)	EW/DSCT	
F19_057188		16 26 49.7 −55 35 34.3	14.36	89.349	35(3)	0.06(2)	CEP	
F19_057199		16 26 49.0 −56 29 35.0	15.39	81.855	2.43(2)	0.09(5)	VAR	
F19_057227		16 26 48.4 −56 55 38.3	14.45	80.714	0.43083(7)	0.26(2)	EW	
F19_057232	*s*	16 26 48.5 −56 47 31.4	12.57	297.676	61(5)	0.012(4)	VAR	
F19_057315		16 26 49.1 −55 39 21.4	12.19	80.687	0.10047(3)	0.009(6)	DSCT	
F19_057432	*s*	16 26 47.2 −56 57 51.6	13.50	94.896	21(2)	0.03(2)	VAR	
F19_057437		16 26 47.5 −56 43 08.8	11.63	···	···	···	LP	
F19_057510		16 26 47.3 −56 34 54.5	13.93	···	···	···	LP	
F19_057568		16 26 46.6 −56 53 23.9	14.92	81.015	0.4348(3)	0.07(3)	EW	
F19_057630	*s*	16 26 46.9 −56 15 29.3	12.94	80.730	0.06088(2)	0.011(8)	DSCT	
F19_057670		16 26 46.5 −56 26 51.6	12.76	95.979	11.1411(1)	···	VAR	
F19_057688	*s*	16 26 47.2 −55 36 05.6	11.77	···	···	···	LP	
F19_057693	*c*	16 26 46.0 −56 47 13.2	14.58	80.777	0.3665(2)	0.06(3)	EW	F19_057822
F19_057698		16 26 46.3 −56 32 30.2	14.68	81.173	0.6044(2)	0.30(3)	EB	
F19_057713		16 26 46.7 −55 58 02.1	13.26	286.199	84(6)	0.21(2)	VAR	
F19_057734		16 26 46.1 −56 34 09.7	12.68	83.102	6.10(4)	0.036(7)	ROT	
F19_057766	*c*	16 26 45.6 −56 48 05.3	13.14	81.373	5.20(3)	0.12(2)	CEP	
F19_057822	*c*	16 26 45.4 −56 47 11.5	14.38	80.777	0.3665(2)	0.04(2)	EW	F19_057693
F19_057899		16 26 46.2 −55 37 28.9	13.08	135.407	58(2)	0.17(2)	CEP	
F19_057905	*c*	16 26 46.2 −55 28 31.4	13.88	81.055	0.4463(2)	0.15(3)	EW	
F19_057967	*s*	16 26 45.8 −55 37 46.3	13.84	91.993	6.67(7)	0.02(2)	ROT	
F19_058073	*c*⋆	16 26 45.0 −56 02 33.7	14.26	88.240	3.79(2)	0.11(3)	EB	
F19_058114		16 26 45.2 −55 33 57.7	13.79	81.135	8.02(6)	0.05(2)	EB	
F19_058238		16 26 43.6 −56 27 45.4	12.26	···	···	···	SR	
F19_058272	*c*	16 26 43.6 −56 15 42.3	11.98	93.756	39(2)	0.13(2)	VAR	
F19_058303		16 26 42.8 −56 47 01.2	15.94	80.691	0.3536(2)	0.08(7)	EW/DSCT	
F19_058368	⋆	16 26 42.6 −56 38 33.0	13.98	80.956	5.24(2)	0.12(2)	EA	
F19_058376		16 26 43.2 −56 01 30.7	15.26	80.972	0.3355(2)	0.11(4)	EW	
F19_058408	*c*	16 26 42.9 −56 14 39.3	14.83	80.715	0.3652(2)	0.2(1)	EW	
F19_058412		16 26 43.2 −55 58 31.2	11.71	···	···	···	SR	
F19_058510		16 26 42.1 −56 29 57.7	14.78	81.075	2.133(3)	0.27(4)	EA	
F19_058517	⋆	16 26 42.6 −56 00 40.2	16.74	80.806	1.19833(1)	5(1)	EA	
F19_058676	*s*	16 26 42.3 −55 29 26.3	13.18	278.195	42(2)	0.05(2)	VAR	
F19_058683		16 26 41.0 −56 42 36.2	14.81	92.605	3.517(1)	0.35(1)	EA	
F19_058701	*c*	16 26 41.7 −55 51 09.5	15.63	80.694	0.5656(3)	0.7(1)	RR	
F19_058806	*c*	16 26 40.4 −56 38 48.2	11.77	89.445	19.6(5)	0.10(2)	CEP	
F19_058893		16 26 40.9 −55 40 58.7	12.38	···	···	···	SR	
F19_058932		16 26 39.6 −56 42 32.8	14.57	82.680	9.163(1)	0.18(1)	EB	
F19_058934	*s*	16 26 39.7 −56 32 33.7	16.07	80.866	0.4881(7)	0.07(7)	VAR	
F19_058951	*s*	16 26 39.2 −56 49 56.3	14.14	90.355	10.6(3)	0.03(2)	ROT	
F19_058982		16 26 39.4 −56 37 24.4	11.99	93.543	23.4(8)	0.06(2)	VAR	
F19_059018	*s*	16 26 39.6 −56 16 57.8	12.85	82.193	10.3(1)	0.03(1)	VAR	
F19_059070	*s*	16 26 38.6 −56 47 14.4	13.66	80.891	0.3191(2)	0.01(2)	EW/DSCT	
F19_059080		16 26 38.9 −56 30 06.4	15.52	80.674	0.17802(7)	0.11(5)	DSCT	
F19_059087		16 26 39.1 −56 14 09.9	16.01	80.795	0.8641(5)	0.35(7)	EA	
F19_059117		16 26 38.7 −56 34 12.5	14.72	81.002	0.3744(2)	0.06(2)	EW/DSCT	
F19_059156	*c*	16 26 38.3 −56 30 49.6	12.99	80.680	0.3700(1)	0.07(2)	EW	F19_059242

Table E.5: Variable stars in field F19 (continued).

BEST ID	F	α (J2000.0) h m s	δ ° ′ ″	R_B [mag]	T_0 [d] [rHJD]	p [d]	A [mag]	Type	Other Names
F19_059194	*c*	16 26 39.2	−55 45 23.9	14.28	81.287	0.777(2)	0.03(2)	VAR	F19_059295
F19_059227		16 26 39.2	−55 32 06.7	12.10	...	...	...	LP	
F19_059242	*c*	16 26 38.0	−56 30 47.0	12.81	80.679	0.36997(8)	0.056(8)	EW	F19_059156
F19_059295	*c*	16 26 38.6	−55 45 18.1	14.61	81.275	0.777(2)	0.03(3)	VAR	F19_059194
F19_059296	*cs*	16 26 38.7	−55 43 08.5	13.57	81.105	0.5777(7)	0.011(8)	VAR	F19_059297
F19_059297	*cs*	16 26 38.6	−55 43 04.3	13.56	81.096	0.5777(6)	0.01(2)	VAR	F19_059296
F19_059342		16 26 37.5	−56 27 47.5	10.10	...	...	...	SR	
F19_059559	*s*⋆	16 26 35.9	−56 52 49.7	15.04	82.824	3.4122	0.063	EA	
F19_059595	*s*	16 26 35.9	−56 46 26.9	15.63	80.785	0.3329(2)	0.3(2)	EW/DSCT	
F19_059665	*c*	16 26 35.8	−56 33 10.4	14.68	80.694	0.47665(8)	0.40(3)	EW	
F19_059739	*c*⋆	16 26 35.6	−56 24 39.7	13.05	92.720	1.15601(1)	0.39(1)	EA	
F19_059861		16 26 34.3	−56 56 54.0	16.59	81.234	0.644(2)	0.1(2)	VAR	
F19_059963		16 26 33.8	−56 57 34.3	15.38	80.877	0.43773(8)	0.47(5)	EW	
F19_060048	*c*	16 26 33.9	−56 32 32.8	12.50	...	...	...	SR	
F19_060202		16 26 34.0	−55 46 50.3	11.49	...	...	...	LP	
F19_060242		16 26 33.9	−55 45 25.1	16.00	81.222	0.9074(9)	0.14(7)	EA	
F19_060320	*c*	16 26 32.8	−56 18 32.3	12.70	82.437	1.894(3)	0.10(3)	EA	
F19_060360	*s*	16 26 32.9	−56 00 44.8	15.51	80.992	0.5010(3)	0.15(6)	EW	
F19_060421	*c*	16 26 32.7	−55 53 08.2	14.97	81.220	0.5898(3)	0.25(4)	EB	
F19_060473	*c*	16 26 32.6	−55 36 31.7	13.38	80.720	0.5359(2)	0.20(2)	EW	F19_060561, F19_060637
F19_060516	*s*	16 26 31.1	−56 34 38.0	11.41	91.728	26.7(9)	0.05(2)	VAR	
F19_060552		16 26 31.3	−56 18 15.9	13.69	90.120	23.0(8)	0.05(2)	ROT	
F19_060561	*c*	16 26 32.4	−55 36 31.3	13.15	80.721	0.5359(2)	0.17(3)	EW	F19_060473, F19_060637
F19_060637	*c*	16 26 31.8	−55 36 36.4	13.56	80.719	0.5359(2)	0.19(4)	EW	F19_060473, F19_060561
F19_060728		16 26 30.8	−56 07 01.3	12.19	...	...	...	SR	
F19_060756		16 26 30.1	−56 26 50.5	14.21	80.792	0.3637(2)	0.03(2)	EW	
F19_060775	*s*	16 26 31.2	−55 33 51.7	13.25	81.005	0.3845(6)	0.01(1)	VAR	
F19_060815		16 26 31.2	−55 29 11.9	12.80	97.925	43(4)	0.04(2)	VAR	
F19_060821	*c*	16 26 29.4	−56 44 05.8	15.12	80.954	0.3601(2)	0.05(4)	EW/DSCT	F19_060822
F19_060822	*c*	16 26 29.4	−56 44 00.5	15.12	80.959	0.3601(2)	0.04(4)	EW/DSCT	F19_060821
F19_060883		16 26 29.6	−56 22 05.2	11.93	...	...	...	SR	
F19_060945		16 26 30.6	−55 23 45.7	16.98	80.773	0.2490(2)	0.5(2)	VAR	
F19_060952		16 26 28.6	−56 48 09.3	11.58	...	...	...	LP	
F19_061031	*c*	16 26 28.1	−56 52 03.6	14.99	80.985	0.4142(3)	0.12(6)	EW	
F19_061146	*s*	16 26 28.6	−56 05 32.6	14.93	80.746	0.4550(3)	0.11(6)	EB	
F19_061381	*c*	16 26 26.9	−56 30 11.3	12.30	80.723	0.10919(3)	0.08(3)	RR	
F19_061420	*c*	16 26 26.8	−56 25 25.4	13.23	...	...	...	SR	
F19_061453	*c*	16 26 26.0	−56 49 51.3	15.54	81.022	0.4190(2)	0.13(5)	EW	
F19_061497	*s*	16 26 26.3	−56 29 00.7	14.69	88.965	11.1(3)	0.08(3)	EB	
F19_061501	*c*⋆	16 26 26.6	−56 20 15.0	13.60	81.377	1.1389(4)	0.61(4)	EA	
F19_061559		16 26 25.4	−56 57 25.8	14.18	80.901	0.25681(6)	0.10(2)	EW/DSCT	
F19_061569	*c*⋆	16 26 26.4	−56 13 13.0	13.48	122.666	4.745(1)	0.09(1)	EA	
F19_061690		16 26 26.6	−55 35 18.7	12.80	80.692	0.11932(4)	0.014(8)	DSCT	
F19_061741	*c*⋆	16 26 25.8	−56 00 28.5	12.43	93.820	37.64(1)	0.5(1)	EA	
F19_061839		16 26 24.3	−56 38 08.1	13.12	82.407	1.938(8)	0.06(2)	ROT	
F19_061925	*s*	16 26 24.7	−56 12 00.8	13.16	...	...	...	SR	
F19_061939	*c*	16 26 25.3	−55 39 04.9	14.49	80.745	0.19613(9)	0.03(3)	DSCT	F19_062062
F19_062047		16 26 23.8	−56 20 51.5	15.35	82.964	5.22(8)	0.10(5)	ROT	
F19_062062	*c*	16 26 24.8	−55 39 08.5	14.93	80.738	0.19614(9)	0.04(4)	DSCT	F19_061939
F19_062158	*c*	16 26 23.3	−56 16 55.3	14.71	80.770	0.2938(1)	0.08(3)	EW/DSCT	
F19_062192		16 26 23.6	−55 54 50.4	15.18	88.231	10.2(2)	0.11(4)	ROT	
F19_062229		16 26 23.4	−55 56 21.2	15.48	80.711	0.16903(7)	0.05(5)	VAR	
F19_062291		16 26 22.4	−56 20 21.3	15.26	80.759	0.3291(2)	0.14(4)	EW	
F19_062334	*s*	16 26 23.0	−55 57 25.8	15.78	80.710	0.4859(4)	0.09(6)	EB	
F19_062347	*s*	16 26 21.0	−57 00 45.0	12.08	...	...	...	SR	
F19_062431	*s*	16 26 22.0	−56 16 54.8	14.91	80.694	0.26336(9)	0.04(3)	EW/DSCT	
F19_062544	*c*	16 26 22.1	−55 44 13.6	12.57	184.930	70(6)	0.28(3)	VAR	
F19_062573		16 26 21.6	−56 00 56.9	14.92	80.672	0.4111(2)	0.5(2)	EW	
F19_062751		16 26 21.1	−55 46 38.5	14.68	81.259	6.22(5)	0.14(3)	CEP	
F19_063000		16 26 20.1	−55 37 42.4	14.18	93.966	27.0(9)	0.10(2)	CEP	
F19_063074	*s*	16 26 18.0	−56 40 23.9	13.12	81.194	5.3(2)	0.014(8)	VAR	
F19_063332	*c*	16 26 16.6	−56 39 32.4	10.47	...	...	...	LP	
F19_063342		16 26 17.2	−56 15 47.8	12.17	...	...	...	SR	
F19_063613	⋆	16 26 15.7	−56 11 44.0	12.56	82.971	12.2(4)	0.027(8)	VAR	
F19_063687		16 26 15.1	−56 22 07.9	12.97	267.599	54(4)	0.049(7)	ROT	
F19_063932	*c*	16 26 13.7	−56 22 44.8	14.35	80.781	0.2128(2)	0.06(4)	DSCT	F19_064038
F19_064038	*c*	16 26 13.2	−56 22 50.0	14.08	80.788	0.21284(9)	0.06(2)	DSCT	F19_063932
F19_064118	*c*	16 26 12.4	−56 33 37.5	13.47	...	...	...	SR	
F19_064248		16 26 12.8	−55 55 33.3	11.25	...	...	...	SR	
F19_064265	⋆	16 26 11.1	−56 51 24.9	13.83	80.719	4.4663(1)	0.23(1)	EA	
F19_064319		16 26 12.4	−56 03 03.7	15.26	80.872	0.3065(2)	0.05(4)	EW/DSCT	
F19_064489		16 26 12.2	−55 37 12.5	14.77	80.931	2.015(8)	0.05(3)	VAR	
F19_064526	*s*	16 26 11.3	−56 00 32.6	14.54	80.831	0.2659(1)	0.05(4)	EW/DSCT	
F19_064528		16 26 11.3	−55 57 17.5	13.31	...	...	...	SR	
F19_064545	*s*	16 26 09.5	−56 53 53.2	11.58	326.111	100(6)	0.028(6)	VAR	
F19_064572	*c*⋆	16 26 09.9	−56 38 04.2	12.78	81.142	0.9355(4)	0.14(2)	EA	
F19_064600		16 26 11.8	−55 33 47.8	14.28	81.588	2.85(3)	0.02(2)	VAR	
F19_064642	*s*	16 26 11.6	−55 32 24.0	12.34	88.806	4.21(5)	0.016(8)	VAR	
F19_064663		16 26 11.0	−55 50 02.7	11.35	...	...	...	SR	
F19_064698		16 26 11.0	−55 41 16.2	15.83	81.863	9.7(2)	0.10(6)	ROT	
F19_064742		16 26 08.9	−56 39 55.1	15.22	80.710	0.3341(2)	0.09(4)	EW/DSCT	
F19_064782	*c*⋆	16 26 09.0	−56 31 34.1	13.26	179.604	36(1)	0.26(2)	CEP	
F19_064820	*c*	16 26 08.5	−56 45 35.3	14.50	81.071	0.656(2)	0.07(3)	VAR	
F19_064963	*c*⋆	16 26 08.6	−56 14 41.5	12.64	...	...	...	LP	
F19_064974		16 26 09.9	−55 32 56.9	14.64	82.467	1.874(2)	1.02(9)	EA	
F19_064975	*cs*	16 26 10.0	−55 29 26.8	15.13	80.696	0.1932(2)	0.04(4)	VAR	F19_065260
F19_064998		16 26 07.9	−56 31 20.0	15.11	81.359	0.9322	0.050	EA	
F19_065007		16 26 08.8	−56 04 53.9	16.19	81.120	0.5348(4)	0.15(8)	EA	

Table E.5: Variable stars in field F19 (continued).

BEST ID	F	α (J2000.0) h m s	δ ° ′ ″	R_B [mag]	T_0 [d] [rHJD]	p [d]	A [mag]	Type	Other Names
F19_065080		16 26 08.5	−55 58 22.1	15.18	80.688	0.25834(7)	0.09(4)	EW	
F19_065084	⋆	16 26 09.0	−55 40 43.9	13.77	139.540	8.059(1)	0.13(1)	EA	
F19_065205	*c*	16 26 06.7	−56 37 38.4	14.80	81.252	0.6897(6)	0.07(3)	EW	
F19_065260	*cs*	16 26 08.6	−55 29 24.3	14.40	80.682	0.1933(2)	0.02(2)	VAR	F19_064975
F19_065333	*cs*	16 26 06.5	−56 21 34.7	12.33	82.424	13.8(3)	0.016(7)	ROT	
F19_065405		16 26 05.8	−56 31 27.0	14.78	80.716	0.28755(5)	0.25(3)	EW	
F19_065501	*c*	16 26 05.4	−56 28 52.4	11.56	...	...	...	SR	
F19_065510		16 26 05.8	−56 13 55.7	14.79	92.930	2.6603(1)	0.22(1)	EA	
F19_065715	*c*	16 26 04.1	−56 30 38.2	13.17	89.539	5.47(7)	0.11(3)	ROT	F19_065852
F19_065815		16 26 03.9	−56 25 21.6	13.44	80.694	0.3062(2)	0.03(2)	EW/DSCT	
F19_065852	*c*	16 26 03.5	−56 30 36.2	12.97	83.990	5.47(2)	0.106(8)	ROT	F19_065715
F19_065856	⋆	16 26 03.7	−56 26 11.3	13.48	81.923	5.33(2)	0.12(2)	EA	
F19_065882	*c*	16 26 02.5	−56 53 31.0	15.07	82.847	7.6(2)	0.08(3)	ROT	F19_065977
F19_065926	*c*⋆	16 26 03.7	−56 12 48.9	14.08	81.180	3.69(1)	0.11(3)	EA	
F19_065977	*c*	16 26 02.1	−56 53 27.7	14.87	91.797	7.6(2)	0.07(3)	ROT	F19_065882
F19_066096	*c*	16 26 03.4	−55 55 05.7	14.63	80.715	0.30026(9)	0.12(3)	EW	F19_066210
F19_066114	*s*	16 26 01.6	−56 43 56.7	15.93	80.691	0.16148(6)	0.05(7)	VAR	
F19_066118	⋆	16 26 02.2	−56 32 10.6	11.49	247.570	13.917(1)	0.23(1)	EA	
F19_066159		16 26 02.1	−56 26 12.6	13.95	80.731	0.31787(9)	0.04(2)	EW	
F19_066184		16 26 04.0	−55 25 21.1	11.73	...	...	...	SR	
F19_066210	*c*	16 26 02.9	−55 55 07.7	14.35	80.715	0.30026(8)	0.08(2)	EW	F19_066096
F19_066438		16 25 59.4	−56 56 59.2	12.77	...	...	...	SR	
F19_066513	*c*	16 26 00.1	−56 22 22.2	13.26	80.829	0.2934(1)	0.07(4)	EW	F19_066641
F19_066533	⋆	16 25 59.3	−56 49 45.8	13.62	81.005	0.7200(2)	0.72(6)	EA	
F19_066641	*c*	16 25 59.5	−56 22 24.6	12.98	80.831	0.29336(8)	0.04(1)	EW	F19_066513
F19_066647		16 25 59.9	−56 12 55.2	14.47	80.725	0.3004(2)	0.03(2)	EW/DSCT	
F19_066730		16 25 57.8	−56 58 37.1	14.31	152.425	21.9(8)	0.05(2)	ROT	
F19_066737	*c*	16 25 58.6	−56 38 39.4	12.59	...	...	...	SR	
F19_066792	*s*	16 26 00.5	−55 37 59.0	16.27	80.776	0.1754(2)	0.07(9)	VAR	
F19_066817		16 25 59.2	−56 11 28.0	16.36	80.699	0.07065(1)	0.3(1)	DSCT	
F19_066934		16 25 59.0	−55 59 11.9	15.71	82.368	9.34302(1)	0.4(1)	EA	
F19_066944		16 25 59.5	−55 43 53.1	11.67	...	...	...	SR	
F19_066946		16 25 59.6	−55 41 14.9	13.10	89.267	15.2(6)	0.03(2)	VAR	
F19_066981		16 25 59.6	−55 37 14.2	12.52	...	...	...	LP	
F19_067055	*s*	16 25 56.2	−56 58 52.0	11.60	...	...	...	LP	
F19_067060		16 25 56.9	−56 40 04.2	12.99	97.489	10.2(2)	0.022(8)	VAR	
F19_067102	*c*	16 25 56.2	−56 49 33.1	14.15	80.698	1.0288(8)	0.08(2)	EA	F19_067275, F19_067276
F19_067132		16 25 58.8	−55 40 21.5	14.00	81.524	14.1(2)	0.11(2)	EB	
F19_067266	*cs*	16 25 58.0	−55 44 17.3	15.42	80.696	0.2661(2)	0.1(1)	VAR	F19_067388
F19_067270	*c*⋆	16 25 58.4	−55 31 09.2	13.39	81.254	0.7469(2)	0.31(2)	EW	
F19_067275	*c*	16 25 55.5	−56 49 39.2	15.20	80.696	1.029(2)	0.15(5)	EA	F19_067102, F19_067276
F19_067276	*c*	16 25 55.5	−56 49 29.4	14.58	80.697	1.029(1)	0.11(4)	EA	F19_067102, F19_067275
F19_067302	*c*	16 25 58.3	−55 29 57.3	15.07	80.879	0.28572(9)	0.07(3)	EW	F19_067337
F19_067337	*c*	16 25 58.1	−55 29 59.7	15.10	80.879	0.28572(9)	0.08(4)	EW	F19_067302
F19_067375		16 25 55.2	−56 40 07.6	13.28	83.609	10.9(3)	0.020(8)	VAR	
F19_067387		16 25 57.0	−55 52 16.1	15.14	80.786	1.0452(7)	0.7(2)	EA	
F19_067388	*cs*	16 25 57.3	−55 44 22.7	15.99	80.677	0.2661(2)	0.06(8)	VAR	F19_067266
F19_067466	*s*	16 25 54.2	−56 54 30.7	13.30	81.731	1.277(3)	0.02(2)	VAR	
F19_067553	*c*	16 25 54.7	−56 30 09.3	14.85	80.682	0.4577(2)	0.18(4)	EW	
F19_067580		16 25 55.0	−56 18 47.3	15.30	81.325	0.9626(6)	0.42(4)	EA	
F19_067632	*c*⋆	16 25 54.1	−56 33 33.8	13.50	82.190	1.733(1)	0.32(3)	EA	
F19_067768	*c*	16 25 53.9	−56 19 16.7	14.16	80.695	0.4412(2)	0.12(3)	EW	
F19_067820		16 25 55.4	−55 32 25.7	14.50	80.875	0.6150(2)	0.20(3)	EW	
F19_067878		16 25 53.8	−56 07 13.8	14.01	81.584	57(5)	0.08(3)	VAR	
F19_067947	*c*	16 25 54.7	−55 33 59.6	13.39	81.038	0.7707(7)	0.08(2)	RR	F19_068064
F19_067975	⋆	16 25 53.8	−55 55 38.3	14.10	81.810	10.936(1)	0.15(1)	EA	
F19_068060		16 25 53.9	−55 43 34.2	14.78	80.900	0.3892(2)	0.04(3)	EW	
F19_068064	*c*	16 25 54.2	−55 33 55.6	13.35	81.039	0.7707(5)	0.07(2)	RR	F19_067947
F19_068107	⋆	16 25 51.7	−56 30 57.7	12.80	81.052	1.2023(5)	0.24(3)	EB	
F19_068127	*s*	16 25 54.0	−55 28 08.3	16.18	80.731	0.18889(6)	0.06(8)	VAR	
F19_068404	*c*⋆	16 25 48.8	−56 58 36.0	13.76	80.890	0.44391(6)	0.22(2)	EW	
F19_068415		16 25 50.1	−56 27 12.7	14.77	83.331	8.19(6)	0.18(3)	VAR	
F19_068597		16 25 51.3	−55 31 37.4	13.98	...	...	...	LP	
F19_068634		16 25 50.9	−55 39 28.5	15.26	100.765	80(2)	0.07(4)	VAR	
F19_068684	*c*	16 25 48.3	−56 37 19.6	14.93	80.834	0.34317(8)	0.17(3)	EW	
F19_068782	*c*	16 25 49.1	−56 02 44.8	12.17	...	...	...	LP	
F19_068846	*c*	16 25 49.0	−55 56 54.5	12.87	...	...	...	LP	
F19_068853		16 25 49.9	−55 33 05.4	11.83	...	...	...	LP	
F19_068881		16 25 48.9	−55 53 00.3	16.24	80.798	3.79(2)	0.3(2)	EA	
F19_068932	*c*⋆	16 25 47.6	−56 10 53.0	13.33	81.194	1.0072(9)	0.08(2)	EA	
F19_068981	*s*	16 25 48.9	−55 40 18.2	13.12	81.215	1.673(4)	0.04(2)	RR	
F19_069047		16 25 48.4	−55 44 11.2	13.34	...	...	...	SR	
F19_069173	*c*	16 25 45.8	−56 28 04.7	15.16	80.740	0.34024(8)	0.23(4)	EW	
F19_069217		16 25 45.9	−56 23 01.9	13.84	81.109	0.6534(5)	0.05(2)	EW	
F19_069235	*c*	16 25 47.7	−55 37 02.6	13.11	80.978	0.5075(3)	0.18(5)	EW	F19_069388
F19_069304	⋆	16 25 46.8	−55 49 02.1	12.82	80.879	3.119(7)	0.054(8)	EA	
F19_069388	*c*	16 25 47.0	−55 36 57.4	12.88	80.988	0.5075(3)	0.07(2)	EW	F19_069235
F19_069441	*s*	16 25 43.4	−56 51 27.3	15.66	81.641	3.04(3)	0.06(5)	VAR	
F19_069531	*s*	16 25 45.3	−55 55 32.6	15.34	80.989	0.884(2)	0.05(4)	VAR	
F19_069551	*c*	16 25 44.5	−56 10 11.7	12.85	80.898	0.3482(3)	0.04(2)	DSCT	F19_069621
F19_069554	⋆	16 25 44.9	−56 01 14.6	13.27	91.226	5.56(2)	0.22(2)	EB	
F19_069621	*c*	16 25 44.3	−56 10 09.1	12.74	80.905	0.3482(3)	0.034(8)	DSCT	F19_069551
F19_069648	⋆	16 25 43.6	−56 20 32.3	15.27	83.086	8.7742	0.11	EA	
F19_069719		16 25 43.0	−56 26 53.2	11.28	177.802	23(1)	0.10(3)	VAR	
F19_069735	*s*	16 25 44.9	−55 42 56.6	14.38	80.793	0.16883(8)	0.02(2)	VAR	
F19_069789	*c*	16 25 43.8	−55 59 33.8	14.22	80.983	0.3226(1)	0.07(2)	EW	
F19_069796	⋆	16 25 44.4	−55 45 35.9	12.63	81.100	0.8864(2)	0.399(8)	EB	
F19_069853		16 25 42.7	−56 17 08.4	14.42	315.323	70(3)	0.05(2)	VAR	

Table E.5: Variable stars in field F19 (continued).

BEST ID	F	α (J2000.0) h m s	δ ° ′ ″	R_B [mag]	T_0 [d] [rHJD]	p [d]	A [mag]	Type	Other Names
F19_069893	*c*	16 25 41.1	−56 47 44.8	13.44	...	...	...	SR	
F19_069906	*s*	16 25 42.5	−56 14 51.2	12.60	...	...	...	LP	
F19_069997		16 25 43.6	−55 38 03.2	12.57	105.096	27(1)	0.09(2)	CEP	
F19_070000	*c*	16 25 40.7	−56 47 43.7	13.47	...	...	...	SR	
F19_070013		16 25 42.3	−56 04 55.5	14.17	88.127	3.97(2)	0.24(3)	EA	
F19_070092	*c*	16 25 43.0	−55 39 47.0	14.99	80.763	0.3414(2)	0.09(4)	EW	
F19_070132		16 25 39.9	−56 48 52.4	11.88	303.011	83(4)	0.17(2)	VAR	
F19_070189		16 25 42.7	−55 36 55.8	14.13	80.825	0.17946(9)	0.04(3)	VAR	
F19_070359	*s*	16 25 41.6	−55 41 21.2	11.60	...	...	...	LP	
F19_070505	*c*	16 25 39.2	−56 18 56.0	15.34	80.875	0.2910(2)	0.09(6)	EW/DSCT	F19_070722
F19_070644		16 25 40.6	−55 29 18.4	11.41	...	...	...	SR	
F19_070683	⋆	16 25 37.3	−56 37 46.9	13.68	91.722	7.4907(1)	0.07(1)	EA	
F19_070722	*c*	16 25 37.9	−56 18 57.1	13.97	80.877	0.2910(2)	0.02(2)	EW/DSCT	F19_070505
F19_070938		16 25 38.2	−55 47 25.2	11.46	...	...	...	SR	
F19_070995	*s*	16 25 37.3	−56 01 07.3	11.51	82.560	11.6(2)	0.05(2)	VAR	
F19_071025	*s*	16 25 37.2	−55 59 04.3	15.37	81.169	3.36(3)	0.07(4)	EA	
F19_071038	*c*⋆	16 25 35.1	−56 42 50.0	12.92	81.049	0.8630(3)	0.157(8)	EB	
F19_071161		16 25 38.0	−55 25 17.8	11.23	82.435	3.92(3)	0.038(7)	VAR	
F19_071386	*s*	16 25 34.9	−56 01 60.0	16.18	80.708	0.3204(2)	0.10(8)	EW	
F19_071401	*c*	16 25 36.4	−55 30 02.6	13.25	100.810	58(4)	0.08(2)	VAR	
F19_071424	*c*	16 25 35.0	−55 57 44.7	14.35	91.907	6.7(2)	0.06(3)	VAR	F19_071480
F19_071480	*c*	16 25 34.7	−55 57 50.1	14.73	91.769	6.77(9)	0.08(4)	VAR	F19_071424
F19_071609		16 25 33.5	−56 09 33.3	12.17	80.681	75(7)	0.017(6)	VAR	
F19_071721	*s*⋆	16 25 34.5	−55 34 51.3	13.36	92.791	6.46(5)	0.027(8)	ROT	
F19_071755		16 25 30.3	−56 58 39.1	13.34	80.946	0.4281(2)	0.032(8)	EW	
F19_071780	*c*	16 25 33.6	−55 44 09.1	15.27	81.171	0.6203(4)	0.08(4)	EA	
F19_071796	*c*	16 25 31.9	−56 21 43.4	13.01	82.491	2.117(4)	0.050(8)	ROT	
F19_071837	*c*⋆	16 25 31.6	−56 24 13.2	13.79	81.009	0.56259(8)	0.42(2)	EB	
F19_071850	*c*⋆	16 25 32.7	−55 57 54.8	14.56	95.680	4.4205(1)	0.16(1)	EA	
F19_071866		16 25 34.1	−55 27 04.0	12.44	80.705	0.12079(4)	0.018(8)	DSCT	
F19_071874	*c*	16 25 31.4	−56 22 59.1	14.05	81.223	0.6884(3)	0.08(2)	EA	F19_071934
F19_071934	*c*	16 25 31.1	−56 22 54.2	14.34	81.224	0.6884(3)	0.16(3)	EA	F19_071874
F19_071971	*s*	16 25 31.7	−56 04 31.7	12.01	...	...	...	LP	
F19_072013		16 25 31.9	−55 56 33.1	13.63	81.067	0.4020(2)	0.07(2)	EB	
F19_072059	*c*	16 25 28.9	−56 54 07.6	13.71	80.958	0.7250(4)	0.14(2)	RR	F19_072126
F19_072089		16 25 28.4	−56 58 22.4	12.52	...	...	...	LP	
F19_072126	*c*	16 25 28.6	−56 54 03.7	14.09	80.957	0.7250(4)	0.23(3)	RR	F19_072059
F19_072151		16 25 32.1	−55 37 23.7	14.43	80.731	0.4382(2)	0.05(4)	EA	
F19_072311		16 25 28.4	−56 36 57.0	12.63	80.674	0.06765(2)	0.01(2)	DSCT	
F19_072356		16 25 28.8	−56 27 42.3	11.90	80.867	0.35078(8)	0.07(1)	EW	
F19_072375	*s*	16 25 30.8	−55 41 36.0	13.69	80.674	0.2143(2)	0.01(2)	DSCT	
F19_072384	*c*	16 25 27.7	−56 45 31.2	15.05	80.925	0.31794(8)	0.19(4)	EW	F19_072385
F19_072385	*c*	16 25 27.7	−56 45 25.5	15.20	80.926	0.31794(6)	0.31(4)	EW	F19_072384
F19_072553		16 25 26.7	−56 46 30.7	15.02	81.185	0.5628(3)	0.17(4)	EA	
F19_072610		16 25 26.1	−56 53 40.1	12.80	80.687	0.07038(2)	0.02(2)	DSCT	
F19_072821	*s*	16 25 26.1	−56 31 02.4	15.02	100.093	13.2(3)	0.06(4)	VAR	
F19_072846	*c*	16 25 25.0	−56 47 02.8	11.82	88.888	13.9(2)	0.025(8)	VAR	
F19_072875	⋆	16 25 24.8	−56 50 54.8	15.18	80.882	0.35114(7)	0.28(4)	EW	
F19_072897		16 25 28.7	−55 31 23.5	11.81	...	...	...	LP	
F19_072946	*c*	16 25 24.8	−56 43 14.2	14.54	80.816	0.35544(7)	0.18(2)	EW	F19_073066
F19_072960		16 25 26.1	−56 14 06.3	16.62	99.015	39(3)	0.2(2)	VAR	
F19_073014	*s*	16 25 25.3	−56 23 53.6	14.12	88.841	11.7(3)	0.05(3)	ROT	
F19_073066	*c*	16 25 24.3	−56 43 15.2	14.59	80.816	0.35544(7)	0.17(2)	EW	F19_072946
F19_073189		16 25 27.2	−55 30 18.1	12.63	...	...	...	SR	
F19_073243		16 25 25.0	−56 05 53.9	13.44	83.992	20.6(9)	0.026(8)	VAR	
F19_073249	*c*	16 25 25.7	−55 51 36.8	14.31	83.171	3.373(7)	0.24(4)	EA	F19_073306
F19_073290		16 25 23.0	−56 37 29.3	14.89	81.151	0.6403(2)	0.24(3)	EB	
F19_073306	*c*	16 25 25.4	−55 51 42.6	14.71	83.184	3.373(7)	0.20(4)	EA	F19_073249
F19_073361	*c*	16 25 24.0	−56 11 18.4	15.48	80.753	0.27710(8)	0.15(5)	EW	F19_073423
F19_073367	*s*	16 25 25.2	−55 48 43.7	15.55	93.969	7.7(3)	0.08(5)	ROT	
F19_073380		16 25 22.1	−56 46 33.2	13.49	...	...	...	SR	
F19_073423	*c*	16 25 23.6	−56 11 23.9	15.61	80.751	0.27710(9)	0.12(5)	EW	F19_073361
F19_073431	*c*⋆	16 25 24.7	−55 50 31.6	14.88	80.845	2.216(3)	0.22(5)	EA	
F19_073540	*c*	16 25 24.3	−55 45 15.8	13.95	81.734	3.392(4)	0.19(3)	EA	
F19_073607		16 25 23.6	−55 54 22.6	14.46	80.718	0.053556(4)	0.14(2)	DSCT	
F19_073638	*s*	16 25 23.8	−55 45 51.3	12.47	...	...	...	SR	
F19_073702	⋆	16 25 22.3	−56 06 35.9	12.59	80.995	0.3538(2)	0.077(8)	DSCT	
F19_073779		16 25 23.8	−55 31 36.4	11.98	185.298	69(5)	0.19(3)	VAR	
F19_073795		16 25 20.0	−56 42 08.9	12.44	...	...	...	SR	
F19_073882	*c*⋆	16 25 18.8	−56 55 27.5	14.23	80.836	0.40057(6)	0.31(3)	EW	
F19_073952	*c*⋆	16 25 20.0	−56 26 05.0	14.94	80.953	0.6501(3)	0.27(3)	EA	
F19_073969	*s*	16 25 22.2	−55 41 38.1	16.47	80.842	0.17324(8)	0.1(1)	DSCT	
F19_073980		16 25 18.4	−56 52 50.5	11.13	...	...	...	SR	
F19_074014		16 25 22.9	−55 25 01.8	13.63	81.089	0.4546(5)	0.03(3)	VAR	
F19_074065	*c*	16 25 20.4	−56 08 46.4	15.26	80.771	0.42513(7)	0.55(5)	EW	
F19_074076		16 25 21.9	−55 38 59.4	13.90	...	...	...	SR	
F19_074085		16 25 22.5	−55 27 07.5	16.20	80.909	0.4018(2)	0.25(8)	EW/DSCT	
F19_074152		16 25 19.8	−56 09 50.0	14.27	80.914	0.3076(2)	0.01(2)	EW	
F19_074277		16 25 17.2	−56 44 37.2	12.87	81.086	0.650(2)	0.03(3)	RR	
F19_074316		16 25 18.6	−56 16 00.2	12.46	...	...	...	SR	
F19_074336	*c*	16 25 16.3	−56 56 57.0	12.49	...	...	...	LP	
F19_074350	*s*	16 25 18.6	−56 10 18.1	13.35	81.505	6.49(5)	0.025(8)	EB	
F19_074424		16 25 17.7	−56 22 34.6	14.14	81.897	5.80(4)	0.07(2)	ROT	
F19_074467	*cs*	16 25 20.0	−55 34 03.2	13.76	80.744	0.13397(6)	0.01(2)	DSCT	F19_074571
F19_074500		16 25 19.4	−55 44 21.4	15.53	82.347	4.94(7)	0.10(5)	ROT	
F19_074539		16 25 19.1	−55 46 35.8	16.34	89.727	5.61(7)	0.2(1)	ROT	
F19_074547		16 25 15.6	−56 49 41.6	15.04	82.800	5.29(5)	0.16(4)	CEP	
F19_074571	*cs*	16 25 19.6	−55 33 58.6	13.82	80.751	0.13397(6)	0.02(2)	DSCT	F19_074467

Table E.5: Variable stars in field F19 (continued).

BEST ID	F	α (J2000.0) h m s	δ ° ′ ″	R_B [mag]	T_0 [d] [rHJD]	p [d]	A [mag]	Type	Other Names
F19_074621		16 25 17.3	−56 09 19.2	15.94	80.734	0.3126(2)	0.13(6)	EW	
F19_074676		16 25 16.2	−56 25 55.3	11.16	···	···	···	LP	
F19_074719	$s\star$	16 25 16.4	−56 17 15.2	12.58	···	···	···	EA	
F19_074824		16 25 17.9	−55 39 56.7	15.14	123.456	12.6(2)	0.08(4)	EB	
F19_074891	$c\star$	16 25 14.5	−56 33 11.8	13.37	80.981	1.0284(4)	0.38(3)	EW	
F19_074935	$\star$	16 25 14.8	−56 22 37.6	16.13	81.170	0.9582(5)	1.1(2)	EA	
F19_075011		16 25 15.2	−56 08 27.7	12.58	···	···	···	SR	
F19_075094		16 25 13.4	−56 33 03.7	11.32	···	···	···	SR	
F19_075144		16 25 16.8	−55 26 58.8	14.21	92.394	8.2(2)	0.09(3)	VAR	
F19_075170	s	16 25 15.4	−55 51 32.3	11.25	···	···	···	SR	
F19_075266		16 25 15.6	−55 35 36.1	11.16	82.452	13.6(3)	0.031(8)	VAR	
F19_075397	s	16 25 10.6	−56 52 23.0	12.11	90.572	11.3(3)	0.013(6)	ROT	
F19_075402		16 25 11.7	−56 32 57.7	14.91	187.257	16.9(6)	0.11(4)	VAR	
F19_075433		16 25 14.8	−55 34 57.5	14.84	83.721	31(3)	0.11(3)	VAR	
F19_075532		16 25 14.0	−55 42 42.0	14.60	80.851	0.3140(1)	0.05(2)	EW	
F19_075666	$cs\star$	16 25 09.5	−56 46 34.1	12.51	81.135	1.875(4)	0.015(6)	EA	
F19_075779	c	16 25 12.8	−55 34 14.3	15.07	139.086	31(2)	0.08(4)	VAR	
F19_075788	s	16 25 08.7	−56 49 17.8	14.74	80.981	0.3467(2)	0.02(3)	EW/DSCT	
F19_075856		16 25 12.8	−55 31 52.3	12.92	···	···	···	SR	
F19_075884	c	16 25 12.5	−55 34 16.1	14.70	141.055	31(2)	0.05(3)	VAR	
F19_075997		16 25 10.7	−55 53 57.6	10.36	···	···	···	LP	
F19_076012		16 25 07.7	−56 44 10.6	14.73	80.912	0.26616(8)	0.06(3)	EW	
F19_076048		16 25 09.2	−56 14 33.2	15.32	80.800	0.33117(6)	0.37(4)	EW	
F19_076092		16 25 09.8	−56 01 01.1	15.42	80.960	0.31421(9)	0.17(5)	EW	
F19_076211		16 25 08.7	−56 06 22.9	11.64	308.347	100(2)	0.033(8)	VAR	
F19_076324	s	16 25 10.7	−55 23 59.4	13.20	82.901	15.3(5)	0.04(2)	CEP	
F19_076327	s	16 25 05.6	−56 48 47.0	15.72	123.360	18.4(6)	0.11(5)	EB	
F19_076345	$\star$	16 25 08.6	−55 56 28.0	13.53	109.940	2.9632(1)	0.05(1)	EB	
F19_076351		16 25 10.2	−55 27 56.3	13.08	95.144	34(2)	0.07(2)	ROT	
F19_076396		16 25 07.4	−56 11 02.9	16.80	80.743	0.4884(3)	0.5(2)	EA	
F19_076426		16 25 08.0	−55 58 00.7	15.14	152.187	44(5)	0.08(4)	VAR	
F19_076455	cs	16 25 07.6	−56 02 01.5	14.69	80.688	0.22552(6)	0.03(3)	EW/DSCT	F19_076589
F19_076529	s	16 25 08.4	−55 40 41.7	12.27	···	···	···	LP	
F19_076582		16 25 06.1	−56 14 54.5	11.95	···	···	···	SR	
F19_076589	cs	16 25 06.9	−56 02 01.3	14.73	80.687	0.22552(7)	0.05(4)	EW/DSCT	F19_076455
F19_076609		16 25 04.5	−56 39 58.0	12.53	80.676	0.1971(1)	0.009(6)	VAR	
F19_076711	c	16 25 02.9	−56 54 11.5	13.71	80.811	0.2502(2)	0.03(1)	DSCT	F19_076837
F19_076788	c	16 25 05.6	−56 00 38.2	15.07	80.736	0.14438(5)	0.08(4)	DSCT	F19_076909
F19_076807	c	16 25 03.6	−56 36 26.2	13.66	80.756	0.20588(5)	0.09(2)	DSCT	
F19_076827	$c\star$	16 25 06.6	−55 43 31.6	13.59	82.576	2.602(3)	0.17(4)	EA	
F19_076837	c	16 25 02.4	−56 54 13.1	13.79	80.810	0.2502(2)	0.04(2)	DSCT	F19_076711
F19_076846		16 25 03.8	−56 26 50.1	14.36	94.658	23(1)	0.04(2)	ROT	
F19_076894	s	16 25 02.4	−56 47 37.9	16.48	141.123	21(2)	0.2(1)	VAR	
F19_076909	c	16 25 05.1	−56 00 37.0	15.06	80.735	0.14438(5)	0.07(3)	DSCT	F19_076788
F19_076992		16 25 02.0	−56 43 06.9	15.39	90.265	5.21(7)	0.06(4)	ROT	
F19_077020		16 25 03.5	−56 13 07.2	13.00	···	···	···	LP	
F19_077041	s	16 25 01.4	−56 49 41.0	13.73	95.875	26(2)	0.06(3)	EB	
F19_077205		16 25 00.4	−56 49 04.8	15.68	80.857	0.41900(9)	0.42(6)	EW	
F19_077225	s	16 25 03.1	−56 02 35.2	12.39	80.734	0.4300(5)	0.01(1)	VAR	
F19_077258	$c\star$	16 25 04.5	−55 36 36.6	15.39	81.044	0.4240(2)	0.40(6)	EW	
F19_077290	$\star$	16 25 01.0	−56 31 02.8	15.22	80.905	0.7349(3)	0.44(4)	EA	
F19_077346	c	16 24 59.6	−56 48 31.1	13.55	81.045	0.4051(2)	0.022(8)	EW	
F19_077481		16 25 01.7	−56 01 08.6	16.41	80.716	0.055750(8)	0.12(9)	DSCT	
F19_077523		16 24 59.2	−56 36 49.1	12.67	···	···	···	LP	
F19_077574	s	16 25 01.2	−56 01 39.3	14.53	82.569	2.55(2)	0.03(2)	VAR	
F19_077589	c	16 25 03.2	−55 28 29.2	12.88	···	···	···	LP	
F19_077593	c	16 25 03.5	−55 23 24.1	15.79	80.869	0.3934(2)	0.43(7)	EB	
F19_077643	s	16 25 01.3	−55 54 42.9	12.02	273.064	67(9)	0.13(3)	VAR	
F19_077652		16 25 02.5	−55 34 28.7	15.58	80.885	0.3229(2)	0.07(5)	EW	
F19_077665		16 24 58.7	−56 34 09.5	15.10	80.680	0.9581(8)	0.13(4)	EA	
F19_077755	c	16 24 57.1	−56 52 25.5	14.76	80.902	0.29133(9)	0.07(3)	EW	F19_077882
F19_077767	$c\star$	16 24 58.6	−56 26 45.7	15.33	80.802	2.185(4)	0.08(4)	EA	
F19_077838	$\star$	16 25 00.3	−55 50 55.4	14.06	81.118	1.1191(6)	0.15(2)	EA	
F19_077882	c	16 24 56.5	−56 52 25.4	14.75	80.902	0.29133(8)	0.08(3)	EW	F19_077755
F19_077956		16 24 57.4	−56 27 27.5	13.26	···	···	···	LP	
F19_077973	$\star$	16 25 00.0	−55 44 57.6	11.82	91.940	8.616(1)	0.2(1)	EA	
F19_078013		16 25 01.1	−55 25 46.6	13.42	···	···	···	LP	
F19_078186		16 24 55.7	−56 36 31.4	11.96	···	···	···	LP	
F19_078206		16 24 59.5	−55 35 14.4	12.30	80.749	0.11420(4)	0.02(2)	DSCT	
F19_078229	s	16 24 56.2	−56 25 55.9	15.20	81.025	0.3936(3)	0.04(4)	EW/DSCT	
F19_078273	s	16 24 58.0	−55 51 04.8	14.91	80.731	0.2304(2)	0.02(3)	VAR	
F19_078350	$c\star$	16 24 54.4	−56 43 51.5	14.16	81.631	1.169(2)	0.06(2)	EB	
F19_078431	s	16 24 56.2	−56 07 11.0	11.41	80.696	0.054974(9)	0.008(7)	DSCT	
F19_078469		16 24 57.7	−55 40 58.0	15.62	80.874	0.4516(2)	0.22(5)	EA	
F19_078494		16 24 56.5	−55 57 50.4	14.78	112.643	27(2)	0.14(3)	VAR	
F19_078549		16 24 55.5	−56 06 59.5	13.92	80.804	0.5968(3)	0.19(3)	EW	
F19_078636		16 24 55.0	−56 07 43.8	14.13	82.674	2.233(4)	0.16(7)	EA	
F19_078722	s	16 24 53.6	−56 21 42.3	13.07	81.178	0.599(2)	0.02(2)	VAR	
F19_078758	s	16 24 55.9	−55 42 29.6	14.33	80.735	0.2718(1)	0.03(2)	EW	
F19_078865		16 24 53.2	−56 15 33.3	13.53	82.131	5.8(2)	0.02(1)	ROT	
F19_078880		16 24 55.9	−55 32 21.2	11.60	···	···	···	LP	
F19_078917		16 24 50.3	−56 55 22.4	16.45	81.279	1.618(3)	0.2(2)	EA	
F19_078941	c	16 24 53.8	−55 59 45.8	11.49	···	···	···	LP	
F19_078951	c	16 24 56.0	−55 27 04.2	11.82	···	···	···	SR	
F19_078985		16 24 50.4	−56 48 29.7	13.35	82.452	2.41(1)	0.05(2)	VAR	
F19_079009		16 24 53.6	−55 57 12.1	14.68	80.872	2.38(2)	0.03(3)	VAR	
F19_079015		16 24 54.6	−55 41 51.9	14.93	80.983	0.3568(2)	0.12(3)	EW	
F19_079023	s	16 24 50.2	−56 48 59.3	11.02	···	···	···	SR	

Table E.5: Variable stars in field F19 (continued).

BEST ID	F	α (J2000.0) h m s	δ ° ′ ″	R_B [mag]	T_0 [d] [rHJD]	p [d]	A [mag]	Type	Other Names
F19_079051	*s*	16 24 54.8	−55 35 59.2	13.52	146.508	14.6(4)	0.04(2)	VAR	
F19_079057	*s*	16 24 49.6	−56 54 07.8	11.78	80.699	1.144(3)	0.02(1)	VAR	
F19_079208		16 24 54.4	−55 29 03.4	12.19	82.523	3.1921(1)	0.023(1)	EB	
F19_079221		16 24 49.5	−56 42 44.7	13.20	...	...	...	SR	
F19_079253	*c*	16 24 48.4	−56 57 42.4	13.69	...	...	...	LP	
F19_079278	*c*	16 24 48.1	−56 57 45.4	13.64	...	...	...	LP	
F19_079282	*c*⋆	16 24 48.6	−56 51 14.9	14.99	81.155	0.6707(4)	0.24(6)	EB	
F19_079285	*s*	16 24 49.2	−56 41 38.6	11.84	146.322	66(5)	0.010(4)	VAR	
F19_079299		16 24 51.8	−56 01 25.6	14.19	...	...	...	LP	
F19_079335	*s*	16 24 53.0	−55 39 14.9	13.62	82.697	3.84(3)	0.05(2)	CEP	
F19_079563	*c*	16 24 51.4	−55 44 50.0	15.75	80.673	0.3562(2)	0.3(1)	EW	F19_079707
F19_079581	⋆	16 24 48.9	−56 20 09.3	13.76	81.830	2.395(6)	0.05(2)	EB	
F19_079647		16 24 47.5	−56 36 57.3	13.51	80.692	0.19517(7)	0.04(2)	DSCT	
F19_079707	*c*	16 24 50.7	−55 44 54.3	15.74	80.675	0.3562(2)	0.17(9)	EW	F19_079563
F19_079713	⋆	16 24 51.8	−55 28 28.4	12.07	81.396	1.223(2)	0.070(8)	VAR	
F19_079741		16 24 49.8	−55 55 45.7	14.47	80.976	0.939(2)	0.06(3)	EW	
F19_079766	*c*	16 24 49.0	−56 04 12.1	11.82	...	...	...	VAR	
F19_079814	*c*	16 24 45.8	−56 49 11.6	11.47	...	...	...	LP	
F19_079865	*s*	16 24 49.4	−55 51 32.0	13.82	80.771	0.4819(3)	0.03(2)	EB	
F19_079888		16 24 47.4	−56 20 55.6	11.30	...	...	...	SR	
F19_080007		16 24 44.5	−56 54 50.5	14.79	80.728	0.2105(2)	0.04(6)	DSCT	
F19_080025		16 24 47.4	−56 10 21.5	13.07	...	...	...	LP	
F19_080038		16 24 49.3	−55 39 20.0	13.94	96.138	8.31(5)	0.09(2)	EB	
F19_080047	*s*	16 24 44.4	−56 51 31.3	14.04	81.297	2.71(2)	0.04(2)	ROT	
F19_080048		16 24 44.8	−56 48 01.5	14.71	275.871	42(3)	0.13(3)	EB	
F19_080135	*s*	16 24 43.8	−56 53 42.0	13.26	91.390	6.89(5)	0.02(2)	ROT	
F19_080161	*c*	16 24 48.0	−55 50 35.2	14.59	81.683	1.223(4)	0.05(3)	VAR	
F19_080181		16 24 44.9	−56 32 22.2	15.61	80.712	0.4031(2)	0.13(5)	EB	
F19_080243	*cs*	16 24 44.5	−56 34 30.1	15.20	80.687	0.4243(3)	0.04(4)	EB	F19_080444
F19_080257		16 24 47.0	−55 57 00.3	12.80	...	...	...	SR	
F19_080272		16 24 43.8	−56 42 11.5	14.69	80.882	0.4060(2)	0.04(2)	EW	
F19_080273	*c*	16 24 44.3	−56 33 38.7	14.35	80.780	0.4065(2)	0.17(2)	RR	
F19_080297	*c*	16 24 48.8	−55 28 45.8	13.48	...	...	...	LP	
F19_080321		16 24 46.9	−55 53 34.4	11.76	...	...	...	LP	
F19_080385		16 24 45.9	−56 01 36.7	10.39	80.678	0.09663(4)	0.02(2)	DSCT	
F19_080387	*s*	16 24 46.7	−55 50 58.7	12.71	187.821	29(2)	0.018(8)	VAR	
F19_080444	*cs*	16 24 43.5	−56 34 27.5	15.00	80.686	0.4243(3)	0.05(3)	EB	F19_080243
F19_080508		16 24 43.6	−56 26 24.1	15.35	81.067	0.4084(2)	0.12(4)	EB	
F19_080552	*c*⋆	16 24 46.0	−55 48 07.1	15.35	81.017	0.4822(2)	0.77(6)	RR	
F19_080612	*s*	16 24 43.4	−56 21 35.1	14.75	80.718	0.2820(2)	0.02(3)	EW/DSCT	
F19_080659		16 24 40.9	−56 56 23.4	12.33	127.479	19.9(5)	0.07(2)	VAR	
F19_080672	*c*	16 24 42.6	−56 28 39.8	13.75	80.757	0.3767(2)	0.03(3)	EW/DSCT	F19_080803
F19_080803	*c*	16 24 42.0	−56 28 44.0	13.50	80.950	0.3766(2)	0.03(2)	EW/DSCT	F19_080672
F19_080871		16 24 42.7	−56 12 04.6	12.30	270.970	128(7)	0.126(8)	EB	
F19_080971	*c*⋆	16 24 43.6	−55 50 07.9	13.68	80.717	0.34913(6)	0.26(3)	EW	
F19_080985		16 24 40.2	−56 39 03.8	12.81	...	...	...	LP	
F19_080993	⋆	16 24 40.8	−56 28 25.8	13.16	126.244	48(3)	0.80(9)	VAR	
F19_081002		16 24 42.3	−56 07 36.4	12.74	81.909	1.346(4)	0.05(2)	ROT	
F19_081022		16 24 39.4	−56 48 17.4	14.74	80.748	0.2780(1)	0.12(8)	EW	
F19_081025	*s*	16 24 39.7	−56 42 26.1	11.41	100.362	14.9(2)	0.05(2)	VAR	
F19_081038		16 24 43.2	−55 49 37.8	15.31	80.987	0.3200(2)	0.08(6)	EW	
F19_081099		16 24 41.9	−56 03 56.3	15.49	81.116	0.4586(3)	0.13(6)	EW	
F19_081117		16 24 39.3	−56 40 11.0	15.41	97.243	36(4)	0.07(4)	VAR	
F19_081134		16 24 43.7	−55 35 51.2	11.99	96.578	19.4(6)	0.08(2)	VAR	
F19_081169		16 24 44.0	−55 29 08.1	11.94	...	...	...	LP	
F19_081228		16 24 42.6	−55 43 31.3	15.52	80.677	0.28573(7)	0.18(5)	EW	
F19_081297		16 24 38.1	−56 43 45.9	14.95	80.671	0.26935(8)	0.06(3)	EW	
F19_081389	*c*	16 24 37.8	−56 39 43.4	13.42	95.305	18.0(3)	0.07(2)	VAR	
F19_081503	*c*	16 24 40.4	−55 50 35.4	14.28	80.815	0.4846(2)	0.09(2)	EB	
F19_081575	*c*	16 24 41.2	−55 37 13.5	16.11	80.855	0.3856(2)	0.5(1)	EW	
F19_081630	*s*	16 24 39.3	−55 59 20.3	11.73	...	...	...	SR	
F19_081744		16 24 37.7	−56 11 51.6	16.28	82.183	1.719(2)	0.4(2)	EA	
F19_081748	*c*	16 24 39.5	−55 46 41.8	14.13	81.444	7.8(1)	0.13(4)	ROT	F19_081913
F19_081770	*c*	16 24 36.2	−56 30 53.0	14.26	81.051	0.4765(6)	0.03(2)	EW/DSCT	F19_081898
F19_081850	*c*	16 24 33.9	−56 56 21.5	14.70	80.842	0.42888(8)	0.25(3)	EW	
F19_081868	*s*	16 24 37.5	−56 05 42.0	13.72	95.666	17.9(6)	0.02(1)	ROT	
F19_081898	*c*	16 24 35.7	−56 30 51.3	14.39	81.054	0.4766(5)	0.04(2)	EW/DSCT	F19_081770
F19_081913	*c*	16 24 38.7	−55 46 42.6	13.80	81.201	7.8(2)	0.06(3)	ROT	F19_081748
F19_082185	*c*⋆	16 24 34.4	−56 25 28.1	13.55	81.977	2.486(2)	0.36(2)	EA	
F19_082197		16 24 38.6	−55 25 33.3	11.03	81.830	2.502(6)	0.067(8)	VAR	
F19_082232		16 24 32.5	−56 47 21.3	14.10	80.836	0.7168(2)	0.25(2)	EW	
F19_082399	*s*	16 24 30.7	−56 59 57.4	13.00	81.068	0.6441(4)	0.010(8)	EA	
F19_082487	*s*	16 24 36.6	−55 33 14.2	13.68	80.778	0.939(2)	0.03(2)	RR	
F19_082503		16 24 31.6	−56 39 42.0	12.36	80.736	0.3464(2)	0.009(4)	EW/DSCT	
F19_082553	*s*	16 24 36.4	−55 29 12.5	14.61	80.715	0.3967(3)	0.04(3)	VAR	
F19_082627	*s*	16 24 35.4	−55 38 22.8	15.95	80.939	0.3060(2)	0.07(7)	EW	
F19_082629		16 24 29.6	−56 57 15.5	13.39	95.635	34(2)	0.07(2)	CEP	
F19_082633		16 24 31.2	−56 34 07.8	11.70	...	...	...	SR	
F19_082749		16 24 35.5	−55 28 10.9	14.52	95.877	23.7(6)	0.22(3)	CEP	
F19_082935		16 24 31.7	−56 05 50.9	12.72	171.822	21.2(7)	0.04(2)	VAR	
F19_083040		16 24 28.5	−56 41 12.0	12.60	...	...	...	LP	
F19_083148		16 24 30.5	−56 04 41.6	15.52	82.336	2.068(3)	0.33(7)	EA	
F19_083180	⋆	16 24 31.7	−55 46 38.6	13.52	91.480	6.02(6)	0.03(1)	ROT	
F19_083357	*c*	16 24 26.5	−56 43 56.7	14.37	80.962	0.4058(2)	0.07(3)	EW	F19_083416
F19_083416	*c*	16 24 26.1	−56 44 00.9	14.09	80.963	0.4058(2)	0.07(3)	EW	F19_083357
F19_083423		16 24 28.2	−56 13 43.3	12.49	...	...	...	LP	
F19_083511	*c*	16 24 24.5	−56 58 42.2	13.41	80.854	0.6818(3)	0.09(2)	EW	
F19_083584		16 24 25.8	−56 36 38.8	11.98	80.687	0.045986(6)	0.012(8)	DSCT	

Table E.5: Variable stars in field F19 (continued).

BEST ID	F	α (J2000.0) δ	R_B	T_0 [d]	p [d]	A	Type	Other Names
		h m s ° ′ ″	[mag]	[rHJD]		[mag]		
F19_083682		16 24 29.5 −55 41 40.0	14.85	81.018	0.5516(4)	0.14(4)	RR	
F19_083756		16 24 23.4 −56 54 58.2	15.59	80.758	0.3847(3)	0.09(5)	EW/DSCT	
F19_083834	c	16 24 24.2 −56 39 41.0	11.07	...	...	...	LP	
F19_083852	c	16 24 27.0 −56 00 52.8	14.30	96.995	11.7(4)	0.05(2)	ROT	F19_083941
F19_083857		16 24 29.0 −55 35 32.7	14.13	96.322	23.3(7)	0.06(3)	VAR	
F19_083941	c	16 24 26.5 −56 00 58.0	14.18	96.886	11.7(3)	0.09(3)	ROT	F19_083852
F19_084092	c	16 24 24.0 −56 22 21.5	14.11	81.048	0.3936(2)	0.06(2)	EW	F19_084093
F19_084093	c	16 24 24.1 −56 22 15.0	14.03	81.047	0.3936(2)	0.05(3)	EW	F19_084092
F19_084138	s	16 24 20.9 −56 58 36.4	15.83	80.794	0.17578(9)	0.08(7)	VAR	
F19_084139	⋆	16 24 21.6 −56 50 53.5	15.66	81.537	1.2309(7)	0.55(6)	EA	
F19_084280	s	16 24 24.7 −55 58 19.7	14.48	80.736	0.10283(3)	0.03(2)	DSCT	
F19_084284	s	16 24 25.8 −55 44 17.5	16.11	80.816	0.2946(2)	0.1(2)	EW/DSCT	
F19_084298		16 24 20.7 −56 50 06.9	16.14	80.719	0.060730(9)	0.1(2)	DSCT	
F19_084352	c	16 24 26.1 −55 36 56.1	12.41	...	...	...	LP	
F19_084369		16 24 22.7 −56 17 56.2	14.73	80.677	0.41132(9)	0.20(3)	EW	
F19_084403		16 24 24.1 −55 56 51.5	12.10	82.123	16.9(3)	0.040(7)	EB	
F19_084494		16 24 19.0 −56 54 27.3	13.75	83.501	7.8(1)	0.02(2)	VAR	
F19_084495		16 24 19.2 −56 53 33.7	14.91	80.790	0.17885(9)	0.06(3)	DSCT	
F19_084572		16 24 22.0 −56 11 56.0	12.46	134.273	23.6(7)	0.09(3)	VAR	
F19_084611		16 24 24.0 −55 43 08.3	13.02	96.445	11.6(4)	0.034(8)	VAR	
F19_084725	s	16 24 20.6 −56 17 21.4	13.93	82.199	1.690(4)	0.02(2)	VAR	
F19_084877	s	16 24 20.3 −56 09 30.8	13.96	127.726	80(2)	0.05(2)	VAR	
F19_084994		16 24 16.7 −56 49 26.4	14.66	81.470	1.393(4)	0.04(3)	VAR	
F19_085032	s	16 24 18.2 −56 27 31.8	11.95	270.961	100(1)	0.011(4)	VAR	
F19_085166	s⋆	16 24 18.4 −56 14 49.9	14.81	88.870	12.1736	0.11	EA	
F19_085187		16 24 16.0 −56 43 32.4	11.55	82.357	4.72(5)	0.019(6)	ROT	
F19_085229		16 24 18.5 −56 10 13.5	14.97	81.357	1.354(4)	0.07(4)	VAR	
F19_085244	s	16 24 14.6 −56 55 59.8	15.73	81.640	1.606(3)	0.10(6)	EA	
F19_085308	s	16 24 15.1 −56 46 00.7	12.09	...	...	...	SR	
F19_085335	s	16 24 14.2 −56 56 27.6	12.10	80.687	0.2714(1)	0.005(4)	EW/DSCT	
F19_085415		16 24 17.7 −56 05 59.2	14.26	81.457	0.904(2)	0.05(3)	VAR	
F19_085545	c	16 24 14.5 −56 35 18.5	14.04	80.817	0.3029(2)	0.10(6)	EW	F19_085595
F19_085556	s	16 24 17.6 −55 56 28.5	13.06	81.134	0.679(2)	0.02(2)	RR	
F19_085575	s	16 24 17.6 −55 54 09.0	16.29	141.206	27(2)	0.3(1)	CEP	
F19_085595	c	16 24 14.1 −56 35 26.4	13.44	80.814	0.3029(2)	0.022(8)	EW	F19_085545
F19_085628	c	16 24 13.6 −56 41 17.0	14.96	81.095	0.5400(8)	0.04(3)	VAR	F19_085677
F19_085677	c	16 24 13.3 −56 41 22.2	14.98	81.061	0.5401(7)	0.03(3)	VAR	F19_085628
F19_085720	c	16 24 14.8 −56 18 31.4	12.25	...	...	...	SR	
F19_085723		16 24 15.9 −56 05 34.3	14.42	80.939	0.6974(6)	0.05(2)	EB	
F19_085771	c⋆	16 24 11.4 −56 56 51.4	14.92	81.411	2.644(3)	0.42(5)	EA	
F19_085862		16 24 13.9 −56 21 40.7	15.49	81.553	1.037(2)	0.12(7)	EW	
F19_086047		16 24 10.6 −56 49 42.3	13.68	188.354	56(2)	0.17(2)	CEP	
F19_086088		16 24 13.3 −56 13 53.0	11.84	80.749	0.5257(3)	0.020(6)	RR	
F19_086184		16 24 14.9 −55 45 51.9	14.09	135.779	16.1(3)	0.17(3)	CEP	
F19_086208		16 24 12.8 −56 10 13.8	15.16	80.783	0.11865(5)	0.04(3)	DSCT	
F19_086209		16 24 13.3 −56 04 10.5	15.84	81.300	0.7126(5)	0.32(8)	EA	
F19_086212		16 24 13.7 −55 58 01.0	13.82	92.828	6.71(2)	0.07(2)	EB	
F19_086369		16 24 12.0 −56 10 43.7	11.59	80.788	0.15373(7)	0.01(2)	DSCT	
F19_086429	s	16 24 09.7 −56 33 26.0	14.31	81.448	0.886(2)	0.03(2)	EB	
F19_086476	s	16 24 13.3 −55 46 08.1	12.24	...	...	...	SR	
F19_086607	s	16 24 08.4 −56 36 38.2	15.36	80.756	0.13794(4)	0.05(5)	DSCT	
F19_086614		16 24 09.7 −56 21 27.8	12.71	80.721	0.057823(9)	0.01(1)	DSCT	
F19_086712	c⋆	16 24 06.7 −56 48 55.4	14.39	80.734	0.4679(2)	0.40(5)	RR	
F19_086745	c	16 24 12.9 −55 33 58.6	13.79	80.685	0.4117(2)	0.04(2)	EW/DSCT	F19_086787
F19_086787	c	16 24 12.6 −55 34 03.7	13.90	80.692	0.4117(2)	0.04(2)	EW/DSCT	F19_086745
F19_086809	s	16 24 09.7 −56 05 33.8	15.17	97.229	12.8(3)	0.12(4)	EB	
F19_086812	s	16 24 10.7 −55 52 32.9	12.56	...	...	...	SR	
F19_086922	c	16 24 12.1 −55 29 59.0	15.65	80.830	0.4515(2)	0.24(6)	EW	
F19_086960		16 24 06.2 −56 37 07.5	11.17	...	...	...	SR	
F19_086963	s	16 24 06.6 −56 33 34.9	14.18	80.714	0.488121(1)	...	EA	
F19_086972	c	16 24 08.4 −56 11 09.6	11.87	...	...	...	LP	
F19_087086		16 24 05.5 −56 37 57.1	15.87	80.971	0.5713(2)	0.68(7)	EW	
F19_087129		16 24 08.7 −55 57 19.2	14.29	80.938	0.32236(9)	0.09(3)	EW	
F19_087169		16 24 11.4 −55 23 21.6	11.12	...	...	...	LP	
F19_087211	c	16 24 06.6 −56 16 25.8	14.50	80.734	0.34916(9)	0.14(3)	EW	
F19_087319	c	16 24 04.1 −56 38 02.8	15.70	81.103	0.6254(5)	0.15(5)	EW	F19_087347
F19_087347	c	16 24 03.9 −56 38 07.6	15.70	81.103	0.6254(5)	0.12(5)	EW	F19_087319
F19_087542	⋆	16 24 05.3 −56 10 55.0	14.66	94.710	17.177(1)	0.4(1)	EA	
F19_087584	⋆	16 24 05.9 −56 01 45.8	15.63	81.204	1.886(2)	0.60(6)	EA	
F19_087590	c⋆	16 24 07.3 −55 45 12.1	14.20	80.726	0.7971(2)	0.32(2)	EW	
F19_087731		16 24 07.6 −55 30 25.8	16.01	81.194	0.5466(3)	0.34(8)	EA	
F19_087744	s	16 24 03.1 −56 21 08.2	13.85	99.168	14.0(5)	0.02(2)	VAR	
F19_087792	s	16 24 04.2 −56 05 53.1	13.91	277.294	58(6)	0.03(2)	VAR	
F19_087819	s	16 24 03.2 −56 16 36.6	15.07	80.792	0.3220(2)	0.03(3)	EW/DSCT	
F19_087821	c	16 24 04.5 −56 00 56.6	14.77	80.822	0.3739(2)	0.18(6)	EW/DSCT	
F19_087840	c	16 24 01.0 −56 40 09.0	15.29	80.721	0.22692(9)	0.15(4)	RR	F19_087948
F19_087859		16 24 05.7 −55 44 27.9	12.53	...	...	...	SR	
F19_087945	c	16 23 58.8 −56 58 50.1	11.34	90.374	37(2)	0.08(2)	CEP	
F19_087948	c	16 24 00.3 −56 40 07.9	15.16	80.715	0.2269(2)	0.10(4)	RR	F19_087840
F19_088042	c	16 24 06.4 −55 24 50.8	11.75	80.704	0.18899(4)	0.08(1)	DSCT	
F19_088056	s	16 24 00.8 −56 27 44.6	13.93	135.061	15.8(5)	0.03(2)	ROT	
F19_088110	⋆	16 23 58.3 −56 54 18.9	15.23	82.357	1.822(2)	0.26(5)	EA	
F19_088185	⋆	16 23 58.8 −56 43 52.4	12.83	81.797	2.600(7)	0.066(8)	VAR	
F19_088207	s	16 24 02.1 −56 04 29.7	15.32	80.672	0.06299(2)	0.04(4)	DSCT	
F19_088251		16 23 57.2 −56 57 35.0	14.45	247.883	14.6(3)	0.12(3)	CEP	
F19_088257		16 23 58.9 −56 38 41.4	10.58	81.003	0.5814(8)	0.07(3)	RR	
F19_088316	s	16 24 04.1 −55 36 04.2	15.01	80.905	0.4366(3)	0.04(4)	EW	
F19_088325		16 23 57.8 −56 47 50.7	14.16	89.304	9.9(2)	0.06(2)	VAR	

Table E.5: Variable stars in field F19 (continued).

BEST ID	F	α (J2000.0) h m s	δ ° ′ ″	R_B [mag]	T_0 [d] [rHJD]	p [d]	A [mag]	Type	Other Names
F19_088429		16 23 59.0	−56 27 07.8	13.48	...	...	...	LP	
F19_088491	*s*	16 24 00.8	−56 00 41.0	14.71	80.768	0.653(3)	0.03(3)	VAR	
F19_088494		16 24 01.9	−55 49 00.8	11.79	171.413	80(2)	0.022(4)	VAR	
F19_088547		16 24 00.6	−55 59 16.5	15.49	80.837	0.2490(2)	0.08(5)	RR	
F19_088582	⋆	16 24 00.1	−56 04 13.4	13.61	80.922	1.382(2)	0.04(1)	EB	
F19_088595		16 24 03.4	−55 25 36.7	14.95	80.721	0.15470(4)	0.15(3)	DSCT	
F19_088615		16 24 00.7	−55 55 10.4	17.17	80.728	0.26124(7)	1.3(4)	EW	
F19_088628		16 23 56.5	−56 42 13.4	15.92	80.850	0.3784(2)	0.24(6)	EW	
F19_088708	*c*	16 23 58.2	−56 17 31.3	14.94	80.937	0.4314(3)	0.05(3)	EW	
F19_088755		16 23 58.0	−56 16 24.6	14.44	80.931	0.3893(2)	0.04(3)	EW/DSCT	
F19_088757	*cs*	16 23 58.0	−56 15 38.2	14.22	81.233	0.838(2)	0.04(3)	VAR	F19_088839
F19_088816		16 23 58.4	−56 07 14.0	13.58	...	...	...	SR	
F19_088839	*cs*	16 23 57.5	−56 15 34.7	13.98	81.240	0.838(2)	0.02(2)	VAR	F19_088757
F19_088856		16 24 00.2	−55 44 57.7	17.17	80.865	1.127(1)	0.5(3)	EA	
F19_088903	*ck*⋆	16 23 56.4	−56 23 40.1	13.96	80.912	0.45493(6)	1.05(3)	RR	KK Nor
F19_088915	*s*	16 23 57.6	−56 09 43.8	14.56	80.682	0.2899(1)	0.02(2)	EW	
F19_089075		16 23 59.4	−55 40 40.6	15.05	81.207	0.9160(9)	0.09(4)	EA	
F19_089080	*s*	16 23 53.0	−56 50 11.0	15.16	81.835	29(2)	0.05(4)	VAR	
F19_089132		16 23 59.9	−55 29 58.2	12.57	122.839	71(4)	0.32(3)	CEP	
F19_089192	*ck*⋆	16 23 52.6	−56 47 54.1	11.25	81.166	0.8523(3)	0.73(4)	EA	EO Nor
F19_089277	⋆	16 23 55.0	−56 15 53.4	13.46	89.969	17.8(2)	0.15(3)	EA	
F19_089326		16 23 52.5	−56 41 05.5	15.50	80.840	0.17765(8)	0.10(7)	DSCT	
F19_089340		16 23 56.2	−55 58 19.3	13.27	...	...	...	SR	
F19_089366	*c*	16 23 54.9	−56 11 07.3	12.73	...	...	...	LP	
F19_089393		16 23 52.6	−56 36 19.0	11.29	80.986	0.3254(2)	0.022(8)	EW	
F19_089408		16 23 55.0	−56 07 52.4	15.53	80.928	0.5367(3)	0.8(1)	RR	
F19_089448		16 23 57.9	−55 34 22.4	13.57	82.355	2.085(8)	0.02(2)	VAR	
F19_089581	*s*	16 23 52.7	−56 22 56.5	13.41	94.343	16.6(4)	0.05(2)	VAR	
F19_089600		16 23 56.0	−55 45 04.3	15.55	90.283	10.4(3)	0.12(5)	ROT	
F19_089655	*s*	16 23 51.5	−56 31 43.6	11.66	80.685	0.053699(9)	0.010(8)	DSCT	
F19_089763	*s*	16 23 51.4	−56 24 18.4	13.32	80.992	0.8265(7)	0.09(4)	EB	
F19_089827	⋆	16 23 50.7	−56 29 08.8	15.45	120.840	4.393(1)	0.22(1)	EA	
F19_089918	*s*	16 23 50.1	−56 28 19.4	12.12	...	...	...	SR	
F19_089942		16 23 47.8	−56 54 31.7	13.22	...	...	...	LP	
F19_089977		16 23 49.8	−56 29 21.6	14.91	267.692	65(5)	0.19(3)	CEP	
F19_090050		16 23 50.7	−56 14 26.1	15.43	80.766	0.3409(2)	0.09(5)	EW/DSCT	
F19_090077	*s*	16 23 50.0	−56 19 57.1	14.78	80.689	0.4523(4)	0.02(3)	EW	
F19_090080		16 23 50.5	−56 15 18.3	11.80	80.678	0.046626(6)	0.013(7)	DSCT	
F19_090092		16 23 52.5	−55 52 58.8	16.12	88.756	4.70(5)	0.14(9)	VAR	
F19_090104	*s*	16 23 47.2	−56 50 39.8	15.59	95.551	57(9)	0.07(5)	VAR	
F19_090146	*s*	16 23 50.6	−56 10 32.5	15.13	81.914	2.81(3)	0.06(4)	ROT	
F19_090151	*c*	16 23 51.3	−56 02 43.4	11.84	...	...	...	LP	
F19_090226	*s*	16 23 51.9	−55 51 52.7	12.47	...	...	...	LP	
F19_090272	*s*	16 23 47.3	−56 38 24.3	13.42	81.193	0.6516(9)	0.03(2)	RR	
F19_090302		16 23 47.2	−56 37 18.7	16.34	81.001	0.3602(2)	0.2(1)	EW	
F19_090344	*c*	16 23 49.9	−56 06 08.6	13.56	...	...	...	SR	
F19_090425	*s*	16 23 47.8	−56 22 44.2	11.39	80.732	0.11176(4)	0.006(6)	DSCT	
F19_090511	⋆	16 23 52.8	−55 26 31.3	15.37	80.888	0.6850(3)	0.52(6)	EA	
F19_090532	*c*	16 23 48.4	−56 10 32.0	14.77	81.017	0.5202(4)	0.09(4)	EW	F19_090668
F19_090544	*c*	16 23 52.4	−55 28 12.0	13.21	...	...	...	LP	
F19_090610	*s*	16 23 50.7	−55 40 50.1	15.18	80.932	0.3996(2)	0.07(4)	EB	
F19_090668	*c*	16 23 47.8	−56 10 30.3	14.74	81.017	0.5201(4)	0.07(3)	EW	F19_090532
F19_090756	*c*	16 23 45.9	−56 25 01.5	14.92	80.916	0.32235(7)	0.25(4)	EW	
F19_090799	*s*	16 23 49.6	−55 43 49.2	14.83	80.744	0.4525(4)	0.02(4)	EW/DSCT	
F19_090811		16 23 43.4	−56 48 50.6	14.23	80.735	0.830(2)	0.02(2)	VAR	
F19_090820		16 23 45.9	−56 22 27.2	13.90	80.910	1.616(2)	0.07(2)	EA	
F19_090832	*s*	16 23 48.8	−55 51 08.2	15.69	81.412	3.04(2)	0.17(6)	VAR	
F19_090923		16 23 47.2	−56 00 25.7	12.14	...	...	...	SR	
F19_090954	*s*	16 23 49.3	−55 37 18.8	11.79	...	...	...	SR	
F19_091017		16 23 44.9	−56 20 14.6	12.33	...	...	...	SR	
F19_091034	*s*	16 23 41.2	−57 00 03.5	13.91	80.686	0.025452(2)	0.01(2)	DSCT	
F19_091092	*s*	16 23 41.0	−56 57 33.1	12.78	82.288	9.7(3)	0.017(7)	ROT	
F19_091154	*cs*	16 23 47.6	−55 43 18.9	13.23	90.953	49(9)	0.03(2)	VAR	
F19_091292	*cs*	16 23 47.0	−55 43 20.2	13.20	93.536	48(9)	0.03(2)	VAR	
F19_091323	*s*	16 23 48.1	−55 27 35.7	13.43	...	...	...	SR	
F19_091335		16 23 41.5	−56 35 55.5	13.85	...	...	...	LP	
F19_091351		16 23 47.4	−55 33 22.6	12.04	...	...	...	SR	
F19_091696		16 23 41.6	−56 15 12.7	11.96	80.707	0.058365(8)	0.04(2)	DSCT	
F19_091720	*s*	16 23 41.1	−56 18 26.5	15.18	89.529	5.33(3)	0.04(4)	VAR	
F19_091731		16 23 44.2	−55 46 00.7	12.34	80.805	0.2337(2)	0.011(8)	VAR	
F19_091870		16 23 38.3	−56 39 12.7	13.18	237.147	34(2)	0.032(8)	VAR	
F19_091879		16 23 39.7	−56 22 53.7	10.11	...	...	...	SR	
F19_091890	⋆	16 23 43.5	−55 44 04.4	15.47	82.890	2.5636(1)	0.22(1)	EA	
F19_092066	*s*	16 23 36.7	−56 44 25.2	12.40	81.271	0.697(2)	0.02(2)	VAR	
F19_092152	*cs*	16 23 35.7	−56 49 42.2	12.26	...	...	...	SR	
F19_092153	⋆	16 23 36.1	−56 45 11.8	16.92	82.316	2.0803(1)	2(1)	EA	
F19_092172	*s*	16 23 42.2	−55 41 55.9	14.34	...	...	...	LP	
F19_092186	*c*	16 23 37.1	−56 31 58.1	10.60	...	...	...	SR	
F19_092188		16 23 37.3	−56 29 30.0	17.76	80.690	0.2974(1)	0.6(4)	EW	
F19_092313	*c*⋆	16 23 39.9	−55 56 12.7	13.95	81.447	1.0487(4)	0.29(2)	EA	
F19_092316	*c*	16 23 40.5	−55 50 44.5	14.79	80.753	0.39147(7)	0.32(3)	EW	
F19_092320		16 23 40.9	−55 45 26.7	15.65	80.725	0.07661(2)	0.20(7)	DSCT	
F19_092549	*s*	16 23 33.3	−56 50 53.7	14.71	80.900	0.3083(2)	0.03(3)	EW	
F19_092675		16 23 38.0	−55 52 58.6	13.79	81.380	1.117(3)	0.03(2)	VAR	
F19_092709		16 23 31.9	−56 54 36.2	14.10	81.024	0.6046(5)	0.02(2)	EB	
F19_092811		16 23 36.4	−56 01 43.3	14.46	80.775	0.4845(3)	0.06(2)	EW	
F19_092878	*s*	16 23 36.7	−55 54 26.5	12.54	81.586	2.093(4)	0.025(8)	EB	
F19_092899		16 23 33.3	−56 27 47.7	12.08	...	...	...	SR	

Table E.5: Variable stars in field F19 (continued).

BEST ID	F	α (J2000.0) h m s	δ ° ′ ″	R_B [mag]	T_0 [d] [rHJD]	p [d]	A [mag]	Type	Other Names
F19_092912		16 23 36.8	−55 52 37.4	11.16	...	...	...	SR	
F19_093008		16 23 35.1	−56 04 30.1	14.17	80.862	0.6016(2)	0.23(2)	EW	
F19_093029		16 23 30.5	−56 51 10.1	14.76	80.810	0.4797(2)	0.19(3)	EB	
F19_093032	c	16 23 30.9	−56 46 12.5	12.66	...	...	...	LP	
F19_093059		16 23 37.3	−55 39 32.5	13.09	95.726	18.2(8)	0.06(2)	ROT	
F19_093116	cs	16 23 29.6	−56 54 55.2	12.69	159.802	28(2)	0.024(8)	ROT	
F19_093144	c	16 23 31.4	−56 33 10.9	14.99	80.864	0.3730(2)	0.13(5)	EW	
F19_093183	c	16 23 31.6	−56 29 17.3	15.04	100.759	45(3)	0.16(4)	CEP	
F19_093198	c	16 23 36.0	−55 44 57.4	15.17	82.665	2.9043(1)	0.35(1)	EA	
F19_093317		16 23 34.0	−55 57 20.2	12.80	93.195	6.85(5)	0.026(7)	ROT	
F19_093445		16 23 28.4	−56 46 12.4	15.58	80.680	0.31720(8)	0.25(5)	EW	
F19_093466	s	16 23 33.4	−55 55 16.9	16.22	311.472	58(7)	0.3(1)	CEP	
F19_093482		16 23 27.9	−56 48 37.6	12.21	...	...	...	SR	
F19_093551	c	16 23 29.2	−56 31 11.4	11.66	122.756	18.0(8)	0.08(2)	SR	
F19_093599	c	16 23 35.1	−55 31 50.7	11.94	...	...	...	SR	
F19_093711	ck	16 23 34.2	−55 35 16.6	10.97	...	...	...	LP	IZ Nor
F19_093755	s	16 23 28.6	−56 27 20.1	12.46	...	...	...	LP	
F19_093972		16 23 30.4	−55 56 27.7	13.32	83.370	3.81(3)	0.022(8)	VAR	
F19_093979	s	16 23 33.0	−55 32 03.1	12.49	80.689	0.042986(7)	0.01(1)	VAR	
F19_094088	c	16 23 25.1	−56 43 12.0	13.77	81.469	0.8159(7)	0.07(2)	EW	
F19_094143		16 23 23.5	−56 57 34.5	11.46	188.524	41(2)	0.07(1)	VAR	
F19_094170		16 23 23.5	−56 54 56.4	13.78	90.049	48(4)	0.15(2)	CEP	
F19_094174	$\star$	16 23 25.7	−56 32 02.8	13.08	81.287	1.0397(4)	0.14(2)	EA	
F19_094224	s	16 23 22.6	−57 00 31.7	14.22	80.962	0.2942(2)	0.02(2)	EW/DSCT	
F19_094231	cs	16 23 24.4	−56 41 52.5	14.78	83.921	5.7(2)	0.03(3)	ROT	F19_094288
F19_094288	cs	16 23 24.2	−56 41 55.9	14.70	83.438	5.66(6)	0.03(3)	ROT	F19_094231
F19_094306		16 23 29.8	−55 43 55.8	12.51	81.210	0.771(1)	0.040(8)	VAR	
F19_094521	s	16 23 26.1	−56 07 41.5	13.38	94.348	14.5(3)	0.03(2)	ROT	
F19_094587		16 23 25.7	−56 08 16.9	12.39	289.253	80(2)	0.011(4)	VAR	
F19_094644	s	16 23 20.5	−56 56 11.0	13.92	81.058	0.714(2)	0.02(2)	VAR	
F19_094732	c	16 23 19.6	−56 58 53.2	15.05	80.814	0.3150(2)	0.03(3)	EW/DSCT	F19_094828
F19_094752	c	16 23 27.1	−55 42 30.2	15.24	135.831	48(3)	0.25(4)	VAR	
F19_094761		16 23 21.9	−56 32 48.0	11.32	...	...	...	SR	
F19_094828	c	16 23 18.9	−56 58 57.2	15.41	80.813	0.3150(2)	0.07(4)	EW/DSCT	F19_094732
F19_094866	s	16 23 23.5	−56 10 18.4	16.39	80.698	0.08495(2)	0.1(1)	DSCT	
F19_094889	c	16 23 20.0	−56 45 04.8	14.46	81.029	0.48679(7)	0.39(2)	EB	
F19_094961		16 23 21.2	−56 29 05.0	14.37	122.222	58(6)	0.11(2)	EB	
F19_094966	s	16 23 22.2	−56 18 56.2	10.51	295.298	41(2)	0.019(6)	VAR	
F19_095097		16 23 19.3	−56 40 29.8	12.43	247.441	48(3)	0.013(4)	VAR	
F19_095227		16 23 18.3	−56 44 08.3	16.29	94.279	10.2(2)	0.44(9)	CEP	
F19_095365	s	16 23 25.7	−55 26 08.1	12.75	82.392	7.8(2)	0.019(8)	ROT	
F19_095405	$c\star$	16 23 16.7	−56 48 31.9	14.35	92.640	1.13477(1)	0.05(1)	EA	
F19_095549		16 23 22.2	−55 48 45.6	15.09	80.817	0.44175(9)	0.30(3)	EW	
F19_095558	c	16 23 16.5	−56 43 03.4	13.97	...	...	...	LP	
F19_095676		16 23 18.9	−56 11 13.5	11.13	...	...	...	LP	
F19_095687		16 23 22.9	−55 33 21.5	12.63	80.917	0.3944(2)	0.05(2)	EW	
F19_095744		16 23 14.4	−56 50 58.8	11.83	81.626	1.42(2)	0.014(6)	VAR	
F19_095780	s	16 23 14.8	−56 44 50.4	15.31	81.019	0.612(2)	0.05(4)	RR	
F19_095825		16 23 18.0	−56 12 02.7	13.31	269.535	56(5)	0.036(8)	ROT	
F19_095861		16 23 18.9	−56 01 43.3	13.58	83.643	22.9(6)	0.057(8)	CEP	
F19_095888	s	16 23 18.2	−56 06 54.2	14.36	83.048	23.2(9)	0.07(3)	VAR	
F19_095946	$c\star$	16 23 19.5	−55 50 49.5	14.46	246.575	5.188(1)	0.21(1)	EA	
F19_095985		16 23 21.5	−55 30 53.7	12.07	80.742	0.10849(3)	0.02(1)	DSCT	
F19_096002	s	16 23 16.9	−56 13 12.7	13.19	...	...	...	LP	
F19_096150		16 23 15.8	−56 15 41.7	13.01	96.982	10.0(2)	0.16(4)	CEP	
F19_096235	$\star$	16 23 19.2	−55 40 20.3	13.78	81.646	1.453(4)	0.10(3)	ROT	
F19_096310	s	16 23 10.8	−56 53 55.6	11.86	...	...	...	VAR	
F19_096351	c	16 23 10.7	−56 51 48.5	15.17	159.695	43(4)	0.18(6)	VAR	
F19_096429		16 23 11.6	−56 37 39.9	12.47	...	...	...	SR	
F19_096432		16 23 12.9	−56 24 35.1	13.42	92.949	12.3(3)	0.04(2)	VAR	
F19_096475	$\star$	16 23 14.1	−56 12 54.7	13.18	82.204	2.383(4)	0.025(8)	EA	
F19_096504	cs	16 23 13.3	−56 17 47.2	14.85	80.725	0.14938(6)	0.03(3)	DSCT	F19_096529
F19_096529	cs	16 23 13.3	−56 17 41.5	14.54	80.728	0.14936(7)	0.02(2)	DSCT	F19_096504
F19_096546		16 23 18.7	−55 25 57.9	11.39	...	...	...	LP	
F19_096554		16 23 10.8	−56 39 33.5	12.01	88.252	18.1(6)	0.021(6)	ROT	
F19_096559	$\star$	16 23 11.8	−56 30 28.7	13.62	120.810	5.9045(1)	0.075(1)	EA	
F19_096568		16 23 13.2	−56 16 32.0	14.50	80.714	0.069411(9)	0.19(5)	DSCT	
F19_096636	c	16 23 18.2	−55 26 40.4	14.35	81.136	0.5046(2)	0.13(3)	EB	
F19_096642	$s\star$	16 23 10.1	−56 40 15.7	13.69	96.690	24.22(1)	0.09(1)	EA	
F19_096653	$\star$	16 23 13.2	−56 10 21.6	17.01	82.102	2.41974(1)	4.5(1)	EA	
F19_096792	s	16 23 17.2	−55 28 02.1	12.97	80.685	0.07542(2)	0.01(1)	DSCT	
F19_096863	$c\star$	16 23 09.1	−56 38 38.7	12.94	81.062	0.6401(8)	0.024(8)	VAR	
F19_096912	c	16 23 09.4	−56 34 00.8	14.80	80.772	0.18957(9)	0.04(3)	VAR	F19_096946
F19_096929	s	16 23 13.9	−55 51 45.1	14.34	80.803	0.2575(1)	0.02(2)	EW/DSCT	
F19_096946	c	16 23 09.2	−56 34 05.4	14.83	80.751	0.18957(9)	0.04(3)	VAR	F19_096912
F19_096957	c	16 23 11.8	−56 09 58.8	14.00	92.024	6.52(7)	0.05(2)	VAR	F19_096986
F19_096986	c	16 23 11.6	−56 10 04.6	14.39	92.042	6.51(5)	0.10(2)	VAR	F19_096957
F19_097016		16 23 10.9	−56 14 25.1	16.10	109.407	10.9(3)	0.14(8)	ROT	
F19_097022		16 23 12.5	−55 59 40.8	12.55	...	...	...	LP	
F19_097048	s	16 23 09.7	−56 24 03.3	15.11	80.787	0.16303(8)	0.04(4)	VAR	
F19_097119	s	16 23 11.7	−56 01 32.2	15.57	80.821	0.2007(2)	0.07(6)	DSCT	
F19_097254	$s\star$	16 23 09.1	−56 18 41.1	14.43	96.690	51.88(1)	0.1(1)	EA	
F19_097348		16 23 09.9	−56 06 44.1	10.35	...	...	...	LP	
F19_097445		16 23 12.0	−55 42 24.9	14.84	81.081	0.5375(3)	0.16(4)	EW/DSCT	
F19_097488	s	16 23 03.3	−56 59 43.4	14.52	80.741	0.1980(1)	0.03(3)	DSCT	
F19_097514		16 23 03.8	−56 53 02.5	13.99	92.454	13.5(4)	0.09(3)	VAR	
F19_097536		16 23 09.6	−55 59 55.6	15.54	80.749	0.5943(5)	0.13(5)	EW	
F19_097606	c	16 23 04.7	−56 39 39.4	14.62	81.170	0.53718(8)	0.51(2)	RR	

Table E.5: Variable stars in field F19 (continued).

BEST ID	F	α (J2000.0) h m s	δ ° ′ ″	R_B [mag]	T_0 [d] [rHJD]	p [d]	A [mag]	Type	Other Names
F19_097617	*c*	16 23 08.5	−56 04 22.4	14.24	91.201	13.4(4)	0.10(3)	ROT	
F19_097675		16 23 08.2	−56 04 33.2	12.86	80.733	0.07012(2)	0.009(7)	DSCT	
F19_097839		16 23 07.9	−55 59 19.1	13.32	81.031	0.5822(9)	0.014(8)	VAR	
F19_098041		16 23 00.5	−56 56 10.1	12.63	...	...	...	LP	
F19_098062	*s*	16 23 10.3	−55 26 30.5	11.12	81.035	1.041(2)	0.014(6)	EB	
F19_098131		16 23 03.8	−56 20 29.5	12.23	...	...	...	SR	
F19_098149	*s*	16 23 07.5	−55 47 41.8	15.62	80.875	0.3280(2)	0.07(6)	EW/DSCT	
F19_098326	*cs*	16 23 03.1	−56 16 38.0	15.51	80.697	0.2276(2)	0.04(5)	VAR	F19_098500
F19_098447	*ck*⋆	16 23 01.0	−56 28 58.2	10.61	...	...	...	LP	NSV 7658
F19_098448	*c*	16 23 01.9	−56 20 51.9	10.16	...	...	...	LP	
F19_098500	*cs*	16 23 02.2	−56 16 34.4	15.53	80.686	0.2276(2)	0.05(5)	VAR	F19_098326
F19_098505		16 23 03.7	−56 02 46.6	12.61	92.951	18.5(6)	0.05(2)	VAR	
F19_098551		16 22 58.1	−56 50 01.8	14.16	80.695	7.33(9)	0.03(2)	ROT	
F19_098565	*s*	16 23 03.4	−56 01 43.3	15.35	81.056	0.4518(6)	0.05(4)	VAR	
F19_098579	⋆	16 23 07.7	−55 23 43.1	13.31	81.002	1.757(2)	0.26(4)	EA	
F19_098584	⋆	16 22 59.3	−56 37 05.8	12.16	81.963	1.4275(8)	0.080(8)	EA	
F19_098692	⋆	16 23 04.3	−55 47 52.3	13.70	90.668	2.7439(1)	0.15(1)	EA	
F19_098701	*c*	16 23 06.6	−55 27 01.3	14.64	81.038	0.4969(4)	0.04(3)	EB	F19_098775
F19_098753		16 22 58.0	−56 40 29.6	12.97	...	...	...	LP	
F19_098775	*c*	16 23 06.2	−55 26 56.0	15.02	81.043	0.4969(3)	0.11(4)	EB	F19_098701
F19_098815	⋆	16 22 58.5	−56 31 36.1	14.33	81.513	1.881(2)	0.19(3)	EB	
F19_098865		16 23 05.2	−55 30 53.4	11.67	...	...	...	SR	
F19_098890	*s*	16 23 01.5	−56 00 52.8	15.76	81.072	1.382(6)	0.10(7)	VAR	
F19_098961		16 22 55.2	−56 54 29.7	14.22	80.902	1.248(1)	0.06(2)	EA	
F19_098975		16 23 01.9	−55 53 15.9	13.02	96.391	10.9(2)	0.033(8)	VAR	
F19_099040	*cs*	16 23 01.6	−55 52 49.1	14.41	80.757	0.25054(7)	0.02(3)	EW/DSCT	F19_099221
F19_099094	*s*	16 22 57.7	−56 23 45.2	12.72	...	...	...	SR	
F19_099118		16 22 55.2	−56 45 27.8	14.91	80.843	0.7065(4)	0.35(4)	RR	
F19_099196	*s*	16 22 54.0	−56 52 12.0	12.52	...	...	...	LP	
F19_099207	*c*	16 22 56.6	−56 27 13.2	13.53	81.105	0.4743(3)	0.09(3)	EB	
F19_099221	*cs*	16 23 00.7	−55 52 42.7	15.62	80.756	0.25054(7)	0.07(7)	EW/DSCT	F19_099040
F19_099255		16 22 54.1	−56 48 00.3	12.54	...	...	...	SR	
F19_099313	*s*	16 22 55.3	−56 34 16.3	16.38	81.061	0.843(2)	0.11(9)	VAR	
F19_099331	*s*	16 23 01.5	−55 38 57.4	16.08	80.868	0.2573(3)	0.10(9)	VAR	
F19_099353	*s*	16 22 59.2	−55 57 29.1	12.02	80.816	0.4428(3)	0.011(6)	EW	
F19_099360	*s*	16 23 01.5	−55 36 43.9	13.60	...	...	...	VAR	
F19_099373		16 22 54.0	−56 42 05.1	15.06	80.708	0.2807(1)	0.06(3)	EW	
F19_099381	*c*⋆	16 22 55.5	−56 28 22.8	13.60	82.754	3.358(3)	0.67(4)	EA	
F19_099412		16 22 57.8	−56 07 20.6	12.79	...	...	...	LP	
F19_099424	*c*	16 23 02.9	−55 23 39.0	15.61	80.675	0.5727(3)	0.49(9)	EB	
F19_099434		16 22 54.7	−56 32 29.4	13.18	80.697	0.15914(6)	0.014(8)	DSCT	
F19_099469		16 22 55.7	−56 21 20.4	12.79	90.243	15.3(4)	0.07(2)	VAR	
F19_099476	⋆	16 22 58.6	−55 56 11.9	15.02	80.899	0.30656(4)	0.82(4)	EW	
F19_099489	*c*⋆	16 22 51.3	−56 59 48.3	13.39	80.788	0.31699(5)	0.35(2)	RR	
F19_099521		16 22 52.5	−56 47 20.3	13.62	91.366	12.4(4)	0.02(1)	ROT	
F19_099576	*s*	16 22 51.2	−56 56 23.9	16.16	82.285	3.88(4)	0.3(2)	ROT	
F19_099590		16 22 56.9	−56 05 38.7	15.58	157.535	5.433(1)	0.35(1)	EA	
F19_099740		16 22 59.8	−55 33 11.1	15.71	99.034	56(5)	0.39(7)	CEP	
F19_099784	*s*	16 22 51.3	−56 43 42.9	11.35	91.334	13.4(3)	0.05(2)	VAR	
F19_099982	*s*	16 22 52.1	−56 27 28.2	14.94	81.239	60(1)	0.09(5)	EB	
F19_100004	*s*	16 22 59.5	−55 24 26.1	12.30	135.025	23.7(6)	0.03(2)	VAR	
F19_100042	*c*	16 22 58.2	−55 33 52.3	14.85	81.004	0.3625(1)	0.16(4)	EW	
F19_100121		16 22 50.0	−56 39 33.2	15.59	127.055	21(1)	0.09(5)	VAR	
F19_100160	*c*⋆	16 22 53.1	−56 10 59.1	13.01	80.846	0.8822(2)	0.35(2)	EA	
F19_100251	*cs*	16 22 48.5	−56 46 35.0	15.31	80.796	0.13162(4)	0.04(4)	DSCT	
F19_100256		16 22 50.0	−56 33 59.6	14.94	81.040	2.143(4)	0.04(3)	EA	
F19_100269	*cs*	16 22 55.4	−55 46 06.3	14.17	80.718	0.09248(3)	0.02(2)	DSCT	F19_100361
F19_100314	*cs*	16 22 48.5	−56 43 46.6	11.84	81.245	11.9(3)	0.027(8)	VAR	
F19_100326	*s*	16 22 53.3	−56 02 05.2	11.88	197.144	18.2(4)	0.021(7)	VAR	
F19_100347		16 22 48.7	−56 40 22.2	14.47	80.794	0.4345(2)	0.09(2)	ROT	
F19_100361	*cs*	16 22 55.0	−55 46 02.9	14.02	80.715	0.09248(3)	0.02(2)	DSCT	F19_100269
F19_100475	*s*	16 22 54.4	−55 45 03.4	12.90	80.792	0.14288(9)	0.009(7)	DSCT	
F19_100631		16 22 45.0	−56 58 39.7	13.58	94.738	7.2(2)	0.03(1)	ROT	
F19_100638		16 22 47.5	−56 35 51.2	12.66	...	...	...	LP	
F19_100773	*s*	16 22 51.7	−55 53 09.9	13.95	81.982	2.59(2)	0.03(2)	VAR	
F19_100878	*c*	16 22 51.4	−55 51 25.3	14.55	81.080	8.32(5)	0.33(8)	EA	
F19_100915	⋆	16 22 46.8	−56 27 30.8	14.37	80.888	0.39881(5)	0.39(3)	EW	
F19_100956	⋆	16 22 53.3	−55 31 20.0	13.68	109.725	10.945(1)	0.55(1)	EA	
F19_101011		16 22 50.1	−55 54 31.9	12.91	80.684	0.08963(2)	0.01(1)	DSCT	
F19_101067	*s*	16 22 46.7	−56 20 55.5	12.56	200.111	38(2)	0.04(2)	VAR	
F19_101069		16 22 47.4	−56 15 38.3	13.02	...	...	...	SR	
F19_101105	*c*	16 22 46.3	−56 22 13.1	11.86	121.447	55(5)	0.053(6)	VAR	
F19_101121	*c*	16 22 51.6	−55 37 58.3	13.26	...	...	...	LP	
F19_101145	*s*	16 22 50.0	−55 49 27.5	14.17	80.731	0.13443(6)	0.01(2)	DSCT	
F19_101160		16 22 42.8	−56 49 05.6	13.83	80.978	0.35861(5)	0.21(2)	EW	
F19_101258		16 22 48.4	−55 57 18.9	15.37	80.813	0.3815(2)	0.30(7)	EW	
F19_101306	*c*⋆	16 22 48.0	−55 57 49.8	12.92	81.104	9.32(6)	0.094(8)	CEP	
F19_101330		16 22 44.5	−56 26 03.9	14.99	80.799	0.1888(2)	0.02(3)	VAR	
F19_101347		16 22 42.7	−56 41 01.2	14.70	80.872	0.33331(7)	0.25(4)	EW	
F19_101349	*s*⋆	16 22 44.3	−56 26 24.1	13.45	80.871	0.7695	0.0066	EA	
F19_101504		16 22 46.0	−56 04 01.9	11.75	...	...	...	LP	
F19_101520	*c*	16 22 42.3	−56 33 54.4	13.90	81.020	0.4315(2)	0.18(3)	EW	
F19_101611	*c*	16 22 50.5	−55 24 24.8	11.57	...	...	...	SR	
F19_101673		16 22 45.9	−55 57 52.7	11.67	...	...	...	LP	
F19_101837		16 22 46.8	−55 43 12.5	11.41	...	...	...	LP	
F19_102095	*cs*	16 22 38.4	−56 39 58.9	12.00	270.983	52(3)	0.11(4)	VAR	
F19_102097	*c*	16 22 38.8	−56 36 40.9	14.53	80.712	0.5042(1)	0.27(3)	EW	
F19_102193	*c*	16 22 40.3	−56 19 42.8	14.41	81.050	0.4492(2)	0.16(4)	EW	

Table E.5: Variable stars in field F19 (continued).

BEST ID	F	α (J2000.0) δ	R_B	T_0 [d]	p [d]	A	Type	Other Names
		h m s ° ′ ″	[mag]	[rHJD]		[mag]		
F19_102262	*c*	16 22 45.4 −55 34 09.3	14.35	80.904	0.5414(2)	0.26(4)	EB	F19_102390, F19_102537
F19_102313	*c*	16 22 46.4 −55 25 44.4	13.68	80.938	0.4896(2)	0.08(2)	EB	
F19_102335		16 22 45.1 −55 35 36.1	12.91	···	···	···	SR	
F19_102337	*c*	16 22 45.2 −55 33 46.4	11.49	···	···	···	LP	
F19_102363		16 22 42.3 −55 56 31.5	14.97	122.979	12.0(5)	0.11(4)	ROT	
F19_102390	*c*	16 22 44.9 −55 34 09.1	13.76	80.904	0.5414(3)	0.18(5)	EB	F19_102262, F19_102537
F19_102395		16 22 35.5 −56 51 26.6	11.43	···	···	···	LP	
F19_102447		16 22 34.9 −56 52 08.1	13.31	81.310	0.6899(4)	0.051(8)	EW	
F19_102537	*c*	16 22 44.0 −55 34 09.6	13.27	80.901	0.5414(3)	0.051(8)	EB	F19_102262, F19_102390
F19_102538		16 22 44.9 −55 27 23.3	11.92	···	···	···	SR	
F19_102550	*cs*	16 22 37.1 −56 28 58.3	13.62	83.436	20(2)	0.04(2)	ROT	F19_102679
F19_102559	*c*⋆	16 22 39.7 −56 07 29.6	14.11	80.712	0.30119(4)	0.30(2)	EW	
F19_102608	⋆	16 22 33.3 −56 57 53.1	12.54	81.018	2.720(2)	0.34(2)	EA	
F19_102613		16 22 34.4 −56 48 41.7	14.49	81.912	1.714(4)	0.10(3)	VAR	
F19_102676		16 22 36.0 −56 32 31.7	11.41	···	···	···	SR	
F19_102679	*cs*	16 22 36.5 −56 28 56.2	13.63	83.615	20.4(6)	0.05(2)	ROT	F19_102550
F19_102758	*c*⋆	16 22 35.1 −56 34 43.1	13.81	80.740	0.40817(6)	0.22(2)	EW	
F19_102802	*cs*	16 22 39.7 −55 57 13.9	15.36	80.868	0.3762(3)	0.05(4)	EW/DSCT	
F19_102900		16 22 38.0 −56 06 18.4	14.61	267.784	33(2)	0.09(3)	VAR	
F19_102977	*cs*	16 22 33.7 −56 37 44.4	14.55	184.085	40(3)	0.07(3)	VAR	
F19_102987	*c*	16 22 36.3 −56 15 59.9	12.01	80.977	0.761(2)	0.03(1)	RR	
F19_103027	⋆	16 22 42.1 −55 28 31.1	14.87	90.885	9.364(1)	0.31(1)	EA	
F19_103054		16 22 38.0 −55 57 59.5	14.60	83.513	3.78(1)	0.09(3)	EA	
F19_103163	*c*	16 22 41.7 −55 23 33.2	13.57	80.882	0.5412(4)	0.02(2)	EW/DSCT	F19_103214
F19_103168		16 22 31.3 −56 47 49.3	15.86	80.997	0.3711(2)	0.10(6)	EW/DSCT	
F19_103214	*c*	16 22 41.6 −55 23 31.8	13.56	81.139	0.5412(4)	0.02(2)	EW/DSCT	F19_103163
F19_103215		16 22 29.8 −56 58 22.6	16.44	80.851	0.3576(2)	0.5(2)	EW	
F19_103221		16 22 33.5 −56 26 52.9	13.76	81.384	1.524(2)	0.14(3)	EB	
F19_103255		16 22 32.9 −56 29 41.7	12.96	···	···	···	SR	
F19_103397		16 22 35.2 −56 05 46.5	13.55	···	···	···	SR	
F19_103469		16 22 39.0 −55 33 31.0	15.15	94.749	27(2)	0.11(6)	VAR	
F19_103479	*s*	16 22 29.1 −56 52 11.0	13.17	81.217	0.989(6)	0.013(8)	VAR	
F19_103539	*c*	16 22 33.1 −56 15 09.9	15.70	80.756	0.11868(2)	0.52(8)	DSCT	
F19_103555		16 22 38.3 −55 33 55.2	13.86	91.511	44(6)	0.09(3)	VAR	
F19_103592	*s*	16 22 29.8 −56 40 39.7	12.70	81.627	10.3(2)	0.012(7)	ROT	
F19_103649		16 22 30.5 −56 30 56.5	16.55	81.129	0.5006(3)	0.4(2)	EW	
F19_103768	*c*⋆	16 22 28.5 −56 41 43.2	14.15	80.740	3.0198(1)	0.17(1)	EA	
F19_103791	*s*	16 22 27.9 −56 44 40.6	11.48	···	···	···	SR	
F19_103798	*s*	16 22 30.6 −56 23 04.0	15.69	80.746	0.2507(2)	0.09(6)	VAR	
F19_103840		16 22 34.1 −55 54 43.6	12.96	82.385	34(3)	0.03(1)	EB	
F19_104039	*s*	16 22 26.5 −56 44 54.8	11.76	···	···	···	SR	
F19_104080	*c*	16 22 31.4 −56 03 21.1	14.25	83.275	27(1)	0.09(2)	VAR	F19_104201
F19_104094	⋆	16 22 35.2 −55 34 28.1	14.73	80.688	0.35244(4)	1.08(3)	RR	
F19_104122		16 22 31.7 −56 00 03.3	14.20	···	···	···	LP	
F19_104201	*c*	16 22 30.9 −56 03 18.9	14.21	82.264	27.1(8)	0.09(2)	VAR	F19_104080
F19_104266	⋆	16 22 35.3 −55 25 14.1	14.77	100.630	2.06891(1)	0.43(1)	EA	
F19_104459	*k*⋆	16 22 27.1 −56 20 43.8	11.20	81.343	0.7383(2)	0.301(7)	EW	EM Nor
F19_104525		16 22 22.0 −56 57 26.3	11.47	···	···	···	SR	
F19_104694		16 22 30.8 −55 40 10.5	11.40	···	···	···	SR	
F19_104736	*c*⋆	16 22 21.2 −56 54 34.7	12.77	81.207	0.6636(1)	0.270(8)	EW	
F19_104765	*s*	16 22 31.7 −55 30 35.5	11.18	80.720	0.15301(6)	0.012(8)	DSCT	
F19_104777		16 22 23.1 −56 36 49.5	15.87	81.214	0.5968(3)	0.46(9)	EW	
F19_104819		16 22 24.8 −56 21 31.6	11.53	···	···	···	SR	
F19_104936		16 22 28.5 −55 47 15.9	13.29	···	···	···	SR	
F19_104979		16 22 29.5 −55 38 57.5	14.09	82.939	6.7(1)	0.19(5)	VAR	
F19_105062		16 22 25.1 −56 08 12.5	13.84	80.939	2.8527	0.061	EA	
F19_105065		16 22 26.0 −56 00 56.7	11.54	···	···	···	LP	
F19_105100	*s*	16 22 28.6 −55 40 33.4	13.23	89.232	4.46(4)	0.014(8)	VAR	
F19_105176	⋆	16 22 27.4 −55 46 04.7	14.59	197.550	20.256(1)	0.35(1)	EA	
F19_105204	*c*	16 22 26.6 −55 51 03.0	14.40	90.896	11.5(4)	0.04(2)	ROT	F19_105263
F19_105232	*s*	16 22 25.0 −56 01 41.0	11.77	···	···	···	SR	
F19_105261		16 22 24.2 −56 07 31.7	14.56	81.205	4.42(3)	0.08(3)	VAR	
F19_105263	*c*	16 22 26.4 −55 50 58.5	14.61	91.031	11.4(5)	0.05(3)	ROT	F19_105204
F19_105285	*c*	16 22 21.6 −56 27 05.3	10.80	309.987	89(6)	0.098(8)	EB	
F19_105297		16 22 26.2 −55 49 54.8	15.36	91.683	2.34615(1)	0.24(1)	EA	
F19_105306		16 22 17.5 −56 57 36.4	15.48	80.892	0.7481(4)	0.14(5)	EA	
F19_105310		16 22 19.7 −56 40 22.3	14.27	82.075	3.1440	0.098	EA	
F19_105331	⋆	16 22 29.2 −55 26 59.4	12.42	81.978	1.493(1)	0.075(8)	EA	
F19_105334		16 22 17.7 −56 54 33.9	14.36	80.681	3.151(6)	0.10(2)	EA	
F19_105599	*c*	16 22 24.8 −55 48 14.3	14.69	80.733	0.3526(2)	0.05(3)	EW/DSCT	F19_105662
F19_105662	*c*	16 22 24.4 −55 48 18.8	14.94	80.732	0.3526(2)	0.11(3)	EW/DSCT	F19_105599
F19_105689		16 22 26.5 −55 31 44.5	13.56	90.829	13.5(4)	0.05(2)	VAR	
F19_105776		16 22 22.9 −55 54 53.3	15.87	80.885	0.4165(3)	0.13(6)	EW/DSCT	
F19_105792	*c*	16 22 17.6 −56 34 17.0	14.72	81.178	0.913(1)	0.07(3)	EW	
F19_105802	*s*	16 22 22.3 −55 58 06.3	12.58	80.784	0.5874(8)	0.03(3)	RR	
F19_105837	*s*	16 22 25.9 −55 29 06.2	12.27	···	···	···	VAR	
F19_105868		16 22 13.7 −57 00 30.9	13.11	···	···	···	LP	
F19_105967	*c*	16 22 19.5 −56 10 19.1	14.88	80.684	0.4348(3)	0.06(3)	EB	F19_106036, F19_106112
F19_106001		16 22 17.9 −56 22 16.0	14.04	81.492	7.31(7)	0.03(2)	VAR	
F19_106006		16 22 19.9 −56 06 20.3	11.41	92.542	66(6)	0.028(8)	VAR	
F19_106036	*c*	16 22 19.3 −56 10 22.8	15.00	80.691	0.4347(3)	0.05(3)	EB	F19_105967, F19_106112
F19_106085		16 22 16.0 −56 32 49.6	15.06	80.914	1.1615(9)	0.17(4)	EA	
F19_106107		16 22 15.1 −56 39 26.3	14.47	80.773	0.30561(6)	0.14(2)	EW	
F19_106112	*c*	16 22 18.8 −56 10 16.3	14.83	80.681	0.4347(4)	0.03(3)	EB	F19_105967, F19_106036
F19_106139	*s*	16 22 19.8 −56 01 02.0	14.92	80.726	1.598(4)	0.07(3)	ROT	
F19_106202	*c*	16 22 15.4 −56 31 32.1	12.19	···	···	···	LP	
F19_106260		16 22 17.1 −56 16 24.0	11.08	80.677	0.08868(3)	0.008(8)	DSCT	
F19_106288	*s*	16 22 22.0 −55 38 01.6	12.76	···	···	···	LP	

Table E.5: Variable stars in field F19 (continued).

BEST ID	F	α (J2000.0) h m s	δ ° ′ ″	R_B [mag]	T_0 [d] [rHJD]	p [d]	A [mag]	Type	Other Names
F19_106372	*s*	16 22 22.9	−55 27 43.0	16.03	81.595	5.47(7)	0.11(8)	VAR	
F19_106417		16 22 19.7	−55 48 04.0	14.75	80.684	0.2058(2)	0.04(4)	DSCT	
F19_106444	*s*	16 22 22.5	−55 26 24.4	13.74	156.058	38(2)	0.04(2)	VAR	
F19_106528	*s*	16 22 09.9	−56 57 38.9	14.34	80.821	0.1913(2)	0.02(2)	VAR	
F19_106531		16 22 10.6	−56 51 55.1	11.56	276.961	24.6(8)	0.11(3)	ROT	
F19_106541	*s*	16 22 12.2	−56 38 16.5	13.12	90.472	12.3(3)	0.03(1)	ROT	
F19_106588	⋆	16 22 19.8	−55 39 39.4	14.32	80.921	0.39903(8)	0.17(2)	EW	
F19_106609	*s*	16 22 16.2	−56 05 43.2	13.64	81.251	9.6(2)	0.02(2)	VAR	
F19_106642	*s*	16 22 18.1	−55 49 33.7	15.49	90.882	15.4(5)	0.10(5)	VAR	
F19_106715		16 22 11.1	−56 39 17.1	14.54	80.677	0.07733(2)	0.05(3)	DSCT	
F19_106721	*c*	16 22 13.9	−56 17 47.4	12.21	80.695	0.3622(2)	0.010(6)	EW/DSCT	
F19_106724		16 22 14.2	−56 15 32.8	14.64	93.426	9.3(2)	0.06(4)	ROT	
F19_106824		16 22 18.9	−55 35 38.2	12.94	...	...	...	SR	
F19_106886	*c*	16 22 11.0	−56 31 14.5	16.02	80.673	0.31256(9)	0.26(7)	EW	
F19_106941	*s*	16 22 10.1	−56 36 16.8	13.23	82.943	21(2)	0.03(2)	VAR	
F19_107001	*c*⋆	16 22 10.2	−56 32 07.6	13.65	80.794	0.5406(2)	0.19(2)	EB	
F19_107057	*s*	16 22 13.9	−56 02 31.2	13.37	100.785	31(2)	0.12(3)	SR	
F19_107145	*c*⋆	16 22 13.1	−56 05 01.8	15.16	80.979	0.45095(8)	0.87(5)	EB	
F19_107150	*c*⋆	16 22 15.1	−55 49 50.0	13.79	81.272	0.8087(3)	0.23(2)	EB	
F19_107182	*c*	16 22 16.2	−55 41 19.4	14.04	80.779	0.3818(2)	0.02(2)	EW/DSCT	
F19_107301	*s*	16 22 13.6	−55 54 59.9	13.58	80.674	0.043606(6)	0.02(2)	DSCT	
F19_107373	*c*	16 22 08.5	−56 28 28.3	13.18	80.869	0.20054(7)	0.07(2)	DSCT	F19_107504
F19_107469		16 22 04.1	−56 59 18.6	15.46	95.420	7.52(9)	0.27(9)	VAR	
F19_107504	*c*	16 22 07.9	−56 28 32.2	13.15	80.864	0.20055(5)	0.09(2)	DSCT	F19_107373
F19_107560	*c*	16 22 05.8	−56 40 56.1	14.38	81.018	0.9528(5)	0.34(5)	EA	
F19_107563	*c*	16 22 07.2	−56 30 19.4	15.07	80.976	0.4336(3)	0.09(4)	EW	F19_107589
F19_107589	*c*	16 22 07.1	−56 30 24.1	15.09	80.978	0.4336(3)	0.12(5)	EW	F19_107563
F19_107628	*c*	16 22 10.2	−56 05 57.3	10.85	95.075	9.52(8)	0.081(8)	CEP	F19_107751
F19_107690	*s*	16 22 09.1	−56 12 00.5	11.57	80.718	0.1946(2)	0.007(7)	VAR	
F19_107751	*c*	16 22 09.7	−56 05 55.2	10.87	95.193	9.5(2)	0.08(2)	CEP	F19_107628
F19_107780	*s*	16 22 12.4	−55 43 55.8	15.10	80.871	0.25693(9)	0.03(4)	EW/DSCT	
F19_107786	*k*	16 22 14.6	−55 28 40.7	10.55	...	...	...	LP	IX Nor
F19_107802		16 22 07.7	−56 17 02.2	12.61	...	...	...	SR	
F19_107837	*s*	16 22 06.9	−56 21 46.8	11.31	...	...	...	SR	
F19_107844	⋆	16 22 11.5	−55 47 35.1	13.88	81.267	3.5972(1)	0.14(1)	EA	
F19_107857	*c*⋆	16 22 03.4	−56 47 33.4	15.23	80.772	0.6378(4)	0.26(5)	EB	
F19_107863		16 22 07.9	−56 13 59.0	14.92	80.715	4.47(5)	0.06(3)	VAR	
F19_107899	⋆	16 22 11.3	−55 46 16.7	11.79	81.627	1.5578(9)	0.19(2)	EB	
F19_107943	*s*	16 22 05.8	−56 24 03.0	14.99	83.646	3.78(4)	0.07(4)	VAR	
F19_107988	*s*	16 22 12.0	−55 37 20.4	12.37	237.847	76(9)	0.014(7)	VAR	
F19_108007		16 22 10.0	−55 50 55.3	15.18	80.729	0.30496(8)	0.16(4)	EW	
F19_108074		16 22 05.0	−56 24 22.9	16.11	80.801	0.4612(2)	0.62(9)	EW	
F19_108146		16 22 03.8	−56 29 02.2	14.34	80.733	0.6294(4)	0.06(2)	EB	
F19_108186		16 22 05.9	−56 12 10.8	13.80	200.263	63(3)	0.12(2)	VAR	
F19_108199		16 22 11.7	−55 30 13.5	12.89	...	...	...	SR	
F19_108235	*c*	16 21 59.9	−56 54 12.1	13.94	89.056	4.86(4)	0.08(2)	ROT	
F19_108250		16 22 06.5	−56 04 18.8	12.88	...	...	...	SR	
F19_108322		16 22 01.3	−56 40 21.6	12.37	80.882	1.302(3)	0.032(8)	VAR	
F19_108448	*c*	16 22 03.9	−56 15 21.4	11.02	...	...	...	LP	
F19_108465		16 21 58.0	−56 58 29.7	11.75	80.813	0.4553(6)	0.02(2)	VAR	
F19_108498		16 22 00.6	−56 36 46.9	13.60	80.885	0.4220(3)	0.10(2)	RR	
F19_108501	*s*	16 22 02.2	−56 24 57.8	12.16	91.995	21.4(6)	0.08(2)	VAR	
F19_108571		16 22 08.8	−55 35 01.3	10.96	...	...	...	LP	
F19_108593		16 22 06.7	−55 49 10.8	11.43	91.153	25.7(7)	0.13(2)	VAR	
F19_108601	*s*	16 22 09.8	−55 26 33.5	11.36	95.676	7.96(6)	0.028(7)	VAR	
F19_108634		16 22 09.2	−55 29 20.7	14.12	81.235	0.8704(7)	0.09(2)	EW	
F19_108639		16 22 00.7	−56 29 35.2	14.06	82.561	2.18(1)	0.05(2)	VAR	
F19_108770		16 22 04.1	−55 59 55.6	11.35	92.952	18.8(5)	0.04(2)	VAR	
F19_108778		16 22 07.0	−55 39 47.5	12.15	80.935	0.4394(4)	0.022(7)	RR	
F19_108845	*c*	16 21 57.8	−56 42 16.2	12.97	297.983	40(4)	0.06(2)	VAR	
F19_108897	*c*	16 22 06.3	−55 38 42.1	14.45	81.153	1.0494(6)	0.29(7)	EA	
F19_108919		16 22 02.5	−56 04 18.2	11.76	80.688	0.13591(5)	0.02(2)	DSCT	
F19_108953		16 22 07.9	−55 25 49.5	11.09	182.285	19.3(7)	0.12(3)	VAR	
F19_108976		16 21 54.5	−56 59 47.7	15.67	80.914	0.5647(2)	0.73(7)	RR	
F19_109034	⋆	16 22 06.3	−55 33 30.8	16.03	93.921	6.67(3)	1.2(2)	EA	
F19_109156	*s*	16 21 58.6	−56 23 02.4	11.82	99.690	64.136(1)	0.08(1)	EA	
F19_109228		16 21 57.4	−56 29 06.6	15.02	81.112	2.359(4)	0.12(3)	EA	
F19_109259	*cs*	16 21 55.8	−56 37 57.9	14.71	80.703	0.3137(2)	0.06(8)	EW/DSCT	
F19_109276	*s*	16 22 02.9	−55 47 55.7	15.54	80.859	0.3834(2)	0.10(7)	EW	
F19_109301	*s*	16 21 58.4	−56 17 46.9	13.56	80.673	0.14698(7)	0.01(2)	DSCT	
F19_109395	*c*	16 21 57.3	−56 21 35.9	13.77	80.783	0.25547(6)	0.15(2)	DSCT	F19_109501
F19_109450	⋆	16 21 59.3	−56 05 23.2	13.47	80.678	0.5721(2)	0.19(2)	EB	
F19_109473		16 21 54.5	−56 39 25.0	13.66	96.984	11.1(3)	0.03(2)	VAR	
F19_109477		16 21 57.0	−56 20 28.8	13.42	99.958	32(1)	0.08(3)	SR	
F19_109501	*c*	16 21 56.7	−56 21 33.3	13.76	80.785	0.25547(7)	0.12(2)	DSCT	F19_109395
F19_109533	*c*	16 21 52.9	−56 48 13.1	13.76	81.245	2.4148	0.067	EA	
F19_109602		16 21 54.6	−56 33 06.3	11.13	...	...	...	SR	
F19_109609	*c*	16 22 00.4	−55 50 37.6	14.34	92.356	27(2)	0.06(2)	ROT	F19_109674
F19_109621	*c*	16 21 52.3	−56 49 43.8	15.31	80.856	0.5769(2)	0.49(4)	EA	
F19_109658		16 21 54.6	−56 31 01.5	14.15	80.874	0.3173(2)	0.03(3)	EW	
F19_109674	*c*	16 22 00.1	−55 50 33.5	14.36	92.501	27(2)	0.07(2)	ROT	F19_109609
F19_109704		16 22 00.8	−55 45 14.8	13.55	91.010	50(2)	0.10(2)	EB	
F19_109723		16 21 53.5	−56 35 52.0	14.73	99.924	15.8(2)	0.17(4)	EB	
F19_109763		16 21 57.0	−56 09 09.6	13.37	...	...	...	LP	
F19_109817	*cs*	16 21 55.5	−56 18 01.6	15.03	92.332	6.40(5)	0.05(4)	ROT	F19_109840
F19_109823		16 21 57.4	−56 03 19.7	12.26	...	...	...	VAR	
F19_109840	*cs*	16 21 55.2	−56 18 06.0	14.65	92.476	6.4(2)	0.04(3)	ROT	F19_109817
F19_109856		16 22 01.9	−55 31 47.5	15.74	80.775	0.2578(2)	0.14(6)	VAR	

Table E.5: Variable stars in field F19 (continued).

BEST ID	F	α (J2000.0) h m s	δ ° ′ ″	R_B [mag]	T_0 [d] [rHJD]	p [d]	A [mag]	Type	Other Names
F19_109861		16 21 50.8	−56 49 49.6	14.19	83.781	4.01(3)	0.03(2)	VAR	
F19_109893	⋆	16 21 49.7	−56 57 01.7	13.57	90.262	14.6(3)	0.07(2)	EB	
F19_109913		16 21 56.6	−56 05 46.5	13.64	81.016	0.4899(4)	0.02(2)	EW/DSCT	
F19_109922		16 21 59.5	−55 45 20.7	14.03	80.779	0.24783(6)	0.05(2)	EW	
F19_109942		16 21 53.6	−56 25 50.9	12.23	90.170	15.1(6)	0.018(8)	ROT	
F19_109955		16 21 58.6	−55 50 31.1	12.91	···	···	···	SR	
F19_109983		16 21 57.0	−56 00 55.6	13.00	125.480	10.02(1)	0.11(1)	EA	
F19_110070		16 21 50.3	−56 45 28.1	12.30	···	···	···	SR	
F19_110113	*c*	16 21 55.5	−56 06 03.5	11.51	···	···	···	LP	
F19_110170	*s*	16 22 00.9	−55 26 46.8	12.21	···	···	···	SR	
F19_110244	*s*	16 21 52.1	−56 24 34.1	15.27	80.835	0.18633(8)	0.04(4)	VAR	
F19_110339		16 21 52.1	−56 20 16.2	11.22	···	···	···	LP	
F19_110355	*c*	16 21 48.6	−56 44 34.7	13.22	···	···	···	SR	
F19_110372		16 21 56.9	−55 44 55.3	13.24	90.405	61(3)	0.10(2)	CEP	
F19_110451	*s*	16 21 50.1	−56 30 11.5	11.00	···	···	···	SR	
F19_110481	*c*	16 21 50.0	−56 29 10.9	13.86	80.775	0.22700(6)	0.14(2)	DSCT	F19_110630
F19_110504	⋆	16 21 46.4	−56 54 53.7	14.56	82.684	13.125(1)	0.09(1)	EA	
F19_110524	*s*	16 21 56.7	−55 40 39.7	11.04	96.721	17.4(3)	0.05(2)	VAR	
F19_110532		16 21 46.1	−56 55 36.8	12.14	80.686	0.06963(2)	0.03(2)	DSCT	
F19_110584		16 21 45.1	−57 00 26.9	12.83	81.058	0.4244(3)	0.02(2)	EW/DSCT	
F19_110630	*c*	16 21 49.3	−56 29 11.4	13.99	80.774	0.22700(7)	0.12(3)	DSCT	F19_110481
F19_110663	*s*	16 21 51.2	−56 13 15.8	14.67	83.856	5.20(5)	0.03(3)	ROT	
F19_110699		16 21 45.0	−56 55 49.3	14.29	80.703	0.2952(2)	0.03(2)	EB	
F19_110745		16 21 52.3	−56 01 08.1	10.69	···	···	···	LP	
F19_110868	*c*⋆	16 21 47.5	−56 31 00.3	14.90	80.961	0.4358(2)	0.23(4)	EW	
F19_110927		16 21 50.6	−56 06 08.3	12.30	···	···	···	SR	
F19_110968		16 21 56.1	−55 27 47.6	14.17	244.007	85(8)	0.09(2)	VAR	
F19_110971	*s*	16 21 43.9	−56 52 10.9	12.86	···	···	···	LP	
F19_110979		16 21 47.2	−56 27 55.4	13.62	81.208	0.5666(4)	0.02(2)	EA	
F19_110990		16 21 52.5	−55 51 01.2	16.81	80.764	0.3159(2)	0.9(3)	EW	
F19_111022		16 21 49.2	−56 12 37.2	15.39	91.807	50(4)	0.12(5)	VAR	
F19_111039	*c*	16 21 53.4	−55 42 55.5	13.09	80.821	0.16163(8)	0.014(8)	DSCT	
F19_111041	*s*	16 21 53.8	−55 41 29.2	12.59	81.385	2.68(2)	0.017(7)	VAR	
F19_111051	*c*	16 21 45.8	−56 35 51.1	15.55	80.852	2.219(3)	0.33(6)	EA	F19_111141
F19_111138	*cs*	16 21 44.2	−56 43 30.8	14.59	80.674	0.16413(7)	0.02(2)	DSCT	F19_111167
F19_111141	*c*	16 21 45.3	−56 35 48.5	16.02	80.851	2.219(4)	0.43(9)	EA	F19_111051
F19_111167	*cs*	16 21 44.0	−56 43 33.4	14.88	80.672	0.16413(7)	0.03(3)	DSCT	F19_111138
F19_111344		16 21 52.6	−55 37 13.1	11.63	···	···	···	LP	
F19_111426	*s*	16 21 45.4	−56 22 49.4	12.92	94.604	10.5(2)	0.03(2)	VAR	
F19_111495	*s*	16 21 46.9	−56 10 14.2	13.79	···	···	···	LP	
F19_111530		16 21 47.4	−56 05 17.4	11.00	···	···	···	SR	
F19_111535		16 21 49.0	−55 54 10.7	12.49	···	···	···	SR	
F19_111595	*c*⋆	16 21 48.0	−55 58 30.6	13.78	82.098	6.71(3)	0.57(6)	EA	
F19_111606		16 21 52.8	−55 27 37.0	13.22	172.403	66(8)	0.15(3)	CEP	
F19_111607	*c*	16 21 52.8	−55 27 07.8	12.89	···	···	···	LP	
F19_111712	*ck*	16 21 50.0	−55 41 00.7	12.78	81.176	0.8742(2)	0.91(4)	EA	UV Nor
F19_111768		16 21 45.1	−56 11 48.9	14.02	80.800	0.2001(2)	0.04(2)	DSCT	
F19_111770		16 21 46.2	−56 04 57.7	13.67	···	···	···	LP	
F19_111778	*c*	16 21 50.5	−55 36 25.2	15.53	80.864	0.3550(2)	0.07(5)	EW/DSCT	F19_111895
F19_111780	*s*	16 21 50.7	−55 34 37.3	12.89	89.967	10.2(2)	0.04(2)	VAR	
F19_111785	*s*	16 21 40.2	−56 45 57.5	13.99	82.153	4.79(5)	0.02(2)	VAR	
F19_111838		16 21 38.7	−56 53 42.2	15.13	82.249	1.979(3)	0.33(7)	EA	
F19_111895	*c*	16 21 49.6	−55 36 17.8	15.76	80.871	0.3550(2)	0.11(7)	EW/DSCT	F19_111778
F19_111916	*c*	16 21 45.3	−56 03 57.2	13.95	80.845	0.42231(5)	0.33(2)	EW	
F19_111961	*s*	16 21 49.5	−55 35 37.4	11.18	···	···	···	SR	
F19_112010		16 21 44.4	−56 07 11.5	13.28	···	···	···	SR	
F19_112013	*c*	16 21 45.0	−56 02 33.2	14.64	81.434	1.5697	0.082	EA	F19_112143
F19_112027	*s*	16 21 37.9	−56 51 37.9	14.27	81.057	2.138(8)	0.11(3)	CEP	
F19_112143	*c*	16 21 44.4	−56 02 33.9	14.66	81.432	1.5697	0.067	EA	F19_112013
F19_112232		16 21 41.2	−56 20 20.7	12.46	248.124	70(2)	0.04(2)	VAR	
F19_112251		16 21 36.6	−56 52 36.4	14.26	88.382	8.5(2)	0.04(2)	ROT	
F19_112252	*c*	16 21 36.8	−56 50 33.4	15.46	80.742	0.4309(3)	0.06(5)	EW/DSCT	F19_112346
F19_112270	*c*	16 21 42.1	−56 12 50.3	12.20	···	···	···	LP	
F19_112329	*c*	16 21 41.7	−56 12 44.7	12.23	···	···	···	LP	
F19_112341		16 21 48.6	−55 27 15.4	14.85	80.750	0.2778(1)	0.05(3)	EW	
F19_112346	*c*	16 21 36.2	−56 50 26.7	15.51	80.746	0.4309(3)	0.07(5)	EW/DSCT	F19_112252
F19_112394	*cs*	16 21 47.6	−55 31 27.0	14.27	80.969	0.4212(3)	0.03(2)	EW	
F19_112494		16 21 45.0	−55 44 15.6	12.53	80.711	0.054442(8)	0.02(1)	DSCT	
F19_112563		16 21 38.9	−56 21 51.9	11.57	···	···	···	SR	
F19_112611		16 21 37.4	−56 29 29.5	13.57	81.798	2.478(8)	0.05(2)	VAR	
F19_112711	⋆	16 21 41.9	−55 55 31.5	12.61	80.689	0.29341(8)	0.08(1)	RR	
F19_112732		16 21 36.1	−56 34 09.6	17.06	83.094	5.7(1)	0.3(2)	VAR	
F19_112758		16 21 37.0	−56 26 34.6	15.75	80.723	0.13309(4)	0.06(6)	DSCT	
F19_112784	⋆	16 21 33.9	−56 47 00.3	13.08	82.742	3.776(4)	0.30(2)	EB	
F19_112831		16 21 42.4	−55 47 53.6	16.15	80.962	0.4257(3)	0.16(9)	EW/DSCT	
F19_112836		16 21 43.8	−55 38 39.8	12.55	92.411	17(2)	0.014(7)	ROT	
F19_112910		16 21 45.2	−55 27 56.6	14.90	82.927	3.1620	0.058	EA	
F19_112933	*cs*	16 21 41.4	−55 50 44.6	13.00	···	···	···	SR	
F19_112937		16 21 43.5	−55 37 22.2	13.61	93.627	13.7(4)	0.03(2)	ROT	
F19_112958		16 21 37.2	−56 17 00.9	11.86	···	···	···	LP	
F19_112961	*s*	16 21 37.8	−56 13 50.9	14.49	80.771	0.16467(7)	0.02(3)	DSCT	
F19_113157		16 21 30.0	−56 59 49.9	14.36	80.697	0.051590(7)	0.1(1)	DSCT	
F19_113249		16 21 38.4	−55 58 08.0	14.66	81.435	1.0678(8)	0.60(7)	EA	
F19_113256	*cs*	16 21 43.2	−55 26 50.5	14.24	80.819	0.3590(2)	0.07(4)	EW	
F19_113267	*c*	16 21 35.9	−56 13 38.8	15.55	80.742	0.1785(1)	0.04(5)	VAR	F19_113357
F19_113274		16 21 40.0	−55 46 01.7	15.68	81.350	0.7231(4)	0.36(9)	EB	
F19_113322		16 21 31.3	−56 42 03.7	14.82	82.057	2.690(6)	0.14(4)	EB	
F19_113357	*c*	16 21 35.5	−56 13 45.3	14.69	80.743	0.17848(8)	0.05(4)	VAR	F19_113267

Table E.5: Variable stars in field F19 (continued).

BEST ID	F	α (J2000.0) h m s	δ ° ′ ″	R_B [mag]	T_0 [d] [rHJD]	p [d]	A [mag]	Type	Other Names
F19_113407	*s*	16 21 33.1	−56 27 21.4	15.18	81.139	10.1(2)	0.06(4)	ROT	
F19_113440		16 21 35.1	−56 12 17.4	14.63	80.752	0.18279(7)	0.10(4)	DSCT	
F19_113449		16 21 37.9	−55 52 59.8	12.63	...	...	...	LP	
F19_113465		16 21 32.0	−56 32 09.4	13.96	80.835	0.17802(9)	0.03(2)	DSCT	
F19_113509		16 21 35.6	−56 06 43.7	15.12	80.734	0.3987(2)	0.14(5)	EW	
F19_113516	*s*	16 21 39.4	−55 41 29.7	13.35	81.917	1.836(3)	0.04(2)	VAR	
F19_113520	*c*	16 21 41.4	−55 28 10.2	14.40	91.487	6.96(4)	0.06(3)	EA	
F19_113524		16 21 27.8	−56 58 34.8	12.68	80.937	0.989(2)	0.03(2)	EB	
F19_113569	⋆	16 21 32.7	−56 24 06.3	15.04	80.821	1.2224	0.045	EA	
F19_113583	*s*	16 21 27.9	−56 56 30.3	14.05	80.964	1.133(4)	0.05(2)	VAR	
F19_113597	*cs*	16 21 37.1	−55 52 41.9	12.50	...	...	...	SR	
F19_113606	*s*	16 21 41.8	−55 22 57.0	13.65	90.564	18.5(5)	0.04(2)	VAR	
F19_113717	*c*	16 21 29.1	−56 40 04.2	14.35	81.040	0.5337(2)	0.11(2)	EW	
F19_113752	*s*	16 21 34.4	−56 03 44.3	11.72	...	...	...	SR	
F19_113846	⋆	16 21 34.6	−55 58 32.8	12.29	80.797	0.9443(7)	0.04(2)	EA	
F19_113876	*c*	16 21 32.1	−56 14 29.9	14.18	81.003	0.5194(2)	0.10(2)	EW	F19_113953
F19_113933	*c*	16 21 37.3	−55 38 03.7	12.09	...	...	...	LP	
F19_113953	*c*	16 21 31.6	−56 14 34.1	14.14	81.004	0.5194(2)	0.16(2)	EW	F19_113876
F19_113990		16 21 36.0	−55 45 06.8	11.06	...	...	...	LP	
F19_114035		16 21 29.5	−56 24 09.4	12.04	...	...	...	LP	
F19_114041		16 21 34.1	−55 54 19.1	12.96	82.188	35(2)	0.10(3)	CEP	
F19_114045	*s*	16 21 36.3	−55 40 06.6	12.90	...	...	...	SR	
F19_114163		16 21 31.3	−56 08 13.9	14.16	80.723	0.4112(2)	0.11(3)	EW	
F19_114165	*s*	16 21 32.2	−56 01 36.5	12.81	80.964	0.907(2)	0.02(2)	VAR	
F19_114178	*c*	16 21 24.6	−56 53 22.3	15.53	80.854	0.41436(9)	0.50(6)	EW	
F19_114253		16 21 31.2	−56 05 14.4	15.33	83.948	4.34(6)	0.07(4)	ROT	
F19_114268	*c*	16 21 24.9	−56 47 02.2	14.66	80.840	0.6081(2)	0.28(3)	EB	
F19_114280	⋆	16 21 29.4	−56 15 52.2	12.99	82.160	1.754(2)	0.18(2)	EA	
F19_114371		16 21 28.0	−56 21 48.5	14.86	81.557	1.959(4)	0.21(4)	EA	
F19_114403		16 21 34.1	−55 41 30.6	14.99	80.792	0.3493(2)	0.07(4)	EW	
F19_114505	*c*	16 21 25.2	−56 34 11.4	14.14	80.759	0.2404(2)	0.05(3)	VAR	F19_114626
F19_114625		16 21 24.4	−56 35 32.2	12.16	...	...	...	SR	
F19_114626	*c*	16 21 24.7	−56 34 16.3	13.69	80.750	0.2404(2)	0.02(2)	VAR	F19_114505
F19_114648		16 21 33.7	−55 35 19.2	14.22	82.624	3.36(2)	0.05(2)	ROT	
F19_114650		16 21 34.1	−55 32 07.4	16.74	83.560	3.427(8)	0.4(2)	EA	
F19_114702	*c*	16 21 29.2	−56 01 33.2	15.51	82.358	1.973(4)	0.33(6)	EA	
F19_114704	*c*	16 21 30.2	−55 55 05.3	12.57	...	...	...	LP	
F19_114721	*c*	16 21 24.4	−56 31 17.2	14.26	80.813	0.25919(9)	0.03(2)	EW	F19_114773
F19_114744		16 21 20.8	−56 56 19.7	11.58	171.573	53(4)	0.10(3)	CEP	
F19_114745		16 21 21.4	−56 51 04.6	11.45	80.715	0.09860(2)	0.04(1)	DSCT	
F19_114773	*c*	16 21 24.2	−56 31 24.3	14.36	80.811	0.25919(9)	0.04(2)	EW	F19_114721
F19_114802		16 21 24.1	−56 30 46.1	11.52	96.896	21.7(6)	0.11(2)	VAR	
F19_114890		16 21 23.7	−56 29 41.7	12.45	80.676	0.7612(5)	0.08(2)	EW	
F19_114970		16 21 19.0	−56 58 01.9	13.59	82.189	2.698(7)	0.13(4)	EA	
F19_115084		16 21 29.4	−55 46 19.1	11.77	...	...	...	SR	
F19_115169		16 21 22.5	−56 26 12.5	16.21	80.757	0.3158(1)	0.23(8)	EW	
F19_115203	*c*	16 21 28.4	−55 47 31.0	13.14	...	...	...	LP	
F19_115234	*s*	16 21 30.5	−55 33 25.8	11.87	...	...	...	SR	
F19_115281	*c*	16 21 23.8	−56 14 04.7	11.76	...	...	...	SR	
F19_115288		16 21 30.8	−55 30 03.2	11.02	94.819	40(3)	0.024(6)	VAR	
F19_115315		16 21 19.2	−56 42 28.8	14.86	80.676	0.13720(2)	0.36(3)	DSCT	
F19_115389	⋆	16 21 26.9	−55 49 30.3	14.08	80.922	0.8604(3)	0.82(7)	EA	
F19_115483	*c*⋆	16 21 22.9	−56 10 58.4	14.33	81.086	0.6681(6)	0.10(3)	EA	
F19_115503		16 21 19.9	−56 29 05.8	12.80	93.078	12.7(5)	0.04(2)	ROT	
F19_115517		16 21 25.9	−55 50 44.4	12.57	81.272	18.9(5)	0.05(2)	VAR	
F19_115576	*c*	16 21 21.1	−56 18 29.9	14.54	80.943	0.784(2)	0.04(3)	VAR	F19_115634
F19_115602	*s*	16 21 20.4	−56 21 35.0	13.91	81.836	4.19(3)	0.03(2)	VAR	
F19_115634	*c*	16 21 21.0	−56 18 28.5	14.52	80.965	0.784(3)	0.03(3)	VAR	F19_115576
F19_115686		16 21 20.3	−56 19 50.4	13.78	81.770	1.6256	0.052	EA	
F19_115763	*s*	16 21 21.7	−56 07 19.1	11.42	...	...	...	SR	
F19_115766		16 21 23.7	−55 54 38.0	16.04	80.680	0.32052(5)	0.83(9)	EW	
F19_115767	*s*	16 21 24.1	−55 50 57.7	13.94	80.721	0.060332(8)	0.01(2)	DSCT	
F19_115812	*c*⋆	16 21 18.6	−56 24 46.9	13.46	182.465	2.0013(1)	1.55(1)	EA	
F19_115980		16 21 15.5	−56 39 19.4	14.27	81.220	0.6139(6)	0.05(2)	RR	
F19_116033		16 21 26.7	−55 27 10.0	15.00	81.043	0.5148(4)	0.05(4)	EW/DSCT	
F19_116088	*s*	16 21 20.8	−56 01 57.2	11.36	...	...	...	SR	
F19_116108	*c*	16 21 14.4	−56 42 34.4	11.85	...	...	...	LP	
F19_116118		16 21 19.4	−56 09 37.9	15.80	81.696	4.67(2)	0.15(7)	EA	
F19_116168	*c*	16 21 16.6	−56 25 05.0	15.10	81.040	0.5251(2)	0.32(4)	EB	
F19_116180	*s*	16 21 25.7	−55 28 14.2	12.86	89.690	16.7(5)	0.018(8)	ROT	
F19_116201		16 21 21.3	−55 54 49.0	11.64	...	...	...	LP	
F19_116230	*c*	16 21 22.3	−55 46 25.3	12.08	80.689	0.045551(5)	0.02(2)	DSCT	F19_116320
F19_116235		16 21 13.2	−56 44 33.4	16.02	81.033	0.38848(8)	0.56(8)	EW	
F19_116287	*s*	16 21 21.1	−55 51 44.1	12.32	...	...	...	VAR	
F19_116305		16 21 14.1	−56 36 37.1	14.43	81.375	1.749(7)	0.04(3)	ROT	
F19_116320	*c*	16 21 22.1	−55 46 22.3	12.11	80.689	0.045551(5)	0.02(2)	DSCT	F19_116230
F19_116322	*ck*	16 21 22.6	−55 41 40.3	12.07	...	...	...	LP	PW Nor
F19_116351		16 21 12.6	−56 43 22.5	14.41	80.755	0.33926(5)	0.27(2)	EW	
F19_116385	*s*	16 21 17.1	−56 13 08.6	14.75	80.714	0.16522(7)	0.05(5)	VAR	
F19_116424		16 21 17.4	−56 09 43.2	12.17	...	...	...	LP	
F19_116490	⋆	16 21 10.4	−56 53 29.1	13.66	81.142	0.5326(2)	0.14(2)	EW	
F19_116516	⋆	16 21 12.0	−56 40 31.9	12.93	80.685	0.6047(2)	0.21(2)	ROT	
F19_116532		16 21 17.4	−56 05 05.9	15.28	123.764	70(2)	0.11(4)	VAR	
F19_116546		16 21 11.1	−56 45 03.5	12.61	80.691	0.041613(5)	0.02(2)	DSCT	
F19_116574	*c*	16 21 13.2	−56 30 32.1	13.72	83.504	34(3)	0.04(2)	VAR	F19_116575
F19_116575	*c*	16 21 13.2	−56 30 27.6	13.56	82.247	34(3)	0.04(2)	VAR	F19_116574
F19_116621		16 21 18.7	−55 54 45.6	12.39	...	...	...	SR	
F19_116703		16 21 14.6	−56 17 40.1	15.18	80.944	0.31962(8)	0.18(4)	EW	

Table E.5: Variable stars in field F19 (continued).

BEST ID	F	α (J2000.0) δ	R_B	T_0 [d]	p [d]	A	Type	Other Names
		h m s ° ′ ″	[mag]	[rHJD]		[mag]		
F19_116778		16 21 10.5 −56 40 23.3	14.08	80.965	0.4740(2)	0.20(3)	EW	
F19_116805	c	16 21 12.6 −56 25 14.5	13.80	81.130	0.4824(3)	0.18(5)	EW	F19_116925, F19_117039
F19_116873		16 21 13.0 −56 20 20.2	14.84	80.764	0.4049(2)	0.06(3)	EW	
F19_116898		16 21 10.8 −56 32 46.8	14.65	80.855	0.2709(2)	0.04(3)	EA	
F19_116910		16 21 18.8 −55 43 05.9	11.89	99.556	20(2)	0.05(2)	ROT	
F19_116925	c	16 21 11.8 −56 25 20.3	11.67	81.130	0.4824(2)	0.12(2)	EW	F19_116805, F19_117039
F19_116930		16 21 14.0 −56 11 36.1	11.42	···	···	···	SR	
F19_116967		16 21 21.6 −55 24 07.2	13.29	81.467	1.516(2)	0.06(2)	EA	
F19_116989		16 21 17.6 −55 47 25.3	15.17	80.797	0.16909(6)	0.11(5)	DSCT	
F19_117039	c	16 21 11.1 −56 25 17.8	11.60	81.130	0.4824(2)	0.09(2)	EW	F19_116805, F19_116925
F19_117069	c	16 21 11.4 −56 23 12.6	11.51	···	···	···	LP	
F19_117086	c	16 21 07.3 −56 48 09.5	11.49	···	···	···	LP	
F19_117172	⋆	16 21 08.3 −56 38 03.2	13.27	81.008	0.4436(1)	0.11(2)	EW	
F19_117258		16 21 09.8 −56 25 15.7	12.44	···	···	···	LP	
F19_117342		16 21 10.6 −56 16 26.1	12.10	···	···	···	SR	
F19_117409	s	16 21 09.5 −56 20 45.3	15.41	81.230	1.134(2)	0.09(5)	EB	
F19_117464	s	16 21 12.2 −56 02 60.0	15.00	100.028	21(2)	0.08(4)	ROT	
F19_117534	c	16 21 16.0 −55 36 23.3	12.67	···	···	···	LP	
F19_117540		16 21 02.8 −56 59 08.0	12.09	82.322	6.72(9)	0.03(2)	ROT	
F19_117574		16 21 05.1 −56 42 57.2	11.63	96.624	20.3(8)	0.06(3)	VAR	
F19_117603	c	16 21 16.2 −55 33 39.8	13.37	···	···	···	SR	
F19_117648	⋆	16 21 11.6 −55 59 57.4	14.43	99.685	3.1079(1)	0.087(1)	EA	
F19_117795	c	16 21 05.4 −56 32 41.4	14.84	80.902	0.3024(1)	0.09(3)	EW	F19_117910
F19_117871	⋆	16 21 13.6 −55 39 39.1	13.28	81.397	0.9237(2)	0.54(2)	EA	
F19_117910	c	16 21 04.7 −56 32 45.2	14.71	80.900	0.3024(2)	0.05(3)	EW	F19_117795
F19_117942		16 21 06.4 −56 21 06.4	15.33	82.682	19.1(8)	0.17(4)	CEP	
F19_118011	c	16 20 60.0 −56 59 39.3	14.41	91.675	14.0(3)	0.08(3)	VAR	F19_118212
F19_118032		16 21 07.8 −56 09 26.5	15.41	80.684	0.3641(2)	0.27(8)	EW	
F19_118071	⋆	16 21 13.0 −55 36 10.6	13.64	83.650	4.8788(1)	0.09(1)	EA	
F19_118132	c	16 21 01.6 −56 43 07.6	11.53	281.123	56(5)	0.25(4)	VAR	
F19_118212	c	16 20 58.6 −56 59 36.6	15.32	91.294	14.0(3)	0.25(7)	VAR	F19_118011
F19_118219		16 21 00.3 −56 49 31.0	14.86	80.736	0.19105(9)	0.03(3)	VAR	
F19_118423	s	16 20 57.4 −57 00 36.0	15.49	80.774	0.2042(2)	0.08(5)	VAR	
F19_118431	c⋆	16 21 03.1 −56 24 53.7	13.76	80.956	0.8218(6)	0.04(3)	EA	
F19_118451	c	16 20 59.2 −56 48 15.9	14.84	80.927	0.3744(2)	0.13(3)	EW/DSCT	
F19_118482		16 21 01.3 −56 33 22.3	14.85	80.801	1.288(2)	0.13(4)	EA	
F19_118491	c	16 21 05.4 −56 07 29.2	14.41	82.309	2.230(8)	0.07(2)	VAR	F19_118585
F19_118543	c	16 21 02.9 −56 21 38.3	11.67	···	···	···	LP	
F19_118555	s	16 21 06.8 −55 56 44.1	15.14	96.248	8.3(2)	0.06(5)	VAR	
F19_118584		16 21 04.4 −56 10 18.8	12.56	188.403	57(4)	0.14(3)	ROT	
F19_118585	c	16 21 05.0 −56 07 28.2	14.83	82.280	2.230(8)	0.12(3)	VAR	F19_118491
F19_118651	s	16 21 03.0 −56 16 45.2	13.71	94.153	16.1(4)	0.07(3)	VAR	
F19_118672	s	16 21 11.8 −55 24 07.6	15.51	80.897	0.5221(5)	0.08(6)	EW	
F19_118716		16 21 01.4 −56 25 26.2	13.05	···	···	···	LP	
F19_118729	s	16 21 10.6 −55 28 42.0	13.62	88.086	17.5(3)	0.04(2)	ROT	
F19_119025	c	16 21 06.9 −55 41 03.9	14.64	80.924	0.3456(2)	0.10(4)	EW	
F19_119034		16 20 54.4 −56 56 32.1	13.25	80.828	3.13(3)	0.10(5)	SR	
F19_119107	c⋆	16 20 60.0 −56 19 25.5	13.24	80.724	0.52400(9)	0.40(3)	EW	
F19_119140	c	16 20 60.0 −56 17 56.7	13.19	80.775	0.4758(3)	0.03(2)	EW	F19_119199
F19_119143		16 21 01.3 −56 09 50.5	15.02	82.655	3.818(6)	0.33(6)	EA	
F19_119199	c	16 20 59.6 −56 17 51.0	13.44	80.772	0.4758(3)	0.07(3)	EW	F19_119140
F19_119213		16 21 06.9 −55 35 09.0	14.65	81.250	3.64(2)	0.26(3)	VAR	
F19_119294	c	16 21 04.5 −55 46 39.0	14.18	80.748	0.2679(2)	0.03(3)	DSCT	
F19_119408	s	16 21 07.0 −55 27 51.0	12.98	···	···	···	VAR	
F19_119424		16 20 57.3 −56 24 23.4	13.62	81.602	19.0(7)	0.05(2)	VAR	
F19_119433		16 21 03.8 −55 44 30.4	14.44	80.700	0.2273(2)	0.02(3)	VAR	
F19_119523	c	16 20 58.0 −56 16 28.8	11.18	112.548	58(6)	0.16(4)	CEP	
F19_119525		16 20 59.7 −56 06 45.4	14.30	89.117	17.9(7)	0.04(2)	VAR	
F19_119537		16 21 04.5 −55 37 41.8	15.14	82.702	2.552(4)	0.22(5)	EA	
F19_119548	s	16 20 54.1 −56 40 11.2	15.76	80.679	0.068287(9)	0.07(6)	DSCT	
F19_119563	c⋆	16 21 05.9 −55 28 54.4	14.07	81.224	1.687(2)	0.23(2)	EA	
F19_119587	c⋆	16 21 03.3 −55 42 59.1	13.28	81.138	0.46852(7)	0.38(2)	EW	
F19_119660	s	16 21 05.0 −55 30 58.7	13.20	95.919	21.2(7)	0.07(3)	VAR	
F19_119698		16 20 52.2 −56 46 26.2	15.03	80.719	0.6070(4)	0.16(4)	EW	
F19_119740		16 20 54.5 −56 30 18.4	14.98	80.741	0.3510(2)	0.09(4)	EW/DSCT	
F19_119863	s	16 21 01.9 −55 41 40.4	16.31	81.410	3.75(5)	0.1(1)	ROT	
F19_119899	c	16 20 50.6 −56 48 47.0	11.58	···	···	···	LP	
F19_119916		16 21 00.0 −55 51 26.4	12.95	122.670	19(1)	0.05(3)	ROT	
F19_119951	c⋆	16 20 59.0 −55 55 41.9	13.56	81.059	0.9051(3)	0.41(2)	EA	
F19_119985	c⋆	16 20 59.8 −55 50 33.6	13.69	80.871	0.37797(5)	0.36(3)	EW	
F19_120000	s	16 20 49.6 −56 50 51.3	12.97	81.143	0.5608(9)	0.02(2)	VAR	
F19_120101		16 20 58.2 −55 55 30.1	14.91	80.746	0.4337(3)	0.14(4)	EB	
F19_120121		16 20 51.4 −56 35 22.6	17.33	81.078	0.4642(3)	0.8(3)	EW	
F19_120127	c	16 20 54.7 −56 15 57.1	11.86	···	···	···	LP	
F19_120217		16 20 58.8 −55 48 14.9	12.39	···	···	···	LP	
F19_120272	c	16 20 53.6 −56 16 38.4	11.35	···	···	···	LP	
F19_120278		16 20 57.4 −55 54 04.3	15.35	80.829	0.37623(6)	0.68(5)	EW	
F19_120307		16 20 56.2 −56 00 27.2	13.19	93.008	18.4(4)	0.08(3)	VAR	
F19_120380		16 20 59.4 −55 39 30.8	13.56	94.289	53(5)	0.06(2)	VAR	
F19_120419		16 20 46.6 −56 55 16.1	15.67	80.779	0.32809(5)	0.59(6)	EW	
F19_120441	cs	16 20 59.3 −55 37 59.1	13.37	81.108	0.5203(6)	0.02(2)	RR	
F19_120634		16 20 52.2 −56 12 37.8	14.92	80.986	1.729(3)	0.17(6)	EA	
F19_120759		16 20 57.4 −55 37 53.9	14.35	80.902	0.7888(3)	0.27(2)	EB	
F19_120762		16 20 59.0 −55 28 14.6	14.54	80.835	0.4965(3)	0.07(3)	EB	
F19_120792		16 20 44.6 −56 52 45.2	13.29	80.679	0.11803(3)	0.06(3)	DSCT	
F19_120885	s	16 20 50.4 −56 14 28.9	14.65	92.287	6.30(8)	0.05(3)	VAR	
F19_120924		16 20 56.1 −55 39 54.7	15.59	80.726	0.3729(2)	0.12(6)	EW/DSCT	
F19_120951		16 20 51.8 −56 04 06.1	14.28	80.882	0.2310(2)	0.02(3)	VAR	

Table E.5: Variable stars in field F19 (continued).

BEST ID	F	α (J2000.0) h m s	δ ° ′ ″	R_B [mag]	T_0 [d] [rHJD]	p [d]	A [mag]	Type	Other Names
F19_120957	*s*	16 20 55.7	−55 41 14.1	12.53	90.808	40(3)	0.22(4)	VAR	
F19_121161		16 20 47.7	−56 20 21.7	15.53	80.986	0.38924(8)	0.45(6)	EW	
F19_121167		16 20 50.5	−56 03 50.1	13.82	123.799	12.4(2)	0.07(3)	ROT	
F19_121231	⋆	16 20 48.4	−56 14 32.6	11.57	81.620	0.963(3)	0.06(4)	RR	
F19_121240	*cs*	16 20 53.4	−55 45 33.2	14.21	157.603	40(2)	0.09(3)	EB	
F19_121291	*c*	16 20 54.9	−55 35 18.9	14.12	83.577	3.91(3)	0.04(2)	VAR	F19_121292
F19_121292	*c*	16 20 54.9	−55 35 14.3	14.14	83.826	3.89(2)	0.03(2)	VAR	F19_121291
F19_121326		16 20 44.5	−56 33 59.6	11.53	...	...	...	LP	
F19_121336		16 20 48.4	−56 10 21.3	14.39	80.804	0.40277(9)	0.15(2)	EW	
F19_121342	⋆	16 20 53.6	−55 40 17.3	11.54	...	...	...	SR	
F19_121409		16 20 51.7	−55 49 07.2	11.59	...	...	...	LP	
F19_121682		16 20 45.3	−56 16 10.8	14.11	...	...	...	LP	
F19_121744		16 20 49.2	−55 51 25.1	13.30	...	...	...	LP	
F19_121769		16 20 48.3	−55 55 42.5	14.17	125.790	9.1402(1)	0.07(1)	EA	
F19_121862		16 20 46.0	−56 06 27.4	15.47	80.919	0.29075(6)	0.35(5)	EW	
F19_121864	*c*⋆	16 20 46.5	−56 03 29.5	13.34	82.132	2.1281	0.060	EA	
F19_121927	*c*	16 20 50.0	−55 41 09.6	14.74	80.844	0.3510(2)	0.18(5)	EW	
F19_121967	⋆	16 20 46.7	−55 57 50.2	13.03	80.743	1.78155(1)	0.14(1)	EA	
F19_121982		16 20 38.4	−56 46 05.2	13.12	80.727	0.11535(5)	0.01(2)	DSCT	
F19_122042	*s*⋆	16 20 44.6	−56 06 52.9	13.78	90.830	19.207(1)	0.07(1)	EA	
F19_122092	*s*	16 20 42.2	−56 18 16.9	15.12	80.745	0.4291(3)	0.06(5)	EW	
F19_122181		16 20 48.1	−55 41 47.3	14.91	182.132	40(4)	0.20(4)	CEP	
F19_122252		16 20 37.2	−56 42 02.8	14.45	80.682	0.18298(7)	0.09(3)	DSCT	
F19_122355		16 20 41.0	−56 17 02.1	15.26	80.794	0.15112(6)	0.05(4)	DSCT	
F19_122357	*c*	16 20 43.9	−56 00 03.8	11.20	...	...	...	LP	
F19_122447	*c*	16 20 46.7	−55 41 08.0	14.25	80.761	0.3362(2)	0.03(4)	EW/DSCT	F19_122573
F19_122458	*c*	16 20 34.1	−56 53 35.2	11.93	...	...	...	LP	
F19_122573	*c*	16 20 46.1	−55 41 13.2	14.57	80.921	0.3362(2)	0.11(5)	EW/DSCT	F19_122447
F19_122643		16 20 47.2	−55 31 59.0	13.48	80.793	0.6423(9)	0.02(2)	VAR	
F19_122732	⋆	16 20 46.5	−55 32 32.2	12.79	141.708	3.8906(1)	0.61(1)	EA	
F19_122902		16 20 31.1	−56 55 07.3	14.93	81.280	2.209(4)	0.20(4)	EA	
F19_122943		16 20 37.9	−56 12 57.7	12.20	90.012	25(2)	0.14(4)	ROT	
F19_123012	*s*	16 20 45.4	−55 29 00.3	13.74	139.880	30(2)	0.06(2)	CEP	
F19_123035		16 20 44.4	−55 33 53.2	12.48	...	...	...	SR	
F19_123041	*c*	16 20 30.0	−56 55 53.5	13.52	80.931	0.6168(2)	0.17(2)	EW	
F19_123174	*s*	16 20 29.6	−56 53 09.3	14.00	81.640	1.415(3)	0.04(3)	EB	
F19_123203		16 20 32.4	−56 35 19.4	15.28	80.698	0.1846(2)	0.13(9)	DSCT	
F19_123207	*c*	16 20 33.3	−56 29 30.7	14.26	80.712	0.053739(8)	0.05(4)	DSCT	F19_123330
F19_123285		16 20 40.7	−55 45 37.6	13.69	82.968	2.5522(1)	0.29(1)	EA	
F19_123297		16 20 31.0	−56 40 36.4	13.60	...	...	...	LP	
F19_123321	*c*⋆	16 20 29.4	−56 48 38.9	11.88	95.223	10.86(6)	0.25(3)	EB	
F19_123330	*c*	16 20 32.8	−56 29 33.3	14.56	80.710	0.053738(8)	0.06(4)	DSCT	F19_123207
F19_123354		16 20 41.8	−55 37 44.9	14.06	81.777	1.546(8)	0.05(3)	ROT	
F19_123419		16 20 31.8	−56 31 52.6	11.00	80.927	0.899(2)	0.04(4)	VAR	
F19_123557	*c*	16 20 32.7	−56 20 19.0	13.48	...	...	...	LP	
F19_123592	*s*⋆	16 20 32.8	−56 19 18.7	12.85	...	...	...	EA	
F19_123709	*c*	16 20 31.9	−56 20 36.5	14.62	80.753	0.3694(2)	0.08(3)	EW	F19_123741
F19_123741	*c*	16 20 31.8	−56 20 43.9	15.20	80.754	0.3694(2)	0.08(5)	EW	F19_123709
F19_123874		16 20 37.5	−55 43 27.4	12.81	...	...	...	LP	
F19_124100	⋆	16 20 27.8	−56 30 37.3	14.28	83.110	4.63122(1)	0.22(1)	EA	
F19_124158	*c*	16 20 29.2	−56 19 36.2	14.63	81.085	0.4481(3)	0.11(4)	EW	F19_124251
F19_124199		16 20 39.0	−55 25 12.2	11.50	...	...	...	SR	
F19_124221	⋆	16 20 28.1	−56 24 14.5	13.99	80.703	0.10204(3)	0.2(1)	RR	
F19_124241		16 20 37.3	−55 33 28.3	14.76	80.675	0.1936(1)	0.04(3)	VAR	
F19_124251	*c*	16 20 28.9	−56 19 37.8	14.53	81.083	0.4480(3)	0.08(3)	EW	F19_124158
F19_124359		16 20 23.7	−56 45 18.3	10.97	...	...	...	LP	
F19_124362	*c*⋆	16 20 25.1	−56 36 13.2	14.29	82.306	2.5782	0.055	EA	
F19_124390		16 20 29.8	−56 08 37.2	14.54	81.042	0.5837(2)	0.36(5)	EB	
F19_124508		16 20 35.4	−55 34 34.7	12.31	157.920	51(5)	0.13(3)	VAR	
F19_124512	*c*	16 20 20.5	−56 57 49.9	12.63	80.820	0.4533(3)	0.07(3)	EW	F19_124576
F19_124576	*c*	16 20 20.2	−56 57 43.2	12.63	81.047	0.4533(2)	0.12(2)	EW	F19_124512
F19_124597		16 20 28.9	−56 06 43.3	13.24	...	...	...	SR	
F19_124609	*c*	16 20 25.3	−56 25 52.5	13.34	81.374	10.3(3)	0.11(4)	ROT	
F19_124815	*s*	16 20 29.1	−55 58 01.6	15.49	80.949	0.4392(4)	0.09(5)	EB	
F19_124816	*s*	16 20 29.1	−55 57 53.1	14.70	80.976	0.4145(3)	0.04(3)	EW	
F19_124834	⋆	16 20 24.0	−56 26 08.0	12.18	80.942	1.294(3)	0.11(5)	EB	
F19_124896		16 20 29.5	−55 53 16.0	14.44	81.001	0.3993(2)	0.16(3)	EW	
F19_124969		16 20 26.4	−56 06 56.4	15.14	81.057	0.4899(3)	0.19(5)	EW	
F19_125082	*s*	16 20 19.5	−56 42 25.6	13.22	83.521	19.1(6)	0.04(3)	VAR	
F19_125166		16 20 26.2	−56 01 59.4	15.38	80.896	0.40208(9)	0.36(5)	EW	
F19_125184	*s*	16 20 16.1	−56 57 59.5	15.16	80.791	0.4117(3)	0.06(5)	EW	
F19_125267		16 20 20.2	−56 30 38.5	10.81	...	...	...	SR	
F19_125393		16 20 27.5	−55 46 39.3	13.94	81.775	1.415(4)	0.07(3)	VAR	
F19_125445	*c*⋆	16 20 16.6	−56 45 50.8	12.54	80.828	0.36416(5)	0.42(4)	EW	
F19_125453		16 20 22.8	−56 10 59.9	14.90	81.032	0.3804(2)	0.11(3)	EW/DSCT	
F19_125473	*c*⋆	16 20 16.9	−56 43 27.1	13.12	83.416	4.52(1)	0.22(4)	EA	
F19_125509		16 20 19.5	−56 27 17.5	15.12	81.018	0.5932(5)	0.10(4)	EB	
F19_125528		16 20 15.0	−56 52 17.3	14.76	82.129	12.2(4)	0.09(4)	ROT	
F19_125562		16 20 17.8	−56 34 55.4	12.30	82.018	21(2)	0.05(5)	CEP	
F19_125697	⋆	16 20 23.3	−55 59 31.7	14.97	81.814	6.0947(1)	0.7(1)	EA	
F19_125757		16 20 21.4	−56 07 51.8	13.70	83.381	9.9(3)	0.09(6)	ROT	
F19_125783		16 20 21.9	−56 03 55.8	14.32	81.992	1.375(4)	0.04(3)	ROT	
F19_125821		16 20 15.2	−56 40 06.3	13.28	91.890	32(4)	0.09(5)	CEP	
F19_125848		16 20 11.9	−56 58 16.0	12.64	...	...	...	SR	
F19_126154		16 20 11.0	−56 52 21.8	15.01	80.818	0.6075(4)	0.12(4)	EW	
F19_126156		16 20 11.7	−56 48 12.1	16.03	80.759	0.3508(2)	0.09(7)	EW/DSCT	
F19_126288		16 20 10.1	−56 51 42.8	15.49	80.828	0.4095(3)	0.10(5)	EA	
F19_126341		16 20 19.2	−56 00 21.8	15.68	81.001	0.3776(2)	0.23(6)	EW	

Table E.5: Variable stars in field F19 (continued).

BEST ID	F	α (J2000.0) h m s	δ ° ′ ″	R_B [mag]	T_0 [d] [rHJD]	p [d]	A [mag]	Type	Other Names
F19_126349	⋆	16 20 24.0	−55 34 07.4	13.62	112.930	11.901(1)	0.13(1)	EA	
F19_126444	*c*	16 20 12.5	−56 33 23.6	12.52	···	···	···	LP	
F19_126475		16 20 17.3	−56 05 36.6	15.56	80.753	0.32971(5)	0.75(7)	EW	
F19_126542		16 20 17.9	−55 59 20.8	17.45	80.677	0.4264(3)	0.5(3)	EW	
F19_126543		16 20 18.8	−55 54 38.4	15.03	82.807	3.68(2)	0.13(4)	EB	
F19_126563	*c*⋆	16 20 14.2	−56 18 24.9	14.20	81.381	1.1828(7)	0.20(4)	EA	
F19_126804	*c*	16 20 20.4	−55 37 50.1	12.93	80.930	0.34456(5)	0.27(2)	EW	F19_126900
F19_126871	⋆	16 20 18.9	−55 43 56.0	12.90	80.723	0.3630(1)	0.18(4)	EW	
F19_126900	*c*	16 20 19.8	−55 37 55.1	13.19	80.931	0.3446(1)	0.21(5)	EW	F19_126804
F19_126986	*c*	16 20 17.2	−55 48 44.6	12.03	89.769	18.1(4)	0.22(4)	EB	
F19_127068	⋆	16 20 07.7	−56 37 20.5	14.95	80.878	0.6184(2)	0.39(4)	EA	
F19_127112	*s*	16 20 17.7	−55 42 44.2	13.10	···	···	···	SR	
F19_127167	*s*	16 20 19.6	−55 30 26.1	13.11	···	···	···	SR	
F19_127212		16 20 10.3	−56 17 45.6	13.31	96.720	80(2)	0.04(2)	VAR	
F19_127247	*s*	16 20 18.0	−55 36 02.3	14.62	80.676	0.1687(2)	0.03(4)	VAR	
F19_127501		16 20 18.0	−55 28 25.0	14.44	80.852	0.18499(7)	0.08(3)	DSCT	
F19_127524		16 20 17.5	−55 30 05.1	10.85	81.537	70(7)	0.06(3)	VAR	
F19_127586		16 20 16.2	−55 35 01.7	11.94	94.835	21(2)	0.05(3)	VAR	

Acknowledgments

It is a pleasure to thank those who made this thesis possible.

First of all, I want to kindly thank my inspiring supervisor Prof. Heike Rauer for the opportunity to pursue my Ph.D. thesis in one of the most exciting fields in astronomy. I am also deeply indebted to Dr. Anders Erikson, who patiently guided me through the ups and downs of this work with ever-available advice.

My work with BEST II would not have been possible without those people who committed themselves for the installation and operation of this telescope in its very remote environment. I am particularly grateful to Dr. Petr Kabath, who not only shared his detailed knowledge of BEST II with me, but also introduced me to photometric observations and data reduction in general, and kept on motivating me throughout this work. I enjoyed the collaboration with Prof. Rolf Chini and his group at the Ruhr-Universität Bochum and sincerely appreciate their invaluable, fast and uncomplicated help with any technical concerns in Chile. Furthermore, I would like to thank Hartmut Korsitzky and Dr. Philipp Eigmüller for their help in preparing and setting up the new BEST II instrument.

I want to express my gratitude to all colleagues within the department "Extrasolar Planets and Atmospheres" for inspiring discussions, questions, advice, and motivation. In particular, I would like to thank Dr. Juan Cabrera and Dr. Szilárd Csizmadia for sharing their broad scientific knowledge with me whenever needed, and my roommate Thomas Pasternacki for always willing to discuss my work.

The acquisition, treatment and analysis of the large amount of data in this thesis was only made possible with the invaluable help of several people. I am particularly indebted to the BEST II observers for their sleepless nights, to Sabrina Kirste for her assistance with the calibration, to Dr. Szilárd Csizmadia for the modeling of the planetary candidates, to Dr. Petr Kabath and Dr. Davide Gandolfi for the reduction and analysis of spectroscopic data, to Julian Petrasch for screening all LRa02 light curves, and to Sabrina Kirste and Dr. Claudia Dreyer for a first sorting of stellar variability in fields F17 and F19. Furthermore, I enjoyed shaping the profile of "our" pipeline together with Thomas Pasternacki, who shares my bold dream of a fully automated, structured, documented, validated, and optimized data reduction.

I would like to express my sincere gratitude to Dr. Juan Cabrera, Dr. Szilárd Csizmadia, Dr. Anders Erikson, Dr. Lee Grenfell, and Dr. Ruth Titz-Weider for careful reading of the manuscript and their insightful comments and suggestions.

Finally, I would not have made it without the strong company, encouragement and continuous support of my family. My greatest thanks goes to Antje for always being there for me.

Further Acknowledgments

- This research has made extensive use of NASA's excellent **Astrophysics Data System** (ADS) Bibliographic Services.
- Based on **CoRoT** data publicly available from http://idoc-corot.ias.u-psud.fr/.
- This work used data from **ASTEP**, a project supervised by the Observatoire de la Côte d'Azur, and installed at the Concordia station, Antarctica with support from the Institut Paul Emile Victor.
- This research made use of **Aladin**, the **SIMBAD** database, and the **VizieR** catalogue access tool, all operated at CDS, Strasbourg, France.
- This research made use of the International **Variable Star Index** (VSX) database, operated at AAVSO, Cambridge, Massachusetts, USA.
- This publication makes use of data products from the **Two Micron All Sky Survey**, which is a joint project of the University of Massachusetts and the Infrared Processing and Analysis Center/California Institute of Technology, funded by the National Aeronautics and Space Administration and the National Science Foundation.
- The **Guide Star Catalogue-II** is a joint project of the Space Telescope Science Institute and the Osservatorio Astronomico di Torino. Space Telescope Science Institute is operated by the Association of Universities for Research in Astronomy, for the National Aeronautics and Space Administration under contract NAS5-26555. The participation of the Osservatorio Astronomico di Torino is supported by the Italian Council for Research in Astronomy. Additional support is provided by European Southern Observatory, Space Telescope European Coordinating Facility, the International GEMINI project and the European Space Agency Astrophysics Division.

Bibliography

Abe, F., Allen, W., Banks, T., Bond, I. et al.: *The MOA Project.* In R. Ferlet, J.-P. Maillard, and B. Raban (Eds.), *Proc. of the 12th IAP Astrophysics meeting: Variable Stars and the Astrophysical Returns of Microlensing Surveys*, pp. 75–80, 1997.

Abe, L., Gonçalves, I., Agabi, A., Alapini, A. et al.: *The Secondary Eclipses and Phases of WASP-19b as seen by the ASTEP400 Telescope from Antarctica.* A&A (submitted), 2012.

Agol, E., Steffen, J., Sari, R., and Clarkson, W.: *On detecting terrestrial planets with timing of giant planet transits.* MNRAS, **359**:567–579, 2005.

Aigrain, S., Favata, F., and Gilmore, G.: *Characterising stellar micro-variability for planetary transit searches.* A&A, **414**:1139–1152, 2004.

Alapini, A. and Aigrain, S.: *An iterative filter to reconstruct planetary transit signals in the presence of stellar variability.* MNRAS, **397**:1591–1598, 2009.

Alard, C.: *Image subtraction using a space-varying kernel.* A&AS, **144**:363–370, 2000.

Alard, C. and Lupton, R. H.: *A Method for Optimal Image Subtraction.* ApJ, **503**:325–331, 1998.

Alcock, C., Allsman, R. A., Alves, D. R., Axelrod, T. S. et al.: *The MACHO Project: Microlensing Results from 5.7 Years of Large Magellanic Cloud Observations.* ApJ, **542**:281–307, 2000.

Alibert, Y., Mordasini, C., and Benz, W.: *Extrasolar planet population synthesis. III. Formation of planets around stars of different masses.* A&A, **526**:A63, 2011.

Almenara, J. M., Deeg, H. J., Aigrain, S., Alonso, R. et al.: *Rate and nature of false positives in the CoRoT exoplanet search.* A&A, **506**:337–341, 2009.

Alonso, R., Brown, T. M., Charbonneau, D., Dunham, E. W. et al.: *The Transatlantic Exoplanet Survey (TrES): A Review.* In C. Afonso, D. Weldrake, and T. Henning (Eds.), *Transiting Extrapolar Planets Workshop*, *Astronomical Society of the Pacific Conference Series*, vol. 366, pp. 13–22, 2007.

Alonso, R., Auvergne, M., Baglin, A., Ollivier, M. et al.: *Transiting exoplanets from the CoRoT space mission. II. CoRoT-Exo-2b: a transiting planet around an active G star.* A&A, **482**:L21–L24, 2008.

Alonso, R., Alapini, A., Aigrain, S., Auvergne, M. et al.: *The secondary eclipse of CoRoT-1b.* A&A, **506**:353–358, 2009.

Alonso, R., Guenther, E., Almenara, J.-M., Endl, M. et al.: *Transiting exoplanets from the CoRoT space mission. XXIV. CoRoT-24: validating a transiting multi-planet system.* A&A (submitted), 2012.

Andersen, M. I., Freyhammer, L., and Storm, J.: *Gain calibration of array detectors by shifted and rotated exposures.* In P. Benvenuti (Ed.), *Calibrating and Understanding HST and ESO Instruments*, *European Southern Observatory Conference and Workshop Proceedings*, vol. 53, pp. 87–92, 1995.

Angel, R.: *Direct detection of terrestrial exoplanets: comparing the potential for space and ground telescopes.* In M. Fridlund, T. Henning, and H. Lacoste (Eds.), *Earths: DARWIN/TPF and the Search for Extrasolar Terrestrial Planets*, ESA SP-539, pp. 221–230, 2003.

Anglada-Escudé, G., Arriagada, P., Vogt, S. S., Rivera, E. J. et al.: *A Planetary System around the nearby M Dwarf GJ 667C with At Least One Super-Earth in Its Habitable Zone.* ApJ, **751**:L16, 2012.

Appourchaux, T., Michel, E., Auvergne, M., Baglin, A. et al.: *CoRoT sounds the stars: p-mode parameters of Sun-like oscillations on HD 49933.* A&A, **488**:705–714, 2008.

Aristidi, E. and Mekarnia, D.: *AstroConcordia & ASTEP winterover report.* Concordia Station, Antarctica, 2011.

Aristidi, E., Fossat, E., Agabi, A., Mékarnia, D. et al.: *Dome C site testing: surface layer, free atmosphere seeing, and isoplanatic angle statistics.* A&A, **499**:955–965, 2009.

Ashley, M. C. B., Burton, M. G., Storey, J. W. V., Lloyd, J. P. et al.: *South Pole Observations of the Near-Infrared Sky Brightness.* PASP, **108**:721–723, 1996.

Ashley, M. C. B., Burton, M. G., Lawrence, J. S., and Storey, J. W. V.: *Robotic telescopes on the Antarctic plateau.* Astronomische Nachrichten, **325**:619–625, 2004.

Ashley, M. C. B., Burton, M. G., Calisse, P. G., Phillips, A., and Storey, J. W. V.: *Site testing at Dome C - cloud statistics from the ICECAM experiment.* Highlights of Astronomy, **13**:932–934, 2005.

Auvergne, M., Bodin, P., Boisnard, L., Buey, J.-T. et al.: *The CoRoT satellite in flight: description and performance.* A&A, **506**:411–424, 2009.

Baglin, A., Auvergne, M., Barge, P., Deleuil, M. et al.: *Scientific Objectives for a Minisat: CoRoT.* In M. Fridlund, A. Baglin, J. Lochard, and L. Conroy (Eds.), *The COROT Mission Pre-Launch Status*, ESA SP-1306, pp. 33–37, 2006.

Bakos, G., Noyes, R. W., Kovács, G., Stanek, K. Z., Sasselov, D. D., and Domsa, I.: *Wide-Field Millimagnitude Photometry with the HAT: A Tool for Extrasolar Planet Detection.* PASP, **116**:266–277, 2004.

Bakos, G. Á., Lázár, J., Papp, I., Sári, P., and Green, E. M.: *System Description and First Light Curves of the Hungarian Automated Telescope, an Autonomous Observatory for Variability Search.* PASP, **114**:974–987, 2002.

Bakos, G. Á., Csubry, Z., Penev, K., Bayliss, D. et al.: *HATSouth: A Global Network of Fully Automated Identical Wide-Field Telescopes.* PASP (in press), 2013.

Ballot, J., Gizon, L., Samadi, R., Vauclair, G. et al.: *Accurate p-mode measurements of the G0V metal-rich CoRoT target HD 52265.* A&A, **530**:A97, 2011.

Baraffe, I., Chabrier, G., and Barman, T.: *The physical properties of extra-solar planets.* Reports on Progress in Physics, **73**, 1:016901, 2010.

Barge, P., Léger, A., Ollivier, M., Rouan, D., Schneider, J., and Exoplanet COROT Team: *Photometric Search for Transiting Planets.* In M. Fridlund, A. Baglin, J. Lochard, and L. Conroy (Eds.), *The COROT Mission Pre-Launch Status*, ESA SP-1306, pp. 83–92, 2006.

Barge, P., Baglin, A., Auvergne, M., Rauer, H. et al.: *Transiting exoplanets from the CoRoT space mission. I. CoRoT-Exo-1b: a low-density short-period planet around a G0V star.* A&A, **482**:L17–L20, 2008.

Barnes, J. W.: *Effects of Orbital Eccentricity on Extrasolar Planet Transit Detectability and Light Curves.* PASP, **119**:986–993, 2007.

Barnes, T. G. and Evans, D. S.: *Stellar angular diameters and visual surface brightness - I. Late spectral types.* MNRAS, **174**:489–502, 1976.

Batygin, K. and Stevenson, D. J.: *Inflating Hot Jupiters with Ohmic Dissipation.* ApJ, **714**:L238–L243, 2010.

Baudin, F., Barban, C., Belkacem, K., Hekker, S. et al.: *Amplitudes and lifetimes of solar-like oscillations observed by CoRoT. Red-giant versus main-sequence stars.* A&A, **529**:A84, 2011.

Bayliss, D. D. R. and Sackett, P. D.: *The SkyMapper Transit Survey.* In C. Afonso, D. Weldrake, and T. Henning (Eds.), *Transiting Extrapolar Planets Workshop*, *Astronomical Society of the Pacific Conference Series*, vol. 366, pp. 320–325, 2007.

Bayliss, D. D. R. and Sackett, P. D.: *The Frequency of Hot Jupiters in the Galaxy: Results from the SuperLupus Survey.* ApJ, **743**:103, 2011.

Bayliss, D. D. R., Weldrake, D. T. F., Sackett, P. D., Tingley, B. W., and Lewis, K. M.: *The Lupus Transit Survey for Hot Jupiters: Results and Lessons.* AJ, **137**:4368–4376, 2009.

Beatty, T. G. and Gaudi, B. S.: *Predicting the Yields of Photometric Surveys for Transiting Extrasolar Planets.* ApJ, **686**:1302–1330, 2008.

Belikov, A. N. and Röser, S.: *A general method of estimating stellar astrophysical parameters from photometry.* A&A, **489**:1107–1119, 2008.

Belkacem, K., Samadi, R., Goupil, M.-J., Lefèvre, L. et al.: *Solar-Like Oscillations in a Massive Star.* Science, **324**:1540–1542, 2009.

Benedict, G. F., McArthur, B., Nelan, E., Story, D. et al.: *Astrometry with Hubble Space Telescope Fine Guidance Sensor number 3: Position-mode stability and precision.* PASP, **106**:327–336, 1994.

Benedict, G. F., McArthur, B. E., Forveille, T., Delfosse, X. et al.: *A Mass for the Extrasolar Planet Gliese 876b Determined from Hubble Space Telescope Fine Guidance Sensor 3 Astrometry and High-Precision Radial Velocities.* ApJ, **581**:L115–L118, 2002.

Benner, S. A.: *Defining Life.* Astrobiology, **10**:1021–1030, 2010.

Bertin, E. and Arnouts, S.: *SExtractor: Software for source extraction.* A&AS, **117**:393–404, 1996.

Bessell, M. S.: *UBVRI passbands.* PASP, **102**:1181–1199, 1990.

Bessell, M. S. and Brett, J. M.: *JHKLM photometry - Standard systems, passbands, and intrinsic colors.* PASP, **100**:1134–1151, 1988.

Blažko, S.: *Mitteilung über veränderliche Sterne.* Astronomische Nachrichten, **175**:325, 1907.

Bodenheimer, P., Lin, D. N. C., and Mardling, R. A.: *On the Tidal Inflation of Short-Period Extrasolar Planets.* ApJ, **548**:466–472, 2001.

Bodin, P.: *The CoRot Instrument.* In M. Fridlund, A. Baglin, J. Lochard, and L. Conroy (Eds.), *The COROT Mission Pre-Launch Status*, ESA SP-1306, pp. 153–154, 2006.

Boisse, I., Bouchy, F., Hébrard, G., Bonfils, X., Santos, N., and Vauclair, S.: *Disentangling between stellar activity and planetary signals.* A&A, **528**:A4, 2011.

Bonner, C. S., Ashley, M. C. B., Cui, X., Feng, L. et al.: *Thickness of the Atmospheric Boundary Layer Above Dome A, Antarctica, during 2009.* PASP, **122**:1122–1131, 2010.

Bonomo, A. S. and Lanza, A. F.: *Modelling solar-like variability for the detection of Earth-like planetary transits. I. Performance of the three-spot modelling and harmonic function fitting.* A&A, **482**:341–347, 2008.

Bonomo, A. S., Aigrain, S., Bordé, P., and Lanza, A. F.: *Modelling solar-like variability for the detection of Earth-like planetary transits. II. Performance of the three-spot modelling, harmonic function fitting iterative nonlinear filtering, and sliding boxcar filtering.* A&A, **495**:647–653, 2009.

Borkovits, T. and Hegedüs, T.: *On the invisible components of some eclipsing binaries.* A&AS, **120**:63–75, 1996.

Borucki, W. J., Koch, D., Basri, G., Batalha, N. et al.: *Kepler Planet-Detection Mission: Introduction and First Results.* Science, **327**:977–980, 2010.

Bouchy, F., Pepe, F., and Queloz, D.: *Fundamental photon noise limit to radial velocity measurements.* A&A, **374**:733–739, 2001.

Brack, A.: *Liquid water and the origin of life.* Origins of Life and Evolution of the Biosphere, **23**:3–10, 1993.

Bradley, A., Abramowicz-Reed, L., Story, D., Benedict, G., and Jefferys, W.: *The flight hardware and ground system for Hubble Space Telescope astrometry.* PASP, **103**:317–335, 1991.

Brown, T. M.: *Expected Detection and False Alarm Rates for Transiting Jovian Planets.* ApJ, **593**:L125–L128, 2003.

Brown, T. M., Latham, D. W., Everett, M. E., and Esquerdo, G. A.: *Kepler Input Catalog: Photometric Calibration and Stellar Classification.* AJ, **142**:112, 2011.

Buda, L. S.: *Search for eclipsing O-type binaries.* Master's thesis, Ruhr-Universität Bochum, 2011.

Burrows, A., Hubbard, W. B., Lunine, J. I., and Liebert, J.: *The theory of brown dwarfs and extrasolar giant planets.* Reviews of Modern Physics, **73**:719–765, 2001.

Burrows, A., Sudarsky, D., and Hubeny, I.: *Spectra and Diagnostics for the Direct Detection of Wide-Separation Extrasolar Giant Planets.* ApJ, **609**:407–416, 2004.

Burrows, A., Sudarsky, D., and Hubeny, I.: *Theory for the Secondary Eclipse Fluxes, Spectra, Atmospheres, and Light Curves of Transiting Extrasolar Giant Planets.* ApJ, **650**:1140–1149, 2006.

Burrows, A., Hubeny, I., Budaj, J., and Hubbard, W. B.: *Possible Solutions to the Radius Anomalies of Transiting Giant Planets.* ApJ, **661**:502–514, 2007.

Burrows, A., Budaj, J., and Hubeny, I.: *Theoretical Spectra and Light Curves of Close-in Extrasolar Giant Planets and Comparison with Data.* ApJ, **678**:1436–1457, 2008.

Burton, M. G.: *Astronomy in Antarctica.* A&A Rev., **18**:417–469, 2010.

Cabrera, J., Fridlund, M., Ollivier, M., Gandolfi, D. et al.: *Planetary transit candidates in CoRoT-LRc01 field.* A&A, **506**:501–517, 2009.

Cabrera, J., Csizmadia, S., Erikson, A., Rauer, H., and Kirste, S.: *A study of the performance of transit detection tool DST in space-based surveys. Application of the CoRoT pipeline to Kepler data.* A&A (in press), 2012.

Caldwell, D. A., Borucki, W. J., Showen, R. L., Jenkins, J. M. et al.: *Detecting Extrasolar Planet Transits from the South Pole.* In R. Norris and F. Stootman (Eds.), *Proceedings of the International Astronomical Union: Bioastronomy 2002 – Life Among the Stars (IAU S213)*, pp. 93–96. Astronomical Society of the Pacific, 2004.

Candidi, M. and Lori, A.: *Status of the Antarctic Base at Dome C and perspectives for Astrophysics.* Mem. Soc. Astron. Italiana, **74**:29–36, 2003.

Cannon, A. J.: *The Henry Draper extension.* Annals of Harvard College Observatory, **100**:1–226, 1936.

Cannon, A. J. and Mayall, M. W.: *The Henry Draper extension II.* Annals of Harvard College Observatory, **112**:1–295, 1949.

Cannon, A. J. and Pickering, E. C.: *The Henry Draper catalogue.* Annals of Harvard College Observatory, **91–99**, 1918–1924.

Carone, L., Gandolfi, D., Cabrera, J., Hatzes, A. P. et al.: *Planetary transit candidates in the CoRoT LRa01 field.* A&A, **538**:A112, 2012.

Carpano, S., Cabrera, J., Alonso, R., Barge, P. et al.: *Planetary transit candidates in Corot-IRa01 field.* A&A, **506**:491–500, 2009.

Casertano, S., Lattanzi, M. G., Sozzetti, A., Spagna, A. et al.: *Double-blind test program for astrometric planet detection with Gaia.* A&A, **482**:699–729, 2008.

Cassan, A., Kubas, D., Beaulieu, J.-P., Dominik, M. et al.: *One or more bound planets per Milky Way star from microlensing observations.* Nature, **481**:167–169, 2012.

Catala, C.: *PLATO: PLAnetary Transits and Oscillations of stars.* Experimental Astronomy, **23**:329–356, 2009.

Catanzarite, J. and Shao, M.: *The Occurrence Rate of Earth Analog Planets Orbiting Sun-like Stars.* ApJ, **738**:151, 2011.

Charbonneau, D., Brown, T. M., Latham, D. W., and Mayor, M.: *Detection of Planetary Transits Across a Sun-like Star.* ApJ, **529**:L45–L48, 2000.

Charbonneau, D., Brown, T. M., Burrows, A., and Laughlin, G.: *When Extrasolar Planets Transit Their Parent Stars.* In B. Reipurth, D. Jewitt, and K. Keil (Eds.), *Protostars and Planets V*, pp. 701–716. University of Arizona Press, Tucson, 2007.

Charbonneau, D., Berta, Z. K., Irwin, J., Burke, C. J. et al.: *A super-Earth transiting a nearby low-mass star.* Nature, **462**:891–894, 2009.

Chazelas, B., Pollacco, D., Queloz, D., Rauer, H. et al.: *NGTS: a robotic transit survey to detect Neptune and super-Earth mass planets.* In *Ground-based and Airborne Telescopes IV*, Proc. SPIE 8444, pp. 84440E(1–10), 2012.

Christiansen, J. L., Derekas, A., Kiss, L. L., Ashley, M. C. B. et al.: *The University of New South Wales Extrasolar Planet Search: a catalogue of variable stars from fields observed between 2004 and 2007.* MNRAS, **385**:1749–1763, 2008.

Ciardi, D. R., von Braun, K., Bryden, G., van Eyken, J. et al.: *Characterizing the Variability of Stars with Early-release Kepler Data.* AJ, **141**:108, 2011.

Collier Cameron, A., Pollacco, D., Street, R. A., Lister, T. A. et al.: *A fast hybrid algorithm for exoplanetary transit searches.* MNRAS, **373**:799–810, 2006.

Collier Cameron, A., Wilson, D. M., West, R. G., Hebb, L. et al.: *Efficient identification of exoplanetary transit candidates from SuperWASP light curves.* MNRAS, **380**:1230–1244, 2007.

Cox, A.: *Allen's Astrophysical Quantities.* Springer, 2000.

Crouzet, N., Guillot, T., Agabi, A., Rivet, J. et al.: *ASTEP South: an Antarctic Search for Transiting ExoPlanets around the celestial south pole.* A&A, **511**:A36, 2010.

Crouzet, N., Guillot, T., Agabi, K., Daban, J.-B. et al.: *ASTEP: Towards the detection and characterization of exoplanets from Dome C.* In F. Bouchy, R. Díaz, and C. Moutou (Eds.), *Detection and Dynamics of Transiting Exoplanets*, EPJ Web of Conferences 11, id.06001, 2011.

Crouzet, N., Schmider, F.-X., Rivet, J.-P., Bondoux, E. et al.: *An analysis of 4 years of data from ASTEP South.* In M. G. Burton, X. Cui, and N. F. H. Tothill (Eds.), *Proceedings of the International Astronomical Union: Astrophysics from Antarctica (IAU S288).* Cambridge University Press, 2012.

Csizmadia, S., Moutou, C., Deleuil, M., Cabrera, J. et al.: *Transiting exoplanets from the CoRoT space mission. XVII. The hot Jupiter CoRoT-17b: a very old planet.* A&A, **531**:A41, 2011.

Cui, X.: *CSTAR and future plans for Dome A.* Highlights of Astronomy, **15**:639–640, 2010.

Cumming, A., Marcy, G. W., and Butler, R. P.: *The Lick Planet Search: Detectability and Mass Thresholds.* ApJ, **526**:890–915, 1999.

Cumming, A., Butler, R. P., Marcy, G. W., Vogt, S. S., Wright, J. T., and Fischer, D. A.: *The Keck Planet Search: Detectability and the Minimum Mass and Orbital Period Distribution of Extrasolar Planets.* PASP, **120**:531–554, 2008.

Daban, J.-B., Gouvret, C., Guillot, T., Agabi, A. et al.: *ASTEP 400: a telescope designed for exoplanet transit detection from Dome C, Antarctica.* In L. M. Stepp, R. Gilmozzi, and H. J. Hall (Eds.), *Ground-based and Airborne Telescopes III*, Proc. SPIE 7733, pp. 77334T(1–9), 2010.

Damé, L., Andretta, V., and The Arena Solar Astrophysics Working Group Members: *ARENA Solar Astrophysics Working Group Reporting on Dome C Exceptional Potential for Solar Observations.* In L. Spinoglio and N. Epchtein (Eds.), *3rd ARENA Conference: An Astronomical Observatory at Concordia (Dome C, Antarctica)*, *EAS Publication Series*, vol. 40, pp. 451–466, 2010.

D'Angelo, G., Durisen, R. H., and Lissauer, J. J.: *Giant Planet Formation.* In Seager, S. (Ed.), *Exoplanets*, pp. 319–346. University of Arizona Press, 2010.

de Mooij, E. J. W., Brogi, M., de Kok, R. J., Koppenhoefer, J. et al.: *Optical to near-infrared transit observations of super-Earth GJ 1214b: water-world or mini-Neptune?* A&A, **538**:A46, 2012.

De Ridder, J., Barban, C., Baudin, F., Carrier, F. et al.: *Non-radial oscillation modes with long lifetimes in giant stars.* Nature, **459**:398–400, 2009.

Debosscher, J., Sarro, L. M., Aerts, C., Cuypers, J. et al.: *Automated supervised classification of variable stars. I. Methodology.* A&A, **475**:1159–1183, 2007.

Debosscher, J., Sarro, L. M., López, M., Deleuil, M. et al.: *Automated supervised classification of variable stars in the CoRoT programme. Method and application to the first four exoplanet fields.* A&A, **506**:519–534, 2009.

Deeg, H.: *UTM, a universal simulator for lightcurves of transiting systems.* In F. Pont, D. D. Sasselov, and M. J. Holman (Eds.), *Proceedings of the International Astronomical Union: Transiting Planets (IAU S253)*, pp. 388–391. Cambridge University Press, 2009.

Deeg, H. J., Gillon, M., Shporer, A., Rouan, D. et al.: *Ground-based photometry of space-based transit detections: photometric follow-up of the CoRoT mission.* A&A, **506**:343–352, 2009.

Deeg, H. J., Moutou, C., Erikson, A., Csizmadia, S. et al.: *A transiting giant planet with a temperature between 250K and 430K.* Nature, **464**:384–387, 2010.

Deeming, T. J.: *Fourier Analysis with Unequally-Spaced Data.* Ap&SS, **36**:137–158, 1975.

Degroote, P., Aerts, C., Baglin, A., Miglio, A. et al.: *Deviations from a uniform period spacing of gravity modes in a massive star.* Nature, **464**:259–261, 2010a.

Degroote, P., Aerts, C., Samadi, R., Miglio, A. et al.: *Asteroseismology of OB stars with CoRoT.* Astronomische Nachrichten, **331**:1065, 2010b.

Dekker, H., D'Odorico, S., Kaufer, A., Delabre, B., and Kotzlowski, H.: *Design, construction, and performance of UVES, the echelle spectrograph for the UT2 Kueyen Telescope at the ESO Paranal Observatory.* In M. Iye and A. F. Moorwood (Eds.), *Optical and IR Telescope Instrumentation and Detectors*, Proc. SPIE 4008, pp. 534–545, 2000.

Deleuil, M., Deeg, H. J., Alonso, R., Bouchy, F. et al.: *Transiting exoplanets from the CoRoT space mission. VI. CoRoT-Exo-3b: the first secure inhabitant of the brown-dwarf desert.* A&A, **491**:889–897, 2008.

Deleuil, M., Meunier, J. C., Moutou, C., Surace, C. et al.: *Exo-Dat: An Information System in Support of the CoRoT/Exoplanet Science.* AJ, **138**:649–663, 2009.

Deleuil, M., Bonomo, A. S., Ferraz-Mello, S., Erikson, A. et al.: *Transiting exoplanets from the CoRoT space mission. XX. CoRoT-20b: A very high density, high eccentricity transiting giant planet.* A&A, **538**:A145, 2012.

Deming, D., Seager, S., Winn, J., Miller-Ricci, E. et al.: *Discovery and Characterization of Transiting Super Earths Using an All-Sky Transit Survey and Follow-up by the James Webb Space Telescope.* PASP, **121**:952–967, 2009.

Derue, F., Marquette, J.-B., Lupone, S., Afonso, C. et al.: *Observation of periodic variable stars towards the Galactic spiral arms by EROS II.* A&A, **389**:149–161, 2002.

Dumusque, X., Pepe, F., Lovis, C., Ségransan, D. et al.: *An Earth-mass planet orbiting α Centauri B.* Nature (in press), 2012.

Eigmüller, P. and Eislöffel, J.: *TEST The Tautenburg Exoplanet Search Telescope.* In *Proceedings of the International Astronomical Union: Transiting Planets (IAU S253)*, pp. 340–342. Cambridge University Press, 2009.

Enoch, B., Collier Cameron, A., and Horne, K.: *Factors affecting the radii of close-in transiting exoplanets.* A&A, **540**:A99, 2012.

Erikson, A., Santerne, A., Renner, S., Barge, P. et al.: *Planetary transit candidates in the CoRoT-SRc01 field.* A&A, **539**:A14, 2012.

ESA: *The HIPPARCOS and TYCHO catalogues.* ESA SP-1200, 1997.

ESO: *World's Biggest Eye on the Sky to be Located on Armazones, Chile.* ESO Press Release no. 1018, 2010.

Evans, T. M. and Sackett, P. D.: *An a Priori Investigation of Astrophysical False Positives in Ground-Based Transiting Planet Surveys.* ApJ, **712**:38–51, 2010.

Eyer, L. and Mowlavi, N.: *Variable stars across the observational HR diagram.* In L. Gizon and M. Roth (Eds.), *Proceedings of the Second HELAS International Conference*, *Journal of Physics Conference Series*, vol. 118, pp. 012010(1–21), 2008.

Fabrycky, D. and Tremaine, S.: *Shrinking Binary and Planetary Orbits by Kozai Cycles with Tidal Friction.* ApJ, **669**:1298–1315, 2007.

Flower, P. J.: *Transformations from Theoretical Hertzsprung-Russell Diagrams to Color-Magnitude Diagrams: Effective Temperatures, B-V Colors, and Bolometric Corrections.* ApJ, **469**:355–365, 1996.

Fortney, J. J. and Nettelmann, N.: *The Interior Structure, Composition, and Evolution of Giant Planets.* Space Sci. Rev., **152**:423–447, 2010.

Fortney, J. J., Demory, B.-O., Désert, J.-M., Rowe, J. et al.: *Discovery and Atmospheric Characterization of Giant Planet Kepler-12b: An Inflated Radius Outlier.* ApJS, **197**:9, 2011.

Fressin, F., Guillot, T., Schmider, F. X., Agabi, K. et al.: *A Step: Towards a Successor to CoRoT on Dome C, Antarctica.* In M. Fridlund, A. Baglin, J. Lochard, and L. Conroy (Eds.), *The COROT Mission Pre-Launch Status*, ESA SP-1306, pp. 513–516, 2006.

Fressin, F., Guillot, T., Morello, V., and Pont, F.: *Interpreting and predicting the yield of transit surveys: giant planets in the OGLE fields.* A&A, **475**:729–746, 2007.

Fressin, F., Guillot, T., and Nesta, L.: *Interpreting the yield of transit surveys: are there groups in the known transiting planets population?* A&A, **504**:605–615, 2009.

Fressin, F., Torres, G., Rowe, J., Charbonneau, D. et al.: *Two Earth-sized planets orbiting Kepler-20.* Nature, **482**:195–198, 2012.

Fröhlich, H.-E., Küker, M., Hatzes, A. P., and Strassmeier, K. G.: *On the differential rotation of CoRoT-2a.* A&A, **506**:263–268, 2009.

Fruth, T.: *Perspektiven für die Transitsuche: Vergleich des Standortes Dome C (Antarktis) mit Standorten gemäßigter Breite.* Master's thesis, Freie Universität Berlin, 2008.

Fruth, T., Kirste, S., and Pasternacki, T.: *DLR Photometric Pipeline User's Manual (version 1.0).* DLR, 2011.

Fruth, T., Kabath, P., Cabrera, J., Chini, R. et al.: *Improved Variable Star Search in Large Photometric Data Sets: New Variables in CoRoT Field LRa02 Detected by BEST II.* AJ, **143**:140, 2012.

Gandolfi, D., Alcalá, J. M., Leccia, S., Frasca, A. et al.: *The Star Formation in the L1615/L1616 Cometary Cloud.* ApJ, **687**:1303–1322, 2008.

Gandolfi, D., Hébrard, G., Alonso, R., Deleuil, M. et al.: *Transiting exoplanets from the CoRoT space mission. XIV. CoRoT-11b: a transiting massive "hot-Jupiter" in a prograde orbit around a rapidly rotating F-type star.* A&A, **524**:A55, 2010.

Gardner, J. P., Mather, J. C., Clampin, M., Doyon, R. et al.: *The James Webb Space Telescope.* Space Sci. Rev., **123**:485–606, 2006.

Gaulme, P., Deheuvels, S., Weiss, W. W., Mosser, B. et al.: *HD 46375: seismic and spectropolarimetric analysis of a young Sun hosting a Saturn-like planet.* A&A, **524**:A47, 2010.

Gillingham, P. R.: *Prospects for an Antarctic Observatory.* Proceedings of the Astronomical Society of Australia, **9**:55, 1991.

Gillon, M., Triaud, A. H. M. J., Fortney, J. J., Demory, B.-O. et al.: *The TRAPPIST survey of southern transiting planets. I. Thirty eclipses of the ultra-short period planet WASP-43 b.* A&A, **542**:A4, 2012.

Giménez, A.: *The Apsidal Motion Test in Eclipsing Binaries.* In W. I. Hartkopf, E. F. Guinan, and P. Harmanec (Eds.), *Proceedings of the International Astronomical Union: Binary Stars as Critical Tools & Tests in Contemporary Astrophysics (IAU S240)*, pp. 290–298. Cambridge University Press, 2007.

Giordano, C., Vernin, J., Chadid, M., Aristidi, E., Agabi, A., and Trinquet, H.: *Dome C Site Characterization in 2006 with Single-Star SCIDAR.* PASP, **124**:494–506, 2012.

Giovannelli, F.: *Cataclysmic Variables: A Review.* Chinese Journal of Astronomy and Astrophysics Supplement, **8**:237–258, 2008.

Gould, A., Dong, S., Gaudi, B. S., Udalski, A. et al.: *Frequency of Solar-like Systems and of Ice and Gas Giants Beyond the Snow Line from High-magnification Microlensing Events in 2005-2008.* ApJ, **720**:1073–1089, 2010.

Grec, G., Fossat, E., and Pomerantz, M.: *Solar oscillations - Full disk observations from the geographic South Pole.* Nature, **288**:541–544, 1980.

Guenther, E. W., Gandolfi, D., Sebastian, D., Deleuil, M., Moutou, C., and Cusano, F.: *Multi-object spectroscopy of stars in the CoRoT fields. II. The stellar population of the CoRoT fields IRa01, LRa01, LRa02, and LRa06.* A&A, **543**:A125, 2012.

Guillot, T.: *The Interiors of Giant Planets: Models and Outstanding Questions.* Annual Review of Earth and Planetary Sciences, **33**:493–530, 2005.

Guillot, T. and Showman, A. P.: *Evolution of "51 Pegasus b-like" planets.* A&A, **385**:156–165, 2002.

Haas, M., Chini, R., Ramolla, M., Pozo Nuñez, F. et al.: *Photometric AGN reverberation mapping - an efficient tool for BLR sizes, black hole masses, and host-subtracted AGN luminosities.* A&A, **535**:A73, 2011.

Haghighipour, N., Vogt, S. S., Butler, R. P., Rivera, E. J. et al.: *The Lick-Carnegie Exoplanet Survey: A Saturn-Mass Planet in the Habitable Zone of the Nearby M4V Star HIP 57050.* ApJ, **715**:271–276, 2010.

Hardie, R.: *Photoelectric reductions.* In W. Hiltner (Ed.), *Astronomical Techniques*, pp. 178–208. University of Chicago Press, Chicago, 1962.

Hartman, J. D., Bakos, G., Stanek, K. Z., and Noyes, R. W.: *HATNET Variability Survey in the High Stellar Density "Kepler Field" with Millimagnitude Image Subtraction Photometry.* AJ, **128**:1761–1783, 2004.

Hartman, J. D., Bakos, G. Á., Noyes, R. W., Sipőcz, B. et al.: *A Photometric Variability Survey of Field K and M Dwarf Stars with HATNet.* AJ, **141**:166, 2011a.

Hartman, J. D., Bakos, G. Á., Torres, G., Latham, D. W. et al.: *HAT-P-32b and HAT-P-33b: Two Highly Inflated Hot Jupiters Transiting High-jitter Stars.* ApJ, **742**:59, 2011b.

Hatzes, A. P., Fridlund, M., Nachmani, G., Mazeh, T. et al.: *The Mass of CoRoT-7b.* ApJ, **743**:75, 2011.

Hebb, L., Collier-Cameron, A., Triaud, A. H. M. J., Lister, T. A. et al.: *WASP-19b: The Shortest Period Transiting Exoplanet Yet Discovered.* ApJ, **708**:224–231, 2010.

Hegedüs, T., Giménez, A., and Claret, A.: *Eccentric Eclipsing Binary Systems – the Up-Dated Catalogue.* In A. Claret, A. Giménez, and J.-P. Zahn (Eds.), *Tidal Evolution and Oscillations in Binary Stars*, *Astronomical Society of the Pacific Conference Series*, vol. 333, pp. 88–94, 2005.

Hellier, C., Anderson, D. R., Cameron, A. C., Gillon, M. et al.: *An orbital period of 0.94days for the hot-Jupiter planet WASP-18b.* Nature, **460**:1098–1100, 2009.

Hellier, C., Anderson, D. R., Collier-Cameron, A., Miller, G. R. M. et al.: *On the Orbit of the Short-period Exoplanet WASP-19b.* ApJ, **730**:L31, 2011.

Henry, G. W., Marcy, G. W., Butler, R. P., and Vogt, S. S.: *A Transiting "51 Peg-like" Planet.* ApJ, **529**:L41–L44, 2000.

Heyl, J. S. and Gladman, B. J.: *Using long-term transit timing to detect terrestrial planets.* MNRAS, **377**:1511–1519, 2007.

Hoffleit, D.: *New Variable Stars in MWF 175.* Harvard College Observatory Bulletin, **884**:10–20, 1931.

Holman, M. J. and Murray, N. W.: *The Use of Transit Timing to Detect Terrestrial-Mass Extrasolar Planets.* Science, **307**:1288–1291, 2005.

Howard, A. W., Marcy, G. W., Bryson, S. T., Jenkins, J. M. et al.: *Planet Occurrence within 0.25 AU of Solar-type Stars from Kepler.* ApJS, **201**:15, 2012.

Howarth, I. D.: *On stellar limb darkening and exoplanetary transits.* MNRAS, **418**, 2:1165–1175, 2011.

Huber, K. F., Czesla, S., Wolter, U., and Schmitt, J. H. M. M.: *Planetary eclipse mapping of CoRoT-2a. Evolution, differential rotation, and spot migration.* A&A, **514**:A39, 2010.

Huber, M. E., Everett, M. E., and Howell, S. B.: *Color and Variability Characteristics of Point Sources in the Faint Sky Variability Survey.* AJ, **132**:633–649, 2006.

IAU: *IAU Working Group on Extrasolar Planets – Position statement on the definition of a planet. http://www.dtm.ciw.edu/boss/definition.html*, 2003.

IAU: *Resolution B5 – Definition of a Planet in the Solar System. http://www.iau.org/static/resolutions/Resolution_ GA26-5-6.pdf*, 2006.

Ichikawa, T.: *Future plans for astronomy at Dome Fuji.* Highlights of Astronomy, **15**:632–633, 2010.

Indermuehle, B. T., Burton, M. G., and Maddison, S. T.: *The History of Astrophysics in Antarctica.* PASA, **22**:73–90, 2005.

Johnson, J. A., Butler, R. P., Marcy, G. W., Fischer, D. A. et al.: *A New Planet around an M Dwarf: Revealing a Correlation between Exoplanets and Stellar Mass.* ApJ, **670**:833–840, 2007.

Johnson, J. A., Aller, K. M., Howard, A. W., and Crepp, J. R.: *Giant Planet Occurrence in the Stellar Mass-Metallicity Plane.* PASP, **122**:905–915, 2010.

Johnson, J. A., Winn, J. N., Bakos, G. Á., Hartman, J. D. et al.: *HAT-P-30b: A Transiting Hot Jupiter on a Highly Oblique Orbit.* ApJ, **735**:24, 2011.

Jurcsik, J., Sódor, Á., Szeidl, B., Hurta, Z. et al.: *The Konkoly Blazhko Survey: is light-curve modulation a common property of RRab stars?* MNRAS, **400**:1006–1018, 2009.

Kabath, P.: *Characterization of the stellar variability in CoRoT fields with BEST telescopes.* Ph.D. thesis, Technische Universität Berlin, 2009.

Kabath, P., Eigmüller, P., Erikson, A., Hedelt, P. et al.: *Characterization of COROT Target Fields with BEST: Identification of Periodic Variable Stars in the IR01 Field.* AJ, **134**:1560–1569, 2007.

Kabath, P., Eigmüller, P., Erikson, A., Hedelt, P. et al.: *Characterization of CoRoT Target Fields with the Berlin Exoplanet Search Telescope: Identification of Periodic Variable Stars in the LRa1 Field.* AJ, **136**:654–661, 2008.

Kabath, P., Erikson, A., Rauer, H., Pasternacki, T. et al.: *Periodic variable stars in CoRoT field LRa02 observed with BEST II.* A&A, **506**:569–587, 2009a.

Kabath, P., Fruth, T., Rauer, H., Erikson, A. et al.: *Characterization of CoRoT Target Fields With Berlin Exoplanet Search Telescope. II. Identification of Periodic Variable Stars in the LRc2 Field.* AJ, **137**:3911–3919, 2009b.

Kalas, P.: *Direct imaging of massive extrasolar planets.* In A. Sozzetti, M. G. Lattanzi, and A. P. Boss (Eds.), *Proceedings of the International Astronomical Union: Astrophysics of Planetary Systems – Formation, Structure, and Dynamical Evolution (IAU S276)*, pp. 279–286. Cambridge University Press, 2011.

Kaltenegger, L. and Traub, W. A.: *Transits of Earth-like Planets.* ApJ, **698**:519–527, 2009.

Kane, S. R. and Gelino, D. M.: *On the Inclination Dependence of Exoplanet Phase Signatures.* ApJ, **729**:74, 2011.

Kane, S. R. and von Braun, K.: *Exoplanetary Transit Constraints Based upon Secondary Eclipse Observations.* PASP, **121**:1096–1103, 2009.

Kane, S. R., Schneider, D. P., and Ge, J.: *Simulations for multi-object spectrograph planet surveys.* MNRAS, **377**:1610–1622, 2007.

Kane, S. R., Clarkson, W. I., West, R. G., Wilson, D. M. et al.: *SuperWASP-N extrasolar planet candidates from fields* $06^h < RA < 16^h$. MNRAS, **384**:1097–1108, 2008.

Karoff, C.: *Observational asteroseismology.* Ph.D. thesis, University of Åarhus, 2008.

Karoff, C., Rauer, H., Erikson, A., Voss, H. et al.: *Identification of Variable Stars in COROT's First Main Observing Field (LRc1).* AJ, **134**:766–777, 2007.

Karttunen, H., Kröger, P., Oja, H., Poutanen, M., and Donner, K. J.: *Fundamental Astronomy.* Springer, 5th edn., 2007.

Kennedy, G. M. and Kenyon, S. J.: *Planet Formation around Stars of Various Masses: The Snow Line and the Frequency of Giant Planets.* ApJ, **673**:502–512, 2008.

Kenyon, S. L. and Storey, J. W. V.: *A Review of Optical Sky Brightness and Extinction at Dome C, Antarctica.* PASP, **118**:489–502, 2006.

Kenyon, S. L., Lawrence, J. S., Ashley, M. C. B., Storey, J. W. V., Tokovinin, A., and Fossat, E.: *Atmospheric Scintillation at Dome C, Antarctica: Implications for Photometry and Astrometry.* PASP, **118**:924–932, 2006.

Ketchum, J. A., Adams, F. C., and Bloch, A. M.: *Accretion of Rocky Planets by Hot Jupiters.* ApJ, **741**:L2, 2011.

Kiraga, M.: *ASAS Photometry of ROSAT Sources. I. Periodic Variable Stars Coincident with Bright Sources from the ROSAT All Sky Survey.* Acta Astron., **62**:67–95, 2012.

Knutson, H. A., Charbonneau, D., Noyes, R. W., Brown, T. M., and Gilliland, R. L.: *Using Stellar Limb-Darkening to Refine the Properties of HD 209458b.* ApJ, **655**:564–575, 2007.

Kovács, G., Zucker, S., and Mazeh, T.: *A box-fitting algorithm in the search for periodic transits.* A&A, **391**:369–377, 2002.

Kovács, G., Bakos, G., and Noyes, R. W.: *A trend filtering algorithm for wide-field variability surveys.* MNRAS, **356**:557–567, 2005.

Kruytbosch, W. E.: *Provisional ephemerides of 33 variable stars in the constellations Norma and Ara.* Bull. Astron. Inst. Netherlands, **7**:253, 1935.

Lagrange, A.-M., Desort, M., Galland, F., Udry, S., and Mayor, M.: *Extrasolar planets and brown dwarfs around A-F type stars. VI. High precision RV survey of early type dwarfs with HARPS.* A&A, **495**:335–352, 2009.

Landsman, W. B.: *The IDL Astronomy User's Library.* In R. J. Hanisch, R. J. V. Brissenden, and J. Barnes (Eds.), *Astronomical Data Analysis Software and Systems II*, *Astronomical Society of the Pacific Conference Series*, vol. 52, pp. 246–248, 1993.

Lanza, A. F.: *Searching for star-planet magnetic interaction in CoRoT observations.* Ap&SS, **336**:303–313, 2011.

Lasker, B. M., Lattanzi, M. G., McLean, B. J., Bucciarelli, B. et al.: *The Second-Generation Guide Star Catalog: Description and Properties.* AJ, **136**:735–766, 2008.

Latham, D. W., Rowe, J. F., Quinn, S. N., Batalha, N. M. et al.: *A First Comparison of Kepler Planet Candidates in Single and Multiple Systems.* ApJ, **732**:L24, 2011.

Laughlin, G., Crismani, M., and Adams, F. C.: *On the Anomalous Radii of the Transiting Extrasolar Planets.* ApJ, **729**:L7, 2011.

Lawrence, J. S.: *Infrared and Submillimeter Atmospheric Characteristics of High Antarctic Plateau Sites.* PASP, **116**:482–492, 2004.

Lawrence, J. S., Ashley, M. C. B., Tokovinin, A., and Travouillon, T.: *Exceptional astronomical seeing conditions above Dome C in Antarctica.* Nature, **431**:278–281, 2004.

Lawrence, J. S., Ashley, M. C. B., Storey, J. W. V., Jolissaint, L., and Travouillon, T.: *Adaptive Optics Sky Coverage for Dome C Telescopes.* PASP, **120**:1119–1127, 2008.

Léger, A., Rouan, D., Schneider, J., Barge, P. et al.: *Transiting exoplanets from the CoRoT space mission. VIII. CoRoT-7b: the first super-Earth with measured radius.* A&A, **506**:287–302, 2009.

Li, L., Zhang, F., Han, Z., Jiang, D., and Jiang, T.: *The evolutionary status of W Ursae Majoris-type systems.* MNRAS, **387**:97–104, 2008.

Lindegren, L.: *Gaia: Astrometric performance and current status of the project.* In S. A. Klioner and M. H. Seidelmann, P. K. Soffel (Eds.), *Proceedings of the International Astronomical Union: Relativity in Fundamental Astronomy Dynamics, Reference Frames, and Data Analysis (IAU S261)*, pp. 296–305. Cambridge University Press, 2010.

Lodders, K.: *Exoplanet Chemistry.* In R. Barnes (Ed.), *Formation and Evolution of Exoplanets*, pp. 157–186. Wiley-VCH Verlag GmbH & Co. KGaA, 2010.

Lovis, C. and Mayor, M.: *Planets around evolved intermediate-mass stars. I. Two substellar companions in the open clusters NGC 2423 and NGC 4349.* A&A, **472**:657–664, 2007.

Lovis, C., Mayor, M., Pepe, F., Queloz, D., and Udry, S.: *Pushing Down the Limits of the Radial Velocity Technique.* In N. C. Santos, L. Pasquini, A. C. M. Correia, and M. Romaniello (Eds.), *Precision Spectroscopy in Astrophysics*, ESO Astrophysics Symposia, pp. 181–184. Springer, 2008.

Lovis, C., Ségransan, D., Mayor, M., Udry, S. et al.: *The HARPS search for southern extra-solar planets. XXVIII. Up to seven planets orbiting HD 10180: probing the architecture of low-mass planetary systems.* A&A, **528**:A112, 2011.

Luyten, W. J.: *Neue Veränderliche am Südhimmel.* Astronomische Nachrichten, **258**, 8:121–126, 1936.

Maciejewski, G., Dimitrov, D., Neuhäuser, R., Tetzlaff, N. et al.: *Transit timing variation and activity in the WASP-10 planetary system.* MNRAS, **411**:1204–1212, 2011.

Madore, B. F.: *The period-luminosity relation. IV - Intrinsic relations and reddenings for the Large Magellanic Cloud Cepheids.* ApJ, **253**:575–579, 1982.

Majaess, D. J., Turner, D. G., and Lane, D. J.: *Characteristics of the Galaxy according to Cepheids.* MNRAS, **398**:263–270, 2009.

Malkov, O. Y., Oblak, E., Snegireva, E. A., and Torra, J.: *A catalogue of eclipsing variables.* A&A, **446**:785–789, 2006.

Mandel, K. and Agol, E.: *Analytic Light Curves for Planetary Transit Searches.* ApJ, **580**:L171–L175, 2002.

Marks, R. D., Vernin, J., Azouit, M., Manigault, J. F., and Clevelin, C.: *Measurement of optical seeing on the high antarctic plateau.* A&AS, **134**:161–172, 1999.

Martioli, E., McArthur, B. E., Benedict, G. F., Bean, J. L., Harrison, T. E., and Armstrong, A.: *The Mass of the Candidate Exoplanet Companion to HD 136118 from Hubble Space Telescope Astrometry and High-Precision Radial Velocities.* ApJ, **708**:625–634, 2010.

Mayor, M. and Queloz, D.: *A Jupiter-mass companion to a solar-type star.* Nature, **378**:355–359, 1995.

Mayor, M., Pepe, F., Queloz, D., Bouchy, F. et al.: *Setting New Standards with HARPS.* The Messenger, **114**:20–24, 2003.

Mazeh, T. and Faigler, S.: *Detection of the ellipsoidal and the relativistic beaming effects in the CoRoT-3 lightcurve.* A&A, **521**:L59, 2010.

McCullough, P. R., Stys, J. E., Valenti, J. A., Fleming, S. W., Janes, K. A., and Heasley, J. N.: *The XO Project: Searching for Transiting Extrasolar Planet Candidates.* PASP, **117**:783–795, 2005.

Meeus, J.: *Astronomical Algorithms.* Willmann-Bell, Richmond, 2nd edn., 1998.

Meinunger, I.: *Bearbeitung von 101 Veränderlichen am Südhimmel (Feld eta Arae, Teil I).* Zentralinstitut für Astrophysik Sternwarte Sonneberg, Mitteilungen über Veränderliche Sterne, **5**:156–158, 1970.

Meinunger, I.: *Veränderliche Sterne am Südhimmel. Teil VII.* Veröffentlichungen der Sternwarte Sonneberg, **9**:107–123, 1979.

Michel, E., Baglin, A., Auvergne, M., Catala, C. et al.: *CoRoT Measures Solar-Like Oscillations and Granulation in Stars Hotter Than the Sun.* Science, **322**:558–560, 2008.

Mochejska, B. J., Stanek, K. Z., Sasselov, D. D., Szentgyorgyi, A. H. et al.: *Planets in Stellar Clusters Extensive Search. IV. A Detection of a Possible Transiting Planet Candidate in the Open Cluster NGC 2158.* AJ, **131**:1090–1105, 2006.

Monet, D. G.: *The 526,280,881 Objects in the USNO-A2.0 Catalog.* Bulletin of the American Astronomical Society, **30**:1427, 1998.

Monet, D. G., Levine, S. E., Canzian, B., Ables, H. D. et al.: *The USNO-B Catalog.* AJ, **125**:984–993, 2003.

Moore, A., Allen, G., Aristidi, E., Ashley, M. et al.: *Gattini: a multisite campaign for the measurement of sky brightness in Antarctica.* In L. M. Stepp and R. Gilmozzi (Eds.), *Ground-based and Airborne Telescopes II*, Proc. SPIE 7012, pp. 701226(1–10), 2008.

Mordasini, C., Alibert, Y., and Benz, W.: *Extrasolar planet population synthesis. I. Method, formation tracks, and mass-distance distribution.* A&A, **501**:1139–1160, 2009a.

Mordasini, C., Alibert, Y., Benz, W., and Naef, D.: *Extrasolar planet population synthesis. II. Statistical comparison with observations.* A&A, **501**:1161–1184, 2009b.

Mordasini, C., Alibert, Y., Benz, W., Klahr, H., and Henning, T.: *Extrasolar planet population synthesis IV. Correlations with disk metallicity, mass, and lifetime.* A&A, **541**:A97, 2012.

Morton, T. D. and Johnson, J. A.: *Discerning Exoplanet Migration Models Using Spin-Orbit Measurements.* ApJ, **729**:138, 2011.

Mosser, B. and Aristidi, E.: *Duty Cycle of Doppler Ground-based Asteroseismic Observations.* PASP, **119**:127–133, 2007.

Mosser, B., Buey, T., Catala, C., Appourchaux, T. et al.: *SIAMOIS: asteroseismology in Antarctica.* Communications in Asteroseismology, **158**:337, 2009.

Moutou, C., Pont, F., Barge, P., Aigrain, S. et al.: *Comparative blind test of five planetary transit detection algorithms on realistic synthetic light curves.* A&A, **437**:355–368, 2005.

Moutou, C., Aigrain, S., Almenara, J., Alonso, R. et al.: *Expected Performance of the CoRoT Planet Search from Light Curve Beauty Contests.* In C. Afonso, D. Weldrake, and T. Henning (Eds.), *Transiting Extrapolar Planets Workshop*, *Astronomical Society of the Pacific Conference Series*, vol. 366, pp. 127–132, 2007.

Moutou, C., Pont, F., Bouchy, F., Deleuil, M. et al.: *Planetary transit candidates in the CoRoT initial run: resolving their nature.* A&A, **506**:321–336, 2009.

Muirhead, P. S., Johnson, J. A., Apps, K., Carter, J. A. et al.: *Characterizing the Cool KOIs. III. KOI 961: A Small Star with Large Proper Motion and Three Small Planets.* ApJ, **747**:144, 2012.

Nagasawa, M., Ida, S., and Bessho, T.: *Formation of Hot Planets by a Combination of Planet Scattering, Tidal Circularization, and the Kozai Mechanism.* ApJ, **678**:498–508, 2008.

Nascimbeni, V., Bedin, L. R., Piotto, G., De Marchi, F., and Rich, R. M.: *An HST search for planets in the lower main sequence of the globular cluster NGC 6397.* A&A, **541**:A144, 2012.

Newberry, M. V.: *Signal-to-noise considerations for sky-subtracted CCD data.* PASP, **103**:122–130, 1991.

Nguyen, H. T., Rauscher, B. J., Severson, S. A., Hereld, M. et al.: *The South Pole Near Infrared Sky Brightness.* PASP, **108**:718–720, 1996.

Norton, A. J. and the SuperWASP Consortium: *Time-Domain Astrophysics with SuperWASP.* In E. Griffin, R. Hanisch, and R. Seaman (Eds.), *Proceedings of the International Astronomical Union: New Horizons in Time-Domain Astronomy (IAU S285)*, pp. 382–384. Cambridge University Press, 2011.

O'Donovan, F. T., Charbonneau, D., Torres, G., Mandushev, G. et al.: *Rejecting Astrophysical False Positives from the TrES Transiting Planet Survey: The Example of GSC 03885-00829.* ApJ, **644**:1237–1245, 2006.

Omiya, M., Izumiura, H., Han, I., Lee, B.-C. et al.: *A Massive Substellar Companion to the Massive Giant HD 119445.* PASJ, **61**:825–831, 2009.

Orosz, J. A., Welsh, W. F., Carter, J. A., Fabrycky, D. C. et al.: *Kepler-47: A transiting circumbinary multiplanet system.* Science, **337**:1511–1514, 2012.

Owen, T.: *The Search for Early Forms of Life in Other Planetary Systems - Future Possibilities Afforded by Spectroscopic Techniques.* In M. D. Papagiannis (Ed.), *Strategies for the Search for Life in the Universe*, *Astrophysics and Space Science Library*, vol. 83, pp. 177–185. Reidel, Dordrecht, 1980.

Pál, A. and Bakos, G. Á.: *Astrometry in Wide-Field Surveys.* PASP, **118**:1474–1483, 2006.

Pallé, E., Zapatero Osorio, M. R., Barrena, R., Montañés-Rodríguez, P., and Martín, E. L.: *Earth's transmission spectrum from lunar eclipse observations.* Nature, **459**:814–816, 2009.

Papaloizou, J. C. B. and Terquem, C.: *Planet formation and migration.* Reports on Progress in Physics, **69**:119–180, 2006.

Pasternacki, T.: *Optimierte photometrische Datenauswertung zur Suche variabler Sterne und Planetentransits in BEST-Daten.* Master's thesis, Freie Universität Berlin, 2009.

Pasternacki, T., Csizmadia, S., Cabrera, J., Eigmüller, P. et al.: *A Variable Star Census in a Perseus Field.* AJ, **142**:114, 2011.

Patat, F., Ugolnikov, O. S., and Postylyakov, O. V.: *UBVRI twilight sky brightness at ESO-Paranal.* A&A, **455**:385–393, 2006.

Pepe, F., Lovis, C., Ségransan, D., Benz, W. et al.: *The HARPS search for Earth-like planets in the habitable zone. I. Very low-mass planets around HD 20794, HD 85512, and HD 192310.* A&A, **534**:A58, 2011.

Pepe, F. A. and Lovis, C.: *From HARPS to CODEX: exploring the limits of Doppler measurements.* Physica Scripta Volume T, **130**, 1:014007, 2008.

Pepper, J. and Burke, C. J.: *Survey for Transiting Extrasolar Planets in Stellar Systems. IV. Variables in the Field of NGC 1245.* AJ, **132**:1177–1188, 2006.

Perryman, M. A. C.: *The Exoplanet Handbook.* Cambridge University Press, 2011.

Perryman, M. A. C., de Boer, K. S., Gilmore, G., Høg, E. et al.: *GAIA: Composition, formation and evolution of the Galaxy.* A&A, **369**:339–363, 2001.

Petersen, J. O. and Andreasen, G. K.: *Studies of Cepheid-type variability. V. The Fourier phases of type II Cepheids with periods of 1–3 days.* A&A, **176**:183–187, 1987.

Phillips, A., Burton, M. G., Ashley, M. C. B., Storey, J. W. V. et al.: *The Near-Infrared Sky Emission at the South Pole in Winter.* ApJ, **527**:1009–1022, 1999.

Pilello, A.: *Photometric data reduction and variability characterisation of BEST target field F8.* Master's thesis, Università degli Studi di Padova, 2010.

Pojmanski, G.: *The All Sky Automated Survey. Catalog of about 3800 Variable Stars.* Acta Astron., **50**:177–190, 2000.

Pojmanski, G.: *The All Sky Automated Survey. Catalog of Variable Stars. I. 0^h–6^h Quarter of the Southern Hemisphere.* Acta Astron., **52**:397–427, 2002.

Pollacco, D. L., Skillen, I., Collier Cameron, A., Christian, D. J. et al.: *The WASP Project and the SuperWASP Cameras.* PASP, **118**:1407–1418, 2006.

Pont, F. and Bouchy, F.: *Exoplanet Transit Search at Dome C.* In M. Giard, F. Casoli, and F. Paletou (Eds.), *Dome C Astronomy and Astrophysics Meeting, EAS Publications Series*, vol. 14, pp. 155–160, 2005.

Pont, F., Bouchy, F., Melo, C., Santos, N. C. et al.: *Doppler follow-up of OGLE planetary transit candidates in Carina.* A&A, **438**:1123–1140, 2005.

Pont, F., Zucker, S., and Queloz, D.: *The effect of red noise on planetary transit detection.* MNRAS, **373**:231–242, 2006.

Poppenhäger, K., Robrade, J., Schmitt, J. H. M. M., and Hall, J. C.: *51 Pegasi – a planet-bearing Maunder minimum candidate.* A&A, **508**:1417–1421, 2009.

Poretti, E., Michel, E., Garrido, R., Lefèvre, L. et al.: *HD 50844: a new look at δ Scuti stars from CoRoT space photometry.* A&A, **506**:85–93, 2009.

Poretti, E., Mantegazza, L., Niemczura, E., Rainer, M. et al.: *Pulsational content and abundance analysis of some δ Scuti stars observed by CoRoT.* Astronomische Nachrichten, **331**:1049–1052, 2010.

Queloz, D., Bouchy, F., Moutou, C., Hatzes, A. et al.: *The CoRoT-7 planetary system: two orbiting super-Earths.* A&A, **506**:303–319, 2009.

Rafikov, R. R.: *Constraint on the Giant Planet Production by Core Accretion.* ApJ, **727**:86, 2011.

Rauer, H. and Deeg, H.: *Time Series Observations at Dome C.* In L. Spinoglio and N. Epchtein (Eds.), *3rd ARENA Conference: An Astronomical Observatory at Concordia (Dome C, Antarctica)*, *EAS Publications Series*, vol. 40, pp. 349–360, 2010.

Rauer, H. and Erikson, A.: *The Transit Method.* In Dvorak, R. (Ed.), *Extrasolar Planets: Formation, Detection and Dynamics*, pp. 207–240. Wiley-VCH Verlag GmbH & Co. KGaA, Weinheim, Germany, 2007.

Rauer, H., Eislöffel, J., Erikson, A., Guenther, E. et al.: *The Berlin Exoplanet Search Telescope System.* PASP, **116**:38–45, 2004.

Rauer, H., Fruth, T., and Erikson, A.: *Exo-planet Search from Dome C and Space – A Comparative Study.* In H. Zinnecker, N. Epchtein, and H. Rauer (Eds.), *2nd ARENA Conference: The Astrophysical Science Cases at Dome C*, *EAS Publications Series*, vol. 33, pp. 41–47, 2008a.

Rauer, H., Fruth, T., and Erikson, A.: *Prospects of Long-Time-Series Observations from Dome C for Transit Search.* PASP, **120**:852–859, 2008b.

Rauer, H., Queloz, D., Csizmadia, S., Deleuil, M. et al.: *Transiting exoplanets from the CoRoT space mission. VII. The "hot-Jupiter"-type planet CoRoT-5b.* A&A, **506**:281–286, 2009.

Rauer, H., Erikson, A., Kabath, P., Hedelt, P. et al.: *Pre-Discovery Observations of CoRoT-1b and CoRoT-2b with the BEST Survey.* AJ, **139**:53–58, 2010.

Rauer, H., Gebauer, S., Paris, P. V., Cabrera, J. et al.: *Potential biosignatures in super-Earth atmospheres. I. Spectral appearance of super-Earths around M dwarfs.* A&A, **529**:A8, 2011.

Raymond, S. N., Armitage, P. J., and Gorelick, N.: *Planet-Planet Scattering in Planetesimal Disks. II. Predictions for Outer Extrasolar Planetary Systems.* ApJ, **711**:772–795, 2010.

Reylé, C., Robin, A. C., Schultheis, M., and Marshall, D. J.: *The Besançon Galaxy model: comparisons to photometric surveys and modelling of the Galactic bulge and disc.* In S. Boissier, M. Heydari-Malayeri, R. Samadi, and D. Valls-Gabaud (Eds.), *SF2A-2010: Proceedings of the Annual meeting of the French Society of Astronomy and Astrophysics*, pp. 51–54, 2010.

Ribas, I.: *Binaries as Astrophysical Laboratories: Open Questions.* In C. Aerts and C. Sterken (Eds.), *Astrophysics of Variable Stars*, *Astronomical Society of the Pacific Conference Series*, vol. 349, pp. 55–70, 2006.

Robin, A. C., Reylé, C., Derrière, S., and Picaud, S.: *A synthetic view on structure and evolution of the Milky Way.* A&A, **409**:523–540, 2003.

Rogers, L. A. and Seager, S.: *Three Possible Origins for the Gas Layer on GJ 1214b.* ApJ, **716**:1208–1216, 2010.

Rosenblatt, F.: *A Two-Color Photometric Method for Detection of Extra solar Planetary Systems.* Icarus, **14**:71, 1971.

Sahu, K. C., Casertano, S., Bond, H. E., Valenti, J. et al.: *Transiting extrasolar planetary candidates in the Galactic bulge.* Nature, **443**:534–540, 2006.

Samus, N. N., Durlevich, O. V., Kazarovets, E. V., Kireeva, N. N., Pastukhova, E. N., and Zharova, A. V.: *General Catalogue of Variable Stars (Samus+ 2007–2012).* VizieR Online Data Catalog, B/GCVS, 2009.

Sasselov, D. D.: *Astronomy: Extrasolar planets.* Nature, **451**:29–31, 2008.

Sato, B., Fischer, D. A., Henry, G. W., Laughlin, G. et al.: *The N2K Consortium. II. A Transiting Hot Saturn around HD 149026 with a Large Dense Core.* ApJ, **633**:465–473, 2005.

Saunders, W., Lawrence, J. S., Storey, J. W. V., Ashley, M. C. B. et al.: *Where Is the Best Site on Earth? Domes A, B, C, and F, and Ridges A and B.* PASP, **121**:976–992, 2009.

Schneider, J., Dedieu, C., Le Sidaner, P., Savalle, R., and Zolotukhin, I.: *Defining and cataloging exoplanets: the exoplanet.eu database.* A&A, **532**:A79, 2011.

Schulze, M.: *Photometrische Datenauswertung zur Suche nach variablen Sternen und Transits extrasolarer Planeten im BEST-Datensatz F15.* Master's thesis, Technische Universität Berlin, 2010.

Schwarzenberg-Czerny, A.: *Fast and Statistically Optimal Period Search in Uneven Sampled Observations.* ApJ, **460**:L107–L110, 1996.

Schwarzenberg-Czerny, A.: *Optimum Period Search: Quantitative Analysis.* ApJ, **516**:315–323, 1999.

Schwarzenberg-Czerny, A. and Kaluzny, J.: *Metallicity of clusters from RRab pulsators: results of an automatic analysis.* MNRAS, **300**:251–256, 1998.

Seager, S. and Mallén-Ornelas, G.: *A Unique Solution of Planet and Star Parameters from an Extrasolar Planet Transit Light Curve.* ApJ, **585**:1038–1055, 2003.

Selsis, F., Kasting, J. F., Levrard, B., Paillet, J., Ribas, I., and Delfosse, X.: *Habitable planets around the star Gliese 581?* A&A, **476**:1373–1387, 2007.

Silva-Valio, A., Lanza, A. F., Alonso, R., and Barge, P.: *Properties of starspots on CoRoT-2.* A&A, **510**:A25, 2010.

Sims, G., Ashley, M. C. B., Cui, X., Everett, J. R. et al.: *Airglow and Aurorae at Dome A, Antarctica.* PASP, **124**:637–649, 2012a.

Sims, G., Ashley, M. C. B., Cui, X., Everett, J. R. et al.: *Precipitable Water Vapor above Dome A, Antarctica, Determined from Diffuse Optical Sky Spectra.* PASP, **124**:74–83, 2012b.

Skrutskie, M. F., Cutri, R. M., Stiening, R., Weinberg, M. D. et al.: *The Two Micron All Sky Survey (2MASS).* AJ, **131**:1163–1183, 2006.

Smith, A. M. S., Collier Cameron, A., Christian, D. J., Clarkson, W. I. et al.: *The impact of correlated noise on SuperWASP detection rates for transiting extrasolar planets.* MNRAS, **373**:1151–1158, 2006.

Smith, C. H. and Harper, D. A.: *Mid-Infrared Sky Brightness Site Testing at the South Pole.* PASP, **110**:747–753, 1998.

Smith, G. A., Saunders, W., Bridges, T., Churilov, V. et al.: *AAOmega: a multipurpose fiber-fed spectrograph for the AAT.* In A. F. M. Moorwood and M. Iye (Eds.), *Ground-based Instrumentation for Astronomy*, Proc. SPIE 5492, pp. 410–420, 2004.

Snellen, I. A. G., de Mooij, E. J. W., and Albrecht, S.: *The changing phases of extrasolar planet CoRoT-1b.* Nature, **459**:543–545, 2009.

Soszyński, I., Poleski, R., Udalski, A., Szymański, M. K. et al.: *The Optical Gravitational Lensing Experiment. The OGLE-III Catalog of Variable Stars. I. Classical Cepheids in the Large Magellanic Cloud.* Acta Astron., **58**:163–185, 2008.

Soszyński, I., Udalski, A., Pietrukowicz, P., Szymański, M. K. et al.: *The Optical Gravitational Lensing Experiment. The OGLE-III Catalog of Variable Stars. XIV. Classical and Type II Cepheids in the Galactic Bulge.* Acta Astron., **61**:285–301, 2011.

Southworth, J., Hinse, T. C., Dominik, M., Glitrup, M. et al.: *Physical Properties of the 0.94-Day Period Transiting Planetary System WASP-18.* ApJ, **707**:167–172, 2009.

Spiegel, D. S. and Turner, E. L.: *Bayesian analysis of the astrobiological implications of life's early emergence on Earth.* PNAS, **109**:395–400, 2011.

Spiegel, D. S., Burrows, A., and Milsom, J. A.: *The Deuterium-burning Mass Limit for Brown Dwarfs and Giant Planets.* ApJ, **727**:57, 2011.

Sterken, C. and Jaschek, C.: *Light Curves of Variable Stars, A Pictorial Atlas.* Cambridge University Press, 1996.

Stetson, P. B.: *On the Automatic Determination of Light-Curve Parameters for Cepheid Variables.* PASP, **108**:851–876, 1996.

Stilz, M.: *Transit Timing Variation with BEST II.* Bachelor's thesis, Freie Universität Berlin, 2012.

Storey, J. W.: *Antarctica: the potential for interferometry.* In W. A. Traub (Ed.), *New Frontiers in Stellar Interferometry*, Proc. SPIE 5491, pp. 169–175, 2004.

Struve, O.: *Proposal for a project of high-precision stellar radial velocity work.* The Observatory, **72**:199–200, 1952.

Sumi, T., Kamiya, K., Bennett, D. P., Bond, I. A. et al.: *Unbound or distant planetary mass population detected by gravitational microlensing.* Nature, **473**:349–352, 2011.

Surace, C., Alonso, R., Barge, P., Cautain, R. et al.: *The oversampling mode for CoRoT exo-field observations.* In A. Bridger and N. M. Radziwill (Eds.), *Advanced Software and Control for Astronomy II*, Proc. SPIE 7019, pp. 70193B(1–8), 2008.

Swain, M. R. and Gallée, H.: *Antarctic Boundary Layer Seeing.* PASP, **118**:1190–1197, 2006.

Swain, M. R., Vasisht, G., Henning, T., Tinetti, G., and Beaulieu, J.: *THESIS: the terrestrial habitable-zone exoplanet spectroscopy infrared spacecraft.* In J. M. Oschmann Jr., M. C. Clampin, and H. A. MacEwen (Eds.), *Space Telescopes and Instrumentation 2010: Optical, Infrared, and Millimeter Wave*, Proc. SPIE 7731, pp. 773125(1–7), 2010.

Tamuz, O., Mazeh, T., and Zucker, S.: *Correcting systematic effects in a large set of photometric light curves.* MNRAS, **356**:1466–1470, 2005.

Tinetti, G., Beaulieu, J. P., Henning, T., Meyer, M. et al.: *EChO – Exoplanet Characterisation Observatory.* Experimental Astronomy, **34**:311–353, 2012.

Tingley, B.: *A rigorous comparison of different planet detection algorithms.* A&A, **403**:329–337, 2003a.

Tingley, B.: *Improvements to existing transit detection algorithms and their comparison.* A&A, **408**:L5–L7, 2003b.

Tingley, B.: *Using color photometry to separate transiting exoplanets from false positives.* A&A, **425**:1125–1131, 2004.

Tingley, B., Bonomo, A. S., and Deeg, H. J.: *Using Stellar Densities to Evaluate Transiting Exoplanetary Candidates.* ApJ, **726**:112, 2011.

Tirard, S., Morange, M., and Lazcano, A.: *The Definition of Life: A Brief History of an Elusive Scientific Endeavor.* Astrobiology, **10**:1003–1009, 2010.

Titz-Weider, R.: *Auf der Suche nach Planeten um andere Sonnen: Astrophysik.* Physik in unserer Zeit, **37**:286–294, 2006.

Tonry, J. L., Howell, S. B., Everett, M. E., Rodney, S. A., Willman, M., and VanOutryve, C.: *A Search for Variable Stars and Planetary Occultations in NGC 2301. I. Techniques.* PASP, **117**:281–289, 2005.

Torres, G.: *On the Use of Empirical Bolometric Corrections for Stars.* AJ, **140**:1158–1162, 2010.

Town, M. S., Walden, V. P., and Warren, S. G.: *Cloud Cover over the South Pole from Visual Observations, Satellite Retrievals, and Surface-Based Infrared Radiation Measurements.* Journal of Climate, **20**:544–559, 2007.

Travouillon, T., Ashley, M. C. B., Burton, M. G., Storey, J. W. V., and Loewenstein, R. F.: *Atmospheric turbulence at the South Pole and its implications for astronomy.* A&A, **400**:1163–1172, 2003.

Triaud, A. H. M. J., Collier Cameron, A., Queloz, D., Anderson, D. R. et al.: *Spin-orbit angle measurements for six southern transiting planets. New insights into the dynamical origins of hot Jupiters.* A&A, **524**:A25, 2010.

Udalski, A.: *The Optical Gravitational Lensing Experiment. Real Time Data Analysis Systems in the OGLE-III Survey.* Acta Astron., **53**:291–305, 2003.

Udalski, A., Paczynski, B., Zebrun, K., Szymanski, M. et al.: *The Optical Gravitational Lensing Experiment. Search for Planetary and Low-Luminosity Object Transits in the Galactic Disk. Results of 2001 Campaign.* Acta Astron., **52**:1–37, 2002a.

Udalski, A., Zebrun, K., Szymanski, M., Kubiak, M. et al.: *The Optical Gravitational Lensing Experiment. Search for Planetary and Low- Luminosity Object Transits in the Galactic Disk. Results of 2001 Campaign – Supplement.* Acta Astron., **52**:115–128, 2002b.

Udalski, A., Szymanski, M. K., Kubiak, M., Pietrzynski, G. et al.: *The Optical Gravitational Lensing Experiment. Planetary and Low-Luminosity Object Transits in the Fields of Galactic Disk. Results of the 2003 OGLE Observing Campaigns.* Acta Astron., **54**:313–345, 2004.

von Braun, K., Kane, S. R., and Ciardi, D. R.: *Observational Window Functions in Planet Transit Surveys.* ApJ, **702**:779–790, 2009.

Voss, H.: *Developing a ground-based search system for transits of extrasolar planets.* Ph.D. thesis, Technische Universität Berlin, 2006.

Walkowicz, L. M., Becker, A. C., Anderson, S. F., Blook, J. S. et al.: *The Impact of the Astro2010 Recommendations on Variable Star Science.* ArXiv Astrophysics e-prints, **0902.3981**, 2009.

Wambsganss, J.: *Astronomy: Bound and unbound planets abound.* Nature, **473**:289–291, 2011.

Wang, L., Macri, L. M., Krisciunas, K., Wang, L. et al.: *Photometry of Variable Stars from Dome A, Antarctica.* AJ, **142**:155, 2011.

Watson, C. L., Henden, A. A., and Price, A.: *The International Variable Star Index (VSX).* In B. D. Warner, J. Foote, D. A. Kenyon, and D. Mais (Eds.), *Symposium on Telescope Science*, Proceedings for the 25th Annual Conference, pp. 47–56. Society for Astronomical Sciences, 2006.

Welsh, W. F., Orosz, J. A., Seager, S., Fortney, J. J. et al.: *The Discovery of Ellipsoidal Variations in the Kepler Light Curve of HAT-P-7.* ApJ, **713**:L145–L149, 2010.

West, A. A., Hawley, S. L., Bochanski, J. J., Covey, K. R. et al.: *Constraining the Age-Activity Relation for Cool Stars: The Sloan Digital Sky Survey Data Release 5 Low-Mass Star Spectroscopic Sample.* AJ, **135**:785–795, 2008.

Wiese, T.: *Analyse stellarer Lichtkurven zur Suche nach Transits extrasolarer Planeten.* Master's thesis, Freie Universität Berlin, 2007.

Winn, J. N. and Holman, M. J.: *Obliquity Tides on Hot Jupiters.* ApJ, **628**:L159–L162, 2005.

Wolszczan, A. and Frail, D. A.: *A planetary system around the millisecond pulsar PSR1257+12.* Nature, **355**:145–147, 1992.

Wolter, U., Schmitt, J. H. M. M., Huber, K. F., Czesla, S. et al.: *Transit mapping of a starspot on CoRoT-2. Probing a stellar surface with planetary transits.* A&A, **504**:561–564, 2009.

Worthey, G. and Lee, H.-c.: *An Empirical UBV RI JHK Color-Temperature Calibration for Stars.* ApJS, **193**:1, 2011.

Yang, H., Allen, G., Ashley, M. C. B., Bonner, C. S. et al.: *The PLATO Dome A Site-Testing Observatory: Instrumentation and First Results.* PASP, **121**:174–184, 2009.

Yang, H., Kulesa, C. A., Walker, C. K., Tothill, N. F. H. et al.: *Exceptional Terahertz Transparency and Stability above Dome A, Antarctica.* PASP, **122**:490–494, 2010.

Zacharias, N., Monet, D. G., Levine, S. E., Urban, S. E., Gaume, R., and Wycoff, G. L.: *The Naval Observatory Merged Astrometric Dataset (NOMAD).* In *AAS 205th Meeting: Visible-Light Telescopes, Instruments, and Technology (Session 48)*, *Bulletin of the American Astronomical Society*, vol. 36, p. 1418, 2004.

Zacharias, N., Finch, C., Girard, T., Hambly, N. et al.: *The Third US Naval Observatory CCD Astrograph Catalog (UCAC3).* AJ, **139**:2184–2199, 2010.

Zebrun, K., Soszynski, I., Wozniak, P. R., Udalski, A. et al.: *The Optical Gravitational Lensing Experiment. Difference Image Analysis of LMC and SMC Data. The Catalog.* Acta Astron., **51**:317–329, 2001.

Zhang, X., Deng, L., Xin, Y., and Zhou, X.: *Searching for Variable Stars in the Field of NGC 7789.* Chinese J. Astron. Astrophys., **3**:151–165, 2003.

Zhou, X., Fan, Z., Jiang, Z., Ashley, M. C. B. et al.: *The First Release of the CSTAR Point Source Catalog from Dome A, Antarctica.* PASP, **122**:347–353, 2010.